NETL

Final Report

11122-20.FINAL

Advanced Hydraulic Fracturing Project

11122-20

August 26, 2016

Jordan Ciezobka

R&D Manager, Shale Gas E&P Research

Gas Technology Institute

1700 S. Mount Prospect Road

Des Plaines, IL 60018

LEGAL NOTICE

This information was prepared by Gas Technology Institute ("GTI") for The Research Partnership to Secure Energy for America (RPSEA) and National Energy Technology Laboratory (NETL).

Neither GTI, the members of GTI, the Sponsor(s), nor any person acting on behalf of any of them:

a. Makes any warranty or representation, express or implied with respect to the accuracy, completeness, or usefulness of the information contained in this report, or that the use of any information, apparatus, method, or process disclosed in this report may not infringe privately-owned rights. Inasmuch as this project is experimental in nature, the technical information, results, or conclusions cannot be predicted. Conclusions and analysis of results by GTI represent GTI's opinion based on inferences from measurements and empirical relationships, which inferences and assumptions are not infallible, and with respect to which competent specialists may differ.
b. Assumes any liability with respect to the use of, or for any and all damages resulting from the use of, any information, apparatus, method, or process disclosed in this report; any other use of, or reliance on, this report by any third party is at the third party's sole risk.

Abstract

Hydraulic fracturing is a prerequisite for establishing commercial production from shale and tight sands reservoirs; however, some real and perceived environmental impacts of hydraulic fracturing have become serious public concerns to a level where clear and deterministic understanding of fracturing process for preemptive elimination of these concerns is no longer an option but an imperative. Evolution of hydraulic fracturing technology has been through many years of trial and error with success measured almost solely by short term production enhancements. This approach has led to pumping larger and larger volumes of fracturing fluid leading to undue taxing of fresh water supply and the possibility of excessive fracture dimensions. As hydraulic fracturing has grown to treat many stages in long horizontal wells, the mere large volume of transported water has caused concerns relative to heavy truck traffic, air pollution, and surface disturbances compounding the environmental issues.

Gas Technology Institute (GTI), with funding from Research Partnership to Secure Energy for America (RPSEA), has completed an industry cooperative research project that aims to optimize fracture completion design so as to improve productivity from unconventional shale gas wells and reduce the environmental footprint by reducing the input requirements per MCF of produced gas. A team of experts from 2 universities, one national lab, one research entity and one natural gas producer along with oil & gas service companies have collaborated for this project in the Marcellus Shale play. The goal was to evaluate the completion and stimulation of target wells and identify ways at improving productivity using variable rate fracturing technique. Dedicated research was focused in the areas of reservoir engineering, completion design including fracture spacing design, fracture diagnostics using treatment data, microseismic monitoring, advanced microseismic processing workflows for improved fracture diagnostics and lab scale experiments to monitor passive seismicity during hydraulic fracturing for better understanding of the process.

Some of the key results from these studies are as follows:

- Combined analysis of microseismic monitoring, well completion and logging data (including production logging) have validated the applicability of variable rate fracturing as a method for improved productivity from shale gas wells. In particular, opening of additional perforations and consequent productivity enhancement has been confirmed.
- Hydraulic fracturing operations can be modified to improve hydraulic fracturing efficiency; i.e., minimize the use of fracturing fluid and associated resources per unit of produced gas. Our tests in the Marcellus have demonstrated a potential for ~40% increase in productivity on one of the test wells.

- Fracture spacing can be optimally designed without resorting to the use of expensive specialty logging tools. The project team has successfully demonstrated the use of Artificial Intelligence based predictive modeling approach to optimize stage/ cluster placement during completion.
- Analyzing the attenuation characteristics of pressure pulse post pump shut-in can help understand completion quality by modeling for fracture properties and negate the need for expensive post completion production logging runs.
- Modified microseismic data processing techniques such as use of self-adapting beamforming filters, head wave arrivals for inversion, spectral analysis or semblance have been shown to provide significant improvements in analysis. These have helped derive more value over and above the typical microseismic catalogs that are generated by service companies involved.
- A semi-analytical solution for Bi-Modal production decline analysis has been implemented to better understand hydraulic fracturing performance.
- Laboratory experiments simulating hydraulic fracturing using representative Poly (methyl methacrylate) samples have shown highly promising results in identifying expected mechanisms associated with fracture initiation and activation of pre-existing faults.
- Optimal microseismic survey design strategies for future experiments have been validated using synthetic forward modeling methods. These strategies can be used to improve diagnostics and reduce costs through the use of surface arrays with smaller footprints.
- Work on Hydraulic Fracture Test Site has been initiated with a test site in the Permian Basin. A joint government-industry JIP with multiple industry participants have completed the fracturing tests through a multi-pad multi-well experiment involving 11 horizontal laterals and a slant core well which was used to collect more than 500’ of through fracture cores and are currently evaluating the data/ observations as per project SOW.

Disclaimer

This report was prepared as an account of work sponsored by Research Partnership to Secure Energy for America (RPSEA) and administrated by National Energy Technology Laboratory (NETL). Neither RPSEA, NETL, Gas Technology Institute (GTI), nor any agency thereof, nor any of their employees, makes any warranty, express or implied, or assumes any legal liability or responsibility for the accuracy, completeness, or usefulness of any information, apparatus, product, or process disclosed, or represents that is use would not infringe privately owned rights. Reference herein to any specific commercial product, process, or service by trade name, trademark, manufacturer, or otherwise does not necessarily constitute or imply its endorsement, recommendation, or favoring by RPSEA, NETL, GTI, or any agency thereof. The views and opinions of authors expressed herein do not necessarily state or reflect those of RPSEA, NETL or GTI.

Acknowledgements

We acknowledge the support of RPSEA and NETL for funding the Marcellus Shale Gas project. Many thanks to WPX Energy for providing wells of opportunity, data, cost sharing and technical guidance. Special thanks to Halliburton for providing technical expertise and cost sharing. Funding for this project was provided by RPSEA through the Ultra-Deepwater and Unconventional Natural Gas and Other Petroleum Resources Research and Development Program authorized by the Energy Policy Act (EPAct) of 2005. RPSEA is under contract with the U.S. Department of Energy's National Energy Technology Laboratory to administer three elements of the EPAct Section 999 Program: (1) Ultra-Deepwater architecture and technology; (2) Unconventional natural gas and other petroleum resources exploration and production; and (3) Technology challenges of small producers.

RPSEA is a non-profit corporation established to help meet the nation's growing need for hydrocarbon resources produced from reservoirs in America; formed by a consortium of premier U.S. energy research universities, industry and independent research organizations. The mission of RPSEA is to provide a stewardship role in ensuring the focused research, development and deployment of safe, environmentally sensitive technology that can effectively deliver hydrocarbons from domestic resources to the citizens of the United States. RPSEA will sharply focus its experience, expertise, and capabilities on meeting the program's objectives: to maximize the value of domestic natural gas and oil resources through new technologies to increase production, and to do so in less expensive, safer and more efficient and environmentally benign ways.

The National Energy Technology Laboratory (NETL), part of the U.S. Department of Energy (DOE) national laboratory system, is owned and operated by the DOE. NETL supports the DOE mission to advance the energy security of the United States. NETL implements a broad spectrum of energy and environmental research and development (R&D) programs that will return benefits for generations to come. These include enabling domestic coal, natural gas, and oil to economically power our Nation's homes, industries, businesses, and transportation; and protecting our environment and enhancing our energy independence. NETL has expertise in coal, natural gas, and oil technologies; contract and project management; analysis of energy systems; and international energy issues. In addition to research conducted onsite, NETL's project portfolio includes R&D conducted through partnerships, cooperative research and development agreements, financial assistance, and contractual arrangements with universities and the private sector. Together, these efforts focus a wealth of scientific and engineering talent on creating commercially viable solutions to national energy and environmental problems.

Report Structure

In this report, we will present a brief summary of results and then proceed to reporting details of the work performed under each task. The report is voluminous and includes many details; all of which may not necessarily interest all readers. In order to enhance readability and flexibility for readers, this report has been broken down into multiple sections as defined under the table of contents. Each section can be treated as a standalone document that can be copied or downloaded independently from the rest of the report. The following structure will be followed in this report:

- Section 1: Project Summary
- Section 2: Research Site
- Section 3: Summary of Results
- Section 4: Appendix containing individual reports

Table of Contents

Abstract iii

Disclaimer v

Acknowledgements vi

Report Structure vii

Project Summary & Research Site 10

Summary of Results 12

Hydraulic Fracturing – Variable Rate Pumping 12

Hydraulic Fracture Test Site (HFTS) 13

Hydraulic Fracture Stage (Cluster) Spacing Design Toolbox 14

Enhanced Hydraulic Fracture Mapping Using Self-Focusing Adaptive Beamformer 15

Advanced Microseismic Source Characterization Schemes 16

Semblance Weighted Emission Mapping to understand seismicity behavior 18

Novel Phase Arrival Detection Workflow 19

Pressure Pulse Attenuation for Fracture Diagnostics 20

Hybrid Microseismic Array Design 21

Spreadsheet analysis of bimodal production decline curve in a hydraulically-fractured shale-gas reservoir 21

Benefit Analysis of Reservoir Engineering 22

Laboratory Scale Hydraulic Fracturing Experiments 23

A re-look at contractor supplied geophysical data 23

Technology Transfer 24

Appendix of Individual Reports 27

Appendix A: Hydraulic Fracturing – Variable Rate Pumping 28

Appendix B: Hydraulic Fracture Test Site (HFTS) 39

Appendix BA: Hydraulic Fracture Test Site (HFTS) – Program Strategy Report 39

Appendix BB: Hydraulic Fracture Test Site (HFTS) Phase II Report 73

Appendix BC: Hydraulic Fracturing Test Site (HFTS) Permian Texas Overview 99

Appendix C: Hydraulic Fracture Stage (Cluster) Spacing Design Toolbox 104

Appendix D: Enhanced Hydraulic Fracture Mapping Using Self-Focusing Adaptive Beamformer 127

Appendix E: Advanced Microseismic Source Characterization Schemes 179

Appendix F: Semblance Weighted Emission Mapping to understand seismicity behavior 205

Appendix G: Novel Phase Arrival Detection Workflow 221

Appendix H: Pressure Pulse Attenuation for Fracture Diagnostics 240

Appendix I: Hybrid Microseismic Array Design 259

Appendix J: Spreadsheet analysis of bimodal production decline curve in a hydraulically-fractured shale-gas reservoir 277

Appendix JA: Errata for Silin and Kneafsey (2012) SPE 149489 306

Appendix JB: Numerical Simulations of Gas Production Using One-column Grids with Different Flow Dimensions 306

Appendix JC: Using the Solver Tool in Excel 311

Appendix K: Benefit Analysis of Reservoir Engineering 313

Appendix L: Laboratory Scale Hydraulic Fracturing Experiments 327

Appendix M: A re-look at contractor supplied geophysical data 371

Appendix MA: Temporal b-value maps for all Wootton 10H stages 406

Advance Hydraulic Fracturing Project

A Joint Industry Project Sponsored by

Research Partnership for Secure Energy for America (RPSEA)

Final Report [August 26th 2016]

Gas Technology Institute (GTI)

Project Summary & Research Site

The Advanced Hydraulic Fracturing project is a field based research and development effort in which real producing wells were used to test multiple advanced hydraulic fracturing concepts. The overall objective was to develop advanced methods and techniques to maximize the efficiency of hydraulic fracturing operations in order to minimize environmental impact by minimizing total fluid requirement for stimulation.

The goal is to minimize the amount of water and additives used for fracture stimulation of a unit reservoir volume thereby alleviating the concerns related to excessive use of fresh water, large volume of flow-back water, water disposal injections, and heavy truck traffic.

Two field test sites in the Marcellus shale were utilized to perform field experiments aimed at evaluating and proving the concept of Variable Rate Fracturing (VRF). WPX Energy provided producing wells of opportunity in order to perform the field experiments. The first test site was located in Susquehanna County, Pennsylvania and included two new horizontal wells drilled through the Marcellus shale. The second test site was located in Westmoreland County Pennsylvania, and included 3 new horizontal wells, also drilled through the Marcellus shale. Data collected at the first test site included advanced open hole logs in the horizontal and vertical sections of the test well. Microseismic monitoring was utilized during hydraulic fracturing, and production logs were run to assess production performance from individual perforation clusters once wells were in production.

The testing at the second test site was limited to further evaluating the concept of Variable Rate Fracturing by introducing more aggressive rate changes. A post stimulation production log was run to determine production from individual fracture stages.

The data collected at the test site was shared across the research team comprised of LSU, UCB, Octave Reservoir Engineering, and LBNL for supporting research and analysis. Below is a summary of key project components.

Objectives of the project: Develop advanced methods and techniques for design and execution of environmentally safe and economically efficient hydraulic fracturing operations.

Description of the project: Development of a real-time hydraulic fracturing control methodology through coupled analysis of geophysical fracture diagnostic data and pumping pressure, rate, and fluid density; and verification of results by detailed production testing.

Key deliverables associated with the project: 1) Guideline for environmentally safe and economically optimal fracture stimulation of shale and tight sand reservoirs, 2) Methods and techniques for high resolution microseismic data analysis, 3) Design diagram for the next generation microseismic data acquisition, 4) Shale-specific production decline analysis software for hydraulically fractured shales and other unconventional resources, 5) A complete research quality dataset, and 6) Final Report.

Potential impact of the project: Reduced use of fresh water used for hydraulic fracturing, minimization of truck traffic and corresponding air emissions, and alleviation of public concern relative to seismicity of hydraulic fracturing. The proposed optimization uses minimum amounts of water for stimulation of a unit reservoir volume, thereby improving the economics of production from shales and other unconventional resources.

Participants involved in performing the scope of work: Gas Technology Institute, Lawrence Berkeley National Laboratory, University of California at Berkeley, Louisiana State University, and Octave Reservoir Technologies. WPX Energy provided two test sites for field experiments.

Organizations providing the required cost share: Octave Reservoir Technologies, Louisiana State University, and WPX Energy

Summary of Results

Hydraulic Fracturing – Variable Rate Pumping

Jordan Ciezobka – Gas Technology Institute

Typical hydraulic fracturing designs in shale utilize a predetermined fluid pump rate, which once achieved is held constant throughout the treatment, excluding situations when surface pressure limitations or other conditions disallow. We propose a method of pumping hydraulic fracture stages where the fluid pump rate is rapidly changed from the predetermined maximum rate, to some significantly lower rate, and then rapidly increased back to original maximum rate. This rapid change in the flow rate produces a pressure pulse that travels up and down the wellbore and has the capacity, together with the pump rate change, to open previously unopened perforations, while increasing fracture complexity through fluid diversion.

We observed increased microseismicity during hydraulic fracturing in stages with frequent pump rate changes. Regardless of their type and nature, seismic signals are indicative of fragmentation of the treated zone. This could be from shear shattering or dilatational opening. One can also assume that high signal density is a good measure of fracturing efficiency. To further investigate these observations, we implemented a variable pump rate fracture design in a Marcellus shale well. More specifically, we implemented the variable pump rate frac design in every odd stage, while implementing a constant rate design in every even stage. This was done in order to account for changes in the reservoir along the horizontal lateral.

Production log results showed on average a 19% increase in production for the variable pump rate stages versus the constant pump rate stages. A lower treating pressure was often encountered after the rapid rate changes, leading to the conclusion that unopened perforations were opened with the aid of the induced pressure pulses. Total well production decline was much slower for test well that included variable pump rate changes versus the offset horizontal well which did not include the variable pump rate frac design.

And finally water hammer frequency decay analysis shows a predictable trend in well with variable pump rate stages. Throughout the variable pump rate stages, no proppant transport issues were encountered and the frac stages were completed without any major issues.

Rapid rate changes applied throughout the fracture treatment enhance microseismicity, which could be interpreted as additional fracture complexity. Surface fracturing pressure data shows that rapid pump rate changes open additional perforations without physical flow diverters such as ball sealers or frac balls, while production log data shows higher production. Implementation

of the Variable Rate hydraulic fracturing method results in no additional costs while it increases stimulation efficiency. Below is a summary of results.

Correlations of fluid pump rate, microseismic data, and production data have led us to investigate a new hydraulic fracture design in which the fluid pump rate is rapidly changed to induce a pressure pulse leading to the following effects as determined through data analysis:

1. Pump fluctuations lead to increased microseismic emissions
2. Increased microseismic emissions correlate well with increased production
3. Rapid rate fluctuations induce a pressure pulse that tends to open previously unopened perforations and increase fracture complexity
4. Rapid rate fluctuations added to the frac design have shown to increase production by 19% as compared to stages with a frac design that did not include rapid rate fluctuations

Hydraulic Fracture Test Site (HFTS)

Jordan Ciezobka – Gas Technology Institute

The industry experience has proved that no two gas shale plays are the same in that while they all need some fracture stimulation, every play reacts different from others when subject to hydraulic fracturing. We originally proposed creating a consortium of producing and service companies involved in development of shale plays to perform conclusive field testing of hydraulic fracturing across all major gas shale basins. The following were the consortium objectives:

1. Establish the geometry of the created fracture system by repeated injections, using cores collected in the injection area, and by sidetracking one of the observation wells.
2. Determine whether or not injection pressure provides a reliable method to assess confinement.
3. Compile guidelines for operational practices related to productivity.
4. Demonstrate that microseismic imaging can provide reliable information of fracture dimensions.
5. Characterize the created fractures near and far-field from the wellbore.
6. Verify that fracture models can be calibrated to predict fracture behavior under the prevailing geological and operating conditions.
7. Establish calibration procedures for hydraulic fracture modeling.
8. Develop diagnostic techniques for multi-fractured horizontal wells.
9. Identify, test and verify new techniques for assuring hydraulic fracture geometry and productivity.

Realizing such a project on national scale would cost in excess of 20 million dollars, it can only be implemented by a highly motivated consortium of operators and service companies. As such, the scope of this task was limited to project planning and development of a detailed scope of work.

Phase I – As part of project planning and development of scope of work, three workshops were held by GTI with industry operators and service companies. These workshops were held on:

1. April 2013 in Houston, TX
2. May 2013 in Pittsburgh, PA
3. July 2013 an Online Webinar

Thirty-seven hydraulic fracturing experts from 22 operating and service companies participated.

The workshops resulted in the identification of the intent, scope, and value of the HFTS program. Hydraulic fracturing research needs were prioritized; a preliminary program mission, objectives, design, participation, budget, and schedule was established; an Advisory Board and a Technical Review Committee were started to guide the program; and alignment was reached on the need for the second phase of the project to help define the experimental design for HFTS. A strategy report was created to align the research and funding necessary to implement and execute the test site. The report is in the appendix.

Phase II – Research and Development (R&D) Assessment and Data Review: This phase involved a baseline study to assess the state of the hydraulic fracturing R&D, fracture diagnostics assessment, and the applicability of that data to help define the experimental design of HFTS. A report highlighting these findings is in the appendix.

Phase III – Implementation: In this phase we secured the funding for the HFTS by forming a JIP and developed a scope of work. The test site was created in the Permian Basin Wolfcamp formation and hosted by Laredo petroleum, and it was launched in August of 2015. Details of the test site are in the appendix.

Hydraulic Fracture Stage (Cluster) Spacing Design Toolbox

Dr. Debotyam Maity – Gas Technology Institute

The aim of this study was to identify an easy to implement technique at carrying out engineering cluster/ stage spacing design based on available drilling and logging data. Most techniques available today when it comes to engineering design involves use of specialty logging runs (such as Dipole Sonic or Litho Scanner) or cuttings analysis which could end up creating significant time/ cost constraints. We devised an approach which makes use of available logging data and drilling

data through mud logs which are routinely collected for all new wells being drilled. This results in an inexpensive fracture/ cluster spacing design tool without the need to run new logs.

Our workflow improves the spacing of the perforation clusters along the lateral by taking into account variations in geomechanical properties of the reservoir as well as the presence of gas and potentially natural fractures. GTI has developed a hydraulic Fracture Spacing Design Toolbox which predicts optimal fracture spacing design based on modeling of rock properties as well as hydrocarbon presence using information from mud logs. The reason for not using traditional wireline or tubing based tools is to avoid high costs associated with the same. The Toolbox has been developed in the Matlab environment and is available with a simple to use GUI interface as the front end and powerful Neural Nets/ Fuzzy Classifiers at the back end. The toolbox at this stage is a scientific code and is not ready for commercial applications. Based on tests done on data collected for this project and relevant background data made available by WPX Energy, we have the following observations:

- Good predictability and applicability over both near field (same pad) and far field (100's of miles) Marcellus Shale gas wells.
- Potential for enhanced productivity per specific unit of input used (water, proppant, chemicals, etc.) leading to reduced environmental footprint per unit of gas produced.
- Optimal completion programs without having to resort to expensive post drill logs or expensive LWD tools.
- Results validated with good tie observed when compared with available post completion production logs.
- Results validated for limited well datasets available from prior RPSEA project [09122].

For a more in-depth discussion on the work carried out, refer Appendix C of this Final Report.

Enhanced Hydraulic Fracture Mapping Using Self-Focusing Adaptive Beamformer

Dr. Bernard Widrow – Stanford University

The underlying objective of this study was to try and improve the ability of microseismic analysis to aid in efficient and environmentally safe resource extraction. The aim was to develop algorithms for improved methods of fracture mapping in 3D using microseismic signals. For this, we studied the application of a self-focusing adaptive beam-former to the problem of microseismic event detection and localization. This beamforming system leverages signal-processing techniques that are well established and have been widely successful in a variety of fields including sonar and radar, where arrays of sensors are used to detect and localize faint sources of energy in a large background of noise. Use of this proposed technology is expected to provide significant attenuation of background seismic noise, particularly coherent noise, and

compensate for inaccurate knowledge of local wave propagation. This has enabled the possibility for a more complete and accurate understanding of the activity induced by stimulation treatments. Key activities that have been completed as part of this study are as follows:

- Developed a method for localizing points of origin of microseismic events. Starting with a large event on which to focus a given seismic array, the beam is scanned incrementally to detect smaller events and to localize them relative to the locus of the large event.
- With enough neighboring seismic-event loci, it is possible to delineate geometry of the fracture. We demonstrate this through an example of five identified source points. Once their location in 3-D space was determined, we were able to make a crude map of a fracture.
- We developed a self-focusing adaptive beamformer workflow that is capable of localizing seismic events in 3-D with improvements in signal-to-noise ratios in the order of ~10 db. This provides opportunities for improving location accuracy, reducing the number of geophones and allow manifold increase in the number of seismic events that could be available for analysis.
- We formulated a set of steps necessary to go from raw seismic data to a 3-D fracture map, as follows:
    a. Identify a large seismic event in the geophone signal data.
    b. Use its moveout delay times to focus the beamformer.
    c. Determine seismic velocity from the moveout delays using knowledge of the well geometry and the geometries of the surface/ borehole arrays.
    d. Steer the beam in known increments about the locus of the large event. Search in 3-D for additional seismic events.
    e. Map the fracture by plotting the loci of multiple seismic events relative to that of the large event.
- We developed an experimental Matlab code for implementing this workflow and various operations for localizing events.

Appendix D provides in-depth understanding of self-adaptive beamformer design and implementation for this project.

Advanced Microseismic Source Characterization Schemes

Dr. James W. Rector – University of California, Berkeley

The primary objective of this study was to develop processing techniques which can circumvent some of the limitations posed by limited aperture of downhole microseismic surveys where the survey geometry is governed by existing wellbore locations. As we well understand, typical microseismic data processing involves basic location, moment magnitude estimation, and advanced source parameter and frequency analysis. The event location, as the

basis of almost all other advanced processing, has been routinely conducted by industry. For horizontal wells in shale gas production, it is a common case to have only one nearby monitoring well, the production well, available for microseismic monitoring. This kind of configuration has the advantage that the geophones can be moved to the nearest area of the stimulation. Also, the deep environment eliminates the effect of noise due to surface fracturing operation and surface noise. However, the limited coverage of acquisition geometry makes microseismic processing with only P and S arrival times impossible resulting in the need for 3 component data. The unknown orientation of downhole geophones and poor coupling between geophone and borehole are the challenges associated with 3 component data from borehole deployments. While perforation shots are normally used for geophone orientation calibration, the complexity and anisotropy of shale formation, and the poor coupling of geophones with horizontal wellbore leads to significant uncertainty in the waveform polarization.

In this study we looked at headwaves which can be seen in layered reservoirs with significant angular source to receiver offset. Due to its low velocity nature, headwaves are very common in cross-well seismic and microseismic surveys. When the distance between geophones and source is relatively large, the headwave arrival can precede the direct arrival. Our analysis on microseismic survey conducted on two horizontal wells in Marcellus shale shows that headwave conveys very useful information, which can eliminate the requirement for waveform polarization in microseismic event location. Additionally, our work in the spectral domain has shown value in order to circumvent another common problem with this typical survey geometry – limited aperture leading to an inability to perform moment tensor inversion. Due to the small solid angle, this traditional geometry survey severely limits the ability to understand source mechanism. As a result, working in the spectral domain enables a better understanding of the fracturing events without the added cost of multiple monitoring wells. Key activities that have been completed as part of this study are as follows:

- We have developed a robust microseismic location inversion routine which makes use of headwaves along with traditional P & S wave arrivals.
- We have demonstrated its performance through comparative study of results using traditional approach provided by the service company for data acquired in this project.
- We observe reduced location uncertainty with this approach.
- We have also introduced a novel Bayesian inversion scheme using Maximum-A-Posteriori estimation technique.
- While correlation between pumping parameters and seismicity was not directly accomplished, correlation between source parameters and spectral content was successfully demonstrated.

- Ratio of shear to compressional waveform bandwidth were used to identify and differentiate between opening and shear mode failure.
- Noise, particularly those from tube waves were successfully mitigated using a location based noise characterization and reduction schema.

Appendix E highlights the issues and proposed solutions including our research results in detail.

Semblance Weighted Emission Mapping to understand seismicity behavior

Dr. Debotyam Maity – Gas Technology Institute

Microseismic surveys typically involve surface deployments, wellbore arrays or a combination of the two. Surface microseismic surveys are often very resource intensive due to their large apertures and receiver count. On the other hand, downhole arrays are often deployed within existing wells in the field which leads to constrained design apertures and failure of imaging algorithms traditionally used with surface deployments for characterizing the observed microseismicity. At the same time, hypocentral inversion algorithms used with wellbore arrays have many well understood limitations and their use leads to numerous "valid" events being discarded during processing due to "poor" data quality and signal-to-noise characteristics.

The objective of this study was to look into the possibility of using "unconventional" approaches towards microseismic data processing and analysis which can circumvent some of the limitations posed by traditional inversion and imaging methods in use today and help enhance derivable value from microseismic monitoring operations. We have introduced and developed a simple seismic energy emission mapping approach (semblance weighted emission or SWE) which can be applied on microseismic data from any array (borehole, surface or combined). The method provides a temporal energy emission profile as observed during treatment based on the recorded seismicity. We also share actual field examples and demonstrate the applicability of this attribute for better understanding of reservoir behavior during hydraulic fracturing operations and validate the analysis through independent observations from production log data. Key observations and results from this research are as follows:

- We have introduced a new passive seismic attribute to characterize fracture completions and to better understand interaction with the subsurface during treatment.
- Our proposed processing and analysis approach provides for a more complete picture of seismicity emitted during treatment.
- It can be easily modified to account for non-traditional seismicity observed in reservoirs under hydraulic fracturing such as slow aseismic creep and associated energy release.

- There exists the potential for accurate spatio-temporal emission mapping using independent data (such as phase and polarization) in place of the current temporal mapping [directionally conditioned semblance weighted emission attribute].
- Other attributes (such as from continuous waveform polarization analysis) have also been looked into as a means to better understand hydraulic fracturing operations.

For a more in-depth discussion on the work carried out, refer Appendix F of this Final Report.

Novel Phase Arrival Detection Workflow

Dr. Debotyam Maity – Gas Technology Institute

Most Microseismic event detection algorithms suffer from the issue of noise artifacts in data. Sometimes, noise can be overbearing and can significantly reduce the number of detected events which has an impact on post processing microseismic data analysis. While full waveform based inversion can remove the need to make event/ phase picks, their use is still significantly impacted by noise. Other techniques such as use of advanced filters while useful can still fail to deliver depending on the data quality and type of filtering used. Due to these issues, we generally loose around 5 to 10 times the number of microseisms compared to those that are actually deemed of good quality for typical processing workflows.

The objective of this study was to identify a way to increase the number of "detectable" events by employing advanced processing technique using predictive "move-out" matching scheme. Our proposed methodology makes use of an evolutionary search algorithm to iteratively search for arrivals as recorded by geophone strings in borehole. This allows the process to only model for predictable hyperbolic moveouts which can be modeled as a higher order polynomial. The events are identified based on observed characteristics of the gather along the predicted moveouts. The same technique can be expanded to process data acquired using small surface geophone arrays (tested at HFTS). Key deliverables and results from this research are as follows:

- Developed a hybrid event detection workflow which has significantly enhanced detectability of events from borehole data for potential data processing and analysis.
- This workflow has been extensively tested on microseismic data collected from the WPX Energy Wootton well 10H experiment and results indicate significant improvement over traditional picking approaches.
- The detection approach thus developed has been successfully combined with SWE mapping analysis to improve upon the results without unduly increasing the processing time associated with relatively large datasets.

For a more in-depth discussion on the work carried out, refer Appendix G of this Final Report.

Pressure Pulse Attenuation for Fracture Diagnostics

Dr. Debotyam Maity – Gas Technology Institute

"Water Hammer" pressure transients are generated when there is a sudden change in flow conditions within the wellbore such as a pump shut in or failure. Classically; water hammer, flow and pressure response data at the end of frac treatment has been used to estimate entry friction. Also, Gary Holzhausen has looked into modeling of fluid transients to characterize fracture dimensions, etc. However, methods devised for characterization of single vertical completions requires extension to horizontal mile long laterals which bring in their own unique set of challenges. We tackle these issues by making use of novel modeling/ analysis methods. With the pressure pulse attenuation (PPA) analysis technique, we hope to be able to carry out real time fracture diagnostics with commonly available pressure response data, potentially redesign consecutive fracture stages on the fly, reduce our reliance on expensive production logs and conduct both qualitative and quantitative modeling of production performance.

The PPA analysis of completion data from multiple wells has indicated that a reasonably strong correlation seems to exist between observed production through production log data and modeled fracture dimensions when corrected for possible losses due to diversion and/ or leak-off into prior stages due to ineffective isolation. An experimental code (WHAM-FD) utilizing finite difference solution has been designed and developed within the MATLAB environment for analysis of pressure response data and has been extensively tested on the two sets of data available in this project (WPX Energy Wootton and Corbett wells) as well as data acquired in the HFTS project. Summary of this study and results are itemized below:

- PPA analysis workflow finalized including relevant modeling parameters for using water hammer pressure transients observed during fracturing operations to model for fracture characteristics.
- Robust Evolutionary algorithm used to identify "optimal" solution for model parameters based on observed pressure response.
- Methodology developed to identify potential inter-stage isolation failure and way of quantifying resulting "effectiveness loss" from treatment.
- Correlations developed between PPA modeling results and production logging results to develop site specific "pseudo-production logs".
- Validated opening of previously "non-communicating" perforations through variable rate fracturing operations.

For a more in-depth discussion on the work carried out, refer Appendix H of this Final Report.

Hybrid Microseismic Array Design

Dr. Debotyam Maity – Gas Technology Institute

Optimizing passive seismic survey designs is the key to limiting deployment costs by minimizing geophone requirements and improving processing results. However, design optimization for microseismic surveys can be extremely challenging. Some of the major issues when it comes to optimized microseismic survey design include the presence of too many variables/ cost functions needing optimization, difficulty in quantification and validation of many of these parameters and the differing processing techniques and schemes in use today. The purpose of this study was to identify and implement an optimization workflow based on the known requirements for optimization defined from expected work to be carried out at GTI for future microseismic data acquisition, processing and analysis programs. For this study, we decided to focus on an optimized design framework to get the best possible solutions for a) moment tensor inversion, b) travel time inversion and c) Sabatier's data angle minimization criteria to reduce uncertainty and bias in final solution. This work attempts to validate an integrated framework for optimized multi array passive seismic monitoring programs to optimally characterize event source parameters as best as possible. While the actual microseismic experiment has not been planned as of now, once that happens, we will obtain necessary data to plug into the design framework shared here and optimally place geophone sensors to map the microseisms. As preparatory work, following tasks have been completed internally by GTI:

- Final design framework for survey optimization using an earlier approach developed as part of the RPSEA funded Marcellus Shale Gas Project (09122).
- A new hybrid GA[1]-SA[2] search algorithm to identify the best designs within the limits of specified constraints.
- A new GA based ray-tracer to quickly identify ray-paths used for optimization when considering optimal tomography results or minimizing same/ similar data.

For a more in-depth discussion on the work carried out, refer Appendix I of this Final Report.

Spreadsheet analysis of bimodal production decline curve in a hydraulically-fractured shale-gas reservoir

Dr. Christine Doughty and Dr. George J. Moridis

[1] Genetic Algorithms
[2] Simulated Annealing

The objective of this study is to develop a simple, Excel-based tool for the analysis of the complex problem of gas production from a fractured tight/shale gas reservoir that is based on a model that remains faithful to the underlying physics and can provide rapid estimates of the important parameters governing the system behavior. In this study, we implemented a semi-analytical solution for a modified Bi-Modal production decline curve for hydraulic fractured shale gas reservoirs in an Excel spreadsheet. Curve-fitting has been done using field data to determine transport properties, fracture geometry parameters and etc. based on available information about the reservoir. We list the underlying assumptions, we present and discuss the problem solution, we describe the use of the spreadsheet, and we examine in detail and analyze results from two example datasets. The spreadsheet-based analysis provides improved understanding of hydraulic fracturing performance, enabling future operations to be done more efficiently in addition to providing insights for more economical operation with reduced environmental impact. The following have been successfully delivered by the research team:

- Excel spreadsheet based solver to obtain the semi-analytical model results for shale gas data.
- Complete description of spreadsheet and a step-by-step guide for usage.
- Sample fitting tests with available data from this project as well as 3rd party data.

For a more in-depth discussion on the work carried out, refer Appendix J of this Final Report.

Benefit Analysis of Reservoir Engineering

Xinya Xiong (formerly with GTI) and Dr. Debotyam Maity

In this study, we have evaluated the well performance of four wells on two well pads to compare the advanced variable rate hydraulic fracturing routine with conventional fracturing routine. In each pad, the experiment well is fractured using variable rate in alternating stages with a nearby offset well fractured using conventional routine. The total production of four wells was looked into. The production rates were analyzed using Bi-Modal decline scheme. Bi-Modal production decline analysis scheme is further illustrated in Appendix J. It provides a simple indirect estimate of initial production decline rate and fracture geometry parameters. The second well pad exhibits production decline without too many operational interruptions and is therefore looked into using Bi-Modal decline analysis carefully. The key observations from this study are:

- The experiment well on second pad which went through more rapid fracture rate changes in alternating stages demonstrated a slower decline rate.

- Assuming they are draining from a uniform SRV, the experiment well developed a more effective fracture network than its offset well on the same pad.
- The production logs showed direct indication of 19% increased production in variable rate fracturing stages of experiment well.

We have also looked at using an open source semi-analytical solution to interpret significant mismatch between productivity of wells and look at potential use for applications in the future.

A more detailed discussion on the work carried out can be references in Appendix K of this Final Report.

Laboratory Scale Hydraulic Fracturing Experiments

Dr. Juan M. Lorenzo – Louisiana State University, Baton Rogue

This goal of this study was to conduct laboratory experiments involving passive seismic monitoring to understand hydraulic fracturing process in a controlled environment. The purpose of conducting lab scale representative experiments was to answer some of the questions regarding the actual fracturing process, generation of elastic waveforms associated with accompanying deformation and precise monitoring and calibration of microseismic monitoring techniques. Our deliverables from this study are as follows:

- An experimental setup for representative lab scale hydraulic fracturing tests.
- Experimental descriptions and interpretations of single-component seismic data sets derived under non-dimensional experimental conditions.
- Catalog tables of event location identified and processed during the course of the experiments.
- 'R' based software package to manage and analyze microseismic data (for lab scale tests) and for possible real world applications.
- Understanding the type of fracturing through experimental variations and how they correlate with interpreted seismic mechanisms (Mode-I versus mixed-Mode).
- An analysis and discussion of the scalability of these results to field conditions and comparison to previous laboratory experiments.

A detailed explanation on how the experiments have been designed, the data collection and processing methodology being used as well as our observations have been detailed in Appendix L of this Final Report.

A re-look at contractor supplied geophysical data

Dr. Debotyam Maity – Gas Technology Institute

The aim of this study was to take a second look at the microseismic data supplied by the relevant service company. Most service companies are limited by the amount of processing they do on the raw data and their results. Various factors at play include acquisition artifacts, noise, array geometry limitations or instrumentation issues, data quality, etc. to name a few. Just as an example, prior studies [e.g. RPSEA 09122] have demonstrated significant mismatch between surface and downhole data acquisition results. We decided to take a second look at the data acquired as part of this experiment for the following reasons:

- Independent data quality analysis including presence of any acquisition or processing artifacts.
- Validation of primary microseismic data inversion product (event hypocentral locations).
- Secondary (non-traditional) data analysis to derive additional value from data. These include b-value analysis, identification of long period long duration (LPLD) events, etc.

For a more detailed review of the tasks completed under this study, refer to Appendix M of this report.

Technology Transfer

Presentations were given at various technical conferences and industry consortiums. Apart from presentations, various papers have been submitted and published in relevant technical journals for wider industry outreach. Table 1 shows a list of technology transfer efforts made by GTI and other JIP partners.

Table 1: Technology transfer efforts made by GTI and other project participants

Date	Event/ Publication	City	Venue	Notes
2014	Hydraulic Fracturing Journal	-	-	Authors: A. Taleghani, M. Gonzalez, P. Puyang & J. M. Lorenzo *Post-treatment assessment of induced fracture network* [Volume 1(3), pp. 24 – 33]
October 27-31, 2014	SEG Annual Meeting	Denver, CO	Denver Convention Center	Presentation- Debotyam Maity: *Semblance Weighted Emission Mapping for Improved Hydraulic Fracture Treatment Characterization* Presentation- Debotyam Maity:

				Robust First Break Picker for Microseismic Data Collected Using Borehole Geophone Arrays
October 29-30, 2014	Shale Exchange Workshop	Pittsburgh, PA	CONSOL Energy Center	Presentation- Jordan Ciezobka: *Emerging Technologies: Hydraulic Fracturing Optimization*
December 8-10, 2014	AAPG/SEG SPWLA Hedberg Conference	Austin, TX	-	Presentation – Jordan Ciezobka: *Hydraulic Fracturing Test Site*
December 16, 2014	AGU Annual Meeting	San Francisco, CA	Moscone Center	Presentation- Juan M. Lorenzo: *Effects of fracturing fluid viscosity on Wave Emissions during Hydraulic Fracturing: An Experimental Approach*
July 20-22, 2015	URTeC	San Antonio, TX	-	Presentation – Michael J. Nava: *Identification of Microseismic Attributes Through Spectral Analysis* Presentation – Zhishuai Zhang: *Microseismic Event Location using Multiple Arrivals: Demonstration of Uncertainty Reduction*
October 18-23, 2015	SEG Annual Meeting	New Orleans, LA	Morial Convention Center	Presentation – Michael J. Nava: *Characterization of Microseismic Source Mechanism in the Marcellus Shale through Analysis in the Spectral Domain* Presentation - Zhishuai Zhang: *Improving Microseismic Event Location Accuracy with Head Wave Arrival Time: Case Study Using Marcellus Shale*
November, 2015	Journal of Sustainable Energy Engineering	-	-	Author: D. Maity *Correlating Pressure with Microseismic to Understand Fluid-Reservoir Interactions during Hydraulic Fracturing* [Volume: 3(2), pp. 127 – 142]
2016	Computers & Geosciences	-	-	Authors: D. Maity & I. Salehi *Neuro-evolutionary event detection technique for downhole microseismic surveys* [Volume: 86, pp. 23 – 33]

February 9-11, 2016	SPE Hydraulic Fracturing Technology Conference	The Woodlands, TX	-	Presentation – Jordan Ciezobka: *Variable Pump Rate Fracturing Leads to Improved Production in the Marcellus Shale*
2016	Hydraulic Fracturing Journal	-	-	Authors: D. Maity, J. Ciezobka & I. Salehi *Multi-Stage Hydraulic Fracturing Completion Diagnostics for Real Time Assessment of Stage-Wise Stimulation Effectiveness and Improved Performance* [Volume: 3(2), pp. 8 – 18]
2016	Journal of Sustainable Energy Engineering	-	-	Authors: D. Maity, J. Ciezobka, I. Salehi *Fracture Spacing Design for Multistage Hydraulic Fracturing Completions for Improved Productivity* [Hydraulic Fracturing Special Issue, pending publication]

Appendix of Individual Reports

Appendix A: Hydraulic Fracturing – Variable Rate Pumping

Background

Previously collected hydraulic fracturing and microseismic data in the Marcellus shale led to the finding that substantial rapid changes in the fluid pump rate during hydraulic fracturing result in increased levels of microseismic activity emanating from the reservoir being stimulated. Top of Figure 1 shows a typical hydraulic fracturing treatment in the Marcellus shale with the treating pressure shown in red and the pump rate shown in blue. Bottom of Figure 1 shows borehole microseismic event density aligned to the treatment plot with the blue highlighted columns corresponding to rapid fluctuations in fluid pump rate. As evident in this figure and shown by the shaded blue columns, the microseismic event density significantly increases during rapid pump fluctuations, both positive and negative. However, the exact sequence of these rate changes were not planned and are a result of either pumping equipment constraints or wellbore conditions. Similar pump rate fluctuations and microseismic event density correlations have been attained with a data set consisting of almost 100 fracture stages in the Marcellus shale (Ciezobka et al 2013)(Ciezobka 2013).

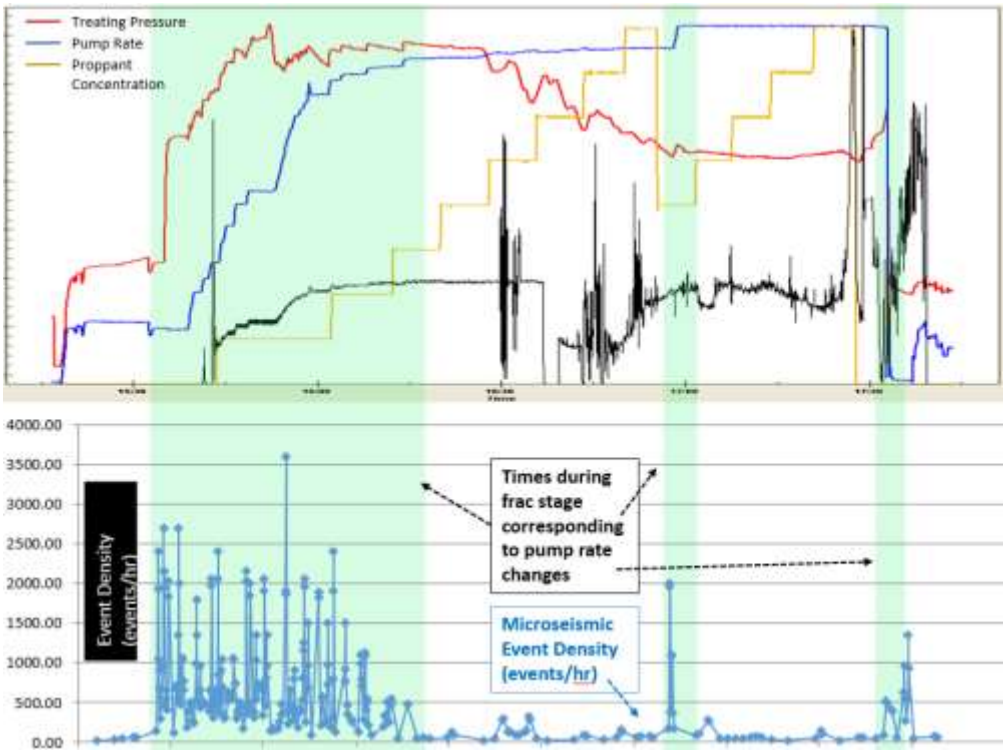

Figure 1: Typical hydrualic fracture stage in the Marcellus shale (top). Microseismic event density during pumping of the hydrualic fracture stage (bottom).

Furthermore, production log data collected in the horizontal lateral and compared with the microseismic survey results show that the microseismic event count and event proximity (proximity of each microseismic event to the next closest recorded event) for each fracture stage correlate well with production from each fracture stage. Figure 2 shows the microseismic data overlaid with the production log results. The production log data shows increased production coming from fracture stages where the microseismic event count is high, and in stages where the event count is low, the production contribution is also reduced.

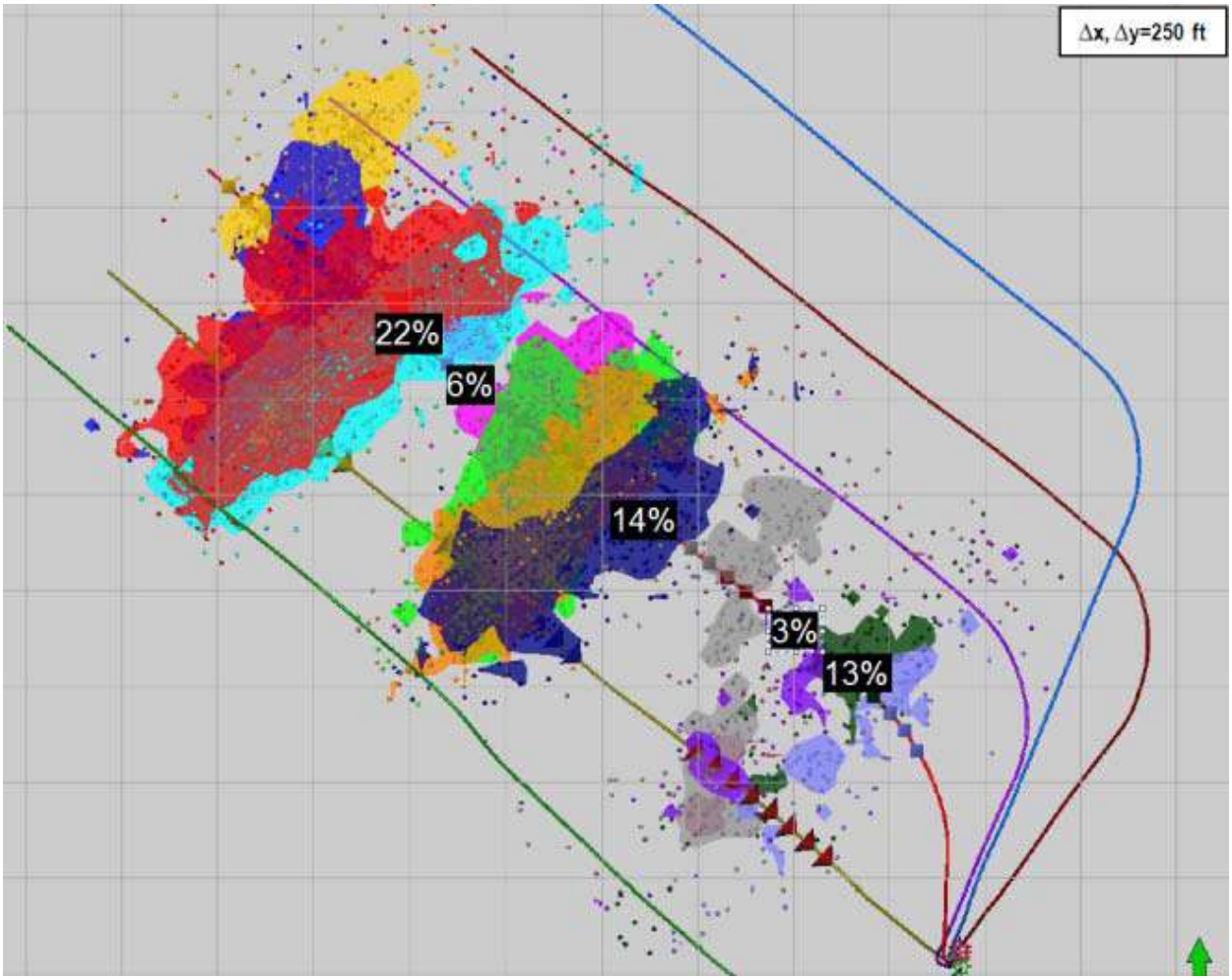

Figure 2: Concentration of microseismis events shown as dots and cluds for the third well from left. Overlaid on top are production log results with production contribution for selcted frac stages.

In summary, these results indicate that pump rate fluctuations produce significantly higher microseism emissions, and higher microseismic emissions correlate with higher production. Based on these findings, we tested a hydraulic fracture design that included rapid rate fluctuations. The pump rate fluctuations we

tested were implemented in a systematic sequence, such that the pump rate fluctuations were intended o designed, and not a result of unanticipated equipment or wellbore conditions. We present the results of the controlled pump rate fluctuations from the Marcellus test in the following sections.

Marcellus Shale Well Pad - Description of Testing Procedure

The experiment wells in this study were wells of opportunity that were hydraulically fractured in the Marcellus shale gas play. Figure 3 shows the well pad diagram highlighting the two laterals which were studied. Another lateral (4H) extends on the other side of well 8H but has not been shown in the diagram. Inter-well separation varies between ~700 ft. to 1000 ft. laterally for wells 6H and 8H. Both wells were designed to land in the lower Marcellus shale play. As observed from the diagram, well 6H had a total of 27 stages and well 8H had a total of 28 stages that were completed.

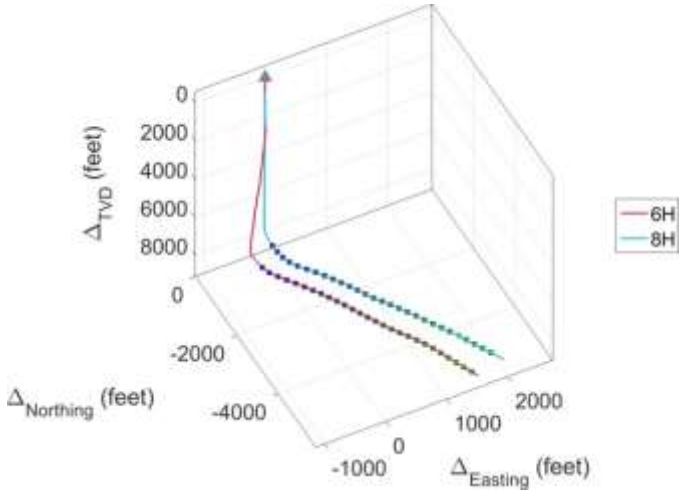

Figure 3: Well pad diagram showing both the 6H and 8H laterals along with location of stage plugs. the dimensions are in feet and relative to the wellhead location.

The frac design involved ~200,000 pounds of proppant (100 and 40/70 mesh white sand) pumped along with ~200,000 gallons of water for well 6H. On the other hand, for stages pumped in well 8H, we had ~ 50% additional proppant (~300,000 pounds of proppant) and higher frac fluid volumes. With higher proppant being pumped for the 8H well, we do expect that initial productivity in terms of gas flow rates from this well to be higher compared to the 6H well.

Results Validating Variable Rate Fracturing

In this study we used four different methods to validate the efficacy of using variable rate fracturing technique when it comes to hydraulic fracturing. These involved both direct and indirect diagnostic techniques.

Production Logging

First, we looked at production log results as observed immediately post completion for well 6H where rate fluctuations were introduced (Figure 4). While we observe significant variability in production behavior over the entire lateral in question due to completion quality as well as exact location of lateral compared with reservoir stratigraphy, we do observe that more often than not, variable rate (odd) stages show higher productivity compared to nearby even stages.

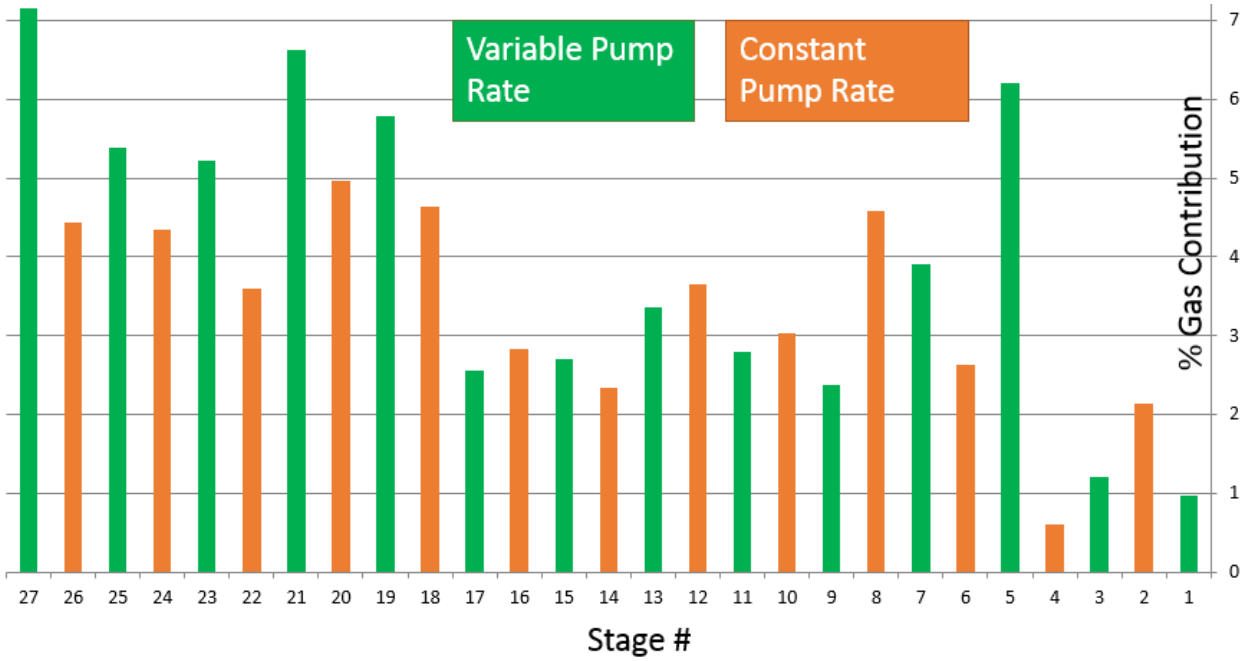

Figure 4: Production logging results for well 6H across producing clusters.

Another inherent assumption with the use of variable rate fracturing approach is that it should ideally open additional perforations which may not have been fully open during the initial breakdown. This should allow for a more uniform distribution of fluid flow into formation across available perforation clusters. We sum the skewness measure for distribution of flow across clusters for each of the 27 stages for well 6H and observe a very low summed measure for odd stages (0.5394) compared to the even stages (4.8528). Looking at overall productivity from odd and even stages separately, the cumulative productivity from odd stages is 915.3 Mscf/d compared to 721.1 Mscf/d for the even stages. Since there is one additional odd stage for this well, the average productivity is evaluated. We still find the same trend, i.e., an average productivity of 65.38 Mscf/d for odd stages and 55.47 Mscf/d for even stages. This represents 17.87% higher productivity with variable rate fracturing.

Pressure Response to Rate Fluctuations

Since we have already seen lower skewness measure for stages completed using variable rate fracturing, we also looked at the behavior of treatment pressure post the introduction of rate fluctuations for these stages. Figure 5 shows two examples of odd stages completed for well 6H and we can clearly see a drop in treatment pressure by 10's to 100's of psi which is indicative of lower entry friction within the system. This could either mean additional opening of perforations due to the pressure transient pulse generated

with the rate fluctuation (i.e., reduced perforation friction). It could also mean a consolidation of non-dominant fractures emanating from the wellbore (reduced tortuosity).

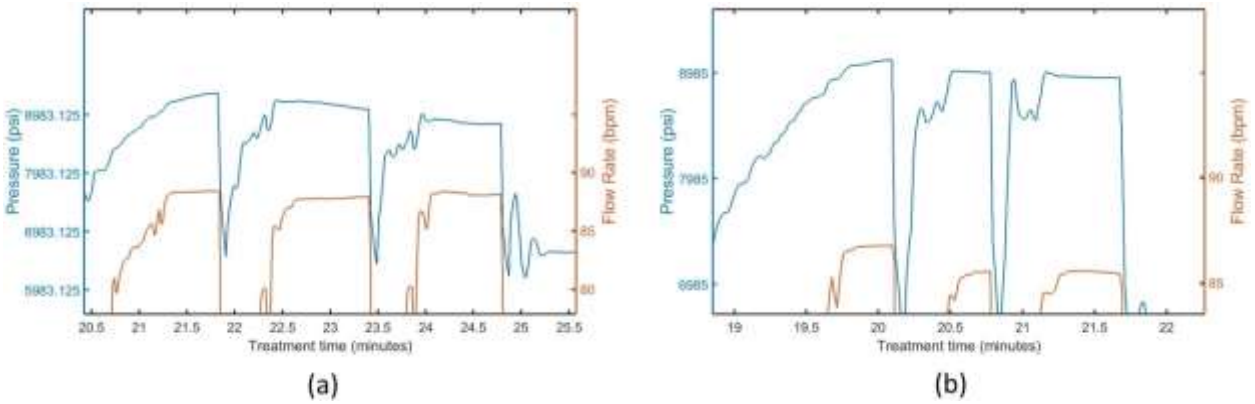

Figure 5: Sample treatment pressure/ flow profiles following introduction of rate fluctuations during stage # 9 and stage # 17 for well 6H.

Post Pumping Shut-down Water Hammer Diagnostics

The wellbore and the associated hydraulically created fractures during the treatment phase of a fracture stage create a complex hydraulically connected conduit where unsteady state transients are common. As the pumping of proppant and slurry ends, the pumps are shut over a short period and time and depending on the shutdown procedure, the transition from steady state constant flow to low or no flow conditions creates single or multiple water hammers within the wellbore. Since the decay in energy over the water hammer cycle is a function of the total frictional head loss as the pressure pulse travels up and down the conduit, it is intuitive to expect the decay in energy to be higher for a longer conduit. In the same vein, the decay should also be higher if an extensive large aperture fracture network is associated with the stage which will consequently absorb more energy as the pressure pulse moves through the network. Moreover, complex fracture network swarms should lead to shorter oscillating pressure response with higher decay rate due to higher frictional losses compared with long singular fracture wings.

While for well 6H, the odd stages were completed using the variable rate approach and the even stages were completed normally; for well 8H, all of the stages were completed using the normal approach with no variable rate fluctuations during completion. Since our hypothesis of additional perforation opening and improved performance through variable rate suggests that a more extensive fracture network is possible with rate fluctuations due to additional fracture propagation and growth with newly opened perforations, we expect those stages which were completed using the variable rate approach to show stronger decay in signal strength with time compared with the normally completed stages. This hypothesis is highlighted through some typical observations from the field in Figure 6.

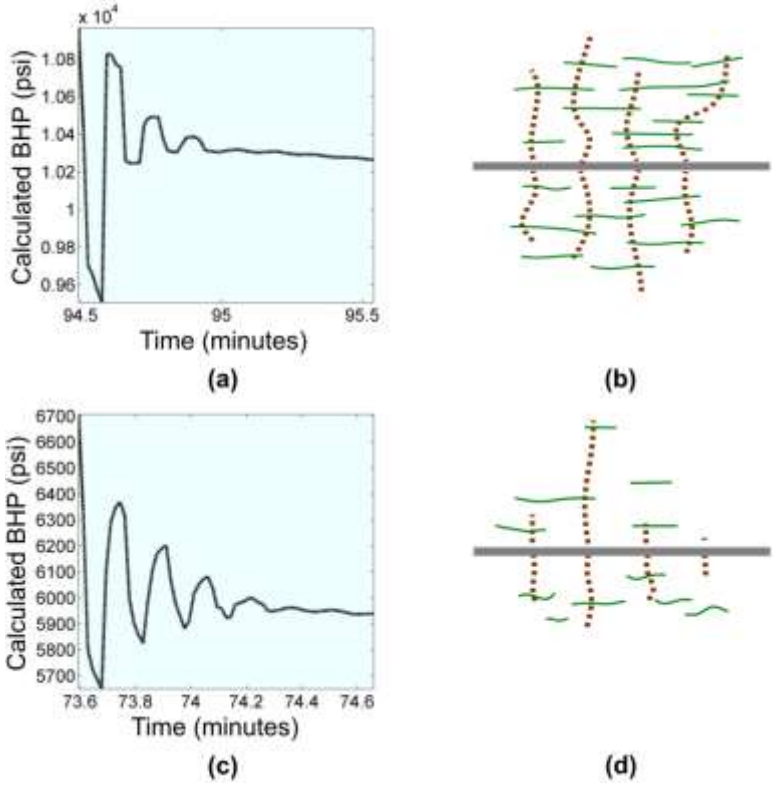

Figure 6: Typical water hammer response with (a) high decay and (c) low decay as well as possible reasons based on our hypothesis (b) and (d).

While exhaustive fluid transient modeling and evaluation techniques have been available for a while (Holzhausen et al. 1988), we use a simple decay rate modeling approach using an exponential decline model to compute the rates of decay in energy observed at pump shutdown for each of the completed stages for two separate wells under study. However, before possible application, one major issue needs to be resolved in relation to behavior of pressure response based on corresponding flow rate variability. While a sharp drop in flow rate or multiple drops followed by short periods of stable flow is desirable for generating sharp water hammer response for modeling, due to non-applicability of typical diagnostic techniques useful with vertical completions, the shutdown procedure for pumps during completion of long lateral multi-stage completions can be quite random. This results in some highly skewed pressure transients which do not allow for easy decay rate computations. In order to resolve this issue a simple de-trending operation is carried out using a polynomial fitting approach. The first step is to fit a second order polynomial to the available data and to subtract the resulting polynomial from the actual data. A secondary higher order polynomial based smoothening step is also used to get a smooth sinusoidal response for modeling. The steps can me mathematically represented as follows:

$$X_{filter\,1} = X - X_{fit\,1} \tag{1}$$

$$X_{filter\,2} = X_{fit\,2} \tag{2}$$

Here subscripts 'filter 1' and 'filter 2' represent filtered data based on the 2nd order and higher order polynomial fitting applied sequentially. The subscripts 'fit 1' and 'fit 2' represent the fitted data from the said procedure. Figure 7 shows the results of this fitting process for two cases; one with a good water hammer response and another with a skewed response. The model used is a sinusoidal pressure response model with an exponential decay. The modeling parameters include the initial amplitude (A), phase (φ) of the response and the decay rate (λ). A standard Evolutionary Algorithm approach is used to minimize the optimization function (CF) which is defined as:

$$X_m = A \times e^{-\lambda \times t} \times \cos\left(2 \times \pi \times \frac{1}{\left[2 \times \frac{1}{f_s} \times Period\right]} \times t + \phi\right) \tag{3}$$

$$CF = \sum_{t=T_{st}}^{T_{end}} \left(X_m - X_{filter\,2}\right)^2 \tag{4}$$

Where T_{st} and T_{end} are the starting and end time stamps which contain the pressure response being modeled. The Period for modeling purposes is extracted from the actual pressure response data. This is done by first identifying all the periods within the identified response. The periods can vary with time due to behavior or the system with time and therefore, a centroid of the periodicity distribution is identified and used in the model.

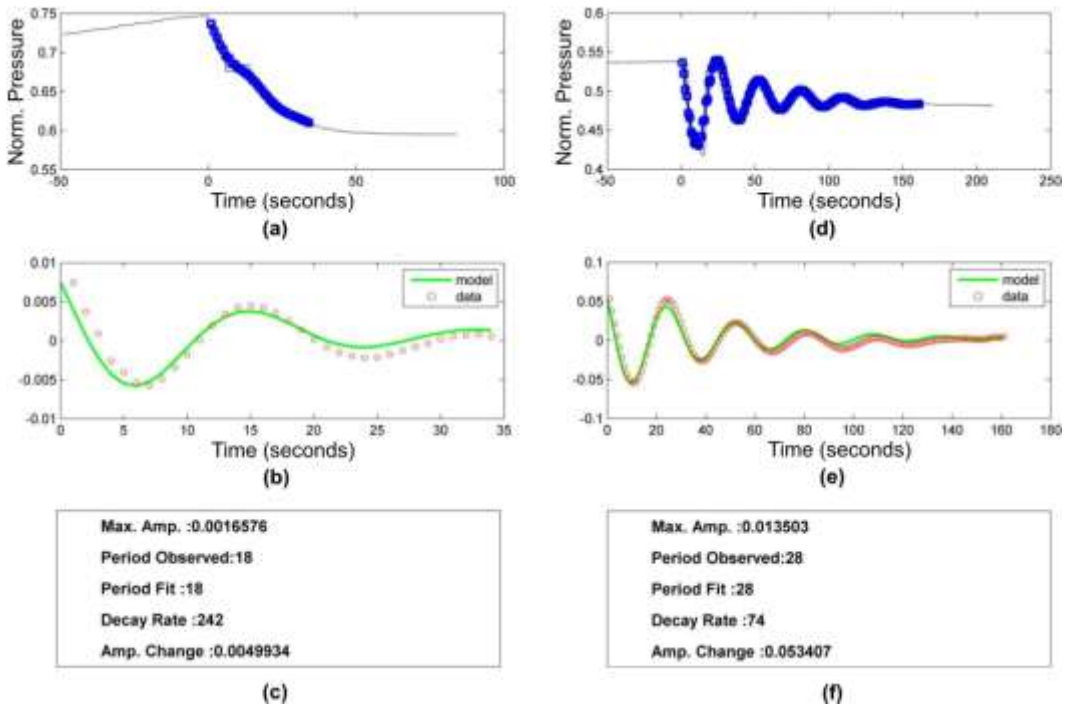

Figure 7 Typical modeling results showing (a) actual data, (b) model fit and (c) modeling results for a skewed pressure response test case and the (d) actual data, (e) model fit and (f) modeling results for a good pressure response case.

This analysis was conducted for the first 26 stages out of the 27 for well 6H and for the first 26 stages out of the 28 for well 8H. First we highlight the modeled decay rate (λ) for all of the stages analyzed in Figure 8.

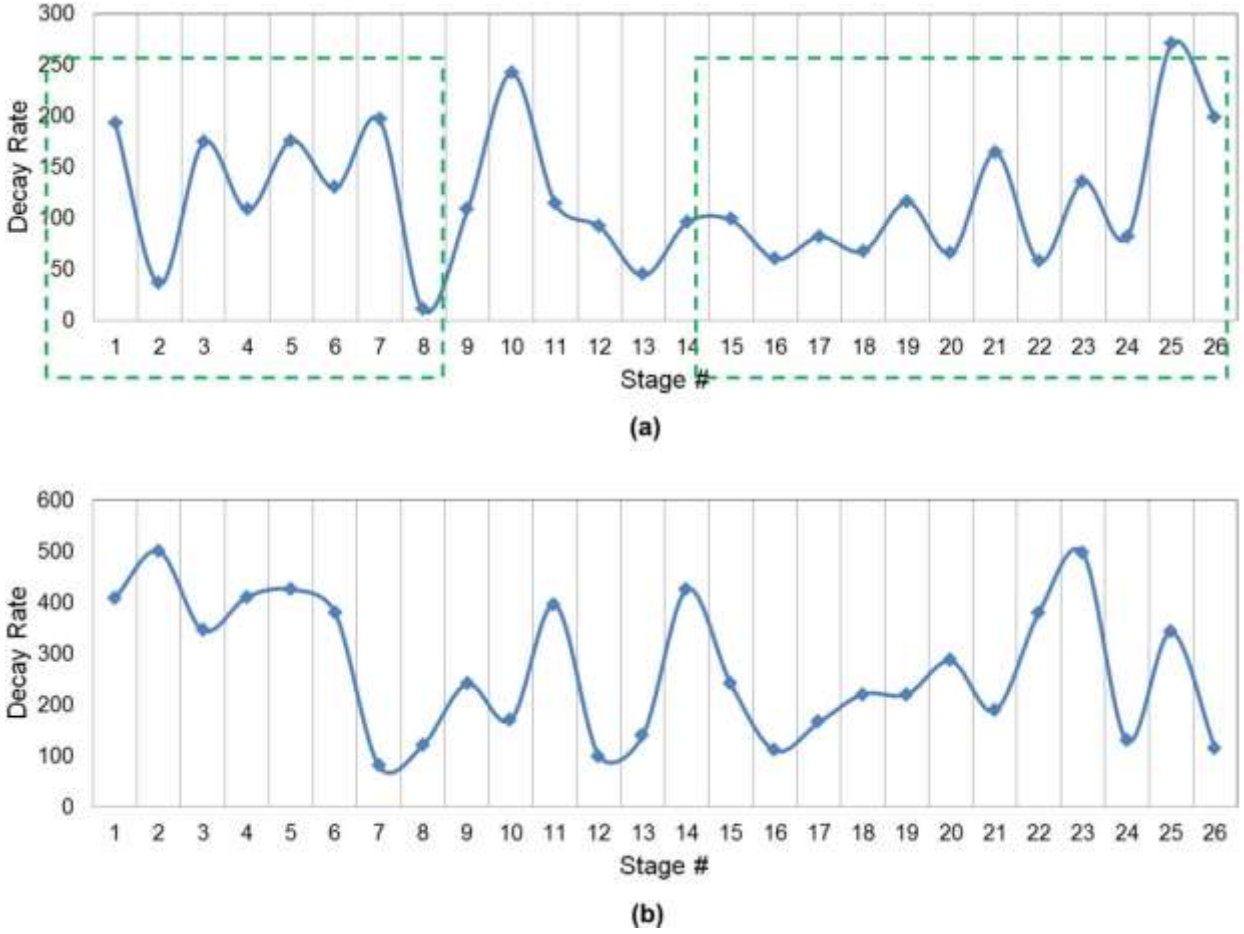

Figure 8: Stage wise decay rate distribution for (a) 6H and (b) 8H.

We can clearly see a discernable trend of odd stages having a higher decay rate compared to the corresponding even stages barring for stages 10 through 14 for well 6H. We do note that the pressure response observed for stages 10 through 13 follow the skewed behavior observed in Figure 5a. This indicates that the observed discrepancy could be a result of modeling failure and not an actual indicator of decay in pressure response. We note that the only other stage where this behavior is observed in stage 26. The average decay rates for the odd and even stages evaluated for well 6H is 143 and 95 respectively while for well 8H is 307 and 334 respectively. Therefore the percentage differential between the odd and even stages for well 6H is much higher (33% higher for odd compared to even) compared to well 8H (8% lower). Also the discernable trend highlighted for well 6H is missing for the results for well 8H. In order to validate the decay models derived using this methodology, we map the model periods (Eq. 3) for the wells and we observed that in general, the period tended to decrease with increasing stage number (lower measured depth) which is as per expectation. Slight variability could be a result of multiple factors

including impact of fractures and inter stage isolation issues. Figure 9 shows the period mapped for the first 26 stages for well 6H to highlight this observation.

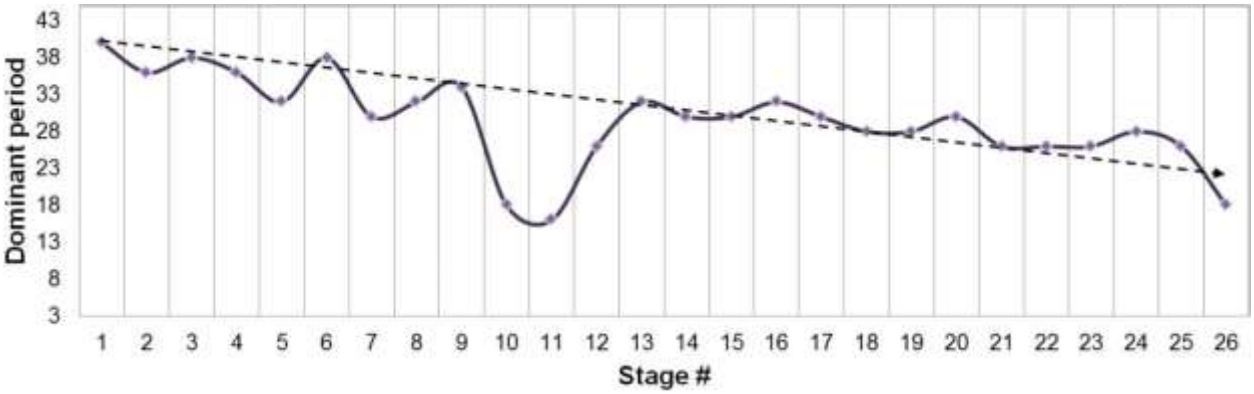

Figure 9: Dominant Period mapped as used for modeling for well 6H across stages 1 through 26.

Post Completion Well Production Performance

We evaluate the production performance of both the wells (6H & 8H) under study. Figure 10 shows the production profiles observed in the first 8 months of operation. The inserts highlight exponential decline functions fitted to relatively clean portions of the profiles (3 month onwards) to understand the decline behavior for these two wells. More robust decline curve analysis tools were not used to limited temporal span in available data. We observe reasonably good fits for both the wells.

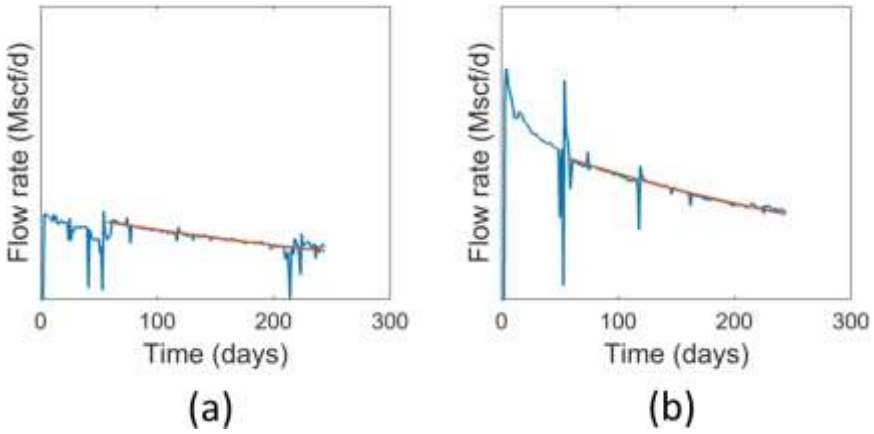

Figure 10: Production profiles for two Marcellus wells.

From our analysis, we find a lower exponential decline rate for well 6H (-0.0022) compared to well 8H (-0.0028). This is despite the fact that well 8H had higher proppant per foot of lateral pumped during completion and it also had access to a larger drainage volume of the reservoir due to the presence of a single well on its left flank compared to well 6H which has wells 8H and 4H flanking it on either side. This

indicates better long term productivity due to lower decline rate thanks to a potentially larger SRV per foot of lateral available for well 6H.

Upscaled field test at the HFTS – Permian Basin

Given the positive production results from applying Variable Rate Fracturing in the Marcellus, we have implemented a scaled up test in another shale formation. The formation in which this test was performed is the Wolfcamp formation in the Permian Basin. As part of the Hydraulic Fracturing Test Site (HFTS), we implemented the VRF design in every stage of an entire well as shown in Figure 11, and will compare production results with its adjacent well, and other offset wells, which have been stimulated in a conventional, constant pump rate approach. In addition to rapidly changing the pump rate in the pad, we have added rate changes throughout the entire treatment, including the proppant stages. We also tested various attributes of the rapid pump rate changes, such as the frequency, duration, and amplitude of each rate change. This was done to determine which rate change parameters have the greatest impact on opening additional perforations and creating additional fractures for increased production.

Unlike the Marcellus shale, which is mostly dry and wet gas, the Wolfcamp formation is an oil shale. We expect the results from the Wolfcamp testing to be positive as well given similar completion type (plug & perf, cemented casing), thus proving that the VRF approach works in both gas and oil shales, which encompasses the majority of US shale formations.

Implementation of the VRF in the Wolfcamp formation and the associated diagnostics were funded by the HFTS project, thus the data and results stemming from that test is confidential to the HFTS project. However, the results will become available once the confidentiality period expires.

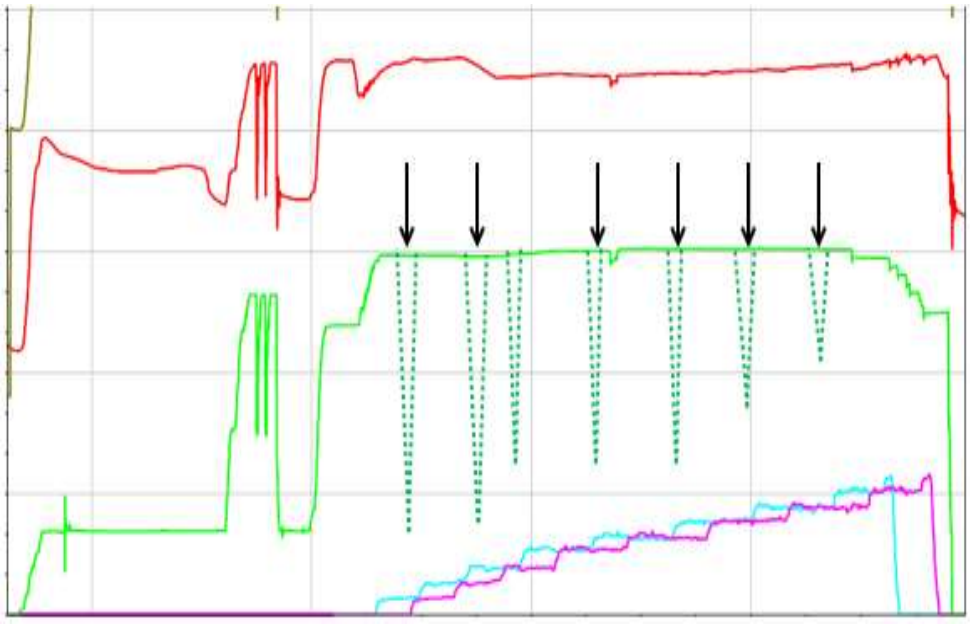

Figure 11: Plot showing surface treatment parameters during fracturing. Green curve is pump rate. Rapid rate changes are implemented in the pad stage, and the black arrows

show planned rapid rate changes implemented throughout the entire treatment. Red curve is pressure, blue and purple curves show surface and bottomhole proppant concentrations.

Conclusions

Correlations of fluid pump rate, microseismic data, and production data have led us to investigate a new hydraulic fracture design in which the fluid pump rate is rapidly changed to induce a pressure pulse leading to the following effects as determined through data analysis:

1. Pump fluctuations lead to increased microseismic emissions
2. Increased microseismic emissions correlate well with increased production
3. Rapid rate fluctuations induce a pressure pulse that tends to open previously unopened perforations and increase fracture complexity
4. Rapid rate fluctuations added to the frac design have shown to increase production by 18% as compared to stages with a frac design that did not include rapid rate fluctuations

Acknowledgements

We would like to thank RPSEA for providing funding for this research project. In addition, we also express our thanks to WPX Energy for providing substantial cost sharing, data, and wells of opportunity.

References

[1] Ciezobka, J., and I. Salehi. "Controlled Hydraulic Fracturing of Naturally Fractured Shales–a Case Study in the Marcellus Shale Examining How to Identify and Exploit Natural Fractures." Paper SPE 164524 presented at the SPE Unconventional Resources Conference, The Woodlands, Texas, USA. 2013.

[2] Ciezobka, J. - Marcellus Shale Gas Project Final Report, RPSEA 09122-04.FINAL – May 10, 2013, http://www.netl.doe.gov/File%20Library/Research/Oil-Gas/Natural%20Gas/shale%20gas/09122-04-final-report.pdf

[3] Holzhausen, G. R., Egan, H. N., Baker, G., Gomez, J. 1988. Characterization of Hydraulic Fractures using Fluid Transients. Project Report [5086-211-1371], Gas Research Institute, Chicago, Illinois (May 1988).

Appendix B: Hydraulic Fracture Test Site (HFTS)

Appendix BA: Hydraulic Fracture Test Site (HFTS) – Program Strategy Report

Abstract

The Hydraulic Fracturing Test Site (HFTS) is a proposed field-based hydraulic fracturing research program for horizontal shale wells with overall objectives of:

- Minimizing potential environmental impacts
- Improving performance and cost efficiency
- Demonstrating safe and reliable operations

Factors such as the evolution of hydraulic fracturing technology, its importance to the global energy market, and the remaining questions regarding environmental impact, performance, efficiency, and safety necessitate the need for advanced technology to adequately characterize, evaluate, and improve the effectiveness of the individual fracture stages. A large, comprehensive hydraulic fracturing research program like the Multi-Site Hydraulic Fracture Diagnostics Project (M-Site Project) in Colorado that was conducted in vertical wells by the Gas Research Institute and Department of Energy in the 1990s has not been performed in long, multi-stage horizontal shale wells.

Prolific volumes of shale gas are being produced. And yet it is well known that not all fracture stages contribute equally to gas production. In many cases, the majority of production in a horizontal well comes from a subset of the total stages treated. There is substantial room for more understanding of the cause and effect relationships between fracture design and more efficient hydrocarbon production in horizontal shale wells. Furthermore, minimization and ultimate elimination of the perceived environmental impacts of hydraulic fracturing needs to be addressed and field verified.

The HFTS program is being developed in three phases.

Phase I – Planning: This phase involves upfront industry interaction to determine their interest in the program, to assess industry research priorities, and to align on the contents of the Program Strategy Report. Planning activities and generation of the final report were funded by the Research Partnership to Secure Energy for America.

Three workshops were held by GTI with industry operators and service companies.

a) April 2013 in Houston, TX

b) May 2013 in Pittsburgh, PA

c) July 2013 an Online Webinar

Thirty-seven hydraulic fracturing experts from 22 operating and service companies participated.

The workshops resulted in the identification of the intent, scope, and value of the HFTS program. Hydraulic fracturing research needs were prioritized; a preliminary program mission, objectives, design, participation,

budget, and schedule was established; an Advisory Board and a Technical Review Committee were started to guide the program; and alignment was reached on the need for the second phase of the project to help define the experimental design for HFTS.

Phase II – Research and Development (R&D) Assessment and Data Review: This phase involves a baseline study to assess the state of the hydraulic fracturing R&D, the availability of data, and the applicability of that data to help define the experimental design of HFTS. A proposal for Phase II has been developed. The project is intended to be completed by 2Q 2014.

Phase III – Implementation: This phase will include the enrollment of participants, the raising of sufficient funding to launch the program, determination of the location and design of the test site itself, and the execution of testing experiments. Phase III is intended to be launched by end of 2014.

Executive Summary

Given the economic importance of hydraulic fracturing and remaining questions regarding environmental impact, performance, efficiency, and safety; Gas Technology Institute (GTI) has proposed the development of a new field-based hydraulic fracturing research program and facility called the Hydraulic Fracturing Test Site (HFTS). Hydraulic fracturing has proven to be an effective form of reservoir stimulation, however, it is known that not all fracture stages contribute equally to production. All fracture stages might contribute to total production, but in many cases the majority of production in a horizontal well comes from a few fracture stages. The purpose of HFTS is to improve shale resource recovery through the evaluation and development of new methods and technologies for increasing the efficiency of the hydraulic fracturing process that leads to fewer wells with higher production output per well, higher cost efficiency, exceptional reliability and safeguards, and smaller environmental impacts.

Under the sponsorship of the Research Partnership to Secure Energy for America (RPSEA), funding was provided for the development of this Program Strategy Report for HFTS. Successful large scale, collaborative hydraulic fracturing research projects have been conducted in the past in vertical wells. Such projects have contributed substantially to increases in hydraulic fracturing effectiveness. However, a large, comprehensive hydraulic fracturing research program of this nature has not been performed in long, multi-stage horizontal shale wells.

A series of consultations with hydraulic fracturing industry experts were conducted in 2013. Three workshops were held by GTI with industry operators and service companies.

1) April 2013 in Houston, TX
2) May 2013 in Pittsburgh, PA
3) July 2013 an Online Webinar

Thirty-seven hydraulic fracturing experts from 22 operating and service companies participated. The participants included experts from:

- Baker Hughes
- BP
- Chesapeake Energy Corporation
- Chevron
- CONSOL Energy
- Core Laboratories (ProTechnics)
- Desert Research Institute
- East Management Services
- EOG Resources, Inc.
- EQT Corporation
- ExxonMobil
- GTI
- GDF Suez
- Hess Corporation
- Pinnacle – a Halliburton Company
- Pitts Oil
- National Oilwell Varco
- Range Resources
- Schlumberger
- Shell Exploration & Production
- Southwestern Energy
- Statoil
- Universal Well Services

These workshops solicited industry feedback regarding the intent, scope, and value of the HFTS program. Industry hydraulic fracturing research needs were identified and prioritized; a preliminary program mission, objectives, design, participation, budget, and schedule was established; an Advisory Board and a Technical Review Committee was started to guide the program; and alignment was reached on the need for a second phase of the project to help inform the experimental design for HFTS.

The following hydraulic fracturing efficiency testing needs were identified:

1) Effects of fluid injection points on fracture geometry (number of perforations, clusters, and spacing, etc.)
2) Effects of natural fractures on fracture geometry (arrest, arrest and offset, pass through, etc.)
3) Effects of connected fracture network conductivity on stimulation efficiency
4) Effects of pump rates on fracture geometry (high, low, varying, etc.)
5) Effects of fracture interference on fracture geometry (stress shadowing, zipper fracture, simultaneous fracture, etc.)
6) Effects of created fracture network connectivity on stimulation efficiency
7) Effects of formation lithology on fracture geometry (clay content, brittleness, etc.)
8) Effects of created fracture network complexity on stimulation efficiency
9) Understanding fracture height growth (landing point, reservoir homogeneity, composite layering, etc.)
10) Effects of fluid properties on fracture geometry (viscosity, foams, surfactants, etc.)
11) Effects of proppants on fracture geometry (diversion, bridging, banking, etc.)

12) Effects of stress anisotropy on fracture geometry (vertical confinement, fracture network width/length, etc.)

13) Testing alternative stimulation techniques (i.e. propellant [controlled explosives], liquefied petroleum gas [LPG], thermal stress cracking from cryogenic fluids, etc.)

The Program Strategy Report outlines a three-phased project plan.

Phase I – Planning: This phase involved upfront industry interaction to determine industry interest in the program, to assess industry research priorities, and to align on the contents of the Program Strategy Report.

Phase II – R&D Assessment and Data Review: This phase involves a baseline study to assess the state of the hydraulic fracturing R&D, the availability of data, and the applicability of that data to inform the design of HFTS.

Phase III – Implementation: This phase includes the enrollment of participants, the raising of sufficient funding to launch the program, determination of the location and design of the test site itself, and the execution of testing experiments.

The site concept for HFTS envisions a central horizontal treatment well flanked by two or more observation wells spaced optimally apart for research. A number of field experiments are planned within the horizontal wells with each drilled and instrumented for specific research purposes. The well configuration is conceptual and subject to final planning by participants.

A series of controlled hydraulic fracturing treatment experiments will be conducted. Each stage will have an individual set of research objectives. The formation will be fully characterized with core data, well logs, drill cuttings, and other formation evaluation techniques, and fully instrumented with sensors and monitoring equipment both in the borehole, outside the casing, and at the surface. The findings of this program will be deduced through the development of cause-and-effect relationships between the inherent properties of the host rock and resulting production stimulation. This will allow many of the results to be transferable to other shale resources.

Anticipated benefits include:

1) Development of advanced technologies that improve safety, lower environmental impacts, and reduce materials and energy required per unit of energy produced.
2) Determination of potential health and environmental consequences of hydraulic fracturing to air, land, and water resources and development of mitigation strategies.
3) Demonstration of safe and reliable hydraulic fracturing operations.
4) Development of optimal instrumentation to reduce the margin of error in interpretation of monitoring and measuring of environmental conditions pre- and post-stimulation.
5) Characterization, measurement, evaluation of hydraulic fracturing efficiency.
6) Improvements to fracture design and evaluation of Stimulated Reservoir Volume (SRV).
7) Assessment of created fracture conductivity as measured with flow between two wells connected by a fracture.

8) Early detection of fracture effectiveness and development of methods and techniques for real-time control of fracturing effectiveness.
9) Development of advanced technologies and methods to maximize resource recovery from each hydraulic fracturing treatment while minimizing the material and energy input requirements
10) Substitution of less effective materials or methods with those more effective.
11) Development of optimal instrumentation to reduce the margin of error in interpretation of monitoring and measuring of created fractures.
12) Evaluation of seismic and other fracture diagnostic techniques.
13) Hydraulic fracture model verification and calibration. Determining spatial and temporal fracture network creation and validate against model.
14) Measurement of effectiveness of downhole perforating techniques.
15) Evaluation of hydraulic fracture directional changes due to stress reorientation.

The cost of a comprehensive program will be a function of the detailed plan, drilling costs, and the number and type of experiments anticipated and is estimated to be approximately $34.5 million with two to four years of performance. It is anticipated that operator and service company funding will be augmented with funds received from various government entities such as the US Departments of Energy and Interior, RPSEA, research institutes and other environmental organizations. A tiered funding mechanism is being considered for operators, whereby funding contribution levels coincide with an operator's opportunity to apply the benefits of the results to its asset portfolio. Details of participation commitment will be determined as the program moves forward into the implementation phase.

Acknowledgements

GTI would like to thank the Research Partnership to Secure Energy for America (RPSEA) and acknowledge the funding it contributed through its Onshore Unconventional Gas Program, which made this HFTS Program Strategy Report possible.
GTI would also like to thank the many industry professionals from operators and services companies that participated in workshops and provided their expert input and feedback, which has informed the content of this document.

Introduction

Context

Hydraulic fracturing has evolved from a single treatment in a vertical well to multiple treatments in a horizontal well with substantial success. Since the earliest applications in the 1940's, it has played a vital role in increasing U.S. energy production—making shale formations commercially viable, positioning the U.S. as the largest natural gas producer in the world, and enabling recent annual increases in U.S. oil production.

Figure 1: Hydraulic Fracturing Operation

Hydraulic fracturing has contributed toward reducing the nation's cost of energy to the consumer, increasing energy security (the natural gas and petroleum trade balance), reducing the nation's CO_2 emissions (displacement of coal for power generation), and potentially revitalizing the nation's manufacturing base (by lowering fuel and feedstock costs). The economic benefits published in the Oxford Energy Forum are summarized in Table 1.

Table 1: Economic Benefits of Hydraulic Fracturing

Economic Benefits of Hydraulic Fracturing	
Global hydraulic fracturing revenues	• $37 B in 2012 • $47.6 B in 2013 (Source: Schlumberger)
U.S. and Canada market share	90%
U.S. employment supported by shale gas industry	• 600,000 jobs in 2010 • 870,000 jobs projected by 2015
Shale gas contribution to U.S. Gross Domestic Product	• $76.9 B in 2010 • $118 B by 2015 • $231 B in 2035 (2010 dollars)

Nonetheless, some critical issues with significant economic and environmental consequences remain unresolved: Are we getting everything we can out of every well? Are we maximizing the effectiveness of each fracture stage? Are we stimulating the maximum volume of reservoir with the least volume of material and energy requirements? What more can be done to ensure safe operations? Are we doing all we can to minimize environmental impact?

Enhancing hydraulic fracturing efficiency, reducing costs, exemplifying safe operations, and minimizing adverse environmental impacts are key challenges in development of unconventional resources. Achieving next-level advancement in these areas will require effective resource recovery from each hydraulic

fracturing stage, while minimizing the material and energy input requirements. Better understanding of the fracturing process and advanced technologies, materials, and methods will lead to further optimization.

Hydraulic Fracturing Efficiency

While hydraulic fracturing is an effective form of production stimulation, it is known that not all fracture stages contribute equally to production. Although each fracture stage might contribute to total production, in many cases the majority of production in a horizontal well comes from a few fracture stages. Figure 2 shows an example of Stimulated Reservoir Volume and Production Log Results for a single well in a multi-well horizontal pad. Results of the production log indicated that 50% of production contribution in the logged well came from 3 fracture stages out of 13 pumped. Many similar cases have been reported by the industry indicating that significant improvement in stimulation efficiency is truly an imperative. Advanced technology to adequately characterize, evaluate, and improve the effectiveness of individual hydraulic fracture stages in horizontal wells is critical to improving cost efficiency, demonstrating safe operations, and minimizing environmental impacts.

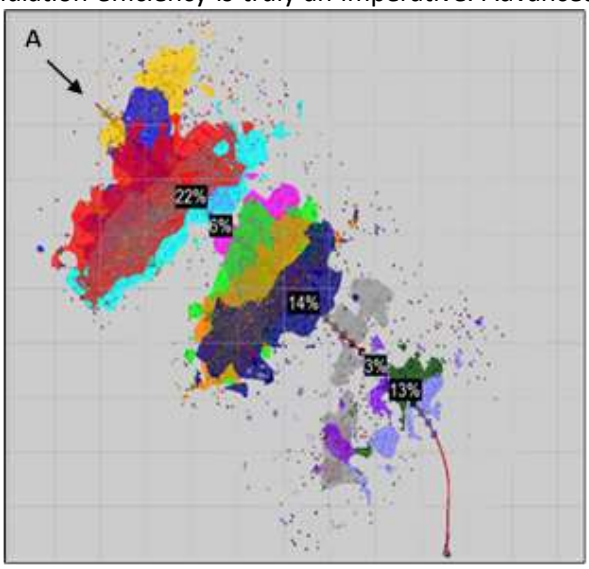

Figure 2: Example of Stimulated Reservoir Volume and Production Log Results for a single well (A) in a multi-well horizontal pad. Results of the production log indicated 50% of production contribution in the logged well came from 3 fracture stages out of 13 pumped.

In the 1990s, Gas Research Institute (GRI) conducted hydraulic fracturing research projects in vertical wells including the Mounds Drill Cuttings Injection Project in Oklahoma, the Four-staged Field Experiments in Texas and Wyoming, and the Multi-Site Hydraulic Fracture Diagnostics Project (M-Site Project) in Colorado. The collaborative M-Site Project, a test site jointly funded with U.S. Department of Energy (DOE), had the objective of performing field-scale experiments and gathering high-quality, independent diagnostic data that would result in increased accuracy in measuring hydraulic fracture dimensions and characterizing the hydraulic fracturing processes. The project led to advancements in fracture diagnostics hardware and data analysis methodologies to the point where commercial hydraulic fracture mapping capabilities were established.

The M-Site project as well as the Mounds and Four-staged Field Experiments projects was conducted in vertical wells. Each field experiment contributed substantially to better understanding of the hydraulic fracturing process and fracturing dynamics, thus enabling future fracture designs that were much more effective. A large, comprehensive hydraulic fracturing research program of this nature has not been performed in long, multi-stage horizontal shale wells.

Hydraulic Fracturing Test Site (HFTS) for Environmental Safety and Stimulation Efficiency

The HFTS program is needed to provide a clearer understanding of the fracturing dynamics key to controlling fracture dimensions and vital to the productivity of fracture networks created in long horizontal wells. To

improve well productivity and reduce environmental footprint, focus will be on improving the efficacy of individual fracture stages. The end result will be improved understanding of the fracturing process and identification of needed technologies and methods to enhance well productivity through more effective hydraulic fracturing treatments that require less water and resources per unit of energy produced. Improving the effectiveness of individual hydraulic fracture stages will lead to cost efficiency, maintaining safe operations, and minimizing environmental impacts. Learnings from this effort will advance operations for all resource production using hydraulic fracturing technology, including shale gas and shale oil.

Phase I – Planning

This Program Strategy Report for HFTS is the output of the first phase of the development process. The strategic planning was made possible through funding from RPSEA. Planning activities included industry workshops, consortia recruitment and coordination, feedback analysis and interpretation, planning meetings and teleconferences, and writing of this report.

Industry Workshops

To evaluate the industry need for field testing of hydraulic fracturing techniques and technologies for shale oil and/or gas reservoirs, GTI invited a committee of producing and service companies involved in development of shale resources to participate in a series of planning workshops. GTI hosted three workshops in the first half of 2013 (Table 2) – one in Houston, one in Pittsburgh, and a webinar – to align on program scope, discuss desired experiments and site selection considerations, refine the goals and objectives, and identify research priorities.

Table 2: HFTS Planning Workshops

HFTS Planning Workshops	
1. Houston	March 20, 2013
2. Pittsburgh	April 16, 2013
3. Webinar	July 2, 2013

Twenty-two participants, comprised of research and industry representatives attended each of the workshops facilitated and mediated by GTI. Involvement in the online workshop grew to over 70 participants. The companies represented include:

- Baker Hughes
- BP
- Chesapeake Energy Corporation
- Chevron
- CONSOL Energy
- Core Laboratories (ProTechnics)
- Desert Research Institute
- East Management Services
- EOG Resources, Inc.
- EQT Corporation
- ExxonMobil
- GTI

Mission

The mission of the HFTS program is to increase shale environmental safety and stimulation efficiency.

This will be accomplished through the evaluation and development of new methods and technologies that leads to fewer wells drilled while enabling higher production output per well, higher cost efficiency, greater reliability and safeguards, and lower environmental impact.

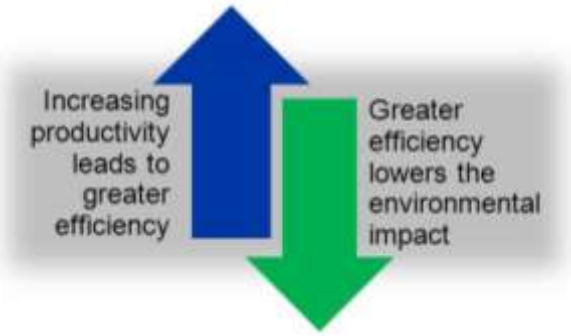

Figure 3: Elements of the HFTS Mission

Program Objectives

The objectives of this program include:

1) Improve fracture design.
2) Early detection of fracture effectiveness.
3) Develop methods and techniques for real-time control of fracturing processes.
4) Optimal instrumentation to reduce the margin of error in interpretation of monitoring/measuring.
5) Evaluate new technologies for increasing the efficiency of fracture treatments.
6) Demonstrate safe and reliable hydraulic fracturing operations.
7) Determine environmental impacts and develop mitigation strategies.
8) Quantify the value of diagnostics, testing, data collection, and analysis.

Intended Outcomes

Anticipated outcomes from the work undertaken in this program will result in ability to:

- Establish the geometry of the created fracture network by utilizing current fracture analysis techniques and confirming with through-fracture cores.
- Determine whether or not injection pressure provides a reliable method to assess confinement.
- Compile guidelines for operational practices that lead to safe, efficient, and environmentally friendly stimulation techniques.
- Determine if micro-seismic imaging can provide reliable measurements of connected fracture dimensions and establish guidelines for such analysis.
- Demonstrate that tiltmeters, both surface and down-hole, in conjunction with microseismic imaging can provide reliable information of fracture dimensions; specifically fracture height.
- Characterize the created fractures near and far-field from the wellbore to determine their flow capacity.
- Calibrate current and future 3D fracture models to improve understanding of fracture behavior under the prevailing geological and operating conditions.
- Create a workflow for optimizing fracturing treatments in real time by utilizing 3D models with constantly updated attributes.
- Determine optimal wellbore spacing based on accurate dimensions of created high-flow capacity fracture networks.
- Determine the fate of the unrecovered fracturing fluids through measurements and coring

HFTS Research Priorities

Results of the three industry workshops conducted by GTI identified the following hydraulic fracturing efficiency testing needs.

1) Effects of fluid injection points on fracture geometry (number of perforations, clusters, and spacing, etc.)
2) Effects of natural fractures on fracture geometry (arrest, arrest and offset, pass through, etc.)
3) Effects of pump rates on fracture geometry (high, low, varying, etc.)
4) Effects of connected fracture network conductivity on stimulation efficiency
5) Effects of fracture interference on fracture geometry (stress shadowing, zipper fracture, simultaneous fracture, etc.)
6) Effects of created fracture network connectivity on stimulation efficiency
7) Effects of formation lithology on fracture geometry (clay content, brittleness, etc.)
8) Effects of created fracture network complexity on stimulation efficiency
9) Effects of fluid properties on fracture geometry (viscosity, foams, surfactants, etc.)
10) Understanding fracture height growth (landing point, reservoir homogeneity, composite layering, etc.)
11) Effects of proppants on fracture geometry (diversion, bridging, banking, etc.)
12) Effects of stress anisotropy on fracture geometry (vertical confinement, fracture network width/length, etc.)

13) Testing alternative stimulation techniques (i.e. propellant [controlled explosives], liquefied petroleum gas [LPG], thermal stress cracking from cryogenic fluids, etc.)

Phase II – R&D Assessment and Data Review

A major point of discussion in the industry workshops was the necessity of HFTS to be cost efficient by avoiding redundant experiments and unnecessary data collection. This can be accomplished by leveraging existing data to establish baseline parameters, to inform the design of experiments for HFTS, and to identify information gaps and where complimentary data sets are valuable. Participants acknowledged the existence of considerable amounts of data from prior hydraulic fracturing research and testing done by research institutes, universities, and industry. However, a comprehensive collection and assessment of that existing hydraulic fracturing R&D and data availability does not exist. Such an assessment would investigate what hydraulic fracturing research has been done, where and by whom, what was accomplished, what data sets are available, and what data are relevant to HFTS.

It was the consensus of the workshop participants that such an assessment helps to inform the design of experiments and site considerations for HFTS and keep costs to a minimum. It was also determined such an assessment is a valuable reference for industry independent of the HFTS program. Therefore, participants recommended a Phase II – R&D Assessment and Data Review project be conducted by GTI. In Phase II, GTI will conduct a comprehensive search to identify prior studies, research, and data sets relevant to advancement of hydraulic fracturing science. This step will identify current technologies and methods so current work under the HFTS will not retrace or duplicate prior work. Gaps in technology and methods that align with participants' needs will become the focus of the experiments considered for the HFTS. Steps to be conducted under this task include:

1) Interviews with participants to identify known research projects and available data
2) Research, review, and compile relevant literature
3) Interview exploration and production companies, service companies, and academia to:
    a. Identify research and data gaps
    b. Inquire data availability
4) Identify relevant data useful to the HFTS project design
5) Develop a searchable database
    a. Establish an agreement with the Society of Petroleum Engineers and create a link with OnePetro for purchase of referenced papers
6) Workshops with the participants to validate data and information gathered and prioritize gaps
7) Summary of information relevant for consideration of the design experiments

Deliverables:

1) Searchable database for participants
2) Summary of relevant data sources for HFTS

Phase III – HFTS Implementation

Program Strategy and Timeline

Based on input from the workshops, a project workflow was designed and presented to the workshop participants. With consideration to comments from the participants the project workflow has been finalized as shown in Figure 4.

This Program Strategy Report concludes Phase I. Phase II is anticipated to be funded and begin at the start of 2014 and last approximately 4 months. Phase III includes enrolling participants, confirming the design of experiments and locating an appropriate site, with the intention of launching the program by the end of 2014.

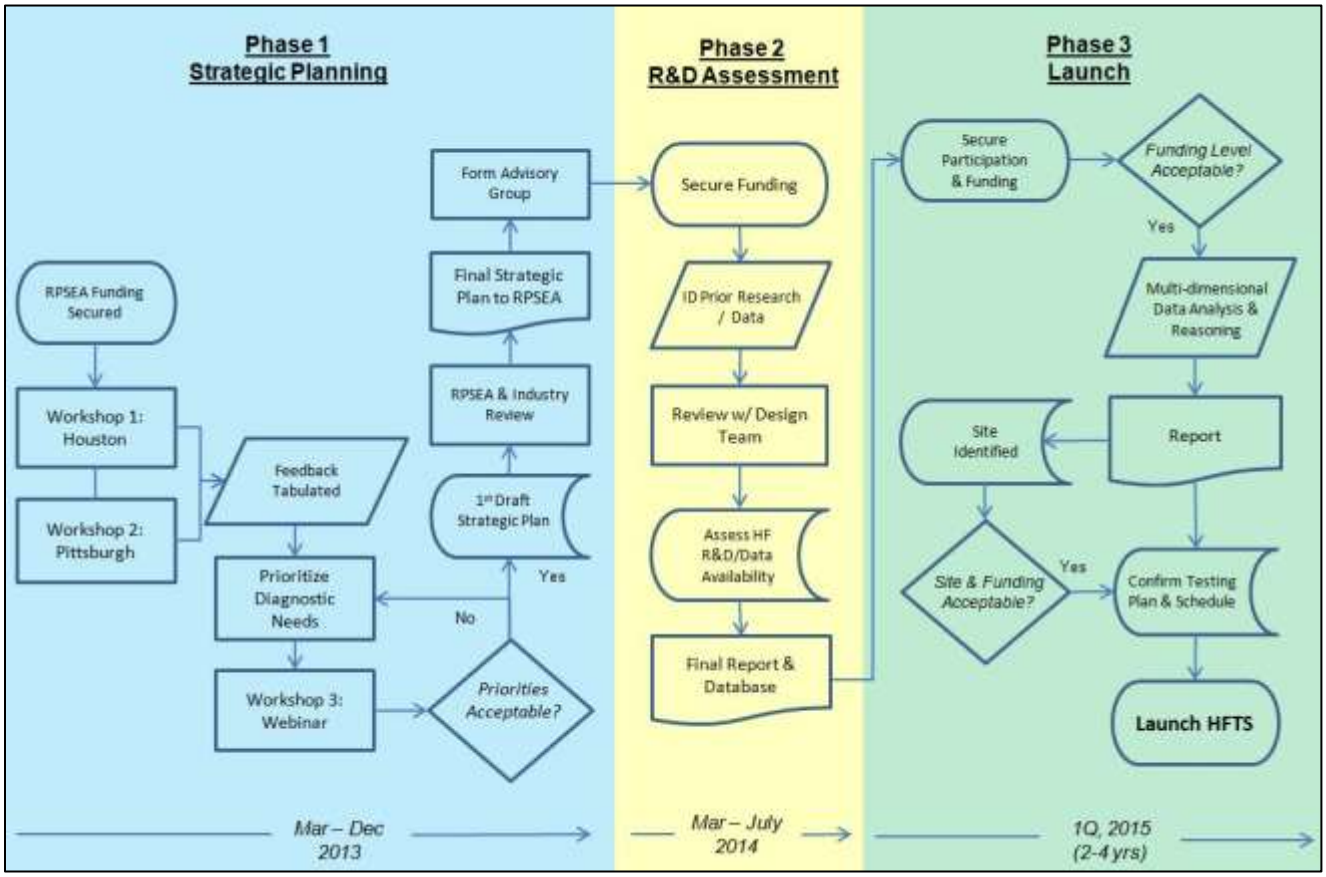

Figure 4: HFTS Program Development Flow Sheet

Advisory Board

Realizing a large scale project of this nature may cost millions of dollars and require substantial commitments of time and resources, participation from a highly recognized, motivated consortium of operators and service companies is essential to ensure the project meets its intended objectives and responds to industry needs. Thus a HFTS Advisory Board is being formed. The role of the HFTS Advisory Board is to set and maintain the direction of the program, site selection, facility and well design.

To expedite decision making, membership will be limited to a maximum ten members. Membership will require written acceptance of a formal invitation and a signed HFTS program participation agreement from the representative company or organization. Selection criteria are based on the level of expertise with hydraulic fracturing, field research, and test wells. Members of the Advisory Board are not yet confirmed. The following industry experts have expressed interest:

1. Paul Huckabee, Shell
2. Karen Olson, Southwestern Energy
3. Kent Perry, RPSEA
4. Norm Warpinski, Pinnacle – A Halliburton Company
5. Iraj Salehi, GTI
6. TBD, Department of Energy

Figure 5 presents the organizational chart for HFTS program development. Overall program management will be performed by Jordan Ciezobka, GTI.

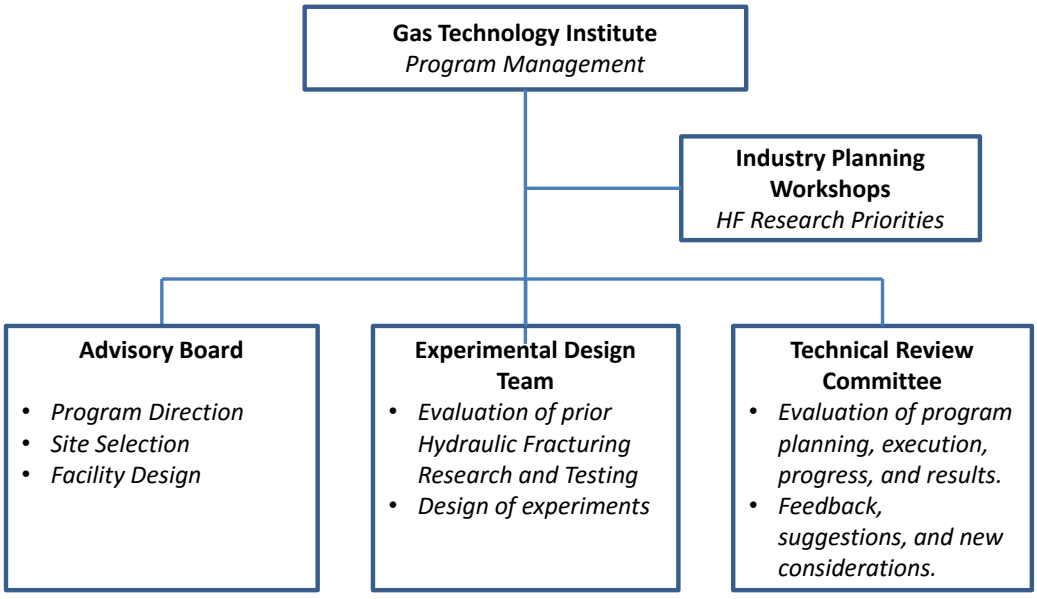

Figure 5: Organizational Chart for HFTS Program Development

Experiment Design Team

The role of the Experiment Design Team is to evaluate the history, results, and lessons from prior hydraulic fracturing research; understand what needs to be done in the HFTS program, and properly design the

research experiments for HFTS. The team will consist of members from GTI and other research organizations with substantial experience with design of experiments. The team will be limited to a maximum ten members. Membership will require written acceptance of a formal invitation and a signed HFTS program participation agreement from the representative company or organization. Selection criteria are based on experience with design of experiments, hydraulic fracturing, and field research. The following organizations are being considered:

1. Operating companies
2. Universities
3. Research institutes
4. National laboratories
5. GTI

Technical Review Committee

The Technical Review Committee is designed for participation from recognized hydraulic fracturing experts from industry, government, non-government, and academia. Its role is to continuously evaluate program planning, execution, progress, and results achieved, and provide feedback, suggestions, and new considerations. A signed HFTS program participation agreement from the representative company or organization is a prerequisite for membership on this committee. The size of the Committee is not limited; however, membership is limited to two represents per company or organization. Advisory Board and Experimental Design Team members are automatically members of the Technical Review Committee. Members are not yet confirmed. The following industry experts have expressed interest:

1) Steve Wolhart, Pinnacle
2) Sanjay Vitthal, Shell
3) Amit Singh, Chevron
4) Mures Zarea, GDF Suez
5) Matt Reeves, Desert Research Institute (DRI)
6) Jordan Ciezobka and Patrick Findle, GTI

Site Selection Considerations

While the geographic location for HFTS is yet to be determined, industry supports the performance of this program in an active producing shale formation so that effectiveness characteristics, such as production per unit volume of fracturing fluid pumped, can be evaluated. Many valuable research experiments can be designed and conducted at a fully controlled field program of this type. The findings of this program will be deduced through the development of cause-and-effect relationships between the inherent properties of the host rock and resulting production stimulation, making many results transferable to other shale resources. Favorable site characteristics were discussed at length in the industry workshops and options are open. Industry feedback on important site considerations included:

- Important to have an operator in an active play with 3D seismic that is willing to operate the site.

- Multiple pay zones to expand experiment options.
- Existing well data in the region to establish a base of reference. Operator experience in the area was seen as very positive attribute.
- A "geologically quiet" area, both structurally and tectonically, is preferred, while it is recognized the characterization of the site will be a prerequisite to successful experimentation.
- A key influencing factor for the final location determination will be favorable site availability and cost considerations.
    - Biggest growth potential (Eagle Ford, Marcellus, Utica, Permian)
    - Depth of reservoir, where to land the lateral, and what properties to consider? Should consider depths in the 6000 - 8000 ft. range because of cost and pressure implications.
- Wet versus dry gas bearing is not considered important, since technical approaches are similar. However,
    - Oil and liquids rich plays are economically popular at this time and currently relevant
    - Eagle Ford, Wolf Camp, Avalon, western Marcellus and Utica - all liquid rich
    - Dry gas may eliminate some complexity
- The Utica would be interesting to increase formation evaluation data and the understanding of the formation's response to hydraulic fracturing.
- Marcellus will continue to be an important play.

The HFTS program can be sited on private, government, or university land each having its own set of advantages and disadvantages. Land for the site can be bought, leased, or donated into the program. It may be possible for an owner to donate land to the HFTS program and claim tax benefits for the donation.

Research Plan Considerations

A number of field experiments are planned within horizontal wells, each drilled for specific research purposes. The well locations and configuration for experimentation have not been determined and are subject to final planning, but are illustrated conceptually in Figure 6. A central treatment well flanked on either side by observation wells is shown. Observation wells above and below the treatment well could also be considered as well as cored wells intersecting through the fractured zones. A series of controlled hydraulic fracturing experiments will be conducted. Each stage will have an individual set of research objectives. The formation will be fully characterized with core data, well logs, drill cuttings and other formation evaluation techniques and fully instrumented with sensors and monitoring equipment both in the borehole, outside the casing, and at the surface.

The research plan for HFTS will follow a 3 step schedule starting with site planning and characterization; followed by well design, drilling and instrumentation; and finally design and commencement of fracture stimulation experiments. Development of the research plan will be driven by the Advisory Board and will involve input from the Experimental Design Team and Technical Review Committee.

1. **Site Planning and Characterization**

Site planning and characterization is devoted to the understanding of inherent formation and reservoir properties, site preparation, and characterization of the geology in terms of tectonic and state of stress. Site characterization will include drilling and casing a vertical well, geophysical and reservoir engineering studies, and data acquisition and interpretation of 3D seismic, cores, and logs to determine how the formation may behave and to define the physical parameters of the site.

If the suitability of the site is confirmed, an inventory of existing environmental conditions will be performed to establish baseline conditions. Surface facilities will be prepared and execution of horizontal well design, drilling and preparation will proceed.

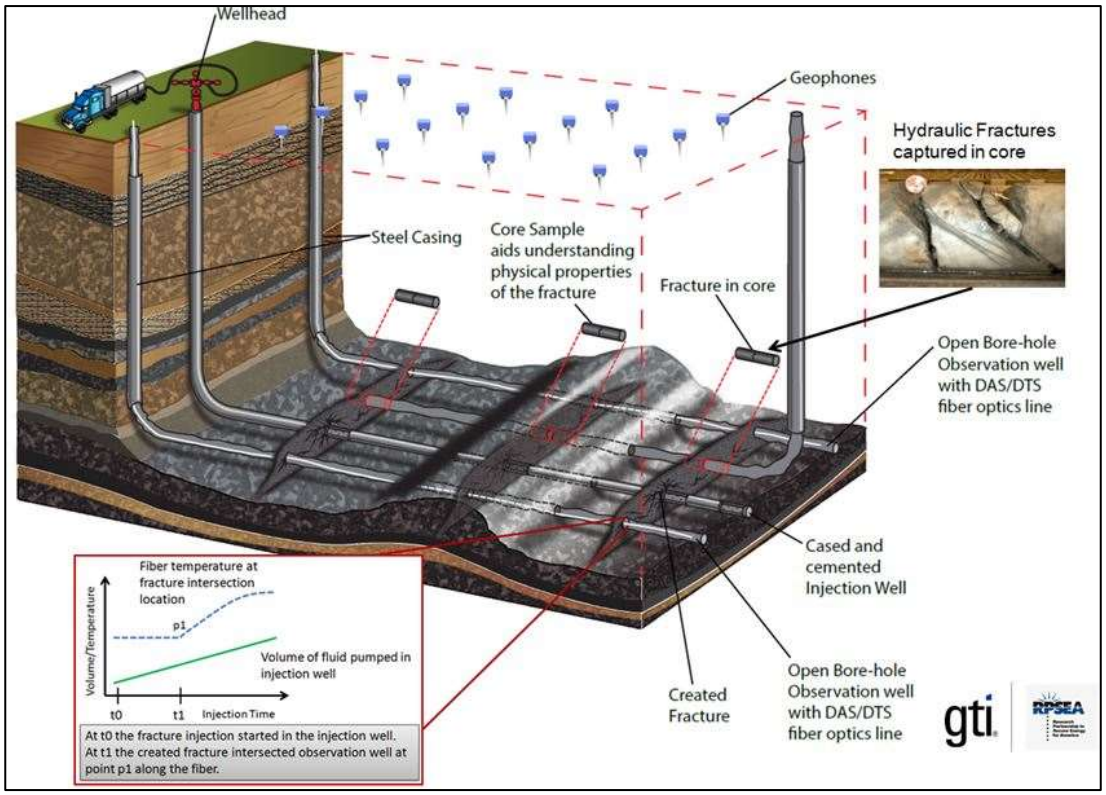

Figure 6: Conceptual Views of the Proposed Site Configuration

2. **Well Design, Drilling, and Instrumentation**

This step is devoted to detailed determination of how many horizontal wells will be drilled, their location, depth, where to land the wells in the formation, and desired well separation or spacing. Wells will be drilled and cased according to a specific schedule that minimizes expenditures while allowing for research and testing to progress.

Necessary surface facilities will be constructed. The site will be fully instrumented at the surface and in the wells to measure and monitor fracture results and potential changes in environmental conditions. HFTS may utilize the following measuring and monitoring instruments:

- Surface and downhole microseismic.
- Seismic hydraulic fracture characterization and coring to establish the ground truth to validate the meaning of signals received.
- Tiltmeter surveys.
- Distributed Temperature Sensing (DTS) and Distributed Acoustic Sensing (DAS)
- Downhole pressure measurements.
- Electrodes to monitor fluid resistivity.
- High precision pressure, rate, and density measurements.
- Integrated long-term data acquisition system and database.
- Air quality monitoring and analysis, including emissions.

3. Experiment Design and Execution

This step is devoted to experiment design, operational planning, and testing of individual experiments. The results of site characterization and assessment of operational constraints will be used to determine the nature and sequence of experiments. Testing operations will commence according to a detailed technical plan and timeline. Data will be collected, assessed, stored, and managed. It is anticipated that data will be distributed broadly to participating companies and academic and scientific institutions for concurrent, comprehensive analysis.

Transferability of Basic Knowledge to All Shale Resources

The findings in this program will be transferable to all shale resources through the development of cause-and-effect relationships between the inherent properties of the host rock, actual fracture properties, and the resulting production data. The approach used at the HFTS is to collect data and perform analysis while augmenting the experimental results with ground-truth measurements, thus reducing ambiguous results that are typically a consequence of inferring fracture attributes through indirect measurements.

The data collected and analysis performed at the HFTS will be validated with real time fracture propagation measurements that are enabled by offset monitoring wells instrumented with optical fiber lines (DTS &DAT). More specifically, the propagating fracture emanating from the injection wellbore during each experiment will be tracked with microseismic surveys and the location and time of arrival at the observation well will be precisely determined. Furthermore, a whole core collected through the created fracture domain will provide indisputable and exact location of the created fractures while allowing measurements of the created fracture attributes including measurements of proppant concentration and type.

We believe the following knowledge and findings will be transferable immediately to other shale formations as wells as other resources that require hydraulic fracturing stimulation:

Developing and Calibrating Complex Fracture Models

Due to deficiencies in our completion and stimulation design tools for Shale resources we often use geometric designs (set number of stages per lateral with a set cluster count per stage) and spreadsheets to design fracture treatments. This translates to using many wells for trial and error of various fracture designs because our models are inadequate, which becomes very expensive and inefficient in the long term. In particular, the fracture models will be updated to reflect ground truth data on:

- Created fracture geometry as governed by rock stresses, elastic and stiffness moduli, and petrophysical properties; thus enabling optimized fracture design based on inherent host rock attributes
- Created fracture geometry resulting from number of injection points (perforations) and spacing, as governed by rock stresses, elastic and stiffness moduli, and petrophysical properties; thus enabling optimal fracture spacing and number of injection points based on inherent host rock properties
- Proppant transport as governed by proppant type and size, injection rate, carrier fluid properties, and host rock properties
    - Proppant concentration in the fracture determined from core analysis; thus enabling optimal design of proppant type, concentration, and ramping strategies
    - Type of proppant and distance carried away from injection wellbore determined from captured fractures in cores; thus enabling selection of optimal proppant type/size for near and far field conductivity

Validating Fracture Diagnostic Tools

Microseismic imaging validation work at the GRI/DOE M-Site in sandstone reservoirs with mainly planar fractures showed that length, height, and azimuth matched with the ground truth data. However, that was a long time ago and we were only looking at microseismic locations to get overall dimensions. Since then we added two complications. First we have some degree of complexity in most of these shale reservoirs that we really do not understand, and second we are trying to use microseismic source mechanism information to extract additional information without any understanding if any of it is meaningful. The HFTS will allow us to do that validation and show what can really be extracted from microseismic data other than fracture geometry. To date, our understanding of interaction between hydraulic fractures and natural fractures has been based on some unsubstantiated analytic reasoning. Accurate monitoring of fracture growth in presence of natural fractures and observation of the ground truth in cored fractures will result in the true understanding of the process that will be beneficial in all fractured shale stimulations. More specifically, microseismic imaging coupled with ground truth measurements will enable:

- Improvements in microseismic location accuracy detection through core sampling and fracture arrival time & location in the observation well; thus providing more accurate microseismic surveys
- Better interpretation methods of microseismic data for understanding hydraulic fracture interaction with natural fractures.
- Development of microseismic data interpretation techniques for discriminating far field unconnected/un-propped fractures with connected propped fractures

Operational Considerations

HFTS may involve some or all of the following operations:

- Site construction and preparation.
- Baseline methane emissions measurement.
- Drilling, logging, coring and well completions.
- Coring through the fracture domain.
- Fracture injection operations.
- Direct observation of induced fractures in core.
- Injection of various tracers to monitor fracture geometry and propagation.
- Monitoring of variations in fluid resistivity in surrounding groundwater.
- Comprehensive analysis of fracture geometry utilizing results of tracer, tilt, microseismic surveys.
- Borehole imaging using Formation Micro Imager.
- Formation evaluation experiments to determine optimum well log suites.
- Production logging over an extended period of time.
- Emissions monitoring & comparison with baseline.
- Facility management.
- Others as designed by the program.
- Oilfield services and technical support services.

Several options are under consideration for how the HFTS might be owned and operated. Two possible options are described below. Additional scenario suggestions are welcome.

Producer Owned and Operated

In this scenario, the HFTS site would be owned and operated by a motivated producing company in a pertinent shale play. The operator would pay for assets associated with production revenue, including site preparation costs as well as costs of drilling, casing, and necessary facilities. The program membership would pay for the incremental costs associated with constructing observation and fracture intersecting wells, instrumentation, diagnostics, testing, and data analysis. Production revenue remains with the owner operator.

Newco Owned and Operated

In this scenario, membership funding would be utilized to form an independent company – HFTS, Inc. for example – to purchase a site, lease a site, or manage a donated site. The company would be set up solely for research similar to how CER was set up for the M-Site project. Newco would hire staff and contractors and would have the expressed purpose of operating HFTS. Site acquisition and preparation, well construction, and costs associated with drilling intersecting and observation wells, instrumentation, diagnostics, testing, and data analysis would be paid through membership funding. If Newco were set up as a non-profit company, membership funding contributions may have tax benefits. Production revenue would fund additional research and potentially additional test sites in other basins.

Preparation, Design, Performance, and Management Functions

The following is a sample of functions that will be needed in the preparation, design, performance, and management of the HFTS. Performance of these functions may involve outside contractor support.

- Experiment Design
- Field Data Systems Operation and Maintenance
- Data Collection, Storage, Analysis and Integration
- Program and Project Management
- Microseismic Data Acquisition
- Microseismic Data Analysis Technical Support
- Fracture Treatment Design, Modeling, and Simulation
- Technical Support
- Environmental monitoring and analysis
- Field Operations and Services, Supervision, Security, and Site Safety

Benefits

The benefits derived from research and testing at the HFTS can be realized according to each of the major program objectives – Environmental Safety and Stimulation Efficiency. Successful experiments at the HFTs will be of substantial benefit to the natural gas industry in developing shale reservoirs, especially since hydraulic fracture stimulation is almost always utilized as part of this development. In addition, concerns about the safe and environmentally responsible application of hydraulic fracturing technology are widespread. For some, hydraulic fracturing connotes something dangerous, unhealthy, and even nefarious. For others, the science needs clearer understanding of the fracturing dynamics that are key to controlling fracture dimensions and vital to the productivity of fracture networks created in long horizontal wells. HFTS is intended to generate substantial data, new knowledge, and enable a pathway to hydraulic fracturing optimization and next generation technology development. Advances in technology will result in fewer wells being needed and higher production output per well. A sample of some of the anticipated benefits includes:

Environmental Safety

- Development and transfer of advanced technologies that improve safety, lower environmental impacts, and reduce materials and energy required per unit of energy produced.
- Determination of potential health and environmental consequences of hydraulic fracturing to air, land, and water resources and development of mitigation strategies.
- Demonstration of safe and reliable hydraulic fracturing operations.
- Development of optimal instrumentation to reduce the margin of error in interpretation of monitoring and measuring of environmental conditions pre- and post-stimulation.

Stimulation Efficiency

- Characterization, measurement, evaluation of hydraulic fracturing efficiency.
- Improvements to fracture design and evaluation of Stimulated Reservoir Volume.
- Assessment of created fracture conductivity as measured with flow between two wells connected by a fracture.

- Early detection of fracture effectiveness and development of methods and techniques for real-time control of fracturing effectiveness.
- Development and transfer of advanced technologies and methods to maximize resource recovery from each hydraulic fracturing treatment while minimizing the material and energy input requirements.
- Substitution of less effective materials or methods with those more effective.
- Development of optimal instrumentation to reduce the margin of error in interpretation of monitoring and measuring of created fractures.
- Evaluation of seismic techniques.
- Hydraulic fracture model verification and calibration. Determining spatial and temporal fracture network creation and validate against model.
- Measurement of effectiveness of downhole perforating techniques.
- Evaluation of hydraulic fracture directional changes due to stress reorientation.

Estimated Funding Requirements and Mechanism

The program consisting of a multi-well, multi-fracture stage test site is being developed in three phases. The summary and anticipated costs of each are described below.

Phase I – Planning

Development of the Program Strategy has been funded by RPSEA and documented in this report. A consortium comprising the producing and service companies, academic, and research institutions has been formed whereby the members contributed toward defining the program research priorities.

Phase II – R&D Assessment and Data Review

A comprehensive assessment of existing hydraulic fracturing research and available data is being proposed as a necessary step toward designing, launching, and implementing the HFTS. This R&D assessment and data review effort will also generate a valuable, searchable data base for industry that is a useful stand-alone product.

Funding requirements for the R&D Assessment and Data Review are approximately $200,000. The preliminary plan is to apply $20,000 in RPSEA funding from the Phase I - Planning project and enroll industry participants at $20,000 each to generate the necessary funding to proceed with Phase II.

Phase III – HFTS Implementation

From past research programs of this nature, multiple wells and fracture treatments in the field are necessary to achieve the testing objectives outline in this report. The cost of a comprehensive program will be a function of the detailed research plan, drilling costs, and the number and type of experiments anticipated.

Total cost for the HFTS testing program conceptualized in Figure 6 is estimated in Table 3. As indicated in the budget scenario below, total funding of approximately $34.5 million is anticipated for a single site with a moderate testing program. It is anticipated the industry funding could potentially be leveraged with funds from various government entities such as the US Department of Energy, Department of Interior, RPSEA, and environmental organizations. The addition of government and other funding commitments is

uncertain and could enable additional research and testing with more treatment, observation, and intersecting wells; and the possibility of additional HFTS sites in different shale formations.

Table 3: Budget Estimate for HFTS Conceptual Testing Program

4000 ft. lateral wells in the Marcellus	Unit $ Million	Total $ Million
Drilling and Casing	3.5	
Coring	1.0	4.5
Logs	.5	5.0
+ 25% cost margin	1.5	6.5
x 3 Wells (1 Test + 2 Observation)		19.5
Tests 1-6 (research priorities)	8	27.5
Tests 7-13 (research priorities)	7	34.5
Total		***34.5**

* Budget reflects a single, conceptual site with three wells as shown in Figure 6 with a moderate testing plan. Does not include site acquisition costs estimated at $2-4 Million. Completion services are reflected in Tests 1-6 and 7-13 and are variable according to the number of tests and extent of testing conducted. Additional treatment, observation, and intersecting wells; additional testing; and additional HFTS sites in different shale formations are possibilities depending on level of funding.

To raise a total estimated budget of $34.5 Million, the example in Table 4 considers a scenario that includes funding from operators and service companies, the federal government, and technology providers. Assuming four operators participate at a Tier 1 level, six at Tier 2, ten at Tier 3, and fifteen at Tier 4, the total funding contribution from operators would be $21.5 Million. Assuming four service companies participate at a contribution of $1.5 Million each; this would total $6 Million. Additional participation and funding support from government sources including RPSEA and/or DOE is estimated at $6 Million. Also, five individual fracturing technology providers each participating with $300k in funding would total $1.5 Million.

A tiered funding mechanism is being considered for operators participating in HFTS, whereby funding contribution levels coincide with a company's opportunity to benefit from the results. As shown in Table

5 there are four tiers or funding levels scaled according to total annual gas production. Other indices that could be considered are total public reserve estimates or total lease acreage. Using the example of total annual gas production, a Tier 1 participant would be an operator producing more than 1000 Bcf/yr of gas and would contribute $1.5 Million to participate in HFTS; a Tier 2 participant would be an operator producing between 500-1000 Bcf/yr of gas and would contribute $1 Million to participate; a Tier 3 participant would be an operator producing between 100-500 Bcf/yr of gas and would contribute $500K to participate; and a Tier 4 participant would be an operator producing less than 100 Bcf/yr of gas and would contribute $300K to participate in HFTS.

Table 4: Possible Funding Scenario

Funding Goal		$34.5 M	
Operator Tiered Funding			21.5
	4 Operators @ Tier 1 ($1.5M)	6	
	6 Operators @ Tier 2 ($1M)	6	
	10 Operators @ Tier 3 ($500k)	5	
	15 Operators @ Tier 4 ($300k)	4.5	
4 Service Company Funding @ $1.5M			6.0
RPSEA/DOE Funding *(uncertain)*			6.0
5 Technology Providers @ $300k			1.5

Table 5: Potential Tiered Operator Funding Mechanism

Operator Tiered Funding**		Millions
	Tier 1 (>1000 Bcf/yr)	1.5
	Tier 2 (500-1000 Bcf/yr)	1.0
	Tier 3 (100-500 Bcf/yr)	.5
	Tier 4 (<100 Bcf/yr)	.3
** Based on an established index or scale (ex. annual oil/gas production, public reserve estimates, or secured shale acreage).		

Summary and Next Steps

Industry input has helped develop a Program Strategy Report that outlines the preliminary intent, planning, scope, design, participation, and funding of the HFTS. This Phase I – Planning for the HFTS has been a successful undertaking and sets the stage for execution of Phase II – R&D Assessment and Data Review and ultimately the Phase III – Implementation. The HFTS program will generate significant value for all shale development stakeholders.

Value of HFTS

Some valuable outcomes from the HFTS program that are expected include:

1) Development of advanced technologies that improve safety, lower environmental impacts, and reduce materials and energy required per unit of energy produced.
2) Determination of potential health and environmental consequences of hydraulic fracturing to air, land, and water resources and development of mitigation strategies.
3) Demonstration of safe and reliable hydraulic fracturing operations.
4) Development of optimal instrumentation to reduce the margin of error in interpretation of monitoring and measuring of environmental conditions pre- and post-stimulation.
5) Characterization, measurement, evaluation of hydraulic fracturing efficiency.
6) Improvements to fracture design and evaluation of Stimulated Reservoir Volume.
7) Assessment of created fracture conductivity as measured with flow between two wells connected by a fracture.
8) Early detection of fracture effectiveness and development of methods and techniques for real-time control of fracturing effectiveness.
9) Development of advanced technologies and methods to maximize resource recovery from each hydraulic fracturing treatment while minimizing the material and energy input requirements
10) Substitution of less effective materials or methods with those more effective.
11) Development of optimal instrumentation to reduce the margin of error in interpretation of monitoring and measuring of created fractures.
12) Evaluation of seismic techniques.
13) Hydraulic fracture model verification and calibration. Determining spatial and temporal fracture network creation and validate against model.
14) Measurement of effectiveness of downhole perforating techniques.
15) Evaluation of hydraulic fracture directional changes due to stress reorientation.

Phase I Accomplishments

The following accomplishments have been achieved by the Phase I planning process:

1) Enrolled a consortium of exceptional hydraulic fracturing professionals from industry in providing input to identify program need, focus, and value.
2) Conducted workshops in Houston and Pittsburgh to gain industry input on program scope and research challenges and validated the feedback and results.
3) Integrated industry input and prioritized research needs into HFTS Program Strategy Report.

4) Established preliminary program mission, objectives, design, participation and rolls, budget, and schedule.

5) Started enrolling an Advisory Board and Technical Review Committee to guide program development and implementation.

6) Identified a Phase II – R&D Assessment and Data Review project to provide a valuable product to the industry and help inform the experimental design for HFTS.

Next Steps

The next steps to move forward successfully with the implementation of the HFTS are listed in Table 6:

Table 6: Milestones and Target Dates

Milestone	Target Date	Status	Funding
Industry Workshop 1 – Houston	Mar. 20, 2013	✓	RPSEA
Industry Workshop 2 – Pittsburgh	Apr. 16, 2013	✓	RPSEA
Industry Workshop 3 – Webinar	July 2, 1013	✓	RPSEA
Hydraulic Fracturing Testing Priorities Identified	July 31, 2013	✓	RPSEA
Publication of the Program Strategy Report	Dec. 15, 2013	✓	RPSEA
Launch of the HFTS Website	Q1, 2013	✓	RPSEA
Confirmation of Advisory Board Members	2Q, 2014		RPSEA
Funding Secured for Phase II – R&D Assessment & Data Review	2Q, 2014		Industry
Confirmation of Experiment Design Team	3Q, 2014		Industry
Completion of Phase II – R&D Assessment & Data Review	Jul. 31, 2014		Industry
Determination of Government Funding Support	2Q, 2014		
Confirmation of Technical Review Committee	3Q, 2014		Industry
Secured participation and funding commitments for HFTS	4Q, 2014		Industry
Identification of HFTS Site	4Q, 2014		Industry
Confirmation of the Research Plan	4Q, 2014		Industry
Launch HFTS	1Q, 2015		Industry

List of Acronyms

Acronym	Description

Bcf	Billion Cubic Feet
CO_2	Carbon Dioxide
DOE	Department of Energy
DRI	Desert Research Institute
E&P	Exploration and Production
GRI	Gas Research Institute (predecessor Gas Technology Institute)
GTI	Gas Technology Institute
HFTS	Hydraulic Fracturing Test Site
LPG	Liquefied Petroleum Gas
M-Site	Multi-Site Hydraulic Fracture Diagnostics
R&D	Research and Development
RPSEA	Research Partnership to Secure Energy for America

Appendices

Legacy of Collaborative Research Programs

Development of unconventional gas in the U.S. was launched with the help of collaborative research programs led by Gas Technology Institute (GTI). These efforts became a catalyst for experimentation and new technology development that unlocked the potential of America's "new" natural gas – including tight sand, coalbed methane and shale gas resources. Other organizations, notably the U.S. Department of Energy and National Energy Technology Laboratory (NETL) also played a critical role in the technological development of unconventional gas in the U.S.

Building on the coalbed methane experience, GTI managed parallel programs for gas shale and tight sands production. These programs led to the advancement of hydraulic fracturing technology and a fundamental understanding of gas adsorption/desorption in rock formations that is critical to shale gas development today. Horizontal drilling, hydraulic fracturing, and high-efficiency downhole tool advancements have contributed to increased shale gas production. In 2000, shale gas production was just 1% of U.S. natural gas supply; by 2011 it rose to 34%; it could reach over 50% by 2035.

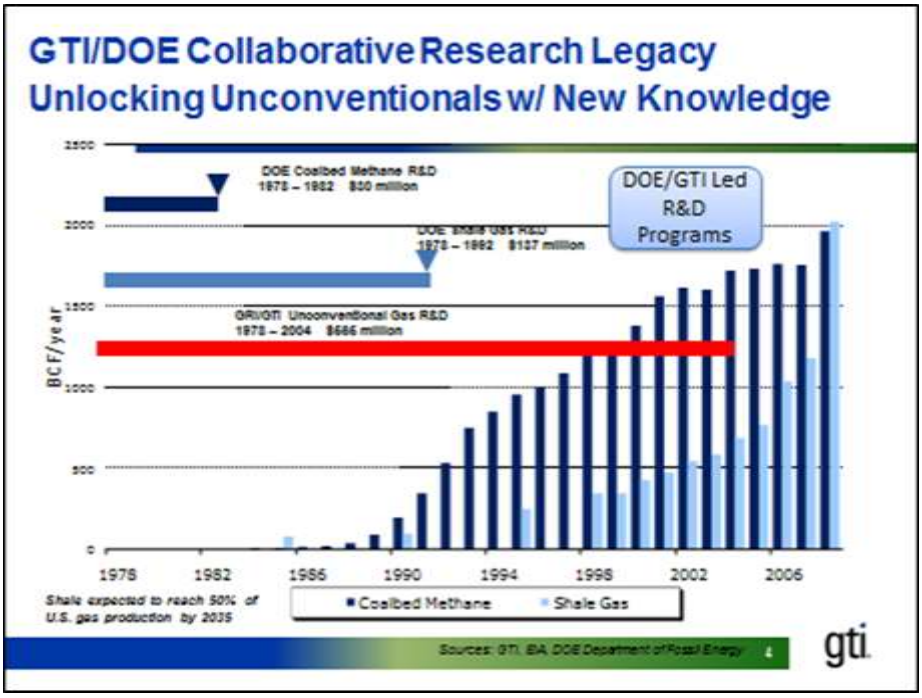

Figure 7: GTI/DOE Collaborative Research Legacy for Unconventional Gas

For more than 35 years, GTI – successor of GRI - has been a catalyst for innovation and technology development to reduce production costs, minimize environmental footprint and expand the supply of clean-burning energy. As a non-profit R&D organization, we are a trusted partner who provides an independent and reliable voice of science and reason.

Since 1978, GTI has led and program managed the operations of more than 30 cooperative research wells, often in close collaboration with the Department of Energy. A sample of relevant past hydraulic fracturing programs and testing facilities includes:

- Advanced Hydraulic Fracturing Project, GTI and RPSEA. 2013 –
- Marcellus Shale Research Project, GTI and RPSEA. 2011- 2013

- New Albany Shale Research Project, GTI and RPSEA. 2008-10
- Underbalanced Completions Program, GTI. 2001
- Mounds Drill Cuttings Injection Project, Gas Research Institute, Oklahoma. 1999
- GRI/DOE Multi-Site Hydraulic Fracture Diagnostics Project (Multi-Well Experiment or MWX), Gas Research Institute, Colorado. 1999
- Four-staged Field Experiments (SFE wells), Texas and Wyoming.
- Cotton Valley Hydraulic Fracture Imaging and Waterfrac Projects, Gas Research Institute. 1999
- Fracturing Fluid Characterization Facility (FFCF), Gas Research Institute and University of Oklahoma. 1991-1998.

M-Site Project Overview (1999)

Project Objective and Initiation Logic

Hydraulic fracturing is an important technique commonly used to improve production performance from gas and oil wells completed in low-permeability reservoirs. Recently, through the implementation of field-scale testing coupled with direct observations of far-field fractures, evidence has been accumulating indicating the fracture propagation process is quite complex. Its fractures are not the symmetric, planar features commonly portrayed, rather; they commonly appear to have multiple strands, secondary fractures, height and length asymmetries, and other complexities.

Since the fracturing process occurs deep in the subsurface and cannot be directly observed, models or various tools/techniques – each having limitations in the real world of complex fracturing – are the only methods available to develop estimates of fracture dimensions. With complex fracturing becoming more apparent, there are many questions such as "What are the critical fracturing parameters?"; "How is the actual fracturing process really unfolding?" and "Is there a technique for more accurately defining fracture growth and geometry?" On the basis of these questions, Gas Research Institute and the U.S. Department of Energy jointly conceived the concept of the Multi-Site Hydraulic Fracture Diagnostics Project (M-Site Project).

The jointly funded M-Site Project had the objective of performing field-scale experiments and gathering high-quality, independent diagnostic data resulting in increased accuracy in measuring hydraulic fracture dimensions and characterizing the hydraulic fracturing processes. The ultimate goal of the project has been to advance the fracture diagnostics hardware and data analysis methodologies to the point where commercial hydraulic fracture mapping capabilities can be established.

The M-Site Project includes comprehensive instrumentation arrays and facilities, which represent a technology system whose scale is beyond that which is envisioned for the commercial fracture mapping capability. However, this complex system is essential to develop and synthesize the various data sets and analytical methods into a cohesive framework. The comprehensive arrays provide an accurate baseline against which the reduced-scale commercial system can be compared. The end result of the M-Site research phase was foreseen to be a simplified and calibrated set of fracture diagnostics tools and techniques providing complementary, yet independent, information regarding hydraulic fracture growth and final dimensions.

Site Characteristics

The site of the former DOE Multi-Well Experiment (MWX) near Rifle, Colorado was chosen in 1992 as the location to conduct the fracture diagnostics and fracture technology experiments of the M-Site Project. An overlay of the M-Site Project wells on an MWX air photo illustrates the close proximity of the wellbores.

The site was found to be attractive for several reasons: 1) multiple thick, laterally continuous sandstone units were known to be present in the upper 700 ft. of the Mesa Verde Group at reasonable operating depths; 2) extensive background data from the MWX project (e.g., cores and core analyses, logs, stress magnitude and direction data, well tests, geophysical data, hydraulic fracture data) were archived and available; 3) the closely spaced MWX wellbores were available for continued research; and 4) surface infrastructure which would facilitate the implementation of the project was already in place.

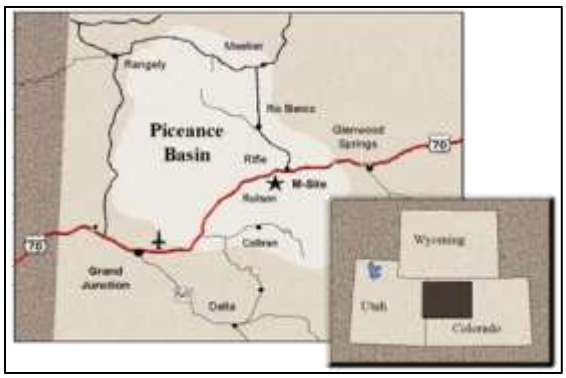

Figure 8: Site Chosen for MWX Project

The informally designated A, B, and C Sands in the upper Mesa Verde Group were targeted for M-Site fracture diagnostics research. The cross-section illustrates several key points:

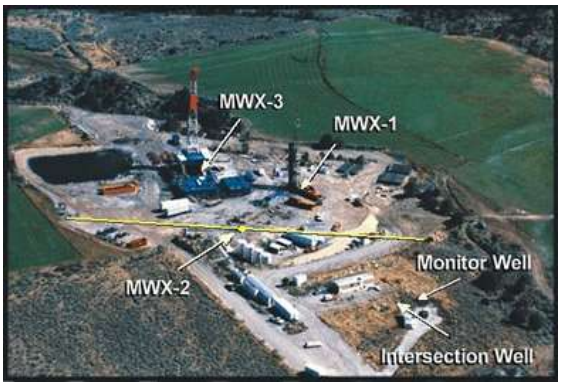

Figure 9: Arial photo of the MWX Site

1. The stacked character of the sandstone units allows for a staged research program to be implemented (i.e., research work proceeds from the deepest to the shallowest interval, "using up" each sand interval before testing begins in the next un-fractured sand interval with a new set of experiment goals);
2. Sandstone units are separated by shale, mudstone, and siltstone of sufficient thickness to reduce the risk of propagating fractures from one target sand zone to another;
3. The continuity and thickness of the target sand units remains relatively constant across the site and therefore provides a suitable subsurface laboratory for conducting fracture diagnostics experiments; and
4. The relatively shallow depths (i.e., 4000 - 5000 ft.) decrease operational costs associated with conducting experiments and promote higher-quality data acquisition from surface-deployed instrument arrays.

The reservoir characteristics of the M-Site targeted sand units were reasonably well known through data collected and analyzed in the MWX and M-Site research programs. Reservoir permeabilities of the A, B, and C Sands range from 0.01 to 0.1 md as determined by core analysis and analysis of extended shut-ins following stress tests. The reservoirs are normally pressured and the core/borehole image log data (including data from deviated boreholes) indicated few natural fractures. The lithologies separating the A, B, and C Sand units are mixed siltstone, mudstone, and shale that resulted in a variable range of laminated stresses ranging from 700 to 1500 psi. Log analyses indicate that the A, B and C Sand units are highly water saturated and are not considered to be capable of sustained gas production. However, the rock does have sufficient gas saturation to be a compressible system and to allow fluid leakoff during injections. Overall, the M-Site targeted sand units do not have a significant distinction from many tight

gas reservoirs that are hydraulically stimulated for production on a routine basis. As such, the technology developed from M-Site research could be successfully extrapolated to many other areas and formations.

Instrumentation Arrays and Wellbore Layouts

Although the A, B, and C Sand experiments each successively included differing wellbore and instrumentation configurations, the M-Site Project principally included the following elements:

- Two remote-well accelerometer arrays (5-level and 30-level) for detecting microseismic events associated with hydraulic fracture propagation
- A vertical array of inclinometers (6 biaxial instruments) deployed in the subsurface to determine the earth's mechanical response to hydraulic fracture opening and closing
- Deviated wellbores which remotely intersect two hydraulic fractures
- Wellbores, surface infrastructure, and data acquisition systems to conduct field experiments.

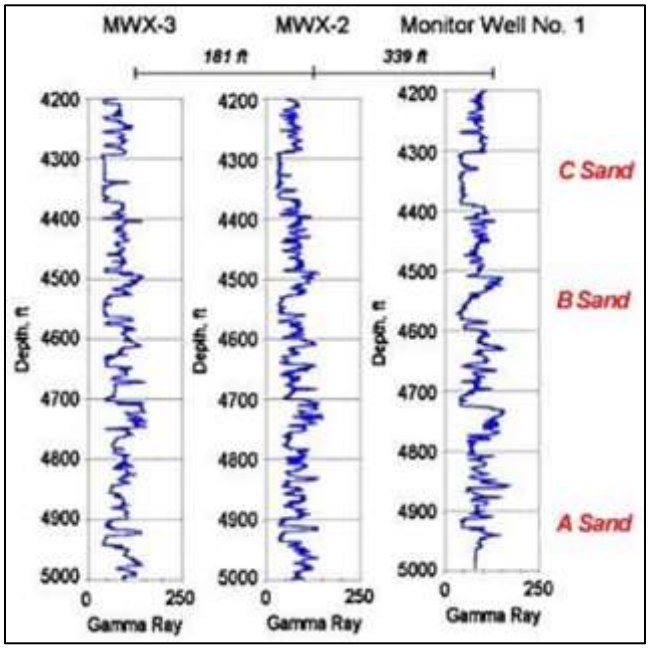

Figure 10: Cross-section of M-Site Target Sand Intervals

The layout of these wellbores and diagnostics arrays, in plan and profile view, is shown for the A, B, and C Sand experiments. The M-Site experiments also included the use of recently emerged advanced-technology instrumentation, fiber-optic telemetry, computers and site infrastructure to enhance data acquisition.

Project Chronology

A-Sand Experiments

Two sets of experiments were performed in the A-Sand, one in October 1992 and another in November 1993. Both sets of experiments were conducted using MWX-3 as the injection well and MWX-2 as a seismic observation well. The initial A-Sand efforts consisted of limited-scope experiments and data acquisition to verify the suitability of the wellbores and assess the capability of remotely detecting seismic signals generated during a mini-fracturing using a single triaxial accelerometer.

Similar to the initial A-Sand injections, the second set of A-Sand experiments also used MWX-3 as the injection well and MWX-2 as a seismic observation well. Three fluid-only injections and a fluid/proppant injection (i.e., Injections 1-A to 4-A) were performed primarily to support the goal of microseismically mapping hydraulic fracture extent.

Facilities and Capabilities Expansion

The cumulative A-Sand results and the realization that the research had the potential for advancing hydraulic fracturing technology provided the incentive for continued expansion of the M-Site facilities and scope of work. The A-Sand experimentation used only four seismic receivers on a fiber-optic wireline for detecting microseismic events. However, comprehensive instrumentation arrays (e.g., permanently

emplaced accelerometers and inclinometers) are required to more accurately map and understand fracture propagation, and to develop reliable fracture diagnostics interpretation methodologies. The most significant expansion effort was the drilling and instrumentation of Monitor Well No. 1 in 1994.

A-Sand experiment results provided guidance in designing the Monitor Well seismic array where it was determined that a 30-accelerometer array with 30-ft spacing between the instruments would be optimal for imaging microseismic events in the B and C Sand intervals. Similarly, an array of six inclinometers located at depths corresponding to above, within, and below the B and C Sands was appropriate. After drilling and casing the Monitor Well to 5,000 ft., the instrumentation arrays and associated cabling systems were systematically secured to the outside of a tubing string, placed at known subsurface depths, and cemented in place.

Figure 11: Monitor Well No. 1

B-Sand Fracture Diagnostics Experiments

M-Site research activities in 1995 focused on performing a series of field operations that were designed to extend fracture mapping capabilities and hydraulic fracturing technology in the B-Sand interval. The B-Sand experiments made full use of the site infrastructure and fracture mapping capabilities made possible by the Monitor Well No. 1 comprehensive instrumentation arrays and wireline-retrievable arrays in MWX-3.

Figure 12: B-Sand Lateral

The initial experimentation conducted in the B-Sand focused on fracture diagnostics and fracture mapping by performing a series of seven hydraulic fracture injections (i.e., Injections 1-B through 7-B) in MWX-2 between April and August 1995. Following the B-Sand injections and fracture diagnostics experimentation, a new well was drilled in October 1995. This intercepted the B-Sand hydraulic fracture(s), verified the accuracy of the microseismic technique, and provided a view of the "far-field" character of the hydraulic fractures.

C-Sand Fracture Diagnostics Experiments

Further verification and development of fracture diagnostic technologies were performed in 1996 in the C-Sand interval, an 80-ft-thick blanket sand above the B-Sand. A deviated borehole, drilled as a kickoff to the existing Intersection Well No. 1, was initially emplaced in the C Sand approximately 300 ft. from the MWX-2 treatment well. A series of six hydraulic fracture injections (i.e., Injections 1-C through 6-C) were then performed, which approached and intersected the C-Sand lateral. These experiments concluded the field data acquisition portion of the M-Site Project in December 1996.

Project Team

The M-Site Project team included contractors to both Gas Research Institute and DOE with expertise in hydraulic fracturing, geophysics, field instrumentation, and field operations. The contacts for the principal investigators in the M-Site Project are also provided.

Benefits of Advanced Fracture Diagnostic Technology

Microseismic fracture mapping has the potential for making a significant impact on hydraulic fracturing economics and field development strategies for improving production. Several examples of this potential include the following:

Treatment Optimization

Fracture diagnostics may provide information on incomplete coverage of the completion interval by the hydraulic fracture or, alternatively, out-of-zone fracture height growth into non-productive or water-productive zones. Recognizing either of these conditions may allow the treatment to be modified, thereby improving production performance and lowering completion costs.

Similarly, treatments may be optimized with information on how much additional length is achieved as the treatment size increases. If the additional treatment size results in undesirable height growth without much length extension, then the treatment may again be modified to reduce treatment costs.

Well Placement Strategies in New Fields and in Maturing Fields

As new fields are developed, knowledge of hydraulic fracture azimuth and final geometry (including possible wing length asymmetries) will result in the optimum well placement strategy for efficiently draining the reservoir from the outset. Similarly, infill drilling programs in maturing fields can be optimized with knowledge of fracture azimuth and geometry. In addition, the effects of hydraulic fracture re-orientation as a result of reservoir drawdown may be observed and compensated for. The end result of the improved well placement strategy will be a higher recovery percentage of the reserves in place.

Multi-zone Completion Optimization

There are many single-well completions which include the simultaneous or sequential stimulation of multiple zones. The vertical coverage of the hydraulic fracture in the target reservoirs may be more accurately assessed with a microseismic image of the hydraulic fracture. Such a map may indicate overlapping hydraulic fractures or zones that did not take fluid and proppant. Either situation may be remedied to improve treatment economics and/or production performance.

References

[1] Hassett, Kevin A. and Aparna Mathur. “Benefits of Hydraulic Fracturing.” Oxford Energy Forum, Issue 91. American Enterprise Institute, Apr 04, 2013. http://www.aei.org/article/economics/benefits-of-hydraulic-fracking/

[2] Ciezobka, Jordan. Marcellus Gas Shale Project. Topical Report: Stimulation and Completion. RPSEA Project 9122-04. Gas Technology Institute. August 25, 2011. http://www.rpsea.org/media/files/project/285ce3d4/09122-04-RT-Marcellus_Shale_Gas_Project-1-08-25-11_P.pdf

[3] Gas Research Institute. GRI/DOE Multi-Site Hydraulic Fracture Diagnostic Project. GRI-99/0117. May 1999.

Appendix BB: Hydraulic Fracture Test Site (HFTS) Phase II Report

Review and Assessment of Published Literature on Diagnostic Technologies

Applied to Unconventional Reservoirs

Prolog

Efficient, cost effective oil and gas production is contingent on a number of technical, economic and political factors. The primary technical factors focus on maximizing reservoir contact area, emplacing high rate conduits that connect the contact areas with the wellbore and ultimately the surface production facilities, and then selecting the best possible well spacing and spatial distribution or well patterns to effectively drain the largest possible reserves in the producible acreage. Typically conventional production depended on high natural productivity reservoirs. They are normally penetrated by vertical wellbores perforated over the entire anticipated net height and if cost effective stimulated with propped hydraulic fractures that are designed to form the highly conductive pathways or conduits connecting remote areas of the reservoir with the wellbore thereby ”stimulating” production. A distinct advantage of hydraulic fracturing is that at depths >2,000 ft. the process generally forms a vertical fracture penetrating the entire net height of the reservoir while extending laterally many hundreds of feet on both sides of the wellbore and where both walls or faces of the emplaced fracture(s) then provide a very large reservoir contact area. Early on reservoir and hydraulic fracture diagnostics were relatively basic and included such things as cased hole logging, core analysis, pre-frac well testing, hydraulic fracturing pressure analysis, treatment fluid rate and rheology, proppant stage concentrations, RA tracers, post frac production logging and production analysis.

As expected the reservoirs exhibiting relatively high production capacity were most economic and developed extensively on a global scale for many decades. However finding new reserves to replace the depleted ones led producers to reservoirs that were deeper and becoming less and less permeable. This then required devising methods of creating longer and longer propped hydraulic fractures. Eventually it became clear that that technology would meet effective limits as the reservoir permeabilities sank into the low microdarcy range. Field scale research later made evident that many of these presumed microdarcy type reservoirs were considerably more complex and misunderstood when taken to be simply homogeneous producing systems. In fact the rock matrix permeability were often found to be in the nanodarcy range with imbedded natural fractures acting as small by ubiquitous conduits that formed an extensive contact area with the matrix resulting in effective or system permeabilities appearing to be in the tens of microdarcy range. The added complexity associated with natural fractures, their extent, interconnectivity and maintaining them as viable conduits is paramount to understanding the well and design, execution and development of the entire hydraulic fracture stimulation process.

The era of the Shales: although gas production from naturally fractured areas of the Devonian shale extends back to the early 1900’s well production was limited even when stimulated with hydraulic fracturing and other techniques. The oil and gas industry took a quantum leap in the late 1990’s when it became apparent that the ultra-tight nanodarcy shale formations known to be a source rock for hydrocarbon development could also become an economic producible resource on a grand scale. Led by George Mitchell of Mitchell Energy the Barnett shale in the Bend Arch-Fort Worth Basin Texas became a test area for such shale development. In early 2000 the developmental process settled on emplacing long horizontal wellbores somewhere near the middle of the shale’s net height and then performing a series

of staged hydraulic fractures along the entire length of the wellbore. All this was done with the expressed intent of increasing the reservoir contact area to the point of enhancing shale gas production that would result in the Barnett shale being an economically producible venture.

Fast forward to the 2010 decade where multiple horizontal wellbores set on single pad locations now with lengths extending beyond 5,000ft and many 10's of clustered hydraulic fracture stages set along their entire length. This generalized type of development is now employed extensively throughout North America in the ultra-tight shales producing gas, liquid and oil and is now serving as a template for shale and other similar resource development worldwide. Understanding the technical complications rooted in this type of advanced production development process and then engineering best practices for efficient, cost effective oil and gas production most certainly requires a synergy of professionals and other diagnostic technologies beyond that normally employed by conventional petroleum engineering. The most current and applicable utilized diagnostics technologies are the focus of this study.

To further complicate the process most of the needed technical information required to achieve success is not directly measureable. Thus the current collection of diagnostics no matter how sophisticated may appear only provide a proxy for those critical parameters or attributes individually and collectively. This review and assessment of current published work is designed to enhance our understanding and utility of those diagnostic techniques and technologies that underpin the industries current approach to full field development.

Diagnostics monitoring technologies

The current categories of hydraulic fracture (HF) diagnostic and reservoir enhancement monitoring technologies considered in this study include the following:

- microseismic arrays
- tiltmeters and hybrid systems
- fiber optic DTS and DAS
- HF and Production tracers
- DFIT
- interference between offset wells
- integrated HF diagnostics

Microseismic technology

The application and proof of concept for microseismic monitoring to identify dynamic HF growth and its spatial dimensions was clearly determined during field scale tests performed under joint sponsorship of the USDOE and GRI during the late 1990's (Warpinski et al, 1995, Peterson et al, 1996). To validate the microseismic data and the interpretations slant wells were emplaced to intersect or be intersected by hydraulic fracture(s) HF(s). They ultimately provided confirmation of the interpreted microseismic data concerning specific HF attributes including initial fluid fracture length, (Branagan et al, 1997), temporal fracture dynamics and fracture azimuth (Warpinski et al, 1997). Further one of the slant wells provided continuous far field downhole hydraulic fracture pressure during execution, intersection and after the

treatment. These and other diagnostic data including tilt, RA tracers, core thoughts of colored proppant stages and borehole imaging of the far field wellbore were acquired during these extensive field tests and the results were subsequently used to re-calibrate the then current industry hydraulic fracture models. The importance of field tests such as these that include multiple independent diagnostic technologies although on their face appear costly are the only viable way for the industry to more accurately evaluate the complexities of the fracturing process and improve and control production enhancement in the development of complex nanodarcy type reserves while valuing the proxies generated by the diagnostics and models themselves.

Commercial deployment of downhole wireline run microseismic arrays in the Barnett shale provided vital information regarding specific HF attributes for individual stage development including fracture length, azimuth , asymmetry, height growth (Fisher et al, 2002, Maxwell et al, 2002). In addition the microseismic data yielded valuable insight into the complexity that was apparently ongoing in the inter-stage reservoir blocks commonly denoted as the stimulated reservoir volume or SRV (Warpinski et al, 2005, Cipolla et al, 2008, Maxwell et al, 2006). Since then microsiesmic monitoring has expanded from downhole arrays in one or two vertical offset wells to tractor deployed arrays in offset horizontal wells (Maxwell et al, 2010), extensive surface and near surface systems (Peyret et al, 2012) and now moving to include fiber optic systems.

The technology for acquiring microseisms that delineate event locations at depth is reasonably well understood (Warpinski et al, 2013, Palmer et al, 2013) but the location accuracy all depend on the acquisition of sufficiently robust p and s waves from specific event(s) that may have traversed numerous depositional layers with differing velocity structures and discontinuities before arriving at the detection array. Given an array that has a well-defined view of the fracturing process and accurate layered geo-mechanical properties the event coordinates are then located on maps in plan and various horizontal planes resulting in a 3-D image of array of points. The events are then interpreted as to their origin and possible location of the HF or some other effect of the stimulation process. The maps are meant to provide the engineers with a visual representation of the HF or process zones in and around the fracture. Often the maps display a clearly defined set of linear features that suggest the appearance of the HF itself, a sort of connect the dots mental process. Other times there appears a cloud of event locations that suggest a more complex fracture system possibly the inclusion of the HF(s) as well as their interaction directly via fluid migration or more indirectly geo-mechanically with existing natural fractures, inherent weaknesses in the rock fabric or bedding planes. The farther events are located away from the expected HF azimuth understandably the perception then shifts to complexity within the SRV.

Moment tensor analysis is designed to aid in assessing the source mechanism of an event by deriving fracture wall motion and the shear or slip direction between the fracture faces. If the first motion indicates opening of a tensile fracture this implies a conductive enhancement of some sort in the reservoir while defining the slip directions provides a measure of orientation and direction of the energized fractures or activation of pre-existing fracture planes. Of course the interconnectivity of the mapped events to one another forming an alleged conductive network which may significantly aid in production is in itself both qualitatively and most certainly quantitatively subjective.

Other complications in the HF process where microseismic data map event locations in non-adjacent layers with no apparent events occurring in the intermediate or connecting layers, i.e. skipped layers (Warpinski et al, 2014). This suggests some sort of indirect, convoluted, none hydraulic causation or

aseismic intervals. Partially open faults and low viscosity fluids such as slick water fracs may create such an environment where thin fluids could generate narrow fracs, or move though open portions of faults and result in very minute or no discernible seismic events. This again goes to point that although one might have an event map with a clearly defined planar appearance and moment analysis depicting numerous shear events it should not be taken with certainty that this is representative of a single or even well connected set of fractures that are interconnected or that they provide conductivity throughout the body of the frac(s).

Nevertheless microseismic mapping and the description of the source mechanisms have been extremely important in the assessment of the HF process and its execution, its potential impact on reservoir enhancement and the source of some of the more critical dimensional aspects of the overall altered reservoir.

Reservoir Complexity

Enhancement of reservoir productivity beyond that provided directly by the faces of the primary propped HF's can be expressed as induced complexity within the natural reservoir system. The forms of induced complexity rooted in geo-mechanics includes alteration of the matrix fabric, shearing of pre-existing natural fractures as well as bedding or other planes of weakness. In shales the effective horizontal stresses may not vary significantly from one another and in fact may approach the vertical component. Thus any newly developed stresses as a result of strains imposed by an open HF or pore pressure increases from frac fluid leak off into the rock fabric can alter the fluid migration process causing pre-existing natural fractures or fissures to destabilize and reduce the shear stress to the point of effecting shear slippage and potential dilation creating complexity in virtually all directions in the SRV. Understanding how and how much complexity effects production from its natural productive state is essential not only because it may provide a measure of the altered or effected permeability, k_{eff} but it supports the derivation of the effective HF half-length, x_f from which to re-calibrate mechanistic HF models and the derivation of ideal HF stage spacing from reservoir production simulators.

An a priori understanding as to the natural state of the reservoir or at least the volume between inter-stage HFs particularly the possible existence of natural fractures or other planes of weakness that might be energized and possibly enhanced by the HF process is a necessary good start at an overall assessment of what may occur during the HF completion process. Mud logs, wellbore imaging, coring and DFIT may provide selected insight into some of these rock features but the scale of the investigation is often restricted to the near wellbore region and limited to feet or 10's of feet within the overall net reservoir. However field or basin scale analysis employing extensive geologic outcrop studies, high resolution wellbore imaging along with gas shows from mud logs were found to aid in mapping natural fracture swarms in the Marcellus (Salehi and Ciezboka, 2013). Microseismic events maps further suggested areas where the HF process most probably induced some sort of complexity or SRV. Those combined data were then used to map length to width ratios of the effected fracture swarms and thus provide a guide to future HF staging locations.

With shale matrix permeability, k_m typically in the nanodarcy to 100 nanodarcy range the addition of complexity creates an effective permeability, k_{eff} that could be at least an order of magnitude or more than k_m. If the complexity is well interconnected and in contact with the faces of the HF, production will

obviously be markedly improved. Quantifying k_{eff} is of significant importance as it pertains to further our definition of fracture half length, x_f and optimizing fracture spacing between stages.

Early in the production cycle fluid migration can be expected to remain in linear flow particularly in these ultra-tight shales for a very long period, years or more (Nair and Miller, 2013). Whether during injection or production the reservoir flowing process can be formation linear and the HF fracture half length, x_f is related to mobility by $\sqrt{\frac{\mu}{k}}$ (Economides and Nolte, 1987). Depending on the formation flow regime transient pressure analysis (PTA) or rate transient analysis (RTA) may yield one or the other, x_f or k_{eff} within the SRV (Cinco-Ley, 1982, Craig and Blasingame, 2006). Since neither of those parameters is known a priori with specificity assessing the overall effectiveness of the stimulation process remains uncertain particularly when in the linear flow regime. Similarly deriving the effectiveness of HF stage spacing and its relationship to fluid mobility is reciprocal square root dependent, $\sqrt{\frac{k}{\mu}}$ and has been shown to vary widely given the uncertainties in k_{eff} which again can easily range from 1 to 100 nanodarcy. (Jin et al, 2013) as shown in the attached graphic provides a rather clear example of optimizing fracture spacing for various values of fluid mobility for oil and gas.

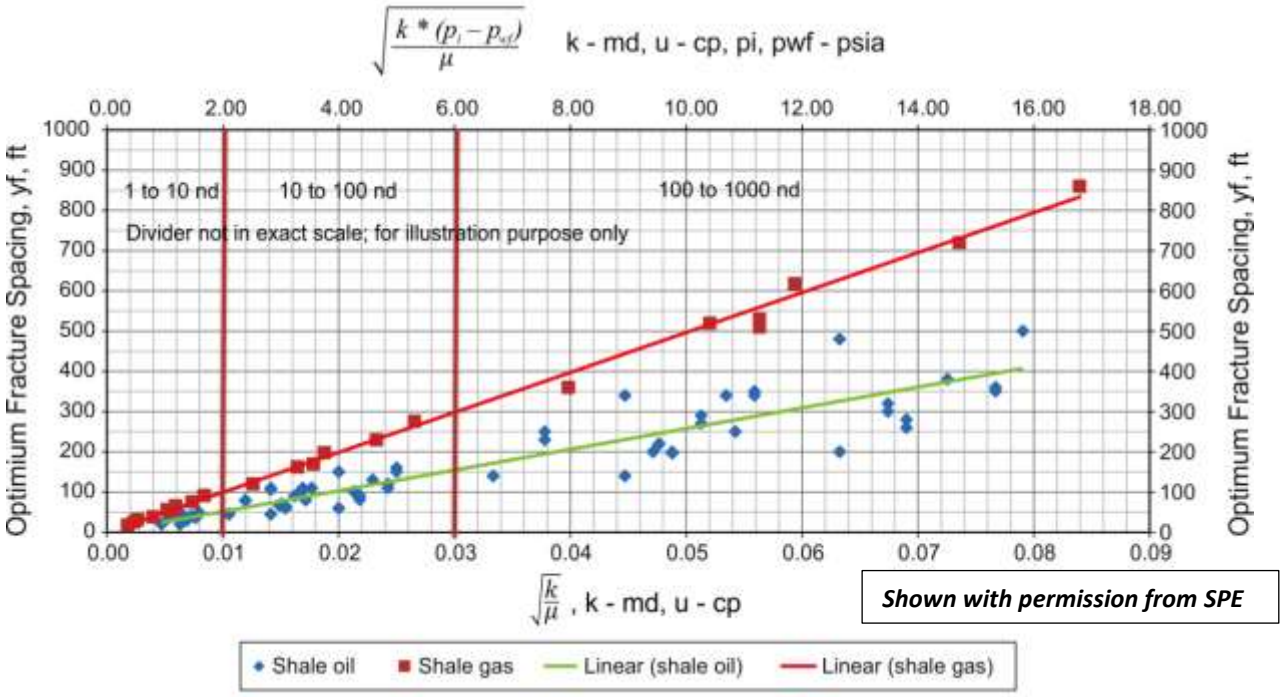

Shown with permission from SPE

Of primary concern is not only whether or not any induced complexity forms some sort of communicative network that adds reservoir contact area to support the main HF fracture thereby improving production but further how to then define that improvement quantitatively both for the HF and complexity. Of course not forgetting that there are N number of fracture stages which individually contribute to overall production and where each may exhibit considerable variation in the complex permeability k_{eff} and effective half length, x_f.

This underscores the need for independent diagnostics that will aid in to assessing the spatial and flow characteristics for each fracture stage as well as define areas where complexity may have occurred.

Tiltmeter technology

Surface Arrays

Surface tiltmeter arrays have been used quite effectively since the 1970's to measuring the minute angular distortions that occur at the grounds surface in response to subsurface rock deformation such as that created by a hydraulic fracture opening or closing. The array will also yield information regarding any residual strains that remain from induced or self-propping of the fracture. Employing an inversion process of the array data both the azimuth and dip of the fracture can be determined (Wright et al, 1998). Since the array data provides fracture dip information it can readily distinguish between vertical, sub-vertical and horizontal fractures. This is important for the shales where variations in the principle stresses may be quite small thus readily allowing the main propagating HF to vary both in azimuth and dip.

Additional information regarding the distributed deformational volume for multiple or complex fractures systems can be derived from the tilt data but becomes quantitatively limited as the fractures tend to be closely spaced and parallel such as might be seen in cluster initiated fractures in horizontal wells. Since the deformations remain from stage to stage when the fractures are propped or not entirely closed it is possible for a new stage deformation to be superimposed and thus the relative stage volumes can be estimated. As one might expect when the superposition of multiple fractures or reorientations of a single fracture grow in number and get more complicated the uniqueness of the inversion becomes less quantitative standing on its own. (Warpinski et al, 2014) expanded on the details of the inversion process discussed by (Wright et al, 2-1998) and suggested refinements to support the geophysical and numerical simulation models. The inversion process when aided by other diagnostic results should support adjustments in the final analysis and improve confidence in the results.

Downhole arrays

An array of downhole tiltmeters was first deployed at depth in a nearby offset well in the monitoring of a series of HF's in tight sands executed through a vertical well (Branagan, et al, 1996). The vertical tiltmeter array was designed to provide an almost ideal data set in that it was in close proximity to the treatment well, straddled the expected height of the HF and at some point positioned to be normal or near normal to the vertical plane during HF growth. Here for the first time a measure of dynamic fracture growth both in height and width could be determined from the inversion process of a the vertical arrays tilt data. Fortunately the tiltmeters were supplemented by a rather large microseismic array in the same offset wellbore which then supported and enhanced the inversion process (Warpinski et al, 2006).

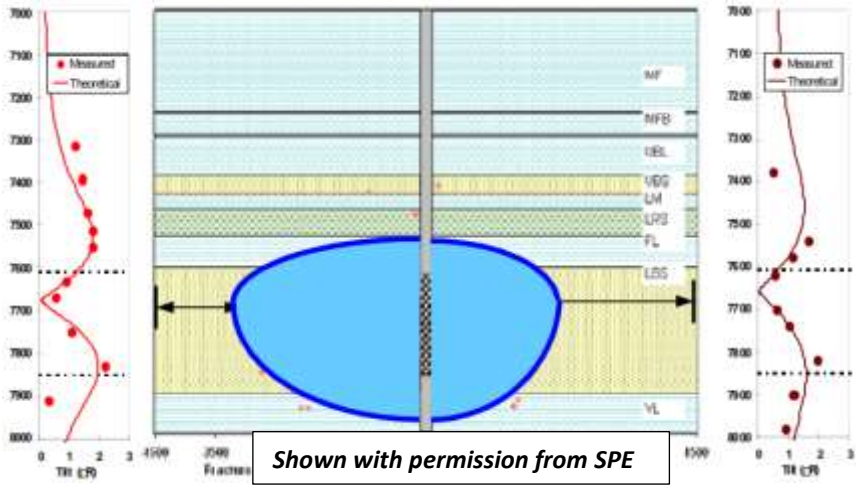

Shown with permission from SPE

(Wright et al, 2-1998) provides some examples of commercial field applications of a wireline deployed vertical tiltmeter array to describe varying types of HF geometries in several wells with divergent length to height ratios and differing widths. The attached graph (Fisher et al,2002) show an example of measured tilts (red dots) from 2 downhole vertical arrays along with the best fit theoretical tilt (red lines) that provided fracture lengths and center lines for frac wing.

In horizontal wells the perforated interval whether clustered or not is confined to a very small vertical portion of the entire producing intervals net height and thus how the fracture grows vertically both upwards and downward attempting to join all the interconnected layers through a simple conductive pathway is of obvious importance. Vertical downhole tiltmeter arrays strategically placed can provide not only information as to the vertical growth pattern through and possibly beyond the net interval but they can also yield an assessment of fracture width. The former is a measure of fracture height and coverage of the net producing interval while the latter a clear implication of interconnected layer fracture and transverse conductivity.

Hybrid arrays

The first simultaneous use of downhole vertical tiltmeter and microseismic arrays in an offset well was employed in the proof of concept tests at the M-Site in Colorado described by (Warpinski et al, 1998) and discussed briefly above. As opposed to that array which was cemented in place at depth the new hybrid systems containing tiltmeters and microseismics detectors are wireline deployed. This allows the simultaneous assessment of the microseismic events and the subsurface deformation during and after the stimulation execution.

In addition the downhole tiltmeter array can provide a measure of the residual deformation of the stimulated interval following the propped HF process and that information coupled with the microseismic analysis can be used to infer alterations in newly induced stress field and how that might affect nearby HF stages yet to be executed.

Fiber Optic Wellbore Monitoring

HF Stage Execution Monitoring

Information regarding the dynamics and stimulation effectiveness of individual HF stages during execution is generally determined by rather sophisticated HF models employing various data that includes surface pressures, fluid and proppant types, concentrations and injection rates, in addition to the near wellbore geophysical rock properties and perforation schemes. Real time monitoring of those data certainly aid in the execution, evaluation and when possible altering of the HF process. However direct evidence of fracture dimensions, pathways, wing symmetry, proppant placement and other are implicitly derived from even the most advanced models. The inclusion of information derived from far field diagnostics such as microseimics and tiltmeter certainly improves on the conceptual definition of the HF process particularly the gross dimensional aspects and superficially its overall stimulation effectiveness. Although in proof of concept fiber optic microseismic can play an important role in delineating HF dimensions.

Fiber optic sensors that include DTS and DAS can certainly advance an awareness of fluid and proppant entry at each of the perforated stage locations as well as other portions of the wellbore. DTS yields a temperature profile often shown in false color which depicts the cooling effects of the incoming fracture

fluids in the wellbore and their exit locations into the reservoir. DAS provides an acoustic signature that indicates areas within the wellbore where significant noise is occurring say at turns or choke points.

Field deployment of fiber optic DTA and DAS diagnostics have shed new light and advanced our understanding as to the actual location of the HF treatment fluids and proppants as they move through the wellbore and exit into the treated zone. A description of the underlying technology, emplacement, and analysis along with some field examples have been well documented for DTS (Huckabee 2009, Holley et al, 2012, Holly et al. 2014) and for DAS (Cox and Molenaar, 2013). DTS provides an almost continuous temperature profile from measurements acquired at small discrete location intervals, (1-3 m) along the entire length of wellbore while DAS provides acoustic emission information based on amplitude and frequency with similar location intervals.

The DTS temperature measurements acquired during a stimulation treatment are indicative of the cooling effect on the wellbore, the perforated exit locations and annular regions behind the wellbore from the presence and passing of the colder injected treatment fluids. Of particular interest of course are the perforation locations themselves, nearby zones or portions of the annular region of the wellbore as well as other previously perforated intervals. (Holley et al, 2014) provides a field example in false color of DTS monitoring of an 11 stage stimulation treatment performed through a vertical well in the Permian basin. The temperature color range is shown with the coolest at 85F in deep purple/blue indicative of the cool injected treatment fluids to the hottest at 155F shown as deep red that corresponding to the near geothermal formation temperature. These so called "waterfall" visualizations provide dynamic snapshots of temperature during the treatment, the "warm back" period following the completion of the treatment as the reservoir temperature tries to recover to its original geothermal temperature and eventually during various periods of production to visualize the inflow of production fluids into the wellbore.

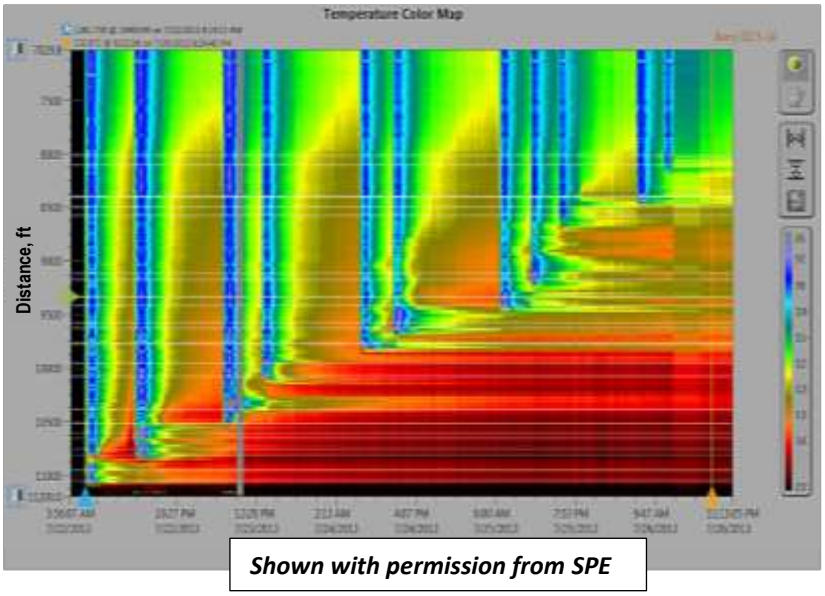

Shown with permission from SPE

Since DTS and DAS data can be acquired along the entire length of the wellbore information although focused on a particular treatment stage during its execution it is nevertheless possible to access stage isolation say from annular intrusion of treatment fluids into poorly cemented annular regions or around a swell packer in an open hole completion (Holley et al, 2012) as well as any unintended interaction with previously executed HF stages.

An example of HF inter-stage complications derived from DTS data is shown for 4 HF stages in a horizontal well in the Barnett and annotated from (Huckabee, 2009). The actual wellbore temperature (^{o}F) during warm-back is shown in line format as a snapshot in time following the execution of all 4 stages. Note the

suggestion of multiple transverse fracs at stage 4, the "fluidized" fracs at stage 2 described by Huckabee as 'injection into natural fractures" while the earliest frac stage 1 appears to show a single transverse frac.

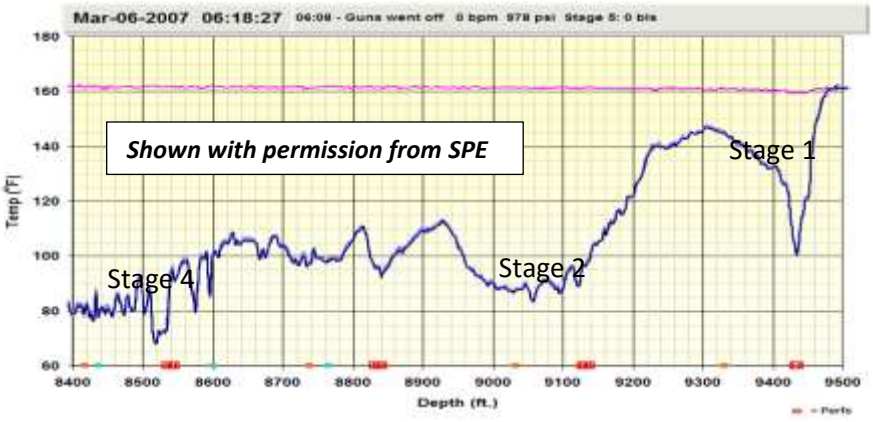

An example of the acoustic emissions or sound field monitoring with DAS from various HF stages of a 10 stage completion in a tight-sand is provided by (MacPhail et al, 2012). The horizontal well was completed open hole with swell packers used to isolate the various frac stages and ball activated frac valves. In addition to monitoring acoustics associated with the HF itself the DAS was meant to be particularly useful in giving information about in well activities such as those from ball seating and activation of frac valves. That information provides immediate feedback of in-situ HF treatment activities thus raising the possibility of an almost real time assessment of the processes which might lead to thoughtful data driven modifications of the treatment. The attached figure shows the DAS measured emissions shown in false color where time is on the vertical axis. The horizontal axis denotes depth advancing toward the toe. The figure is annotated with the locations of the stage packers and intervals. The active emissions are shown for a 3 minute period during ball sealing and valve opening.

Production Monitoring

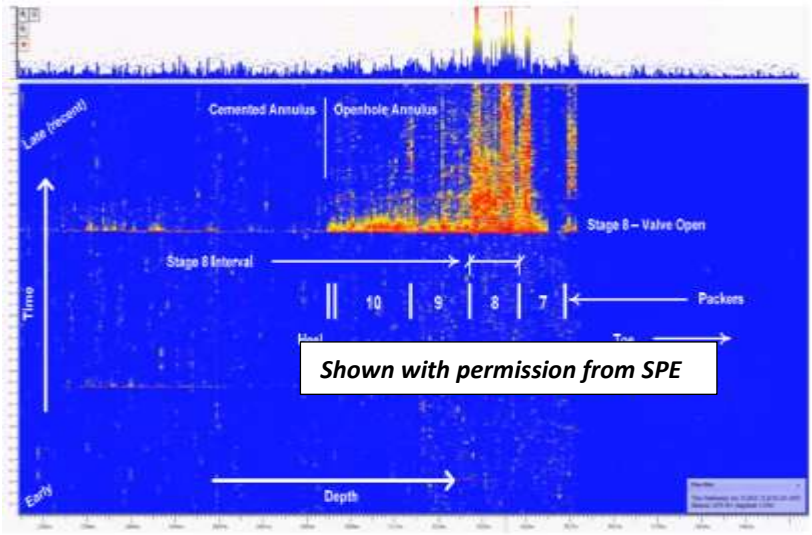

Cumulative fluid production as measured at the surface is of course of primary interest since it represents the ultimate global assessment of the well, stimulation, reserve recovery and economics. However from an engineering point of view it is very important to understand where and how much production can be attributed to each of the perforated and stimulated stages. The far field HF diagnostics provide important information as to which stages appear to have experienced some degree of fracturing, whether they generated symmetric or asymmetric fracture wings, most of the dimensional aspects of the fracture(s), and any apparent complexity induced beyond the main HF fracture(s). Nevertheless those individual diagnostics lack the fidelity necessary to define for each HF stage the total effective producible contact surface area, interconnected complexity, and interconnected conductivity of the primary propped HF.

During production fluids undergo small but measurable transient temperature changes attributed to pressure reductions as described by the Joule–Thompson effect. This pressure dependent effect can occur at choke points in the wellbore generally at fluid entry points such as perforation locations. (Johnson et al, 2006) describes the use of temperature data from DTS acquired during production to obtain inflow profiling in multilayered vertical wells for both dry gas and water production cases. While the actual temperature data can quite often provide a visually qualitative assessment of areas within the wellbore that infer gas or liquid inflow much as it does in the treatment injection cases described above, a quantitative assessment of flow rates based on temperature requires analytic or numeric reservoir modeling. The models create a wellbore temperature profile that is based on simulated fluid flow regimes for each fracture stage, perforation location and the entire wellbore. The derived temperature profiles are then matched with the DTS temperature profile. The best fit temperature profiles then yields the model simulated inflow allocations or rate data. As with all models the results are only as good as the input data whether measured or synthetic. When available the results can also be compared with flow data derived from conventional production logging tools (PLT) and when applicable used to recalibrate the model.

(Cui et al, 2014) discuss combining wellbore, fracture and formation flow/thermal models to derive a temperature profile along an extended length undulating horizontal wellbore with multiple HF stages. For these types of well settings the semi-analytic models are becoming more complex than those for vertical wellbores requiring a priori not just the reservoir and fracture data but the intricacies of the effects on fluid flow within an asymmetric slanted or near horizontal wellbore.

In their paper they provide a field example for a near horizontal well in a liquids rich area of the Eagle Ford. The simulation derived temperature data is shown as a history match to the DTS measured data along with the geothermal temperature. Note that temperature decreases from heel to toe because the well was drilled toe up. With all the model variables but fracture half lengths fixed the best temperature fit as shown above results in flow rates and fracture half lengths for each fracture stage and inflow location.

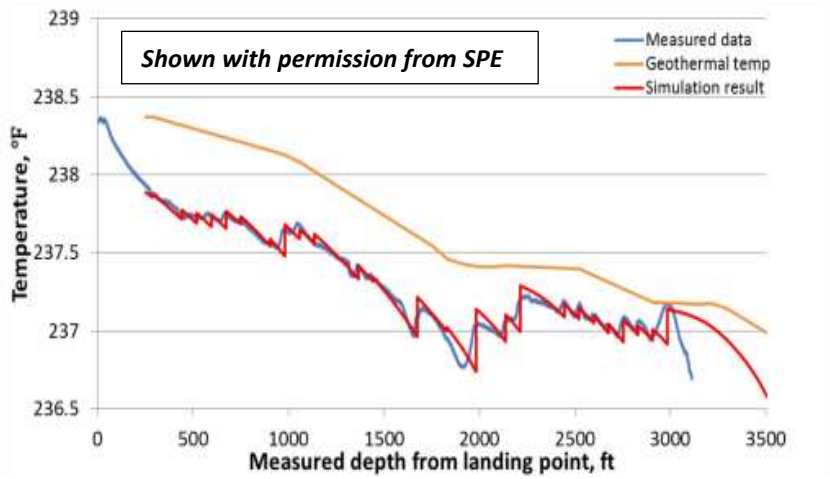

It's rather evident that fiber optic DTS and DAS are fast becoming mature technologies that can provide valuable information regarding the proper execution of individual HF stages and subsequently the effectiveness of individual stages based on their production.

Tracers

Since the 1940's when various radioactive (RA) isotopes became readily available for commercial applications they were used by the oil and gas industry in a variety of ways including as a tracer material

to identify injected treatment fluids and solids. Over the years different short lived low level gamma ray (GR) emitting isotopes have been used as a tracer to identify portions of hydraulic fracture treatments such as various fluids or proppant staging. Currently the 3 most commonly employed are Iridum-192, Scandium-46 and Antimony-124. Spectral analysis of these GR tracer emissions acquired with wireline run logging tools could then simultaneously identify multiple isotopes and the axial location within the wellbore where they reside. A brief historical perspective and cases histories of RA tracing of HF in vertical wells from a variety of field and reservoir settings are provided by (Barree et al, 2002).

Supplementing RA tracing, a variety socially and environmentally friendly chemical tracers are rapidly becoming the mainstay from which to tag and identify HF treatment materials and as well as produced hydrocarbons. With a large available array of chemical tracers individual fluid types and proppant staging for single or multiple HF treatments can be uniquely tagged and ultimately identified during the early cleanup phase of production. Samples captured from the surface flow stream during cleanup can be analyzed employing mass spectroscopy. A mass balancing technique is used to define the unique character and concentration for each of the chemical traced stages. The results of that analysis can then be utilized to indicate the volumetric flowback and cleanup efficiency for each traced stage leading to the implicit assessment of overall post frac production performance or enhancement.

An example of chemically traced treatment fluids for a 3 well case study is provided by (Asadi et al, 2008). These 3 vertical test wells were being completed in tight sandstone in the Carlise shale. Each of the staged treatment fluids from the pre-pad to individual proppant stages was uniquely tagged with chemical tracers. The overall study objective was to determine the most appropriate treatment schedule for both fluids and proppant concentration in order to arrive at increased cleanup or flowback efficiencies that might then improve production. The results from one of the test wells in this study, designated Well B is shown in the attached bar chart. The blue bars indicate the stage by stage fluid volumes injected during the treatment as measured at the surface during execution. The stage by stage volumetric returns shown as red bars and the individual stage flowback efficiencies in yellow were subsequently derived from the tracer concentrations in the sampled production stream during cleanup.

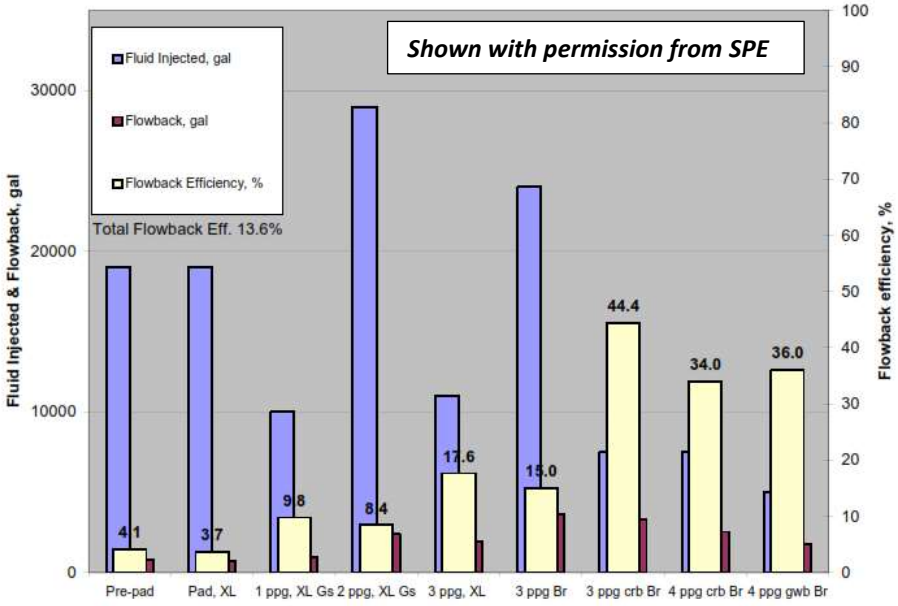

Another series of chemical tracer studies designed to characterize the recover or cleanup of frac fluids that were used in the treatment of multiple HF stages in horizontal wells in the Marcellus, Eagle Ford and Woodford are provide by (Johnson et al, 2013). One of the wells in the gas producing portion of the Eagle Ford had the treatment fluids in each of the 10 HF stages tagged with a unique tracer. The results of that tracer study are shown in the attached bar chart. The total fluid treatment volume by stage that was measured during execution is shown in blue while the recovered fluid stage volume calculated from the individual tracer concentrations that were captured in sampling of the surface effluent stream during cleanup are shown in red. The yellow bars represent the calculated treatment fluid recover efficiency for each stage.

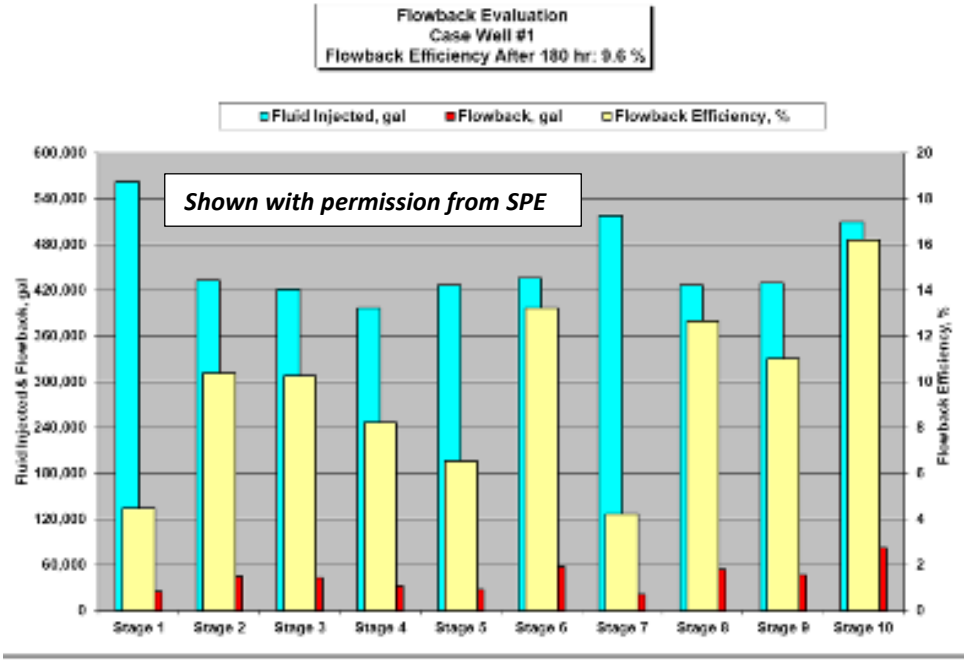

Preliminary results from a successful deployment of chemical tracers in a series of horizontal wells in the Barnett shale are described by (King and Leonard, 2011). Two offset parallel multi-stage HF wells, B1H and B2H were sequentially fractured with each stage chemically traced and monitored with microseismic. The 3-D bar chart in the attached figure displays tracer concentrations recovered in samplings taken from both wells production flow stream during the first 7 days of cleanup. Each color represents a different tracer stage while the sequential bars represent the calculated volumetric flowback from each sample.

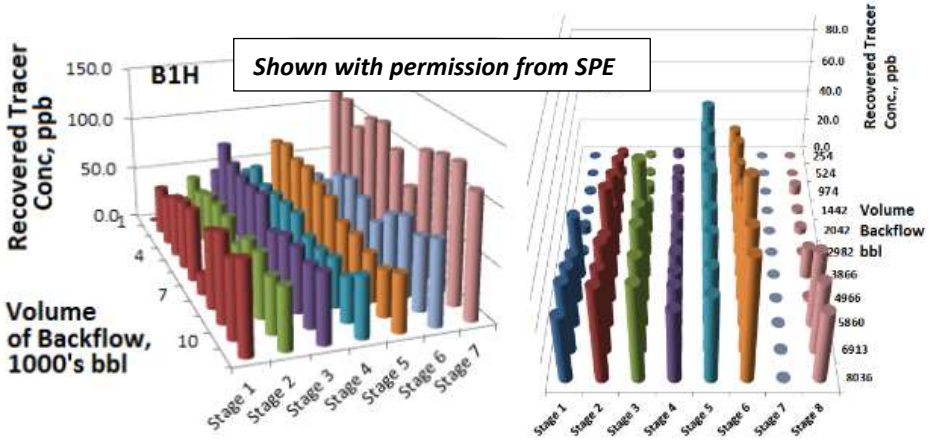

Chemical tracing can also involve the employ of soluble tracers injected in stage by stage HF's. The tracer whether oil (OST) or water (WST) soluble remain within fracture or on its face where the tracers are emitted into the flow stream when contacted by their specific solvent, i.e oil or water. Thus the subsequent production flow stream will then yield a specific tracer concentration for each stage that leads to the relative contribution of the traced reservoir product such as oil or water. An example by (Goswick, 2014) describes the use of OSTs deployed in each stage of 2 horizontal wells with multi-staged HFs. A 3rd well was treated with OSTs and WSTs in each of its HF stages. The objective was to define stage by stage HF oil production contributions for each well, assess HF stage effectiveness and the whether HF's might be affecting or interfering with offset wells. The 3 well study involved offset wells completed in the Lower Marmaton formation in Oklahoma and the attached figure shows a line chart for the percent contribution of oil production for each of the 9 stages vs time from one of those test wells, F-4H. Although time is not defined in their graphs tabular information in the text describes sampling from cleanup through 180 days. (Stegent et al, 2011) describes the use of oil soluble tracers to evaluate treatment efficiencies and the differences between 2 completion strategies in a horizontal wellbore based on their stage by stage production.

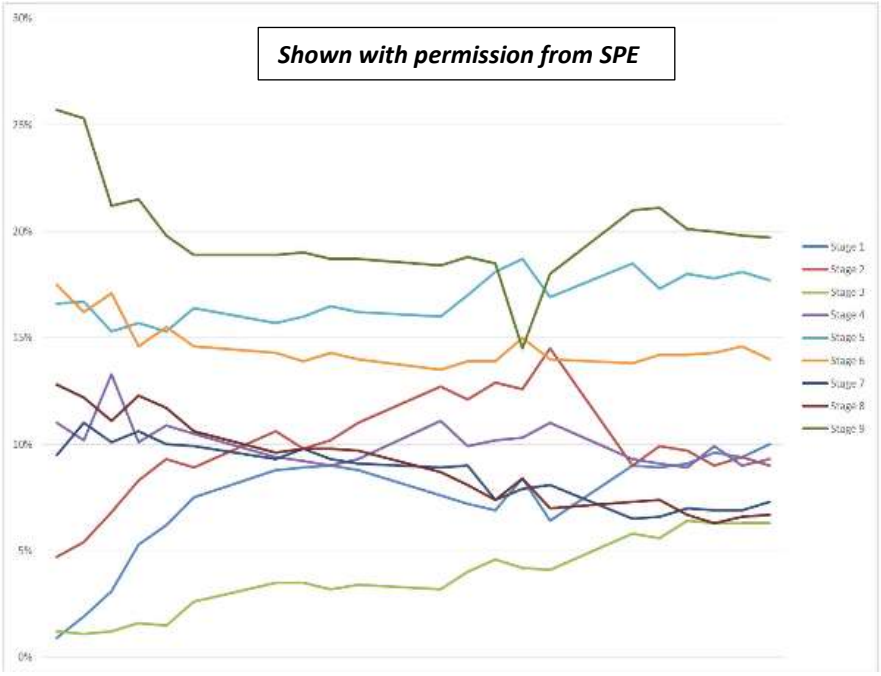

The application of RA and chemical tracer diagnostics individually or combined can certainly assist operators in assessing these complicated multi-stage completion practices. Stage by stage chemical tracing can also provide a quantitative appraisal of the relative production capacity for each HF stage. Further as operators continue to shrink well spacing in an attempt to maximize reserve recovery chemical tracing is an effective diagnostic tool regarding well to well interference or communications.

Diagnostic Fracture Injection Test

Diagnostic fracture injection test (DFIT) involve injecting fluid under high pressure in order to create a HF that by design should enable the analysts to acquire specific data regarding the geophysical and geomechanical properties of the fractured formation as well as ascertain HF and reservoir properties. Early pre frac injection test analysis based on pressure falloff data employed some or a combination of simple pressure vs time, log(Δp) vs log(Δt), square root of time, G-function, and the various derivatives of those relationships, see (Barree et al, 2007). Similar in execution to in-situ stress tests and mini-fracs, DFIT injections are designed to be relatively small HF but sufficient to make contact with the entire formations net height and thus create significant fracture cross-sectional surface area. The acquisition of DFIT pressure during the decline or falloff portion of the test particularly in unconventional reservoir is

however considerably long, requires dynamic high resolution bottom-hole pressures and the overall analytic techniques are more involved since the anticipated data and results extend beyond those normally acquired from either in-situ stress tests or mini-fracs. (Barree et al, 2014) provides a good overview of all aspects of DFIT including execution, data acquisition, analysis and pitfalls.

The need for detailed in-situ rock properties, geomechanical data, HF dimensions as well as a complete characterization of the reservoir cannot be overstated for the ultra-low permeability resources such as shale formations that in addition are completed with multi-staged HF through extended length undulating near horizontal wellbores. Some of the issues with a DFIT are particularly exaggerated in acquiring accurate test data, adhering to analytic formulation assumptions and the interpretation techniques some of which are discussed by (Soliman and Gamadi, 2012, Wallace, et al 2014). As (Wallace, et al 2014) aptly assert DFIT analytic techniques and resulting interpretations have roots in the original work of (Nolte,

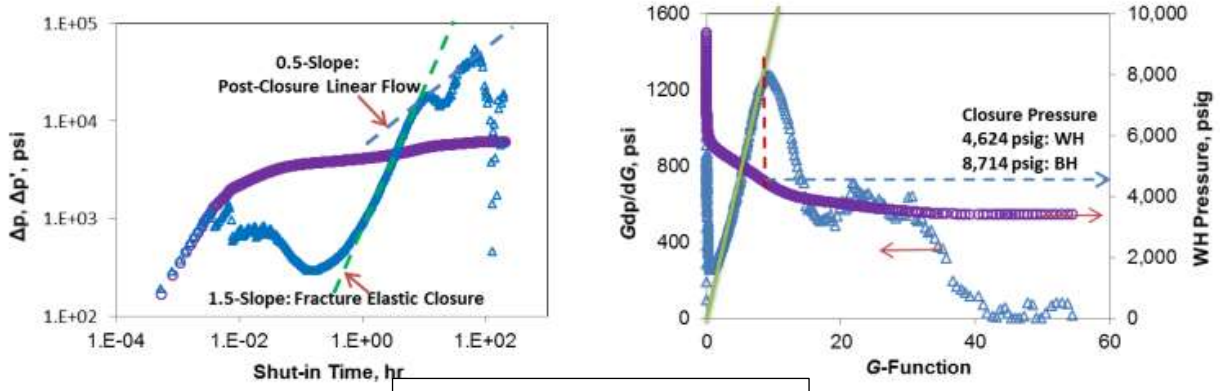

Shown with permission from SPE

1979). That work described analytic techniques and methodology to quantify HF and certain reservoir parameters based on pressure decline data following a HF treatment. Although that work is physically sound it requires rather strict adherence to its base assumptions and limitations, the least of which is not that pressure should be defined at the wellbore edge of the induced fracture.

An example of complications involved in assessing fracture closure pressure from DFIT pressure decline is given in the (Wallace, et al 2014) paper. This nicely illustrates what appears a reasonably appearing real time pressure decline that when analyzed with G function and derivative analysis indicate considerable differing fluid loss processes and complications in simply defining frac closure pressure. The details and their assessment of non-ideal falloff behavior along with some possible physical explanations for such behavior, such as natural fractures, thermal effects and other is certainly worth a careful read. Note in this example that pressures are measured from what appears to be wellhead gages with the implication that bottomhole pressures are then derived. I would add that tubular and fluid compliances, the presence and migration of multiphase fluids with differing compressibility's occupying various positions in the wellbore will adversely affect the derivatives and if not addressed with obviously skew and add a measure of subjective bias to the analysis. The acquisition of bottomhole pressure that is shut-in or isolated from as much of the wellbore as possible is rather imperative given the undefined nuances that can appear in the pressure derivatives and thus their causes then require considerable speculation.

All of that being said DFIT is presently the most advanced and preferred technique in the acquisition of dynamic in-situ rock stress and reservoir properties which if all things in planning, execution and analysis

go as designed it can provide vital and reasonably accurate data related to the effective HF completion of these unconventional complex reservoirs.

Well to Well Interference

Shown with permission from SPE

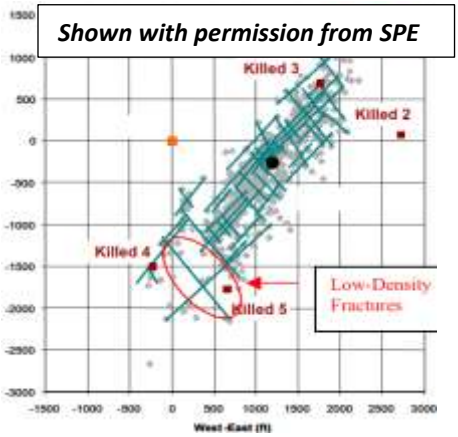

Well to well interference or direct communication between nearby offset wells following the execution of one or more stages of hydraulic fracturing of a newly completed well has been well documented (Sardinha et al, 2014, Yaich et al 2014, Johnson et al, 2013). Early recognition of such behavior in the Barnett shale (Fisher et al, 2002) was quite obvious when multiple wells had production "killed" or seriously affected during the HF execution of a new infill well. In addition to pressure interference or implied communication, treatment fluids, tracers and proppants have been detected in previously completed or producing offset well(s) from newly completed wells (Johnson et al, 2013). Originally well to well interference was considered an adversity to proper well spacing and placement, it now appears that some amount of reservoir or well to well communications through some commonality in the SRV's may facilitate more effective, and efficient reserve recovery particularly in the very low permeability reservoirs which should then increase corporate asset value (Jackson et al, 2013).

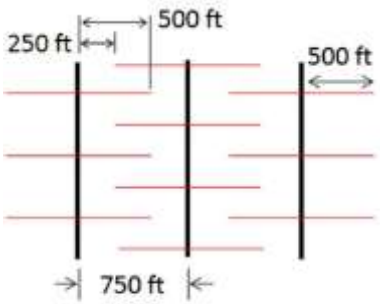

50% SRV Overlap

Shown with permission from SPE

(Sahai et al, 2012) presented a series of reservoir simulations to assess the optimum number of horizontal wells in a section with non-uniform spacing and HF lengths. In a companion paper to (Jackson et al, 2013) the authors expanded their simulations to assess the impact on zipper type fractured horizontal well spacing where fractur s wells shared portions of a common SRV (Sahai et al, 2013). The attached figures show an illustration of the simulated well spacing geometry for the case with 50% overlay between each wells HF's and the resulting analysis for various spacing and thus overlays. The analytic graphs show incremental NPV and normalized cumulative gas production for simulations of 1 to 8 wells per section based on 20 years of production. The optimum number of well per section is then taken as the point when NPV or cumulative production crosses the 50% line thus any additional wells would increase the recovery factor less than 50% of the 1st well. The data symbols show the base case or non-overlapping SRV case (5 wells per section) and the SRV case with 50% overlapping SRV with the dotted line indicating the 50% incremental value.

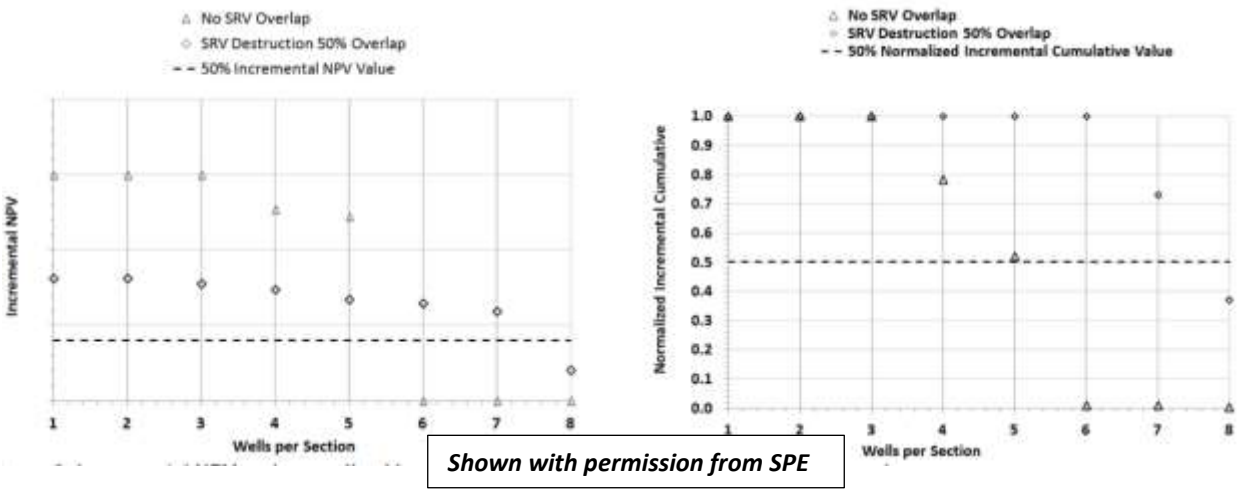

Shown with permission from SPE

Of course the ideal type simulations above are never quite that simply played out in field execution given the geomechanical and depositional complexities. Changes in the stress field that surround an open HF can if sufficiently large alter the direction of an approaching HF (Warpinski and Branagan, 1989). (Manchanda and Sharma, 2012) extended that analysis to include multiple fractures from one horizontal well approaching fractures from an offset well and devised a time staggering of stage treatments for offset wells to minimize the effect.

(Sardinha et al, 2014, Daneshy, 2014) distinguish and discuss the differences of direct and indirect fracture connections between offset well and how they be observed and identified in the pressure records.

It seems rather clear that some level of use of common reservoir area or SRV between wells can be beneficial to cumulative production and thus NPV. To what extend that sort of development can be extrapolated from simulation to field by field or basin by basin of course depends on many factors most of which are probably not known a priori and is yet to be determined.

Integrated HF Diagnostics

The last item in this manuscript study will focus on some field studies that used a combination of the diagnostic technologies described above in order to further their understanding of whether or not and how their current development schemes might be achieving some measure of success.

(Fisher et al, 2002) described the use the combination of diagnostics technologies including microseismic mapping in conjunction with surface and downhole tilt inversion models to enhance the operators understanding of the complexities associated with the early treatment and development of the Barnett shale. The diagnostic results showed what appeared to be a rather formidable fracture network that grew well beyond any imaged singular planar fracture system and sparked the suggestion of an astonishing large SRV surrounding the fracture treatment "fairway". The figure is an example of those complexities along with noted areas that appear aseismic.

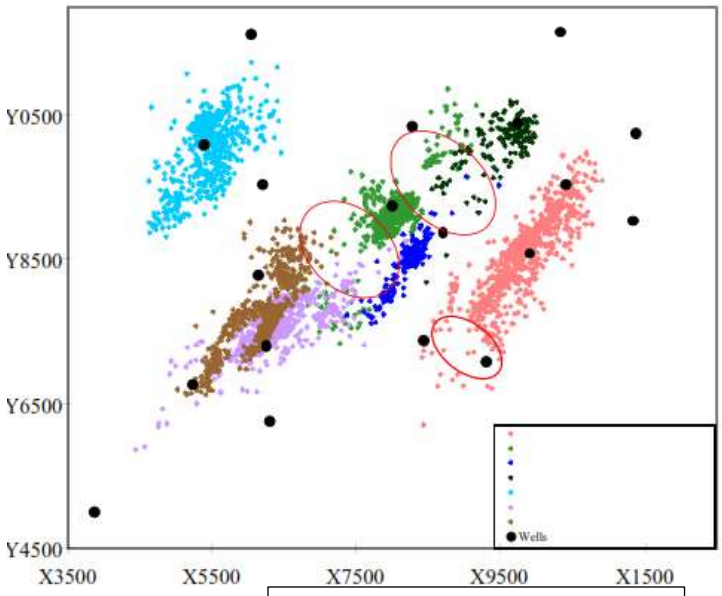

Shown with permission from SPE

Although the paper by (King and Leonard, 2011) is focused on the use and assessment of fluid and proppant tracers applied to multiple horizontal well completions they provide a rather entailed list of data other sources and diagnostics that can aid in assessing the reservoir and completion process. They make use of other diagnostics such as microseismic, fracture treatment information, production logging and other flowback measurements to aid in their overall analysis of the fracturing process and its effects on production. The attached composite figure shows two stages of a multipe staged horizontal well treatment that had steir stages tracer with differing RA tracers along with th corresponding plan view of the mapped microseiemics events from those stages. The RA spectral analysis of stage 5 suggest non-transverse fractures possibly longtiudional ones while the RA signatures from stage 6 fractures appear to be well spaced and transverse.

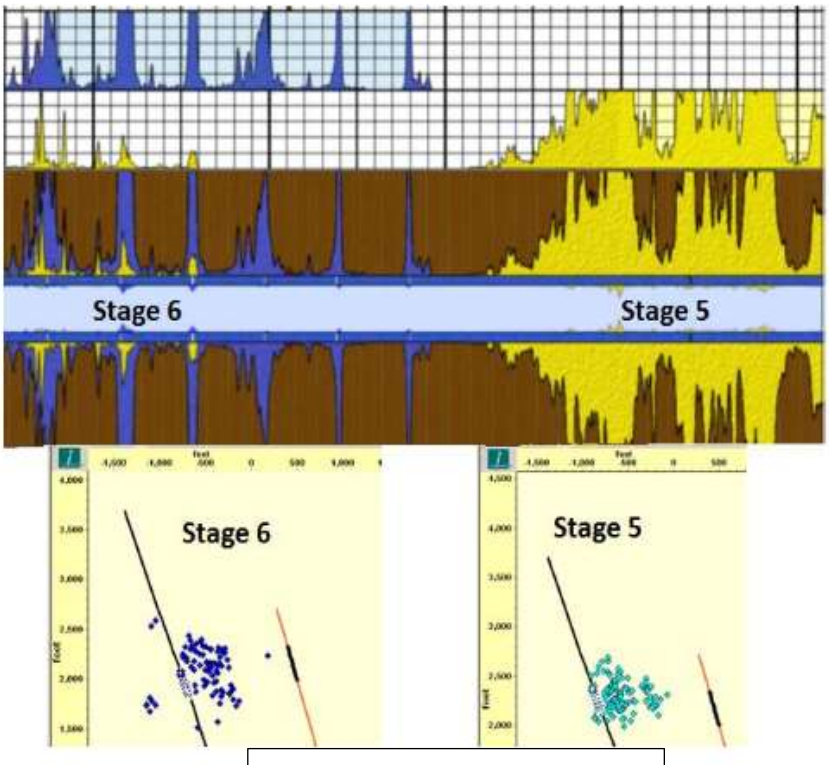

Shown with permission from SPE

They further indicate that the microseismic events suggest a near wellbore fracture for stage 5 as well that might support the stage 5 RA tracer assumption of a longitudinal frac with some added complexity.

(Stegent et al, 2011) describes the use of oil soluble tracers combined with microseismics to evaluate treatment and production efficiencies and reservoir complexity for 2 differing completion strategies in the Eagle Ford. The hydrophobic tracers were successfully injected in 14 of the 16 HF stages. Sampling of the production stream provided stage by stage tracer concentration from which the relative stage oil production bar charts are derived. The attached figure depicts the relative production for each stage of the1H well. The second figure is the final map of microseismic events from all 16 stages of the 1H well treatments.

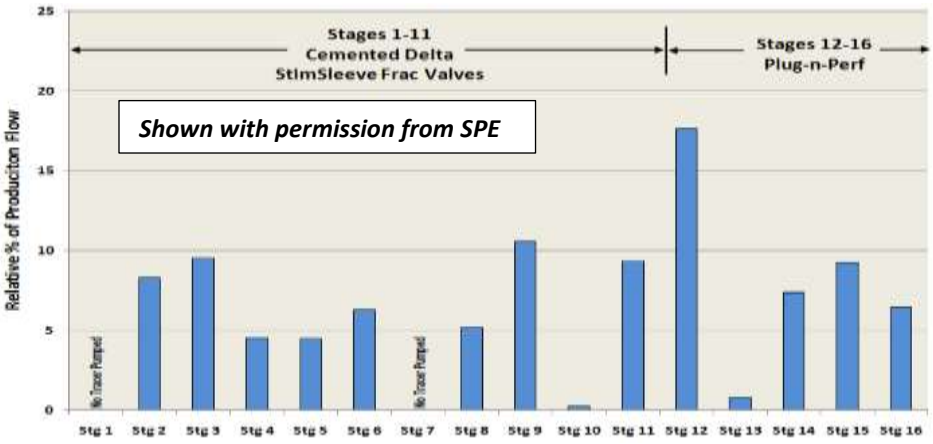

Both of these figures provide data as time snapshots, the microseismic during the treatment period and the tracer production data derived from 14 days of production. It is always instructive with microseismic to view the stage by stage time map to get a better sense of the possible propagation of the stage fracturing process and when and where complexity may be occurring. The authors provide a couple of stage by stage examples in their paper. The operator was able to integrate the tracer and microseismic results from which to favorably compare their completion methodologies.

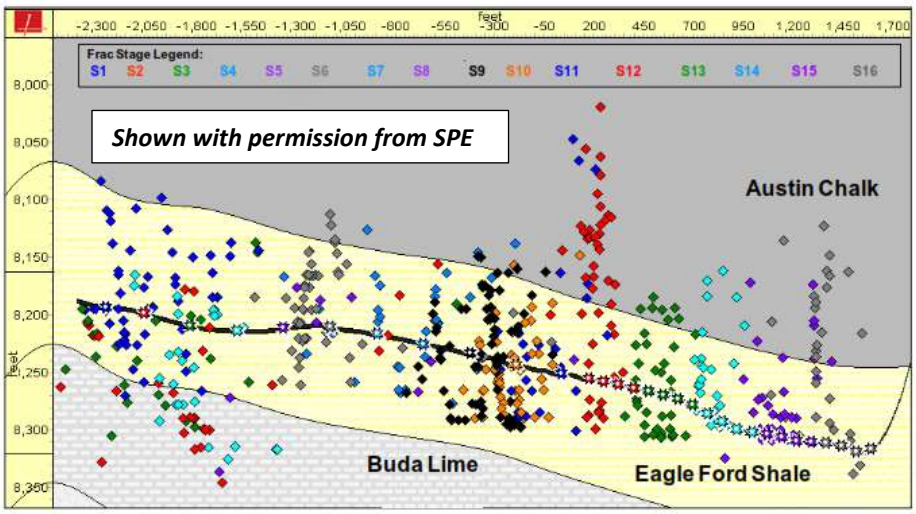

Shown with permission from SPE

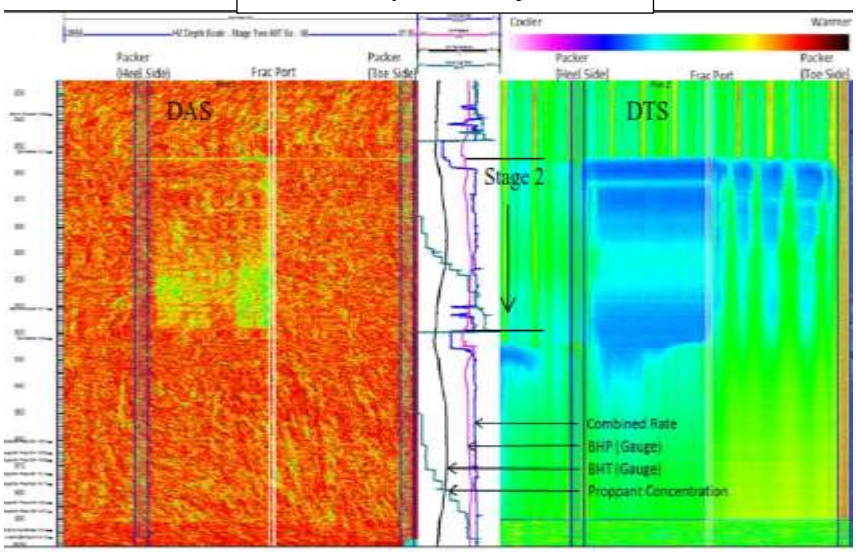

Data, observations and results of a fiber optics DAS deployed in the open-hole completion of a horizontal well with ball activated fracvalues were provided by (MacPhail et al, 2012). In these field tests they included other diagnostic in addition to DAS that included DTS, downhole pressure, microseismic and RA tracers. They were meant to complement the DAS data and their individual and combined interpretations. The attached figure with time on the vertical axis shows data acquired from DAS and DTS during the stgae 2 treatment. In addition they include treatment data such as injection rate, proppant concentration and bottomhole pressure.

Shown with permission from SPE

Will Determine
May Determine
Can Not Determine

GROUP	DIAGNOSTIC	MAIN LIMITATIONS	ABILITY TO ESTIMATE: Length	Height	Width	Azimuth	Dip	Volume	Conductivity
Indirect	Net Pressure Analysis	Modeling assumptions from reservoir description	■	■	■			■	■
	Well Testing	Need accurate permeability and pressure	■		■				■
	Production Analysis	Need accurate permeability and pressure	■		■				■
Direct, near-wellbore	Radioactive Tracers	Depth of investigation 1'-2'		■	■	■	■		
	Temperature Logging	Thermal conductivity of rock layers skews results		■					
	HIT	Sensitive to I.d. changes in tubulars							■
	Production Logging	Only determines which zones contribute to production		■					
	Borehole Image Logging	Run only in open hole – information at wellbore only				■	■		
	Downhole Video	Mostly cased hole – info about which perfs contribute		■					
	Caliper Logging	Open hole, results depend on borehole quality				■			
Direct, Far Field	Surface Tilt Mapping	Resolution decreases with depth	■	■		■	■	■	
	DH Offset Tilt Mapping	Resolution decreases with offset well distance	■	■	■	■	■	■	
	Microseismic Mapping	May not work in all formations	■	■		■	■		
	Treatment Well Tiltmeters	Frac length must be calculated from height and width	■	■	■				

(Barree et al, 2002) discussed the available diagnostic tools currently in use at the time for vertical well completions and categorized their utility in defining HF characterization and reservoir complexities from near wellbore and far field measurements. They further went on to provide a matrix that described their estimation of each of the diagnostics capabilities and their limitations in providing specific attributes of the HF and complexity. Note that in their estimation only far field type diagnostics will yield a determination of HF attributes. It is not surprising that the indirect tools are model or analytic based and are listed in the "may determine" category since they all have self- imposed limitations and adherence to specific input requirements that are rarely achieved.

(Warpinski et al, 2014) expanded on the assessment by Barree to include diagnostic tools as they pertain to horizontal well completions in unconventional reservoir. Although focused on microseismic they detail a number of other diagnostic technologies and how they may contribute by adding character and dimension to the microseismic results. That is of course reciprocal since many of the listed diagnostics in

Horizontal Well Fracture Diagnostic Chart

Technique / Attribute	Length			Far-Field Height	Fracture Width	Fracture Azimuth	Fracture Dip	Asymmetry	Complexity	Stage Isolation	Staging Effectiveness	Diversion
	Total	Propped	Effective									
Wellbore-Based												
Well Testing Analyses												
Production Analyses												
Fracture Pressure Analysis												
Radioactive Tracers												
Chemical Tracers												
Production Logs												
Distributed Temp Sensing												
Distributed Acoustic Sensing												
Offset Horiz Well DTS, DAS, Tracers												
Offset Horiz Well Pressure gauges												
Far-Field Imaging												
Microseismic-Downhole												
Microseismic-Surface												
Tiltmeter-Surface												
Tilt-Downhole Offset Well												

Shown with permission from SPE

Does Not Measure | Provides Estimate | Accurately Measures

the attached chart compare their results to the microseismic maps and interpretation. This chart appears to be indicative and rather inclusive of the current state of the various diagnostic technologies. It's clear that there are numerous limitations that exist in defining the HF and reservoir attributes even if all of the listed technologies are employed and their individual and collective results are considered accurate. Some of these technologies could find themselves moving from the "provides an estimate" category to the "accurately measures" category when using new information or data from advances in other new or developing technologies.

As with most developing technologies when they advance they tend to resolve old issues and solve for our current set of unknowns. This will of course lead the industry to a whole new set of concerns equally or more complicated than our present ones. Recall that not very long ago one of the primary concerns facing the industry was whether to define the singular planar HF width dimensions using the rectangular shaped KGD or elliptical PKN model.

A number of diagnostic techniques have been addressed in this study. Some lead to a rather formidable assessment of one or more particular aspects of the HF process or its subsequent effect on the reservoir while other may provide at best a shaky qualitative appraisal. Achieving developmental success in the complicated environment posed by very tight layered reservoirs such as shales will only occur through the integration and collaboration of the most the pertinent of these diagnostic technologies and ones that are yet to come.

As stated in (Warpinski et al, 2014) ***" The main goal of fracture diagnostics should be to aid in the development and calibration of realistic models that can be used to analyze, design, and predict performance of the stimulations and resulting production. This often requires complicated workflows and calibration of unknown reservoir data, but the insights from such modeling can be extremely valuable for optimizing unconventional development and ensuring the proper balance of reserves recovery and capital expenditure."***

Permian Basin

The Permian basin has long been a mainstay of oil and gas production in the US. The first wells drilled in the early 1920's were the precursor for realizing the basins enormous reserves and production capacity. Historically the various producing intervals such as those in the Spraberry and Wolfcamp formations were developed using vertical wellbores and some stimulation. Following many decades of production the conventional resources went on the decline and the operators turned their attention to the unconventional resources that are prolific in the Spraberry and Wolfcamp shales. Pioneer now estimates that the Spraberry and Wolfcamp shales may contains more than 75 BBOE and ranks it as the largest US oil field.

Throughout the US modern development of shale resources whether oil or gas relies on production from extended length horizontal wellbores with multiple transverse propped hydraulic fractures. And so the development of the unconventional plays in the Permian basin is in lock step.

An integral part of their field development Pioneer Natural Resources makes extensive use of microseismic data and analysis. The microseismic events are obtained primarily from subsurface arrays and that information is used to delineate multi-stage hydraulic fracture geometry. Those results and interpretations will ultimately drive the development of proper well spacing (Hull et al, 2013). (Hull et al, 2013) provides a microseismic example of what they suggest may be stress interference from a hydraulic fracture in one offset well effecting the propagation of a new hydraulic fracture in the new well. Pioneer indicates that microseismics has certainly advanced their understanding of what appears to be complications and variations in fracture propagation azimuths. They also pay particular attention to geomechanical properties in order to define stress

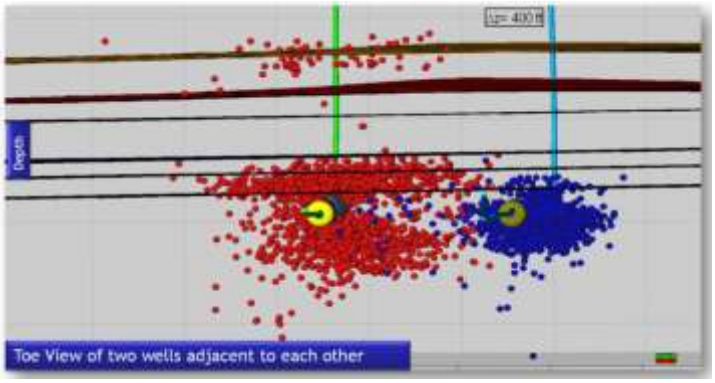

heterogeneities that appear to exist in certain of the many targeted layers and thus influences placement of the wells landing zone.

They indicate that they have had “tremendous” success with the horizontal well development of their Wolfcamp targets employing a systematic approach to understanding well performance (Mohan et al, 2013).

Technology merits and limitations

Microseismic technology

- Microseismic technology as applied to the spatial delineation of the HF process has found wide spread acceptance in the oil and gas industry. Given an array whether surface or downhole with a well-defined view of the fracturing process along with accurate layered geo-mechanical properties locating the events at depth is reasonably well understood.
- With fairly robust events moment tensor analysis can provide information regarding the event source mechanisms. That analysis aids in assessing what physical process is at work in the subsurface whether from the HF directly or more indirectly by inducing slippage or movement of preexisting discontinuities in the rock fabric such as bedding planes and natural fractures.
- The absence or clustering of events during any HF Stage can be a clear indication of fracture asymmetry an ineffective, diverted or missed treatment stage.
- Given a sufficient number of HF stage related events its overall length, azimuth and dip can be estimated.
- When the event locations are numerous the mapped visual representation can be striking. Stage by stage linear features add confidence that they are representing the propagation of a HF. Events location clouds suggest a more complex fracture system i.e. the HF and the induced movement of natural fractures or other.
- The event location maps are in reality a series of individual points in space and ascribing specific spatial dimensions requires considerable subjectiveness.
- Surface arrays require numerous monitoring sites spread over a rather large area. Downhole arrays require vertical offset wells or an offset horizontal wellbore that will provide a quiet unobstructed view of the events associated with the various stages ongoing in the test well.
- The industry has made great strides in developing the unconventional resources with multi-staged HF’s in extended length horizontal wells. Microseismic technology has played a significant role in that regard. It has clarified our understanding of the HF execution process and more importantly how the reservoir is responding to the treatment.

Tiltmeter Technology

- Tiltmeter arrays responds to the deformation of the rock mass imposed by the overall HF volume. A surface array with sufficient resolution can indicate HF azimuth, dip and if it has been significantly diverted.

- A downhole vertical tile array measures the rock deformation in the vertical plane which leads to a measure of fracture height, vertical asymmetry and width.
- A downhole array also responds to the temporal deformation of an open or propped HF indicative of growth. It can also show the residual profile when the HF is completely closed which may reveal proppant location.
- The tiltmeter inversion process constrained by microseismic data instills confidence in the overall model results.
- To effectively define the HF width profile the downhole tiltmeter array needs to straddle the HF interval.
- Surface tilt arrays require multiple buried monitoring sites that surround the footprint of stimulated test well.
- A downhole array requires a vertical offset well that is quiet and straddles the anticipated HF height.
- A hybrid downhole system involving a microseismic and tiltmeter array would of course reduce the requirements for the number of offset vertical wellbores

Fiber Optic Technology

- DTS and DAS are capable of defining temperature or acoustic emissions at small intervals (~3ft) along the entire length of the wellbore.
- The fiber is designed for long term deployment and can be monitored for years to assess the effects of fluid production.
- DTS responding to the thermal cooling from injection frac treatment fluids during execution are clear spatial indicators of the reservoir entry points.
- Post frac wellbore temperatures show the effects of “warmback” and the resulting images from DTS analysis can delineate stage by stage frac locations as well as an indication of fracture shape.
- DTS monitoring during production provides a temperature profile of the entire wellbore denoting the small but measureable temperature changes at fluid entry points. Thermal models are then adjusted for each stage of fracture fluid flow and wellbore effects to find a best fit to the DTS temperature profile.
- DAS measures acoustic emissions during various phases of the wellbore completion process. The emissions delineate high velocity points within the well that can be attributed to fluid and proppant entry locations in the wellbore. Further they can provide emissions associated with in well activities such as from valve opening or packer settings.
- Measurements from DTS and DAS provide valuable data and images that are initially qualitative at their base and suggestive of specific well activity, i.e. fluid and proppant flow, production rates and in well activities.

- Single point fiber optic pressure elements can provide accurate long term BH pressure data to a wide variety of design and analytic fracture and reservoir modeling techniques.
- Those data can be used as a basis for model derivations to further quantify certain specific parameters such as fluid flow.
- Monitoring an offset well may provide information regarding well to well interference or communications.
- The deployment, positioning and shielding of the fiber optic is critical to the effectiveness of the data acquisition and varies depending on the wellbore type and completion design.

HF and Production Tracer Technology

- Specific RA isotopes can be effectively used to trace treatment fluids and proppants. Spectral logging and analysis can then delineate the type and positions in or very near the wellbore where those specific isotopes finally reside.
- A large number of chemical tracers are now available to trace individual HF fluids and proppants stage by stage.
- Injected into each HF stage during the fracturing process their return upon frac cleanup or production can be sampled from the surface flow stream and used to identify the tracer and thus define the relative production from individual stages.
- Oil and water soluble tracers are deployed and injected into the HF in a manner similar to process used with chemical tracers. Upon flowback they provide a unique signature as to the presence in the flow stream of oil and water that can be attributed to individual HF stages. Relative productions can then be ascribed to each HF stage.
- Sampling of offset well production streams for chemical or soluble tracers can an effective diagnostic tool regarding well to well interference or communications.

DFIT Technology

- The DFIT execution process involves creating and propagating a HF while acquiring surface injection rates and pressure during the fracturing process and long after fracture shut-in.
- Those data are used in a variety of analytic techniques to define simple or complicated multiple fracture closure pressure and fluid leakoff as well as reservoir properties such as pore pressure and overall permeability.
- Reliable data and its analysis can be quite valuable in recalibrating HF treatment design and assessing the effected reservoir stimulation.
- Data acquisition and analysis that employ derivatives requires high speed, high resolution bottomhole pressure. This means either measurements from an isolated downhole gage or a surface gage with a well-defined and almost constant wellbore hydrostatic pressure.

- Sufficient time must be allocated for the acquisition of reliable DFIT data especially when performed in nanodarcy type reservoirs where fracture closure may take 10 days or more and many weeks to observe the end of pseudo linear flow or departure into pseudo-radial flow.
- DFIT is presently the most advanced and preferred technique in the acquisition of dynamic in-situ rock and reservoir properties acquired from an injection and falloff data from a small HF.

Well to Well Interference

- As more efficient and effective drainage of reserves appears possible with closer well spacing that includes some level of well to well interference acquiring positive indications from an offset well of new well activities is becoming essential.
- Offset pressure measurements that show a significant pressure increase associated with one or more HF stages from the treatment well would be indicative of a direct conductive communication path between wells. More subtle pressure changes may signify some communication pathway within the SRV between wells or some circuitous path between their HFs.
- Chemical tracer monitoring of the offset well production stream can indicate which stages have communicated directly between wells. When the response is nearly immediate it indicates a direct conductive path. When the response is delayed it may signify some communication pathway within the SRV between wells or some circuitous path between their HFs.
- Periodic monitoring of both well flow streams for chemical tracers from both wells should assist in assessing how the wells and their common communication flow paths might be changing in time.
- Assessing the nature and number of flow paths direct or other that exists between wells will certainly aid in providing a critical parameter for revising reservoir production simulation and recalibrate well spacing and treatment designs.

Technology Gaps in Defining Certain HF and Reservoir Properties

HF Dimensions and Spatial Distribution

Currently the combination of microseismic, tilt and warmback DTS data appear to provide some of the best far field and near well data regarding stage by stage HF dimensions and their spatial distribution. None of the aforementioned are stand- alone diagnostics nor do they provide the accurate dimensional aspects of a fully connected HF. For example the most frequently employed diagnostic tool microseismic data and analysis provide locations in 3-D of seismic events that require some level of confidence to then make valid point by point connections that will form an effective 2-D picture of the lateral or vertical HF dimensions.

As these and addition diagnostic tools are added to and combined the dimensional aspect and locations of individual stages will surely improve our confidence in their interpretation.

HF Flow Properties

The development and use of DTS during production has provided a new measure of stage by stage production profiles. The models that form the basis for defining and quantifying individual stage inflow and wellbore flow effects will improve markedly when combined and recalibrated with other diagnostic tools particularly when multiphase fluids are present.

Chemical tracing, sampling and analysis represents another diagnostic technology that are capable of providing values of stage by stage fluid flow from the production stream. The combination workflow and interaction of results from both DTS and chemical tracers will surely add confidence to their collective defining of production.

The above combined with single point fiber optic DH pressure gage data will provide critical information to RTA, HF and reservoir models and their subsequent recalibration in defining HF and reservoir flow regimes and ultimately HF dimensions.

Fracture Connectivity and Secondary Fracturing

At present defining anything about fracture connections whether within the main HF treatment, those offset to it and induced during the treatment or secondary fracturing relies heavily on perceptions gleaned from microseismic map interpretations, a presumptive change of k_m to k_{eff} resulting from "enhanced" production or other. Microseismic event clouds and their locations often lead to the assumption that they then represent a connected conductive fracture set that greatly improves k_{eff} over k_m.

Appendix BC: Hydraulic Fracturing Test Site (HFTS) Permian Texas Overview

Background

The HFTS is a collaborative, comprehensive hydraulic fracturing diagnostics and testing program in horizontal wells at a dedicated, controlled field-based site. The program emulates the field experiments GRI and NETL http://www.netl.doe.gov/ performed in vertical wells in the 1990s (Mounds, M-Site, and SFEs). Technology has since advanced into long horizontal, multi-stage shale wells creating a new set of challenges and unanswered questions. HFTS will conduct conclusive tests designed and implemented using advanced technologies to adequately characterize, evaluate, and improve the effectiveness of individual hydraulic fracture stages as well as improved wellbore spacing, leading to optimal resource recovery. The highlight of the program features through-fracture cores to undoubtedly identify hydraulic fractures and their attributes, while validating fracture models and fracture diagnostic tools.

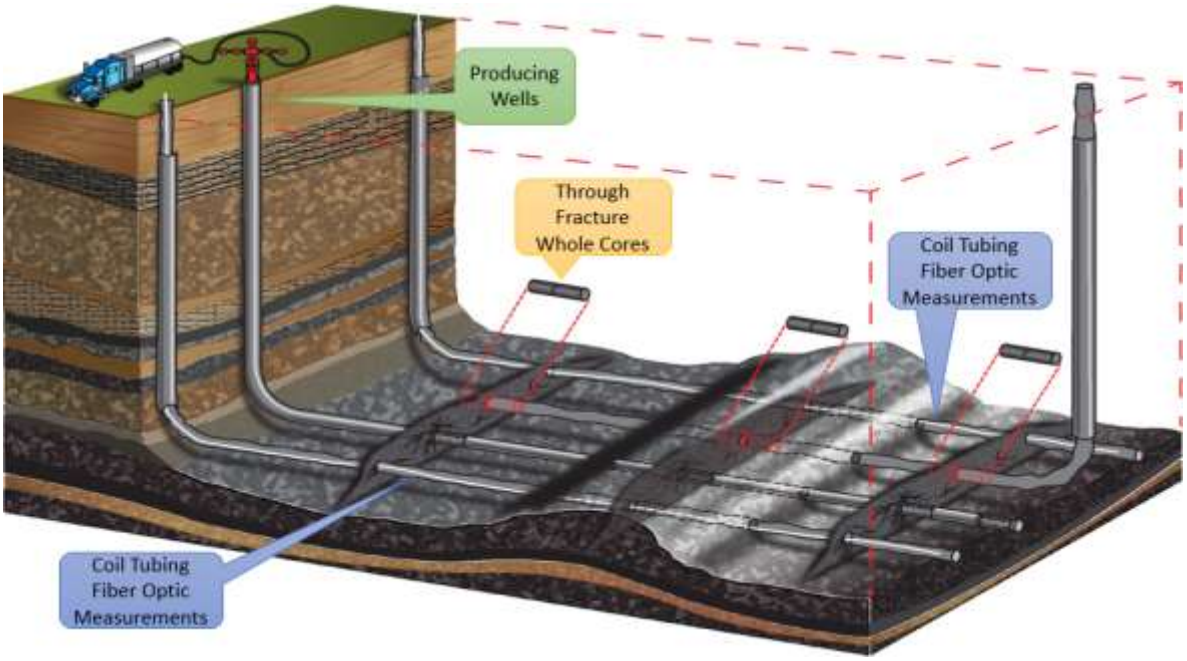

Figure 1: Conceptual test site design

The mission of HFTS is to increase shale environmental safety and stimulation efficiency (Figure 2). This will be accomplished through the evaluation and development of new methods and technologies that lead to higher production output per well with less material and energy inputs (fewer wells drilled), higher cost efficiency, greater reliability and safeguards, and reduced environmental impact.

Developed by Gas Technology Institute (GTI) http://www.gastechnology.org/ and a consortium of hydraulic fracturing experts from industry and government, the program will provide a clearer understanding of the fracturing dynamics key to controlling fracture dimensions and vital to the productivity of fracture networks created in horizontal wells. To improve well productivity and reduce environmental footprint, the program focus will be on improving the efficacy of individual fracture stages. The end result will be improved understanding of the fracturing process and identification of needed technologies and methods to enhance well productivity through more effective hydraulic fracturing treatments that require less water and resources per unit of energy produced. Improving the effectiveness of individual hydraulic fracture stages will lead to cost efficiency, maintaining safe operations, and minimizing environmental impacts. Learnings from this effort will advance operations for all resource production using hydraulic fracturing technology, including shale gas and shale oil.

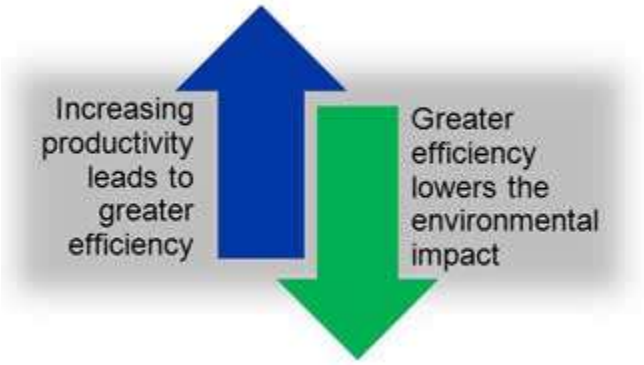

Figure 2: Mission and benefits of the HFTS

HFTS Benefits

Advances in stimulation technology will result in fewer wells being needed and higher production output per well. Anticipated benefits derived from HFTS include:

Benefits of Participation

- Leveraged investment in a dedicated, controlled field experiment.
- Collaboration with GTI and DOE http://www.energy.gov/ and a consortium of industry peers.
- Access to science wells explicitly designed for hydraulic fracturing diagnostics, environmental monitoring, data collection, and technology testing, including:
- Results of analysis verified with through-fracture cores
- Access to verified reservoir characterization techniques and workflow; and a thorough diagnostic data set including seismic, microseismic, cross-well seismic, micro-deformation, advanced logs, cores, production logs, reservoir pressure monitoring, and tracer program
- Access to independent, third-party analysis of the data.
- Early access to new technology commercialization opportunities.

Environmental Safety Benefits

- Development and transfer of advanced technologies that improve safety, lower environmental impacts, and reduce materials and energy required per unit of energy produced.
- Determination of potential health and environmental consequences of hydraulic fracturing to air, land, and water resources and development of mitigation strategies.

- Demonstration of safe and reliable hydraulic fracturing operations.
- Development of optimal instrumentation to reduce the margin of error in interpretation of monitoring and measuring of environmental conditions pre- and post-stimulation.
- Conclusive measurements of fracture height to show fractures are contained

Stimulation Efficiency Benefits

- Characterization, measurement, evaluation of hydraulic fracturing efficiency.
- Improvements to fracture design and evaluation of Stimulated Reservoir Volume.
- Assessment of created fracture conductivity and complexity as determined with reservoir pressure measurements
- Early detection of fracture effectiveness and development of methods and techniques for real-time control of fracturing effectiveness.
- Development and transfer of advanced technologies and methods to maximize resource recovery from each hydraulic fracturing treatment while minimizing the material and energy input requirements.
- Substitution of more effective materials or methods for those less effective.
- Development of optimal instrumentation to reduce the margin of error in interpretation of monitoring and measuring of created fractures.
- Evaluation of seismic techniques.
- Hydraulic fracture model verification and calibration. Determining spatial and temporal fracture network creation and validate against model.

Test Site Host and Location Information

The HFTS (hydraulic fracture test site) will be conducted on an eleven well completion program located on Laredo Petroleum's http://www.laredopetro.com/ Northern Reagan County, Texas acreage (Figure 3). Below is a map that locates Laredo's acreage in the Midland Basin. There are a significant number of operators in the surrounding area.

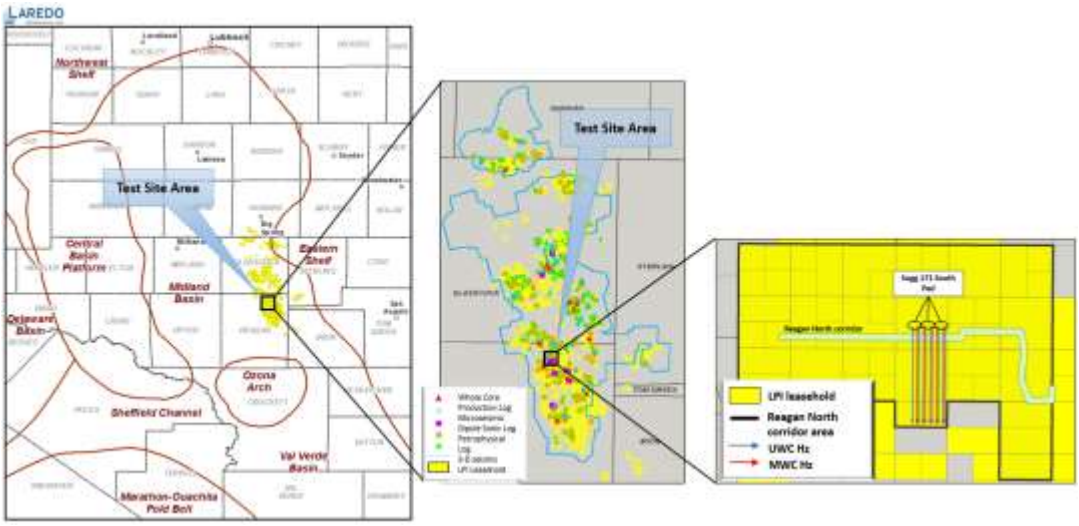

Figure 3: Location of test site, Reagan Co, TX

HFTS Test Site Location and Details (Sugg A 171 South Pad)

- 11 well pad in Reagan County, Texas
- Targeting Upper and Middle Wolfcamp, chevron configuration
- Wolfcamp depth ~7,500'
- All wells are 10,000' laterals to be completed with 36 stage completions

The Project Objectives Are:

- Evaluate and confirm environmentally safe operating procedures
- Determine fracture geometry and confirm maximum height growth
- Evaluate subsurface controls and operational impacts on hydraulic fracture geometry and completion efficiency
- Evaluate inter-well interference
- Understand stimulated rock volume & reservoir depletion over time
- Identify and evaluate the distribution and effectiveness of geological frac barriers
- Evaluate pressure front barriers created in stimulation sequence
- Test alternative frac designs in different wells in a relatively consistent geological setting
- Test production performance by stage/perf cluster post stimulation

Test Plan

- Below diagnostic program is designed to accomplish the above objectives
    - Microseismic and tiltmeter survey
    - Oil tracers
    - RA tracers

- Bottomhole pressure gages during production
- Production logs
- Fiber optics through coil tubing
- OBMI logs
- Pressurized sidewall rotary cores
- DFIT analysis
- High resolution cross well seismic through stimulated interval
- Full core through a stimulated interval
- Reservoir pressure measurement post completion
- Water sampling and air sampling program

The final technical and diagnostic program is being evaluated based on technical feasibility and available funding

Current Status

Started field data acquisition in October 2015 and plan to complete the through fracture core well in February 2016.

Funding

Partial funding for the project in the amount of $7.35MM is provided by the Department of Energy (DOE) and administered by NETL through an award received by GTI in 2014. Remaining funding is provided by industry participants either through in-kind services and cash contributions. We anticipate the total project value to exceed $20MM.

Appendix C: Hydraulic Fracture Stage (Cluster) Spacing Design Toolbox

Summary and Accomplishments

With the aim of improving the spacing of the perforation clusters along the lateral to take into account variations in geomechanical properties of the reservoir as well as the presence of gas and natural fractures, GTI has developed a hydraulic Fracture Spacing Design Toolbox which predicts optimal fracture design based on modeling of rock properties as well as hydrocarbon presence using information from mud logs. The reason for not using traditional wireline or tubing based tools is to avoid high costs associated with the same. The Toolbox has been developed for the Matlab environment and is available with a simple to use GUI interface as the front end and powerful Neural Nets/ Fuzzy Classifiers at the back end. Application on datasets made available by WPX Energy has shown the following:

1. Good predictability and applicability over both near field (same pad) and far field (100's of miles) Marcellus Shale gas wells.
2. Potential for enhanced productivity per specific unit of input used (water, proppant, chemicals, etc.) leading to reduced environmental footprint per unit of gas produced.
3. Optimal completion programs without having to resort to expensive post drill logs or expensive LWD tools.

Motivation

With the current "Cookie-cutter" approach to hydraulic fracturing, we see significant variability between fracture clusters due to multitude of factors both natural as well as engineering which can lead to some clusters showing insignificant to almost zero production creating zonal drops in productivity. Even though there are available solutions which use expensive logging tools to predict reservoir quality and design fracture spacing, we want to find a solution which is within the framework of current hydraulic fracturing approach without having to resort to these tools.

Introduction

While the advent of multi-stage hydraulic fracturing in long lateral completions has revolutionized shale oil and gas production, the process still lacks the robust understanding of what happens downhole within the reservoir and what leads to the significant variability in productivity from completed stages. A significant amount of work has gone into improving our understanding of these completions and some of these observations have provided enough information to try and improve fracture spacing design. Traditional approach to completion design involves use of transient rate-time analysis to identify key design parameters (permeability and fracture half lengths) and using them to predict well performance [1]. Stage spacing is a critical design parameter which is impacted by considerations of reservoir permeability [2], stress shadowing effects [3, 4], SRV considerations [5] and economic considerations such as net present value [6]. Other more elaborate techniques at optimizing stage spacing include use of microseismic data [7],

and fracture network modeling [8] to name a few. In practical applications, what is desirable is to take a holistic view of the completion process and utilize as much data and analysis as possible for design [9]. While holistic design techniques are in place, most methods do not account for variability in reservoir and completion effects along the long laterals. From production logs and distributed acoustic and temperature sensing data, we know that many clusters show insignificant to no production, creating zones with very low productivity. This clearly indicates that the "one size fits all" approach creates sub-optimal fracture design and this has been abundantly recognized by the industry [10]. We believe that while design issues (such as fracturing efficiency) are important; formation quality is critical as sections with lower quality should have modified fracture density to provide for adequate drainage.

Many novel approaches have been suggested in the past few years which involve a thorough investigation of the reservoir properties and the geomechanical aspects of completion in shale formations. One recent example highlighting an engineered fracture spacing design approach uses characterization of reservoir and completion quality which are used to predict proper stage placement [11]. Microseismic monitoring and other geophysical tools can also allow for improvements in design based on observations [12]. Generating pseudo logs for lateral sections of wellbore based on observations from the vertical pilots is an established technique [13] for understanding laterals and improving associated completions. Methods looking at fracability alone and utilizing stochastic optimization techniques have been evaluated [14]. The need for running wireline petrophysical logs for at least the vertical pilots and the need for core analysis and correlation is well understood. These are not routinely available and therefore, we felt there was a need for a technique that can be applied on any well and can provide a quick optimal design suggestion based on the historic field data available for the play in question and the mud log data from the well under consideration.

For this study, we wanted to devise a technique that can systematically distribute fracture stages for more effective drainage of the reservoir without the use of expensive wireline or logging while drilling data. What is unique about our completion design approach is the use of mud log data for completion design in the absence of any wireline petrophysical or geomechanical data from that area. This is expected to work reasonably well provided a predictive model for rock properties can be developed. In our approach, we use a hybrid AI (Artificial Intelligence) based modeling workflow to predict geomechanical properties where stage spacing design utilizes mud log gas shows as well as predicted geomechanical rock properties within a predefined design framework.

Method

For most new field development programs in unconventional plays, vertical pilot wells are drilled, cored and logged in order to gain a robust understanding of the formation before completions can be designed. These pilots provide valuable insights into the rock including the mineralogy, in situ stress state, organic content, lithology, porosity, etc. to name a few. This wealth

of data can be used to predict the behavior of the well laterals drilled from the pilot. Using data from such pilots, we propose to design predictive models for reservoir properties which can be obtained from mud log data alone. This allows for wider applicability of the design methodology without compromising on upfront well completion costs. We propose a hybrid neural network (Neuro-Fuzzy) workflow which uses mud log data and geomechanical predictive models to design fracture density model which can then be used to place fracture clusters.

Mud logs typically provide estimates for observed gas shows, Gamma ray for geo-steering purposes and rate of penetration data. We understand that Gamma ray logs can provide indications of shale layers which have higher natural radioactivity. Gas shows could indicate possible productive or non-productive zones and also potential naturally fractured zones. However, the observed gas shows are influenced by rate of penetration which in turn can be impacted by multitude of factors not all of which are due to reservoir conditions. Gamma ray tool is also influenced by the erratic drilling speeds and varying wellbore conditions encountered during drilling in general. In order to develop the suggested design framework, we have to answer some important questions posed at the outset. The most important is to see how these parameters relate to zonal productivity potential, is the impact verifiable and which parameters are needed for reasonable design solutions? To answer these questions, we use available data from multiple wells from the Marcellus shale play and verify through observations, the necessary framework for proposed design approach.

Impact of Natural Fractures

The initial step is to understand how some factors may play an important role within our fracture spacing design framework. Marcellus and other shale plays are known to have varying natural fracture distributions and depending on the in-situ condition as well as the properties of the injected fluid/ proppant, these could significantly enhance the productivity of the stimulated well. In the Marcellus play, prior data suggests presence of natural fracture swarms as a result of local stress perturbations occurring over geologic timelines [15]. These natural fracture swarms are known to contribute significantly to overall production by providing additional surface area for gas to move from matrix to the connected fractures and eventually to the producing well.

Identification of naturally fractured zones is a key element in accurate understanding of well behavior but this is not easy to achieve due to the need for use of indirect measurement techniques or proxies to identify the zones where the reservoir is fractured a-priori. While there are many available techniques for fracture characterization in reservoirs, we use available microseismic data from one of the wells under study (henceforth Well #1) to characterize fractures. This is made possible due to the ways in which hydraulic fractures interact with naturally fractured rock and the impact such interaction has on the final fractured rock volume in terms of fracture network complexity, fracture network dimensions and magnitude distribution of the microseisms [16].

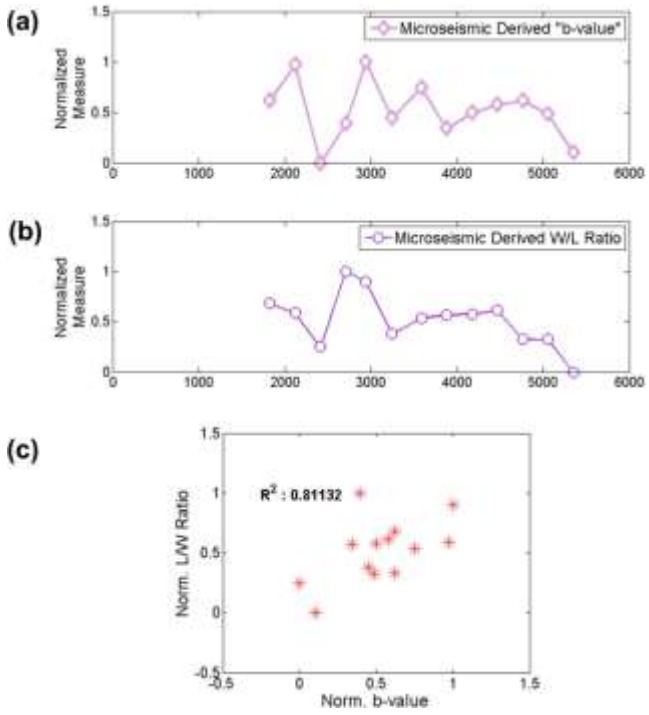

Figure 1- Stage wise distribution of microseismic derived (a) '*b* value' and (b) length-to-width ratio for a study well. Subplot (c) shows cross plot of the two showing a strong positive correlation between the two parameters.

In this context, we look at two different properties evaluated based on the distribution of induced microseismicity associated with the hydraulic fracturing process. The first is the *b* value distribution which is obtained from the Gutenberg-Richter law providing the relationship between the magnitude of the seismic event and the total number of earthquakes in any given region and time period of at least that magnitude [17]. Higher *b* value is indicative of a larger portion of small earthquakes compared to bigger ones. Since in the presence of natural fracture swarms, many re-activations are expected, *b* values tend to be higher when hydraulic fractures interact with such zones [18]. In this study, we look at the overall distribution of events and their *b* value estimates for every completed stage and try to interpret post completion production logs. We expect zones showing higher *b* value to be indicative of presence of natural fractures and therefore, should correlate strongly with gas shows and production log data run for some of these test wells. Similarly, higher length-to-width ratio (or the ratio of the two principal dimensions of the microseismic event cloud) is indicative of an elongated perturbed zone with lower degree of complexity in the created fracture network. On the other hand, a lower length-to-width ratio suggests more complex network which could be due to substantive interaction of the propagating hydraulic fractures with natural fractures [19]. **Fig. 1** shows length-to-width aspect ratio as mapped with borehole microseismic data and how it correlates with evaluated *b* values for the same stages.

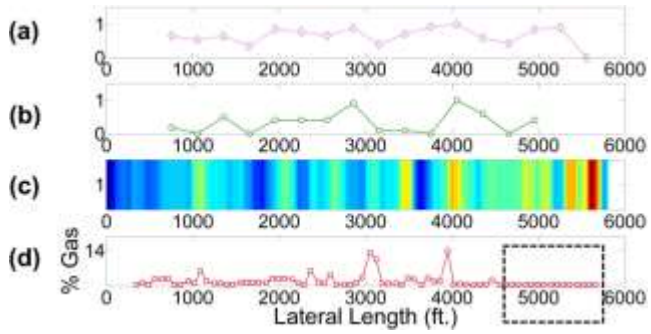

Figure 2- (a) Microseismic derived '*b* value', (b) image log derived fracture density, (c) mud log gas shows (red: 1 and blue: 0) and (d) production log for a study well. The properties (except production log data) are normalized between 0 and 1. The black insert in subplot (d) indicates the section of the wellbore where production log could not be run.

Fig. 2 shows another example where *b* value has been compared with production logs and other relevant data to highlight these observations and how they correlate with mud log gas shows. We observe a poor correlation between *b* values and observed fracture density from image logs which is expected as image logs are subject to interpretation errors (and so is b-value analysis). However, image logs only provide a snapshot of fractures at the wellbore unlike b-value which defines the spatio-temporal seismicity distribution. We observe reasonable correlation between sections showing very high flow contribution and sections indicating highly complex fractured zones from *b* value distribution. Finally, we observe a reasonable correlation between production log and highly fractured sections of the reservoir as well as a reasonably strong correlation between production log and high gas composition from mud log gas show data. The observed correlation between mud log gas shows and production log data over certain depth intervals has been observed for multiple wells and provides one element governing our stage/ cluster spacing optimization workflow. Even though the correlation is not perfect, in conjunction with gamma log readings and rate of penetration data, a strong correlation between the observed production and modeled geomechanical properties governing production in shale reservoirs should be possible as it may take care of some of the outlier observations.

Based on the observations, our design workflow (**Fig. 3**) involves utilizing relevant routinely logged data from mud logs (gas shows, rate of penetration, and gamma ray) and model for rock properties such as Young's Modulus and Poisson's Ratio using data from Well #1. These in turn are used to predict rock brittleness which we correlate with another brittleness measure from lithological distribution to validate the brittleness function before actual use (**Fig. 4**). This is because lithology has an impact on rock properties and therefore, rock brittleness can be considered a function of Young's Modulus and Poisson's Ratio [20]. Broadly speaking, Increasing Young's Modulus or decreasing Poisson's Ratio is indicative of more brittle formations. This modeled brittleness is then used in conjunction with gas shows to identify the optimal hydraulic fracture/ cluster density along the lateral. The basic framework governing our design is to provide for more cluster density in regions susceptible to lower productivity behavior in order to improve

overall production from the completed lateral. Based on this fracture density model, clusters are populated along the length of the lateral by honoring the background modeled density values.

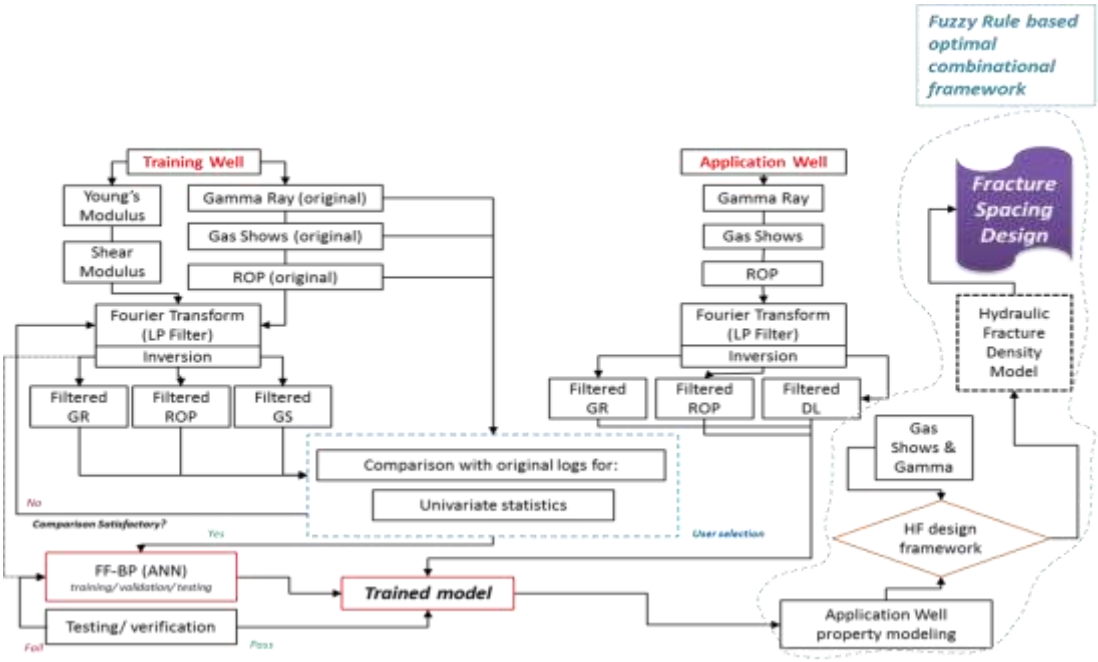

Figure 3: Fracture/ Cluster spacing design workflow.

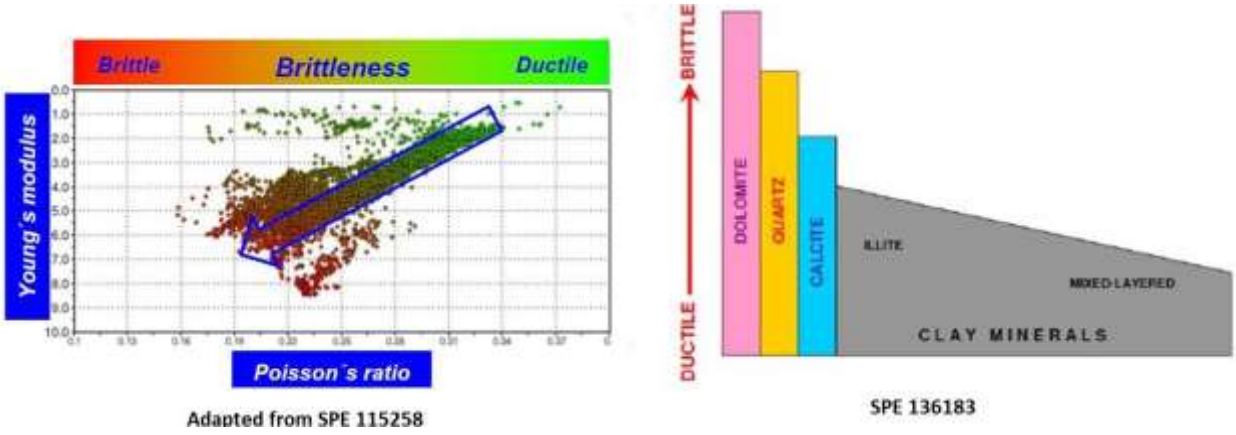

Figure 4: Composite of two correlations showing how rock brittleness can be considered a function of other rock properties or lithology.

Workflow

Apart from the pre-completion drilling data, the proposed workflow requires some rock properties derived from specialty logging such as dipole sonic or spectral azimuthal gamma for representative lithologic layers. This data is typically available for a given field, especially new development fields where a single or multiple pilot wells are drilled before full field development drilling program is implemented. This is necessary to model for the same properties

based on routine mud log data by deriving the necessary models. The workflow involves the following steps:

1. Training wells are nominated based on availability of relevant specialty logging data and the exact position of the well in relation to various shale sub-layers. The original high resolution mud log data is inverted by passing through a low pass filter and the filtered data is compared with the original so as to make sure that the univariate statistics show reasonably good match. Multiple inputs are generated using multiple filters.
2. The filtered mud log data are used as input to design a feed forward back-propagation neural network model. The model is trained to predict desired output rock properties (Young's Modulus and Poisson's ratio). The model design includes the usual training, validation and testing phase. Care is taken to prevent over-fitting of the data as well as having a reasonable network in terms of size. We use a network with single hidden layer and 10:1 ratio for number of hidden layer nodes when compared with number of sample points. Models specific to defined lithological layers are tagged and stored for application.
3. For application of the design, data from candidate well is identified and it is segmented based on predefined lithological layers. Corresponding models are applied after careful filtering of data using the filters obtained in step 1.
4. Based on the generated geomechanical models, a rock brittleness parameter is computed. Resulting parameter is combined within the predefined hydraulic fracture density design framework shared later. It works on the basis of partially weighting mud log gas shows and modeled properties to get the final density values. The density model is normalized and fractures/ clusters are placed based on the behavior of this modeled parameter.

Model Fine-tuning

We need to highlight that there are multiple input properties being used in the modeling process where each comes with varying degrees of associated uncertainties. As an example, modeled rock properties have high degree of uncertainty due to modeling errors particularly at large offset from design wells. Similarly, mud log gas shows can sometimes show erroneous readings due to gas flow into wellbore downstream of drilling bit. Similarly, the framework relating modeled rock properties and gas shows with naturally fractured zones in the reservoir is loosely defined due to lack of adequate corroborative data. Moreover, multiple input sets are generated from singular properties using variable filter parameters. All these add up to create a highly non-unique solution space and therefore, finding the right framework for combining these parameters to define hydraulic fracture density model can be a challenge.

In order to tide over these uncertainties, we use a fuzzy classification technique to identify the definition boundaries with adequate fuzziness so as to classify sections of the lateral in terms of cluster spacing design by taking into account the underlying uncertainty as well. At the same time, if production logs are available and the broad framework is well defined (such as highly brittle rock and high gas shows should lead to a lower modeled hydraulic fracture spacing density, etc.),

we can try to generate the best possible model (and correspondingly, the best possible fuzzy classifier) to match the designed fracture density with the observed production behavior post completion. This is accomplished by using an evolutionary algorithm to minimize a predefined error function which tries to match the inverse of modeled fracture density with the observed cluster wise production. The fuzzy rules set which defines the modeling framework we used is as follows:

- Rule #1: Low modeled brittleness and low gas shows imply very high density.
- Rule #2: Medium modeled brittleness and low gas shows imply very high density.
- Rule #3: High modeled brittleness and low gas shows imply high density.
- Rule #4: Low modeled brittleness and medium gas shows imply high density.
- Rule #5: Medium modeled brittleness and medium gas shows imply medium density.
- Rule #6: High modeled brittleness and medium gas shows imply medium density.
- Rule #7: Low modeled brittleness and high gas shows imply low density.
- Rule #8: Medium modeled brittleness and high gas shows imply low density.
- Rule #9: High modeled brittleness and high gas shows imply very low density.

Here the 'density' values indicate final fracture density (or perforation cluster density) recommendation to be made by the designed fracture density model. We do note that these rules suggest relatively lower fracture cluster count for the so called sweet spots. Since the decision on how much to frac and where is a highly complex one with well economics playing a major role, the workflow is adaptable enough so that the rules can be flipped with the high density recommendations changed to low density recommendations and vice versa. This approach is useful in cases where specific well intervals have a predictable behavior and sensitivity to stimulation.

Need for Artificial Intelligence

There are three computational elements using AI techniques used in this workflow. We need to consider the need for using said methods in this study. We understand that though broad relationships between Gamma Ray measurements and rock properties are expected due to influence of clay content on said properties, the relation may not always hold due to other influences. The same holds true for hydrocarbon indicator used for modeling (mud log gas shows). Due to this non-linearity and in-exactness in the relationship between geomechanical properties and gamma ray, Artificial Neural Nets are ideally suited since they can map highly nonlinear relations if properly modeled and calibrated and are very robust in handling noisy data [21].

Furthermore, a broad correlation between modeled and observed properties and the desired application (hydraulic fracture spacing design) can be easily defined [e.g. higher gas shows and higher modeled brittleness leads to lower cluster density, etc.]. However with the high uncertainty in the available inputs, a simplistic framework for combining said properties may not capture the

relationships accurately. A classic solution to such a classification problem is to use a Fuzzy Inference System. They are easy to understand as they are governed by fuzzy rules which are semantic in nature even though the underlying evaluation is mathematical. They have the ability to optimally search for the best classifier set definitions to match the observed data. They are simple yet highly adaptable and can work with imprecise and incomplete data that we have [22].

Finally, as stated already, the designed fracture density and observed production behavior mismatch is minimized by using an evolutionary search routine. The big advantage with using such an approach is that it is highly scalable and adaptable and can be used to solve for multi-dimensional, non-differential, non-continuous and non-parametric problems. They are intuitive and very easy to build and therefore provide an optimal search algorithm for the problem at hand [23].

Data

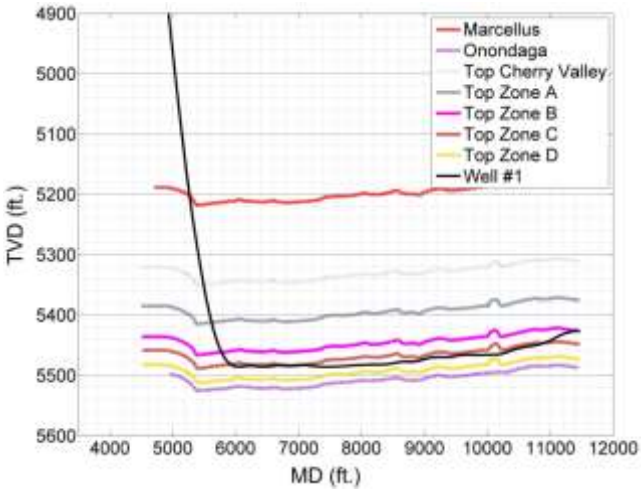

Figure 5- Well #1 cross-section showing well track in reference to the varying lithologic formations in the Marcellus shale play. The lateral is restricted to Zones C & D.

We apply this approach to three wells from two separate well pads (separated by 10's of miles from one another). Henceforth, Pad # 1 & Pad # 2 indicate Wootton & Corbett pads respectively as used in this project. The data from Well #1 for Pad #1 is used as the design data as the well had open-hole logging carried out for the vertical pilot as well as the horizontal section of the well. Two other wells were used as application wells for validating the models as each had a production log available for independent validation. These include Well #2 associated with the same well pad as Well #1 and Well #3 associated with Pad #2. **Fig. 5** shows the various lithological layers of relevance across Well #1. We can clearly observe that the well lateral intersects two layers (Zone C or the target zone and zone B which is the overburden lower Marcellus layer) of interest and we use the available data to model the geomechanical properties for these two layers.

Since we have extensive wireline logging done for this long lateral (Well #1), we can use the data from the logs to estimate geomechanical and other properties which in turn form the basis for our model design framework using artificial neural nets. Apart from the standard mud log gas shows available from drilling records, other wireline tools run for this well (both for the horizontal lateral and the vertical sections) include standard measurements such as density, porosity & resistivity as well as lithological tools to identify mineralogy and organic content. A thorough petrophysical analysis was carried out for the entire logged wellbore and the geomechanical properties were ascertained using the lithology data. Gamma from both the actual wireline logging run and the mud log data was correlated to validate applicability for other "application" wells which lack similar wireline logs.

Using the geomechanical properties and the mud log data available for well #1, the entire dataset was pruned such that two separate datasets were generated. The inputs were expanded using multiple filtering bandwidths to extract features at different frequency spectrums which might hold physical meaning and therefore are valuable in the modeling process. The inputs were in turn used to develop two separate models for two separate reservoir (shale) units, namely Zone C and Zone B as discussed earlier and observed from Fig. 3. However, based on the well trajectory along the lateral, the two sections have varied data density in terms of available sampling points. From the mud logs, while Zone C has approximately 600 data points, zone B only has approximately 70 data points which makes results from model defined for this zone to be susceptible to more errors. **Fig. 6** shows sample rock property (Poisson's Ratio) modeled for these two layers and we can observe relatively higher errors for Lower Marcellus Layer compared to the target layer due to said mismatch.

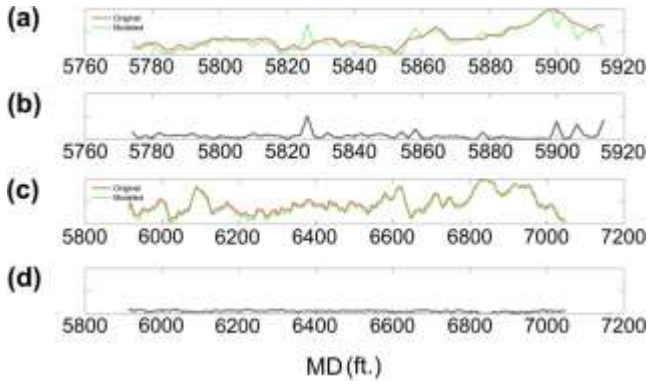

Figure 6- (a) Modeled Poisson's Ratio compared with actual log derived values and (b) corresponding error mismatch for Zone B and (a) Modeled Poisson's Ratio compared with actual log derived values and (d) corresponding error mismatch for Zone C.

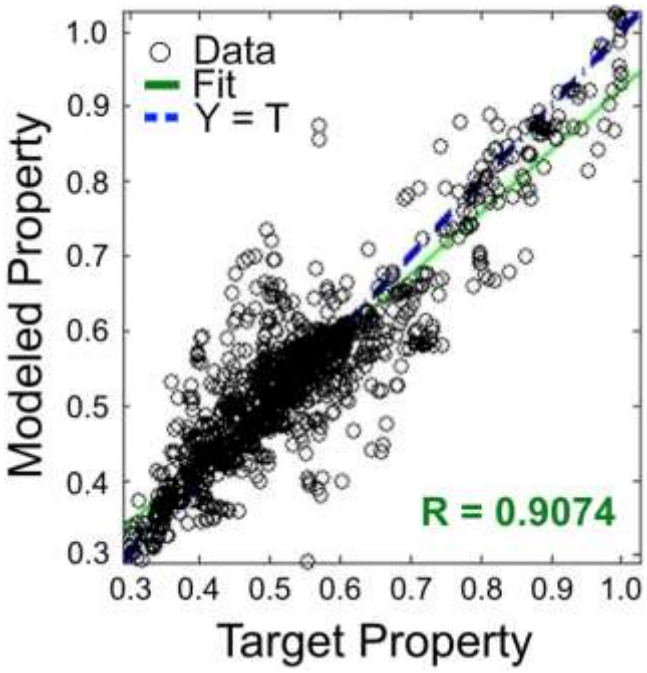

Figure 7- Validation results from a sample neural network training run showing minimized error in modeled property (Poisson's Ratio) compared to target property (actual log derived data). Note: The target data was normalized before modeling run.

For network training, care is necessary to prevent either over-fitting or non-representative dataset generation. Care is taken in the neural network design with the ratio of number of network nodes to the number of data samples kept at less than 0.10. Also, segments from each Zone are combined making sure that they are representative of varying behavioral aspects of the property being modeled (such as sudden rise or drop in value). The final network models are chosen based on the minimized error observed within the network validation process **(Fig. 7)**.

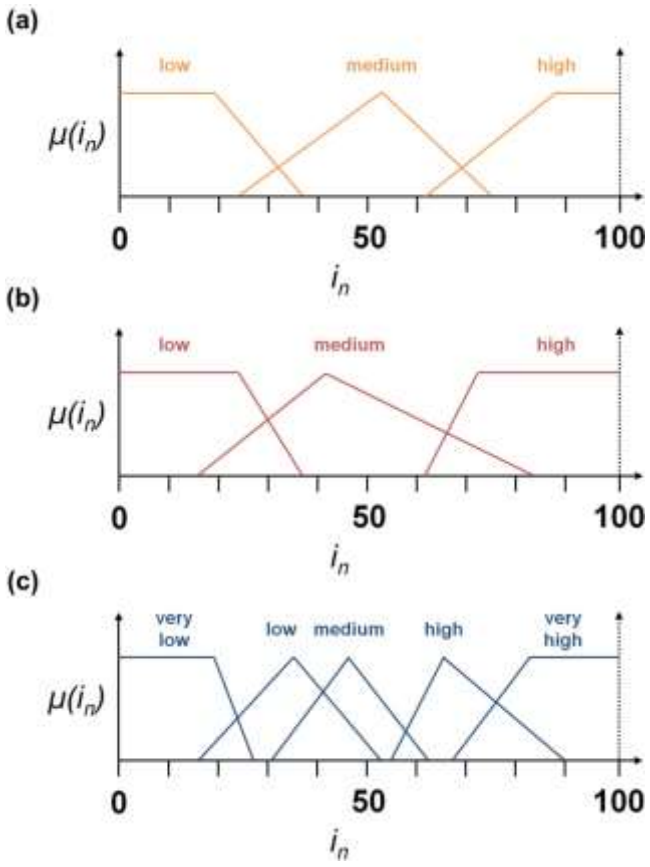

Figure 8- Optimal fuzzy set definitions based on training well data for (a) modeled brittleness, (b) mud log gas shows and (c) output fracture density guidance.

With the individual geomechanical models as well as the composite brittleness model ready for use, the next step is to identify the best fuzzy set definitions corresponding to the rules defined earlier. **Fig. 8** shows the final identified rules set which corresponds with the best match between the predicted fracture density models and the observed production log behavior for Well #1.

Once the model is ready for application, all of the model design parameters are stored for later use with application test scenarios. These include the number of layers in the network, number of nodes in the hidden, input and output layers, trained weights associated with each node in the network, activation functions associated with each node, biases within the network, etc. These saved models are in turn applied to any dataset from "application" wells to generate hydraulic fracture/ cluster density maps. The final fracture density maps need to be rescaled in order to make sure that sufficient "maximum" and "minimum" fracture spacing is maintained before final fracture or perforation cluster placement. These maxima and minima limits can be independently evaluated using other stage design approaches discussed in the introduction to this study.

Results

Before the models can be applied to other wells, they need to be categorized based on lithological layers associated with each portion of the wellbore to be analyzed. This is done by using the same approach as used for the training well (Well #1) as discussed earlier. Once the wellbore has been characterized, these segmented subsections are evaluated for rock properties by using the corresponding rock property predictive artificial neural net derived models. We will share the design results obtained using the models for the two application wells (Well #2 and Well #3) and compare the observations with production log data. This will allow validation of the observed results using independent production log results which is critical as initial production is the key for rapid return on investment in shale gas wells. We again note that while Well # 2 belongs to the same pad as the training well (Well #1), Well #3 is located 10's of miles from the first pad and incorporates a different completion design.

Before we look into the application wells (Well #2 & Well #3), we apply the derived models to data from training well itself (Well #1) using the segmented modeling approach. Based on the wellbore location in reference to lithological units (Fig. 3), separate models are applied to the dataset along the wellbore. **Fig. 9** shows the results for this particular test case and as expected, we get a good match between the suggested fracture density derived from the proposed workflow and the production log data for Well #1.

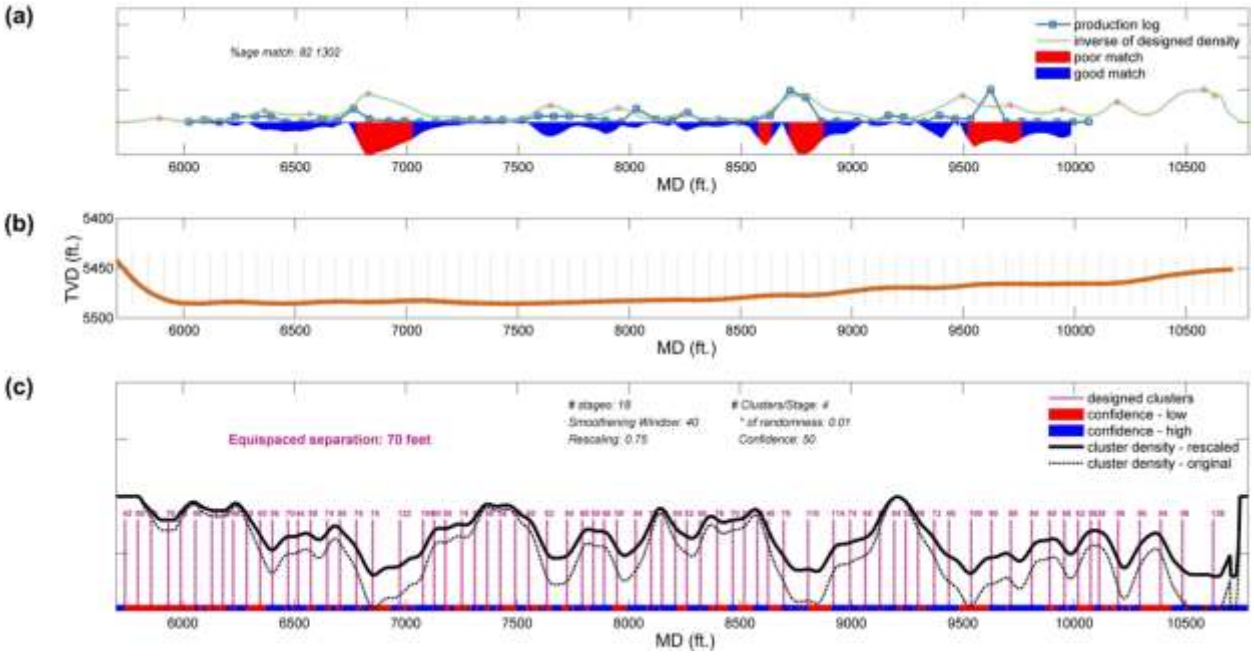

Figure 9- Figure showing (a) the comparison between modeled fracture density and available production log, (b) TVD behavior along lateral with traditional equally spaced perforation locations and (c) the actual fracture spacing recommendation based on the model results for Well #1 incorporating both zone B & zone C models using segmented modeling approach. Red arrow indicates section with significant mismatch between production and designed fracture density.

We note that the original completion for Well #1 involved 18 stages with 4 perforation clusters per stage and an inter-stage separation of ~ 280 feet. The modified spacing design as suggested by the workflow is shown in **Fig. 9(b)**. As observed from these results, significant mismatch is observed close to 6900 ft. (measured depth) which could be due to the wellbore lying either very close to or at the interface of zone B & zone C (Fig. 3). This would make it difficult to interpret as to which model is the right model and applicable for corresponding sections of the wellbore.

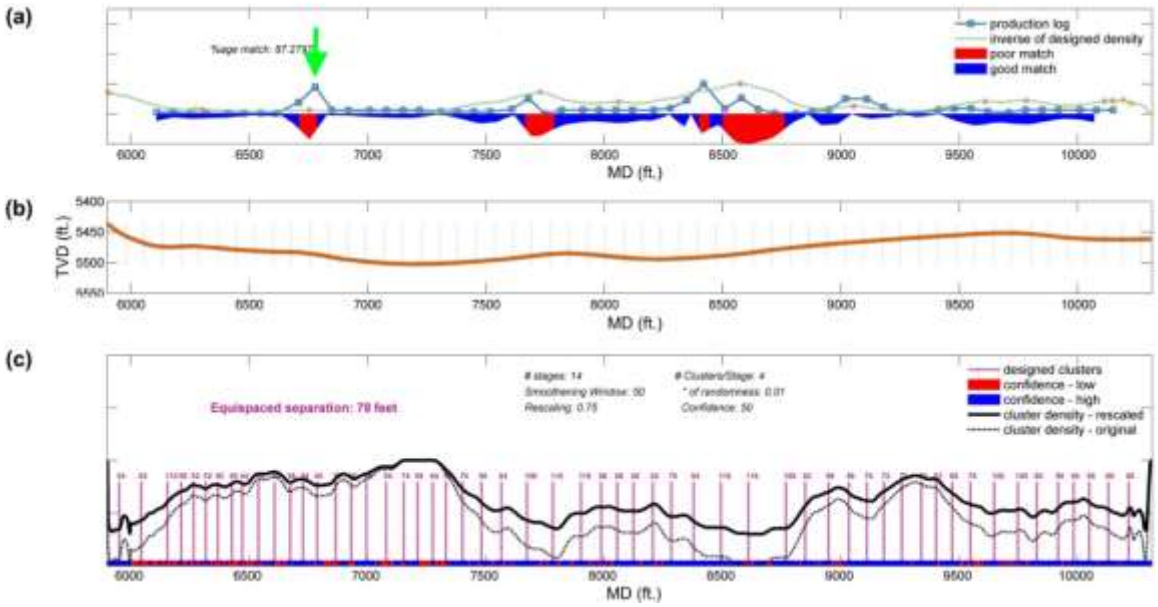

Figure 10- Figure showing (a) the comparison between modeled fracture density and available production log, (b) TVD behavior along lateral with traditional equally spaced perforation locations and (c) the actual fracture spacing recommendation based on the model results for Well #2 incorporating model from zone C. Green arrow indicates section with significant mismatch between production and designed fracture density which corresponds with wellbore section falling outside zone C.

For Well #2, we ran three tests with the first test incorporating model associated with zone C for the entire lateral (Case 2A), the second test incorporating model associated with zone B for the entire lateral (Case 2B) and the third test incorporating segment wise modeling using both models based on location of the lateral in relation to the lithological units (Case 2C). **Fig. 10** shows the modeling and design results for Case 2A, **Fig. 11** shows the results for Case 2B and **Fig. 12** shows the results for Case 2C.

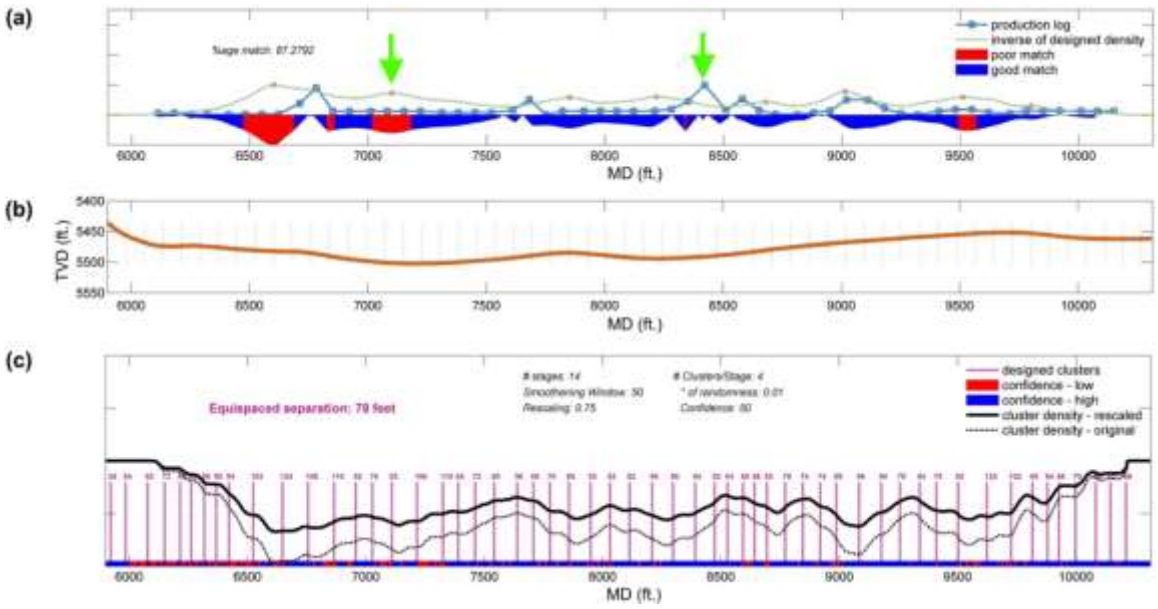

Figure 11- Figure showing (a) the comparison between modeled fracture density and available production log, (b) TVD behavior along lateral with traditional equally spaced perforation locations and (c) the actual fracture spacing recommendation based on the model results for Well #2 incorporating model from zone B. Green arrows indicate sections with significant mismatch between production and designed fracture density some of which corresponds with wellbore section falling outside zone B.

We note that the original completion profile for Well #2 involved 14 stages with 4 perforation clusters per stage with an inter-stage separation of ~300 feet. We can clearly see sections along the wellbore where the design recommendation suggests sparser clusters and other sections which suggest denser cluster spacing. This correlates well with the production log results with sections suggesting denser clusters showing lower productivity and vice versa. This is desirable considering the defined modeling framework discussed earlier. However, for Case 2A & Case 2B, the predicted fracture spacing design does not match well with the observed stage wise productivity behavior at some locations (identified by red arrow). This can be attributed to the model applicability issue in certain sections of the wellbore depending on whether the well track is within the zone defining the applied geomechanical model or not.

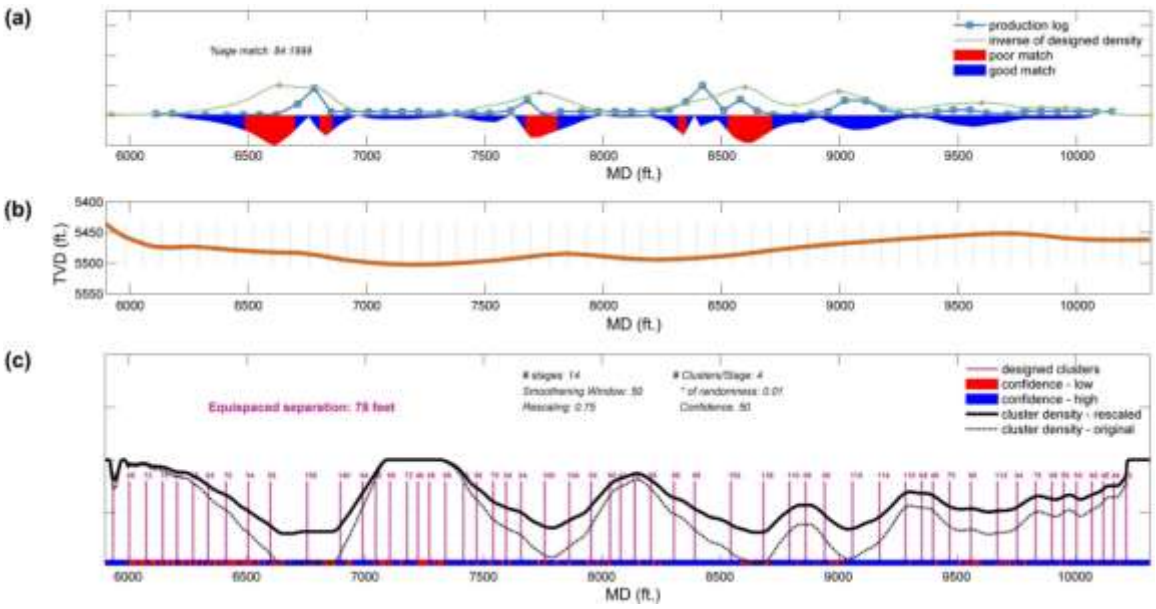

Figure 12- Figure showing (a) the comparison between modeled fracture density and available production log, (b) TVD behavior along lateral with traditional equally spaced perforation locations and (c) the actual fracture spacing recommendation based on the model results for Well #2 incorporating both zone B & zone C models using segmented modeling approach. We do not see any significant mismatch between the predicted fracture density behavior and the productivity of completed perforation clusters.

For Case 2C, we observe a much better match along the entire completed lateral and this is due to segmented modeling approach where the correct model (based on the location of the wellbore in reference to the lithological units) is used (Fig. 12). This validates the applicability of the proposed approach for wells within proximity of well used in training our models.

For Well #3, the completion design was significantly different with 27 stages and 4 perforation clusters per stage with an inter-stage separation of 200 feet. Once again we generate results incorporating model associated with zone C for the entire lateral (Case 3A), the second test incorporating model associated with zone B for the entire lateral (Case 3B) and the third test incorporating segment wise modeling using both models based on location of lateral (Case 3C). Since Well #3 is at an offset of 10's of miles from Well #1, we expect the results to be not as robust as was the case with Well #2. **Fig. 13** shows the modeling and design results for Case 3A, **Fig. 14** shows the results for Case 3B and **Fig. 15** shows the results for Case 3C.

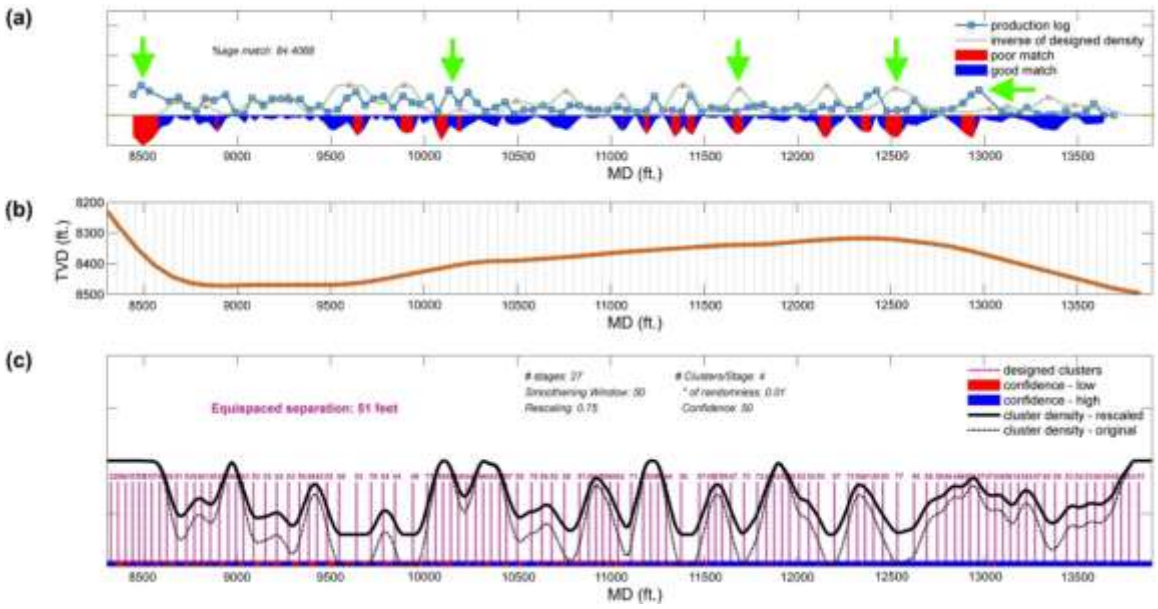

Figure 13- Figure showing (a) the comparison between modeled fracture density and available production log, (b) TVD behavior along lateral with traditional equally spaced perforation locations and (c) the actual fracture spacing recommendation based on the model results for Well #3 incorporating model from zone C. Green arrows indicate sections with significant mismatch between production and designed fracture density some of which corresponds with wellbore section falling outside zone C.

For Case 3A & Case 3B, the predicted fracture spacing design does not match well with the observed stage wise productivity behavior at sections highlighted using red arrows. This can be attributed to the model applicability issue in certain sections of the wellbore depending on whether the track is within the zone defining the applied geomechanical model or not as observed with the earlier test case. Other issues include the robustness of the model at separation of 10's of miles as well as issues with inadequate data for zone B model as highlighted latter.

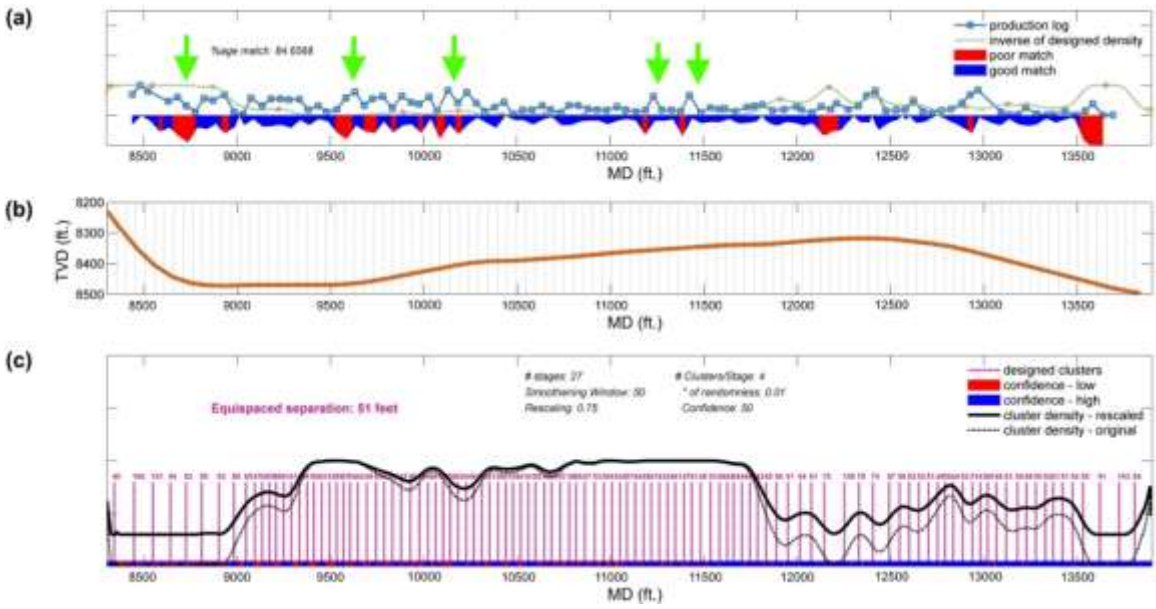

Figure 14- Figure showing (a) the comparison between modeled fracture density and available production log, (b) TVD behavior along lateral with traditional equally spaced perforation locations and (c) the actual fracture spacing recommendation based on the model results for Well #3 incorporating model from zone B. Green arrows indicate sections with significant mismatch between production and designed fracture density some of which corresponds with wellbore section falling outside zone B.

For Case 3C (Fig. 15) using segmented modeling approach, we observe a much better match along the completed lateral. However once again, there are small sections of the lateral where the fracture placement recommendation based on density model does not match well with the production log observations.

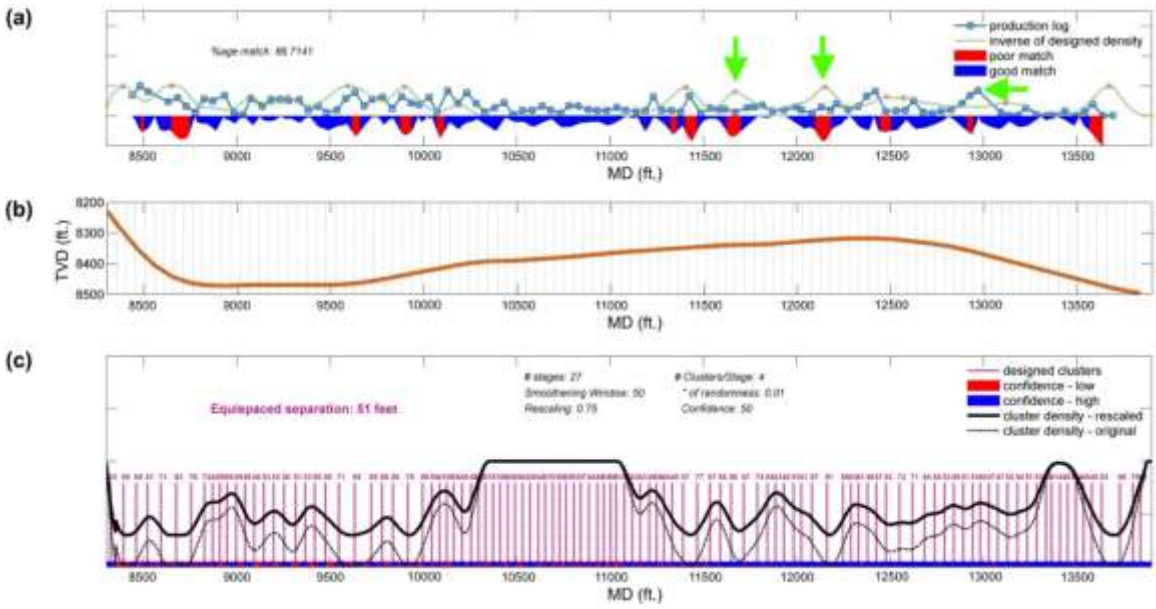

Figure 15- Figure showing (a) the comparison between modeled fracture density and available production log, (b) TVD behavior along lateral with traditional equally spaced perforation locations and (c) the actual fracture spacing recommendation based on the model results for Well #2 incorporating both zone B & zone C models using segmented modeling approach. Green arrows indicate sections with significant mismatch between production and designed fracture density.

Next we highlight the issue of model robustness due to data inadequacy. As observed from Fig. 14, certain section of the modeled fracture density along the wellbore shows significantly poor results suggested by the consistent high values from ~9300 feet to ~11700 feet (measured depth). This is because model from zone B is poorly defined due to lack of adequate data as discussed earlier. While the laterals for both Well #1 and Well #2 falls mostly within the target zone C; significant sections of the wellbore corresponding to the identified depth interval for Well #3 falls within overburden zone B (as observed in Fig. 13 from ~10300 feet measured depth to ~11000 feet measured depth). Therefore these erroneous artifacts are observed for both Case 3B and 3C which makes use of geomechanical models from zone B.

Applicability Considerations

Based on our results, we can say with some degree of confidence that this approach can be useful in designing completions (stage or cluster spacing) of wells within the same well pad provided major sections of the wellbore do not fall very close to or at the interface between geologically distinct layers with significant variability in geomechanical properties. Moreover, presence of local faulting or completion of nearby wells post drilling operations of the candidate well can also have significant impact on results. Since the proposed method works with multiple

models based on a segmented modeling approach, it is critical that each model is robust as well as well-defined and their reliability should be ascertained before application.

For wells at significant offset from those wells used for model design, applicability can suffer depending on lithologic variability across spatial distance as well as other formation properties. However, our results show that properly designed models and segmented modeling approach can still provide reasonably good fracture density maps and spacing recommendations.

Beyond the questions regarding effectiveness of the models, the methodology used, and applicability close to and away from those wells used for model training and design; a more fundamental question is the efficacy of the design framework proposed in this study. **Fig. 16** highlights the broad framework in question as well as one possible alternative framework to highlight this issue.

Since the question of how to proceed with the completion design framework is a complex one with well economics playing an integral part in any decision making process, a more thorough investigation and decision making based on particulars of the wells being completed using this approach is essential. As an example, the decision on which framework to choose could be decided by price factors (gas vs. oil/ condensate rich play) as well as reservoir related considerations (Clay richness, natural fractures, etc. to name just two).

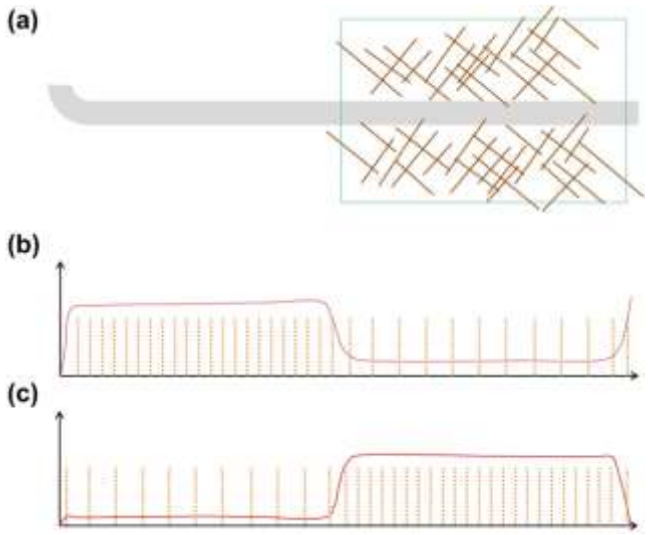

Figure 16- (a) Well schematic showing localized sweet spot due to intersecting natural fracture swarm (green box) and (b) hydraulic fracture density framework suggested in this study with (c) potential alternate framework along the wellbore lateral.

Concluding Remarks

We have introduced a fracture spacing design approach which makes use of routinely collected mud log data apart from some reference wireline specialty logs to model for complex

geomechanical properties of the rock surrounding the wellbore. These models along with observed gas shows are used to propose variable perforation cluster spacing along the wellbore laterals. We have demonstrated this approach to be useful at small (100's of feet) as well as large (10's of miles) geographical offsets from the wells used to train said models. The proposed methodology identifies local sweet spots that require less stimulation and areas where more stimulation is needed. By redistributing the hydraulic fracture density along the wellbore, we aim to balance stimulation costs and long-term production performance.

While many methods have been proposed over the years which utilize data from such specialty wireline logs to predict well behavior or recommend completion design, the key discriminator with our proposed fracture spacing design methodology is the ability to apply the technique at geographically far off wells without having to update the geomechanical models. The key is to use a well-defined modeling framework and production log or other completion quality attributes (such as potentially from fiber-optic data) to constrain the designed models so that they can mimic well behavior with upon completion with reasonable accuracy.

Based on the results we have observed from multiple wells, including those shared in this study, we hypothesize that this approach should work in most situations provided proper care is taken before applying this approach. However, the proposed approach needs to be validated as it may not hold under many situations depending on economic considerations. For future work, we propose to carry out extensive modeling studies and generate guidelines for applicability under varying scenarios as suggested in this work.

In the future, we plan on using a fuzzy or probabilistic classifier to decide on which model to be used depending on the closeness of the well track to a particular lithologic boundary. This is due to significant uncertainty ranging from 10's to 100's of feet when it comes to layer boundaries and exact well location which can make the decision making on models to be used for design very non-representative. We hope to test this approach on multiple wells in other shale plays (Permian Basin). We also expect to conduct similar design work for multiple wells which are geographically spread out and validate these observations.

Acknowledgement

This work was supported by Research Partnership to Secure Energy for America (RPSEA) project number 11122-20. We also acknowledge WPX Energy for providing access to active hydraulically fractured wells of opportunity in Marcellus shale play and Schlumberger for acquiring the wireline and production logs used in this study.

References

[1] Crafton, J. W., and Anderson, D. 2006. Use of Extremely High Time-Resolution Production data to Characterize Hydraulic Fracture Properties. Presented at the SPE Annual Technical

Conference and Exhibition, San Antonio, Texas, 24-27 September. SPE-103591-MS. http://dx.doi.org/10.2118/103591-MS.

[2] Ye, P., Chu, L., Harmawan, I. et al. 2013. Beyond Linear Flow Analysis in an Unconventional Reservoir. Presented at the SPE Unconventional Resources Conference, The Woodlands, Texas, 10-12 April. SPE-164543-MS. http://dx.doi.org/10.2118/164543-MS.

[3] Wu, K., and Olson, J.E. 2013. Investigation of the Impact of Fracture Spacing and Fluid Properties for Interfering Simultaneously or Sequentially Generated Hydraulic Fractures. *SPE Production & Operations* **28** (4): 427-436.

[4] Jonathan, M., and Miskimins, J.L. 2012. Optimization of Hydraulic Fracture Spacing in Unconventional Shales. Presented at the SPE Hydraulic Fracturing Technology Conference, The Woodlands, Texas, 6-8 February. SPE-152595-MS. http://dx.doi.org/10.2118/152595-MS.

[5] Cipolla, C., and Wallace, J. 2014. Stimulated Reservoir Volume: A Misapplied Concept? *Hydraulic Fracturing Journal* **1** (2): 54-75.

[6] Ma, X., Plaksina, T., and Gildin, E. 2013. Optimization of Placement of Hydraulic Fracture Stages in Horizontal Wells Drilled in Shale Gas reservoirs. Presented at the Unconventional Resources Technology Conference, Denver, Colorado, 12-14 August. SPE-168790-MS. http://dx.doi.org/10.1190/URTEC2013-151.

[7] Baig, A., Urbancic, T.I., Mace, K.C. et al. 2012. Assessing the spacing of stages in Plug and Perf Completions through Seismic Moment Tensor Inversion. Presented at the SPE Hydraulic Fracturing Technology Conference, The Woodlands, Texas, 6-8 February. SPE-152547-MS. http://dx.doi.org/10.2118/152547-MS.

[8] Bazan, L.W., Larkin, S.D., Lattibeaudiere, M.G. et al. 2010. Improving Production in the Eagle Ford Shale with Fracture Modeling, Increased Fracture Conductivity, and Optimized Stage and Cluster Spacing along the Horizontal Wellbore. Presented at the Tight Gas Completions Conference, San Antonio, Texas, 2-3 November. SPE-138425-MS. http://dx.doi.org/10.2118/138425-MS.

[9] Kennedy, R.L., Gupta, R. Kotov, S.V. et al. 2012. Optimized Shale Resource Development: Proper Placement of Wells and Hydraulic Fracture Stages, Presented at the Abu Dhabi International Petroleum Conference and Exhibition, Abu Dhabi, UAE, 11-14 November. SPE-162534-MS. http://dx.doi.org/10.2118/162534-MS.

[10] Ciezobka, J. 2013. Marcellus Shale Gas Project. *RPSEA*, August 2013, http://www.rpsea.org/files/3629/ (accessed 11 May 2015).

[11] Ajayi, B., Aso, I.I, Terry, I.J. et al. 2013. Simulation Design for Unconventional Resources. *Oilfield Review* **25** (2): 34-46.

[12] Warpinski, N.R., Mayerhofer, M.J., Davis, E.J. et al. 2014. Integrating Fracture Diagnostics for Improved Microseismic Interpretation and Stimulation Modeling. Presented at the Unconventional Resources Technology Conference, Denver, Colorado, 25-27 August. SPE-2014-1917906-MS. http://dx.doi.org/10.15530/urtec-2014-1917906.

[13] Borstmayer, R., Stegent, N., Wagner, A. et al. 2011. Approach Optimizes Completion Design. *The American Oil & Gas Reporter*.

[14] Jahandideh, A., and Jafarpour, B. 2014. Optimization of Hydraulic Fracturing Design under Spatially Variable Shale Fracability. Presented at the SPE Western North American and Rocky Mountain Joint Meeting, Denver, Colorado, 17-18 April. SPE-169521-MS. http://dx.doi.org/10.2118/169521-MS.

[15] Engelder, T., Lash, G.G., and Uzcategui, R.S. 2009. Joint sets that enhance production from Middle and Upper Devonian gas shales of the Appalachian Basin. *AAPG Bulletin* **93** (7): 857-889.

[16] Bahorich, B., Olson, J.E., and Holder J. 2012. Examining the Effect of Cemented Natural Fractures on Hydraulic Fracture Propagation in Hydrostone Block Experiments. Presented at the SPE Annual Technical Conference and Exhibition, San Antonio, Texas, 8-10 October. SPE-160197-MS. http://dx.doi.org/10.2118/160197-MS.

[17] Gutenberg, B., and Richter, C.F. 1954. *Seismicity of the Earth and Associated Phenomena*, second edition. Princeton, New Jersey: Princeton University Press.

[18] Boroumand, N. 2014. Hydraulic fracture b-value from microseismic events in different regions. Presented at GeoConvention, Calgary, Canada, 12-16 May.

[19] Salehi, I.A., and Ciezobka, J. 2013. Controlled Hydraulic Fracturing of Naturally Fractured Shales: A Case Study in the Marcellus Shale Examining How to Identify and Exploit Natural Fractures. Presented at the SPE Unconventional Resources Conference, The Woodlands, Texas, 10-12 April. SPE-164524-MS. http://dx.doi.org/10.2118/164524-MS.

[20] Rickman, R., Mullen, M.J., Petre, J.E. et al. 2008. A Practical Use of Shale Petrophysics for Stimulation Design Optimization: All Shale Plays Are Not Clones of the Barnett Shale. Presented at the SPE Annual Technical Conference and Exhibition, Denver, Colorado, 21-24 September. SPE-115258-MS. http://dx.doi.org/10.2118/115258-MS.

[21] Haykin, S. 1998. *Neural Networks: A Comprehensive Foundation*, second edition. Saddle River, New Jersey: Prentice Hall.

[22] Ross, T.J. 2009. *Fuzzy Logic with Engineering Applications*, third edition. West Sussex, United Kingdom: John Wiley & Sons.

[23] Goldberg, D. E. 1989. *Genetic Algorithms in Search, Optimization and Machine Learning*, first edition. Boston, Massachusetts: Addison-Wesley Longman.

Appendix D: Enhanced Hydraulic Fracture Mapping Using Self-Focusing Adaptive Beamformer

Project Summary

In order to improve the ability of microseismic analysis to aid in efficient and environmentally safe resource extraction, we propose to study the application of a self-focusing adaptive beam-former to the problem of microseismic event detection and localization. This beamforming system leverages signal-processing techniques that are well established and have been widely successful in a variety of fields including sonar and radar, where arrays of sensors are used to detect and localize faint sources of energy in a large background of noise. Use of this proposed technology is expected to provide significant attenuation of background seismic noise and compensate for inaccurate knowledge of local wave propagation, enabling a more complete and accurate understanding of the activity induced by stimulation treatments. The self-focusing adaptive beamformer has been implemented in the Matlab environment and the source code has been provided for public dissemination.

CONTACT INFORMATION		
GTI Project Sponsor	**Email**	**Phone**
Iraj Salehi	iraj.salehi@gastechnology.org	847-768-0902
Project Manager	**Email**	**Phone**
Scott Taylor	dmtchili@gmail.com	438-882-3680
Principal Investigator	**Email**	**Phone**
Bernard Widrow	widrow@stanford.edu	650-392-5860

Summary and Accomplishments

A final report has been prepared describing the progress of the above project and the significant observations and results emanating from its successful completion.

From only five points whose location in 3-D space was determined, we were able to make a crude map of a fracture.

We developed a self-focusing adaptive beamformer that was capable of localizing seismic events in 3-D.

We formulated a set of steps necessary to go from raw seismic data to a 3-D fracture map, as follows:

(1) Identify a large seismic event in the geophone signal data.

(2) Use its moveout delay times to focus the beamformer.

(3) Determine seismic velocity from the moveout delays using knowledge of the well geometry and the geometries of the surface arrays.

(4) Steer the beam in known increments about the locus of the large event. Search in 3-D for additional seismic events.

(5) Map the fracture by plotting the loci of multiple seismic events relative to that of the large event.

Introduction

The dominant interest of this project was the development of 3-D fracture imaging methods based on adaptive beamforming methods using seismic data from surface geophone arrays. #Surface array signals are much noisier than downhole array signals, but surface arrays are much cheaper to install than downhole arrays. The noise reduction capabilities of adaptive beamformers are important and effective when working with signals from surface arrays. This is the reason that our tests and analysis was limited to surface data from an independent source outside the scope of this project [11122-20].

The Arrays

The data used in this study were recorded digitally and made available to us. We called this data set #2. Data set #2 was collected during hydraulic fracture stimulation of a single horizontal well using a surface array of 1000 single-component (vertical) geophones separated into 13 approximately-linear arrays radiating outward from the frac-well's pad in a star configuration. Fifteen zones of fracture stimulation were performed over the course of four days, and slightly less than 30 hours of continuous array data was recorded. One check shot of known location was performed in the vertical portion of the well prior to stimulation treatment. The horizontal portion of the stimulated well was approximately 1400 meters in length, and was located at a depth of approximately 1700 meters below ground level. The surface array geophones were spaced at approximately 18- meter (60-foot) intervals, and the longest single linear array that we called sensor line 1 spanned approximately 2700 meters parallel to and nearly directly above the horizontal portion of the treatment well, extending well beyond the end of the stimulated region.

We used seismic signal data from two of the thirteen arrays. That data was sufficient for 3-D fracture imaging. Of the fifteen fracturing stages, we used data from the first stage. Scale drawings of the two arrays whose signals were analyzed in this study are shown in Figure 1 and Figure 2. Sensor line 1 had 149 geophones. Sensor line 2 had 141 geophones. The geophone signals were originally recorded with a 500 Hz sampling rate. With interpolation and re- sampling, the data as incorporated in this work was made available with a 1 kHz sampling rate. The reason for the up sampling was to create a set of data that would be suitable for array beamforming with the self-focusing adaptive beamformer.

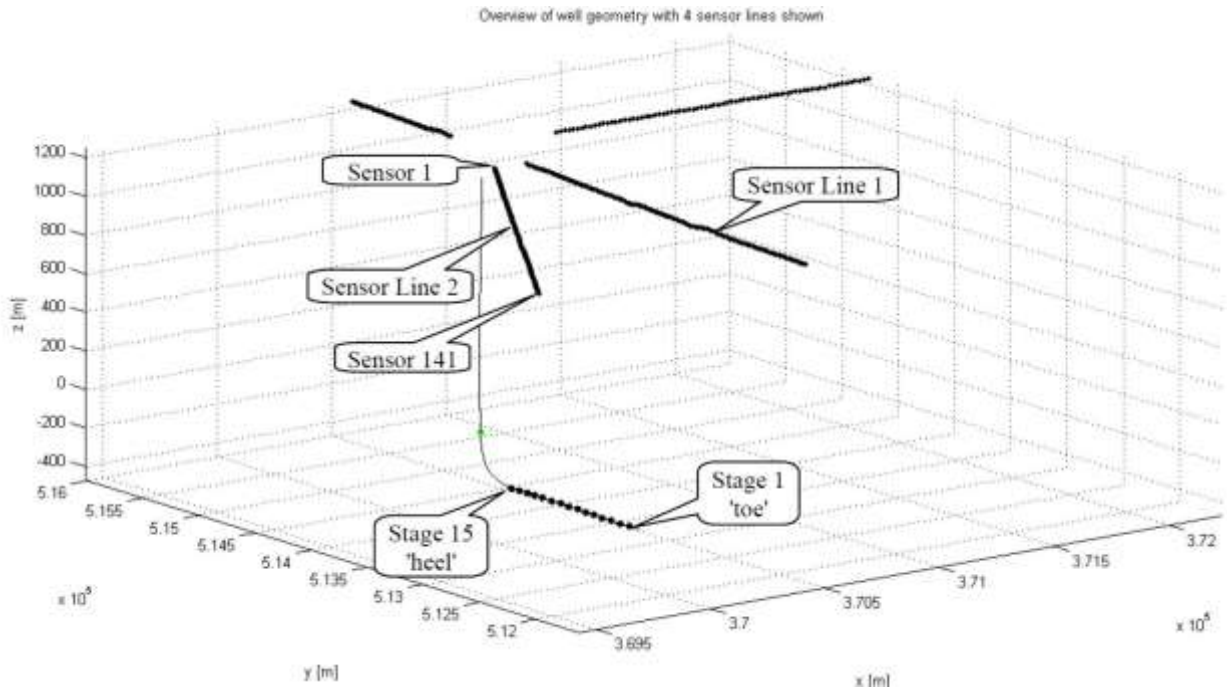

Figure 1: Well geometry with surface seismic sensor lines.

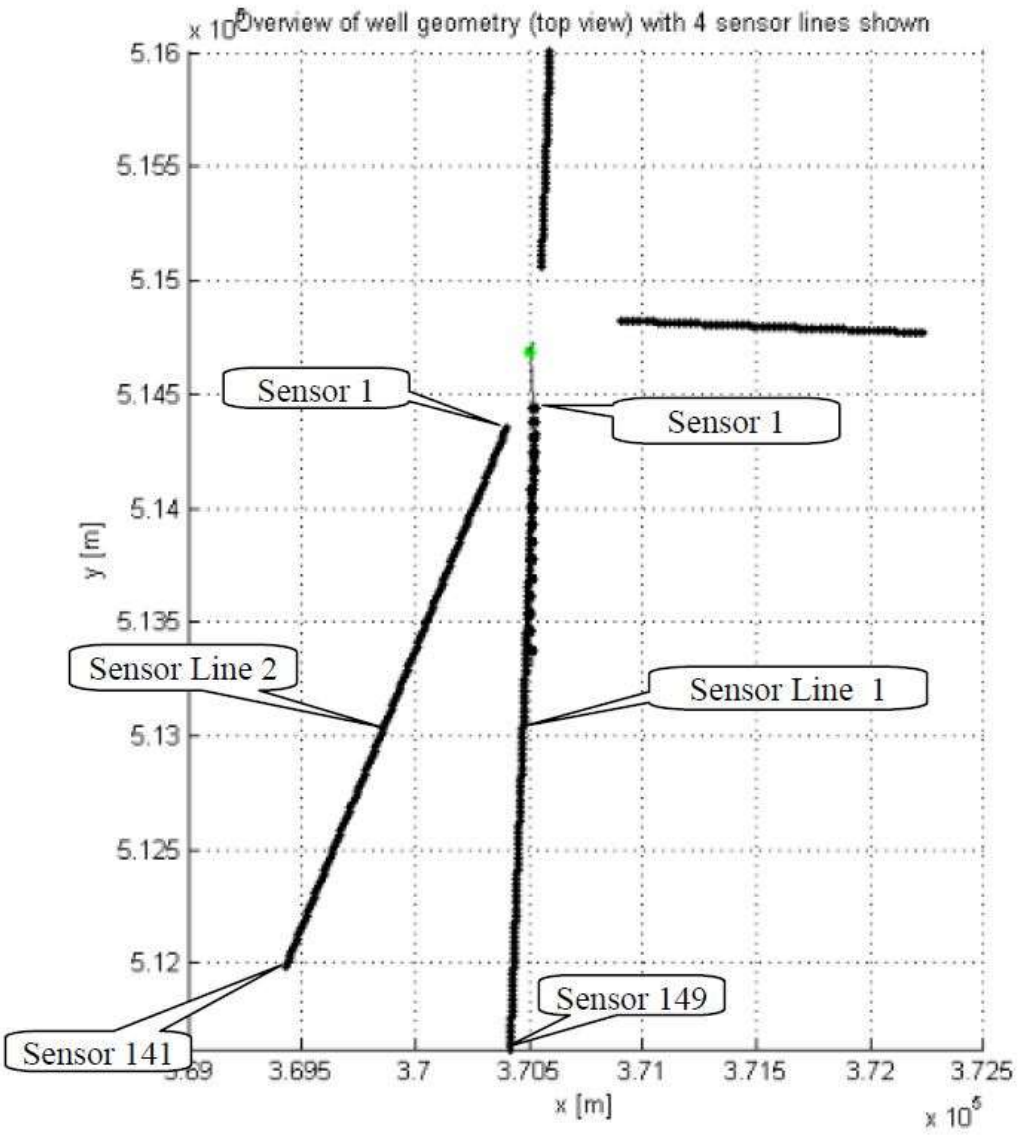

Figure 2: Top view of well geometry with surface seismic sensor lines 1 and 2.

The Self-Focusing Adaptive Beamformer

An adaptive beamformer was used for the detection of seismic events. This requires more computation than conventional time-delay-and-sum beamforming, but adaptive signal processing techniques have been proven to be desirable and essential for processing signals from surface geophone arrays. The resulting improvements in signal to noise ratio allow one to use less geophones in the array and to detect more smaller-amplitude seismic events than would otherwise be possible. The physical length of the surface arrays will remain the same for adaptive

beamforming as for conventional beamforming, in order to preserve the spatial resolution of the ultimate fracture image.

A block diagram of the self-focusing beamformer is shown in Figure 3. In this diagram, the geophones receive signals from a seismic source. The beamsteering delays are adjusted to compensate for the various delay times of the seismic arrivals to the geophone sensors. The adaptive equalizing filters self-adjust to insure that the wave shapes of the seismic signals will all be the same as they are applied to the adaptive beamformer section of the system. There are a number of different configurations of adaptive beamformer that could be used. We chose the Griffith-Jim beamformer for its simplicity and that it computes a time-delay-and-sum beam output as well as an adaptive beamformer output. The Griffith-Jim beamformer is diagrammed in Figure 4.

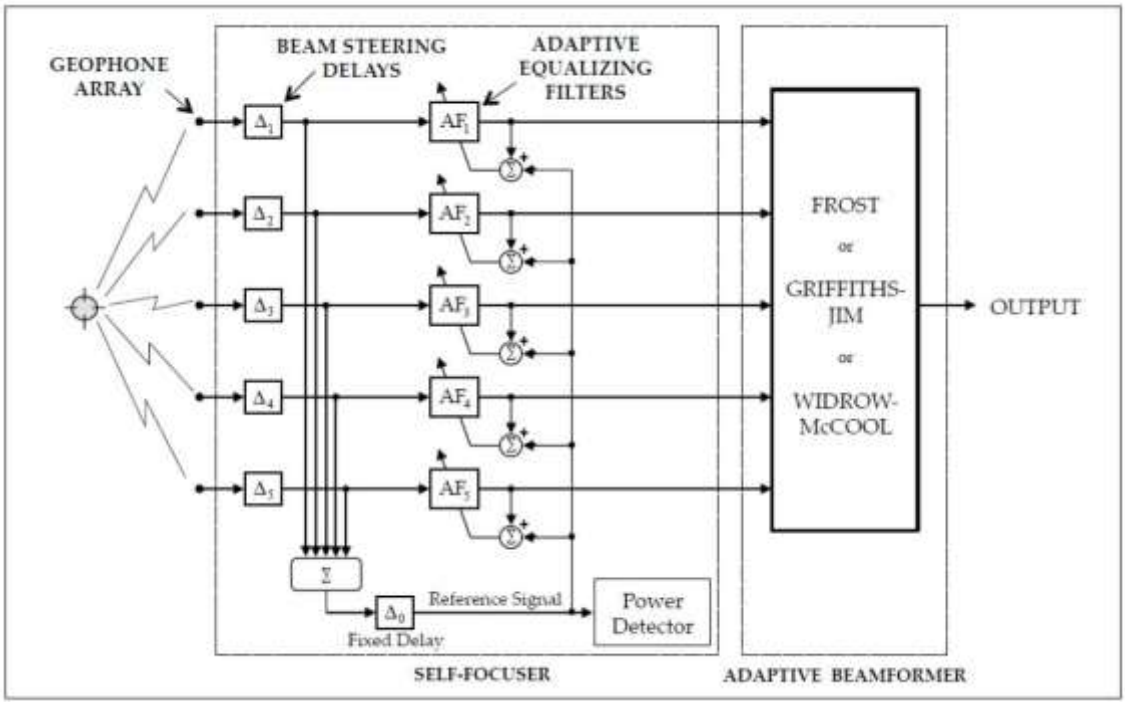

Figure 3: The self-focusing beamformer

Our experience with the seismic-event signals of data set #2 has shown that these events as received by the various geophones were sufficiently similar in their wave shapes that full-blown adaptive equalizing filters were not necessary. These filters were able to be replaced by simple gains that were adjusted to make all the seismic transient signals the same in amplitude as they were then applied as inputs to the adaptive beamformer. Since the beam-steering delays have already been set to compensate for the different arrival times of the seismic signals, which was

necessary to perform equalization, the beam-steering delays of the Griffith-Jim adaptive beamformer shown in Figure 4 should all be set to zero. How this beamformer works is explained simply and in full detail in the book “Adaptive Signal Processing” by Bernard Widrow and Samual D. Stearns, Prentice-Hall, 1985. The Griffith-Jim beamformer is described on pages 418 – 420 and is illustrated by Figure 14.4. Adaptive beamforming in general is described and explained in Chapters 13 and 14.

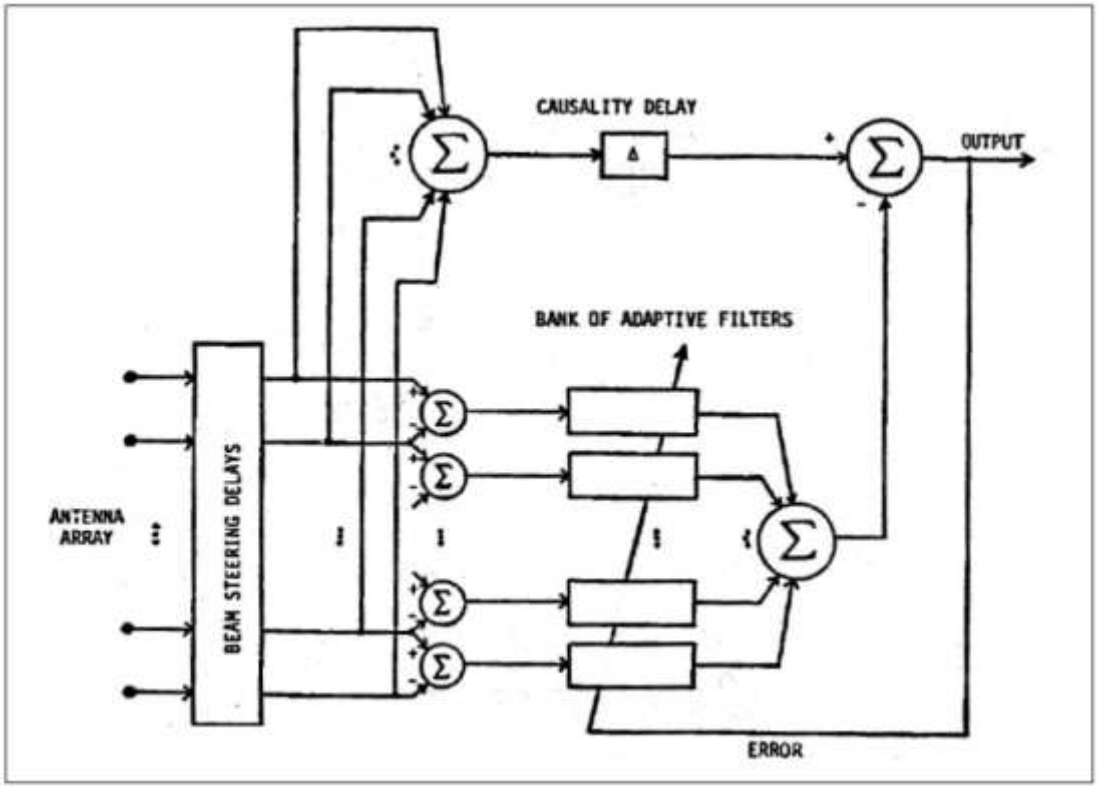

Figure 4: The Griffiths-Jim adaptive beamformer

A very brief discussion of adaptive beamforming follows. A usual description of an adaptive beamformer shows an array of sensors located in a plane, connected to an adaptive processor to provide an output signal. This is a receiving array, not a transmitting array. Adjusting the beam steering delays allows one to point the beam in a desired direction, the “look direction”. The beamformer accepts the signal from the look direction, with a gain of unity. All other signals arriving not in the look direction are rejected as best possible in the least squares sense. The adaptive beam picks up signals from the look direction and adapts to minimize the total power of noise received outside the look direction. It is assumed that the source of the desired signal is located in the far field of the array. The distance from the sensor array to the signal source is

large compared to the aperture of the array, i.e. the physical size of the array. The desired signal is defined in terms of its direction of arrival, not its distance from the sensor array. All this is done in 2-dimensions.

The self-focusing adaptive beamformer for monitoring microseismic signals that are due to hydraulic fracturing differs from the usual adaptive beamformer in that it works in 3-dimensions and works with seismic signals whose point of origin is in the near field of the sensor array. The desired signal is identified with its point of origin in 3-dimensionsional space. Its distance from the array is highly significant. The physical lengths of sensor array 1 and sensor array 2 are comparable to the depth of the well. Sensor array 1 at the surface was 2700 meters long and the depth of the fracture was approximately 1700 meters. The beamforming in this case is definitely near field. The adaptive beamformer will be focused on the point of origin of a seismic event in 3-dimensional space. It will receive signals from this point without distortion and will minimize the power of the total seismic noise coming from anywhere other than the focal point. Instead of a look direction, we have a focal point. In tuning the beam, we have selectivity in the X, Y, and Z directions. This was made possible by the surface arrays being long compared to the depth of the fracture. The array geometry was chosen by the well operator, and it was far from an optimal placement, but it was good enough for us to do fracture mapping. More will be said below about array design. With the seismic data, we have experienced near field beamforming and that is what we want for 3-D localization of seismic events.

High-Energy Seismic Event

A single high-energy microseismic event, observed during the first zone of hydraulic fracture stimulation at the toe of the well, was used as the focus event for all of the initial experiments to be reported here. This high energy event occurred approximately an hour and a half into the two-hour stimulation of zone 1 and generated readily visible arrivals on 9 of the 13 line-arrays, with the strongest arrivals appearing on the southernmost line arrays, including sensor line 1 and sensor line 2. The relative arrival times of the wave front generated by this event indicate that it was located relatively near the perforation interval for zone 1 of the fracture treatment, as may have been expected.

The geophone trace data for this event as observed across sensor line 1 is presented in Figure 5 and across sensor line 2 is in Figure 6. The moveouts were calculated and later used for beam steering. The traces shown in Figure 5 and Figure 6 were high-pass filtered at 5 Hz to eliminate dc offsets and were low passed to eliminate high-frequency noise. No other processing was done. The high-energy event was strong enough to be seen in the individual geophone signals. The geophone outputs for the high-energy event were aligned in time, averaged, and each geophone

signal was given an individual gain to have uniform amplitude of the event across the array. This signal normalization was done by using the average as a template and adjusting each gain to produce a best match to the template. This was done in Figure 3, using simple gains in place of the adaptive equalizing filters. This simple form of equalization was adequate for this fracture. In other cases, full-blown adaptive equalization may be required.

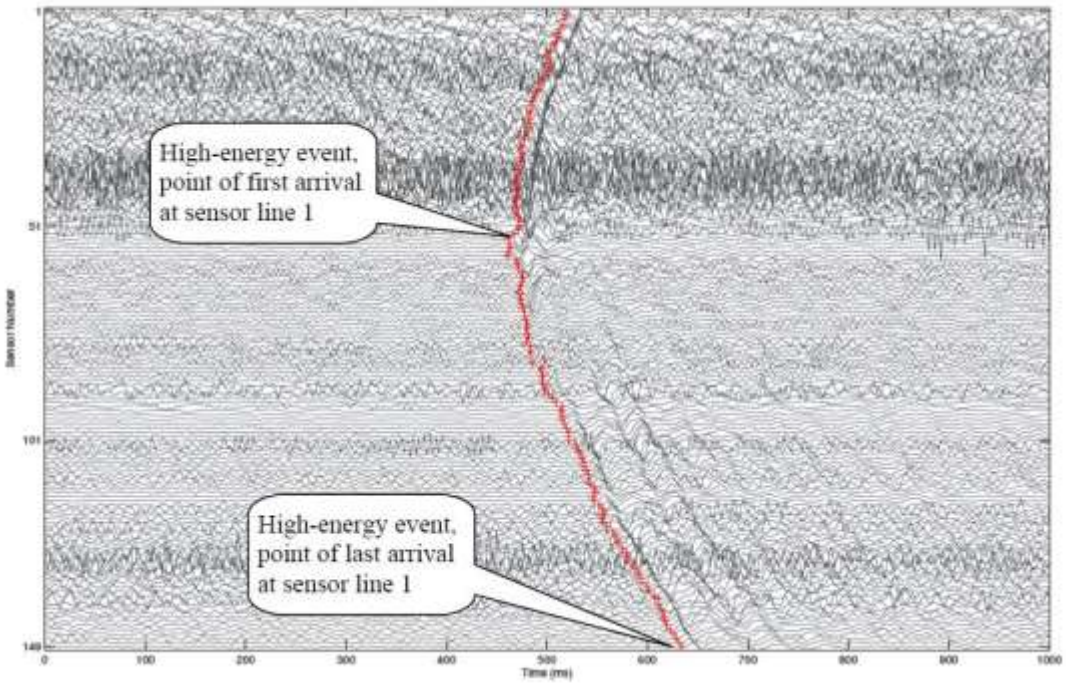

Figure 5: Moveout of high-energy seismic event from Stage 1, measured with sensor line 1. The red line shows the first peaks of this event.

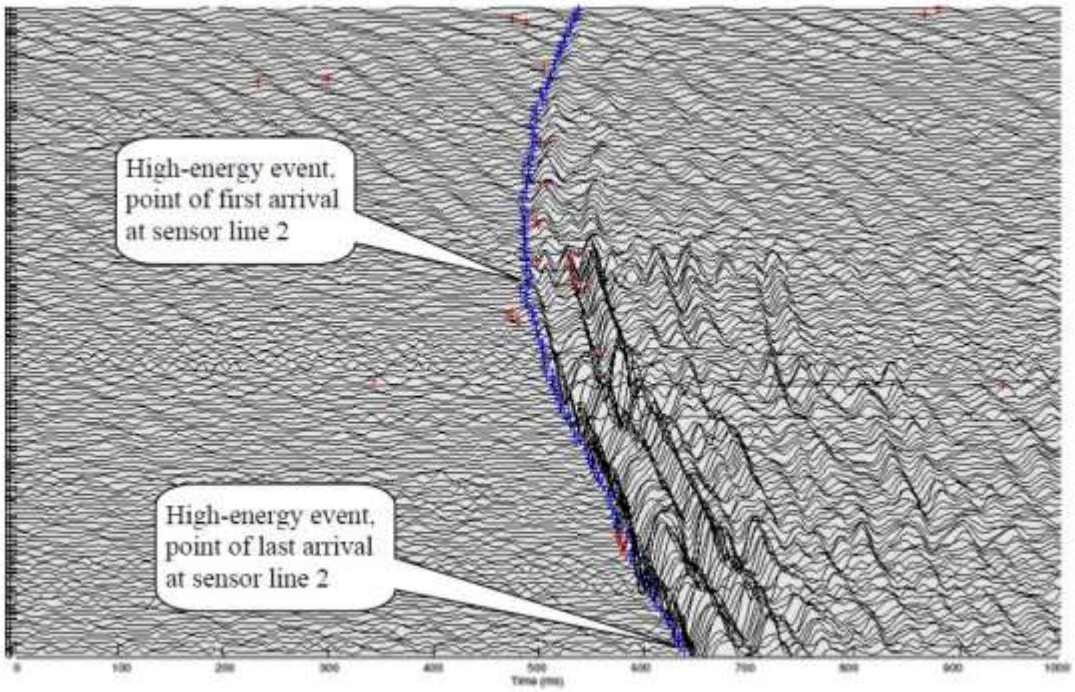

Figure 6: Moveout of high-energy seismic event from Stage 1, measured with sensor line 2. The blue line shows the first peaks of this event.

The results of performing this modified self-focusing procedure using the currently considered focus-event (including normalizing gains) are depicted for sensor line 1 in Figure 7. An SNR-weighted correlation coefficient of 0.98 was achieved between the individual-trace arrival waveforms and an SNR-weighted mean of all individual traces, indicating that the shape of the waveform remains quite consistent across the entire 2700 meter array, and that the event will serve well as a focusing event for use in targeting the event's location.

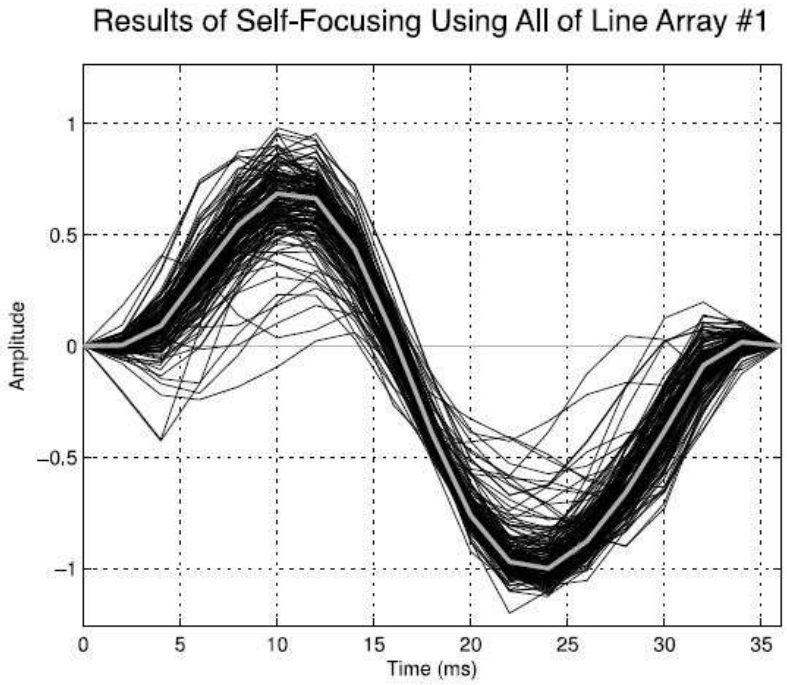

Figure 7: The results of self-focusing for all 149 sensors in line array #1 of data set #2, using a high-energy microseismic event observed during the first zone of hydraulic fracture stimulation. For the 2700-meter long line array, the event's initial arrival waveform remains quite consistent across all sensors, resulting in a fairly high weighted correlation coefficient after self-focusing (0.98) that bodes well for the successful application of the adaptive beamformer. Geophone data has been high-passed at 5 Hz to eliminate DC-bias, and has been low-passed to the event's dominant bandwidth to improve the accuracy of the self-focusing procedure and better illustrate the consistency of the arrival waveform. The white curve is the average.

Improvements in SNR with Adaptive Beamforming

Given the determined focusing parameters, the adaptive beamformer's performance was then compared to the performance of a conventional time-delay-and-sum beamformer by evaluating the SNR improvement achieved by the adaptive beamformer when targeting the location of the focus event over 3 hours and 40 minutes of continuous data that included the entire 2-hour stimulation of the well's first stage. For this experiment, no pre-processing was performed to identify individual noisy or "problematic" sensors within the surface array. Because noise conditions often vary significantly from sensor-to-sensor in surface-array survey data due to local and cultural noise and varying coupling quality between geophones and the ground such pre-processing is generally advantageous or necessary to improve the overall data quality by

eliminating particularly bad sensors; however, such processing often requires the use of ad hoc or heuristic techniques and here we desired to see how the self-focusing adaptive beamformer would naturally handle this issue without any additional processing.

In order to evaluate how the adaptive beamformer performed in various cases, several runs of the experiment were performed. The adaptive beamformer was applied to data using either 25 or 50 taps per adaptive filter of Figure 4 (spanning 50 or 100 milliseconds of signal, respectively), and the array data was either processed raw or pre-processed with a 4-th order Butterworth low-pass filter with a cutoff frequency of 60 Hz in order to remove energy at frequencies above the dominant bandwidth of the focus event. These trials demonstrated that pre-conditioning data through the use of a simple low-pass filter, as is commonly done in microseismic data processing, significantly enhanced the self-focusing adaptive beamformer's ability to improve SNR relative to a conventional time-delay-and-sum beamformer, yielding improvements that were approximately 4.5 dB greater than when low-pass conditioning was not performed. We believe that this occurs because most of the high-frequency content observed by the surface-array geophones is comprised of local noise that is incoherent across the array. The presence of incoherent noise can limit the effectiveness of the adaptive beamforming algorithm, and thus eliminating this content through simple low-pass filtering can greatly enhance the effectiveness of the adaptive beamformer when used with surface arrays. It was also found that increasing the number of filter taps from 25 to 50 provided a modest increase in the advantage of the adaptive beamformer of approximately 0.5 dB. Thus, while the adaptive beamformer may perform slightly better with additional degrees of freedom to optimize (more taps in its adaptive filters), the performance of the adaptive beamformer is not strongly dependent upon high tap counts. The SNR improvements achieved with these various setups over the 3-hours and 40-minutes of processed data are depicted below in Figure 8.

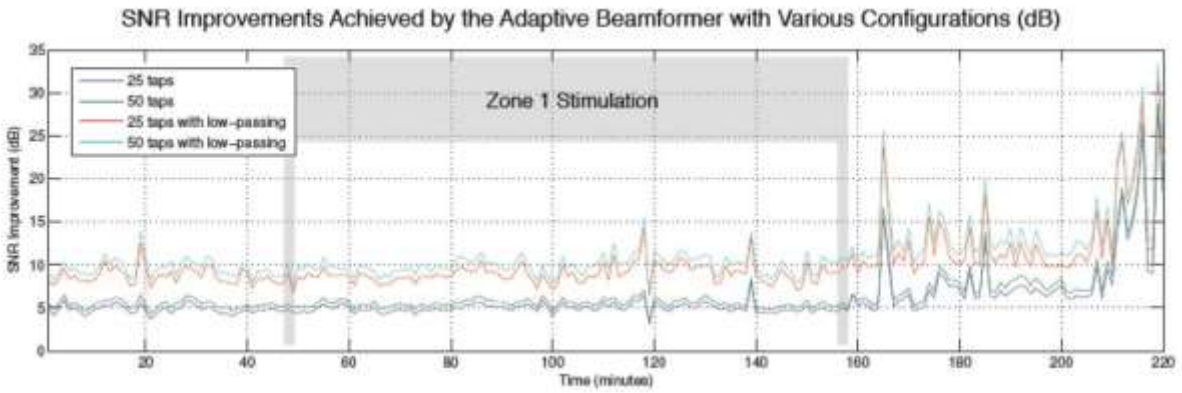

Figure 8: SNR improvements achieved by the adaptive beamformer as compared to a conventional time-delay-and-sum beamformer for each processed one-minute time segment

in a 3-hour and 40-minute time period encompassing the first zone of fracture stimulation, when focusing on a high-energy microseismic event observed during minute 131. The time period corresponding to the treatment of zone 1 is indicated by a shaded gray heading. SNR improvements for 4 runs of the experiment with different beamformer configurations are displayed: either 25 or 50 filter taps were used in the adaptive beamformer's weight matrix (covering 50 or 100 milliseconds of time, respectively), and low-pass filtering either was or wasn't used to pre-condition the array data. It can be observed that in all cases fairly consistent improvements in SNR were achieved for the first 160 minutes and that this level increased somewhat for the last 60 minutes, including intermittent periods where SNR improvements of as much as 25 or 30 dB were achieved. It can also be observed that the adaptive beamformer was able to improve SNR by a substantially greater amount when array data was low-pass filtered prior to application of the adaptive beamformer and that the use of 50 taps rather than 25 provided a modest increase in the SNR improvement achieved by the adaptive beamformer regardless of whether low-pass filtering was performed.

For all of the experimental results that we report, 50 taps spanning 100 milliseconds of data were used in the adaptive beamformer's filters and data was pre-conditioned using the previously described low-pass filter. Figure 9 on the following page highlights the SNR improvements achieved in this case. Averaged across the full duration of the zone 1 treatment, the adaptive beamformer was found to provide a substantial 10.1 dB SNR improvement. Figure 10 shows the output of the conventional and adaptive beamformers for a time period of data that includes the arrival of the targeted focus event, providing a visual example of a 10.1 dB of SNR improvement in data. Figure 9 then presents a close-up of the conventional and adaptive beamformer outputs for the focus-event arrival itself, illustrating that although the adaptive beamformer provides significant noise reduction (as seen in Figure 10), it does not greatly attenuate energy originating from the targeted focus location and thus provides the improvements in SNR described here.

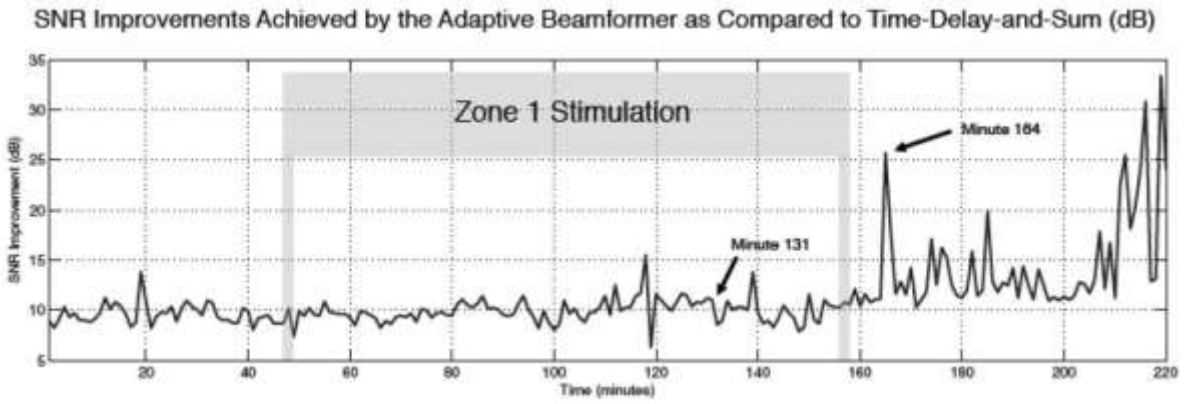

Figure 9: SNR improvements achieved by the adaptive beamformer as compared to a conventional time-delay-and-sum beamformer for each processed one-minute time segment in a 3-hour and 40-minute time period encompassing the first zone of fracture stimulation, when focusing on a high-energy microseismic event observed during minute 131. The adaptive beamformer provides an SNR increase of 10.1 dB on average during the zone 1 stimulation treatment. It can be seen in this plot that the adaptive beamformer is capable of providing significantly greater SNR improvements as well: improvements of as much as 33.4 dB are achieved during the last few minutes of the processed data. An SNR improvement of 25.7 dB achieved during minute 164 of the processed time period has been labeled.

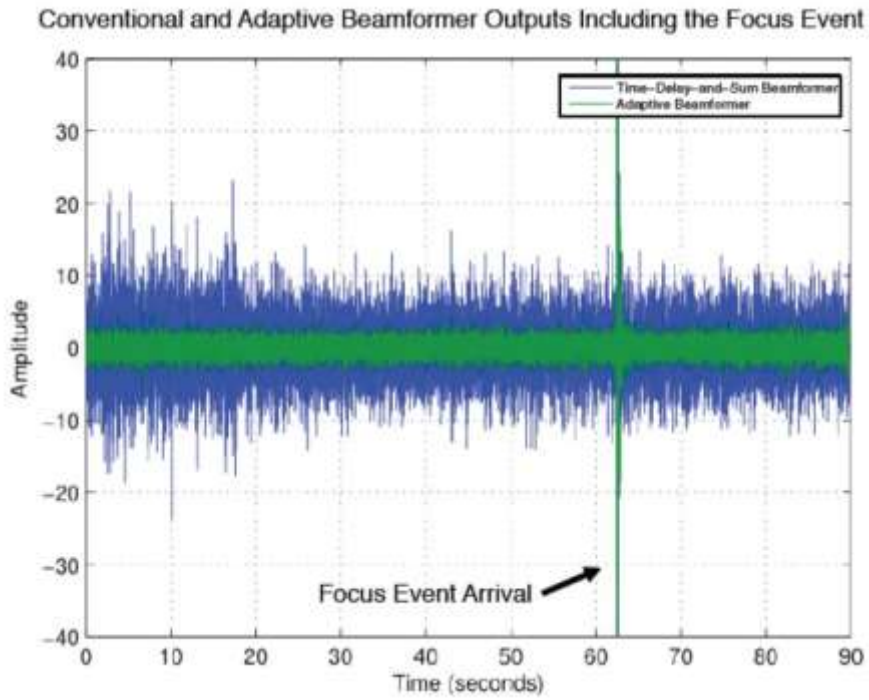

Figure 10: The outputs of a conventional time-delay-and-sum beamformer (dark blue) and the adaptive beamformer (light green) during the time period leading up to and including the arrival of the focus-event energy. This data corresponds to parts of minutes 130 and 131 in Figure 7. The average reduction in noise energy demonstrated in this plot is 10.6 dB. Thus, the noise reduction shown here is representative of the average noise reduction achieved by the adaptive beamformer as compared to the conventional beamformer throughout the duration of stimulation for zone 1 (10.1 dB).

The achieved average SNR improvement of 10.1 dB across the duration of the zone 1 stimulation treatment is very substantial and represents a significant increase in detection and localization ability. While it is somewhat of an oversimplification, this improvement in SNR can be thought of as providing a statistical advantage approximately equal to using a conventional time-delay-and-sum beamformer with 10 times as many sensors spaced over an aperture of the same size or larger. Accordingly, we can expect the self-focusing adaptive beamformer to provide detection ability and localization accuracy similar to what would be achieved using conventional processing techniques on an array with 10 times as many sensors, or, alternatively, we can expect to achieve similar results using the adaptive beamformer using only one tenth of current typical sensor counts.

In addition to the general advantage reflected by this measured increase in signal-to-noise ratio (SNR), we have observed the self-focusing adaptive beamformer to provide particular types of noise reduction that yield even greater SNR increases, eliminate the need for additional data conditioning and pre-processing to eliminate individual problematic sensor signals, and improve the statistics of the remaining noise so as to reduce the number of false-positive event detections. We will present examples of these types of noise reduction in the following section of this report.

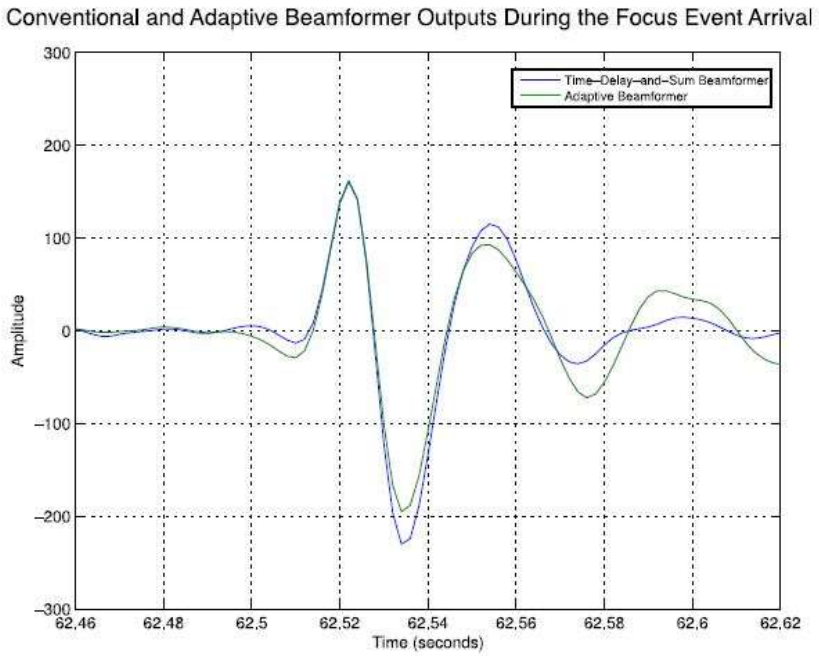

Figure 11: The outputs of a conventional time-delay-and-sum beamformer (dark blue) and the adaptive beamformer (light green) during the arrival of the focus-event energy. The time axis in this figure refers to the same time period as Figure 10, expanded to examine a portion of second 62 that includes the arrival of the focus event waveform. Note that this figure has a different vertical scale than Figure 10. It can be seen in this figure that although the adaptive beamformer provides significant noise reduction (see Figure 10), it does not greatly attenuate the arrival of energy from the targeted focus location: the conventional and adaptive beamformer outputs are very similar for the focus-event arrival, with the adaptive beamformer attenuating the initial arrival only slightly.

Noise Reduction with Adaptive Beamforming

Looking back to Figure 9, it can be seen that the adaptive beamformer achieved SNR improvements significantly greater than 10.1 dB at several times during the processed period of data. This is particularly the case during the hour of data after the zone 1 treatment (minutes 160 to 220), where the median SNR improvement increased to 12.5 dB, the average SNR improvement increased to 20.0 dB, and SNR improvements of as much as 33.4 dB were sustained for 1-minute periods. This increase in the advantage provided by the adaptive beamformer after the zone 1 treatment ended was not anticipated because noise generated by pump trucks and other machinery associated with the hydraulic fracture stimulation typically cause local noise levels to be higher during active treatment, and thus it may be expected that the adaptive

beamformer will be able to provide a greater improvement during treatment by eliminating much of this noise; however, other activities at the well pad may have been causing noise during this time after treatment ended or there may have been an increase in nearby seismic activity.

Figure 12 below shows the average power present in the raw array data recorded by sensor line 1 during the time period of the experiment, and confirms that the average noise level seen across the array did generally decrease after the end of the zone 1 stimulation treatment, although some significant spikes in energy were observed. The ability of the adaptive beamformer to provide even greater SNR improvements during this time period than it generally did during the active stimulation of zone 1 indicates that the noise that was present at this time was likely more directional or coherent across the array than much of the noise that was present during treatment, or that an elevated level of incoherent noise was present during treatment that limited the ability of the adaptive beamformer to provide noise reduction.

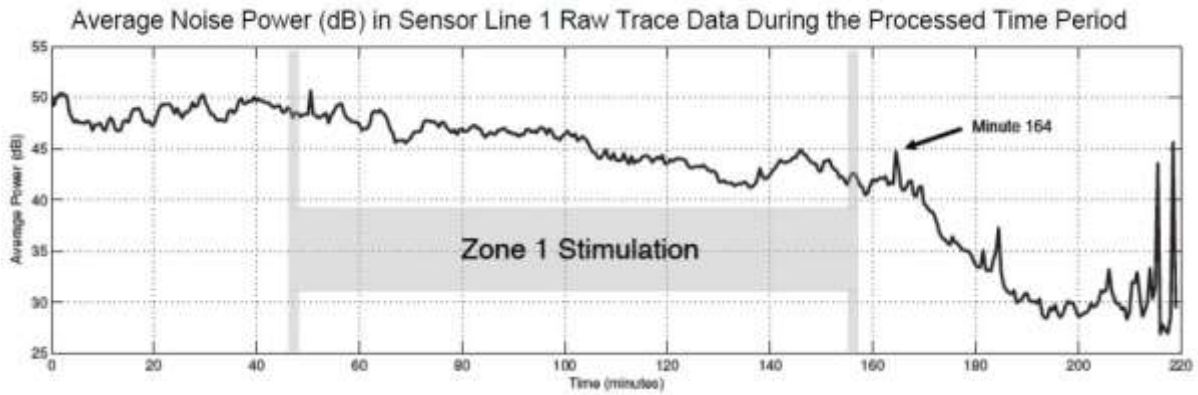

Figure 12: Average power observed by sensor line 1 during the time period of data examined in the current experiment. This figure refers to the same time period as Figure 9. It can be seen in this figure that the overall noise level observed by the array generally decreased after the end of the zone-1 stimulation, but that some temporary increases in energy occurred. Figure 9 shows that the adaptive beamformer was able to provide significant SNR improvements during many of these spikes as well as in general during the last hour of processed data (minutes 160 to 220). The fact that these SNR improvements were greater than the average improvements observed during the zone 1 stimulation treatment suggests that the noise observed during this time period was generally more directional or coherent across the array. Minute 164 of processed data has been labeled; the data corresponding to this time is used as an example and is presented in the subsequent figures of this report.

Examination of the trace data associated with this last hour of processed data found that the noise present during this period did indeed exhibit more directionality and coherence across the array. As an illustrative example of such noise, trace data from minute 164 of the processed time period is presented in Figure 13 and Figure 14 on the following page. Two directional noises are apparent in these figures: a high-energy, long-duration seismic wavefront that has similar amplitude across the entire array and intermittent wavefronts that appear with the most energy at the northernmost sensor (sensor #1) and attenuate as they travel down the array.

While we are unsure of the source of the first of these noises, the second, intermittent directional noise originates from activity at the treatment well-pad, as it appears simultaneously at the innermost sensors of multiple line-arrays surrounding the well-pad and exhibits typical attenuation as it travels and spreads outward.

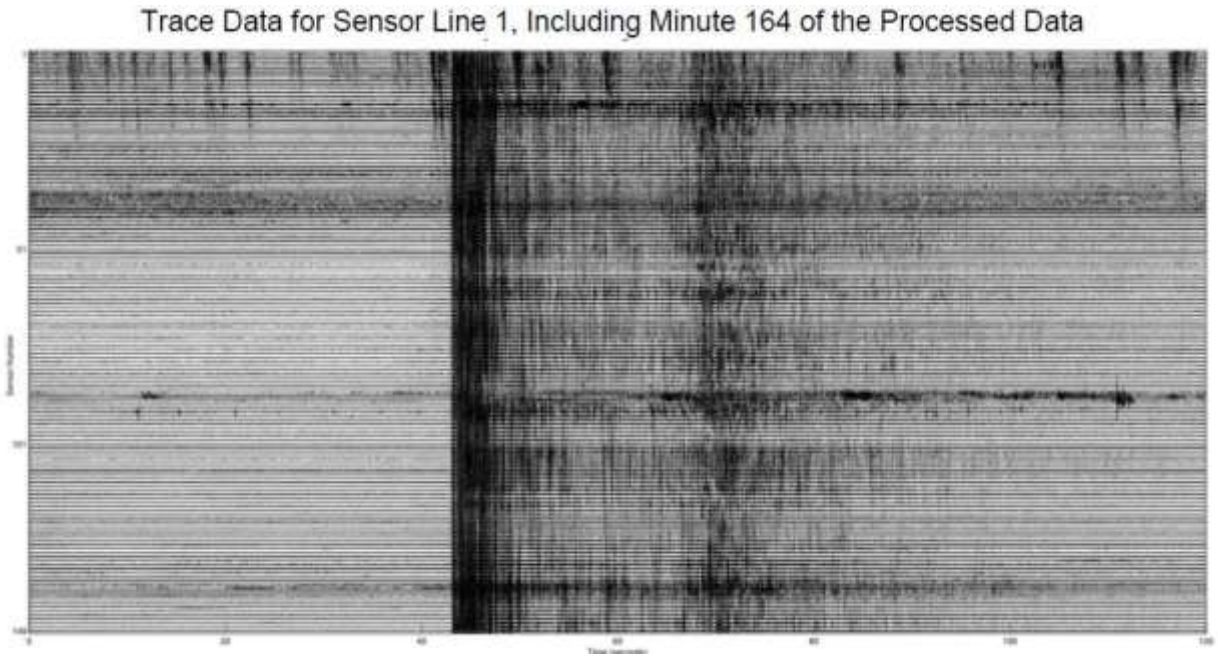

Figure 13: Trace data for sensor line 1 showing a high-energy arrival of directional noise that occurred during minute 164 of the processed data. As reported in Figure 9, the adaptive beamformer was able to provide 25.7 dB of SNR improvement during this time period by eliminating a large portion of the directional noise energy depicted here. Intermittent directional noise associated with activity at the well-pad is also visible in the uppermost traces throughout the 2 minutes of data shown here.

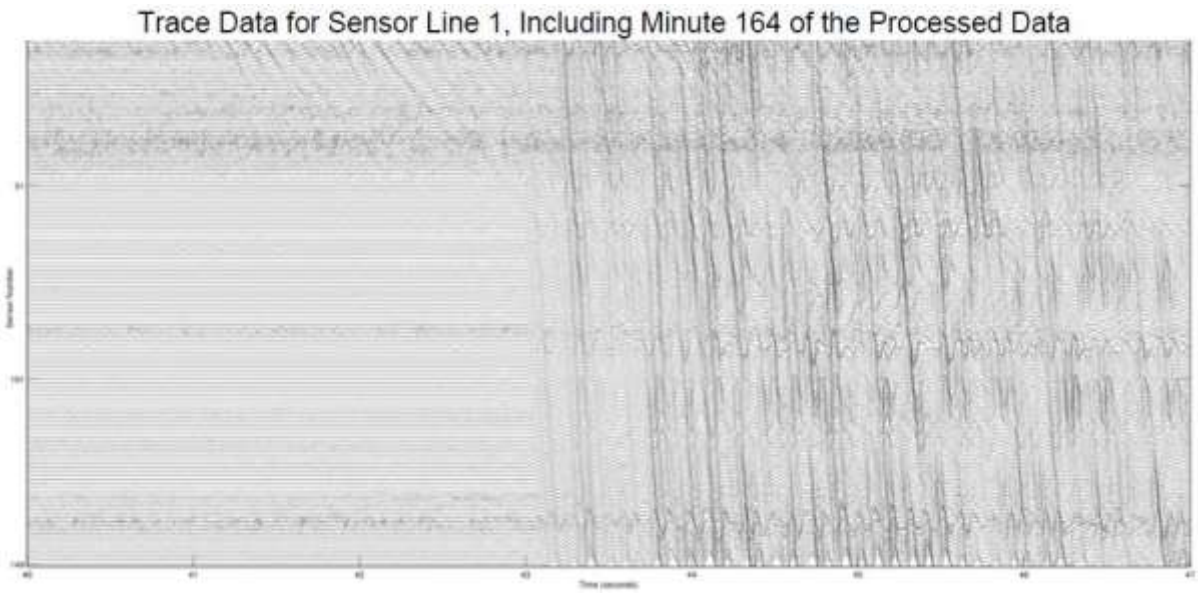

Figure 14: Trace data for sensor line 1 showing a high-energy arrival of directional noise that occurred during minute 164 of the processed data. The time axis in this figure refers to the same time period as Figure 13, expanded to examine a seven-second portion of data that includes the initial arrival of the directional noise. It can be seen in this plot that the high-energy arrival is quite coherent across the entire array and largely exhibits a single move-out indicative of a single location or direction of origin. The adaptive beamformer is able to greatly attenuate any directional signal originating from a location other than the targeted look location, and thus is highly effective at eliminating the noise seen here. Intermittent noise associated with activity at the well-pad can also be seen in the uppermost traces here, and exhibits a different move-out than the high-energy, long-duration noise arrival. The adaptive beamformer works to eliminate both of these directional noises simultaneously.

The high-energy, long-duration wavefront shown in Figure 13 and Figure 14 on the previous page corresponds to a temporary increase in array energy during minute 164 of the processed data that can be seen in Figure 10and that corresponds to a high SNR-improvement, averaged over one minute, of 25.7 dB that is reported in Figure 9. During the peak energy period of this wavefront's arrival, which lasts only a few seconds, the adaptive beamformer provides 33.8 dB of noise reduction. This is shown in Figure 15 and Figure 16. Incredible noise reductions are achieved by the self-focusing adaptive beamformer in this case because the corrupting noise is highly coherent across the array and the adaptive beamformer is able to optimize its directional sensitivity to avoid picking up the wavefront's energy while maintaining essentially constant sensitivity to signals originating at the targeted look location. The intermittent noise from activity at the well-pad that is evident in Figure 13 and Figure 14 on the previous page is present throughout the final hour of processed data and exhibits similar characteristics to noise that is

present during the zone 1 treatment as well; however, as the overall noise levels reduce after the zone 1 treatment ends, this directional noise becomes an increasingly prominent part of the local noise field. It appears that in addition to coherent, directional noise, active treatment may cause elevated levels of incoherent noise across the array. When the energy of this incoherent noise decreases after active treatment has ended, the adaptive beamformer is able to provide even greater increases in SNR, yielding a median improvement of 12.5 dB in the hour after the zone 1 treatment finished. This may prove beneficial for detecting and localizing low-energy microseismic events that occur as the local geology settles after treatment due to newly imposed local stresses.

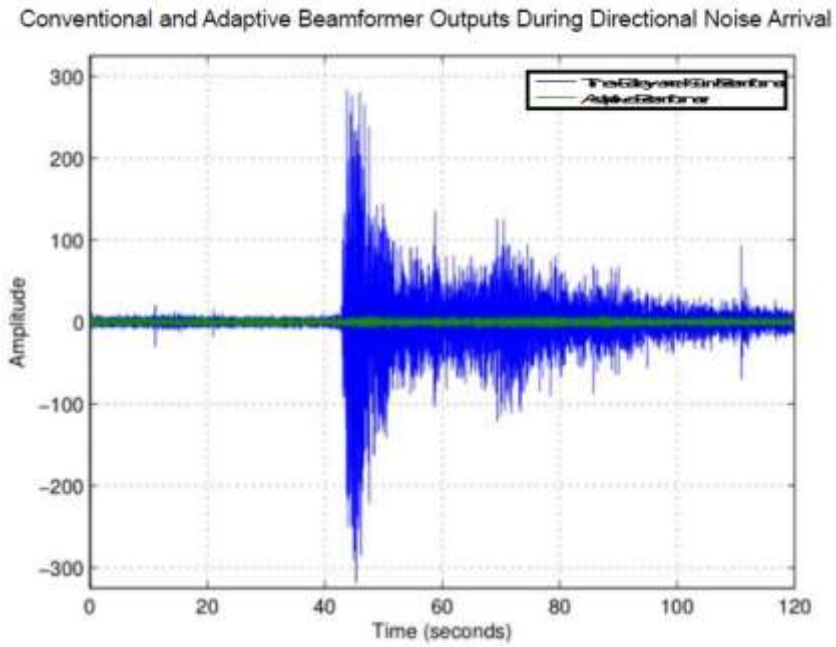

Figure 15: The outputs of a conventional time-delay-and-sum beamformer (dark blue) and the adaptive beamformer (light green) during the time period plotted in Figure 13 that includes minute 164 of the processed data while targeting the location of the focus event. It can be seen in this figure that the adaptive beamformer effectively eliminates the energy increase associated with the high-energy, long-duration wavefront that is strongly evident in the time-delay-and-sum output. The adaptive beamformer does this by optimizing its directional sensitivity to avoid picking up the noise signal while maintaining constant sensitivity to signal originating at the focus event location. If any microseismic events had occurred during this time period, they would not have been detectable through use of a conventional time-delay-and-sum beamformer, but may have been observable through use of the adaptive beamformer. Averaged across the full 2-minute duration of data depicted here, the adaptive beamformer provides a noise reduction of 23.7 dB. During the most energetic portion of the wavefront

arrival (from about 43 to 48 seconds), the adaptive beamformer provides 33.8 dB of noise reduction.

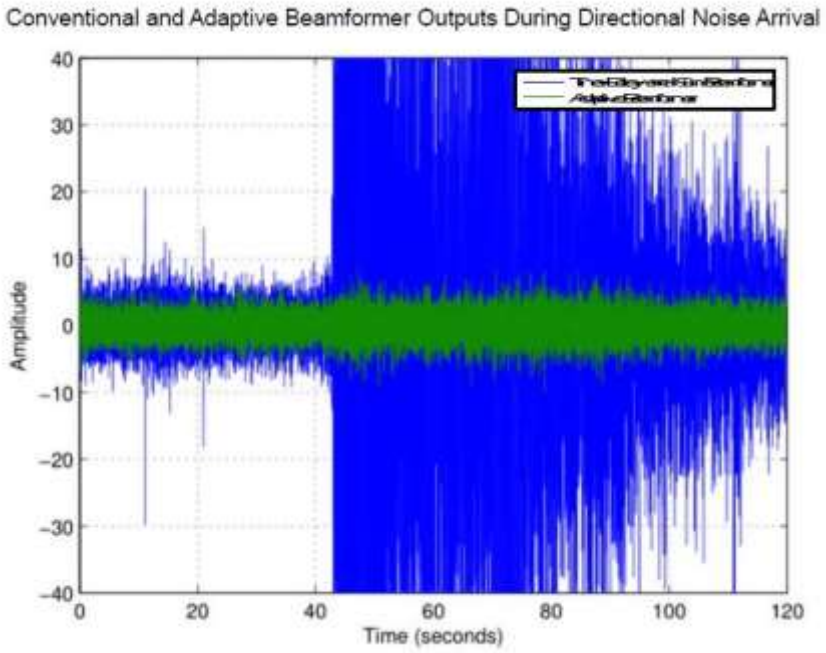

Figure 16: The same data as plotted in Figure 15 on the previous page, but with an increased y-axis scale to show the adaptive beamformer output in more detail. It can be observed in this figure that the adaptive beamformer almost completely eliminates the high-energy seismic wavefront arrival over the full 80-second duration shown here. Additionally, as is discussed below and will be presented in Figure 17 and Figure 18, it can be seen that the adaptive beamformer eliminates transient spikes of energy present in the conventional time-delay-and-sum beamformer output at times of approximately 11, 21, and 113 seconds that may have otherwise been misidentified as arrivals of microseismic event energy.

In addition to the adaptive beamformer's ability to eliminate even very-high-energy arrivals of seismic energy originating from locations other than the targeted look location, the adaptive beamformer is also very effective at detecting and temporarily eliminating particularly noisy sensors, without the need for any additional pre-processing or the implementation of ad hoc or heuristic methods. In fact, nothing additional needs to be done to achieve this: the same optimization that works to eliminate coherent, directional noise signals will inherently work to temporarily eliminate individual, isolated "problematic" sensors whenever they act up. Thus, the self-focusing adaptive beamformer provides an elegant and robust way of dealing with individually problematic sensors and local, intermittent noises in surface arrays.

The true benefit of this property is not always expressed well using a simple SNR measurement. For example, many of the isolated or intermittent noises that are eliminated from the beamformer output in this way will appear at the output of a conventional time-delay-and-sum beamformer as a transient spike that may be mistaken for an event arrival. An example of this is highlighted in Figure 17 and Figure 18. Eliminating this type of transient signal from the output of the adaptive beamformer may not register a large SNR increase when averaged over some duration of time (i.e. over a minute, as done in the experiments reported here), but making noise statistics more normal and eliminating such transient spikes can greatly improve detection confidence and decrease the amount of false-positive event detections that occur for a given SNR and detection threshold. This in turn results in a more confident and clear imaging of the fracture network induced during a hydraulic fracturing treatment as well as the amount of activity induced during a given time period

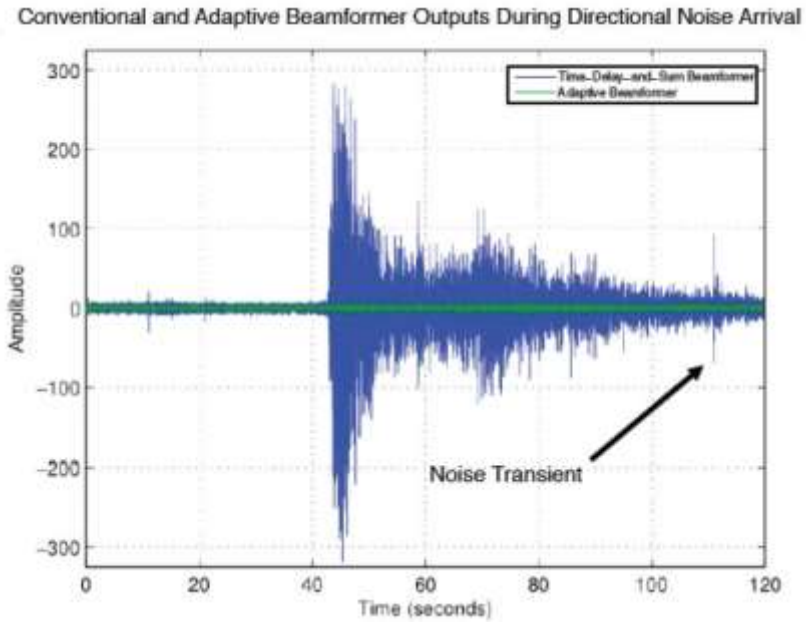

Figure 17: The same data as displayed in Figure 15, but emphasizing a transient signal that occurs after the main high-energy seismic wavefront arrival. This transient spike appears strongly on the conventional time-delay-and-sum beamformer output (blue) but not on the adaptive beamformer output (green), and is an example of a single noisy sensor greatly impacting the output of a conventional beamformer. If examined closely, additional transients may be seen in the conventional beamformer output at times of approximately 11 and 21 seconds. These transients may also be seen in Figure 16 on the previous page.

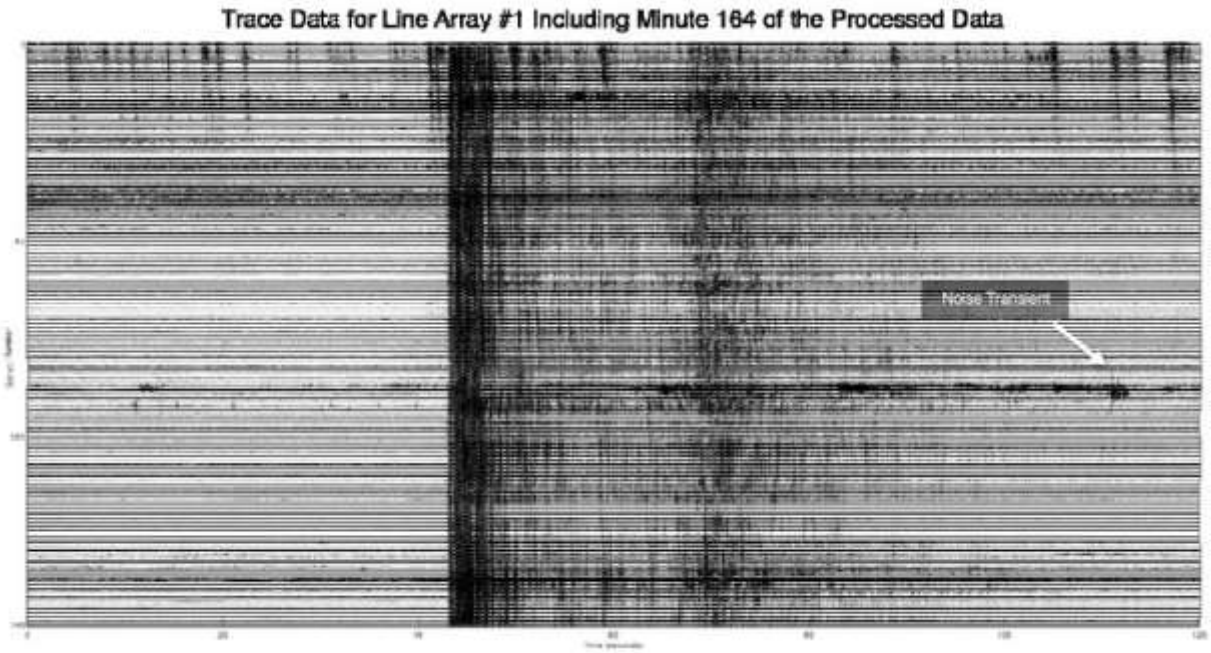

Figure 18: The same data as displayed in Figure 13, this figure shows the array trace data associated with the beamformer outputs plotted in Figure 15 above (the same time periods are shown in both plots on this page). Here we point out a noise transient that has occurred on a single sensor out of the 149-sensor line-array. This isolated disturbance is responsible for the transient spike in the time-delay-and-sum beamformer output emphasized in Figure 17 above. It is evident in this array data that some kind of local disturbance has increased the noise level in that single sensor and perhaps one or two sensors next to it, and that the corresponding spike in the conventional beamformer's output does not indicate the arrival of a microseismic event. While the adaptive beamformer naturally eliminates individual noisy sensors and suppresses this type of spurious transient, additional pre- or post- processing would be required when using a conventional time-delay-and-sum beamformer to avoid declaring this transient as a false-positive microseismic event.

Detection of Previously Undetectable Low-Energy Events

During our study of data set #2, we identified a low-SNR event that occurred at or near the location of the high-energy focus event just prior to the main focus event that was not observable using a conventional time delay-and-sum beamformer but that was readily apparent when using the self-focusing adaptive beamformer. This detection of a "sub-threshold" or low-SNR foreshock demonstrates achievement of a significant goal of the self-focusing adaptive beamformer: enabling the detection of additional low-energy microseismic events that would otherwise be

undetectable in order to provide a more detailed mapping of the fracture network induced during a stimulation treatment.

Figure 19 through Figure 21 below and on the following page demonstrate the uncovering of this low-energy “foreshock”, which precedes the high-energy focus event and must occurs at nearly the same location because it is not eliminated by the adaptive beamformer as would be content arriving from other locations (as previously demonstrated in Figure 15 and Figure 16). It can be seen that by increasing SNR by 10.1 dB, the adaptive beamformer has been able to reduce background noise to a level substantially below the level of this low-energy event, providing a confident detection of microseismic activity that would have gone completely unseen using a conventional time-delay-and-sum beamformer.

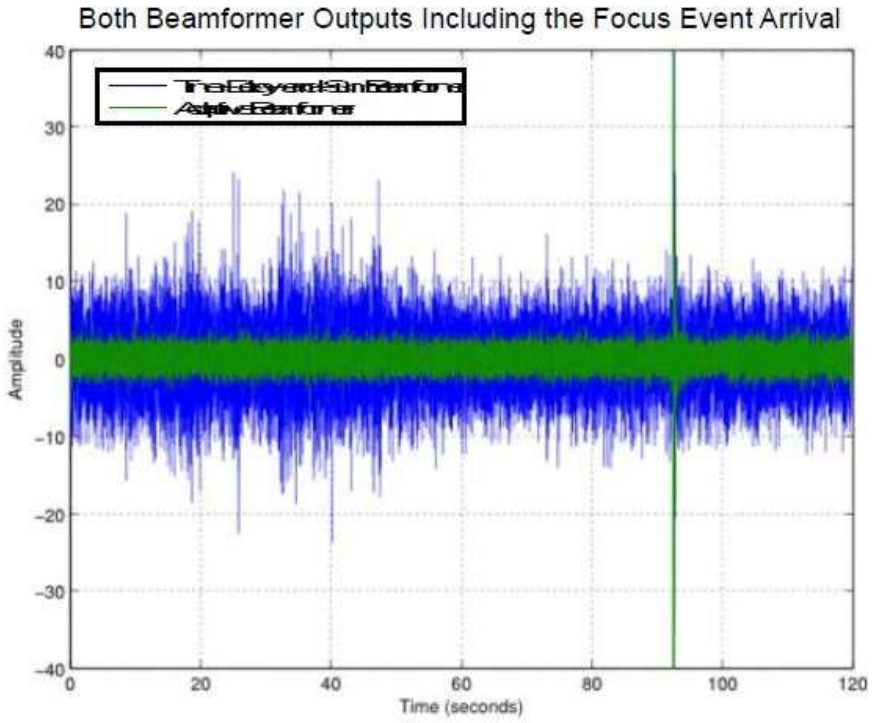

Figure 19: Figure 19 depicts the outputs of both a conventional time-delay-and-sum beamformer (dark blue) and the self-focusing adaptive beamformer (light green) over a time period that includes the focus-event arrival. Looking at Figure 19, it can be seen that this signal is well below the noise level in the time-delay-and-sum beamformer, making the small transient in the adaptive beamformer output difficult to see in that plot.

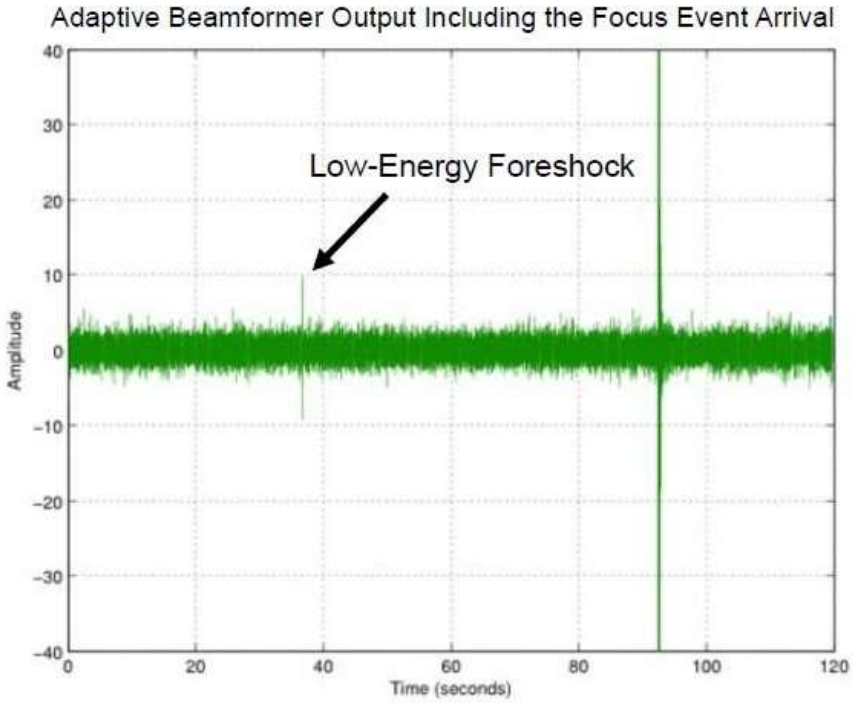

Figure 20: Figure 20 depicts the same data as displayed in Figure 19, but only the adaptive beamformer output is plotted. It is evident in Figure 20 that a transient signal is present at a time of about 37 seconds.

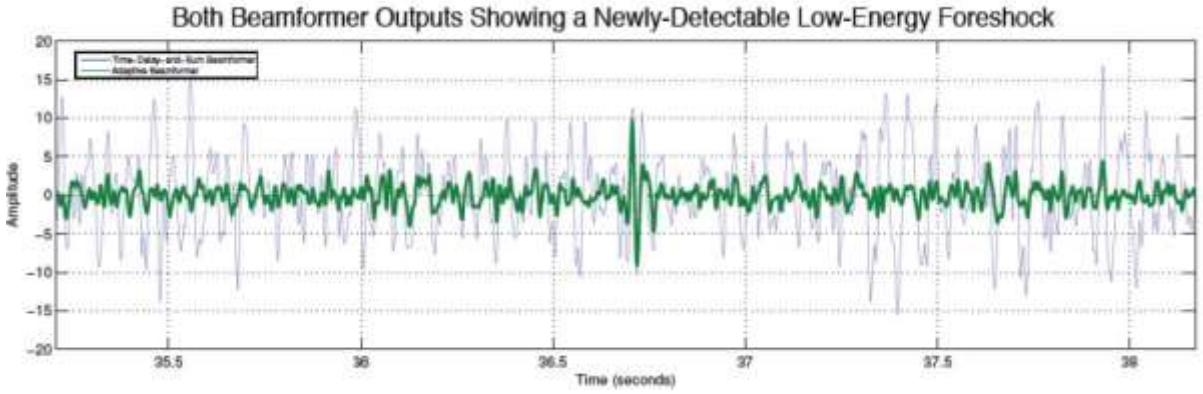

Figure 21: This figure shows the outputs of both a conventional time-delay-and-sum beamformer (light blue) and the adaptive beamformer (dark green) during the arrival of the low-energy foreshock highlighted in Figure 20 on the previous page. This figure demonstrates that the short transient shown in Figure 20 extends well above the noise-floor of the adaptive beamformer output but would not stand out in the output of a conventional beamformer as there are numerous peaks of equal or greater energy in the time-delay-and-sum beamformer's output (light blue) surrounding this arrival.

Figure 22 below provides additional confirmation that this uncovered transient waveform is in fact the arrival of microseismic event energy: although this low-energy foreshock and the subsequent focus-event arrival have substantially different energy levels, they exhibit similar waveforms and similar bandwidth, resulting in wavelet pulses with very similar durations and waveshape.

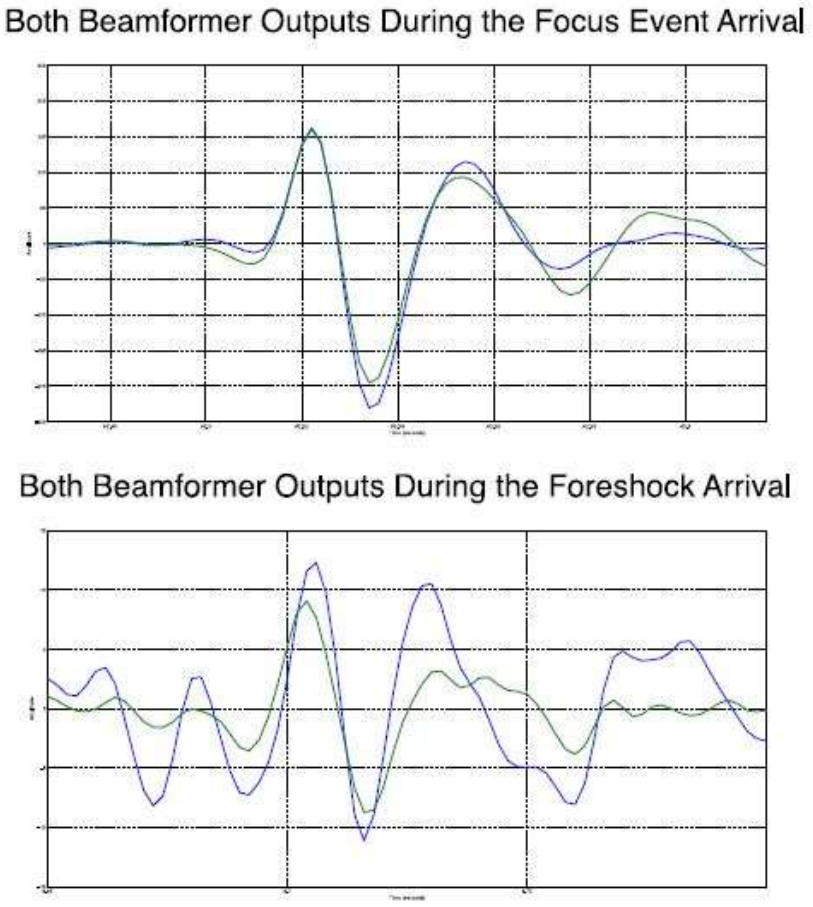

Figure 22: This figure shows the outputs of both a conventional time-delay-and-sum beamformer (blue) and the adaptive beamformer (green) during the arrivals of the focus event and the low-energy foreshock (previously depicted in Figure 18 and Figure 19). The two arrivals (focus event and foreshock) have been plotted on the same time-scale (150 ms) but with different amplitude scaling in order to highlight the similarity of the waveforms exhibited by the two arrivals. The fact that the uncovered low-energy arrival has a waveform with essentially the same duration and waveshape as the high-energy focus event serves as additional confirmation that the newly detectable low-energy transient is in fact an arrival of

microseismic event energy from a location at or near the location of the subsequent focus event.

The results of the study presented here using data set #2 demonstrate that use of the self-focusing adaptive beamformer is highly advantageous for the processing of microseismic data collected using a surface array. The measured average SNR improvement of 10.1 dB represents a substantial increase in detection and localization ability, approximately equivalent to using conventional beamformer techniques with 10 times as many sensors spread over an aperture of the same size or larger. Even greater noise reductions have been demonstrated for coherent noise signals originating at locations other than the targeted look location, and the ability of the adaptive beamformer to reduce false-positive event detections by eliminating spurious transients and individual, problematic sensors in an elegant, natural way has been shown. Comparing the output of an adaptive and conventional beamformer can reveal whether or not an observed transient arrival is a true microseismic event arrival, as event waveforms originating from the targeted look location will appear in both the conventional and adaptive beamformer outputs, while spurious transients and false-positives will appear only in the conventional beamformer output. Furthermore, it has been shown that the advantage afforded by use of the adaptive beamformer can indeed reveal the presence of additional microseismic activity that would be buried in the noise-floor of a conventional beamformer's output. All of these demonstrated properties should result in the ability of the self-focusing adaptive beamformer to provide a more confident, detailed, and complete image of the fracture network induced by a hydraulic fracturing treatment.

Velocity Estimation

Once we have had experience with adaptive beamforming and had demonstrated its effectiveness with SNR improvement, we were ready to use it for detection of large and small seismic events and to localize them in 3- dimensions. Beam steering was essential for this, and in order to do beam steering, knowledge of seismic velocity was required.

We were able to estimate velocity by making use of the moveout delays of the large seismic event. The moveouts observed with sensor line 1 and sensor line 2 can be seen in Figure 5 and Figure 6, respectively. These moveouts are due to the various travel distances from the source of the large seismic event to the individual geophones of the surface arrays.

The relevant geometry for sensor line 1 can be seen in Figure 23. The moveouts for the high-energy event can be seen in Figure 24. In Figure 25, a circle is shown centered at the locus of the high-energy event and tangent to the surface. This is a circle of equi-distance from the locus of the high-energy event. The first arrival will occur at the geophone at the tangent point. Arrivals at the other geophones will be delayed relatively and the amount of delay time turns out to be proportional to the relative distance from the individual geophone to the equidistant circle.

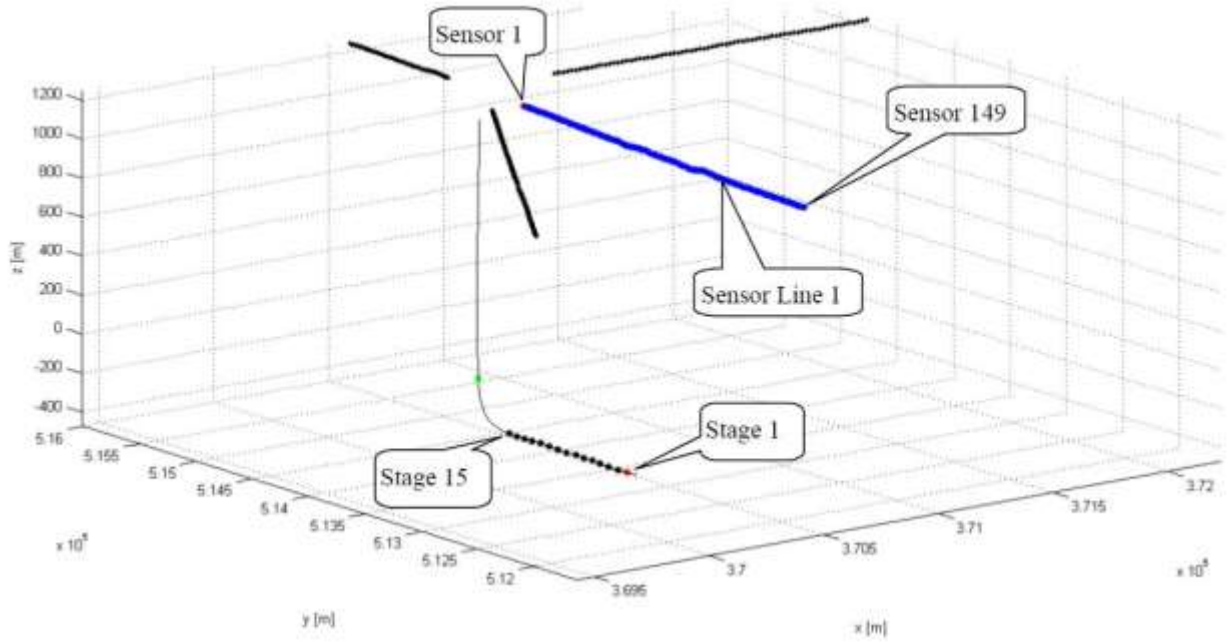

Figure 23: Surface seismic sensor arrays, sensor line 1.

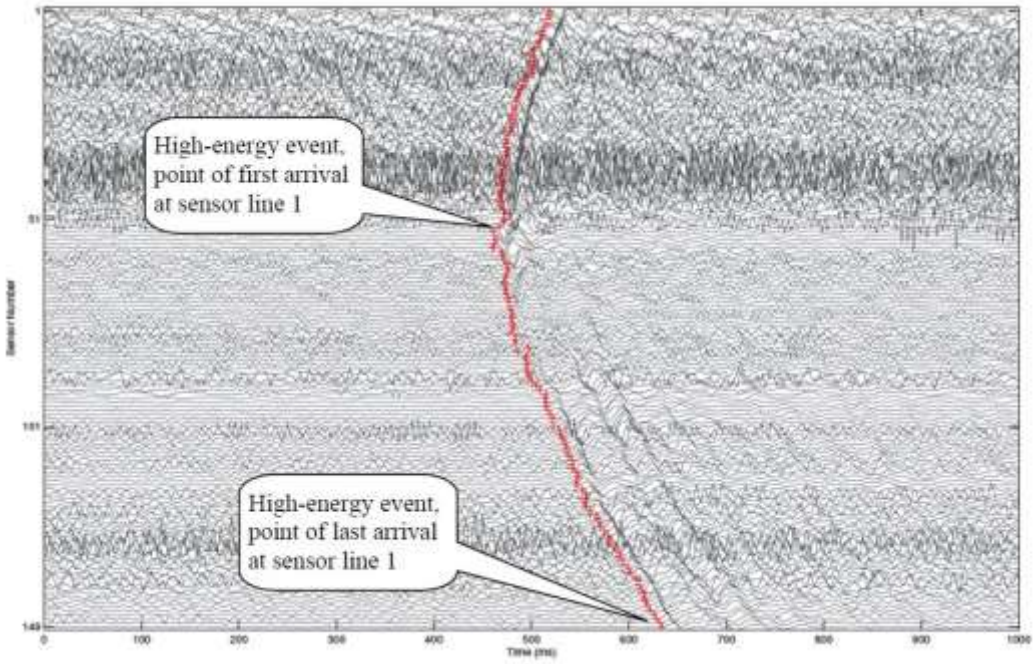

Figure 24: Moveouts of high-energy seismic event from Stage 1. The red line shows the first peaks of this event.

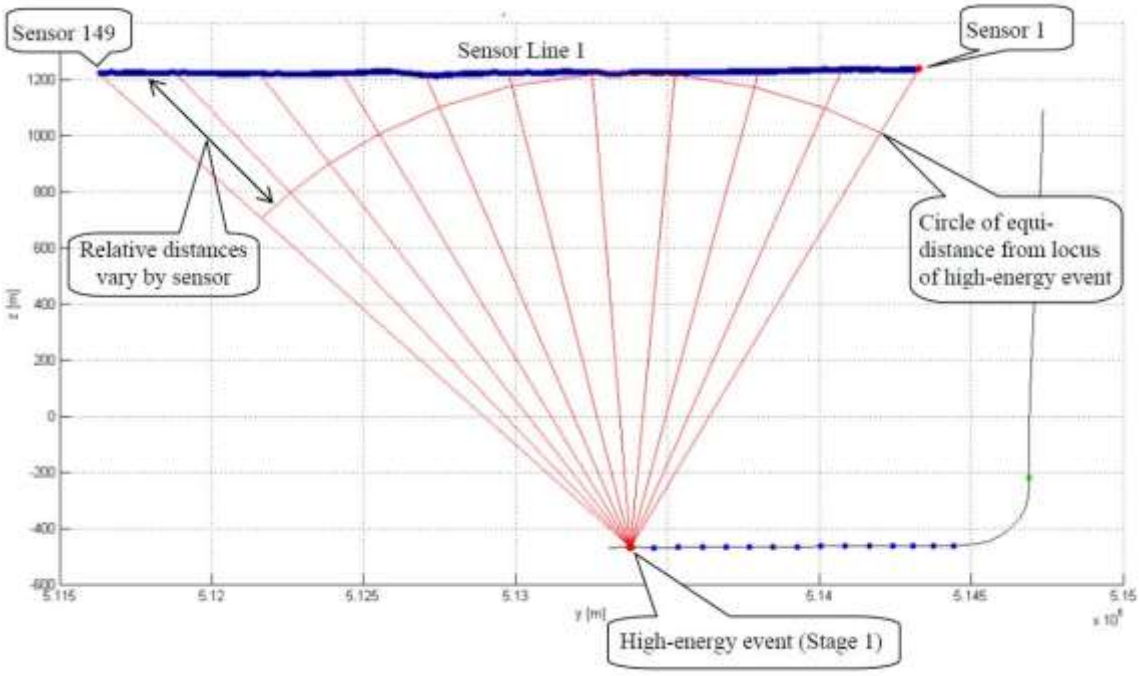

Figure 25: Geometry for calculation of relative distances from the locus of the high-energy event to the individual geophones.

Figure 26 is a plot of relative distance versus relative time delays of the moveouts of the 149 geophone channels of sensor line 1. The red straight line has been fitted by linear least squares regression to 149 points. The slope of the red line gives a velocity estimate of the 8714 m/s. Using this velocity measure, we were able to compute the changes in time delay to steer the beam by measured distances away from the locus of the high energy event, enabling one to search for events that may occurring near the locus of the high-energy event. In like manner, velocity was calculated using moveout data from sensor line 2. In Figure 27 a circle of equidistance from the locus of the high-energy event to the surface geophones of sensor line 2 is drawn. From the circle one can obtain the relative distances to the various geophones. These relative distances turn out to be proportional to the relative time delays of the moveouts. A plot of relative distance vs. relative time delay is shown in Figure 28. The slope of the regression line gives a velocity estimate.

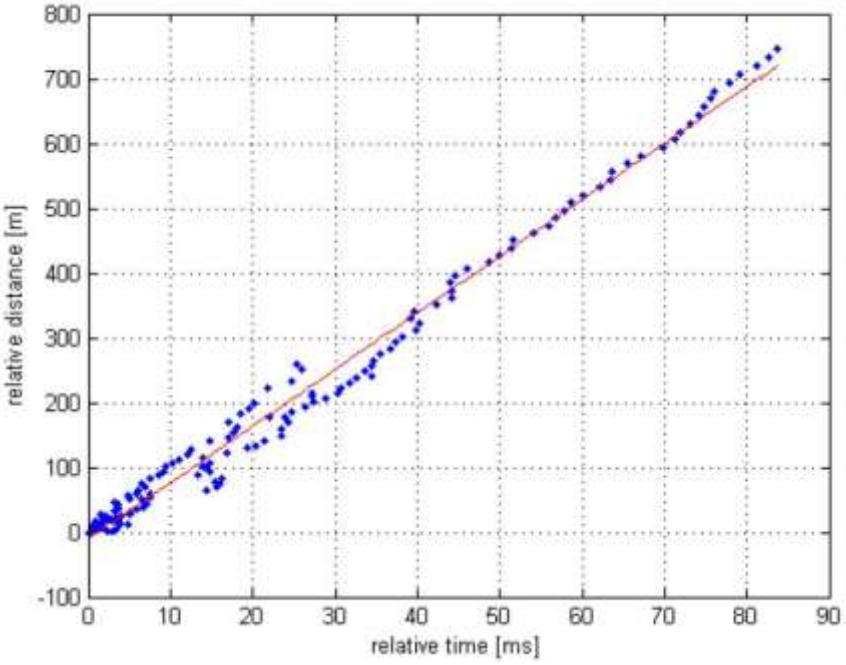

Figure 26: Relative distance versus relative time delays for the high-energy event observed by the 149 geophones of sensor line 1. The slope of the red regression line provides a velocity estimate.

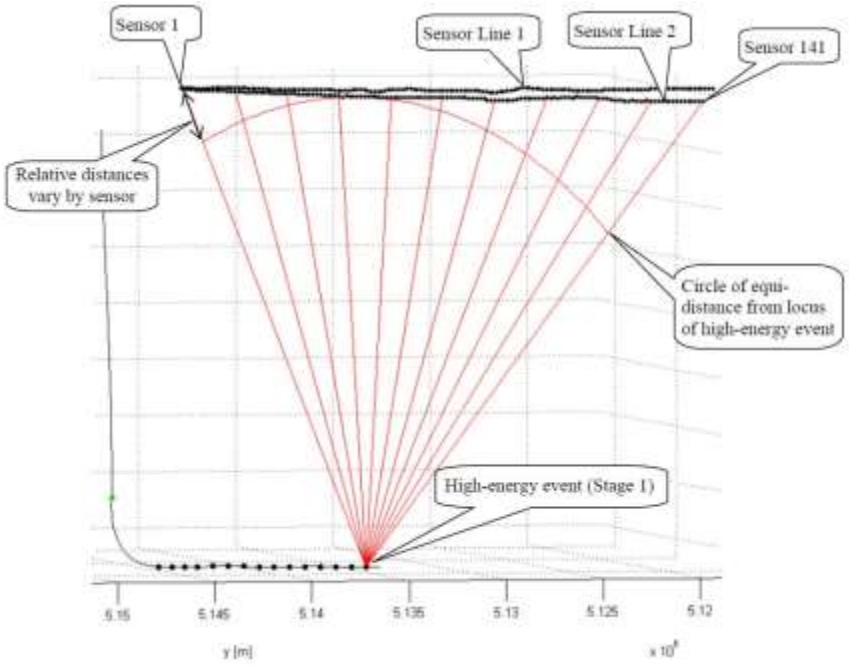

Figure 27: Geometry for calculation of relative distances from the locus of the high-energy event to the individual sensors of line 2.

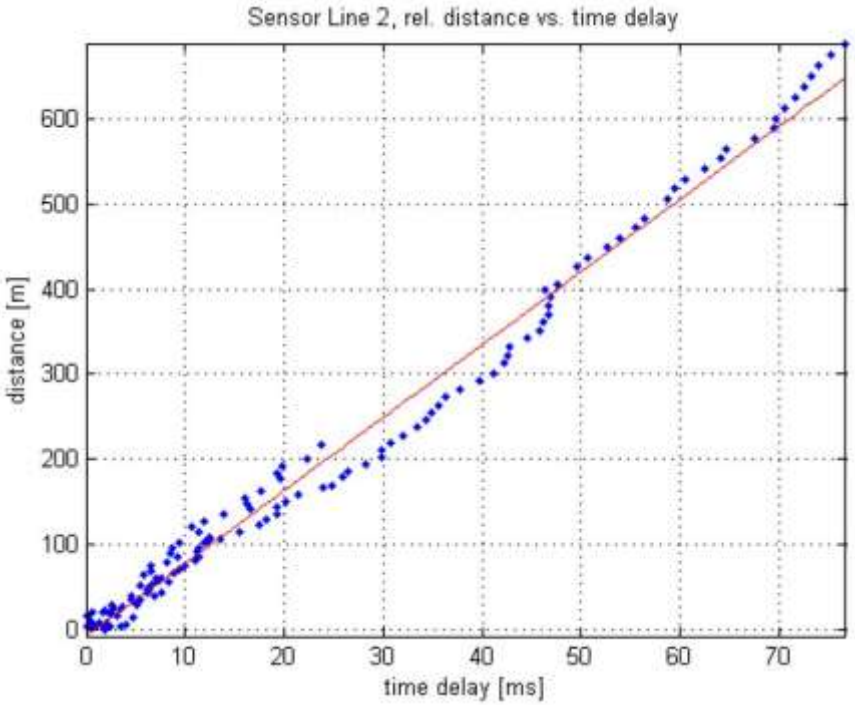

Figure 28: Relative distance versus relative time delays for the high-energy event observed by the 141 sensors of sensor line 2. The slope of the red regression line provides a velocity estimate.

The previous velocity estimate obtained from the moveouts of sensor line 1 was 4362.5 m/s. The velocity for sensor line 2 is estimated at 4282.0 m/s. The two velocity estimates differ by 1.85%. The difference is not really significant. These velocity estimates pertain to volumes of earth from near surface down to about 500 meters. They have been obtained from actual event moveouts instead of velocity logs and velocity profiles.

Beamsteering

The geophone signals from sensor line 1 were fed to the self-focusing adaptive beamformer. Focusing on the large-energy seismic event was accomplished by setting the steering delays to be the inverse of the moveout delays. The geophone signals were summed coherently by the beamformer and since they are aligned in time, maximum output of the large-energy event appeared at the beamformer output. By changing the steering delays, the beam can be deflected to focus on adjacent seismic sources. Small changes result in small deflections. Knowledge of velocity is essential in order to deflect the beam by specific distances.

Figure 29 shows in red selected ray paths (straight line approximations) from the locus of the high-energy event to the surface geophones. In blue are selected ray paths from a focal point

near the locus of the high energy event. The velocity estimate is used to calculate differential time delays between the red and the blue paths. The differential time delays supplement the delays previously used to focus the beamformer on the high energy event. Different distances in displacement away from the high-energy event correspond to various delay supplements. In this way the beam is able to be steered in measured distances away from the locus of the high energy event. Figure 30 is a close-up picture of the focal points.

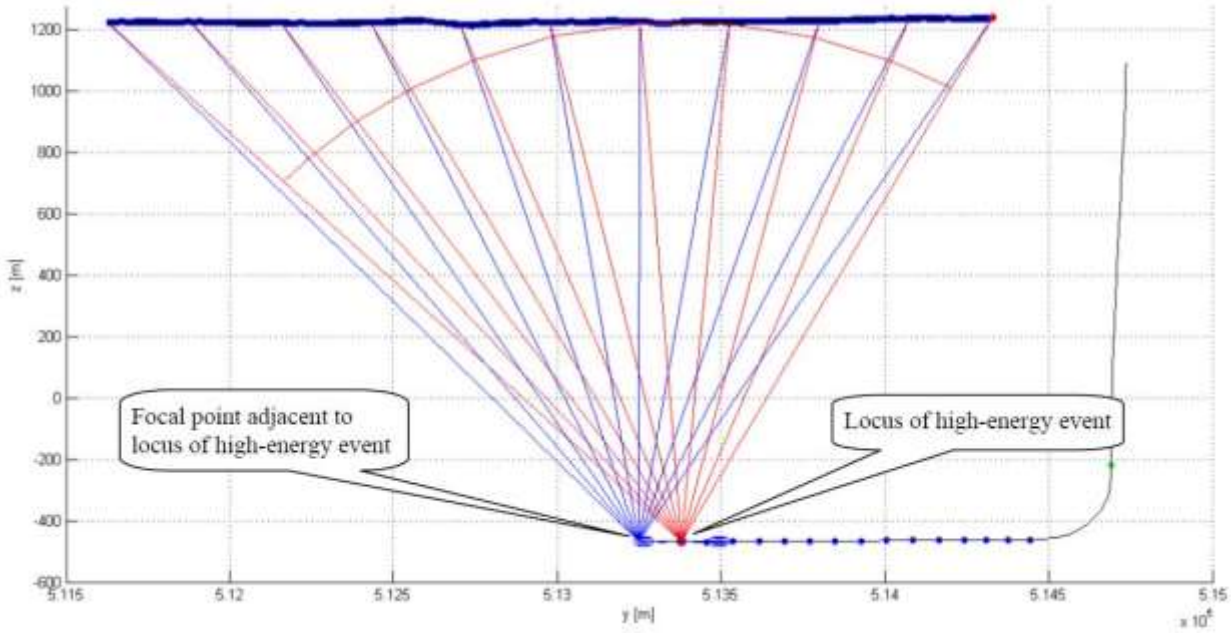

Figure 29: Red ray paths (straight line approximations) from the locus of the high-energy event (Stage 1) to the surface geophones (Sensor Line 1). Blue ray paths from a focal point near the locus of the high-energy event. Differential time delays can be calculated to steer the beam (either conventional time-delay-and-sum beamformer or adaptive beamformer) in measured distances away from the locus of the high-energy event.

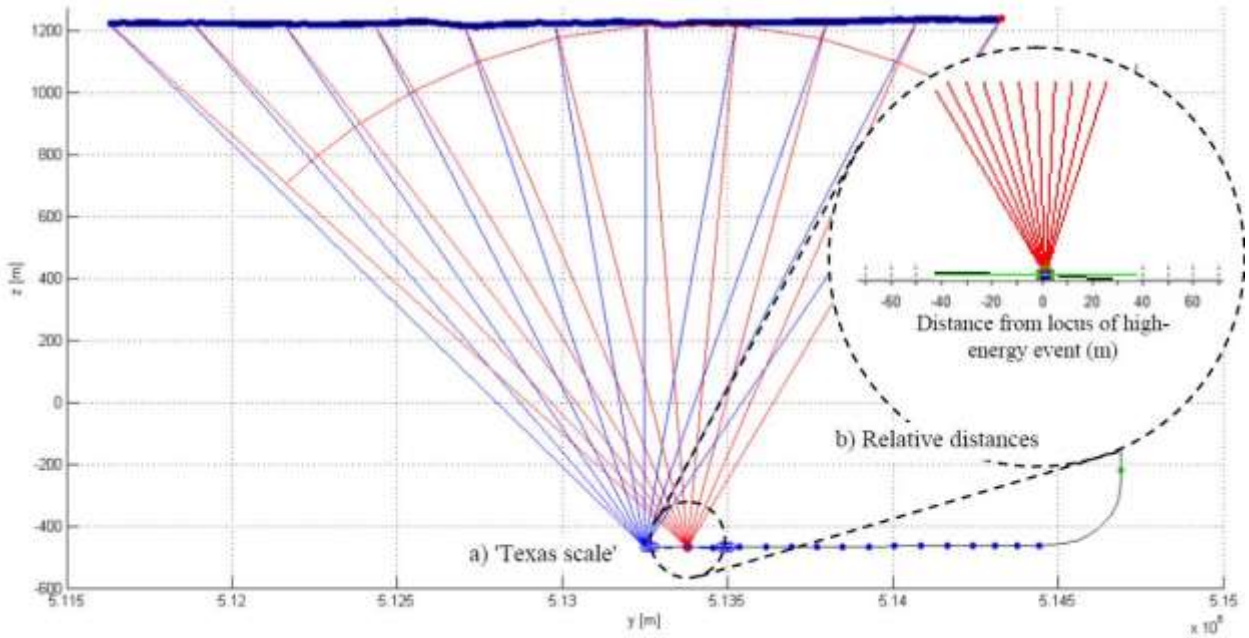

Figure 30: Scales of distance: relative distances from locus of high-energy event.

Figure 31 shows the effect of beamsteering with respect to the high-energy event. Maximum response is obtained by aiming the beam directly at the locus of the high-energy event. Aiming the beam in either direction away from this locus causes a reduction in the beamformer output. Figure 31 shows this effect for both the adaptive beamformer (in red) and for the conventional beamformer (in blue). Distances to the right are in the direction of the well's 'heel', while distances to the left are in the direction of the well's 'toe'. The amplitude measurements shown in the figure are maximum values of the first peak of the event. These peak values are very solid and not noisy, and they are plotted on an arbitrary linear scale. These curves show that both beamformers are able to resolve the position of a microseismic event to within +/-10 meters along the direction of the surface geophone array.

Figure 32 shows the effect of beamsteering with respect to the low-energy event. This event could not be detected without the adaptive beamformer. We had suspected that the low energy event was a 'fore shock' of the high-energy event and that both events emanated from the same volume of earth. We steered the beam of the adaptive beamformer at the locus of the high-energy event and then began to explore the vicinity of this locus. We were surprised to find that the maximum amplitude response was not obtained when the beam was aimed at the locus of the high-energy event, but the maximum was obtained when steering the beam +30 meters away in the direction of the well's heel. Although the amplitude of the low-energy event was much lower than that of the high-energy event, the adaptive beamformer measurements of the low-

energy event were quite solid and not noisy. The response curve shown in Figure 32 appears to be quite reliable and its peak is clearly +30 meters displaced from the locus of the high-energy event. Our conclusion is that the volume of earth where the low energy event took place is quite distinct from the volume of earth where the high-energy took place. The low energy event may or may not be regarded as a 'fore shock' of the high-energy event.

Figure 33 is a superposition of the adaptive beamsteering curves of the low-energy and high-energy events. These curves are plotted on a linear, normalized scale for comparison. The 30 meter relative displacement can be readily seen in this figure.

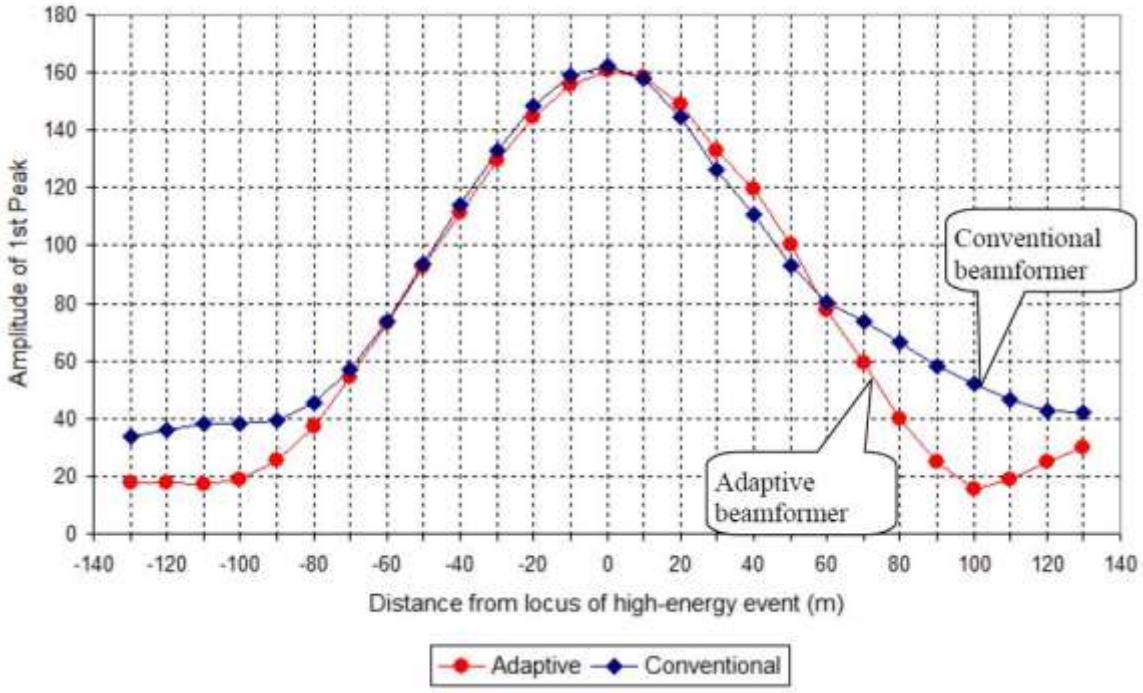

Figure 31: Beamsteering with respect to the high-energy event: output of adaptive versus conventional beamformer.

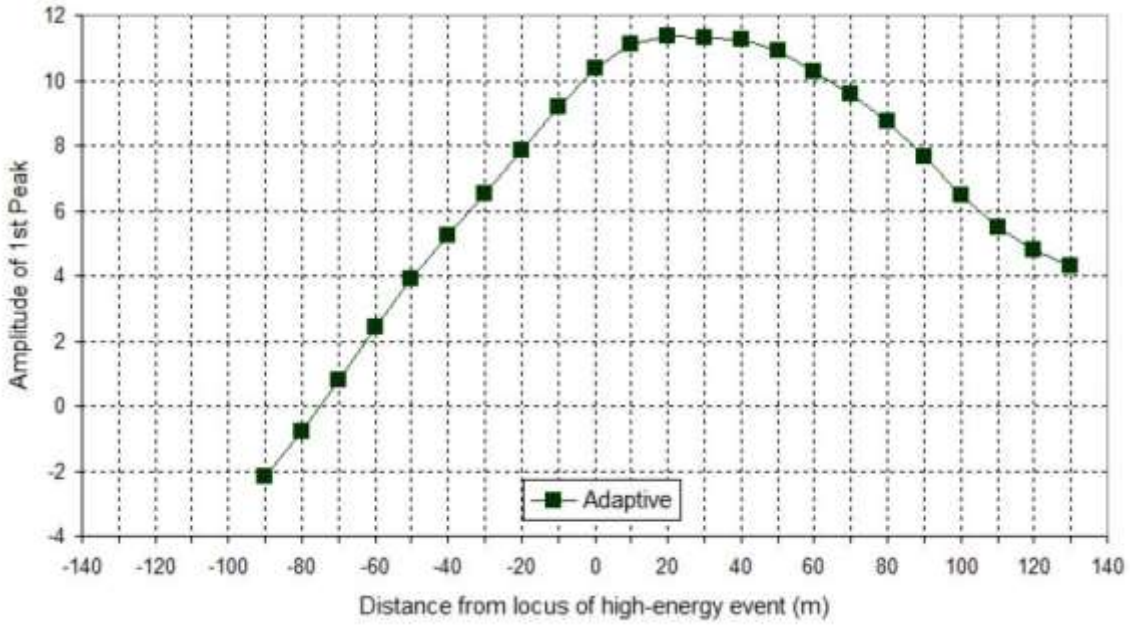

Figure 32: Beamsteering with respect to the low-energy event: output of adaptive beamformer.

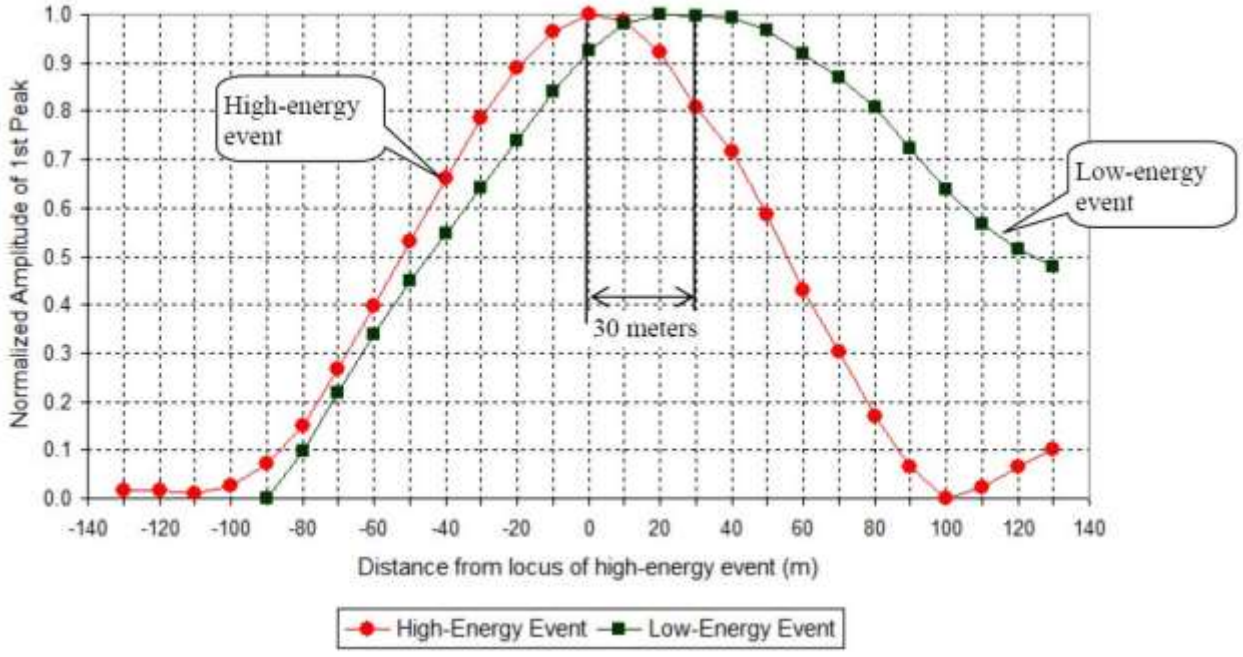

Figure 33: Comparison of beamsteering patterns (peak locations). Note the 30 meter displacement of the low-energy pattern

3-D Beamsteering

The beamsteering described in the previous section was done in 2-dimensions. The goal is beamsteering in 3-dimensions. To do this, we used signals from both sensor lines 1 and sensor line 2. The three dimensional localization cannot be done with a single line array of sensors. At least two such arrays are required. A 3-D coordinate system was established as illustrated in Figure 34. The Y' coordinates coincided with the line of perforations of the horizontal portion of the well, originating at the toe and aiming toward the heel. The X' coordinate was perpendicular to the Y' coordinate and both are in a horizontal plane. The Z' coordinate was perpendicular to the Y' and X' coordinates, and pointed vertically toward the surface. Given these definitions, an additional set of orthogonal coordinates was defined that are called the "event coordinates." They are X, Y, and Z parallel to X', Y', Z' respectively. The origin of the event coordinates is the 3-D locus of the large-energy event. The 3-D localization results reported here will be in the event coordinates.

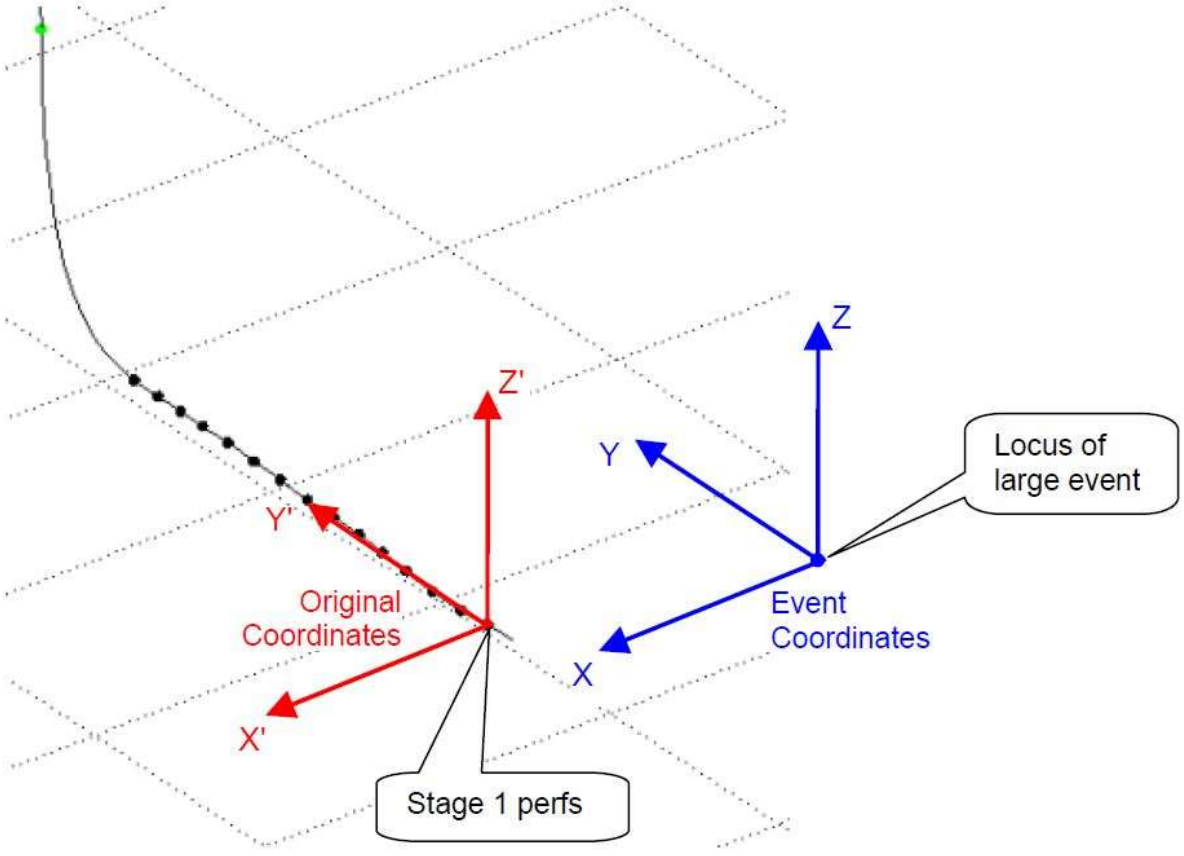

Figure 34: Original coordinate system and event coordinate system.

We did 3-D localization of seismic events using signals from sensor line 1 and sensor line 2. Ideally, one would combine these signals and treat this as a single array, being not a simple straight line array. Because we were not sure about the simultaneousness of the recording time bases, we chose to steer beams from the two sensor lines separately and add their processed outputs rather than coherently add their signal outputs directly. The resulting signal processing was both simple and effective. Figure 35 illustrates beamforming from two sensor lines simultaneously, comprising 3-dimensional beamforming with signals from two independent surface arrays. The basic idea is to process the signals from the two sensor lines independently and combine their outputs into a single output that is to be maximized when focusing on the location of a seismic event in 3-dimensional space. We begin by choosing a trial point in 3-dimensional space and adding the signal outputs of both sensor lines focused at that point. Then we increment the position of this point along the Y-axis in a series of steps and at each displacement of focus noting the sum of the array output signals. Plots of these signal sums versus displacement are shown below.

The objective is to find the Y-position that gives the largest signal sum. An interpolated curve is differentiated to find the peak. Once this is done for the Y-coordinate, a corresponding search is made to find the peak along the X-axis. Once that is done, a peak is found along the Z-axis. Once that is done, the search is resumed along the Y-axis, then again along the X-axis, then again along the Z-axis. This relaxation process is continued until improvements in the summed signal amplitude become negligible, and the relaxation process has converged. This generally requires 3 or 4 complete cycles.

The search for the maximum summed output was in each case done at first with coarse increments, to “get in the ball park” of the maximum. Then the search was switched to fine increments to hone in on the maximum. This was done for both the large and small events. The small event was 14 dB smaller than the large event. Table 1 gives the increments that were used for the coarse and fine searches for both the large and small events. In finding maxima, 4th degree polynomial interpolation was used for the coarse increments, while 8th degree polynomial interpolation was used for the fine increments.

The process began with establishing the 3-D location of the large-energy event. The delays of the beamformers of sensor line 1 and sensor line 2 are set in accord with the moveouts of these arrays for the large energy event. This steers the 3-D event at the source of the large-energy event, as a starting point. Subsequent fine tuning of the delays of both sensor lines produced somewhat higher beamformer outputs and yielded a more precise localization of the high-energy event. The following was the procedure:

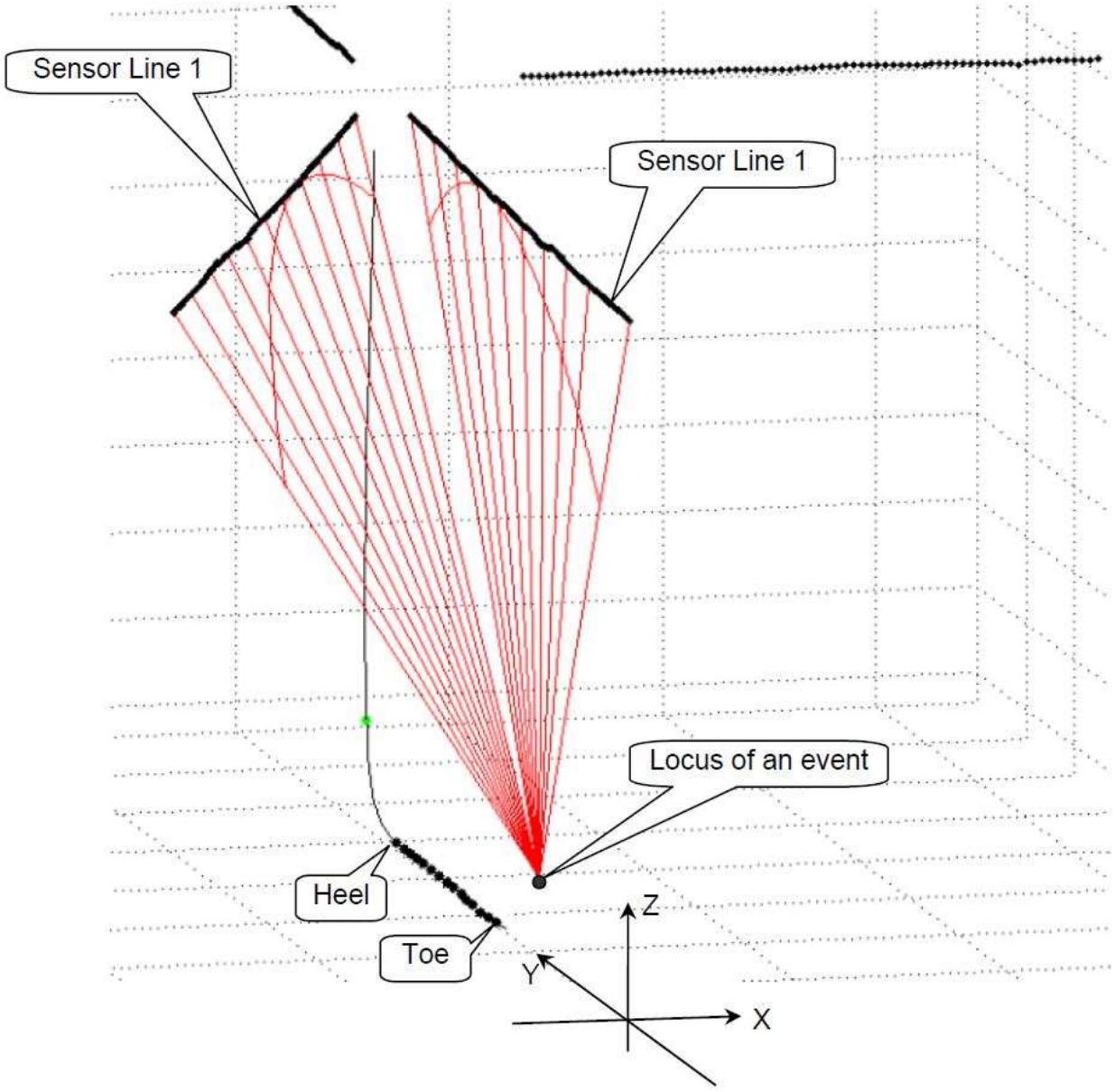

Figure 35: 3-dimensional beamforming.

Table 1: Beamsteering Increments

Axis	Coarse Resolution [meter]	Fine Resolution [meter]
X	20	5

Y	5	2
Z	10	4

Figure 36 is a plot of summed output versus focusing displacement along the Y-axis for the large event, with coarse increments. All displacements are measured relative to the location in 3 dimensions of the large event.

The plot shows the maximum (marked by an x) to be at about -3 meters along. The position of 0 was set to correspond to the moveouts of the large event as seen on sensor lines 1 and 2. The adaptive beamformer found a maximum slightly different from this along the Y-axis, hence the maximum at -3 meters. The maxima along the X and Z-axes for the large event were also slightly different from 0. The plots showing the coarse search along Y, X, and Z-axes are shown in Figure 36, Figure 37, and Figure 38, respectively.

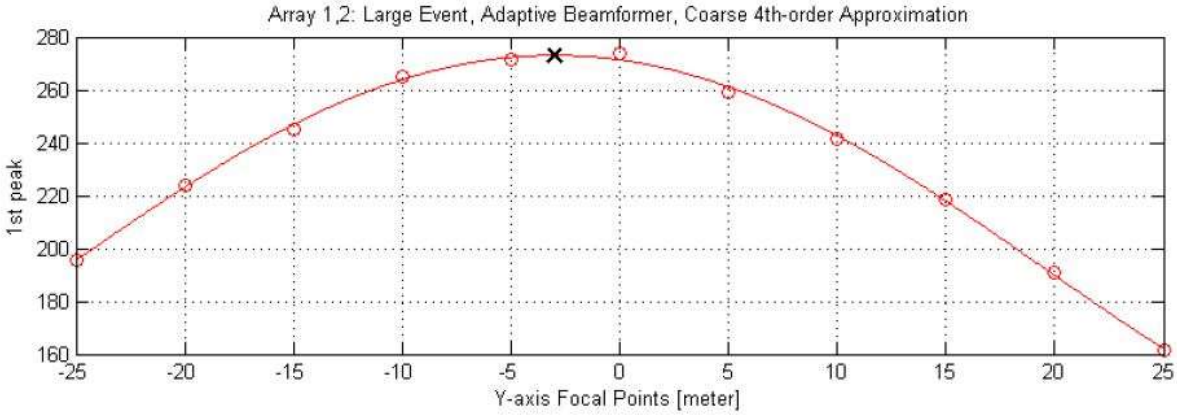

Figure 36: Coarse search for large event, Y-axis, with 4-th order interpolation.

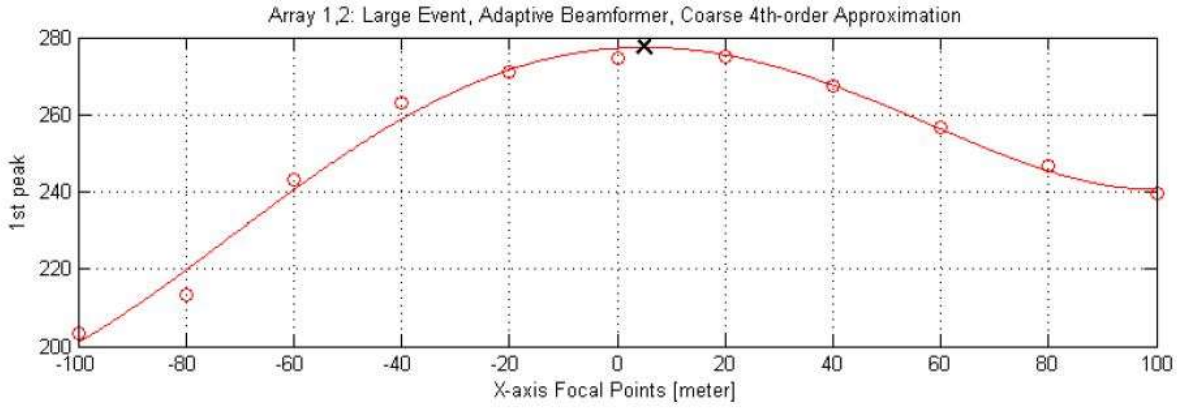

Figure 37: Coarse search for large event, X-axis, with 4-th order interpolation.

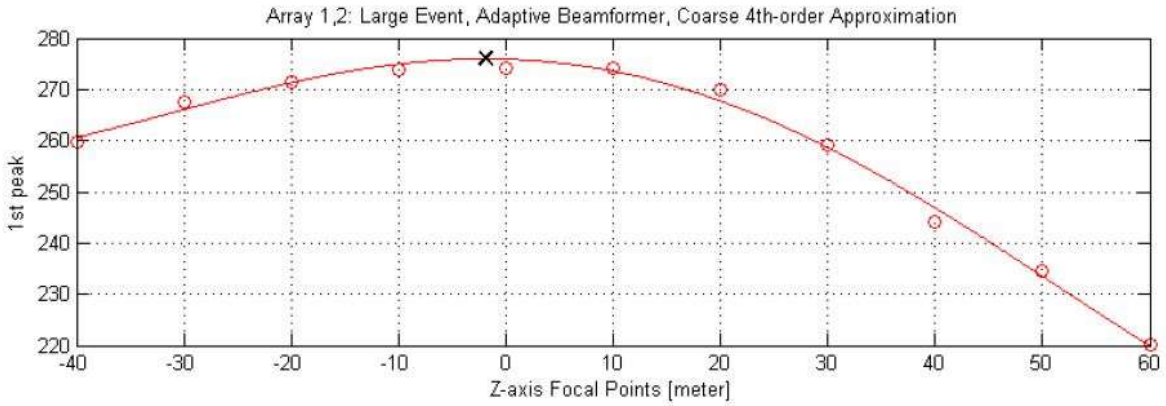

Figure 38: Coarse search for large event, Z-axis, with 4-th order interpolation.

After the coarse search, the fine search was done yielding more precise results. Figure 39, Figure 40, and Figure 41 are plots showing the fine search for the large event, which is located close to 0 along all three coordinates, as would be expected.

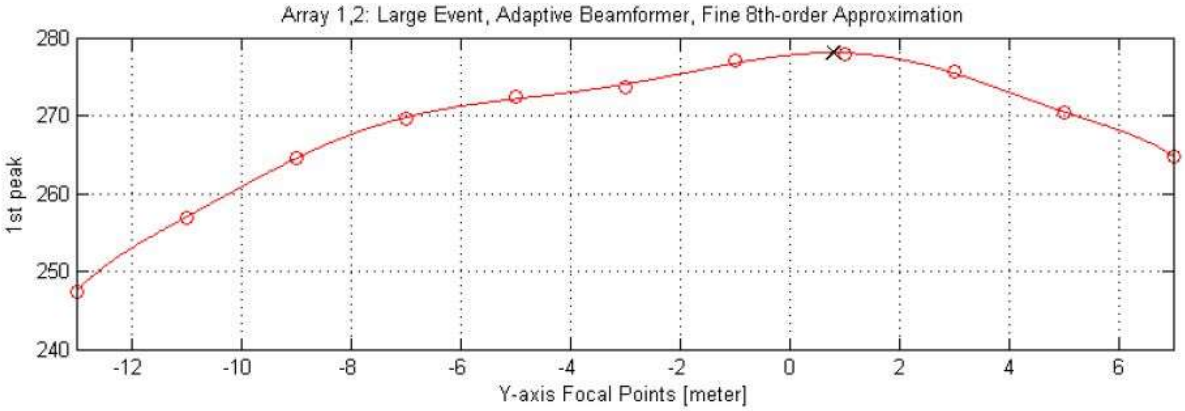

Figure 39: Fine search for large event, Y-axis, with 8-th order interpolation.

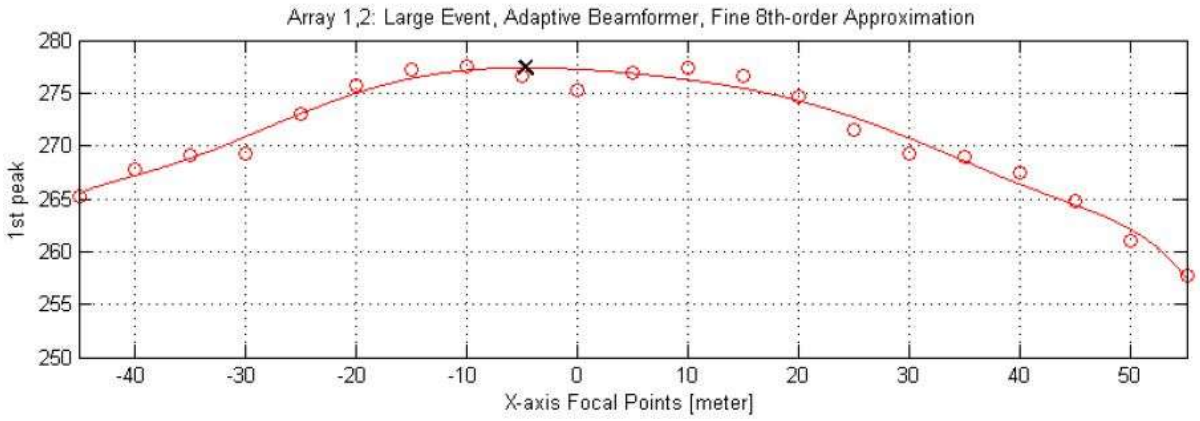

Figure 40: Fine search for large event, X-axis, with 8-th order interpolation.

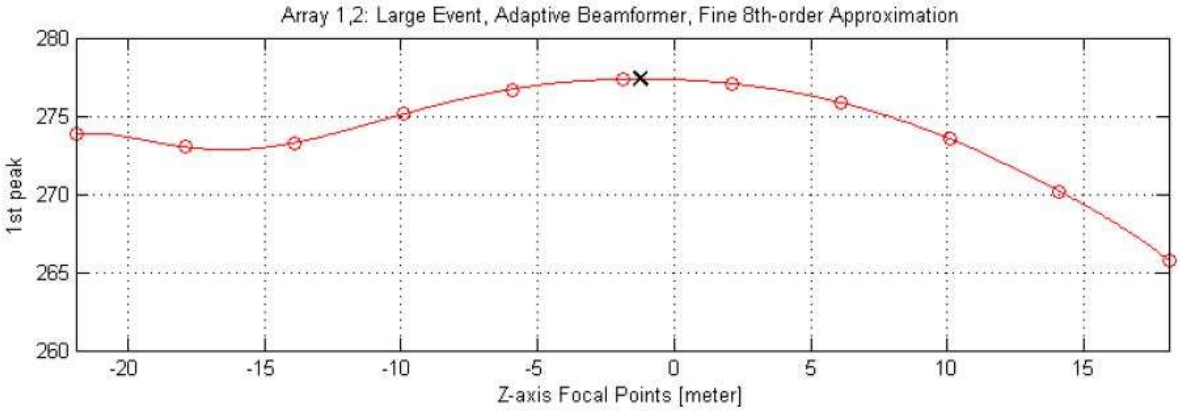

Figure 41: Fine search for large event, Z-axis, with 8-th order interpolation.

The same methods were used for the search for the small event. Figure 42, Figure 43, and Figure 44 show the coarse search along the Y, X, and Z-axes for the small event.

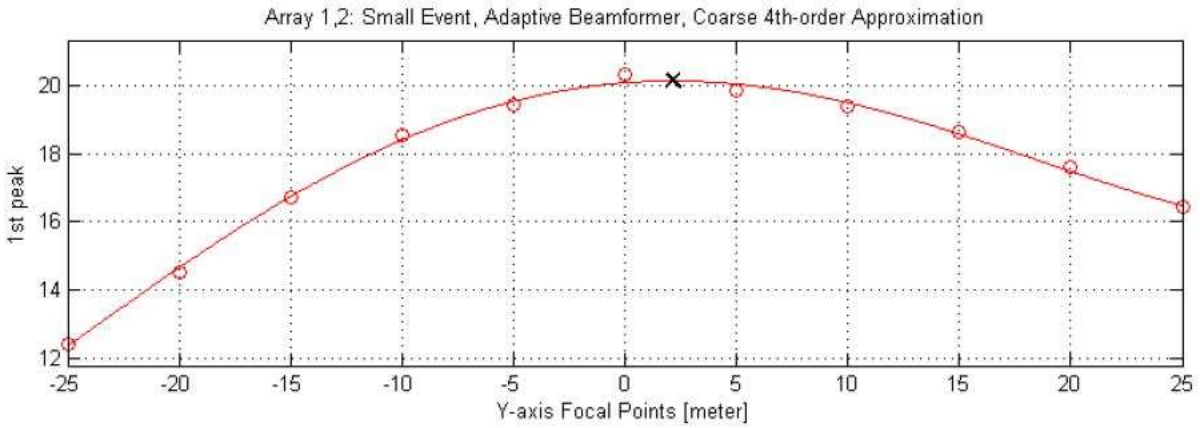

Figure 42: Coarse search for small event, Y-axis, with 4-th order interpolation.

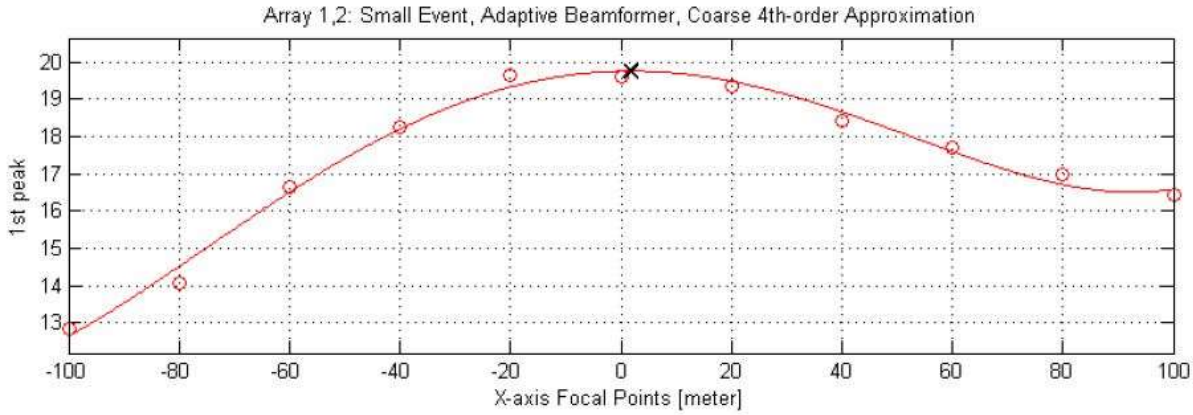

Figure 43: Coarse search for small event, X-axis, with 4-th order interpolation.

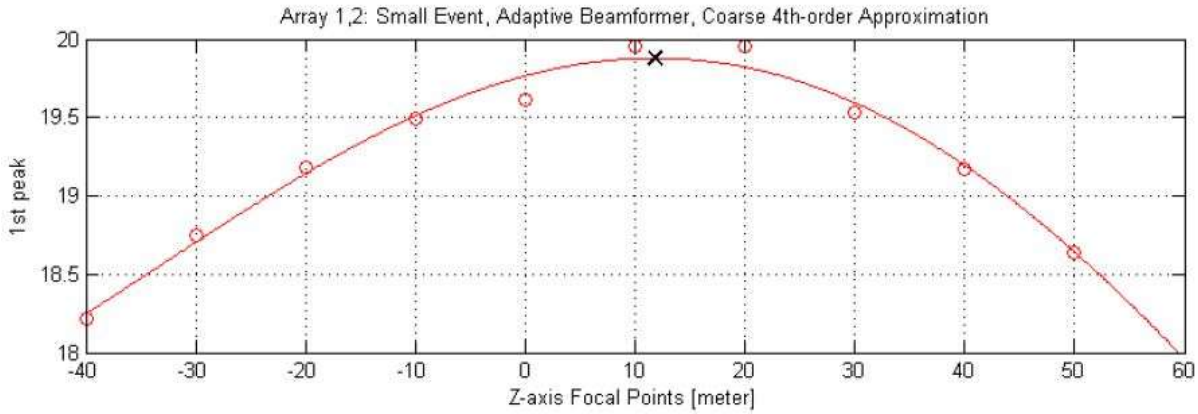

Figure 44: Coarse search for small event, Z-axis, with 4-th order interpolation.

After the coarse search was completed, the fine search began. Figure 45, Figure 46, and Figure 47 show the fine search along the Y, X, and Z axes.

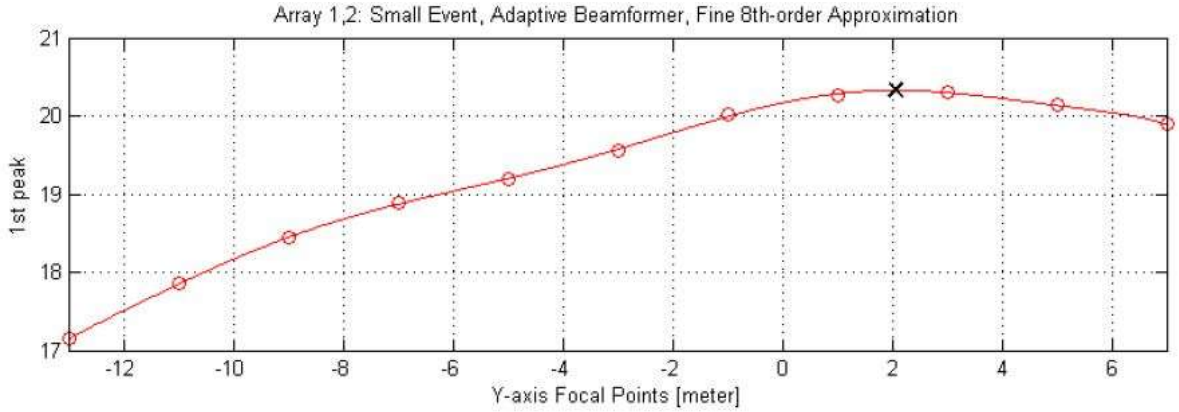

Figure 45: Fine search for small event, Y-axis, with 8-th order interpolation.

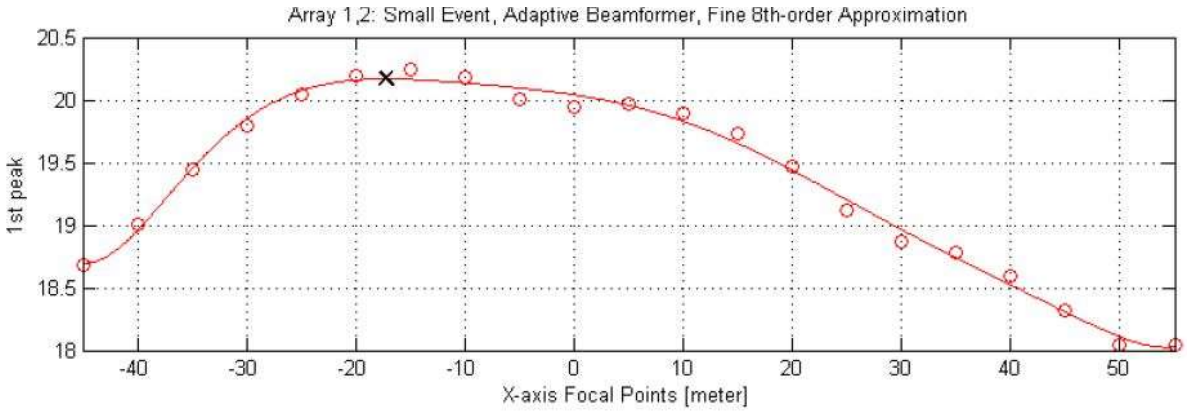

Figure 46: Fine search for small event, X-axis, with 8-th order interpolation.

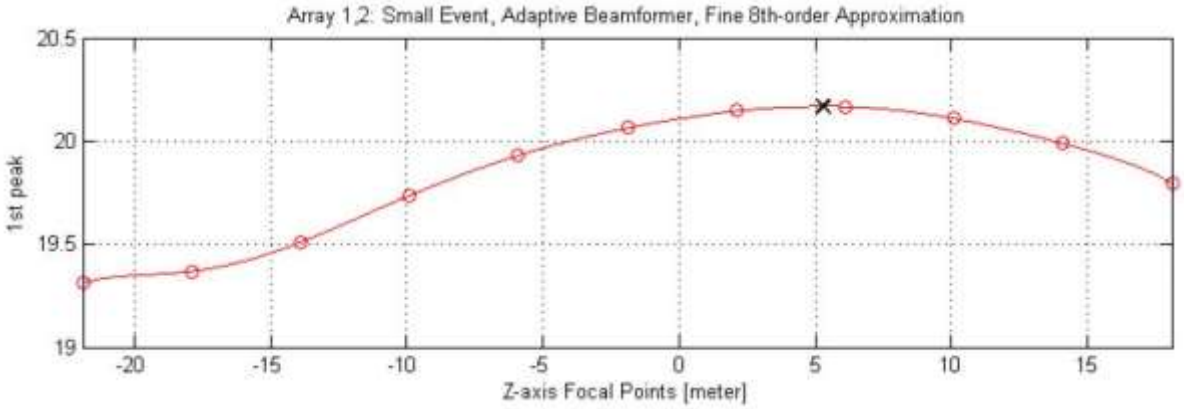

Figure 47: Fine search for small event, Z-axis, with 8-th order interpolation.

Inspection of the above figures reveals that these curves are not parabolic and that the noise level is low. The 8th order interpolation gives curves that well represent the data points, and the peak value of the curves gives maxima that are in good accord with "eyeball" estimates of the location of the maxima. The results of the study are presented in Table 2.

Table 2: Locus of Events [meters]

Axis	Large Event	Small Event	Difference
X	-4.7	-17.2	-12.5
Y	0.8	2.1	1.3
Z	-1.2	2.9	4.1

Referring to Figure 7, the direction of the fracture should be roughly in the direction of the X-axis. Note from Table 2 that the largest difference is -12.5 meters along the X-axis between the two events. The difference is small along the Y-axis since the two events, occurring closely in time, are in the same fracture plane. The small event is shallower by 4.1 meters.

Detection and Localization of Additional Small-Energy Events

The fracture having the high-energy event and the low-energy event as described above had other seismic events during the total pumping period of approximately 1.8 hours. These additional events were relatively small in amplitude compared to the high-energy event and were able to be detected only using the adaptive beamformer. These additional events were localized in 3-dimensional space bringing the total number of localized events to 5. This is too small a number of events to delineate a fracture, nevertheless the results are quite interesting.

The seismic data was recorded in files that were 30 seconds long. The files were numbered consecutively. Most files contained no detectable seismic events. The five files that did have events had only one event per file. Accordingly, we labeled each event with the number of the file in which it occurred. The above described large event is now designated as 470, and the above described small event is now designated 468. Figure 48 shows these two events and their respective file times. Figure 21 shows the times of occurrence and relative amplitude of all 5 detected events.

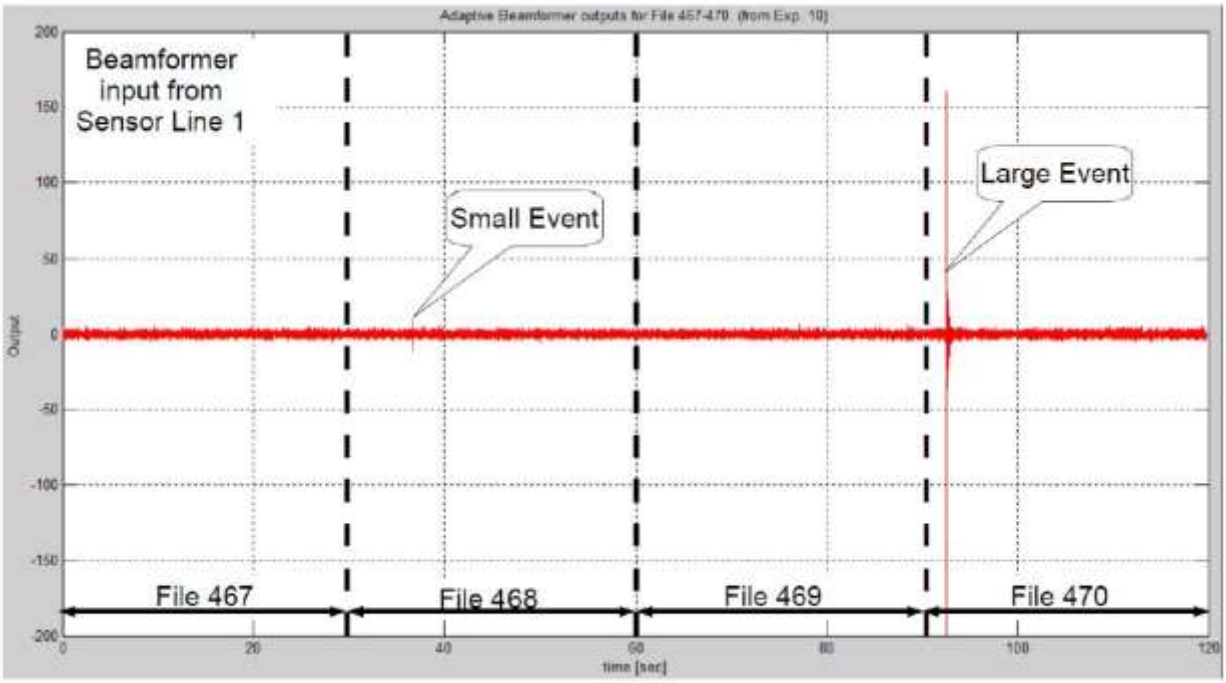

Figure 48: The high-energy (large) event 470 and the low-energy (small) event 468.

The three additional events are 441, 489, and 519. No events were detected for the first 1.1 hours of pumping. All five events occurred between 1.1 and 1.8 hours of pumping. Figure 22, Figure 23, and Figure 24 show the output signals from the adaptive beamformer from sensor line 1 and 2 when events 441, 489, and 519 were detected. These signals were obtained with the beamformer focused on large event 470. Although the adaptive beamformer was not focused on events 441, 489, and 519, they are still able to be detected on both sensor lines 1 and 2.

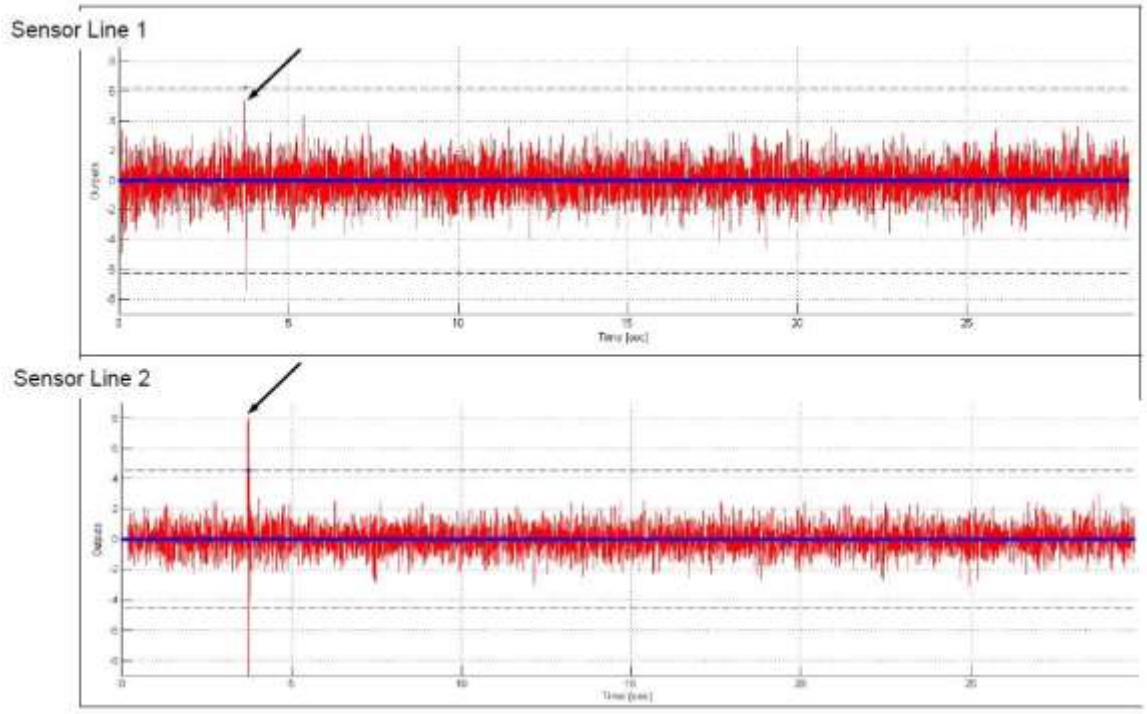

Figure 49: Detection of event 441 with adaptive beamformer focused on large event 470.

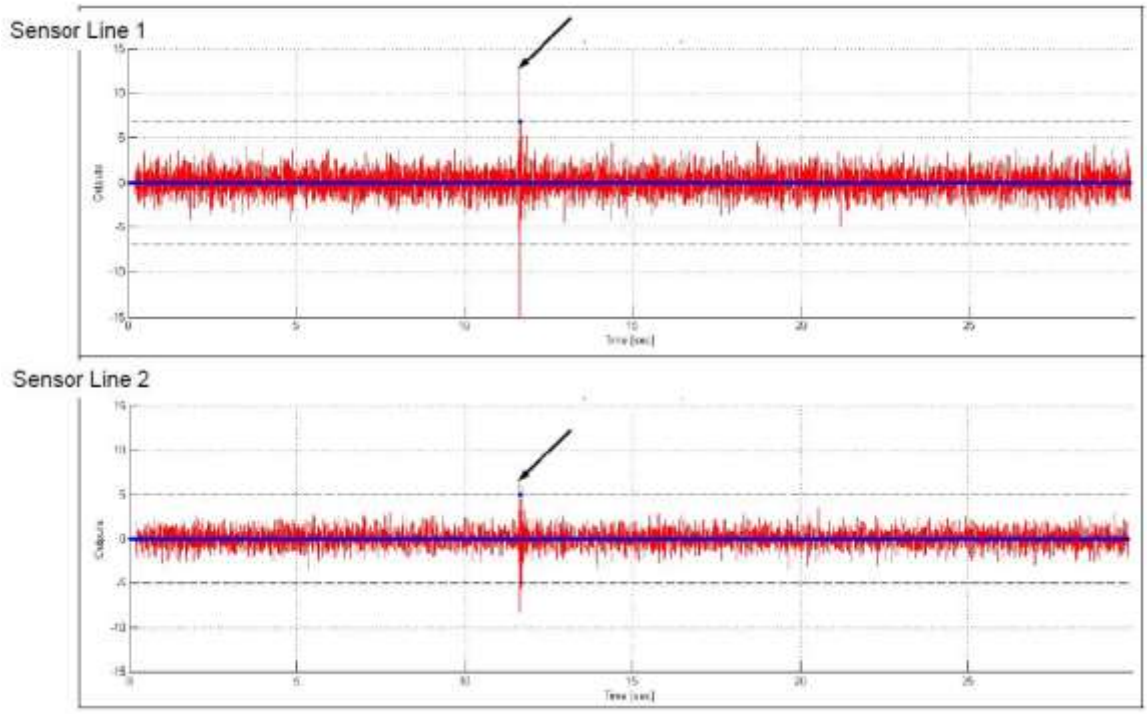

Figure 50: Detection of event 489 with adaptive beamformer focused on large event 470.

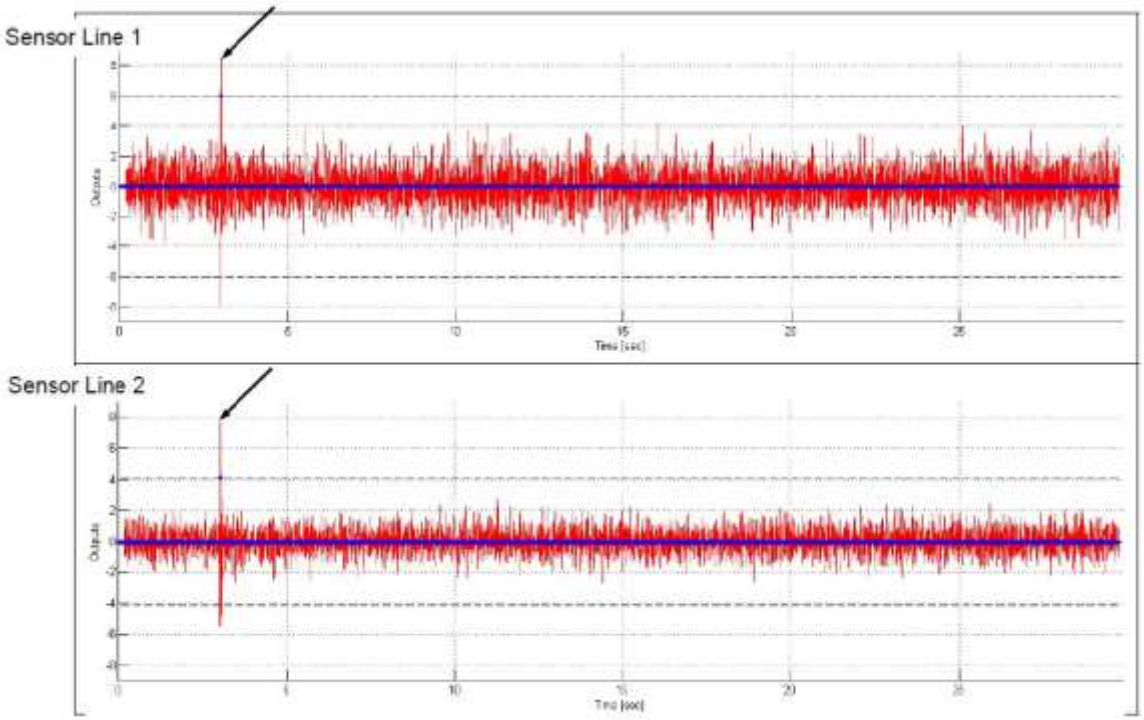

Figure 51: Detection of event 519 with adaptive beamformer focused on large event 470.

Using the above method for localizing the points of origin of events 441, 489, and 519, and adding the resulting information to the previously obtained localizations of large event 470 and small event 468, the following table of events was constructed in chronological order. The chronology and amplitudes of the events are given in Figure 52(a). The 3-D localization data for the 5 events is given in the table of Figure 52(b).

(a)

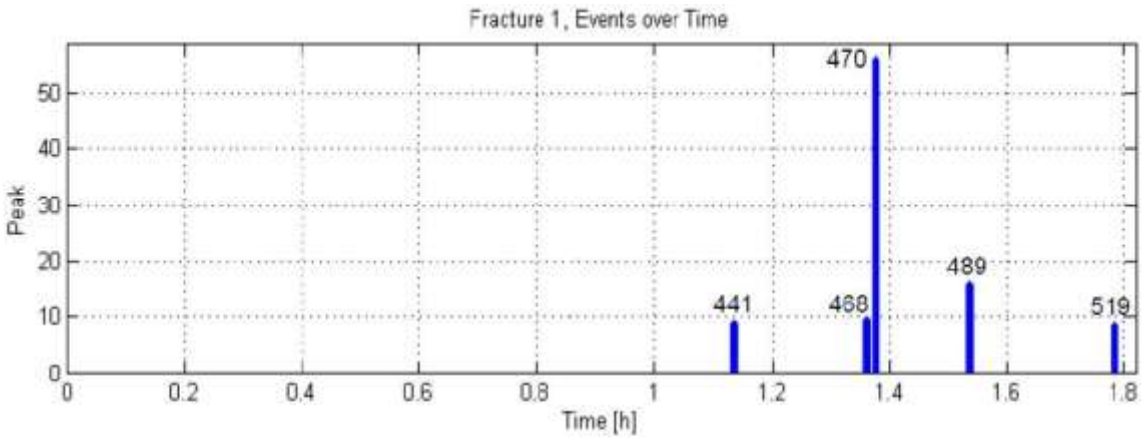

(b)

Location	Event by File No.				
[m]	441	468	470	489	519
X	-72.0	-64.0	-0.8	186.3	1.5
Y	-8.1	14.3	-1.6	36.2	-33.7
Z	31.7	8.9	12.4	3.9	32.6

Figure 52: (a) Timing of events 441, 468, 470, 489, and 519. (b) Table of event localization in 3-D.

A plot of the location of the five events projected onto the 2-dimensional horizontal X/Y plane is shown in Figure 53. The Y-axis is the direction of the well from the toe to the heel. The events occurred roughly along a line parallel to the X-axis, roughly perpendicular to the direction of the well. The depths of the various events are given by the numbers in green.

This is a map view of the points on the fracture. The Y-axis points north. The X-axis points east. The Z-axis points straight up and gives depth information.

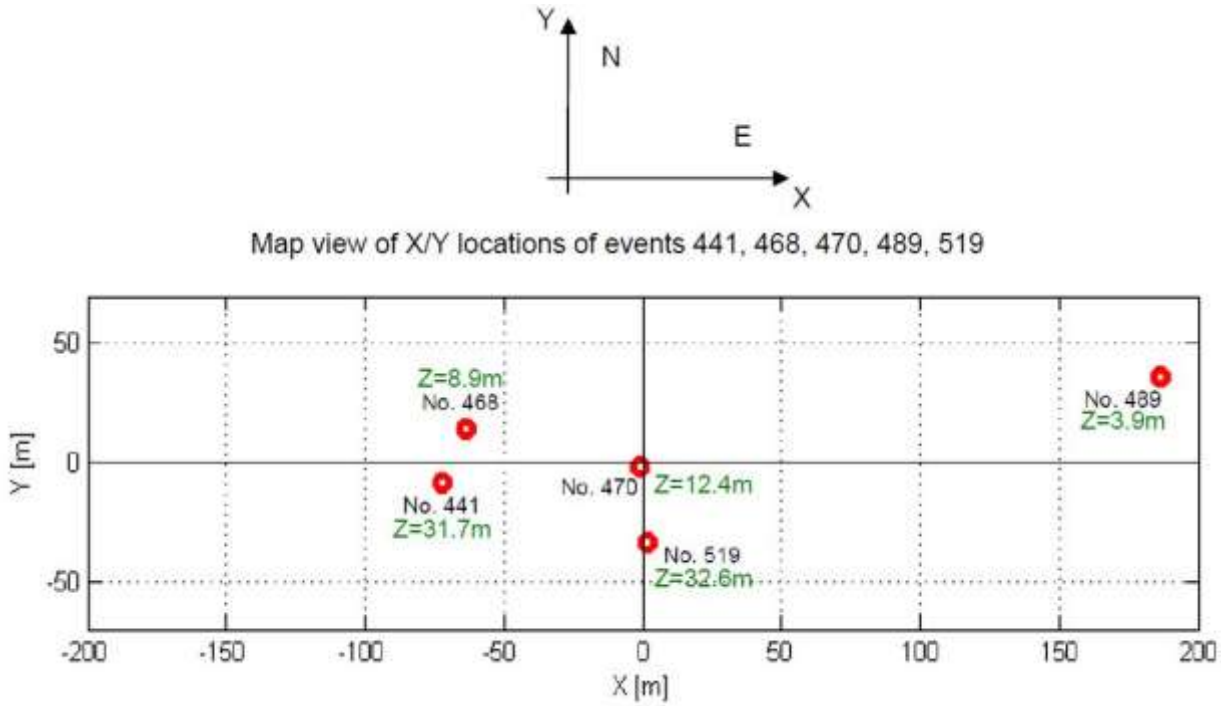

Figure 53: The locations of events 441, 468, 470, 489, 519 projected onto a horizontal X/Y plane. The direction of the well from toe to heel is parallel to the Y-axis. The horizontal line is parallel to the X-axis. The span of the fracture from wing tip to wing tip is about 255 meters, and the range of depths of the events is about 29 meters.

Analysis of the Fracture

With only 5 points, one cannot properly map the fracture and be able to identify which points belong to one wing and which other points belong to the other wing. Making an educated guess, we would say that event 489 belongs to one wing, and the remaining four points belong to the other wing. The total span of the fracture from wing tip to wing tip is about 255 meters, and the depths, from minimum to maximum vary over a range of about 29 meters.

Combining information from Figure 52 and Figure 53, we can speculate about what happened, about the sequence of events. After more than an hour of pumping, event 441 occurred. Next, event 468 occurred. Event 468 is a neighbor to event 441. Event 468 was deeper than 441 by 22.89 meters. Next, event 470 occurred. After that by about 24 minutes, its neighbor event 519 occurred. Event 470 is deeper than event 519 by 20.2 meters. It seems that detectable seismic activity began further out from the perforations than the seismic activity closer to the perforations. In both neighborhoods, the seismic activity began at shallower depths and then with more pumping went deeper, down about 20 meters or so. Event 489 on the opposite

wing of the fracture occurred all by itself fairly late in the pumping, after about 1.5 hours. There may have been many more seismic events that occurred throughout the pumping, but they were too small for us to detect with the adaptive beamformer with a first look.

From events 468 and its neighbor 441, and from event 470 and its neighbor 519, we conclude that the western wing of the fracture was not vertical, but at about 48 degrees from the vertical with the bottom of the fracture to the north east of the top of the fracture. The general direction of the fracture runs from south east to northwest at roughly 45 degrees from the east-west axis.

Array Design

The thirteen arrays with 1000 geophones were not optimally placed for fracture mapping. Only sensor line 1 and sensor line 2 with 290 geophones total were used to do the fracture mapping. The placement of these two arrays was good enough, but a better placement would have been possible. Figure 54 shows a much better placement.

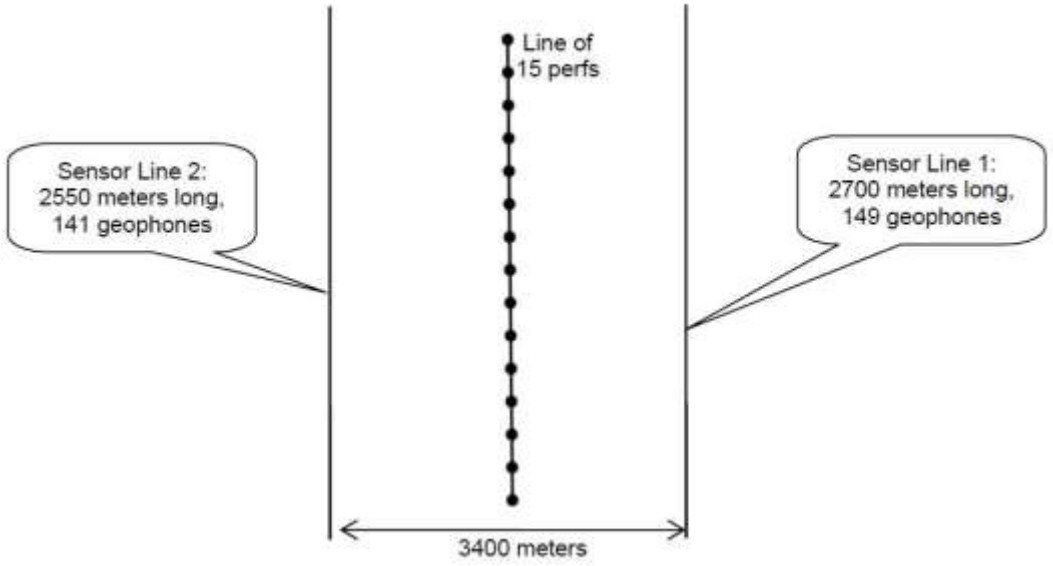

Figure 54: A good array configuration for 3-D fracture mapping.

With given property boundaries, the configuration of Figure 54 may not be possible. Fortunately, the array design is not critical and many other configurations would work. The better the design, however, the sharper will be the spatial resolution of the fracture map.

Conclusion

The objective of this project has been to develop algorithms for improved methods of fracture mapping in 3- D using microseismic signals. To this end, we have done the following:

a) Developed a method for localizing points of origin of microseismic events. Starting with a large event on which to focus a given seismic array, the array's beam is then scanned incrementally to detect smaller events and to localize them relative to the locus of the large event. With enough neighboring seismic-event loci, it is possible to delineate the geometry of the fracture. The seismic velocity needed for beamsteering is obtained from the original moveouts of the large event.
b) Developed a self-focusing adaptive beamformer that can focus on a selected large event and can be scanned incrementally from it to detect and localize other seismic events, some of which could be so small that they would not be detected by any other means. Experience with a given fracture showed an improvement in SNR of about 10 dB when using the adaptive beamformer. This greatly enhances the accuracy of localization, reduces the required number of geophones, and allows a many fold increase in the number of seismic events that could be available for fracture mapping.
c) From 5 detected and localized points, simple mapping was done with a single fracture.

Developed Matlab code for implementing the self-focusing adaptive beamformer and the various operations for localizing microseismic events. This is experimental code and is not yet of commercial grade.

Appendix E: Advanced Microseismic Source Characterization Schemes

Status of Objectives

The original objectives of this study were to correlate event magnitude with pumping parameters, to differentiate between opening mode and shear mode microseismic signals, to develop acquisition methodologies to identify, characterize, and mitigate noise associated with the hydraulic fracturing process, and to correlate production data with fracturing parameters to aid in optimal fracture designs. The scope of this research project was ultimately guided by the quality of data, and as a result, the objectives were updated. One of the updated objectives came out of necessity.

Given the large amount of data, it was necessary to design software that enabled interactive visualization and analysis of the information. This was accomplished by creating a microseismic analysis toolkit in the form of multiple, linked Graphical User Interfaces. With this microseismic analysis toolkit, most of the objectives were met.

For example, event magnitude has been correlated, not with pumping parameters directly, but with calculated event bandwidth. Additionally, through the use of spectral analysis, a sense of shear or compressional energies has been realized.

Through the use of a location-based noise characterization and reduction schema, a significant source of noise has been identified, characterized, and mitigated. While production data was not directly used to improve on fracture design, through the use of head wave analysis, an improvement can be made on monitoring geometry. As a result, with the same traditional monitoring geometry, simply adjusting spacing and the number of downhole geophones may enable a more robust understanding of the main waveforms being produced.

Introduction

In an effort to improve the capabilities of microseismic monitoring with a conventional monitoring geometry, an investigation into microseismic source mechanism and microseismic event location was performed. In order to achieve these objectives, analysis was performed on two major fronts. First, analysis in the spectral domain through interactive analysis was performed in order to better understand microseismic source mechanism through the use of software designed in Matlab. Second, the headwave was incorporated in the modeling and location estimation of microseismic events.

Head Wave Analysis

Summary

We show that the location of microseismic events can be significantly improved by incorporating information on head wave arrival time. The traditional method of using direct arrival times and P-wave polarizations leads to increased error due to the large uncertainty in polarization. We integrated head wave arrival time to P- and S-wave arrival time to achieve better resolution in microseismic event location. To this end, we developed a Bayesian inference framework for joint event location and velocity model

calibration. The developed method was applied for both microseismic event as well as perforation shot location in a project in Marcellus shale. Comparison with location results provided by contractor shows that the developed method can effectively improve the accuracy of microseismic event location. Based on the improvement, we propose a new acquisition geometry and strategy to reduce microseismic monitoring cost and improve event location accuracy.

Introduction

Microseismic processing involves basic location, moment magnitude estimation, and advanced source parameter and frequency analysis (Cipolla et al., 2012; Eisner et al., 2007; Maxwell, 2009, 2014; Warpinski, 2009). The event location, as the basis of almost all other advanced processing, has been routinely conducted by industry. For horizontal wells in shale gas production, it is a common case to have only one nearby well available for microseismic monitoring. Due to the limited azimuthal coverage of acquisition geometry in single horizontal monitor well, microseismic event location with only P- and S-wave arrival time is impossible. An additional constraint on the event location usually comes from direct P-wave polarization (Dreger et al., 1998; Li et al., 2014). However, the unknown orientation of downhole geophones and poor coupling (Gaiser et al., 1988) between geophone and borehole are the challenges to use three component data. These problems, as well as the complexity and anisotropy of shale formation, make the uncertainty in the P-wave polarization significantly large.

Due to shale's low velocity nature, head wave is very common in crosswell seismic (Dong and Toksöz, 1995; Parra et al., 2002; Parra et al., 2006) and microseismic survey (Maxwell, 2010; Zimmer, 2010; Zimmer, 2011) in shale operation. When the distance between geophones and source is relatively large, the head wave arrival can precede direct arrival. Microseismic industry has realized the presence of head wave before direct arrival. Because of its weakness, head wave has been commonly regarded as the contamination of direct arrival. Some preliminary research on making use of head wave has been conducted but mainly on synthetic example of simplified situations (Zimmer, 2010; Zimmer, 2011).

As an inverse problem, the microseismic event location in downhole monitoring can be carried out in various ways. Commonly used methods include least-square travel time inversion (Douglas, 1967; Li et al., 2014), double-difference (Waldhauser and Ellsworth, 2000), coherence scanning (Drew et al., 2005; Duncan and Eisner, 2010), full-waveform inversion. Through effective to a certain extent, these methods don't follow a rigorous statistical framework. The Bayesian inversion (Tarantola, 2005; Tarantola and Valette, 1982) has been used for earthquake (Myers et al., 2007; Myers et al., 2009) as well as microseismic event location (Poliannikov et al., 2014). It has been shown to be an effective tool for joint inversion and uncertainty analysis. However, further work is needed to make full use of this method.

We applied the Bayesian inversion for microseismic event location as well as velocity model calibration. Our event location result on microseismic survey conducted on a single horizontal monitor well in Marcellus shale shows that head wave conveys very useful information. Thus, it can be used to eliminate the requirement for P-wave polarization to improve microseismic event location accuracy.

Theory and Method

Head wave

Head wave is common in microseismic survey in shale (Maxwell, 2010; Zimmer, 2010; Zimmer, 2011). The existence of head wave in Marcellus shale can be shown by the simple yet common configuration in Figure 1. When the angle of incidence equals the critical angle, $\arcsin(V_1/V_2)$, there will be head wave that travels along the interface at the speed of the high velocity layer.

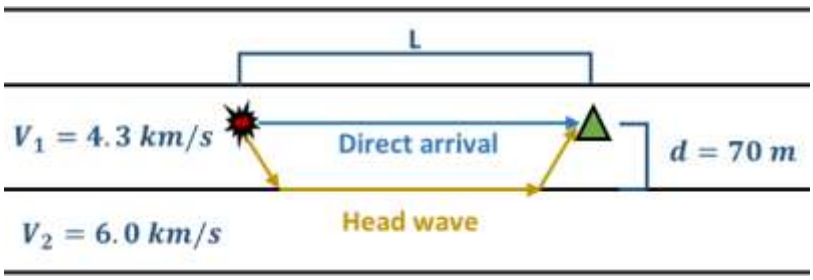

Figure 1: A common configuration for head wave in shale gas operation. Due to the low velocity nature of shale, headwave is common when there is a nearby high velocity layer.

Head wave amplitude decays to be inversely proportional to the square of travel distance while body wave amplitude decays to be inversely proportional to the distance. As such, head wave amplitude is usually low, thus difficult to be identified when it appears after the high amplitude direct arrival. However, as its name implies, head wave is typically faster and arrives ahead of other waves. Figure 2 shows that the head wave can take over direct arrival to be the first arrival after the cross-over distance.

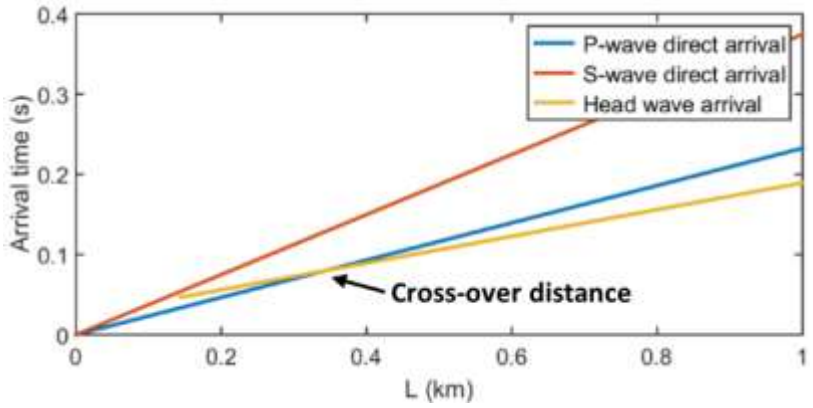

Figure 2: Arrival time of various phases as a function of source receiver distance. When source receiver distance is larger than the cross-over distance, head wave can overtake direct arrival to be the first arrival.

Due to its low amplitude, head wave has been regarded as the contamination of direct arrival, especially when it arrives before direct P arrival. However, our study shows that head wave is actually a valuable source of information that should be not dismissed since its travel path covers a larger area than the direct arrival path.

Bayesian inversion for microseismic event location

To estimate the microseismic event location within a rigorous statistical framework, we applied the Bayesian inversion for microseismic event location. From inverse problem theory (Tarantola, 2005; Tarantola and Valette, 1982), we can demonstrate that under Gaussian assumption, the a posteriori information of the model can be given by:

$$\sigma_{\mathbf{M}}(\mathbf{m}) \propto \exp\left\{-\frac{1}{2}\left[(\mathbf{g}(\mathbf{m})-\mathbf{d}_{\mathbf{obs}})^{T}\mathbf{C}_{\mathbf{D}}^{-1}(\mathbf{g}(\mathbf{m})-\mathbf{d}_{\mathbf{obs}})\right.\right. \quad (1)$$
$$\left.\left.+\left(\mathbf{m}-\mathbf{m}_{\mathbf{prior}}\right)^{T}\mathbf{C}_{\mathbf{m}}^{-1}\left(\mathbf{m}-\mathbf{m}_{\mathbf{prior}}\right)\right]\right\}$$

Here $\mathbf{d}_{\mathbf{obs}}$ is a vector containing the observed data. In the problem of microseismic event location, it can be an array of arrival times of all identifiable phases, and the polarization information if desired. The data covariance matrix $\mathbf{C}_{\mathbf{D}} = \mathbf{C}_{\mathbf{d}} + \mathbf{C}_{\mathbf{T}}$ is the sum of the observation part $\mathbf{C}_{\mathbf{d}}$ and model part $\mathbf{C}_{\mathbf{T}}$. The model parameter vector $\mathbf{m}$, and its prior information $\mathbf{m}_{\mathbf{prior}}$ contain the spatial coordinate and origin time of microseismic events. The parameters describing velocity model can also be a part of the model parameter if we want to do a joint inversion of event locations and velocity model. $\mathbf{C}_{\mathbf{m}}$ is the parameter covariance matrix of the prior information. The forward operator $\mathbf{g}(\mathbf{m})$ is a function of the model parameters $\mathbf{m}$ and will give a prediction on the observable data $\mathbf{d}$ based on the model parameters. We use a ray tracing method as the forward operator to predict the arrival time based on event location and origin time.

The solution to the posterior probability density function (PDF) of model parameter can be challenging (Oliver et al., 2008; Tarantola, 2005). Here, we adopted a Maximum-A-Posteriori (MAP) estimation (Oliver et al., 2008; Zhang et al., 2014) to characterize the posterior PDF of microseismic event location and origin time. The MAP estimation method tries to find the peak of the posterior PDF and regards the model at this point as the most likely case given the prior information and observation. This can be accomplished by minimizing the exponent of the posteriori probability density with a Gauss-Newton method (Zhang et al., 2014).

Microseismic Survey Overview

The hydraulic fracturing was performed in the Marcellus formation in Susquehanna County, Pennsylvania, within Susquehanna River Basin. Two horizontal wells were drilled as shown by Figure 3. The length of the horizontal portion of the monitor and stimulation well are 1.35 and 1.7 km respectively. Average distance between the horizontal portions of the two wells is around 0.22 km.

Eighteen hydraulic fracturing stages were conducted with four perforation shots prior to each stimulation stage (Figure 4). Microseismic monitoring was carried out with an array of eleven three-component geophones. The geophone spacing in the array is approximately 15 m. The array was moved according to the location of hydraulic fracturing stages to minimize the noise due to source receiver distance. The contractor-estimated locations of microseismic events are also shown on Figure 3.

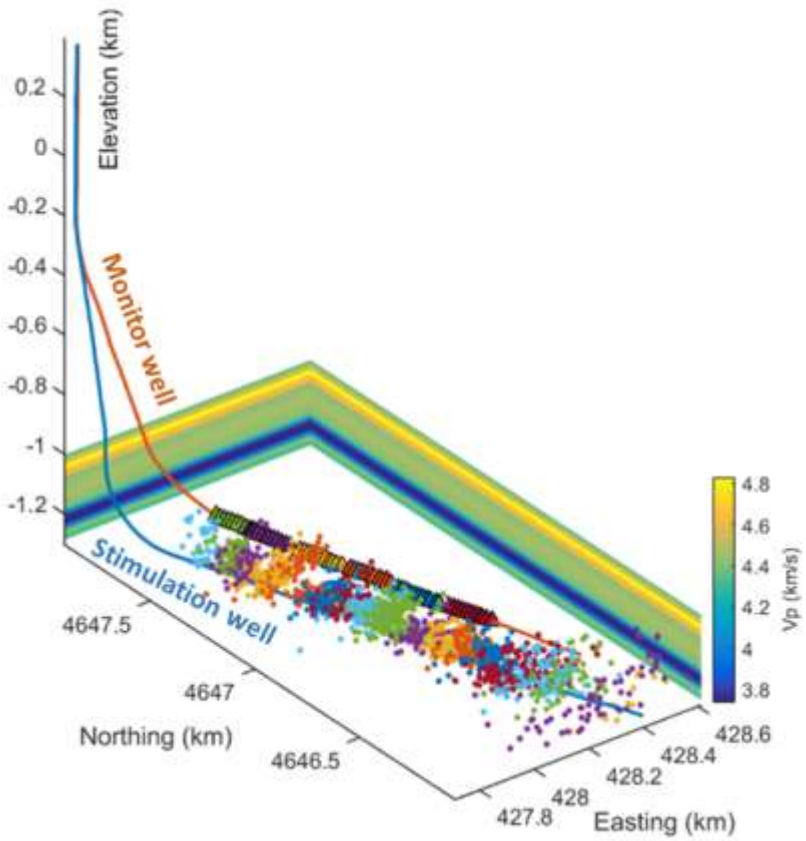

Figure 3: Microseismic survey geometry. The microseismic event location (dots) were processed by contractor. The geophone array is colored according to their locations. Microseismic events are colored according to their associated stimulation stages.

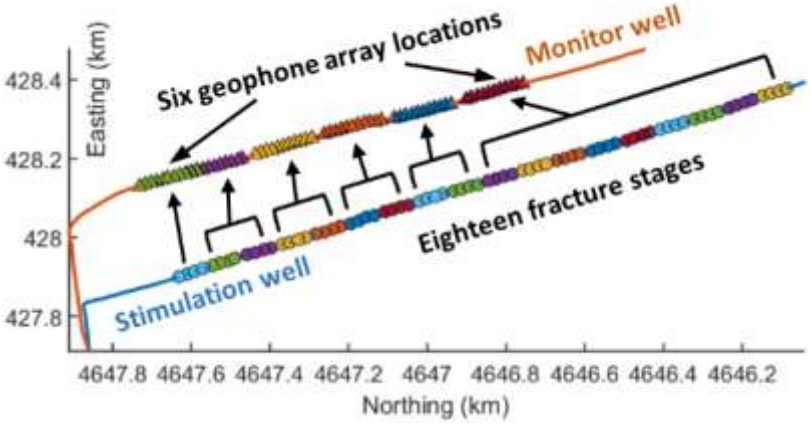

Figure 4: The stimulation was performed in 18 stages and the microseismic signal was recorded by an array of 11 geophones in the nearby monitoring well. The geophone array was moved according to the stimulation stage location to reduce the error due to large observation distance.

In addition to these microseismic events, most of the perforation shots were recorded by the geophone array and can be used for velocity model calibration and location uncertainty analysis.

Observation of Head Wave

Head wave is commonly observed in waveforms of both perforation shots and microseismic events, especially those in the early fracking stages given their relatively large distance from the monitoring geophone array. Figure 5 is a typical set of waveforms and moveout recorded by the geophone array. We can easily identify the head wave arrival based on its low amplitude and high velocity moveout.

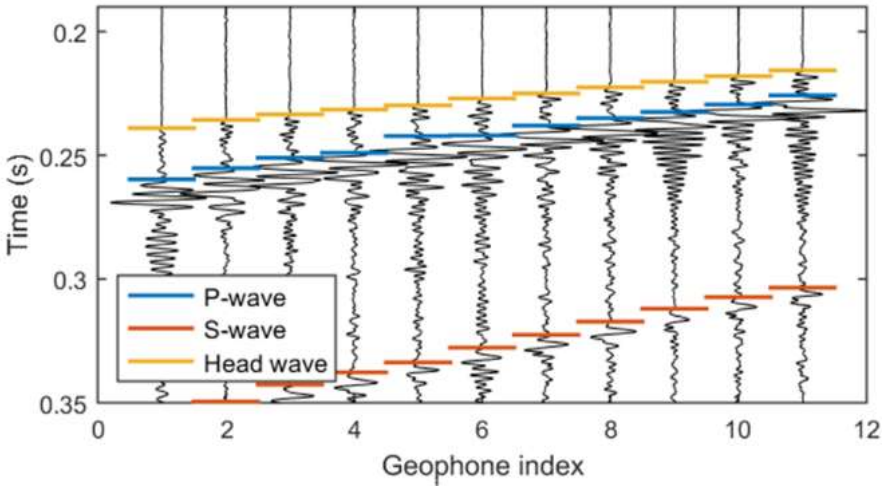

Figure 5: The waveform of a perforation shot recorded by an array of geophones. Head wave can be easily identified based on their low amplitude and high velocity moveout.

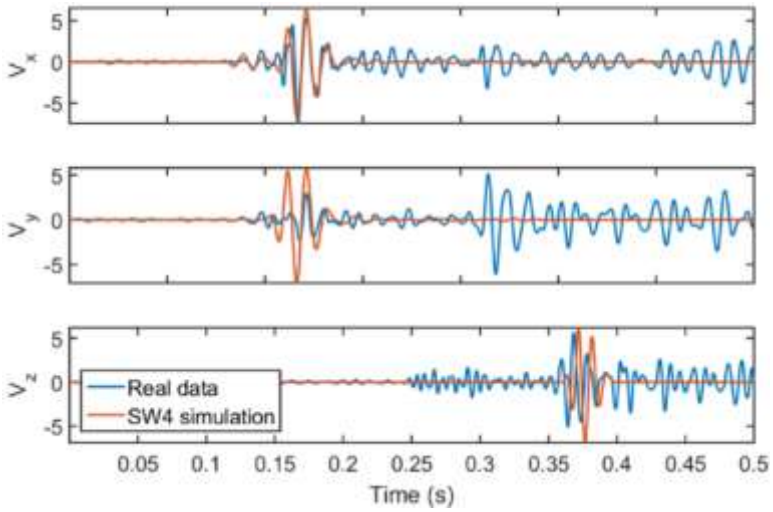

Figure 6: Comparison between synthetic and real waveform. The synthetic waveform matches the real data relatively well. This verified the existence of head wave. The difference on S-wave in x and y components may be because of the unknown source mechanism of the real event for simulation.

To further verify and analyze the head wave, the finite difference simulation of microseismic wave propagation in the configuration of this project was conducted by Lawrence Livermore National

Laboratory's SW4 code (Petersson and Sjogreen, 2013). The existence of head wave can be verified by the comparison between real and synthetic waveform as shown by Figure 6. Both the amplitude and arrival time of head wave in real data match the synthetic waveform well.

Results and Discussion

Velocity model calibration

The original velocity model used by the contractor as shown in Figure 3 was isotropic layered model built based on sonic logs. However, analysis on this velocity model shows that head wave will not take over direct arrival to be the first arrival in this configuration. So the velocity model will need to be calibrated to waveform of perforation shots. This can be carried out by our developed Bayesian inversion code for microseismic event location. We can simply use the velocity model as the model parameter $\mathbf{m}$ and perforation shot location as the observable data $\mathbf{d}$. From the velocity model calibration, we found the stimulation zone can be precisely characterized by the original velocity model ($V_p = 4.31\ km/s$ and $V_s = 2.67\ km/s$). However, the calibration also reveals the existence of a high velocity ($V_p = 6.01\ km/s$) zone approximately 70 m below the geophone array but there was no velocity information in the original model due to lack of sonic log.

Perforation shot location

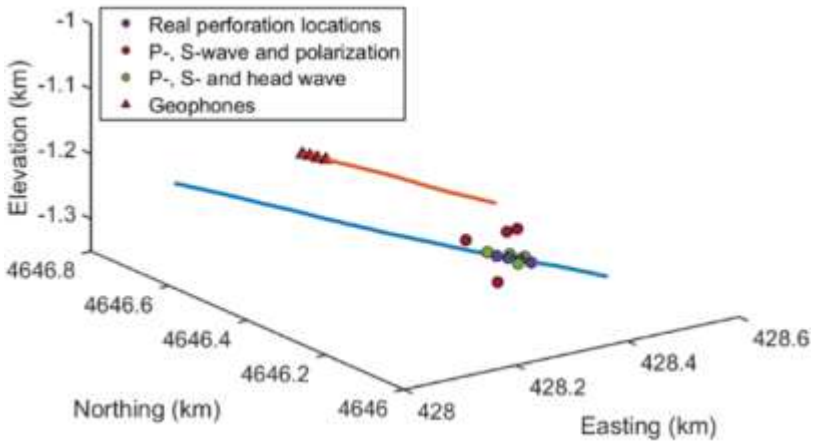

Figure 7: Comparison on estimated perforation shots location and the true perforation location. The perforation shot location estimated with P-, S-, and head waves is very accurate.

To quantify our event location estimation accuracy, we located the perforation shots whose locations are known. Our location result of the four perforation shots on stage two, along with their true location, is shown by Figure 7. What is also shown is the location result with the traditional method, which used direct arrivals and P-wave polarization. Before the location of perforation shots in this analysis, the velocity model was calibrated with all available perforation shots on stages other than stage two. Since the velocity model was not calibrated with perforation shots to be located, these perforation shots on stage two can be treated as normal microseismic events and used for location uncertainty analysis.

From the comparison we found the method using head wave gives an average error of 15 m while the traditional method with polarization gives an error of 49 m. This demonstrates the effectiveness and accuracy of our proposed location method with head wave arrival time.

Relocation of microseismic events on stage two

The map view of the microseismic event location provided by the contractor is shown in Figure 8. Apparently, the microseismic event location on stages two is significantly more scattered than those on later stages. One possible explanation of the scattering is because of the larger stimulated reservoir volume for stage two. Another explanation is simply because of the large location uncertainty due to the long distance of stage two from the geophone array.

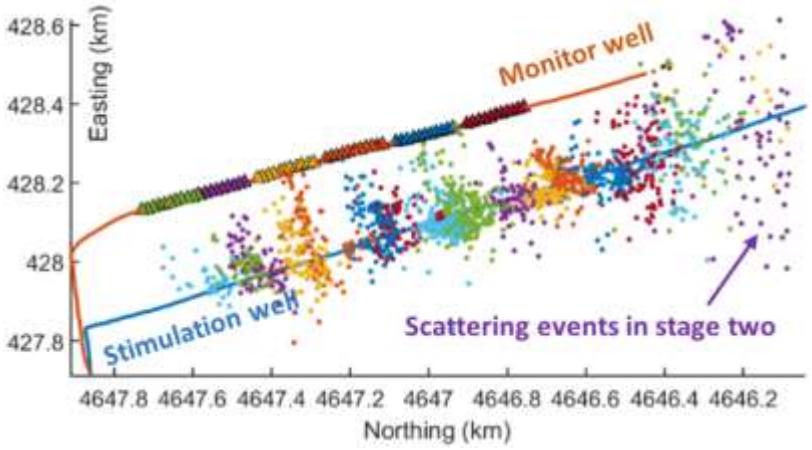

Figure 8: Map view of microseismic event location processed by contractor. The event location on stage two is more scattered than those in later stages.

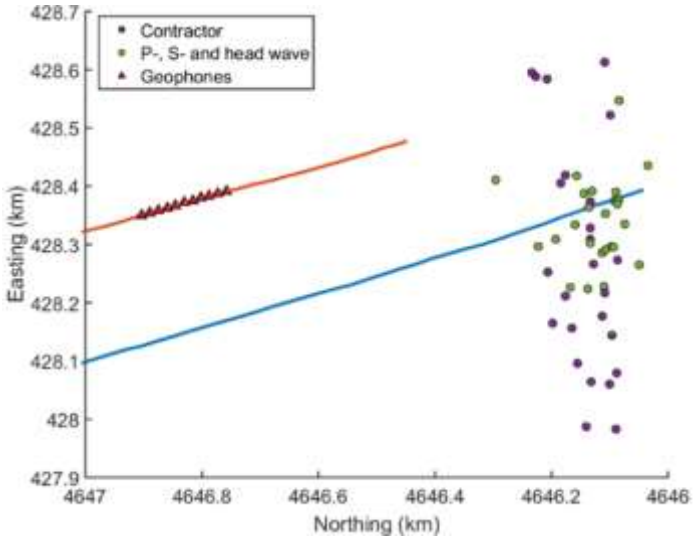

Figure 9: The microseismic event location estimated with P, S and head wave arrival is less scattered when compared to the microseismic event location processed by the contractor.

To find the reason for the scattering of stage two events, we relocated these events with head wave arrival as a substitution for polarization as shown in Figure 9. The relocated events are much less scattered than the result provided by contractor. This shows that the scattering of stage two events in original catalog was due to the large uncertainty in the estimation. Also, it indicates the effectiveness of accounting for head wave in microseismic event location to improve location accuracy.

Since it is difficult to pick head wave that arrives after direct P-wave arrival, we will be forced to use polarization to constrain the event location near the geophones. This traditional method is problematic, as we have shown. We would propose a two-array geophones acquisition geometry for single horizontal well monitoring. One array should be as near to the stimulation zone as possible. And the other array should be at relatively large distance from the stimulation zone for head wave monitoring. This acquisition geometry will be able to use head wave arrivals as well as obtain high S/N ratio.

Conclusion

The existence of head wave in microseismic survey in Marcellus shale is observed and verified. A Bayesian inversion framework was developed for microseismic event location and velocity model calibration. The location result of perforation shots using the developed method verified that the accounting for head wave arrival time as a substitution of P-wave polarization indeed improves the microseismic location accuracy. The relocation result on microseismic events in stage two shows a more reasonable pattern than the original catalog. Based on the developed method, we proposed a new acquisition geometry for single horizontal well hydraulic fracturing monitoring, which enables us to improve microseismic event location accuracy.

Spectral Analysis

Motivation

The monitoring geometry of the hydraulic fracturing project is typical in that the treatment well is drilled horizontally at depth and accompanied by an adjacent horizontal monitoring well. This specific monitoring geometry is frequently used because it is a cost-effective method of monitoring hydraulic fracturing projects. However, there are significant drawbacks to this particular approach. For example, moment tensor inversion is not possible due to a small solid angle (Du et al. 2011; Vavryčuk 2007). In order to perform traditional time-domain analysis techniques, additional monitoring wells are needed at an additional, often, cost-prohibitive amount.

In order to circumvent this inability to perform moment tensor inversion and understand microseismic source mechanism, a new method must be implemented. Traditional time-domain analysis fails due to hard constraints. As such, the spectral-domain is used in order to increase understanding of subsurface fracture phenomena.

Hydraulic Fracturing Microseismic Monitoring Overview

As previously stated, the hydraulic fracturing project was performed in Susquehanna County, Pennsylvania in the Marcellus shale formation and utilized two horizontal boreholes. The microseismic monitoring sensors employed to capture the acoustic energy of the project were miniaturized multi-component borehole sonde strings consisting of eleven geophones, each spaced approximately 50 ft. from one other. While it is certainly preferable to clamp, or lock into place, the geophones in a crosswell monitoring configuration, the geophones in this project were not clamped. As such, the weight of the monitoring instrument was the only coupling force adhering the tool to the borehole casing.

The main focus of monitoring this hydraulic fracturing project was to investigate the potential of increasing stimulation efficiency by only changing operational constraints such as pump rate. As such, a variable pump rate design was implemented in nine of the eighteen stages that were completed in the overall project. Pumping parameters were monitored in an effort to correlate increased gas production with those stages implementing the varied rate design. Preliminary findings, however, were inconclusive as to whether a variable rate design of pumping stages leads to an increase in gas production. Despite this, the hydraulic fracturing project was successful in producing hydrocarbon from the treatment well. In an effort to reduce viewing distance while fracturing each of the eighteen stages, the geophone array was moved six times throughout the hydraulic fracturing project, shown in Figure 10.

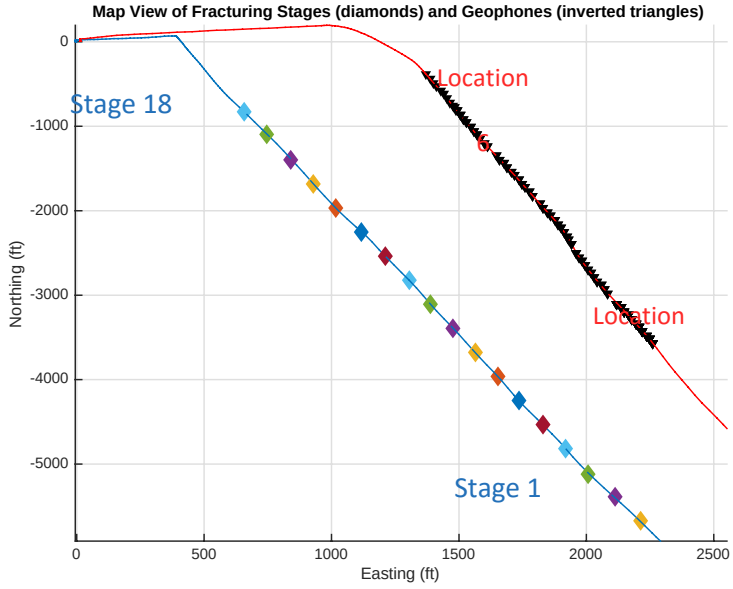

Figure 10: Map view of hydraulic fracturing process in the Marcellus Shale. Relative distances are given in the Easting and Northing directions. Blue line represents the treatment well and the red line indicates the observation well. Multi-colored diamonds represent the locations of perforation shots for each of the eighteen stages. Stage one is at the toe of the well and stage eighteen is at the heel of the well. Black inverted triangles represent the six locations of the geophone array.

A listing of the stages associated with each geophone array location can be seen in Table 1. The decision to relocate the geophone array had both advantages and disadvantages. For instance, with a reduced viewing distance, signal-to-noise was improved as a result of diminished scattering and attenuation effects; however, there was also a dramatic reduction in azimuthal coverage. As such, there was a tradeoff

between reduced noise and a reduced ability to determine specific source mechanisms through traditional means.

Table 1: Description of geophone movement throughout hydraulic fracturing project

Hydraulic Fracturing Stage	Geophone Array Location
1 - 9	1
10 - 11	2
12 - 13	3
14 - 15	4
16 - 17	5
18	6

Data Analysis

Noise Reduction through Location-Based Characterization

Traditional time-domain analysis steps failed due to the geometry of the monitoring well as well as poor signal-to-noise within the raw data. However, as an initial processing step, the raw data were filtered using a Butterworth Low Pass filter with corner frequency of 150Hz. This gave some useful indications. For example, it was noted that large amplitude ringing artifacts were significantly diminished. In order to understand this phenomenon better, a new method of noise reduction was developed and implemented.

Since the triaxial geophones were not clamped to the borehole casing once placed downhole, a significant amount of noise was present in the data as a result. This led to a non-stationary noise characteristic. That is, the specific noise characteristic attributed to clamping issues between the geophone and borehole casing changed from one monitoring location to the next. In order to understand and account for this noise signature, after applying a low pass filter, the Root Mean Square, RMS, values were found for each trace for all events. After these values were found, a two-dimensional averaging technique was used for all events in each of the six monitoring locations. This process resulted in six scalar values, or location-specific noise signatures, and those values were accounted for appropriately.

A useful conclusion that was drawn as a result of this attempt to minimize noise is that, throughout a large subset of the events recorded, ringing artifacts were seen. Upon further investigation, and through a literature review, it was concluded that as a result of the geophones not being clamped to the borehole casing, some of these ringing artifacts are actually tube waves (Gaiser et al. 1988). Tube waves typically have a slower moveout than other waves present in the data and due to the pathway the wave takes through the borehole, it is considered to add no useful information for event location, magnitude, or source mechanism estimates. Figure 11 shows an example of an event containing a tube wave, and that

same event post-processed showing an absence of tube wave energy. Removing this large contributor of noise was valuable; however, more work was required in order to analyze the dataset. For this we turn to the spectral domain and begin our analysis with software developed in Matlab.

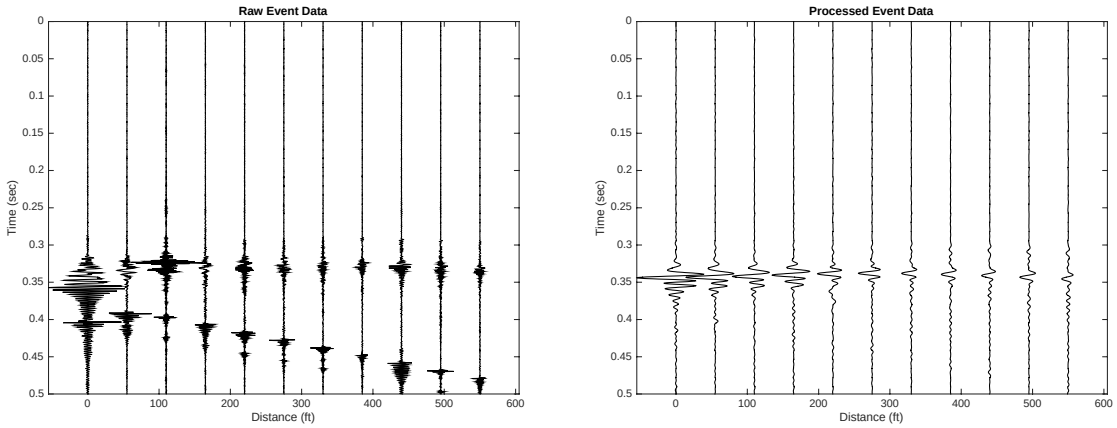

Figure 11: Comparison of raw data (left) showing the presence of a large amplitude artifact, likely caused by interference from a tube wave propagating through the observation well.

Initial Processing Steps

In order to interactively analyze the data through visualization software, a number of steps were first necessary. After the location-based noise characterization and reduction steps were performed, the records were significantly more readable; however, in order to perform spectral analysis steps, the compressional and shear wave events needed to be identified. In order to accomplish this, an automatic picker was designed that would identify both compressional and shear wave arrival times. This approach incorporated the contractor estimates of first arrivals for both waveforms as a baseline. On the newly processed records, these picked times were used and a pre-determined number of sample before and after were considered. The maximum amplitude found within this tolerance was considered the arrival time. It should be noted that this approach used the Hilbert transform to establish a maximum amplitude.

Additionally, as a means of checking the effectiveness of the automatic picker algorithm, the records were also manually picked. This was necessary due to poor signal-to-noise throughout the dataset, which made it difficult for many compressional wave arrivals to be confidently identified. As a result of the combined automatic picker and manual interpretation, the highest confidence in arrival times was achieved. Still, on a significant number of events, it was exceedingly difficult to confidently identify compressional wave arrival time. As such, the windowing of the events relied mainly on the shear wave arrival times, which will be discussed shortly.

After the arrival times were compiled, the individual waveforms were then windowed for follow-on spectral analysis. In order to accomplish this, a Tukey window (Equation 2) was used with an empirically determined r value of 0.25. This window, which is a tapered cosine, was chosen since it minimized edge effects and also retained most of the information present in the data. The length of the window was 100ms, which began 10ms before the first arrival of the waveform. Since the compressional wave first

arrivals could not be confidently identified on a significant number of records, the shear wave arrival time was used as the basis for windowing. That is, the compressional wave window was selected based on the start time of the shear wave window. This allowed the shear wave to be confidently windowed, and the compressional wave to be captured as well. The window length was chosen in order to minimize loss of waveform energy.

$$w(x) = \begin{cases} \frac{1}{2}\left\{1 + cos\left(\frac{2\pi}{r}\left[x - \frac{r}{2}\right]\right)\right\} & , \quad 0 \le x < \frac{r}{2} \\ 1 & , \quad \frac{r}{2} \le x < 1 - \frac{r}{2} \\ \frac{1}{2}\left\{1 + cos\left(\frac{2\pi}{r}\left[x - 1 + \frac{r}{2}\right]\right)\right\} & , \quad 1 - \frac{r}{2} \le x < 1 \end{cases} \tag{2}$$

Spectral Analysis Steps

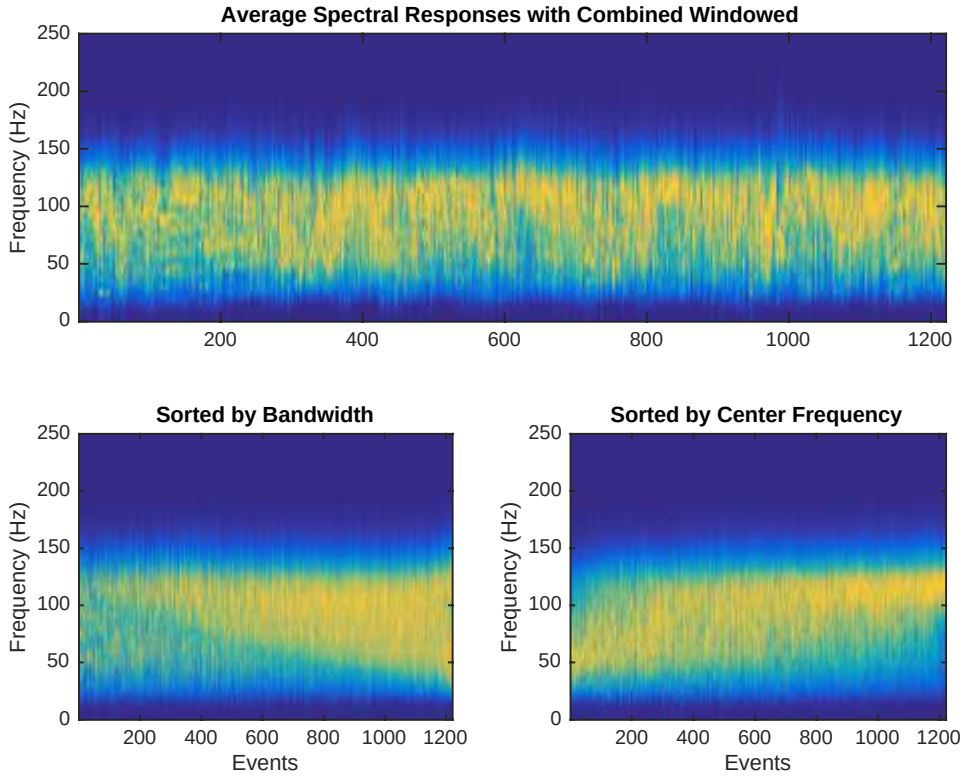

Figure 12: Event spectra of combined windowed data - horizontal axis shows event count, color encodes frequency amplitude where blue is lowest and yellow is greatest amplitude. Unsorted events (top) show that there is a range of variability in frequency response present in the data. Bandwidth-sorted spectra (bottom left) show that there is also variability of narrowband events. Center frequency-sorted events (bottom right) show that at the highest center frequencies (events 1,000 to 1200), the events are more narrowband in nature.

Now that the waveforms are windowed, the processing shifts focus from time-domain to the Fourier-domain in order to gain an understanding of the spectral relationships present within the data. In order to accomplish this some initial processing steps were required. Simply taking the Fourier transform of each trace (eleven traces) for all events (1,221 events) in the dataset produced a very large number of transforms, more than 13,000 Fourier transforms. This proved to be counterproductive since it was difficult to interpret the events in any meaningful way. In order to resolve this issue, an average spectral

response was determined for each event by taking the mean of all traces per record. This was accomplished by taking the mean of the eleven spectral responses. With an average spectral response for each waveform in each event (Figure 12), spectral analysis could begin. The focus of the spectral analysis was on two main spectral measurements: center frequency and bandwidth.

Center Frequency

In order to determine center frequency of the events, Bracewell's centroid method of signal analysis was used (Bracewell 1965). This approach models the event spectra as a distributed load and the first moment is considered. This method enabled the identification of which frequencies contained the greatest amount of energy within a given event. Bracewell's centroid method yields the abscissa$\langle x \rangle$, or center frequency, and is found by considering the integral of the product of signal energy and frequency (Equation 3).

$$f_c \overset{\text{def}}{=} \langle x \rangle = \frac{\int_{-\infty}^{\infty} x f(x) dx}{\int_{-\infty}^{\infty} f(x) dx} \tag{3}$$

The center frequency of event spectra is considered an important characteristic because it gives an indication of what the principal frequency of each event is. Specifically, it can give a relative measure of high or low frequency based on the other events in the dataset. Spectral content has been used in many other ways to give information regarding slip distance, Q determination, and other source parameters (Beresnev 2001; Brune 1970, 1971; Eaton 2011, 2014; Maxwell 2011). We use the center frequency as a means to classify microseismic events based on correlation with event location, pump parameters, and accompanying microseismic attributes that will come with follow-on analysis. This is necessary since the time-domain analysis techniques fail.

Bandwidth

Bandwidth is another important spectral characteristic since it can give an indication of how concentrated the energy is at the frequencies measured by the Fourier transform. Narrowband events are representative of events that have the majority of spectral energy concentrated around a specific frequency. Conversely, broadband events have significant energy distributed around a larger number of frequencies. In order to calculate the narrow or "broadbandedness" of spectral responses, a built-in Matlab function was used. This approach finds the global maximum of each event spectra and classifies this point as the prominence. The width of the signal at one-half the prominence of the signal is then used as the basis for computing the width of the event (Figure 13). This approach gives a relative measure of bandwidth for all event spectra.

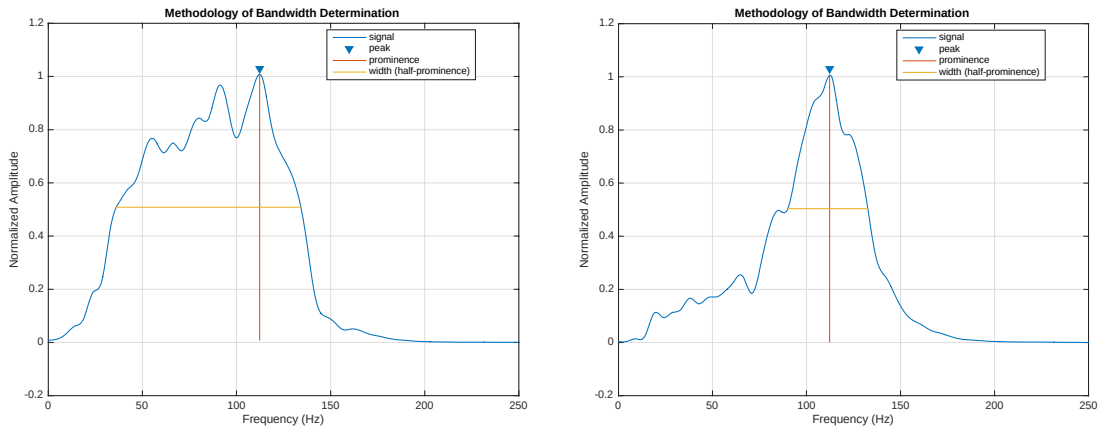

Figure 13: An example event showing how bandwidth is determined. Note that the width of the signal (horizontal line), which we call the bandwidth, is measured at one-half the prominence (vertical line)

Statistical Measures

To better understand the spectral trends reflected in the center frequency and bandwidth measures, a number of processing steps were completed. First, it was important to understand the differences between the windowed compressional and shear waves as well as a combined window. This combined window included both the compressional and shear waves, but nothing before or after. A combined window enabled us to understand the general sense of frequencies at which energy was present within the events. Specifically, the mean of all windowed compressional waves, all windowed shear waves, as well as all combined windowed events were found. From these measurements, it can be seen that both the mean center frequency and the mean bandwidth are higher for windowed shear waves. Additionally, the mean center frequency of the combined window is also higher than the compressional wave parameters (Table 2).

Table 2: Mean values of spectral characteristics for entire dataset

	Mean Center Frequency (Hz)	Mean Bandwidth (Hz)
Compressional Wave	86.0	61.9
Shear Wave	92.3	72.5
Combined Window	88.6	66.0

Software Developed

In order to continue analysis by way of non-traditional methods, a software package was developed using Matlab. This microseismic analysis toolkit uses multiple linked Graphical User Interfaces (GUIs) to allow

the user to interactively analyze the information contained in the dataset. There are three main views: Seismograms, Event Locations, and Spectral Analysis.

Seismogram GUI

The first view of the microseismic analysis toolkit is the Seismogram GUI. The Seismogram GUI is an analysis dashboard that enables the user to quickly and seamlessly progress through the events in order to visually interpret the microseismic records. This instance of the GUI displays an individual event in the form of a seismogram via a wiggle plot. Additionally, another figure displays relevant process information like surface pressure, slurry flow rate, as well as proppant concentration concurrently as a function of time for the stage containing the specific event displayed. Finally, the time at which the current event occurred is shown on the process parameter figure so that the user can quickly access the relevant process information at the time of the event. This allows the user to better understand the state of the hydraulic fracturing process and potentially identify microseismic artifacts on the seismogram.

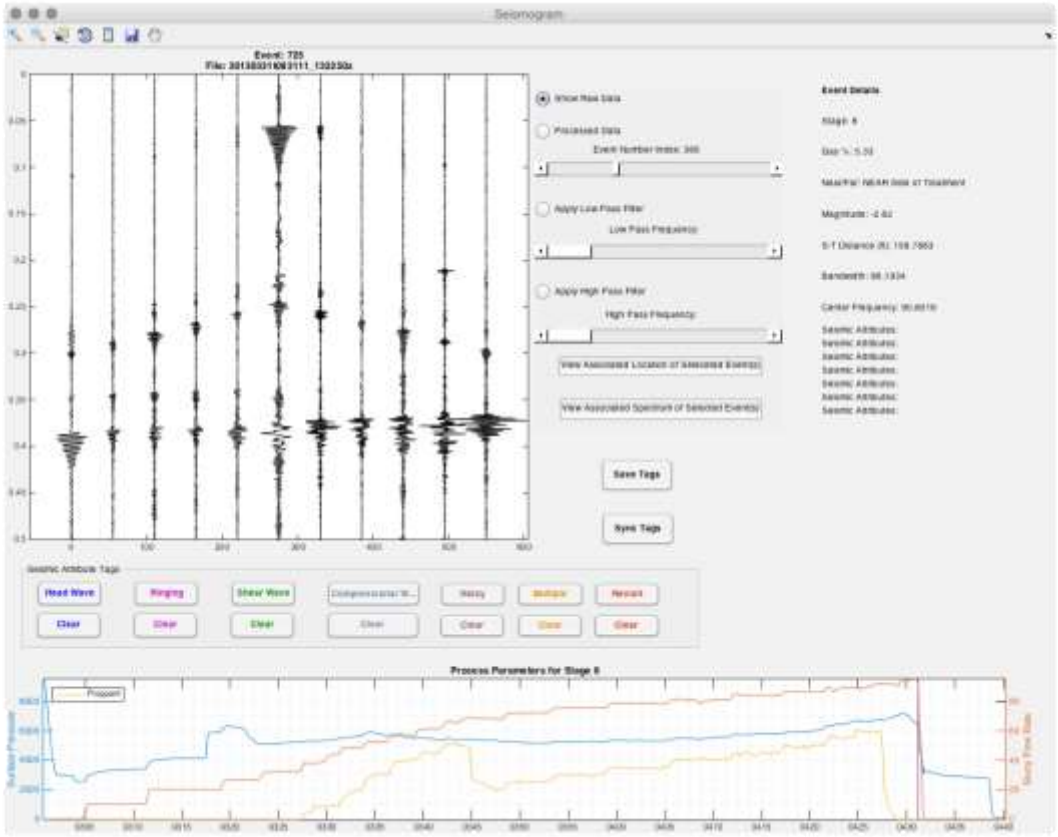

Figure 14: The first GUI displays an event seismogram (top) and pump parameters (bottom). Additionally, event characteristics are displayed on the right. Radio buttons control filtering options to display data dynamically. Sliders enable the user step through dataset and adjust corner frequency of filters. The group of pushbuttons enables the user to assign or clear seismic attributes via tags. Assigned tags are also displayed on the right side of the GUI.

There are also a number of event-specific parameters displayed on this particular view. For example, the right side of the GUI displays the stage in which the current event occurred, the gas production values for

that stage, a binary determination of whether the event occurred between the treatment well and the observation well, which can give an indication of whether the strength of the event is diminished by anticipated means or not (Figure 15). Additionally, the event's magnitude, distance from the treatment well the event occurred, as well as the predominant spectral characteristics bandwidth and center frequency are all displayed for each event viewed.

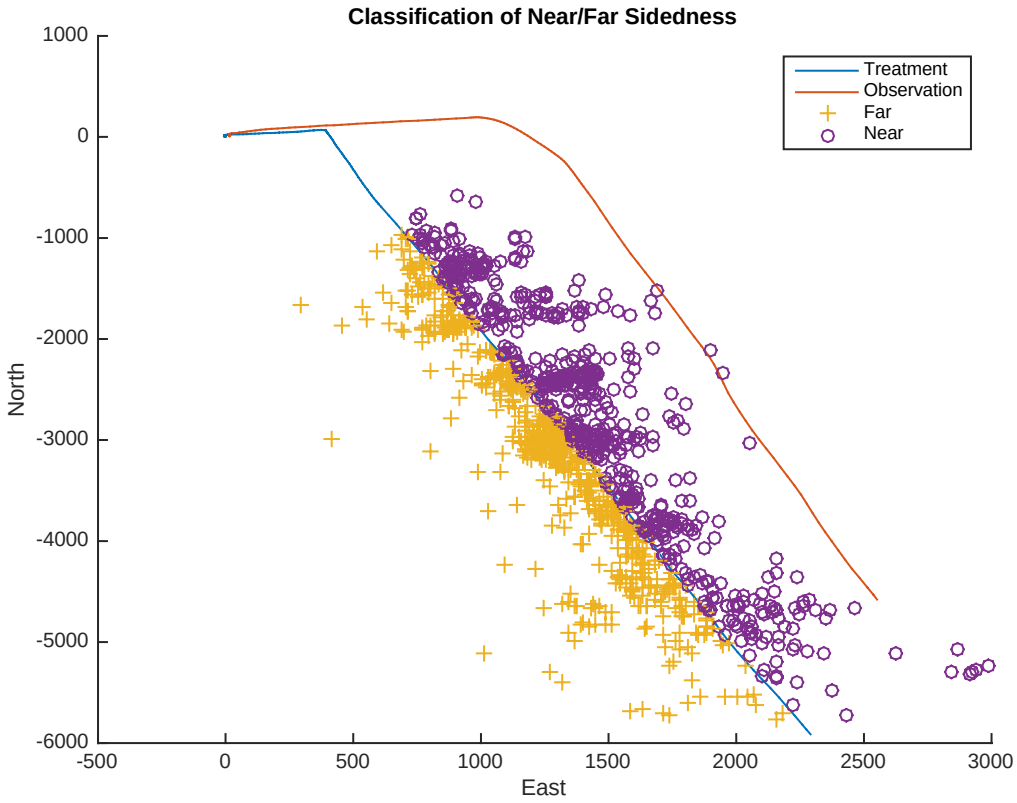

Figure 15: Map view of events in dataset. Gold plus signs depict those events that are located on the "far" side of the treatment well. Purple circles depict those events which lie between the treatment well and the observation well, on the "near" side. This allows the user to determine if signal-to-noise should be investigated since it is typically worse on the far side of the treatment well.

Furthermore, there are a number of options, which allow the user to interactively visualize and analyze the data. Radio buttons allow the user to toggle between raw data, processed data, and filtered data. Specifically, the user can show the dataset containing all records that have been processed with the location-based noise characterization and reduction schema. Moreover, the user can choose to display low pass and high pass filtered events. The user can also adjust the corner frequency of these filters from 10Hz to 200Hz in order to interpret artifacts that occur at different component frequencies.

A central aspect of this microseismic analysis toolkit is the ability to interactively analyze the data. In order to effectively perform this task, it is important to keep record of the microseismic attributes that are observed in specific events in the dataset so that these attributes can later be correlated with observed or measured parameters. In the visualization community, the term "tags" is used to describe

that which is assigned to a specific visualization to link a specific attribute for later interpretation or processing. The Seismogram GUI uses Seismic Attribute Tags in order to better enable interactive analysis.

Specifically, seven different pushbuttons are shown on the Seismogram GUI in order to allow the user to quickly assign various attributes to the event being viewed. Those tags are: Headwave, Ringing, Shear Wave, Compressional Wave, Noisy, Multiple, and Revisit. If the user identifies one or more of these attributes in the microseismic record being viewed, he can select the appropriate tag and later view all events that share these attributes. For example, this functionality enables the user to later plot the locations of all events that have multiple arrivals and also have ringing present in the record. In a sense, this enables for more robust slices of the data to be viewed. All seismic attributes that the user selects are displayed on the Seismogram GUI for quick reference as well.

Since the dataset, and other microseismic datasets, are typically large with a high number of records that are to be analyzed, the Seismogram GUI enables the user to save the tags he as selected and return to the GUI at a later time to continue the analysis. The Save Tags and Sync Tags buttons allow the user to accomplish this.

Locations GUI

The second view of the microseismic analysis toolkit is the Locations GUI, which displays contractor provided event locations in a three-dimensional figure (Figure 16). This instance of the GUI brings with it the full functionality of Matlab visualizations in that the figure can be rotated, zoomed, and panned. This is an important feature since there are a large number of events in the dataset and a two-dimensional projection occludes numerous events. Additionally, a major advantage to the Locations GUI is the ability to visualize event locations based on sorted parameters. This view of the microseismic analysis toolkit enables the user to visualize slices of data that reflect specific microseismic parameters.

Figure 16: The second GUI displays event locations in a three-dimensional space. The user may select all events, or specify a range of events based on the specific task. Events are sorted by stage, magnitude, and distance from source to treatment well.

The user may choose to view all microseismic events in the dataset, which is valuable to determine first order clustering and planar groupings. Additionally, the user may choose to only view a specific stage or stages. In this view, the events are color coded to reflect the various stages selected. Moreover, the user may choose to display the locations of events based on a number of parameters. For example, if the user desired to visualize only the events corresponding to the lowest magnitudes, a slider can be dialed in to only display the smallest magnitude events. Furthermore, the user may also visualize microseismic events based on the source-treatment distance, which is the Euclidian distance from the source to the stage-specific perforation area of the treatment well. This gives an indication of where the events occur relative to the fracture length. Specifically, it enables the user to understand if there is a relationship between azimuth and distance from treatment well.

Finally, the user may step through the entire hydraulic fracturing process by manipulating the sliders associated with time. This enables the user to better understand where each event occurs relative to the previous events. Additionally, this functionality enables the user to view a smaller subset of events particular to a specific range of time to determine if there are similarities in spatial distribution relative to time in stage or overall process.

Spectral Analysis GUI

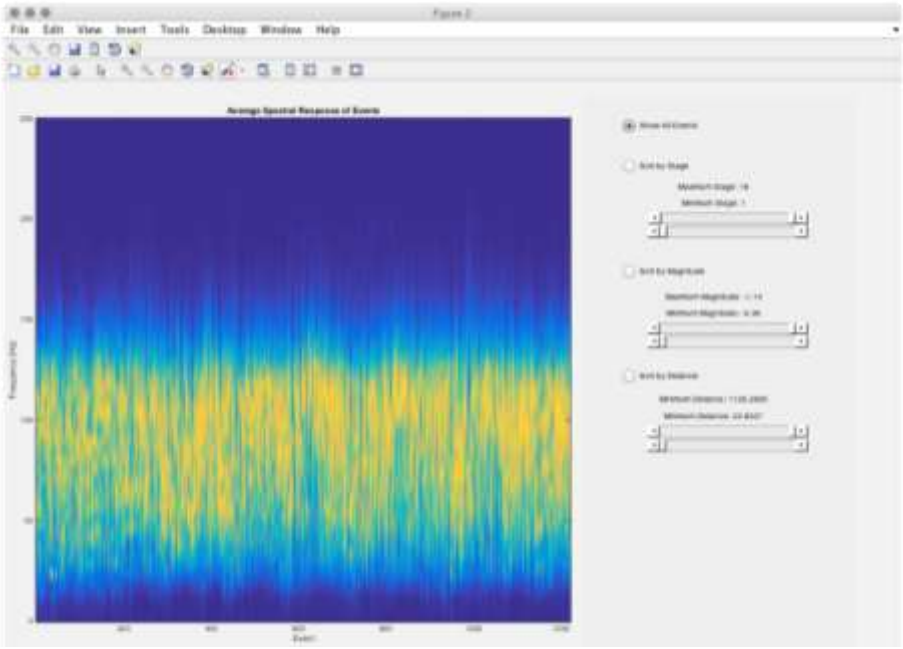

Figure 17: Third GUI displays spectral content. The user may display all events or choose to display events based on stage, magnitude, or source-treatment distance.

The last instance of the microseismic analysis toolkit is the Spectral Analysis GUI (Figure 17). This view of the toolkit enables the user to view spectral information contained in the microseismic events. The Spectral Analysis GUI contains a main figure that dynamically plots event spectra for a number of user-defined ranges of events. For example, the user may choose to display all events chronologically in order to gain a sense of the spectral variability present in the entire dataset. Additionally, the user may view a single stage or a range of stages. This approach enables the user to understand the spectral variability in a subset of the dataset and also gives a quick sense of the number of events in each stage.

In order to further correlate event parameters to spectral content, the user may also visualize event spectra as a function of both magnitude and distance. The sliders associated with these selections enable the user to dial in a specific range of values to display the associated spectra. This functionality enables the user to visually analyze spectral trends related to specific measured or observed parameters. While this version of the Spectral Analysis GUI is limited to the four previously listed options, it is extensible and can therefore support other microseismic parameters for visualizing spectra.

Linking Data for Interactive Analysis

Another important aspect of the microseismic analysis toolkit is the ability to transfer information between the three main views of the toolkit. In the visualization community, the act of transferring information between user interfaces for co-visualization is called “linking.” Through linking the three GUIs in the microseismic analysis toolkit, the user is better able to interpret the information present in the data. For example, if the user recognizes an interesting artifact in the Seismogram GUI, he may choose to also view the location of that specific event. Furthermore, he may wish to also view the spectral response for

that specific event. From the Seismogram GUI, he may push data to both the Location and Spectral Analysis GUIs in order to display the appropriate spatial and spectral information.

Additionally, a single event, or a user-defined range of events currently displayed in the Locations GUI, can be viewed in the Spectral Analysis GUI. This enables the user to view a specific stage, a subset of events with a specific magnitude, or source-treatment distance in the spectral domain in order to determine if there are any relevant relationships present in the dataset.

Results

While the scope of this project changed as a result of limitations stemming from difficulty performing time-domain analysis techniques that would be required for completion of original objectives, the research tasks performed are valuable.

Objective 1: Correlate Event Magnitude with Pump Parameters

Although correlation with pumping parameters like surface pressure, slurry flow rate, and proppant concentration was not directly accomplished, correlation between source parameters and spectral content was successfully performed. Scalar values of bandwidth and center frequency were visualized in order to determine if there was any relationship between those spectral parameters and microseismic event characteristics. As a result of this, it can be seen that there is an inverse relationship between calculated event bandwidth and vent magnitude (Figure 18). Further investigation was performed in order to determine if there was also a relationship between available pumping parameters and the calculated spectral characteristics; however, no clear relationship was seen with confidence.

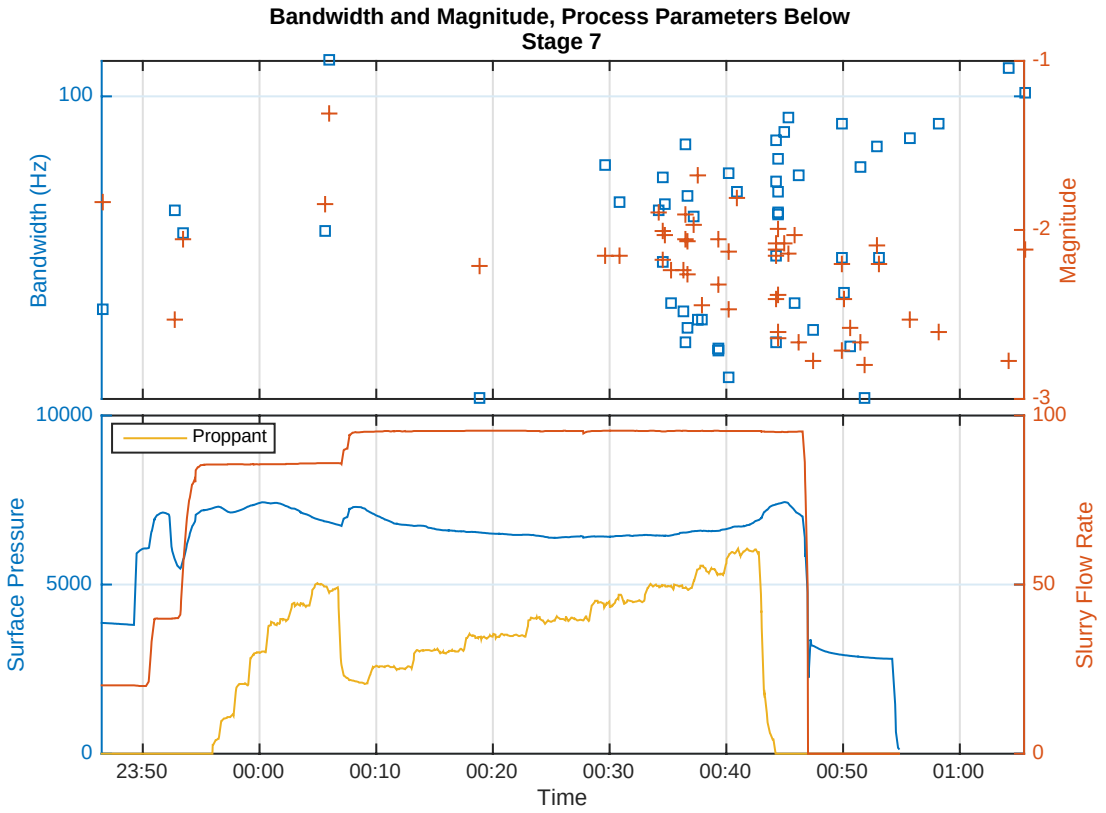

Figure 18: Bandwidth and magnitude shown as a function of time with other process parameters. The top figure shows bandwidth (blue squares) and microseismic event magnitude (red plus) as a function of time. The bottom figure shows process parameters – surface pressure (blue), slurry flow rate (red), and proppant concentration (yellow). Bandwidth and event magnitude display an inverse relationship.

However, one interesting observation was made regarding the magnitude of correlation. Specifically, there was better matching and a more apparent inverse relationship between event magnitude and calculated event bandwidth when the slurry flow rate decreased to zero. An example of this phenomenon can be seen in the final minutes of the seventh stage of the hydraulic fracturing project. One possible explanation for this behavior is that the stress state of the fractured area was returning to a state of lower energy.

Objective 2: Differentiate Opening Mode and Shear Mode Microseismic Signals

As previously stated, the mean center frequency and mean bandwidth of windowed shear waves were both higher than the windowed compressional wave values (Table 2). In order to understand the principal component, opening or shear, the ratio of the shear to compressional bandwidth was considered. This is a similar approach to the time-domain analysis technique; however this approach used the calculated event bandwidth in place of the traditional amplitude. Given that the windowed compressional wave consistently had a lower mean bandwidth and center frequency, a larger S/P bandwidth ratio would signify an event containing mostly a shear component.

In order to better understand the impact of this approach, a map view of event locations is considered (Figure 19). Here, the contractor-provided event locations are signified by diamonds. Additionally, a dual encoding with both color and size is used to demonstrate the S/P bandwidth ratio. A large, yellow diamond depicts the location of an event with primarily shear energy and a small, blue diamond shows the location of an event with mostly compressional energy. From this technique, it is possible to determine more about the locations of high or low shear regions.

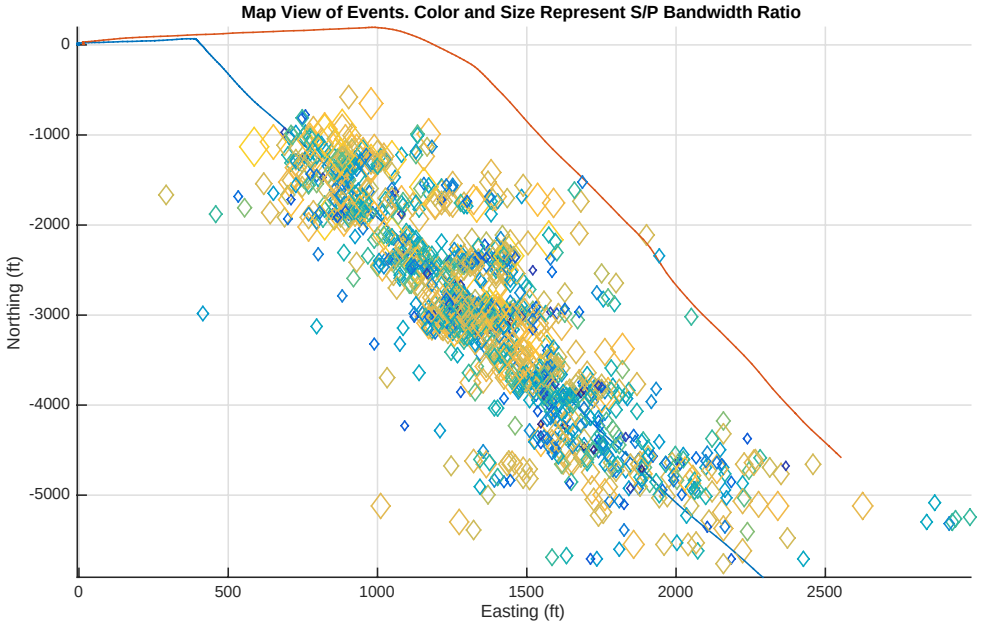

Figure 19: Map view of event locations (diamonds) for all eighteen stages of hydraulic fracturing process. As before, the treatment well is blue and the observation well is shown in red. Color and size of diamonds represent the S/P ratio of bandwidth. As such, larger yellow diamonds indicate events that have mainly shear content. Conversely, small blue diamond represents event dominated by tensile content.

Objective 3: Develop Acquisition and Processing Methodologies to Identify, Characterize, and Attenuate Noise Related to Stimulation Process

Although there were significant issues with signal-to-noise, one of the main identifiable sources of noise that came as a result of stimulation presented itself in the form of tube waves. After initial processing steps, large amplitude ringing artifacts were diminished, but were still present in the microseismic records. After further investigation into the source of these ringing artifacts, these noise artifacts were characterized as tube waves.

Tube waves can be excited in the receiver by incoming waves and present with a linear moveout with velocities nearly equal to or slightly less than shear waves (Mulder 2002). The tube wave is an interfacial wave, which travels along the cylindrical, fluid-solid boundary of the borehole (Hardrage 1981). Furthermore, the vertical profile of the hydraulic fracturing site is more susceptible to forming tube waves. Specifically, a low velocity layer, which is surrounded by high velocity layers, has the potential to generate strong tube waves (Chen 1993).

In order to mitigate this, the location-based noise characterization and reduction schema was developed, as previously described. As a result, the microseismic records contained significantly less noise. The post-processed data allowed for a much more precise analysis of spectral content.

Conclusion

Despite significant drawbacks associated with single monitoring well geometry, which is commonly used in hydraulic fracturing processes, information is still gleaned from existing data through the use of spectral analysis. While traditional moment tensor inversion fails as a result of small solid angle associated with horizontal monitoring geometry, stepping away from time-domain analysis and moving toward frequency-domain techniques is valuable.

After identifying and attenuating complex noise signatures due to the presence of tube waves, event parameters have been correlated with calculated spectral characteristics such as bandwidth and center frequency. Furthermore, by considering the ratio of windowed shear wave and windowed compressional wave energy in the frequency-domain, a greater understanding of shear event locations is also achieved. Continued work in the area of machine learning, with these first order relationships in mind, will lead to a more robust analysis and understanding of subsurface phenomena from traditional monitoring geometry.

References

[1] Beresnev, Igor A. "What we can and cannot learn about earthquake sources from the spectra of seismic waves." *Bulletin of the Seismological Society of America* 91.2 (2001): 397-400.

[2] Bracewell, R. "The Fourier transform and its applications." *McGraw-Hill electrical and electronic engineering series* (1965).

[3] Brune, James N. "Tectonic stress and the spectra of seismic shear waves from earthquakes." *Journal of geophysical research* 75.26 (1970): 4997-5009.

[4] Brune, James N. “Correction.” *Journal of geophysical research* 76 (1971): 5002

[5] Chen, S. T. (1993, January). A single-well profiling tool and tube wave suppression. In *1993 SEG Annual Meeting*. Society of Exploration Geophysicists.

[6] Cipolla, Craig, S. Maxwell, M. Mack, and Robert Downie. "A practical guide to interpreting microseismic measurements." In SPE/EAGE European Unconventional Resources Conference & Exhibition-From Potential to Production. 2012.

[7] Dong, Wenjie, and M. Nafi Toksöz. "Borehole seismic-source radiation in layered isotropic and anisotropic media: Real data analysis." Geophysics 60, no. 3 (1995): 748-757.

[8] Douglas, Alan. "Joint epicenter determination." Nature 215 (1967): 47-48.

[9] Dreger, Douglas, Robert Uhrhammer, Michael Pasyanos, Joseph Franck, and Barbara Romanowicz. "Regional and far-regional earthquake locations and source parameters using sparse broadband networks: A test on the Ridgecrest sequence." Bulletin of the Seismological Society of America 88, no. 6 (1998): 1353-1362.

[10] Drew, Julian Edmund, H. David Leslie, Philip Neville Armstrong, and Gwenola Michard. "Automated microseismic event detection and location by continuous spatial mapping." In SPE Annual Technical Conference and Exhibition. Society of Petroleum Engineers, 2005.

[11] Du, Jing, Ulrich Zimmer, and Norm Warpinski. "Fault Plane Solutions from Moment Tensor Inversion for Microseismic Events using Single-Well and Multi-Well Data." *Focus* (2011).

[12] Duncan, P. and Eisner, L. "Reservoir characterization using surface microseismic monitoring." Geophysics 75, no. 5 (2010): 75A139-75A146.

[13] Eaton, David W. "Q determination, corner frequency and spectral characteristics of microseismicity induced by hydraulic fracturing." *2011 SEG Annual Meeting*. Society of Exploration Geophysicists, 2011.

[14] Eaton, David W. "Magnitude, scaling, and spectral signature of tensile microseisms." *EGU General Assembly Conference Abstracts*. Vol. 16. 2014.

[15] Eisner, Leo and Le Calvez, Joel Herve. "New Analytical Techniques To Help Improve Our Understanding of Hydraulically Induced Microseismicity and Fracture Propagation." (2007).

[16] Gaiser, James E., Terrance J. Fulp, Steve G. Petermann, and Gary M. Karner. "Vertical seismic profile sonde coupling." Geophysics 53, no. 2 (1988): 206-214.

[17] Hardage, B. A. (1981). An examination of tube wave noise in vertical seismic profiling data. *Geophysics*, *46*(6), 892-903.

[18] Li, Junlun, Chang Li, Scott A. Morton, Ted Dohmen, Keith Katahara, and M. Nafi Toksöz. "Microseismic joint location and anisotropic velocity inversion for hydraulic fracturing in a tight Bakken reservoir." Geophysics 79, no. 5 (2014): C111-C122.

[19] Maxwell, Shawn. "Microseismic location uncertainty." CSEG Recorder, April (2009).

[20] Maxwell, Shawn. "Microseismic: Growth born from success." The Leading Edge 29, no. 3 (2010): 338-343.

[21] Maxwell, Shawn C. "What does microseismic tell us about hydraulic fracture deformation." *CSEG Recorder* 36.8 (2011): 31-45.

[22] Maxwell, Shawn. Microseismic imaging of hydraulic fracturing: Improved engineering of unconventional shale reservoirs. No. 17. SEG Books, 2014.

[23] Mulder, W. A., Plessix, R. E., & Fehmers, G. C. (2002, January). Another tube wave filter, based on semblance and correlation. In *2002 SEG Annual Meeting*. Society of Exploration Geophysicists.

[24] Myers, Stephen C., Gardar Johannesson, and William Hanley. "A Bayesian hierarchical method for multiple-event seismic location." Geophysical Journal International 171, no. 3 (2007): 1049-1063.

[25] Myers, Stephen C., Gardar Johannesson, and William Hanley. "Incorporation of probabilistic seismic phase labels into a Bayesian multiple-event seismic locator." Geophysical Journal International 177, no. 1 (2009): 193-204.

[26] Oliver, Dean S., Albert C. Reynolds, and Ning Liu. Inverse theory for petroleum reservoir characterization and history matching. Cambridge University Press, 2008.

[27] Parra, J. O., C. L. Hackert, P-C. Xu, and Hughbert A. Collier. "Attenuation analysis of acoustic waveforms in a borehole intercepted by a sand-shale sequence reservoir." The Leading Edge 25, no. 2 (2006): 186-193.

[28] Parra, Jorge O., Chris L. Hackert, Anthony W. Gorody, and Valeri Korneev. "Detection of guided waves between gas wells for reservoir characterization." Geophysics 67, no. 1 (2002): 38-49.

[29] Petersson, N. Anders, and B. Sjogreen. "User's guide to SW4, version 1.0." LLNL-SM-xxyy, Lawrence Livermore National Laboratory (2013).

[30] Poliannikov, Oleg V., Michael Prange, Alison E. Malcolm, and Hugues Djikpesse. "Joint location of microseismic events in the presence of velocity uncertainty." Geophysics 79, no. 6 (2014): KS51-KS60.

[31] Tarantola, Albert, and Bernard Valette. "Inverse problems= quest for information." J. Geophys 50, no. 3 (1982): 150-170.

[32] Tarantola, Albert. Inverse problem theory and methods for model parameter estimation. siam, 2005.

[33] Vavryčuk, Václav. "On the retrieval of moment tensors from borehole data." *Geophysical Prospecting* 55.3 (2007): 381-391.

[34] Waldhauser, Felix, and William L. Ellsworth. "A double-difference earthquake location algorithm: Method and application to the northern Hayward fault, California." Bulletin of the Seismological Society of America 90, no. 6 (2000): 1353-1368.

[35] Warpinski, Norm. "Microseismic monitoring: Inside and out." Journal of Petroleum Technology 61, no. 11 (2009): 80-85.

[36] Zhang, Zhishuai, Behnam Jafarpour, and Lianlin Li. "Inference of permeability heterogeneity from joint inversion of transient flow and temperature data." Water Resources Research 50, no. 6 (2014): 4710-4725.

[37] Zimmer, Ulrich. "Localization of microseismic events using headwaves and direct waves." In 2010 SEG Annual Meeting. Society of Exploration Geophysicists, 2010.

[38] Zimmer, Ulrich. "Microseismic design studies." Geophysics 76, no. 6 (2011): WC17-WC25.

Appendix F: Semblance Weighted Emission Mapping to understand seismicity behavior

Summary

Microseismic surveys typically involve surface deployments, wellbore arrays or a combination of the two. Surface microseismic surveys are often very resource intensive due to their large apertures and receiver count. On the other hand, downhole arrays are often deployed within existing wells in the field which leads to constrained design apertures and failure of imaging algorithms traditionally used with surface deployments for characterizing the observed microseismicity. At the same time, hypocentral inversion algorithms used with wellbore arrays have many well understood limitations and their use leads to many valid events being discarded. We introduce a simple emission mapping approach which can be applied on microseismic data from either borehole or surface arrays and provides a temporal energy emission profile as observed during treatment. We share an actual field example using data from this project (Wootton pad well 10H) and demonstrate the applicability of this attribute for better understanding of reservoir behavior during hydraulic fracturing and validate the analysis through independent observations from production logging data.

Introduction

Emission tomography is a relatively new yet well understood technique aimed at mapping the microseismic emission fields and localization of seismic source parameters using grid based search algorithms. These algorithms have found increasing acceptability in recent years due to improvements in the field of high performance computing and their ability to surmount some of the shortcomings of traditional inversion algorithms such as phase detection issues, picking inaccuracies and inversion errors. Kho et al. (2004) used a source scanning approach to map earthquake tremors in both space and time. More recently, Lakings et al. (2006), Chebotareva (2010), and others have made the technique more robust and applicable to oil and gas environments. Moreover, the derived attributes have also been used to model other relevant reservoir properties. For example, Geiser et al. (2012) introduced a new modeling approach that utilizes semblance volumes derived using traditional seismic emission tomography to identify potential fracture fairways and permeability maps within unconventional settings. However, the need for utilizing relatively large aperture surface arrays to apply these techniques leads to a substantial loss in detectability due to spherical spreading issues, transmission related losses (subsurface strata), surface noise and its impact, attenuation effects, etc. While monitoring programs using small aperture horizontal and vertical arrays should ideally record more of the observable seismicity, inversion results are

heavily dependent on first arrivals, accurate phase picks as well as the accuracy of local earth model. This leads to a large number of potential microseisms being lost during processing and these are typically not accounted for in interpretations of the data.

In our research work, we have looked at the potential for using emission tomography approach to better understand and interpret hydraulic fracture treatment programs. There exists considerable scope for application of emission tomography approach while using small aperture arrays in getting a more holistic understanding of reservoir behavior during injection. Moreover, when combined with traditional data (such as microseismic event locations or other source parameters), it can be extremely useful in improving our understanding of treatment efficacy and eventual well productivity. We introduce the basic algorithm and workflow to compute semblance weighted emission (SWE) with continuously recorded data. We share a case study where the observed microseismicity during completion of a gas well from Marcellus is processed using our approach and the results are compared with other independent datasets (local geology, microseismic source parameters, production logs, OBMI logs, etc.). We highlight the incremental benefits of this analysis on interpretation of treatment data and its practical applications in the field.

Method

As mentioned earlier, we utilize a standard emission tomography approach to process data acquired using a downhole array (continuously acquired during stimulation of 18 frac stages for a dry gas well). Since our interest is only in the temporal characterization of emission, the actual event location is not characterized using this approach. However, a standard inversion based algorithm utilizing travel time information is used to map out all possible events independently. The method involves a systematic mapping of emission for different trial locations based on defined gridded search space using the observed waveforms and various sensor locations (Kho et al., 2004). The first step is to filter and normalize the synthetic gather as recorded. For N downhole receivers, emission parameter is computed as

$$e(x,y,z,\tau)=\frac{1}{N}\sum_{n=1}^{N}\left\{\sum_{m=-M}^{M}\left|u_n(\tau+t_{x,y,z,n})\right|\right\} \quad (1)$$

where (x, y, z) provides the co-ordinates of the grid point under evaluation, τ is the time at which emission potentially took place, M defines the evaluation window which takes into consideration the uncertainties in the earth model and u, provides the processed seismograms at station ‘n’. The second measure that is computed is a semblance measure based on the predicted moveout from each evaluation grid point. Based on the estimated travel time for

each grid location using the defined velocity model, the semblance measure at any point is computed as

$$s(x,y,z,\tau)=\sum_{n=1}^{N}\frac{\sum_{m=-M}^{M}u_n u_p}{\sqrt{\sum_{m=-M}^{M}u_n^2}\sqrt{\sum_{m=-M}^{M}u_p^2}};\ p=1:N\notin n \tag{2}$$

The final SWE attribute is computed as the product of the two parameters calculated for each grid point and each event time within the global search space.

$$SWE(x,y,z,\tau)=s(x,y,z,\tau)\times e(x,y,z,\tau) \tag{3}$$

Since the search space is continuous, a threshold is used to extract attribute values which show a reasonably strong indication of an event. The threshold is identified by using perforation shot data with the grid search space reduced based on known location during velocity model calibration step. The result of this mapping process is continuous 4D SWE maps which can then be correlated and analyzed with the available treatment data. Figure 1 shows a brief outline of the discussed workflow for reference.

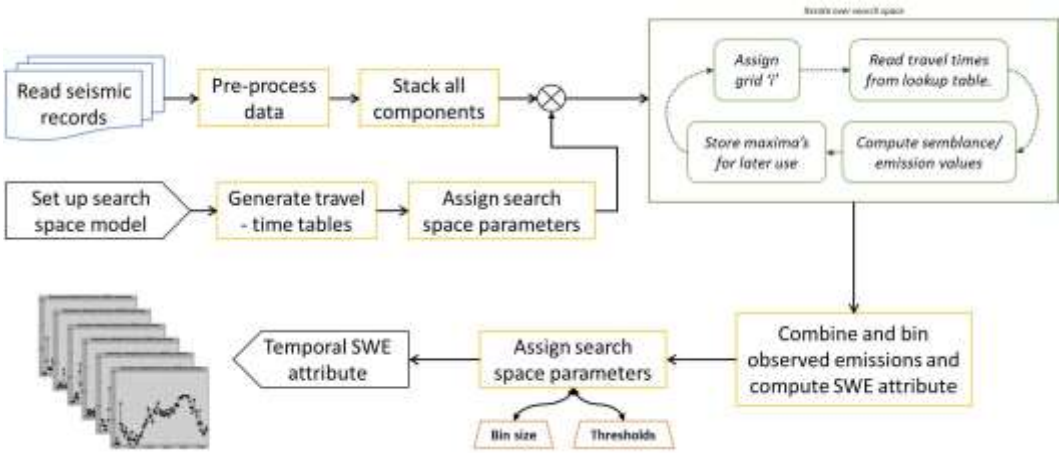

Figure 1: Workflow.

Figure 2 show test results carried out with this algorithm using a synthetic test dataset. The simulated event was placed at the center of the defined search space (Figure 2a) and an elastic wave propagation algorithm was used to generate synthetic seismograms with random noise added to simulate a more realistic scenario (Figure 2b). Figure 2c shows the emission profile as observed for this test case validating the applicability of this workflow to characterize seismic events in a predefined search space. Other tests were also conducted simulating more

complex acquisition geometries including wellbore arrays. Temporal mapping ability was validated for a synthetic event sequence similar to a realistic hydraulic fracturing environment.

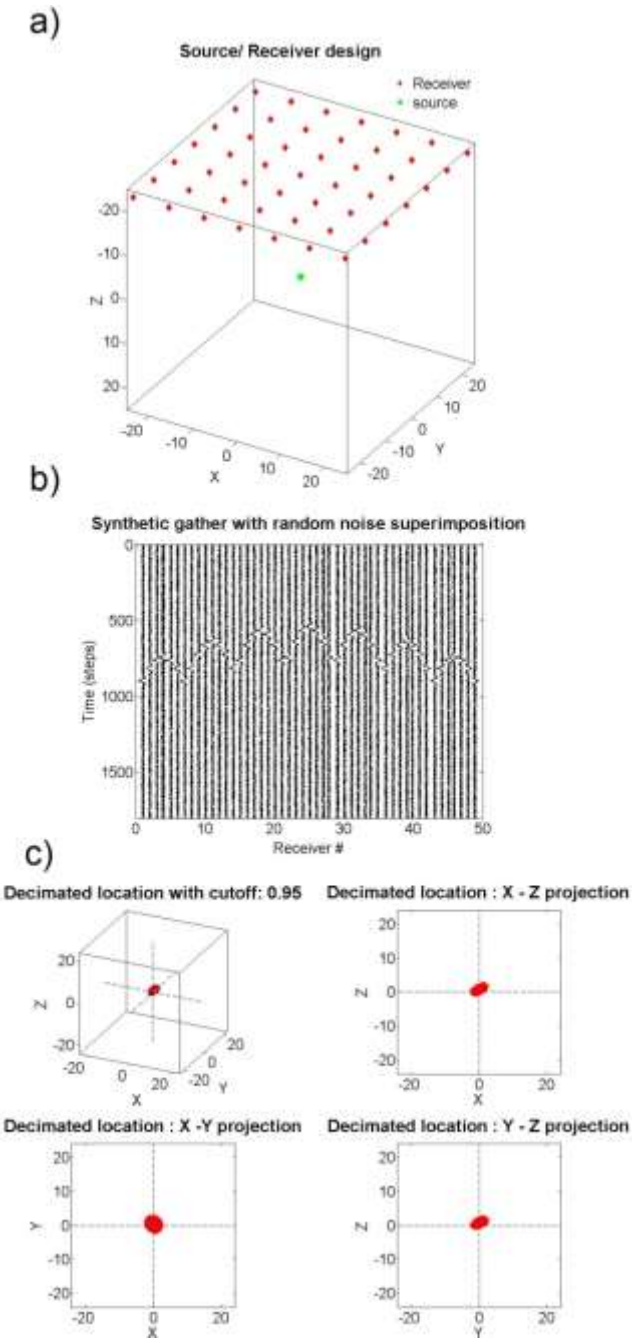

Figure 2: (a) shows a test scenario with 49 surface receivers in a square equi-spaced array along with a subsurface explosive source at the center of the search space (0, 0, 0), (b) shows the generated synthetic gather using a constant wave velocity field and (c) shows the results with the highest emission observed at the center of the search space as expected.

Analysis of data

We highlight application on a gas well form this project. This Marcellus well (Wootton pad, well 10H) has 18 fracture stages (4 perforation clusters per stage). The monitoring well used for this treatment was an offset well at a lateral separation of approximately 1000 feet. Figure 3 shows the wellbores including the treatment (well A) and the monitoring well (well B). The sensors were re-positioned (shifting array) in order to minimize the potential source-receiver separations wherever possible. Due to coupling issues faced with the tool string, there were significant data quality issues that manifested into highly limited catalog with no apparent correlation between observed seismicity and stage behavior in terms of production profiles. Moreover, due to wellbore issues, the tool string could not be pushed beyond ~ 9000 feet (MD) leading to additional constraints during monitoring of the first 7 stages.

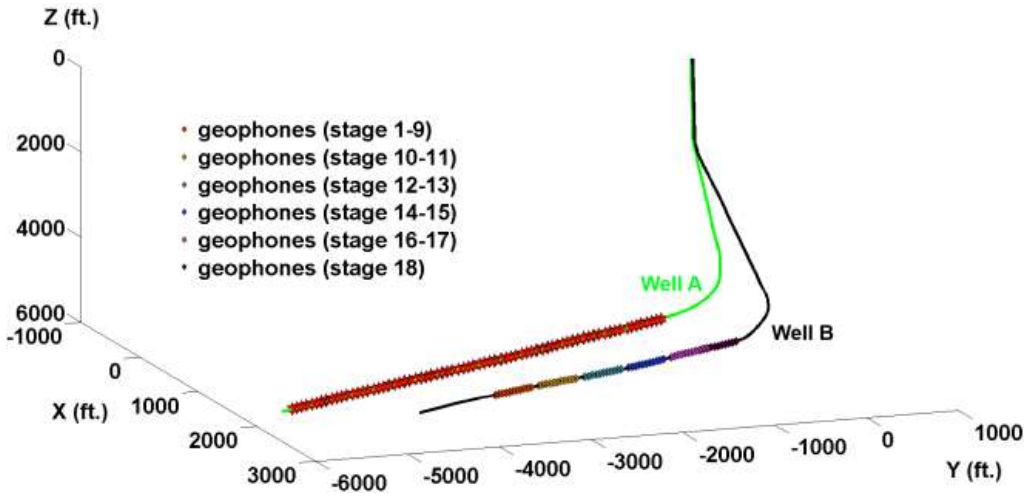

Figure 3: Field case study showing the survey setup used in well B as well as 18 treatment stages in well A. Note the shifted geophone locations to minimize Source – Receiver offsets. All distances are with reference to the grid origin (wellhead).

The microseismic monitoring data generated during this stimulation involved ~ 33000 records (5 seconds each) which was processed to generate equivalent SWE attribute map. Figure 4a shows the slurry and proppant feed and the accompanying microseismicity during stimulation of stage 9. Figure 4b shows the corresponding temporal SWE map (averaged over 1 minute time intervals) generated using the shared workflow. We can observe a gradual build-up in emission as the proppant loading increases with the peak being observed during maximum proppant loading and a sudden drop in emission as soon as injection stops. We can clearly observe that the SWE attribute provides useful information with respect to reservoir behavior

during treatment when compared with the actual inverted microseismic data due to processing issues such as noise artifacts, low phase amplitudes, multiples, missing phase, etc.

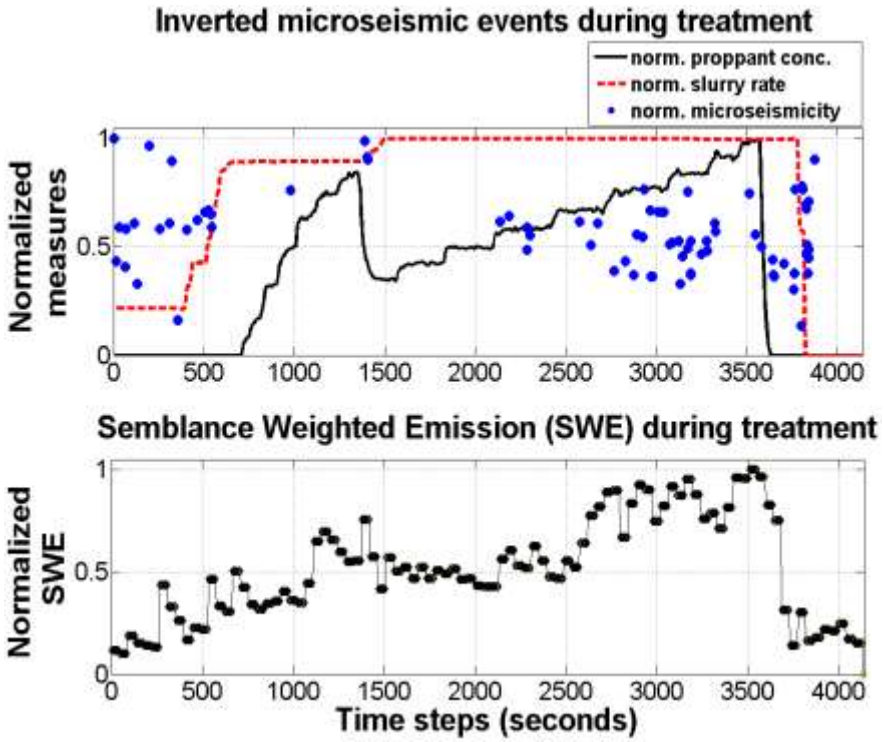

Figure 4: (a) shows the normalized treatment data and the accompanying microseismic events (elevation above 0 indicates relative event magnitude) and (b) shows the SWE attribute mapped in time during the stimulation for stage 9.

The mapped SWE integrated over the treatment duration for individual stages were correlated with the production log for well A which provides the flow contribution of stages to the wellbore. Our tests indicate a positive correlation between the observed gas production (flow contribution) from individual stages and the corresponding cumulative emission. Moreover, such a correlation is absent when we map the actual (inverted) microseismic events (event count) for the same stages. Figure 5 shows this observed correlation and provides validation of SWE as a better QC tool to improve our understanding of completions. It should be noted that production log could not be run for stages 1 through 4 due to wellbore issues. Also, seismicity captured prior to stage 8 are impacted by higher source receiver separations (Figure 3). Despite the reasonably strong correlation observed for this well, we do note that such an observation may not apply under all situations. Nonetheless, it still provides a much better indicator of in-situ stimulation characteristics when compared with inverted (hypo-located) microseismic events or potential event triggers.

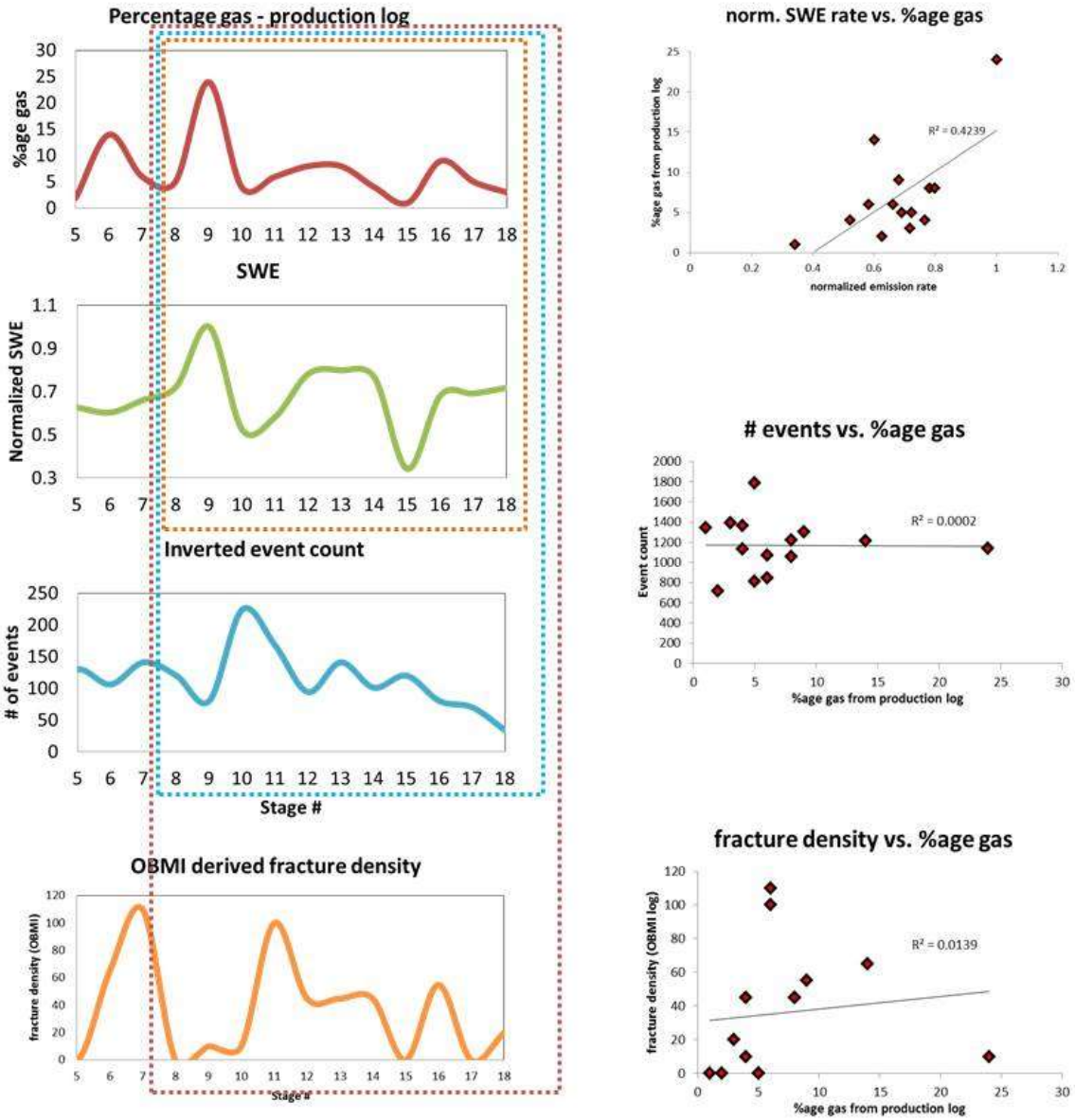

Figure 5: Production log, cumulative SWE, number of inverted microseismic events and finally, observed fractures from OBMI log for well A.

We also look at stage wise emission profiles and compare these with other available data such as microseismic source parameters, image logs etc. Figure 6 shows some sample stages with the observed flow contributions correlated with mapped emission profiles. We can clearly diagnose a major issue with the sample stages shown under case B where there are emission peaks before proppant pumping is initiated which could be indicative of either fluid bypass or stress shadowing issues. For most stages, correlating with observed seismicity through inversion workflows does not allow for such interpretations.

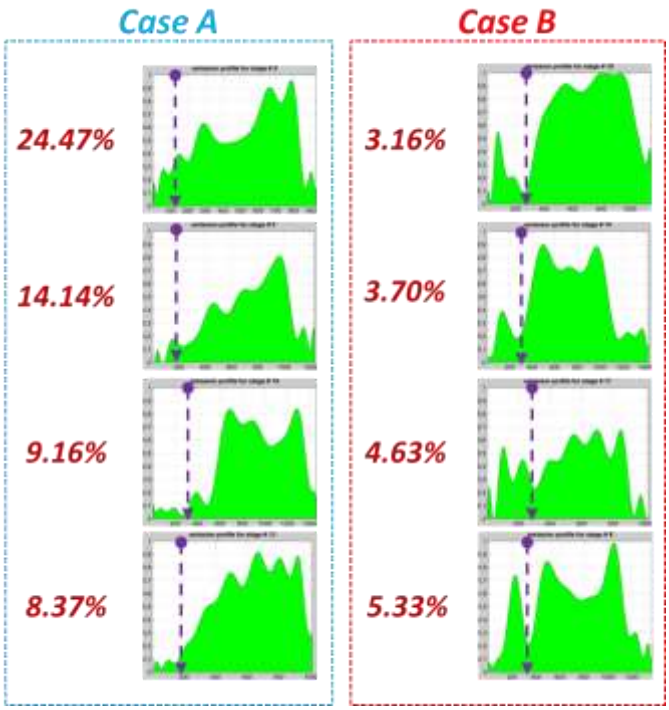

Figure 6: Case A represents emission profiles for sample stages with high gas flow contributions (percentage values) and case B shows sample stages with relatively low flow contributions. The arrows indicate proppant pumping initiation.

Looking at results from all the stages completed for this test well, we categorize those stages that show pre proppant phase injection emission against those that don't and observe an average percentage contribution to gas production at 8.94% compared to those that show pre proppant phase emissions. Even with discarding outlier stages (stage 6/9 based on abnormally high production contribution), we get a percent contribution of 5.48%. Average production contribution from stages without pre-proppant injection emission features is observed at 4.75% and 4.03% if the outlier stage (stage # 13) is discarded from analysis. Therefore the observed reduced production contribution from identified stages stands at ~ 47% (or 27% discarding outliers) and indicates potential underlying issues (such as leak-off) with the identified stages with pre-proppant injection emission.

We also compare overlap observed between stages based on the spatial microseismic event location distribution. To be on the conservative side, 10^{th} and 90^{th} quantile cut-offs are used to remove some of the most far field events for each of the stages in question. The cut-offs are applied on radial separation of events from the cluster center. Table 1 shows the stage pairs under study and the corresponding observations from event distribution/ overlaps as well as pre-proppant injection emission peaks from our analysis. We observe that barring two

pairs of stages, the observed overlap from spatial spread of microseismic hypocenters correlated very strongly with pre-proppant injection emission peaks.

Table 1: Correlating inversion results (observed overlap of stages) with emission results (injection peaks before proppant injection begins)

Stage Pair	Overlap	pre proppant injection emission peak
1/2	Yes	
2/3	No	
3/4	Yes	No
4/5	No	No
5/6	No	No
6/7	No	No
7/8	Yes	Yes
8/9	No	No
9/10	No	No
10/11	Yes	Yes
11/12	Yes	Yes
12/13	Yes	Yes
13/14	No	No
14/15	Yes	Yes
15/16	No	No
16/17	Yes	Yes
17/18	No	Yes

Stage Wise Diagnostics

As part of this study, we try and correlate the observed emissions with the seismicity behavior to understand and interpret the completion in lieu of the known data from production logs. We also look at the completion data and try to understand the reasoning behind some of the observations. Figure 7, Figure 8, Figure 9 and Figure 10 show examples of 4 stages analyzed for our study. The first example is a poorly producing stage. The second example is of a highly productive stage while the last two are examples of stages showing low to very low productivity as per production log readings.

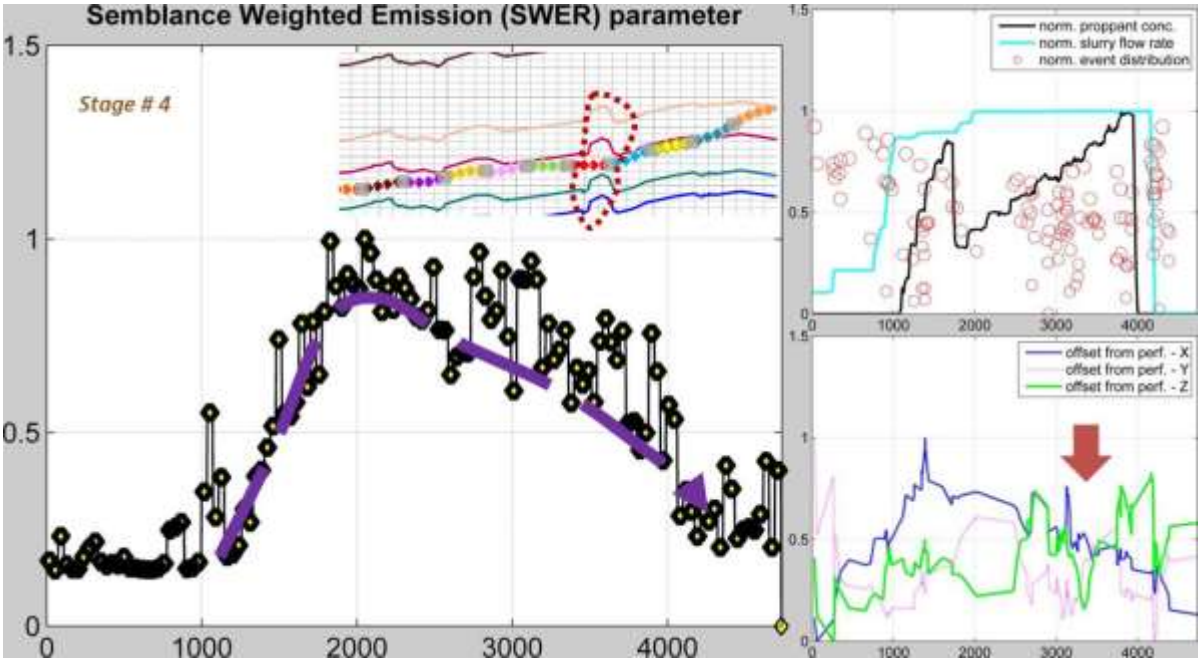

Figure 7: Mapped temporal SWE attribute along with the location of the well lateral w.r.t horizons, completion profile and observed seismicity for stage # 4 (WPX Energy Wootton 10H well).

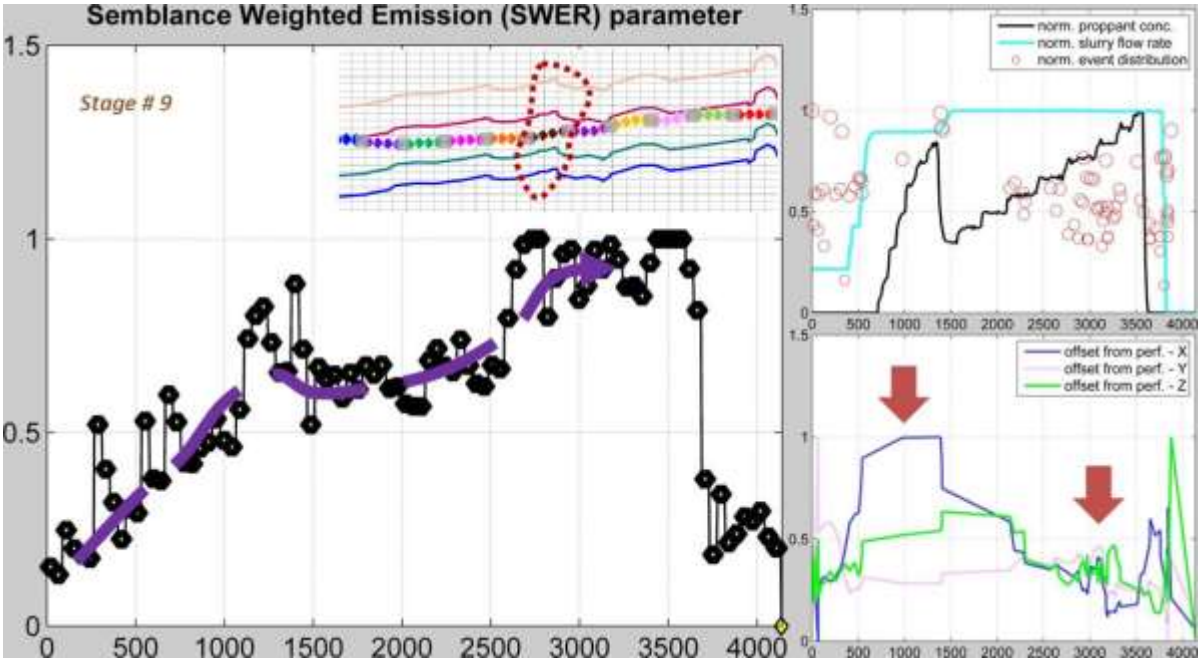

Figure 8: Mapped temporal SWE attribute along with the location of the well lateral w.r.t horizons, completion profile and observed seismicity for stage # 9 (WPX Energy Wootton 10H well).

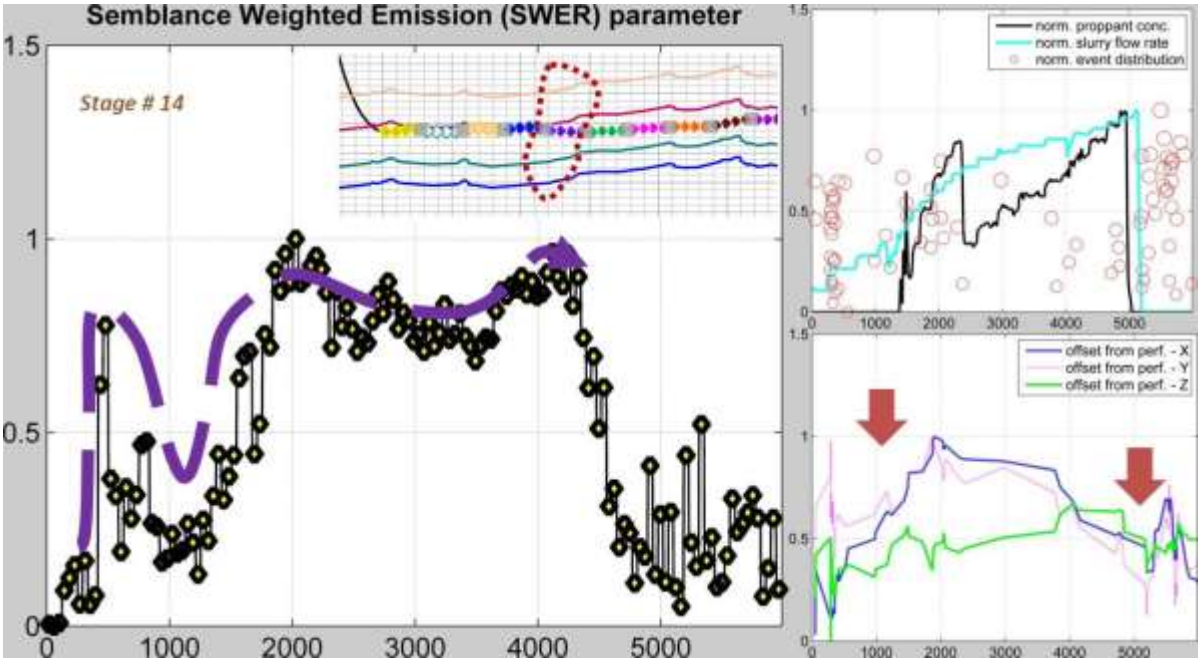

Figure 9: Mapped temporal SWE attribute along with the location of the well lateral w.r.t horizons, completion profile and observed seismicity for stage # 14 (WPX Energy Wootton 10H well).

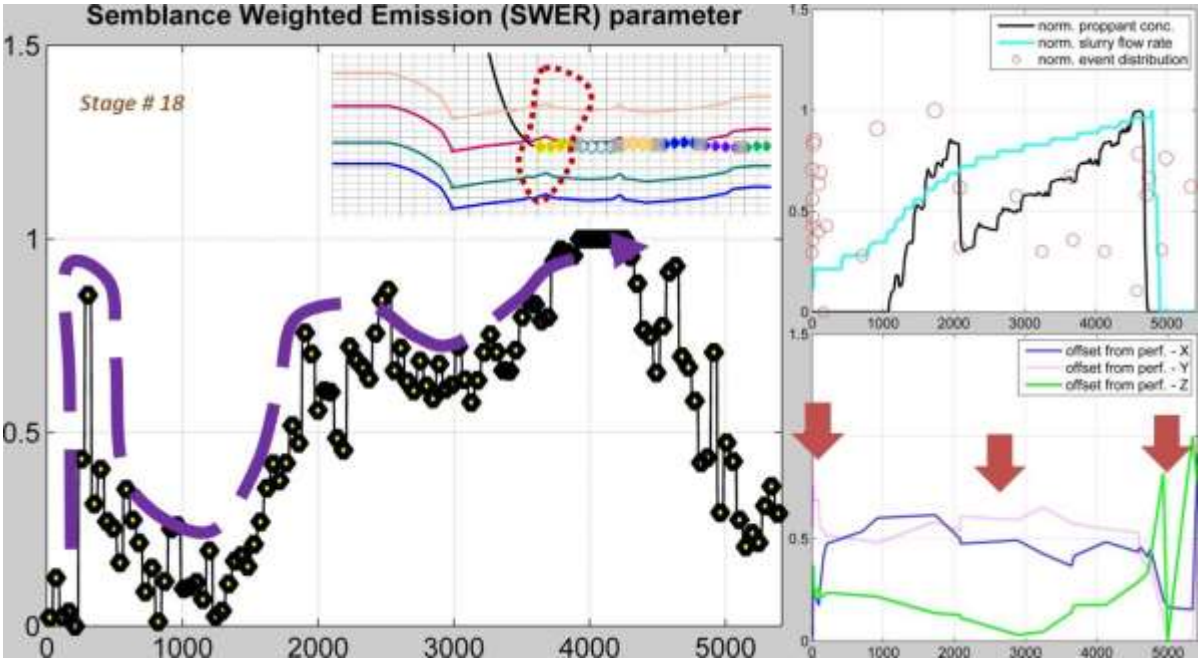

Figure 10: Mapped temporal SWE attribute along with the location of the well lateral w.r.t horizons, completion profile and observed seismicity for stage # 18 (WPX Energy Wootton 10H well).

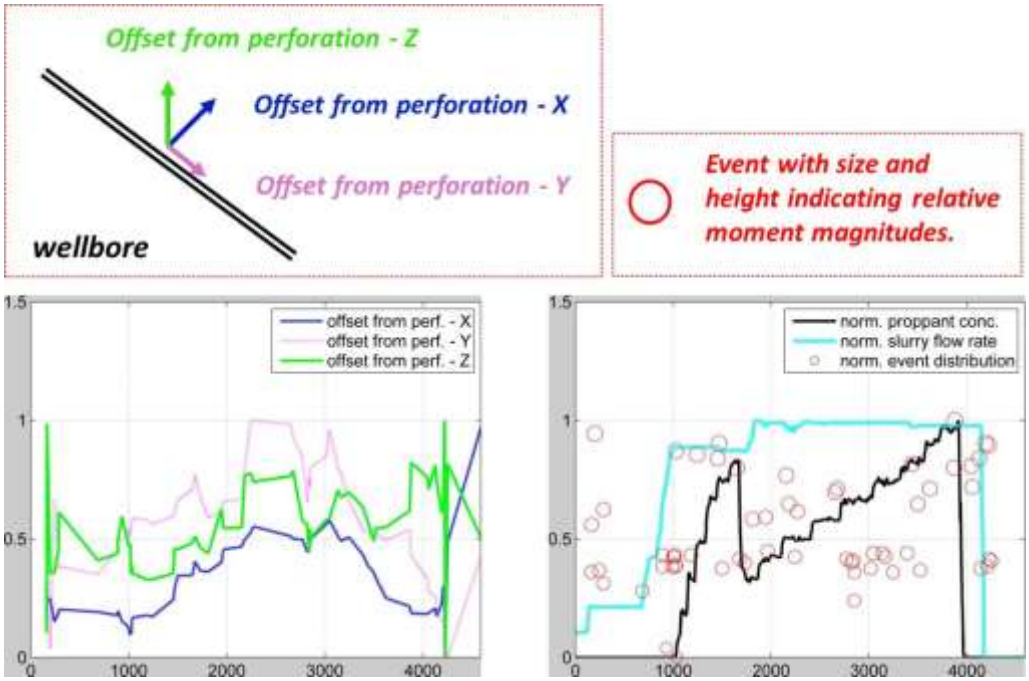

Figure 11: Nomenclature used in the diagnostic plots for reference.

Before getting into the discussion to interpret completions for this well, we look at Figure 11 which shows the nomenclature used in the diagnostics plots. Stage # 4 is in the middle of the highlighted horst structure bounded by faulting. Decline in overall emission but significant events observed during proppant injection indicate possible fluid and proppant loss issues (shear mode induced seismicity). This is further validated by the relatively higher X/ Y/ Z offsets from inversion results and the very low production contribution (2%) for this stage. Stage # 9 is in the middle of the target zone and the emission increases gradually with slurry but jumps significantly with the first proppant slug. A late period emission peak corresponds with the second proppant slug. The event distribution indicates initial far field events and late period seismicity occurring close to the wellbore but then fanning out. This stage shows a very high production contribution (20%) and is typical of most highly productive stages. For stage # 14, it lies very close to the boundary between target zone and overburden strata. We also observe an initial emission peak with slurry injection and subsequent peaks with the proppant slugs. The inversion results show initial and intermediate far field events and relatively low degree of seismicity close to the wellbore. The larger offsets and relatively low production contribution (3%) indicates possible fluid bypass issues. For stage # 18, we again have a stage close to the boundary between target zone and overburden. An initial emission peak is observed with slurry injection and subsequent peaks with proppant slugs. The event distribution indicates far field events during the treatment with very few near wellbore

emissions post injection initiation. Low production contribution (3%) indicates possible fluid bypass issues.

Conclusions

Our work demonstrates the potential use of emission profiling in improved understanding of efficacy of stages developed during hydraulic fracture stimulation programs. We have demonstrated the utility of the defined SWE attribute even for borehole microseismic datasets which are traditionally not considered adequate for imaging applications. Emission profiles derived from SWE attribute maps for stages can be used to diagnose treatments and can provide valuable information regarding fluid/ rock interaction. Moreover, near real time temporal SWE mapping in hydraulic fracturing programs can act as a handy QC tool to improve current/ future treatments. This is made possible with the use of relatively small aperture arrays (such as borehole deployments) and the need for temporal mapping at low resolutions leading to lower computational requirements (other microseismic source parameters can be identified later as desired using either imaging or inversion algorithms). It can allow us to identify potential fluid loss or other issues which can have a detrimental impact on stage productivity. Finally, SWE analysis can provide a robust template for predicting efficacy/ productivity of other wells in the vicinity of the test well without having to wait for well production data which could typically take a few years to allow for reliable time-rate analysis. However, this requires rudimentary microseismic monitoring to generate reasonable SWER attribute maps for wells under investigation and this concept will be validated in our future work.

Additional Work

While the proposed method works very well with time variant mapping of the said attribute, localization is space is highly challenging due to array aperture or “solid angle” limitations. In order to resolve this issue and to be able to model the attribute both temporally as well as spatially using borehole arrays, a modified directionally weighted SWE attribute is proposed. The semblance attribute is calculated in a manner similar to what has already been described under “Methods”. Azimuthal directions (Back-azimuth) as well as inclination (dip) are computed based on the observed polarization of P wave arrival. This limits applicability of this modified approach to those events with discernable P arrivals.

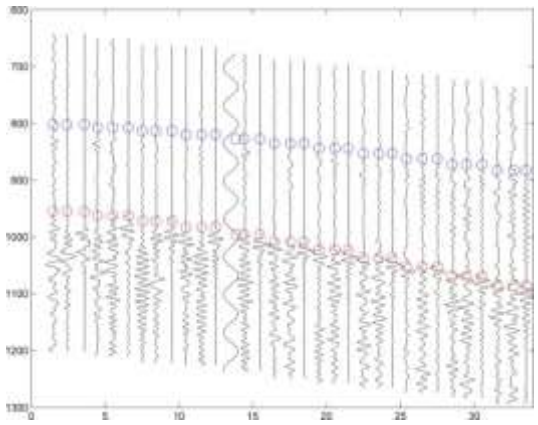

Figure 12: Blown up section of event gather showing the traces from 3 component records as well as identified P and S phase arrivals.

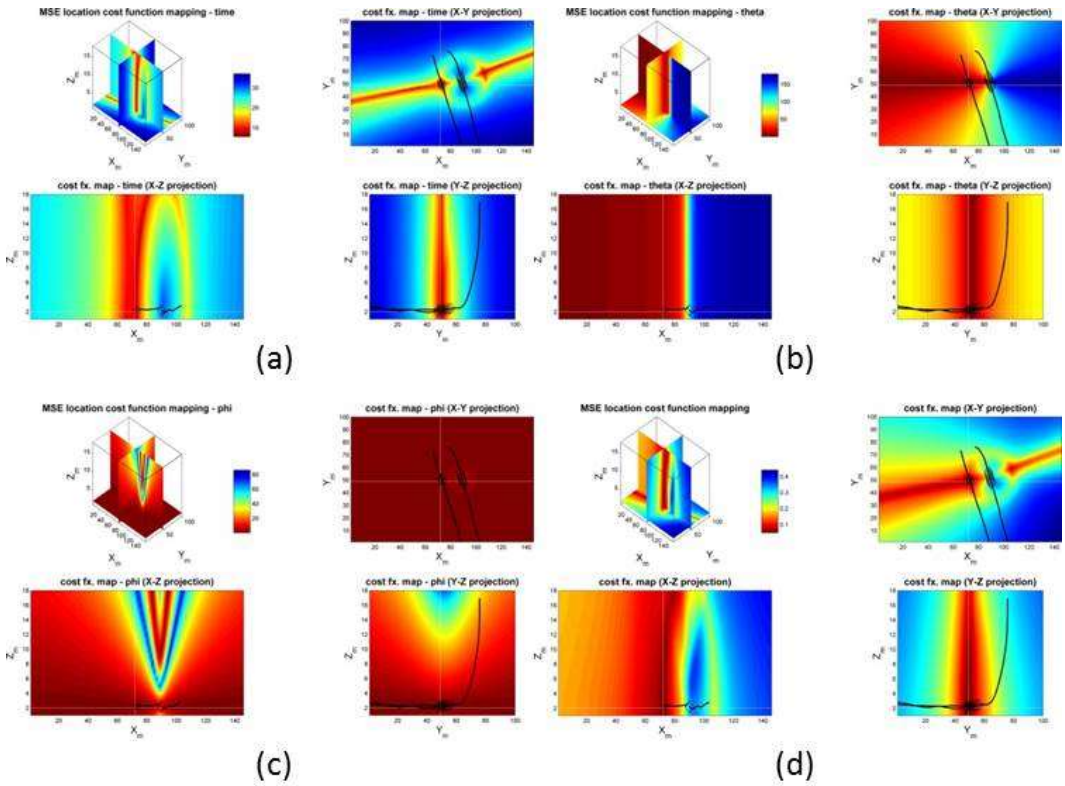

Figure 13: (a) Original semblance, (b) back-azimuth, (c) dip and (d) weighted semblance attributes highlighting the ability of using polarization to spatially map emissions.

Since the purpose is to minimize the modified objective function, the three parameters are separately normalized before combining them. The optimization search space comprises

Δt_{P-S}, $\Delta\theta$, and $\Delta\emptyset$ which are the mismatch between observed and predicted phase arrivals times, azimuths and take off angles. Semblance is weighted using the minimum baseline value measure based on white noise while the angles are normalized to 180˚. Figure 12 shows a sample event file with the original picks. Figure 13 shows the computed attributes including the weighted attribute. Figure 14 shows the identified event location based on the weighted attribute maxima. Figure 15 highlights a set of 7 events with discernable P wave arrivals tested from stage # 11 of well 10H.

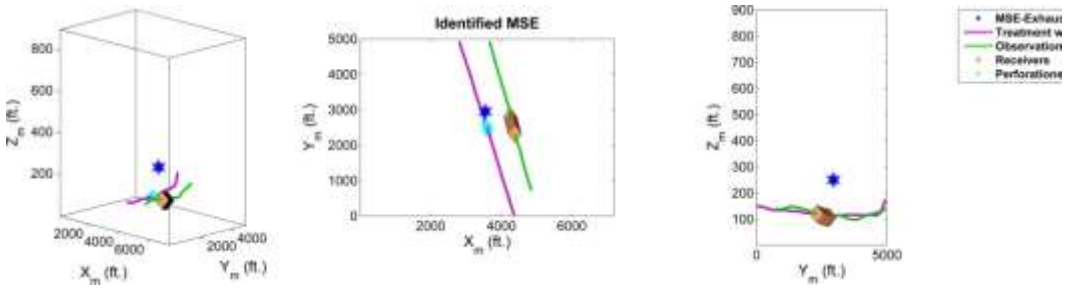

Figure 14: Identified event location by maximizing directionally conditioned SWE attribute.

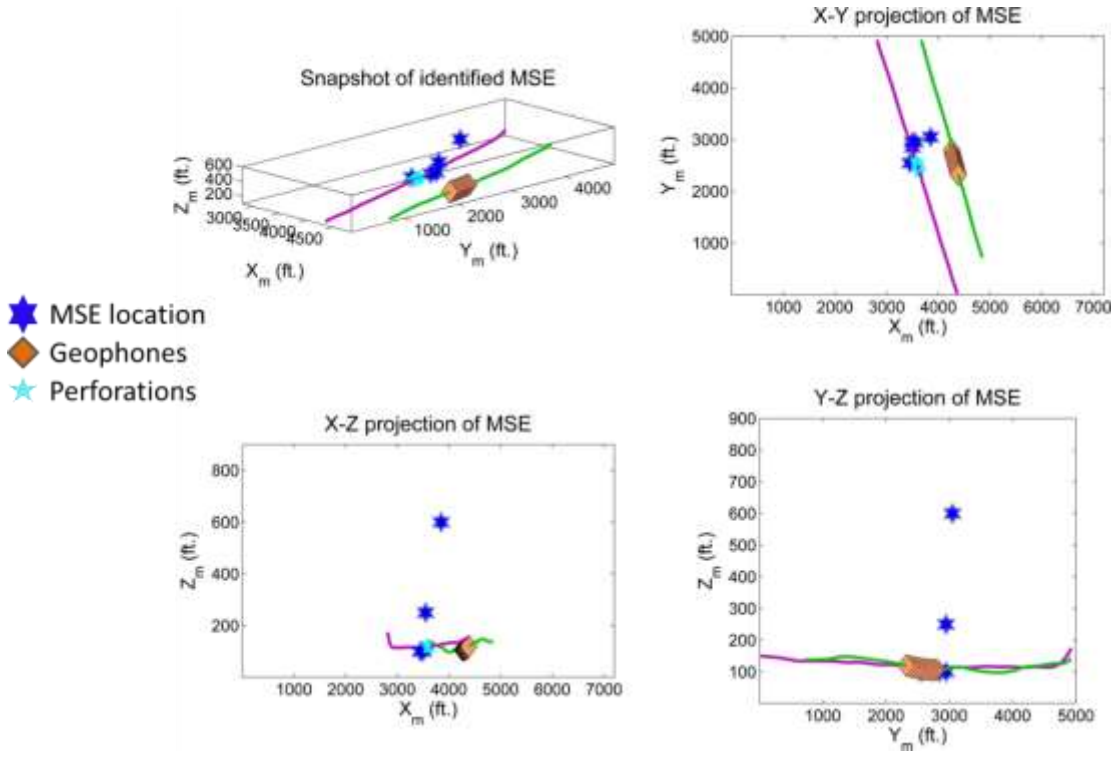

Figure 15: Identified event locations from processing data subset from Wootton 10H completion data (Stage # 11).

References

[1] Chebotareva, I. Y., 2010, New algorithms of emission tomography for passive seismic monitoring of a producing hydrocarbon deposit: Part II. Results of real data processing: Physics of the Solid Earth, 46, no. 3, 199 – 215. doi: 10.1134/S1069351310030031.

[2] Geiser, P., A. Lacazette, and J. Vermilye, 2012, Beyond 'dots in a box': an empirical view of reservoir permeability with tomographic fracture imaging: First Break, 30, no. 7, 63 – 69.

[3] Kao, H., and S. Shan, 2004, Source scanning algorithm: mapping the distribution of seismic sources in time and space: Geophysical Journal International, 157, no. 2, 589 – 594, doi: 10.1111/j.1365-246X.2004.02276.x.

[4] Lakings, J. D., P. M. Duncan, C. Neale, and T. Theiner, 2006, Surface based microseismic monitoring of a hydraulic fracture well stimulation in the Barnett Shale: 76th Annual Meeting, SEG, Expanded Abstracts, 605 – 608. doi: 10.1190/1.2370333.

Appendix G: Novel Phase Arrival Detection Workflow

Summary and Accomplishments

We have developed a hybrid event detection workflow which has significantly enhanced detectability of events from borehole data for potential data processing and analysis. This workflow has been extensively tested on microseismic data collected from the WPX Energy Wootton well 10H experiment and preliminary results indicate significant improvement over traditional picking approaches.

Motivation

Most Microseismic event detection algorithms suffer from the issue of noise artifacts in data. Sometimes, noise can be overbearing and can significantly reduce the number of detected events which has an impact on post processing microseismic data analysis. While full waveform based inversion can remove the need to make event/ phase picks, their use is still significantly impacted by noise. We propose a new methodology which makes use of an evolutionary search method to iteratively search for arrivals as recorded by geophone strings in borehole. This allows the process to only model for predictable hyperbolic moveouts which can be modeled as a higher order polynomial.

Introduction

Microseismic monitoring has become an integral part of most unconventional resource development programs. They have found wide utility in reservoir monitoring as well as resource characterization studies. Phase arrival information is critical in identifying other microseismic source parameters of relevance such as event size and hypocentral location. One of the most common algorithms for detection is the short term averaging / long term averaging (sta/lta) algorithm. Methods based on abrupt changes in attributes of the seismic waveform such as higher order statistics (skewness & kurtosis by Saragiotis et al., 2002) have also seen use. Modern autopickers can use advanced techniques such as cross-correlation analysis, parallelized filters or robust statistical techniques. Noise artifacts can cause autopicker efficacy to gradually degrade though the effect of different types of noise on different autopickers can vary significantly. For downhole sensor deployments, the quality of the first arrival picking is related to sub- surface structure (such as velocity contrasts and layering), source type, receiver geometry, and finally, downhole noise conditions. These factors can lead to complicated wave-trains (such as head

waves and reflections) and require human intervention to prevent miss-picks. Finding a robust methodology to work under extreme noise conditions is a major challenge.

In this research we use a robust hybrid neural network autopicker (Maity et al., 2014) to make initial pick estimates. Then we use an evolutionary algorithm to make the best possible arrival detection based on the initial pick estimates. The basic assumption behind the suggested approach is that moveout behavior is predictable as it is hyperbolic and can be approximated using a high order polynomial function. The algorithm has been extensively tested on real microseismic monitoring data from multiple gas well completions in the Marcellus shale reservoir and the results have been compared with contemporary autopickers in use by the industry to validate, both qualitatively as well as quantitatively, the applicability of our proposed approach. The use of genetic algorithms allows for optimized search and rapid detectability even for extremely large gathers (hundreds of data channels).

Method

Neural network based autopicking algorithm

A robust neural network based autopicking workflow using evolutionary training approach is used to make initial pick estimates. In brief, the workflow involves pre-processing steps such as noise removal through application of frequency filters, data rotation to maximize phase arrival energy on corresponding components, etc. A small representative subset is then carefully selected from the data for training purposes. For network input design, multiple seismic data attributes are evaluated (such as wavelet transform, statistical measures, or available autopicker algorithms, etc.) and redundant attributes are pruned by evaluating a windowed cross-correlation measure across known arrivals for different attribute pairs and pruning attribute from those pairs showing very high correlation and those which are computationally more expensive. A neural network is used to map the input attributes to an output characteristic function which has highs of 1 at the phase onsets and 0 otherwise. The data subset selected is subdivided into training, validation and testing sets using statistical measures such as mean and skewness of distribution. The nodal inputs to the network are defined by the selected attributes. The hidden layer is designed is selected based on the number of input and output layer nodes. An evolutionary algorithm is used for network optimization. The output characteristic function as obtained by applying the trained network on any dataset is used for pick selection as required and we will call this function as AP1 for future reference. While a more detailed discussion on the exact workflow is beyond the scope of this paper, Maity et al. (2014) provides a detailed understanding of the autopicking workflow used for this study and can be used as a reference.

Contemporary picking algorithms

Two contemporary autopicking algorithms were tested in a comparative framework along with the proposed hybrid AP2 workflow in order to test and benchmark its performance. The first method used was the FilterPicker algorithm which involves multiple filters operating in parallel. The final picker characteristic function involves calculating the envelope from a derived function which combines the results from each filter. The first step is to calculate first differences followed by two 1-pole high pass filters and one 1-pole low pass filter.

$$x'(i) = x(i) - x(i-1) \tag{1}$$

$$y_m^{HP1}(i) = c_m^{HP}[y_m^{HP1}(i-1) + x'(i) - x'(i-1)] \tag{2}$$

$$y_m^{HP2}(i) = c_m^{HP}[y_m^{HP2}(i-1) + y_m^{HP1}(i) - y_m^{HP1}(i-1)] \tag{3}$$

$$y_m^{LP}(i) = y_m^{LP}(i-1) + c_m^{LP}[y_m^{HP2}(i) - y_m^{HP2}(i-1)] \tag{4}$$

The filter coefficients c_m^{HP} and c_m^{LP} used in equations (2), (3) and (4) are defined as

$$c_m^{HP} = \frac{W_m}{W_m + \Delta t} \tag{5}$$

$$c_m^{LP} = \frac{\Delta t}{W_m + \Delta t} \tag{6}$$

The weighting factor w_m and associated corner period T_m used to compute filter coefficients are defined as

$$W_m = \frac{T_m}{2\pi} \tag{7}$$

$$T_m = 2^m \times \Delta t \tag{8}$$

The envelope and the characteristic functions are computed for each band '*m*' as

$$e_m(i) = y_m^2(i) \tag{9}$$

$$a_m(i) = \frac{e_m(i) - \langle e_m \rangle (i-1)}{\langle \sigma e_m \rangle (i-1)} \tag{10}$$

Where $\langle e_m \rangle$ is the time average and $\langle \sigma e_m \rangle$ is the standard deviation average calculated till "*i*-1" index from the envelop. The band for "*m*" is chosen such that there is atleast one final t_m value which is greater than the dominant period from the original data. The final autopicker characteristic function at any index "*i*" is the maxima from the derived characteristic functions

from equation (10). Lomax, Satriano and Vassallo (2012) provide a very detailed understanding of the FilterPicker workflow.

The other picking algorithm used is the standard "sta/lta" averaging method as implemented within microseismic monitoring (MIMO) package developed by NORSAR. The signal detections or first break picks are made based on signal-to-noise ratio crossing predefined threshold and falling back below threshold within a reasonable time interval. For the ratio, the short-term average (sta) is computed as

$$sta(i) = \frac{1}{l} \times \sum_{j=1}^{l-1} |x(i-j)| \tag{11}$$

Here "l" is the product of sampling rate of the data and the defined short term window length. The recursive definition of the long-term average (lta) is

$$lta(i) = 2^{-\zeta} \times sta(i-\varepsilon) + (1 - 2^{-\zeta}) \times lta(i-1) \tag{12}$$

Here "ε" is the time delay and "ζ" is a steering parameter for "lta" update rate. Oye and Roth (2003) provide a detailed understanding of the picking and phase detection algorithm used within MIMO package. In brief, the phase onsets are computed based on signal at onset and noise interval and the coefficients of an autoregressive model for noise characteristics are computed and used for error-prediction filtering and computation of Akaike information criteria (AIC) function for onset time determination. The "aic" method assumes that the intervals before and after onset time are two separate stationary processes. The "aic" characteristic function for a seismic trace is computed as follows (Maeda 1985):

$$aic(i) = i \times log\{var(x[1:i])\} + (N - i - 1) \times log\{var(x[i+1:N])\} \tag{13}$$

Here the seismogram **x** has a length N and the onset is the point where the characteristic function has a minimum value. Additional quality control and pick refinement steps within MIMO were not used for this study.

Pick refinement

Based on the output map obtained from any of the mentioned picking workflow, we expect higher values of characteristic function to be indicative of possible pick locations and vice versa. The picking approach involves time averaging of the autopicker characteristic function before using limiting thresholds predefined by the user. As the average moves beyond the defined threshold, a possible pick is declared and then a check is made to ensure that the time averaged value of the characteristic function falls below the defined threshold before a second pick can be considered. Once a pick is declared, the algorithm selects the peak (local maxima) on the picker

characteristic function as potential pick location within the defined pick window (as obtained based on when the value of the time averaged characteristic function rises above and falls below predefined thresholds). A quality control mechanism can be used which checks for ratio of two statistical measures (mean and maximum) across the pick within the identified pick window and picks are quality controlled based on these ratios.

Evolutionary search for optimal pick across gathers

Before final detection using evolutionary search, misclassified picks can be removed if necessary using a weighted pick density criteria which is evaluated for each pick. This criteria and its use is based on the fact that for borehole geophone strings, the moveout is smooth across the gather for seismic events. This indicates that if a pick is located accurately enough, it should be straddled with other picks in close proximity. The density measure is computed for i^{th} trace by using a weighted summation approach along each pick within a predefined evaluation window as

$$\tau_P(i) = \sum_{j=i-N}^{i+N} \sum_{k=\tau(j)-win}^{\tau(j)+win} AP1_{j,k} \tag{14}$$

Here, N defines the traces close to the evaluation trace for calculation which can include all traces across gather. The variable k allows for summation over a predefined window size where presence of other picks increases pick density. This measure is normalized based on the observed maximum and minimum over all picks made using AP1 characteristic function. Finally, the picks associated with the lower n^{th} percentile of the density distribution are pruned as erroneous provided the evaluated signal to noise ratio taken cumulatively for all traces is reasonably low. Figure 1 shows a sample gather with the initial picks and the final pruned picks using this measure. For this study, we use a cutoff at 10^{th} quantile, i.e., any pick location with a probability falling below the 10^{th} quantile of associated probability function is removed.

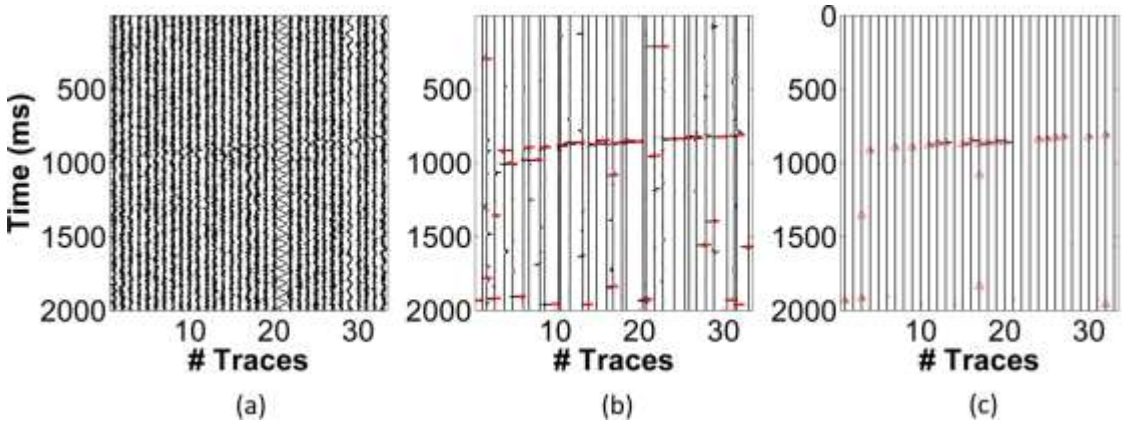

Figure 1: Subplot (a) shows the recorded gather without any processing, (b) shows the AP1 output (picker characteristic function) and preliminary picks while (c) shows the pick probability map and refined picks. The red inserts show the pick location for subplots (b) & (c).

With the picks from the refinement step available for analysis, evolutionary search can be applied to detect events across gather. As indicated earlier, this technique is only applicable for borehole data or with surface data where moveout behavior can be approximated by a high order polynomial function. We use a genetic algorithm which mimics the theory of evolution by natural selection wherein the less fit individuals from each generation are selectively eliminated before a new generation is created. This selection is an iterative process where an objective function is used to evaluate the fitness of each individual in the population and new generations are obtained by probabilistically selecting fitter individuals from current generation. The fitness function is a weighted summation of individual functions relating to minimizing the mean squared error based on the misfit for each pick as well as number of qualified "good picks" identified as those relatively close to the polynomial fit. This closeness is evaluated based on the quality of each pick (the local maximum of the AP1 characteristic function) and the Euclidean distance between the AP1 pick and polynomial fit value. Function "τ" is the final optimization function to be minimized.

$$\theta(x) = 1/\sum_{i=1}^{no.of\ traces} [AP1\_pick_i - fit\_value_i]^2 \quad (15)$$

$$\phi(x) = 1/[\#good\ picks] \quad (16)$$

$$\tau(x) = 1/[\phi(x) \times \theta(x)] \quad (17)$$

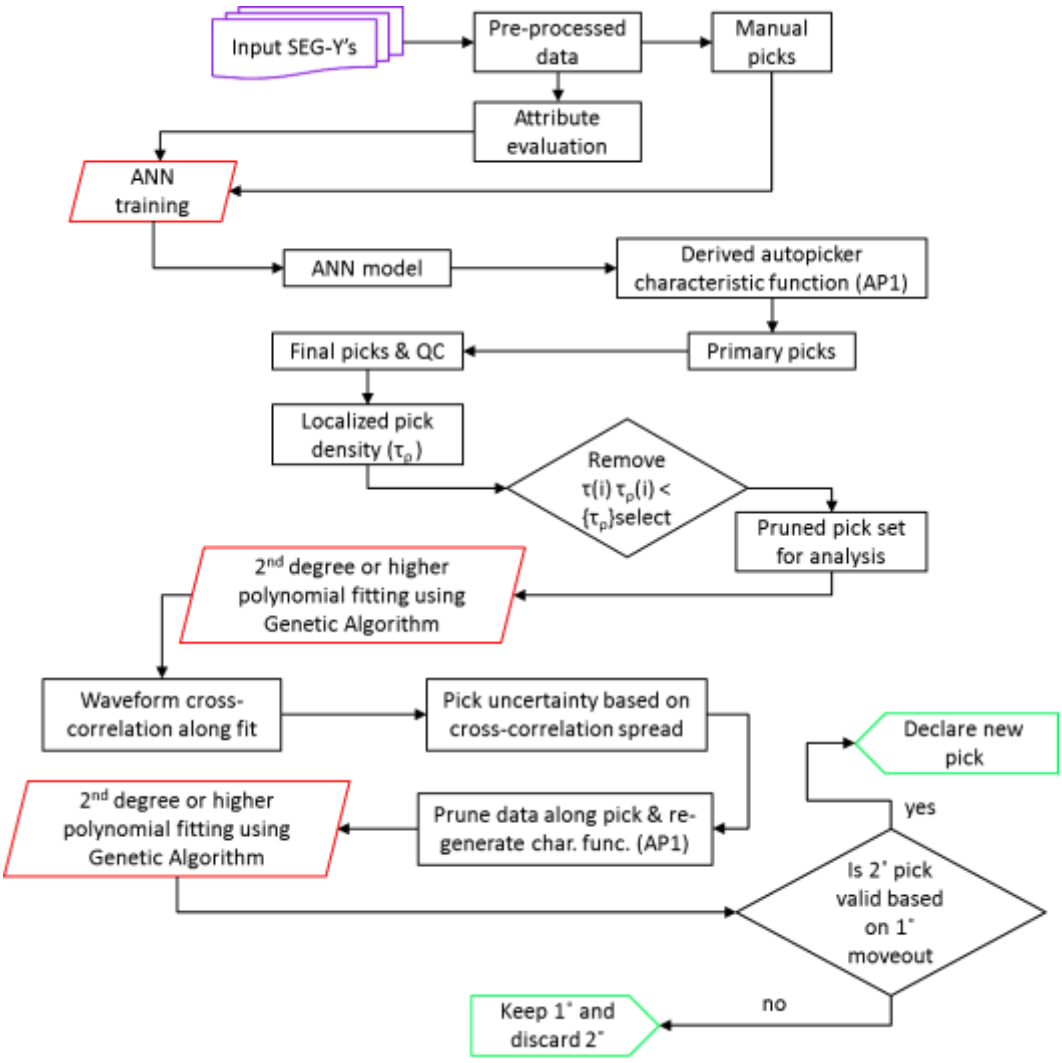

Figure 2: Initial picking and event detection workflow for datasets with predictable moveout.

Beyond these optimization functions, certain hard constraints on fitting can also be used including the concave down condition based on the survey geometry and a constraint of maximum moveout (fit curvature) based on the expected source-receiver separation which also helps remove potential far field events (such as noise artifacts) not associated with the actual hydraulic fracturing treatment. Some members of the parent population are also subjected to genetic operators such as cross-over and mutation to generate new offspring. In short, the fitness function used tries to identify the best possible polynomial fit through the initial picks available provided the error in mismatch is reduced but at the same time, better picks (as per quality of the initial picks) are more heavily weighted through higher scoring of the individuals. A probability measure is used to decide on the percentage of individuals from parent population that will be copied (while the rest undergo cross-over). This probabilistic selection is implemented through a rank selection process where the probability of selection of individual is

inversely proportional to its position in the sorted population list based on fitness. Once selection is made of the candidates for crossover, the operation involves a random subpart from the parent pair being swapped to generate two offspring pair. A uniform crossover technique is used for this study. Finally, a relatively small portion of the offspring population is chosen at random and a randomly chosen bit is flipped in the selected population set to generate a mutated offspring. In order to reduce crowding effects (where similar individuals crowd a population set), fitness sharing strategy is implemented which rescales the evaluated fitness based on the number of similar individuals in a population. The entire workflow involving initial picking followed by evolutionary search for best pick has been described in Figure 2 for reference.

We also measure uncertainty in arrivals by assuming each pick to be accurate and estimating the location of the best pick along other traces with the assumption that the waveforms for all traces at arrival should be similar. This sliding window cross-correlation analysis method allows isolating events with high uncertainty observed as wider spread for cross-correlation maximums. Figure TTT shows two sample traces with high/ low noise artifacts leading to higher/ lower arrival uncertainty as measured with all other traces within the event gather.

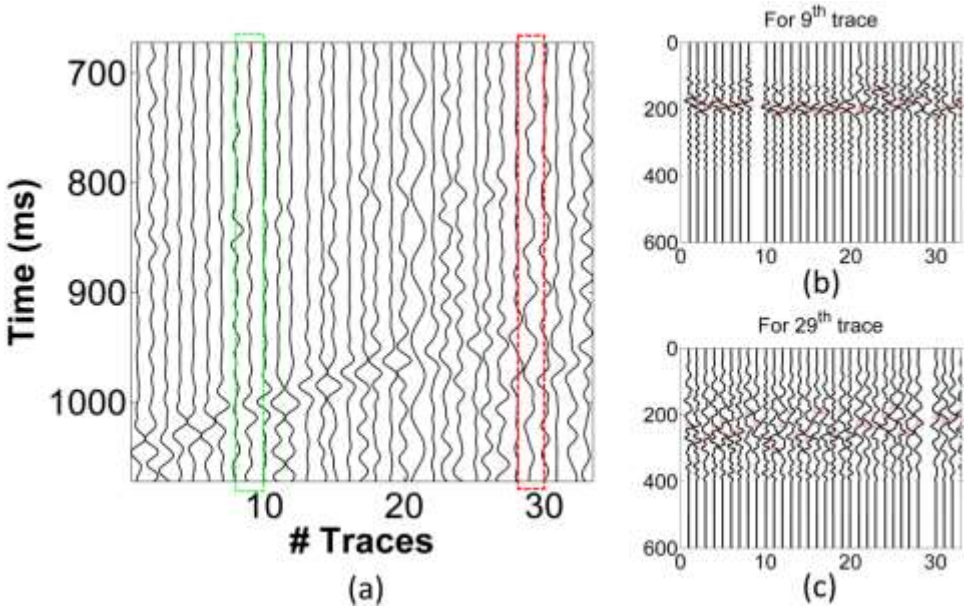

Figure 3: Subplot (a) shows a sample gather with a relatively noisy (29th) and a relatively noise free (9th) trace. Subplots (b) & (c) show cross-correlation results with rest of the traces in the gather at arrival for said traces.

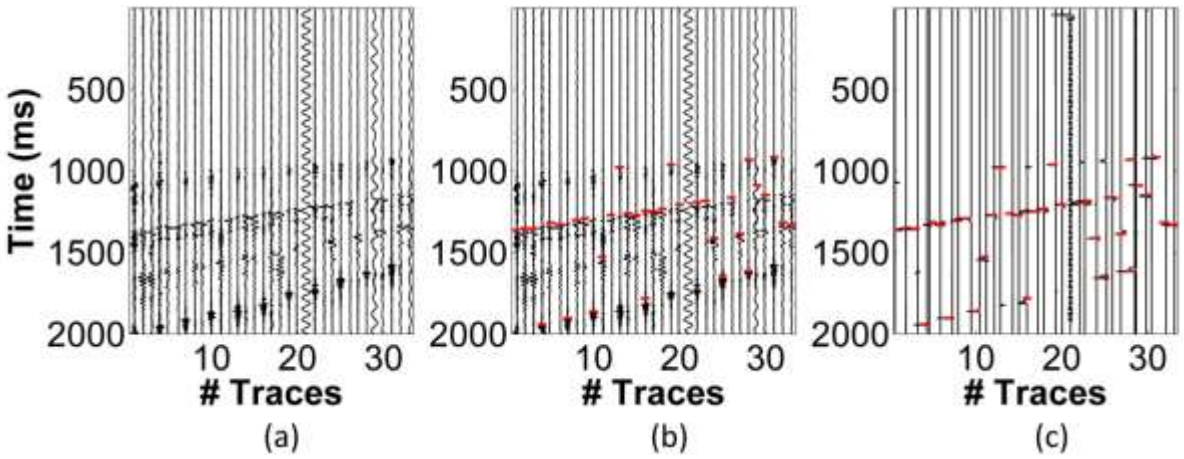

Figure 4: Sample event file showing multiple arrivals with subplot (a) showing the original data, (b) showing band pass filtered data and (c) showing the AP1 picker characteristic function. The red inserts indicate the initial observed picks.

Case study

Let us consider a sample event detection of relatively high signal-to-noise ratio (approximately 10) data and understand the results from the detection workflow as observed. Based on the initial picking algorithm (AP1), picks are made across the gather as observed in Figure 4. We note that each trace is assigned a unique pick based on the maxima observed with the AP1 characteristic function (Figure 4c). This can be modified to allow for multiple picks along each trace based on AP1 derived characteristic function's local behavior. We also note that this event has multiple phase arrivals which are most likely a result of two temporally separate events (by approximately 0.6 seconds).

Based on the initial picks identified by AP1, an initial fit is obtained so as to randomly fit all of the identified picks (Figure 5a). The polynomial fitting routine using an evolutionary algorithm for optimization is run so as to minimize the objective function.

The final pick location is selected based on local maxima in AP1 characteristic function close to the final identified polynomial fit and the pick uncertainty is defined based on a secondary cross correlation analysis close to the identified picks across the gather. Figure 5b depicts the optimization process for the sample event with the iterative search process to identify the optimal pick.

Once the primary pick has been identified, the workflow reruns the AP1 algorithm for segmented data sections before and after the identified pick to detect secondary arrivals. In case an arrival

is detected before the first pick onset, the primary is classified as S phase pick and the new secondary detection is classified as P phase pick. Figure 6 shows the initial estimate using the segmented dataset and the iterative search process leading to optimal secondary detection. Both primary and secondary fits seem to be more or less linear with the primary showing a smaller slope (~ -8) compared with the secondary pick (~ -5.7). This is expected since the primary pick is actually the S phase onset which should show a higher slope due to slower shear velocity. Moreover, the primary pick shows a higher constant (arrival at 1st trace) compared to the secondary pick as expected.

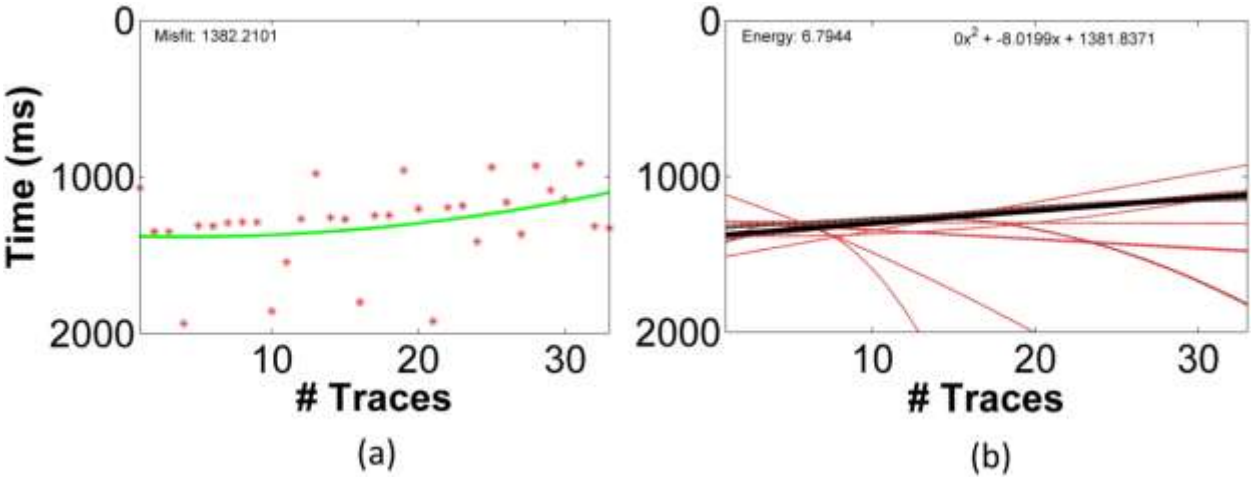

Figure 5: (a) Initial fit before evolutionary search and (b) final search results [black] after iterative optimization of cost function for the primary detection.

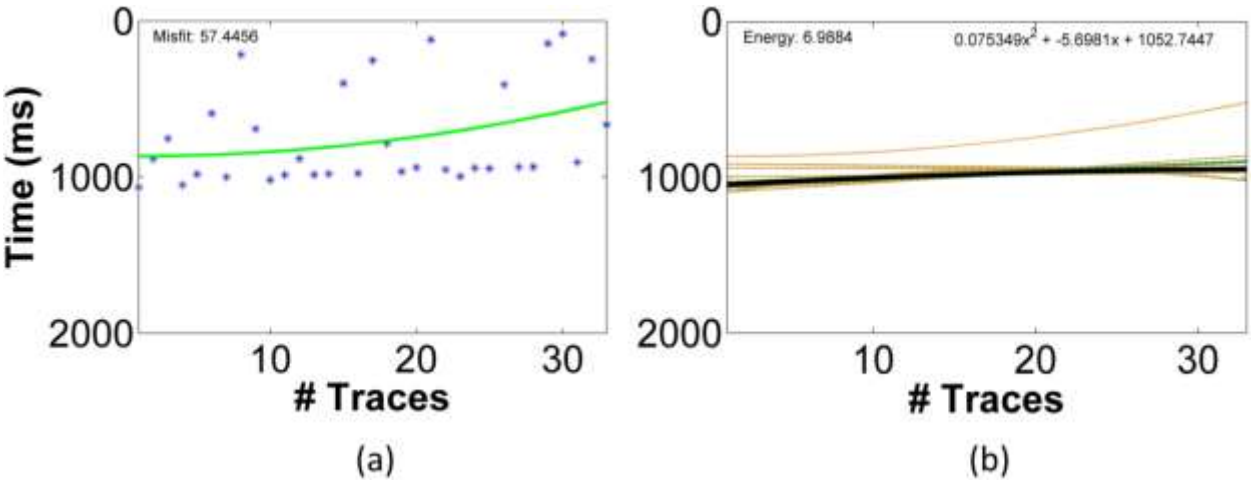

Figure 6: (a) Initial fit over segmented data before evolutionary search and (b) final search results [black] after iterative optimization of cost function for the secondary detection.

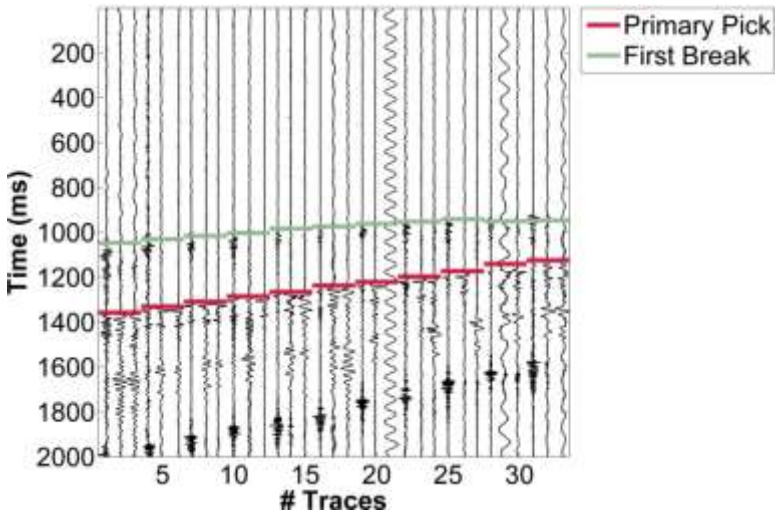

Figure 7: Primary and secondary (first break) arrivals for the reference event showing more robust primary arrival compared to the secondary detection.

The final picks (primary S phase and secondary P phase detection) are shown in Figure 7. We observe relatively accurate P and S phase arrival detection with maximum absolute error in arrival observed as approximately 24 ms and the average error in arrival observed at approximately 7 ms. This seems reasonable for an automated picking workflow which does not include any post detection pick refinement and also does not try for any significant noise reduction prior to picking. However, the sample event shared has relatively high signal to noise ratio and the results should degrade with increased noise.

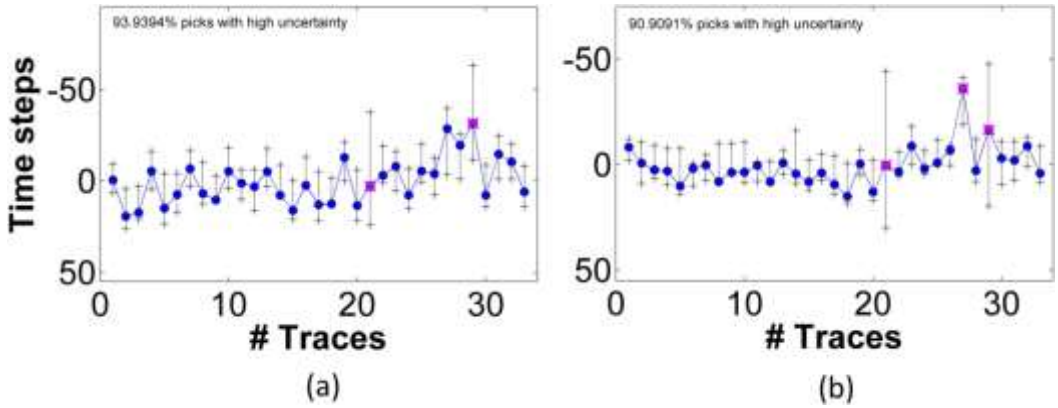

Figure 8: Pick uncertainty estimates with the blue dots showing mean of the spread and vertical bars showing the uncertainty spread. Plot (a) shows pick uncertainty estimates for the primary and (b) shows uncertainty estimates for secondary pick. Picks with relatively high uncertainty are tagged with a cross.

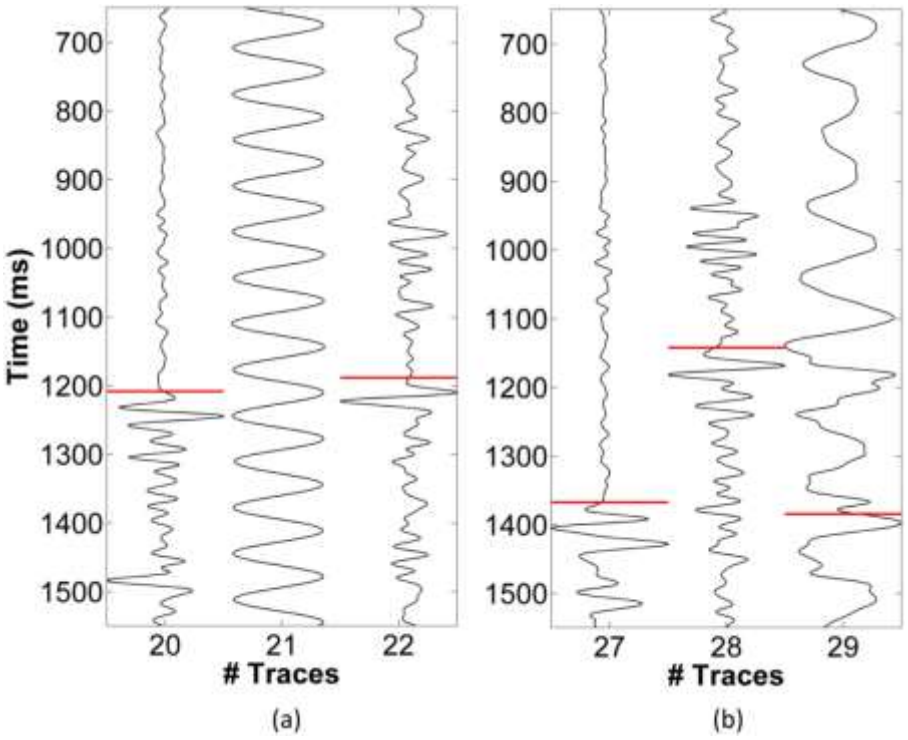

Figure 9: Blow up sections showing trace # 21, 27 and 29 highlighting high uncertainty in S phase (trace # 21 & 29) and P phase (trace # 21, 27 and 29) arrivals.

Looking at the uncertainty estimates for both P and S phase arrivals made for the sample event trigger (Figure 8), we observe high uncertainty for picks on traces 21 and 29 for primary and for picks on traces 21, 27 and 29 for secondary detection. This uncertainty is highlighted through the trace display (Figure 9) which includes the original picks made using the AP1 picker. Trace 21 is observed to be instrument noise, trace 27 has relatively small first break arrival energy and trace 29 has low frequency noise artifact causing high pick uncertainty. Based on the uncertainty estimates and the percentage of uncertain picks classified per event detected, a picked event is declared for comparative analysis.

Results

While the case study discussed highlights a single event file with relatively high signal to noise ratio, the strength of this methodology lies in its ability to isolate hard to detect noisy microseisms. This workflow was applied on monitoring data from multiple hydraulic fracturing stages (> 18) from a few Marcellus gas wells. In this discussion, we limit ourselves to a very small subset (20 event trigger files with a total of 660 traces) of this large dataset for a comprehensive analysis involving visual inspection and manual phase picking as well as comparisons with

available open source contemporary event detection algorithms. Of these 20 files, we share 4 event files in this document to highlight the robustness of this detection workflow. Figure 10 shows four sample event files from this data subset under study and we can clearly see events with moderate to very low signal-to-noise ratios for P phase onset, wave reflection/ interference artifacts as well as potential survey geometry related artifacts. These events depict typical microseismic detections in borehole environments where poor instrument clamping causes low signal strength and potential borehole noise artifacts.

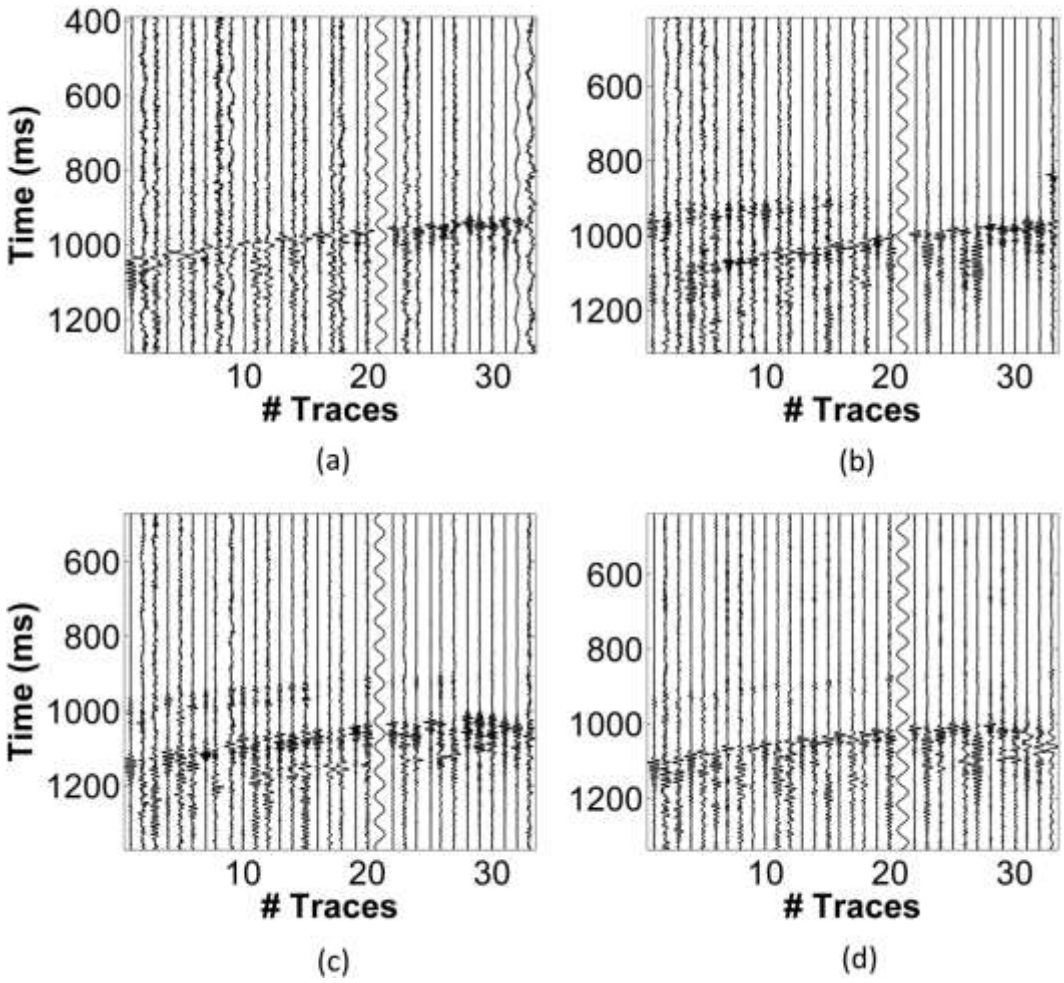

Figure 10: Four sample events showing the arrivals of both P and S phase energy at the geophones. For subplots (a) and (d), the P phase energy onset is very hard to detect. For subplots (b) & (c), the acquisition geometry leads to partial moveouts for P phase energy onset.

The same workflow as discussed under the case study is applied to this data subset and the workflow detects both primary and secondary arrivals for the four sample events shown. Figure 11 shows the detections and highlights the robustness of the automatic event detection routine under relatively low signal-to-noise ratio conditions. We note that in all of the four examples shows, the primary detection is a late period S phase energy arrival while the secondary detection is the first break or possibly P phase arrival. This is expected in borehole environments where S wave is typically the most energetic and shows most strongly on the gathers.

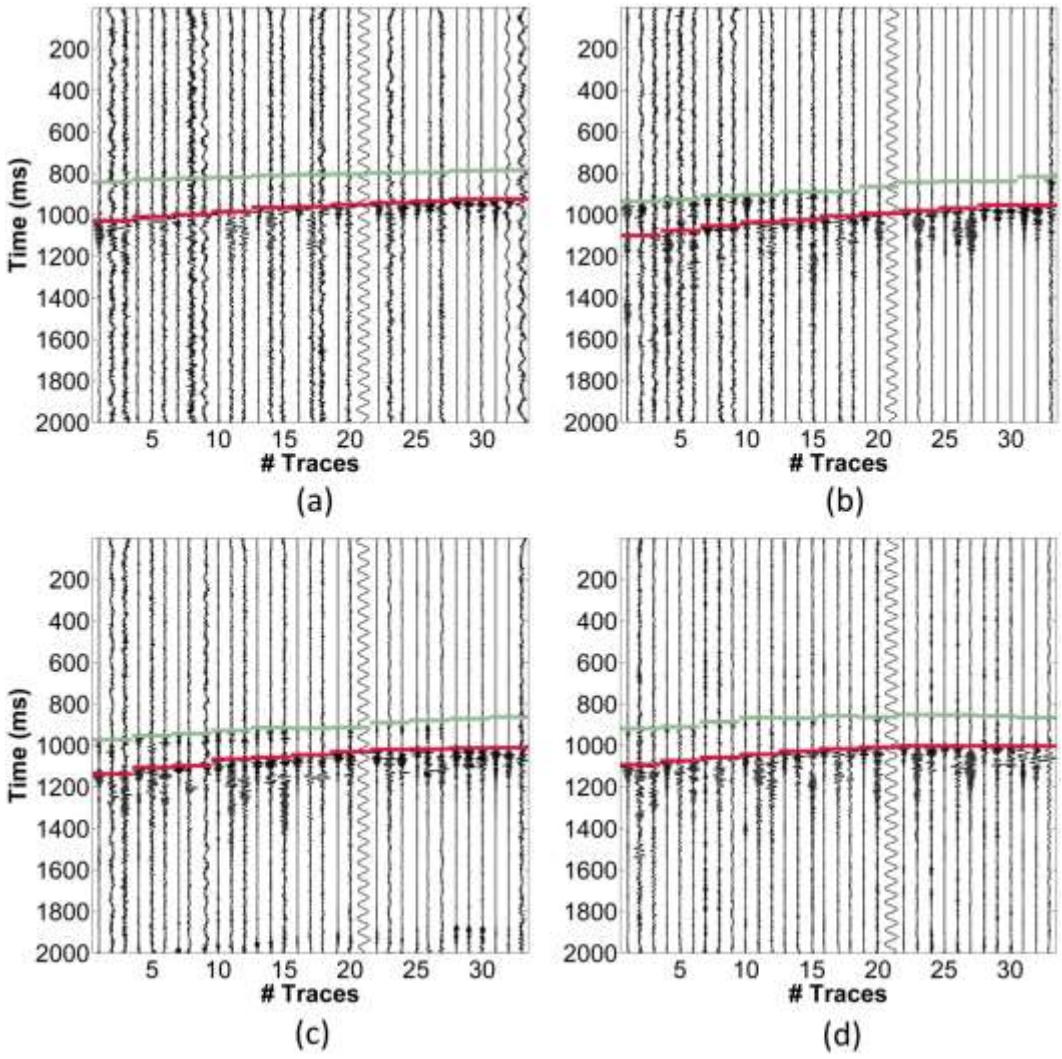

Figure 11: Final phase detections for the four selected events showing both primary and secondary detection. The algorithm works in situations where propagation geometry creates lower energy onsets for sections of the event gather (subplots b & c) or where attenuation leads to lower P phase onset energies (subplots a & d).

For event gathers with propagation artifacts, the devised detection strategy iteratively moves towards the actual arrival based on a limited number of accurate phase detections clustered along the gather. This is highlighted with the plot of the updates observed during evolutionary search for two such sample events (Figure 12).

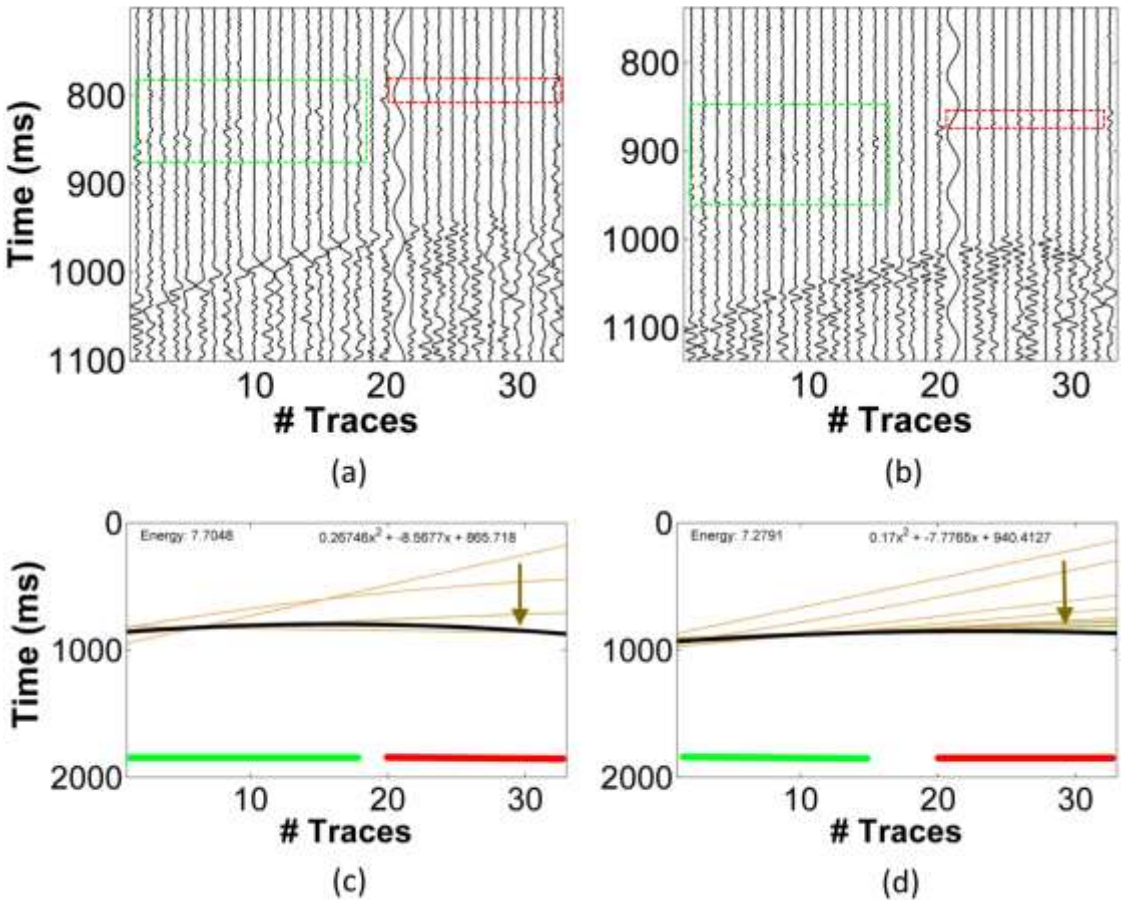

Figure 12: Two sample iterative optimization runs with the final event detection (black inserts) shown as subplots (c) & (d) as they correspond with arrivals shown in subplots (a) & (b). The green section highlights zone with relatively accurate preliminary detections based on AP1 and red inserts show sections of the gather with relatively poor fit or no AP1 derived picks. The arrows highlight the direction of best fit with successive iterations hm.

The results obtained with this workflow (AP2) were compared with the original picks made using the AP1 algorithm as well as two other contemporary event picking algorithms (FilterPicker and MIMO). For comparative analysis, manual picks were made (both P and S phase arrivals) for the

entire data subset under study. Then, the offset of picks from each algorithm was compared with the baseline manual pick. This was done for all picks made provided a corresponding manual pick was available for comparison. The total picks possible for each event gather is 66 (33 P phase picks + 33 S phase picks) giving us potentially 660 P phase picks and 660 S phase picks for analysis. Since all picks could not be identified manually with desired accuracy, the actual number of picks compared was considerable lower (more so for P phase arrivals).

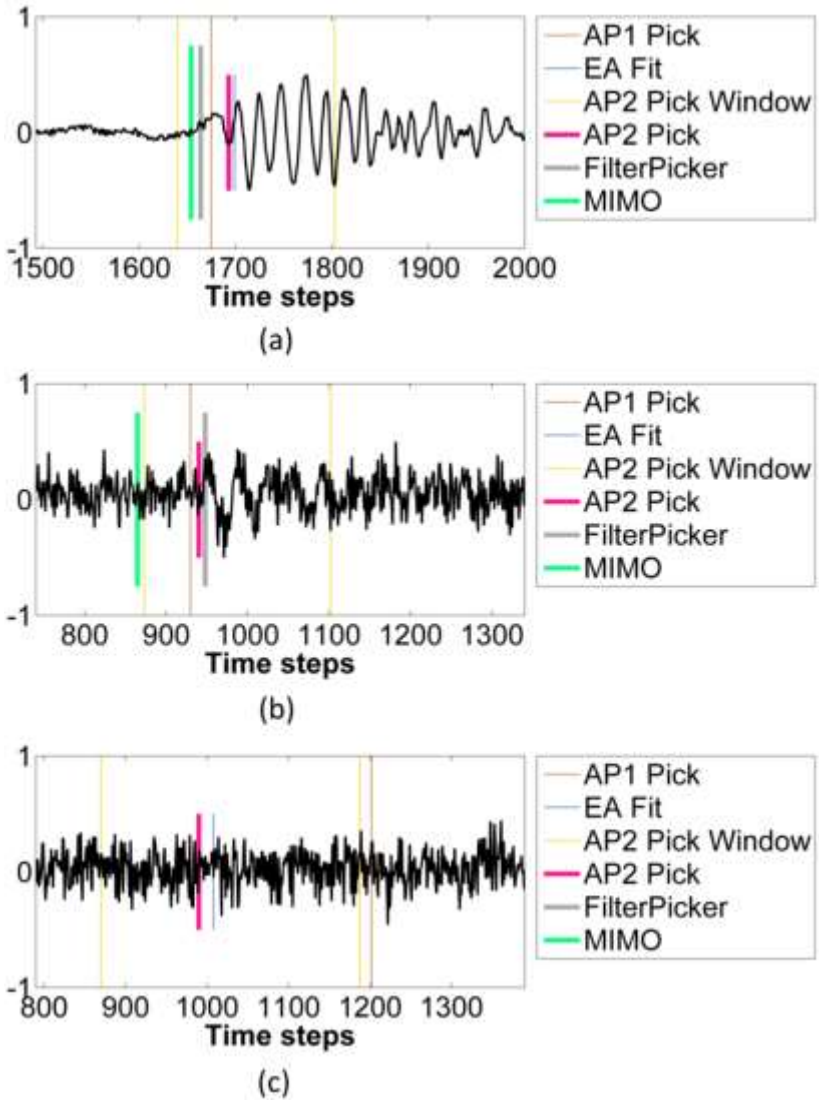

Figure 13: Sample trace blow out sections highlighting the energy arrivals and the corresponding picks made by algorithms under study for a (a) high signal-to-noise, (b) moderate signal-to-noise and (c) very low signal-to-noise test cases.

Figure 13 shows examples of both very high and very low SNR event and the results from the picking routines used in the study. We observe the proposed workflow to perform reasonably

well even in situations where the contemporary routines fail to make a usable pick or make erroneous arrival detections (Figure 13c). With the hybrid detection workflow (AP2), both primary and secondary picks are assigned if the algorithm is able to successfully detect them. However, this may not always be the case, in particular where we have relatively low signal to noise ratios. Figure 14 shows the total P and S phase detections made by the four methods and how they compare with total number of manual picks available.

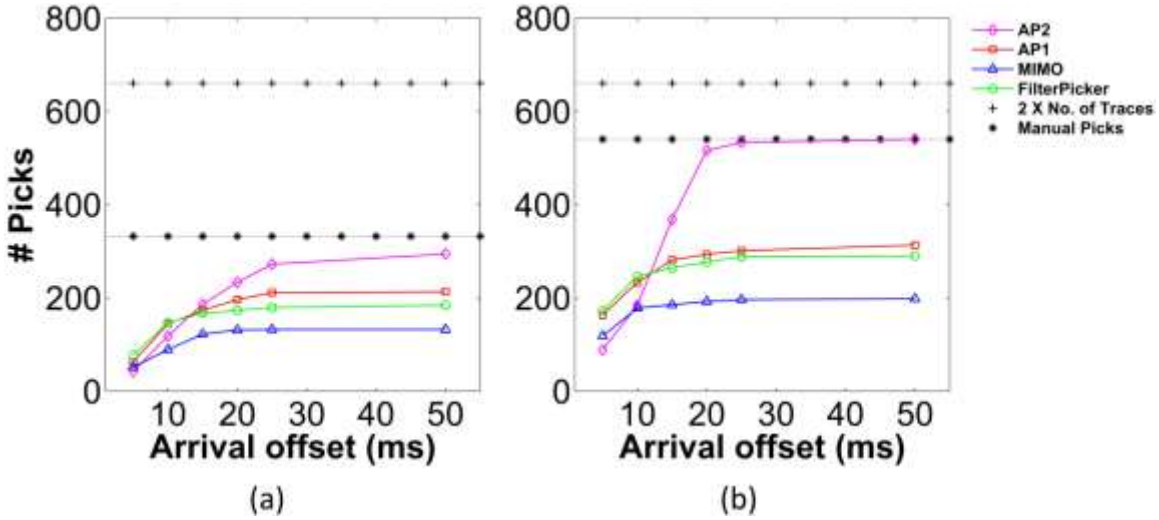

Figure 14: Results from comparative analysis of four picking algorithms. Subplot (a) shows results for P phase detections and (b) shows results for S phase detections.

We can clearly observe that in both cases, we were unable to pick all possible phase arrivals. This problem was particularly acute with P phase where the arrival energies were approximately 2 orders of magnitude lower than for S phase. Of the 660 potential picks for each phase, 20 had to be discarded as they correspond with vertical component (instrument noise issue) for geophone # 7. A total of 541 S phase and 329 P phase manual picks were successfully made. We observe that the proposed hybrid workflow (AP2) shows good results at offsets higher than ~ 13 ms for P phase and ~ 11 ms for S phase data. We also observe that the proposed algorithm is able to resolve almost all S phase arrivals that could be manually picked within ± 25ms. However, we do not observe the same with P phase arrivals for many instances where the algorithm failed to pick due to lack of "preliminary" detections available for fitting. However, we do observe the results to show an overall improvement in arrival detectability albeit with higher uncertainty. We also note that there are many instances where manual picks couldn't be made but the proposed workflow is able to detect a potential phase arrival. This could be true for some instruments (partial gather) as observed in Figure 12 or across the entire gather. Figure 15 shows a sample

event where it is very hard to manually pick P phase onsets but the auto detection workflow is able to identify a possible P phase arrival.

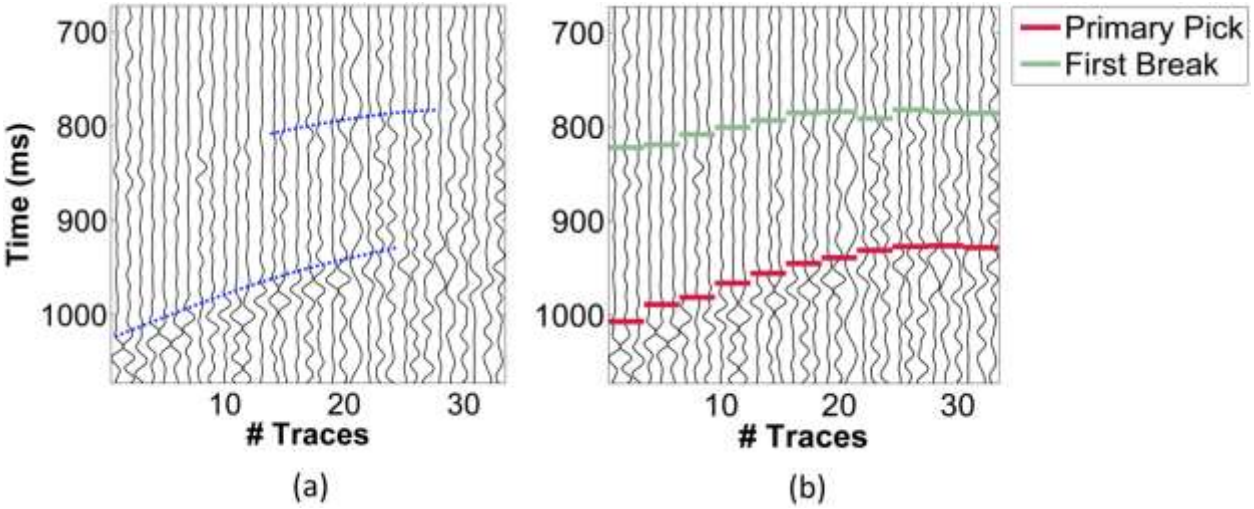

Figure 15: Subplot (a) shows a blowout with a possible event and subplot (b) shows the final primary and secondary detections. The blue dotted inserts show possible P & S arrival as per visual inspection but it is clear that manual picking is extremely hard due to very low signal-to-noise ratio.

Conclusion

A robust event detection routine has been developed which utilizes expected moveout characteristics for downhole sensor deployments to identify potential events from raw microseismic datasets. The workflow also searches for secondary phases if possible to isolate potential P and S phase energy arrivals in the data. Our tests on application with read microseismic monitoring data from the Marcellus shows very high applicability and improved detectability when compared with contemporary event detection algorithms in use. While we have used a neural nets based hybrid autopicker to make the initial picks, the workflow allows flexibility to use any other primary picking algorithms to make these initial pick estimates, provided the picks are reasonably accurate. While the proposed workflow shows relatively high immunity towards incoherent background noise, directional coherent noise artifacts can cause significant misclassifications. In order to tide over this issue, we propose the use of this microseismic event detection algorithm with a robust noise removal tool such as time-delay or adaptive beamformer (Widrow and Sterns, 1985) which can remove coherent noise in a robust manner before the actual detection routine is applied. Future work involves testing the efficacy of such a modified workflow including adaptive noise filtering for downhole microseismic

applications by studying the impact of the same on quality of identified microseismic source parameters.

References

[1] Lomax, A., C. Satriano, and M. Vassallo, 2012, Automatic picker developments and optimization: FilterPicker – a robust, broadband picker for real-time seismic monitoring and earthquake early warning: Seismological Research Letters, 83, 531-540.

[2] Maeda, N., 1985, A method for reading and checking phase times in auto-processing system of seismic wave data: Journal of the Seismological Society of Japan, 38, 365-380.

[3] Maity, D., F. Aminzadeh, and M. Karrenbach, 2014, Novel hybrid artificial neural network based autopicking workflow for passive seismic data: Geophysical Prospecting, 62, 834-847.

[4] Oye, V., and M. Roth, 2003, Automatic seismic event location for hydrocarbon reservoirs: Computers and Geosciences, 29, 851-863.

[5] Saragiotis, C. D., L. J. Hadjileontiadis, and S. M. Panas, 2002, PAI-S/K: A robust automatic seismic P phase arrival identification scheme: IEEE Transactions on Geoscience and Remote Sensing, 40, 1395-1404.

[6] Widrow, B., and S. D. Sterns, 1985, Adaptive Signal Processing: Prentice-Hall. ISBN: 9780130040299.

Appendix H: Pressure Pulse Attenuation for Fracture Diagnostics

Summary and Accomplishments

The Pressure Pulse Attenuation (PPA) analysis of completion data from multiple wells as indicated that a reasonably strong correlation seems to exist between observed production through production log data and modeled fracture dimensions (lumped L×H parameter) which seems intuitive.

An experimental code (WHAM-FD) utilizing finite difference solution has been designed and developed (MATLAB) for analysis of pressure response data and has been extensively tested on the two sets of data available in this project (WPX Energy Wootton and Corbett wells). However, preliminary tests indicate that more elaborate models and problem definitions may be required in order to fully consider other factors impacting pressure attenuation response as observed from surface.

Motivation

"Water Hammer" pressure transients are generated when there is a sudden change in flow conditions within the wellbore such as a pump shut in or failure. Classically; water hammer, flow and pressure response data at the end of frac treatment has been used to estimate entry friction. Also, Gary Holzhausen has looked into modeling of fluid transients to characterize fracture dimensions, etc. However, methods devised for characterization of single vertical completions requires extension to horizontal mile long laterals. This requires the use of novel modeling/ analysis tools. With the pressure pulse attenuation (PPA) analysis technique, we want to carry out real time fracture diagnostics with commonly available pressure response data. Potentially redesign consecutive fracture stages on the fly. Reduce our reliance on expensive production logs and conduct both qualitative and quantitative modeling of production performance.

Introduction

While the advent of multi-stage hydraulic fracturing in long lateral completions has revolutionized shale oil and gas production in the last decade or so, the process still lacks a robust understanding as to what happens downhole within the wellbore and in the formation during the treatment. Inter-stage isolation issues are well documented (Ugueto et al., 2015) and understood to be highly undesirable. Figure 1 shows a ball retrieved

from a stage which faced screen out. We can clearly observe extensive erosion of the ball which invariably would have led to inter-stage isolation issues.

Figure 1: Eroded frac ball from one of the treatment stages from Wootton test pad (well 10H) indicating potential for inter-stage isolation issues during the treatment.

In addition, depending on the actual back pressure and completion design, we could have fewer than desired number of perforations open at any point, thereby impacting stage productivity. Another element of uncertainty is the presence or absence of fluid interaction with opening of natural fractures and how to identify this phenomenon in real time. A lot of research has been done in this regard (Potluri et al., 2005; Kresse and Weng, 2013] but real time characterization still remains elusive for the industry. Natural fractures can provide enhanced productivity of various frac stages but they can also provide conduits for significant fluid loss into nonproductive zones and also divert fluid in previously stimulated zones. There could be other issues contributing to poor stage production as well; such as poor cementing and flow channeling.

Real time treatment and completion diagnostics can be very useful in understanding how good or bad the completions are and whether there is any need for immediate or medium term remediation. Diagnostic methods include well testing, net pressure analysis (fracture modeling), techniques that employ open-hole & cased-hole logs, surface & downhole tilt fracture mapping, microseismic fracture mapping, production data analysis, DAS or DTS, image logging, tracers, etc. Not only can some of these methods be extremely complex, time consuming and expensive; but some of them have not found wide acceptability within the industry due to multitude of reasons. Moreover, there are not that many which can provide meaningful diagnostic information and results in real time. Others have found that methods applicable for vertical fractured wells may not work well with long horizontal

completions. As an example, microseismic monitoring is used to identify issues with completion including fluid or energy loss into previous treatments, or faults. However, the methods used in microseismic data analysis suffer from significant uncertainty and require extensive data workflows for analysis which invariably reduce its application to a post-fact completion analysis tool, not to mention the high costs associated with the method. What is sorely lacking are simple approaches to understanding completions without resorting to expensive and elaborate data collection and processing. Therefore, it is critical that any completion diagnosis and optimization workflow be fast enough to be done in real time, accurate enough to be of practical use and, finally, be economical, particularly in the current reality of low oil prices.

Based on our understanding of hydraulic fracture completion and its propagation, we believe that any attempt to understand the process should ideally involve understanding the effectiveness of the fracturing fluid to easily get through the wellbore and into the formation. Moreover, how the perforations, the stimulated section of the wellbore and the reservoir to be stimulated behave during treatment impacts this “effective penetrability” of the fluid into that stage during completion. This paper is focused on a pressure pulse attenuation modeling approach during the entire treatment based on an existing methodology. This method provides direct indicators for inter-stage isolation issues as well as completion quality. The modeled parameters can be used to carry out fracture diagnostics during, and at the end of, the treatment and help optimize stimulations on the fly. Finally, this approach is simple to incorporate, inexpensive in terms of resource requirements and can be readily accommodated within the current state of the art.

Background and Proposed Methodology

“Water Hammer” pressure transients are generated when there is a sudden change in flow conditions within the wellbore such as a pump shut in or failure, or sudden rate fluctuations. Classically; water hammer flow and pressure response data at the end of hydraulic fracturing treatment has been used to estimate entry friction. Also, Holzhausen and Egan (1986) have looked into modeling of fluid transients to characterize fracture dimensions, etc. However, these methods were devised for characterization of single vertical completions and they require extension to be applicable to horizontal mile long laterals. More recently (Mondal, 2010 and Carey, 2014) attempts have been made to utilize these pressure transients to understand the created hydraulic fractures and other aspects of completion. We propose to further develop this methodology by introducing new modeling parameters and tying our results with observations in the field. With the pressure pulse attenuation (PPA) analysis technique, we want to carry out real time fracture diagnostics with commonly available pressure response data, potentially

redesign fracture stages on the fly, reduce our reliance on expensive diagnostic tools and provide both qualitative and quantitative understanding of completions.

Water hammer “pressure transient” is generated when there is a sudden change in flow conditions within the wellbore such as a valve closure or pump failure. Figure 2 shows how the water hammer response gets generated in a typical wellbore setting.

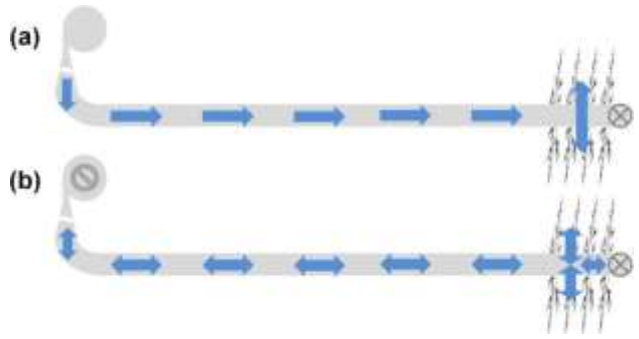

Figure 2: Schematic shows how the change in flow within a wellbore from (a) steady state (constant flow during pumping) to (b) unsteady state (pump closure) conditions creates a water hammer which traverses from surface to the fractured zone.

Though water hammer phenomenon is observed when kinetic energy of a fluid is converted to elastic energy; only rapid changes of flow velocity will produce this effect. The inertia of fluid column prevents it from adjusting to the new situation. The fluid is deformed and pressure transients accompany this deformation process. Their impact can be diminished by providing surge protection devices which are typically chambers filled with fluids (such as air) which can help dissipate this excess energy. As an analogy; longer, more extensive and more complex fracture networks provide more open channels and volume for energy from such pressure pulses to dissipate quickly. Therefore, in pressure transient response data from hydraulic fracture treatments, we expect the water hammer to dissipate much more quickly for stages with bigger and more complex connected fracture networks. However, bigger connected volume for dissipation does not necessarily mean increased productivity from that stage. This is because there are other factors that can also create the same effect, such as lack of inter stage isolation (between adjacent treatment stages) as observed with Figure 1 or communication with shared (previously stimulated) or non-productive (local faulting) zones of the reservoir.

Before we introduce our model parameters for diagnostics, we highlight the mathematical formulation used in solving the water hammer phenomenon. One of the most robust, quick and routinely used techniques involves solving the equation of continuity and equation of momentum using the “method of characteristics” for transient flow behavior. A conceptual description of the ‘water hammer’ phenomenon and the derivation of the

mathematical model as a hyperbolic partial differential equation can be found in many sources, Larock et al. (1999). Here we present a brief description of the model and its derivation.

The equation of continuity and equation of momentum are defined as:

$$\frac{\delta V}{\delta t} + \frac{1}{\rho}\frac{\delta P}{\delta x} + g\frac{dz}{dx} + \frac{f}{2D}V|V| = 0 \tag{1}$$

$$\rho a^2 \frac{\delta V}{\delta x} + \frac{\delta P}{\delta t} = 0 \tag{2}$$

Here x is the axial distance along the wellbore, z is the elevation at any point of the wellbore, V is the mean flow velocity of the fluid, P is the pressure, a is the wave velocity, ρ is the fluid density, f is the friction factor, D is the pipe diameter and g is the acceleration due to gravity. In order to solve these sets of partial differential equations numerically, we introduce a single ordinary differential equation using the Lagrange multiplier as:

$$\left(\lambda\frac{\delta V}{\delta t} + \rho a^2\frac{\delta V}{\delta x}\right) + \left(\frac{\lambda}{\rho}\frac{\delta P}{\delta x} + \frac{\delta P}{\delta t}\right) + \lambda g\frac{dz}{dx} + \lambda\frac{f}{2D}V|V| = 0 \tag{3}$$

Now since we can apply chain rule for V, we get:

$$\lambda\frac{dV(x,t)}{dt} = \lambda\frac{\delta V}{\delta t} + \lambda\frac{\delta V}{\delta x}\frac{dx}{dt} \tag{4}$$

By comparing the coefficients, the first term in equation 3 can be modified by letting:

$$\lambda\frac{dx}{dt} = \rho a^2 \tag{5}$$

Similarly, we can apply chain rule for P to get:

$$\frac{dP(x,t)}{dt} = \frac{\delta P}{\delta x}\frac{dx}{dt} + \frac{\delta P}{\delta t} \tag{6}$$

Again by comparing the coefficients, the second term in equation 3 can be modified by letting

$$\frac{\lambda}{\rho} = \frac{dx}{dt} \tag{7}$$

In order to satisfy both these conditions (equations 5 & 7), we need $\lambda = \pm\rho a$

Applying this condition to our solution, we get a fully differentiable form for equation 3 as:

$$\lambda\frac{dV}{dt}+\frac{dP}{dt}+\lambda g\frac{dz}{dx}+\lambda\frac{f}{2D}V|V|=0 \tag{8}$$

Now choosing the two possible solutions for λ, we can obtain the two solutions as follows:

$$\frac{\mathrm{dV}}{\mathrm{dt}}+\frac{1}{\rho a}\frac{\mathrm{dP}}{\mathrm{dt}}+\mathrm{g}\frac{\mathrm{dz}}{\mathrm{dx}}+\frac{\mathrm{f}}{2\mathrm{D}}\mathrm{V}|\mathrm{V}|=0 \tag{9}$$

$$\frac{\mathrm{dV}}{\mathrm{dt}}-\frac{1}{\rho a}\frac{\mathrm{dP}}{\mathrm{dt}}+\mathrm{g}\frac{\mathrm{dz}}{\mathrm{dx}}+\frac{\mathrm{f}}{2\mathrm{D}}\mathrm{V}|\mathrm{V}|=0 \tag{10}$$

Equations 9 & 10 are referred to as the C+ and the C- characteristic equations. Figure 3 shows the solution space and the straight line relationships on which these sets of equations are valid.

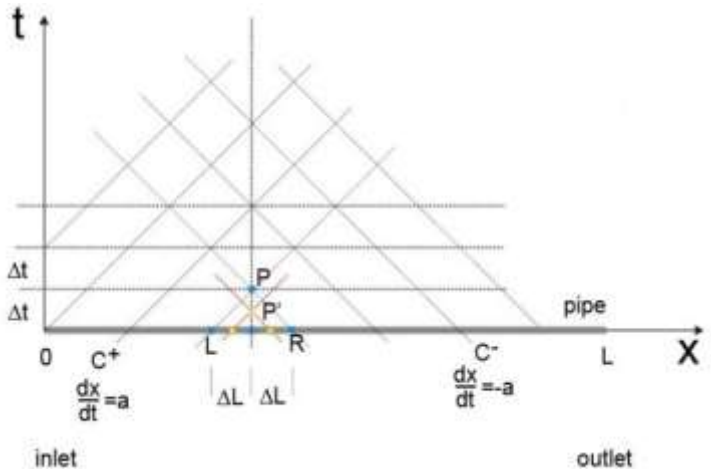

Figure 3: Method of Characteristics solution space for a pipeline showing the straight line relationships between t and x on which C+ and C- are valid and evaluated.

These equations form the basis for finite difference solution for the water hammer problem which we have applied to our modeling. Since the nodal length for simulation is computed based on the selected time step, the Courant–Friedrichs–Lewy criterion for convergence (Courant et al., 1967) is always maintained unless the wellbore length becomes too short (equivalent of travel length corresponding to single time step) or the time step used is too large. For the boundary conditions, the upstream end (wellhead) is guided by the observed flow at the surface from the completion data. For the downstream end (fracture plug/ fractures), an analogous RC circuit is used which is based on what was originally

suggested by Holzhausen (Holzhausen et al., 1988). The equivalent hydraulic equations governing the resistivity and capacitance terms in the model are defined as follows.

$$\Delta P = \left(\frac{\mu l}{kA}\right) Q = RQ \tag{11}$$

$$Q = C\frac{dP}{dt} \tag{12}$$

Here μ is the fluid viscosity, l is the fracture length, k is the permeability and A is the c/s area of the conduit through which fluid is flowing. The resistance term models the combined effect of well perforation friction and flow resistance in the fracture itself. The capacitance models the change in pressure due to fluid flux. By making some basic assumptions regarding the fracture properties, easily solvable linear relationships can be obtained for the resistive (R) & capacitive (C) terms as suggested by Holzhausen and Egan (1986):

$$C = \frac{8\rho g r^3(1-\nu)}{3\mu} \tag{13}$$

$$R = \frac{3k\Delta L}{4gb^3h} \tag{14}$$

It is important to note that the capacitive term is for simple penny shaped crack of radius r and the resistive term is for fracture with maximum fracture half-width b and half height h (Bird et al., 1960).

Based on the R & C parameters modeled, the corresponding fracture dimensions can be evaluated. However, as discussed earlier, there is a possibility of fluid leak off taking place during each water hammer cycle due to communication with natural fracture swarms, previously stimulated zones, local faults and other fluid loss scenarios. In order to account for such loss, we incorporate a flow and corresponding pressure bleed in the downstream boundary and model this fluid loss parameter (FLF) through a fractional multiplier.

$$Q_i = FLF \times Q_{i-1} \tag{15}$$

Here Q denotes the modeled flow at the downstream boundary and subscripts i and i-1 denote the time step. Based on this parameter as well as the modeled fracture volume (V_f) from fracture dimensions, a “penetrability index” (PI) is computed as:

$$PI = FLF * \log V_f \tag{16}$$

Finally, we want to model the potential fluid/ pressure communication with the previous (completed) stage due to frac ball erosion or ball falling off its seat for other reasons. This is done by comparing the modeled pressure transient and the actual pressure data frequency and identifying the difference between the two as a fraction of stage length.

$$LOF = \frac{Model\ Length - Actual\ Length}{Stage\ Length} \tag{17}$$

In order to search for optimal model parameters such that the modeled pressure transient response matches with the actual data, an evolutionary search algorithm is used. We use a genetic algorithm (GA) which mimics the theory of evolution by natural selection wherein the less fit individuals from each generation are selectively eliminated before a new generation is created. This selection is an iterative process where an objective function is used to evaluate the fitness of each individual in the population and new generations are obtained by probabilistically selecting fitter individuals from current generation. The fitness function (Ψ) is a weighted summation of individual functions relating to minimizing the error based on the misfit between data and model. These functions are defined as follows:

$$\Phi(t) = \left| \frac{1}{2 \times w} \left\{ \sum_{t-w}^{t+w} P_m - \sum_{t-w}^{t+w} P_o \right\} \right| \tag{18}$$

$$\theta = \{\#extrema_m - \#extrema_o\}^2 \tag{19}$$

$$\Psi = \sum_{t=start}^{end} \Phi(t)^\theta \tag{20}$$

Here t is the time of evaluation, w is the smoothening window length to tackle high frequency fluctuations, P_m is the modeled pressure response, P_o is the observed pressure response and "# extrema" define the number of troughs and crests observed in the water hammer response. A more robust fitness criterion may also be used as shared under "Field Application" section. In addition to the defined optimization criteria, other hard constraints can also be added to make the search algorithm more robust and responsive. As an example, these could include maximum and minimum pressure observed over modeling time window. Some members of the parent population are also subjected to genetic operators such as cross-over and mutation to generate new offspring. In short, the fitness function used tries to identify the best possible model fit through repetitive perturbation of selected optimization variables (R, C, FLF) provided the error in mismatch is reduced but at the same time, model parameters are more heavily weighted through higher scoring of the individuals. A probability measure is used to decide on the

percentage of individuals from parent population that will be copied (while the rest undergo cross-over). This probabilistic selection is implemented through a rank selection process where the probability of selection of individual is inversely proportional to its position in the sorted population list based on fitness. Once selection is made of the candidates for crossover, the operation involves a random subpart from the parent pair being swapped to generate two offspring pairs. A uniform crossover technique is used for this study. Finally, a relatively small portion of the offspring population is chosen at random and a randomly chosen bit is flipped in the selected population set to generate a mutated offspring. In order to reduce crowding effects (where similar individuals crowd a population set), fitness sharing strategy is implemented which rescales the evaluated fitness based on the number of similar individuals in a population. Figure 4 shows the optimization workflow used for PPA modeling as described.

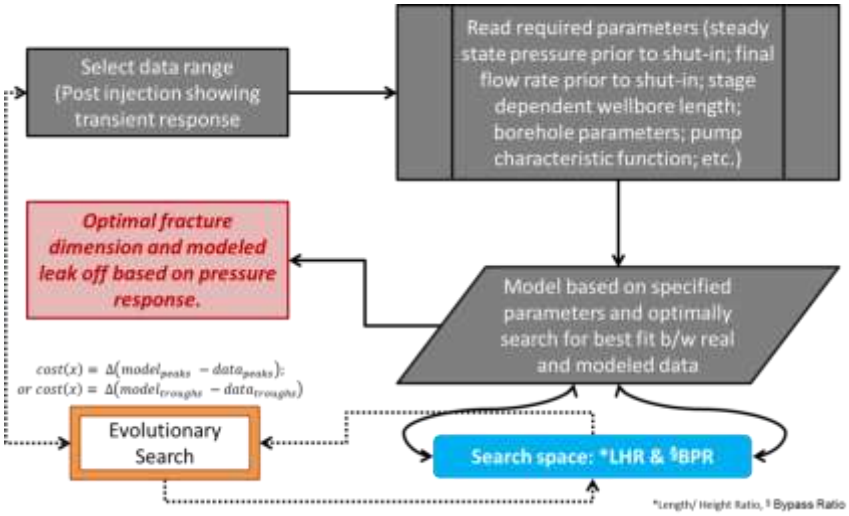

Figure 4: Optimization workflow used for water hammer modeling.

Before examples with application to real datasets, we present results of application of modeling approach to an artificial flow modulation scenario. In this scenario, randomly selected wellbore model and fluid properties are defined and the flow is dropped over a short period (0.33 seconds) from a steady flow rate (50 bpm) to zero. The baseline wellbore length is modeled for 10000 feet and a 5" P-110 grade #21 pipe is selected for the wellbore. For a time step of 0.01 seconds, we have 246 nodes with each nodal span covering ~40 feet. The fluid is assumed to be water at standard temperature and pressure conditions and the flow is assumed to be turbulent with a Reynolds Number of ~5000. The pressure modeling results for some variations in modeling parameters are shown in Figure 5.

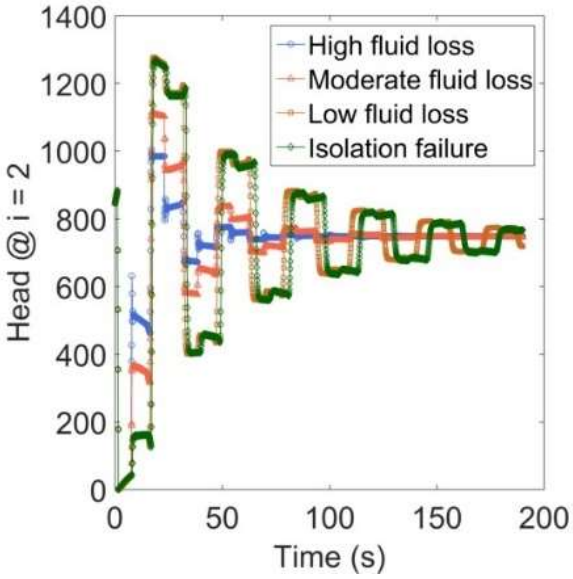

Figure 5: Synthetic runs indicating pressure response under different modeling conditions.

As can be observed from the results, loss of fluid into formation leads to rapid signal attenuation in time as well as significant loss of energy released with the water hammer from the wellbore into the formation. Moreover, we also observe differences in signal frequency when we modify the length of the system through which the signal traverses by removing the inter stage isolation with the previous stage which adds around 300 feet of additional wellbore section.

From synthetic modeling results, it is clear that with careful selection of parameters, we can identify potential inter-stage isolation issues by comparing synthetic and actual data (wavelength) and inverting the relevant model parameters. Also, the pressure response and its development over time indicate the potential to model fluid loss in addition to fracture parameters which can allow for evaluation of how good or bad the completion was using penetrability index (Eq. 16).

Field Application

The proposed pressure pulse attenuation analysis methodology was applied to data acquired from two shale gas wells located in the Marcellus play. These experimental wells were part of the “Advanced Hydraulic Fracturing” Project and were part of this study due to the availability of post completion production log data and relatively high resolution completion data (sampling rate of 1/3 second). The exact wellbore properties were incorporated in the study based on available completion data for the respective wells. The

wellbore length used for comparison was from the surface to the isolation plug. The fluid properties used for modeling were estimates using the average borehole temperature. Figure 6 shows an example of model results when applied to a randomly selected stage from both wells under study. The model was applied to data close to the shut-in post proppant injection phase and they show good match between the actual pressure data and the modeled results.

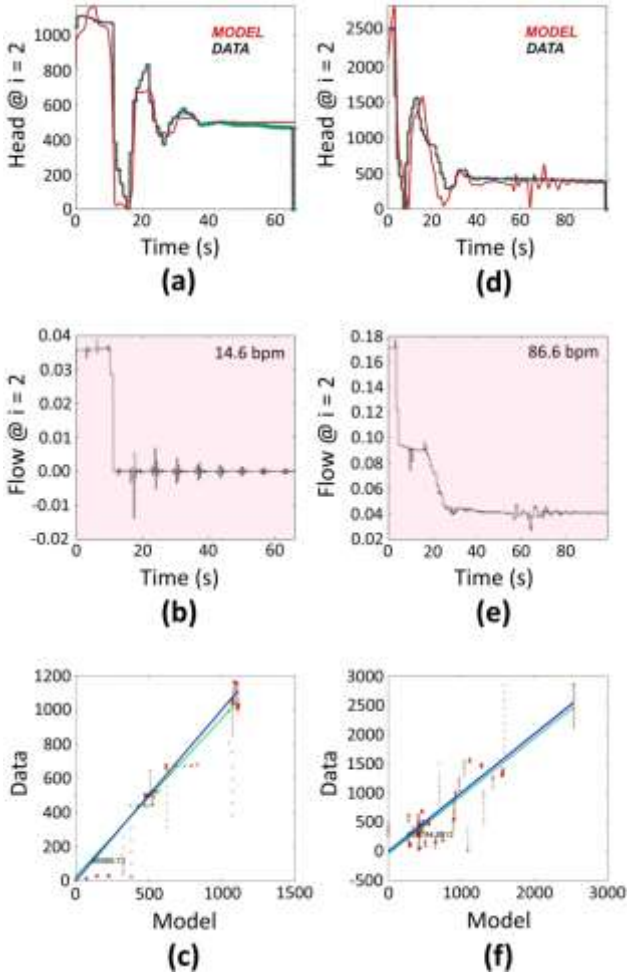

Figure 6: Subplots (a), (b) and (c) show modeling results for a stage from well # 1 and subplots (d), (e) and (f) show modeling results for a stage from well # 2. Subplots (a) and (d) show the model and actual pressure data close to shut-in for a particular set of modeled parameters. Subplots (b) and (e) show the corresponding modeled flow. Subplots (c) and (f) show cross-plots of actual and modeled data (red dots), the best fit (green curve) and the 1:1 plot (blue curve).

The modeled flow was computed by setting the surface flow as equal to the observed flow from completion data. However, propagation effects do creep into the modeled flow as can be observed from Figure 6 (b) and (e). Also, higher weighted multiplier is assigned

to data close to beginning of the evaluation window and lower weighted multiplier to data from late period during optimized search. This is because the effect of the PPA on the system is not accounted for once the unsteady state conditions are initiated (the parameters such as FLF and modeled fracture properties are constant for the duration of modeling). In order to incorporate the weight, an exponential decline function is used and Eq. 18 is modified as follows:

$$WM_t = (1-b)^t \tag{21}$$

$$\Phi(t) = WM_t \times \left| \frac{1}{2 \times w} \left\{ \sum_{t-w}^{t+w} P_m - \sum_{t-w}^{t+w} P_o \right\} \right| \tag{22}$$

Figure 7 shows the impact of using the weighted multiplier as it results in improved match at the beginning but relatively poorer match towards the end of the modeled period.

Results

For the two separate experiments in question, the modeling parameters such as FLF, PI and LOF were tabulated and compared with other available data for these wells. Figure 6 shows the results and the modeled parameters obtained using the GA based fitting approach.

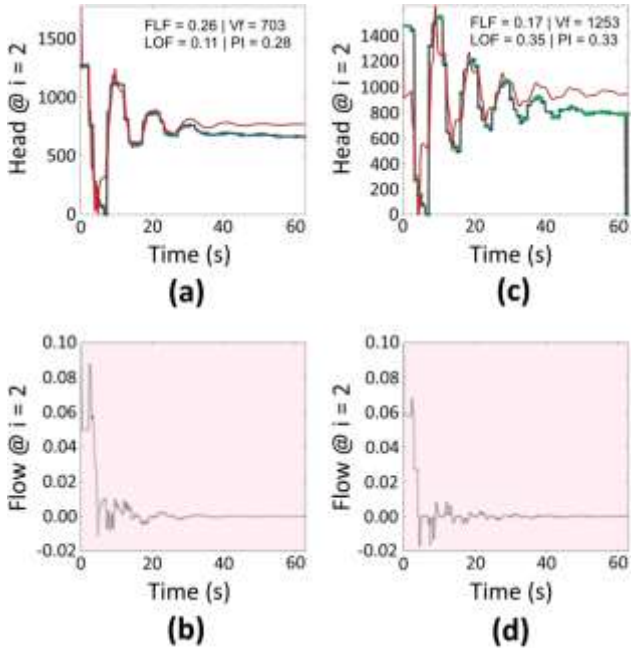

Figure 7: Subplot (a) and (b) show a sample modeling run and modeled parameters for a stage from well # 1 and subplot (c) and (d) show the modeled parameters for a stage from well # 2. The first case shows a relatively poor completion with smaller predicted fractured zone size and lower penetrability index (PI) and vice versa for the second case.

Since the modeled penetrability index (PI) is impacted by modeled fracture volume (from fracture dimensions) as well as fluid loss into formation under unsteady state conditions, we expect some positive correlation between modeled PI and observed stage-wise flow contribution from production logs. Cross-correlation between these two parameters derived independently of each other is shared for both the wells under study in Figure 8.

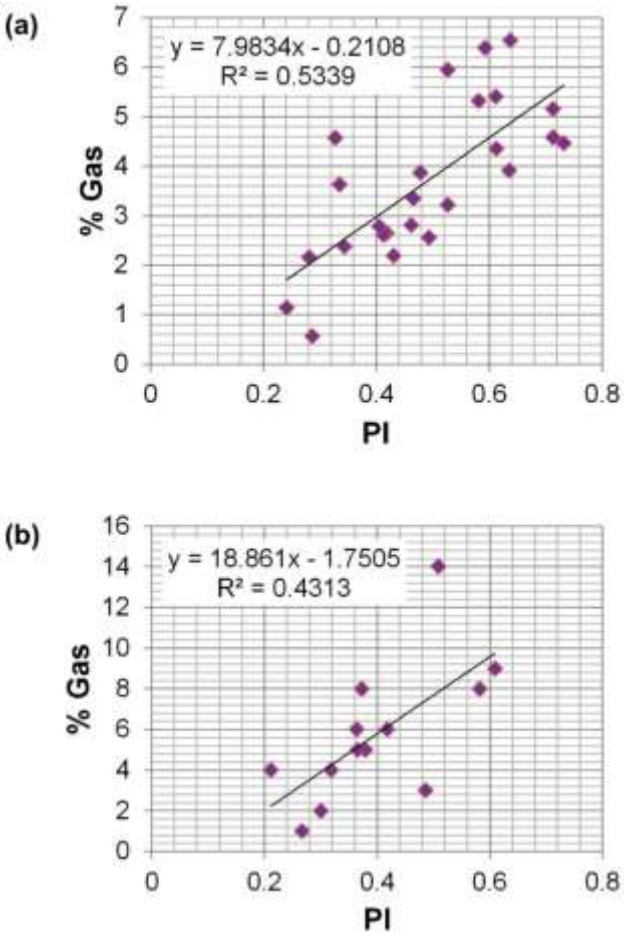

Figure 8: Modeled penetrability index (PI) cross plots with observed gas flow contribution from production logs for (a) well # 1 and (b) well # 2.

Based on the cross-plots, we see relatively weak though firmly positive correlations between the modeled PI and observed gas flow from production logs obtained from these two wells. The lack of very strong positive correlation could be due to multitude of reasons. While the PI parameter does take into account the fractured volume as well as potential fluid loss due to communication with previous fractured or naturally fractured zones as well as near wellbore faults, it does not consider possible parasitic pressure removal due to opening of additional perforations or loss due to inter-stage pressure/ flow communication. We validate this by removing data from those stages which showed high

LOF values for both sets of data and the coefficient of correlation improves for well # 1 from 0.534 to 0.645 and for well # 2 from 0.43 to 0.6. There are other factors which can cause significant uncertainty in both the production log as well as the modeled parameters. Due to multi-phase flow in these gas wells (water + gas), the flow predictions made by the production logs always have some inaccuracies. Moreover, the behavior of the fractured zone and the wellbore might change during the few 10's of seconds of pressure pulse attenuation modeling and this is not incorporated in the modeling approach. This can lead to some error particularly from lack of match from late period model results. Finally, other considerations such as wellbore location with respect to the formation tops can cause significant variability from modeled productivity due to variability in hydrocarbon presence.

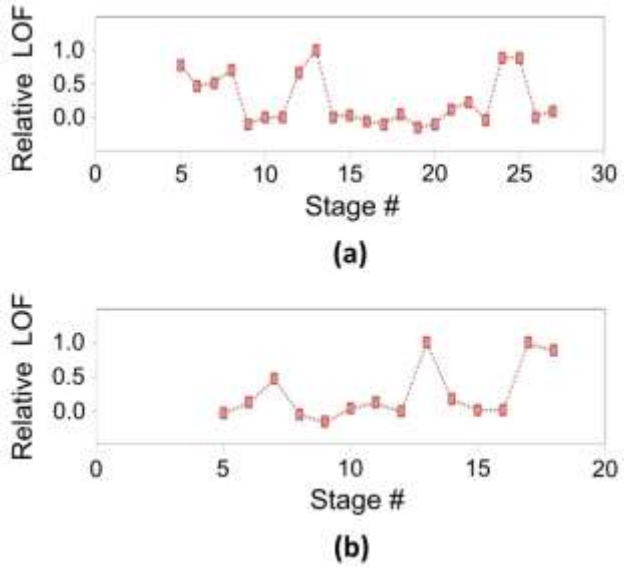

Figure 9: Routine LOF parameter computed for (a) well # 1 and (b) well # 2.

We also model inter-stage isolation parameter LOF (Eq. 17) which gives a robust indicator for non-optimal isolation with prior completed stage. Figure 9 shows the modeled inter stage isolation parameter for both well # 1 and well # 2 under study. We find most stages to not show significant isolation issues. For well # 1, stages 5, 6, 7, 8, 12, 13, 24 and 25 show significant isolation issues based on high LOF value indicating significant mismatch between predicted and observed wave travel length (wellbore). For well # 2, stages 7, 13, 17 and 18 show similar mismatch. While we do not have independent verification of these observations, the frac ball obtained when stage 8 from well # 1 completion was flowed back does indicate significant erosion (Figure 1) and therefore, potential for isolation issues at the end of completion as well. We do however observe higher productivity of prior stages to those showing high LOF values. We consider well # 2 to demonstrate this

due to lower number of stages and significantly less predicted isolation issues (four stages) compared with well # 1 (eight stages). For well # 2, three out of the four stages with high modeled LOF parameter show this behavior (stage 6: 14%, stage 12: 8%, stage 16: 9%, stage 17: 5%, stage avg.: 7%). This could potentially be due to over-stimulation of these stages compared to others due to both fluid and proppant bypass over significant period of stimulation. It is notable that in combination with the modeled FLF parameter, with relatively high or low LOF values, we can identify where the pumped fluid is going in near real time provided we have multiple rate fluctuations incorporated during injection. This is because higher FLF values can indicate loss of fluid either to natural fracture swarms, hydraulically fractured zones completed previously, or local faults, etc. Remedial measures can be taken in near real time in case such observations are made (such as modifying rest of the completion design through schedule, proppant, rates, etc.). Moreover, higher LOF values can help us isolate improper treatments due to partial inter-stage isolation and thereby help prevent potential screen-outs. Remedial actions could also include pumping appropriate diverting agents to improve target zone completion and limit energy loss through proppant and fluid into undesired zones.

Novel completion strategy (namely variable rate fracturing) has been introduced by GTI involving the use of rapid rate fluctuations during treatment (pre- and potentially post-proppant injection phase) and this provides for ideal deployment of our proposed diagnostic technique for analysis (Ciezobka et al., 2016). Odd stages in well # 1 were completed in this manner while even stages were completed in routine fashion. As already discussed, rapid pressure fluctuations can cause some additional perforations to open and communicate fluid during treatment. Figure 10 shows sample treatment with rapid rate fluctuations and observed pressure drop indicating more open perforations.

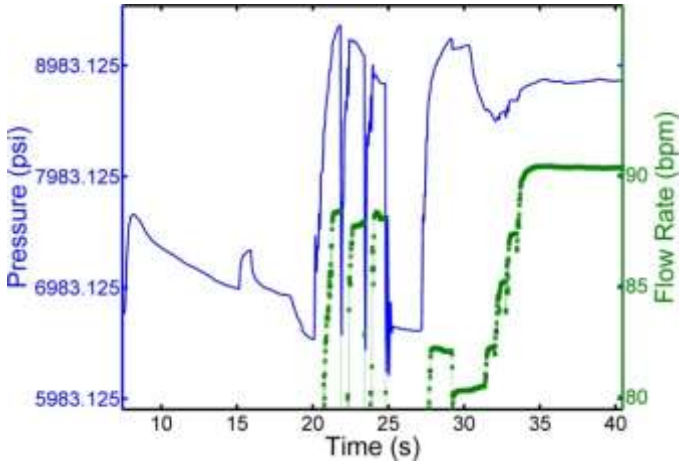

Figure 10: Sample treatment data from a stage where rapid rate fluctuations (variable rate completion) were used prior to proppant injection. We can clearly see that the ΔP drops after each fluctuation suggesting potentially opening of previously closed perforations. We can also see the pressure pulse after the last rate drop due to flow stabilization.

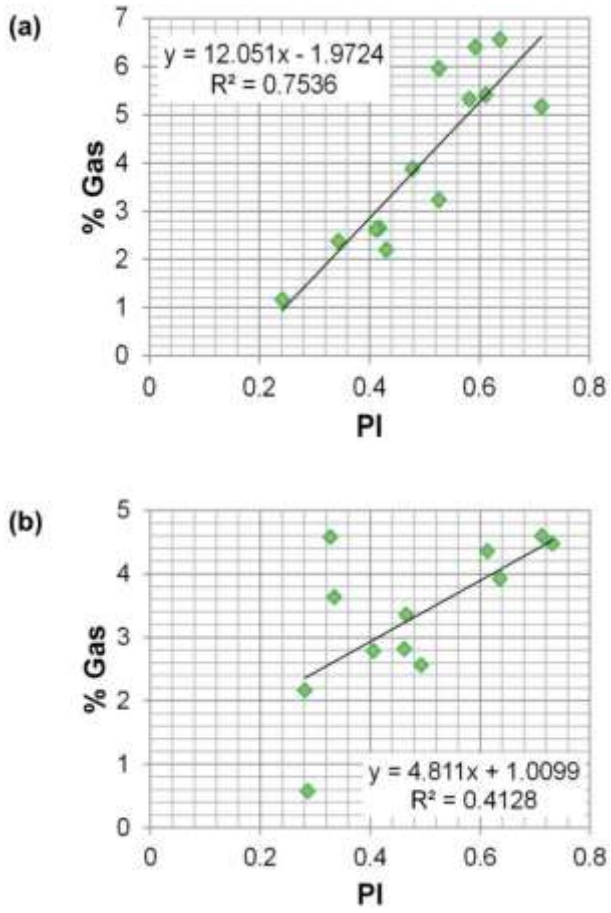

Figure 11: Trimmed data from Figure 8a showing data from only the (a) odd stages and (b) even stages.

We understand that the proposed pressure pulse attenuation analysis does not explicitly consider additional pressure variability in response to this parasitic pressure from unopened perforations. Therefore, due to more open perforations expected from using this approach, we should observe better correlation of productivity index (PI) with production for said stages compared to others not using this approach. Figure 11 shows the correlation observed for all stages with and without using this approach. The overall positive relationship allows us to numerically predict production contribution from any new stage provided this model is available. Moreover, the spatial spreads allow us to compute uncertainty in the estimated production contribution as obtained from the modeled fracture dimensions. Table 1 shows the estimated production contribution based on 4 random lumped fracture dimension draws which could be observed based on this modeling approach in a future well.

Table 1: Sample modeled production contribution as a function of fracture dimensions.

Model # 1	Lumped modeled frac. dimension	Expected Production Contribution
	50	-1.512457978
	100	-0.853549736
	500	4.417716198
	1000	11.00679862
Model # 2	**Lumped modeled frac. dimension**	**Expected Production Contribution**
	50	2.116597369
	100	2.600403882
	500	6.47085598
	1000	11.3089211

Results from random prediction of flow contribution indicate similar values for the upper boundary but significantly different well productivity close to the lower boundary of the curve. Additional data will allow us to obtain refined and more usable models for analysis. In real time application, as each successive stage is completed, the fracture dimensions will be modeled based on observed pressure response and so on. Looking at the modeled contributions, it is clear that other factors may be at play which leads to higher productivity for similar fracture dimensions/ productivity. Finally, data from model #2 based on Field Test #1 shows considerable stability at lower modeled dimensions unlike model #1 from Field Test #2.

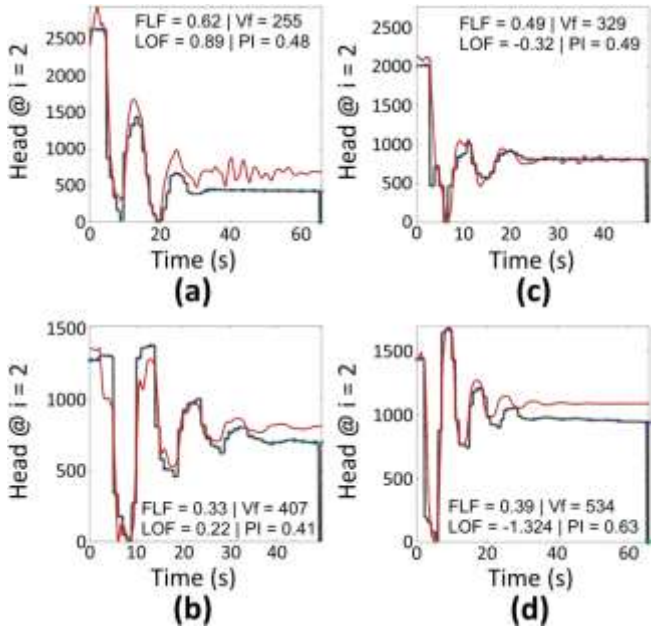

Figure 12: Subplots (a) and (b) show the pressure response and modeling results for pre and post proppant injection respectively for stage A while subplots (c) and (d) show the same for stage B.

The potential for both pre - and post- proppant injection rate fluctuations allows for real time analysis of pressure pulse attenuation phenomenon which occurs due to rapid rate drops. For well # 1, we have many stages with rapid rate drops both before and after proppant injection phase. Careful analysis of results from these responses can help understand how the fracturing develops in near real time. Figure 12 shows two examples of stages (A & B) with multiple responses available for analysis. For both, we observe increase in modeled fracture volume in time (255 to 407 for stage A and 329 to 534 for stage B). We also observe that for both cases, the loss into formation tends to be lower (lower FLF) after proppant injection is complete (0.33 vs. 0.62 for stage A and 0.39 vs. 0.49 for stage B). Finally, we observe that the penetrability of the created fractured zone (PI) decreases for stage A (0.41 vs. 0.48) but increases for stage B (0.63 vs. 0.49). We also note that based on production log results, stage B is more productive (5.32 % Gas) compared to stage A (2.62 % Gas).

Concluding Remarks

Based on the results from two separate field case studies, we have validated the utility of pressure pulse attenuation-based analysis as a diagnostic tool for hydraulic fracturing. While the model in itself is highly simplistic with significant assumptions, the interpretations can be valid provided these limitations are honored. We demonstrate the utility of modeled parameters in identifying completion quality (PI) as well as potential inter-stage isolation issues (LOF). Completion quality (or penetrability index) shows significant positive correlation with observed production behavior of the completed wells. Analysis of results from novel completion technique (variable rate technique) indicates that this approach does allow for opening of previously nonconductive perforations. Moreover, such an approach involving multiple rapid rate fluctuations through the treatment phase can allow multiple opportunities for diagnostics to prevent potentially damaging or sub-optimal fracturing. This methodology provides a valuable real time completion diagnostic tool for hydraulic fracturing without the need for any new tools and by using routinely collected completion data. Its simplicity allows for rapid deployment and analysis either in the field or from remote locations.

References

[1] Bird, R., Stewart, W., & Lightfoot, E.: ‘Transport Phenomena’ 1961 (John Wiley & Sons, New York).

[2] Carey, M. A. 2014. Water Hammer Fracture Diagnostics. M.S. Thesis. The University of Texas at Austin, Austin.

[3] Ciezobka, J., Maity, D., & Salehi, I. Variable Pump Rate Fracturing Leads to Improved Production in the Marcellus Shale. Paper SPE 179107-MS to be presented at the SPE Hydraulic Fracturing Technology Conference, The Woodlands, Texas, 9-11 February.

[4] Courant, R., Friedrichs, K, & Lewy, H. 1967 [1928]. On the partial difference equations of mathematical physics. IBM Journal of Research and Development, 11(2): 215-234.

[5] Holzhausen, G. R., & Egan, H. N. 1986. Fracture Diagnostics in East Texas and Western Colorado using Hydraulic-Impedance Method. Paper SPE 15215 presented at the SPE Unconventional Gas technology Symposium, Louisville, Kentucky, 18-21 May.

[6] Holzhausen, G. R., Egan, H. N., Baker, G., & Gomez, J. 1988. Characterization of Hydraulic Fractures using Fluid Transients. Project Report [5086-211-1371], Gas Research Institute, Chicago, Illinois (May 1988).

[7] Kresse, O., & Weng, X. 2013. Hydraulic Fracturing in Formations with Permeable Natural Fractures. Presented at the ISRM International Conference for Effective and Sustainable Hydraulic Fracturing, Brisbane, Australia, 20-22 May.

[8] Larock, B. E., Jeppson, R. W., & Watters, G. Z.: 'Hydraulics of Pipeline Systems' 1999 (CRC Press).

[9] Mondal, S. 2010. Pressure Transients in Wellbores: Water Hammer Effects and Implications for Fracture Diagnostics. M.S. Thesis. The University of Texas at Austin, Austin.

[10] Potluri, N. K., Zhu, D., & Hill, A. D. 2005. The Effect of Natural Fractures on Hydraulic Fracture Propagation. Paper SPE 94568-MS presented at the SPE European Formation Damage Conference, Sheveningen, The Netherlands, 25-27 May.

[11] Ugueto, G. A., Huckabee, P. T., & Molenaar, M. M. 2015. Challenging Assumptions About Fracture Stimulation Placement Effectiveness Using Fiber Optic Distributed Sensing Diagnostics: Diversion, Stage Isolation and Overflushing. Paper SPE 173348-MS presented at the SPE Hydraulic Fracturing Technology Conference, The woodlands, Texas, 3-5 February.

Appendix I: Hybrid Microseismic Array Design

Summary and Accomplishments

This work attempts to validate an integrated framework for optimized multi array passive seismic monitoring programs to optimally characterize event source parameters as best as possible. While the actual microseismic experiment has not been planned as of now, once that happens, we will obtain necessary data to plug into the design framework shared here and optimally place geophone sensors to map the microseisms. As preparatory work, following tasks have been completed internally by GTI:

- Final design framework for survey optimization using an earlier approach developed as part of the RPSEA funded Marcellus Shale Gas Project [09122].
- A new hybrid GA-SA search algorithm to identify the best designs within the limits of specified constraints.
- A new GA based ray-tracer to quickly identify ray-paths used for optimization when considering optimal tomography results or minimizing same/ similar data.

Introduction

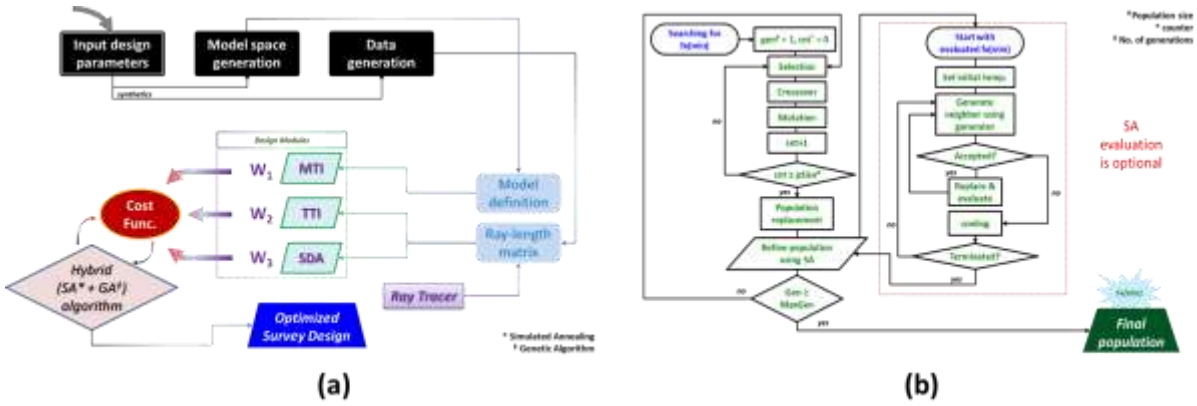

Figure 1: (a) Design framework for microseismic survey optimization and (b) optimization workflow using a hybrid GA (Genetic Algorithm)/ SA (Simulated Annealing) approach.

Some of the major issues when it comes to optimized microseismic survey design include the presence of too many variables/ cost functions needing optimization, difficulty in

quantification and validation of many of these parameters and the differing processing techniques and schemes in use today. Based on the known requirements for optimization defined from expected work to be carried out at GTI for future microseismic data acquisition, processing and analysis programs, we decided to focus on an optimized design framework involving getting the best possible solutions for a) Moment tensor inversion, b) travel time inversion, c) Solid angle minimization [Eaton, 2011] and d) Sabatier's data angle minimization criteria [Sabatier, 1977] to reduce uncertainty and bias in final solution. Figure 1 highlights the design framework we have devised as well as the hybrid GA-SA algorithm (genetic algorithm and simulated annealing approach) to find the optimal solution.

Ray Tracer

For the survey design workflow to be implemented, a 3D ray-tracing methodology was necessary for accurate travel time computation. The entire search space is gridded and computations are carried out independently at each grid point (center of grid). Values within grid but at offsets smaller than grid dimensions are computed using linear interpolation with radial distance as the basis. The designed ray tracing workflow follows the following steps for tracing:

- Initiate ray search for take-off angle θ.
- For each θ, shoot ray from source (center of grid point with co-located source) and take refraction at velocity interface into account (ΔV across each grid and neighboring grid along propagation direction).
- Compute error between the expected ray arrival and actual receiver position along the defined receiver plane.
- Iterate for all θ such that θ → "$\theta - \theta_{off}$" to "$\theta + \theta_{off}$" with step change of Δθ. Parameters θ_{off} & $\Delta\theta$ can be kept small, particularly with relatively simple earth models. The starting value is selected as the take-off angle between a straight line connecting the source and receiver grid centers.
- Identify minimum mismatch error and select corresponding ray as final selection.
- If separation < predefined error threshold, reset Δθ or redefine model parameters and repeat ray search.

Figure 2, Figure 3 and Figure 4 show a sample ray-tracer output for homogeneous increasing, layered perturbed and finally, complex laterally heterogeneous velocity models. The associated search grid is superimposed for reference.

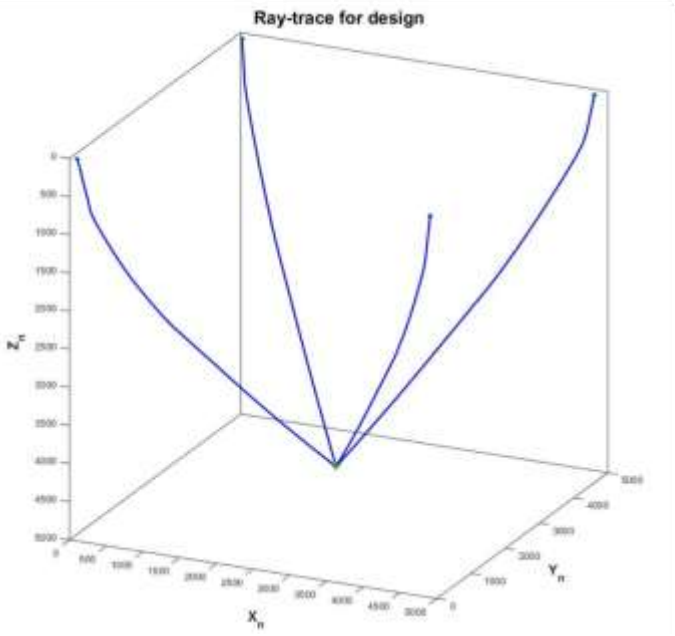

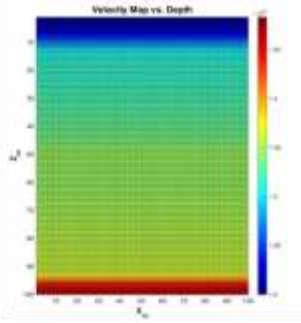

Ray #	Travel Time	Sample Points (sample rate: 0.25 ms)
1	0.4363	1745
2	0.4368	1747
3	0.4361	1744
4	0.4364	1746

Figure 2: Sample simple velocity model and ray tracing results for optimal source-receiver travel path identification based on said model. Note relatively low travel time mismatch.

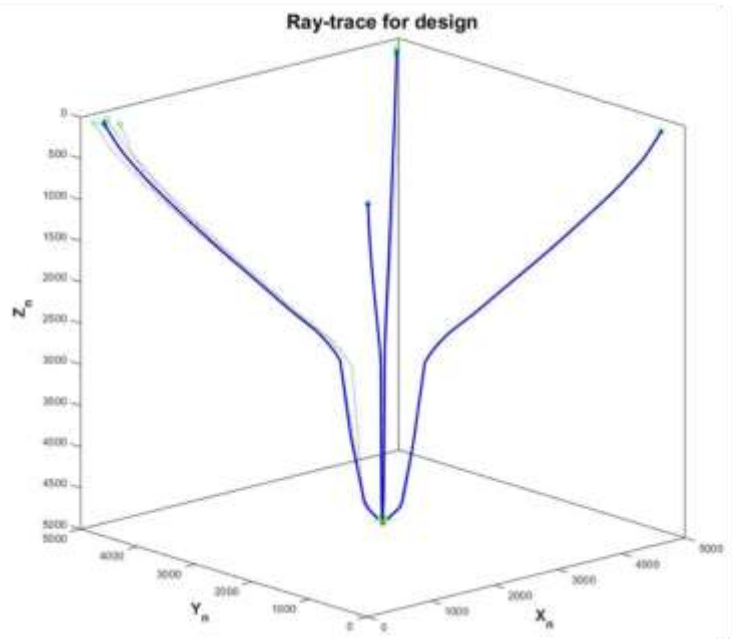

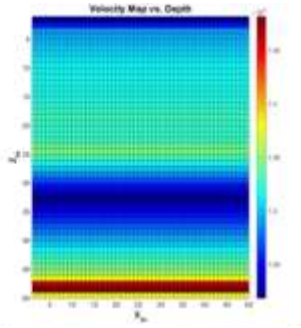

Ray #	Travel Time	Sample Points (sample rate: 0.25 ms)
1	0.46182	1847
2	0.46109	1844
3	0.46108	1844
4	0.46134	1845

Figure 3: Sample layered velocity model and ray tracing results for optimal source-receiver travel path identification based on said model. Note relatively low travel time mismatch.

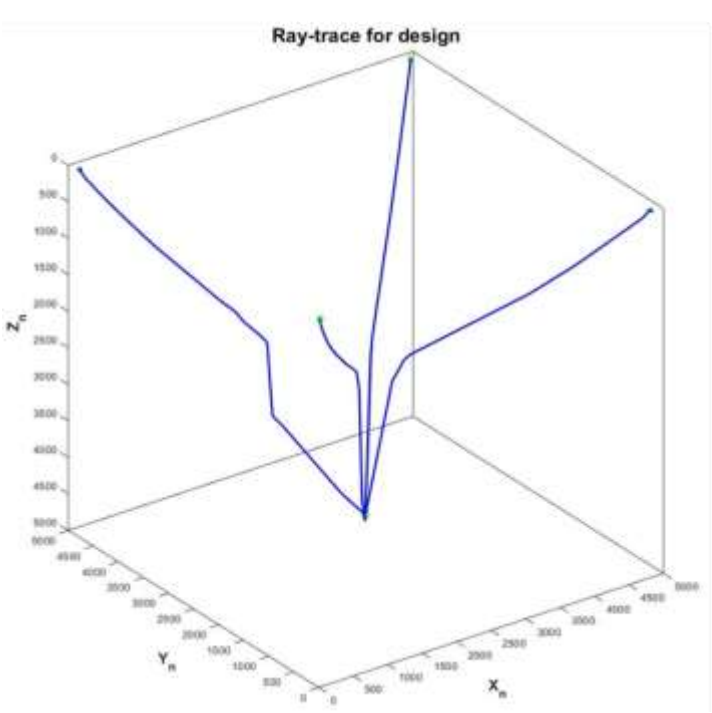

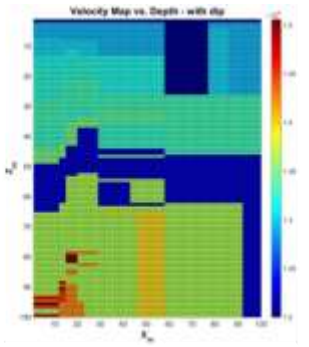

Ray #	Travel Time	Sample Points (sample rate: 0.25 ms)
1	0.4533	1813
2	0.43378	1735
3	0.44713	1788
4	0.44821	1793

Figure 4: Sample complex velocity model and ray tracing results for optimal source-receiver travel path identification based on said model.

Despite the use of a robust optimized search technique, the ray tracer can take significant time to trace rays for tens of thousands of potential source/ receiver location pairs. For eventual implementation, a VC++ [Visual Studio] based platform will be ideal for faster grid based search results. Alternatively, more innovative problem design is needed to improve applicability for very large grid points in search space which is needed for accurate ray tracing. Due to use within Matlab environment, there are current evaluation constraints placed by grid dimension limitations (~ 10^6 cells). These can be solved using more robust memory management techniques. There also exists significant scope for future improvement in methodology to generate better results including hybrid methods (such as additional pseudo bending implementation using the ERT results as starting point), etc. We also note that we obtain very low location error at trace extremities (10's of feet) which is always less than the actual grid dimension and therefore considered as acceptable for analysis. This is particularly true when the data is to be used for grid based analysis workflows such as Semblance Weighted Emission (SWE) mapping highlighted in Appendix F.

Theory/ Results

With the ray-tracing workflow in place, we define the individual optimization (cost) functions to be used in the design workflow. First we look into travel time inversion processing. For the ray path defined by the ray-tracer, the travel time equation is given by:

$$d_i = \int_{\text{ray path j}} \text{slowness}(u)du \quad = \quad \sum_{k=1}^{P} l_{ik} m_k$$

The equation in discretized form sums over individual cells which are covered by the ray path in the discretized earth model. So the inverse problem to solve for model space, m (representing slowness) is defined as:

$$d = A_s m$$

Where the A_S (i × j) matrix is defined based on ray length in ij^{th} grid (l_{ij}). The solution is obtained based on the inversion matrix as:

$$m = \left[A_S{}^T A_S\right]^{-1} A_S{}^T d$$

In the context of survey design, the inversion matrix can be decomposed into eigenvalues and eigenvectors. Positive eigenvalues correspond with independent pieces of information. Eigenvectors provide the actual information corresponding to these eigenvalues. Based on the decomposition, various quality measures can be defined and used depending on how we want to define the optimization problem. If λ_i where i = 1 to P defines the eigenvalues of $A_S{}^T A_S$ in decreasing order of magnitude, the four common quality measures (Curtis, 2004) used are defined as:

$$\theta_1 = \sum_{i=1}^{P} \frac{-1}{\lambda_i + \delta}; \qquad \theta_2 = \sum_{i=1}^{P} \lambda_i \; ; \qquad \theta_3 = \sum_{i=1}^{P} \frac{\lambda_i}{\lambda_1} \; ; \qquad \theta_4 = \prod_{i=1}^{P} \lambda_i$$

Here, measure Θ_1 is computationally expensive but is sensitive to eigenvalues with magnitude around δ which can in turn be used to set a lower sensitivity threshold based on expected data noise levels. Measure Θ_2 evaluates the area under the eigenvalue curve. Maximization of this measure is achieved by increasing the largest eigenvalues at the expense of small ones. It is known to give reliable constraints especially with very few independent pieces of information. Measure Θ_3 evaluates the area under the normalized eigenvalue curve. This measure is increased by increasing the smaller eigenvalues relative to the largest one. This measure provides a more even spread of constraints with more pieces of information (compared to Θ_1).

Measure Θ_4 is more evenly sensitive to the magnitude of all eigenvalues. Maximizing Θ_4 is equivalent to minimizing expected post-survey model parameter uncertainties. Figure 5 shows the optimization test results for a survey setup with a constant velocity model. The selected geophones are highlighted in blue.

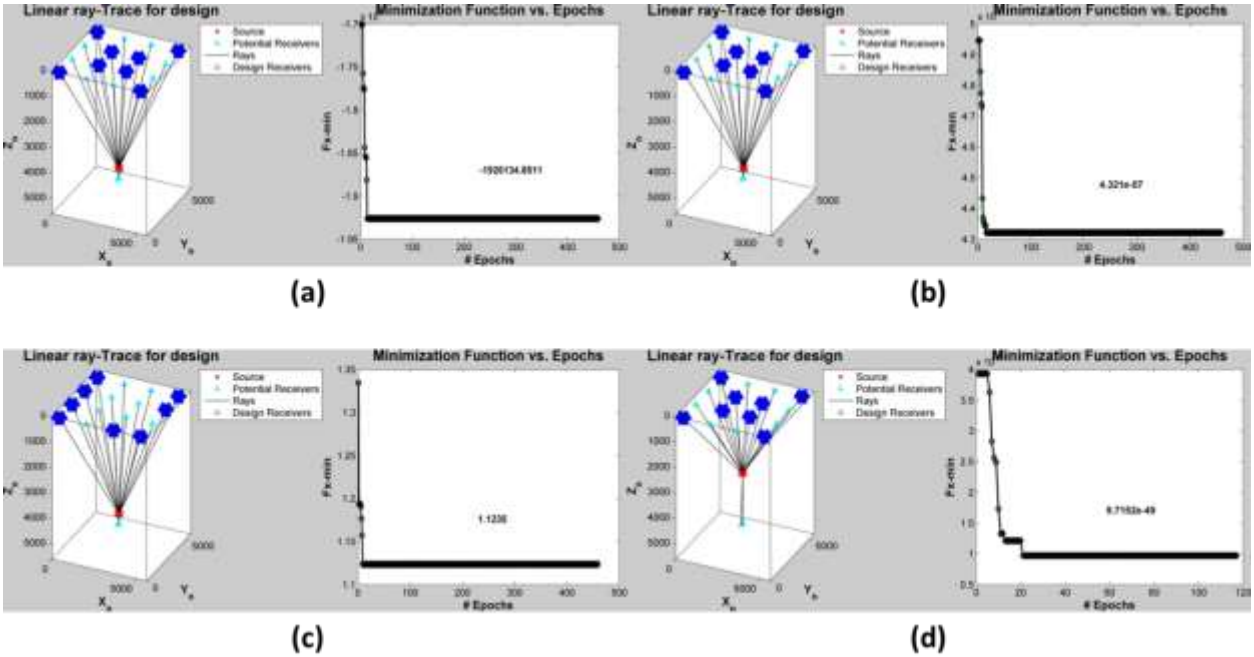

Figure 5: Trial optimization results for (a) θ_1, (b) θ_2, (c) θ_3 and (d) θ_4 parameters for a surface array.

Next we look into optimization for moment tensor solutions. In order to solve for moment tensors, the concept of solid angles can be used. The solid angle subtended by a surface is defined as the surface area of a unit sphere covered by the surface's projection onto the sphere. This can be written as:

$$\Omega \equiv \iint_S \frac{\hat{n} \cdot da}{r^2}$$

Where $\hat{n}$ represents the unit vector from origin normal to da which is the differential area of a surface patch. Finally, r is the distance from origin to the patch. In order to reduce the impact of noise on matrix inversion when solving for the over-determined system (provided we have adequate number of receivers), the solid angle has to be maximized. The design framework involves computing the peripheral receivers within the solution space (of receivers) and

computing the solid angle for selected receiver patch. The maximization of the solid angle is based on the hybrid GA+SA optimization framework as discussed earlier. Figure 6 shows the results from optimization for surface arrays with 8/ 16 receivers showing the optimal solution to lie on a hypothetical sphere as it intersects the receiver plane.

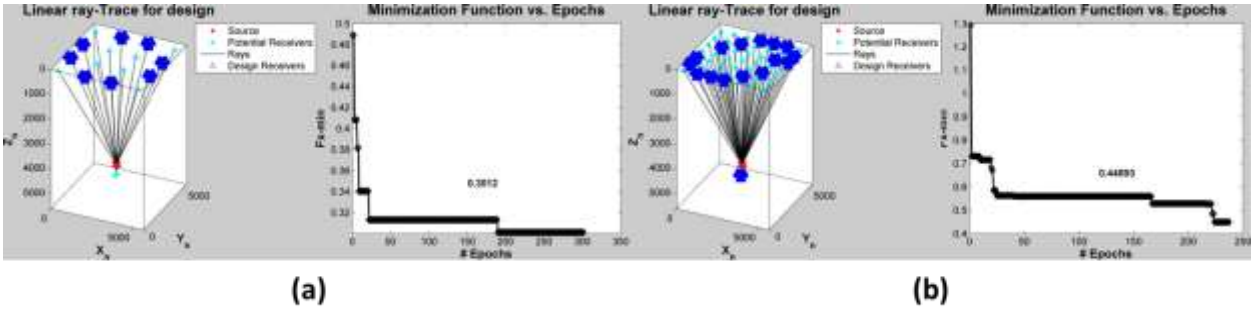

Figure 6: Optimized solution using solid angle technique for (a) 8 surface receivers and (b) 16 surface receivers.

Finally, we look at Sabatier's data angle evaluation. We understand that singularity condition (for eigenvalues) from ray-length vectors (travel time inversion discussion) will occur when rows are linear combination of other rows in the A_S matrix. Sabatier (1977) identified use of this phenomenon to reduce the size of large datasets by removing vectors that are effectively repetitions or combinations of others. The data angle (or angle between two ray vectors) based measure is computed as:

$$\Phi = \sum_{i=1}^{n_R} \sum_{j=1,\, j\neq i}^{n_R} \left[1 - \frac{\left|a_i \odot a_j\right|}{\|a_i\|\|a_j\|}\right]$$

The optimization workflow is as follows:

- For each selected receiver, compute data angle measures summed for all possible receiver pairs.
- Identify the best solution using an iterative GA or GA+SA approach where the identified maximum is selected as final design.
- The pairs with minimal separation are progressively pruned.

Figure 7 shows the results from optimization for surface arrays with 8/ 16 receivers showing the identified optimal solution.

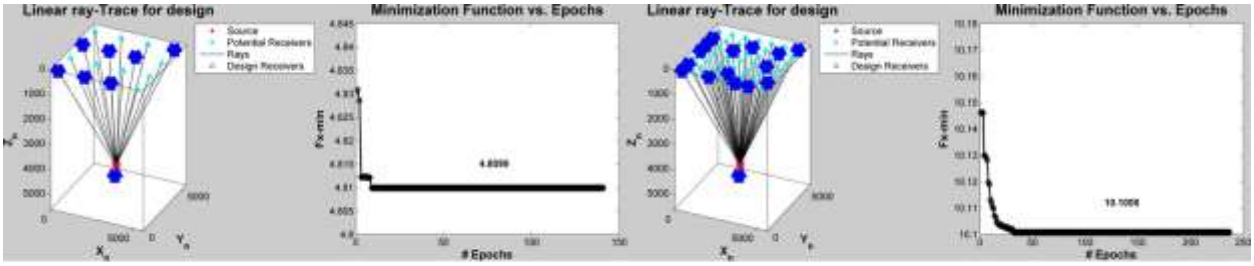

Figure 7: Optimized solution using Sabatier's data angle technique for (a) 8 surface receivers and (b) 16 surface receivers.

The final optimization step will involve solving for identified parameter or a combination of parameters by using suitable weighting coefficients to get modified cost function for optimization.

As an independent design optimization check, displacement modeling will be used (such as Brune model or Abercrombie model) and the same will be correlated with instrument spectra in order to verify suitability of selected geophones/ survey design used in study. Figure 8 shows the modeled displacement spectra's for a varying magnitude (M_W) events using Brune model. Figure 9 shows the same for Abercrombie model. Figure 10 and Figure 11 show the amplitude spectra for Brune and Abercrombie models respectively. The red plots are for surface receivers and blue plots are for borehole receivers. The models are defined as follows:

Brune Model:

$$\Omega(f) = \frac{\Omega_o}{\sqrt{1 + \left(\frac{f}{f_c}\right)^2}}$$

$$\Omega_o = \frac{F_R S_a}{4\pi\sqrt{\rho_r \rho_s {v_r}^5 {v_s}^5}} \frac{M_o}{R_h}$$

$$M_o = 10^{\frac{2}{3}M_w + 9}$$

$$f_c = \frac{K v_s}{2\pi R_o}$$

$$R_o = \sqrt[3]{\frac{7}{16}\frac{M_o}{\sigma_o}}$$

Abercrombie Model:

$$\Omega(f) = \frac{\Omega_o}{\left(1 + \left(\frac{f}{f_c}\right)^{\gamma n}\right)^{\frac{1}{\gamma}}} e^{\frac{\pi f r_h}{Q\sqrt{v_s v_r}}}$$

Here, Ω denotes the amplitude from spectrum, f is the frequency from the spectrum, f_c is the corner frequency which is inversely proportional to the size of a seismic source, γ is the high frequency fall off rate (computed from a log-log plot), M_0 is the seismic moment, M_w gives the moment magnitude, V_s and V_r are velocities at source and receiver location respectively while ρ_r and ρ_s are the densities of the medium at said locations, Q is a quality factor characterizing the inelastic attenuation of the medium. The Abercrombie model is considered more robust as it takes care of high frequency roll-off with slope n and sharpness γ. It also takes into consideration attenuation effect through 'Q'. The analysis is conducted for all source-receiver pairs and the smallest magnitude events detectable at different receivers are mapped. For a more detailed understanding of earthquake far-field displacement models shared here, refer to relevant publications [Brune, 1970 & Abercrombie, 1995].

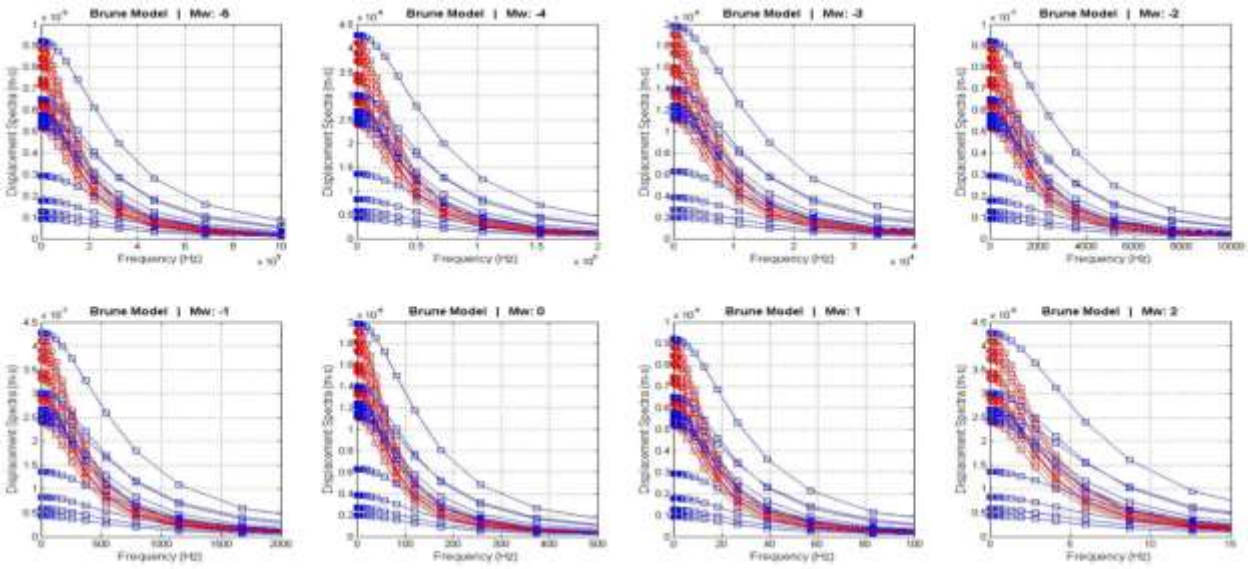

Figure 8: Displacement spectra using Brune earthquake model.

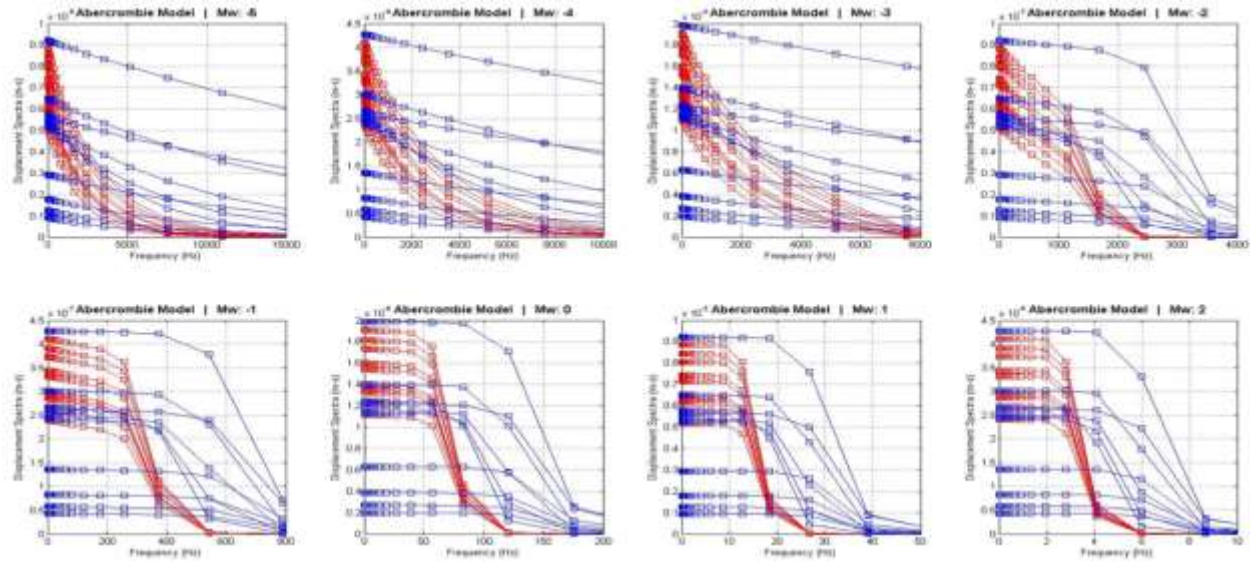

Figure 9: Displacement spectra using Abercrombie earthquake model.

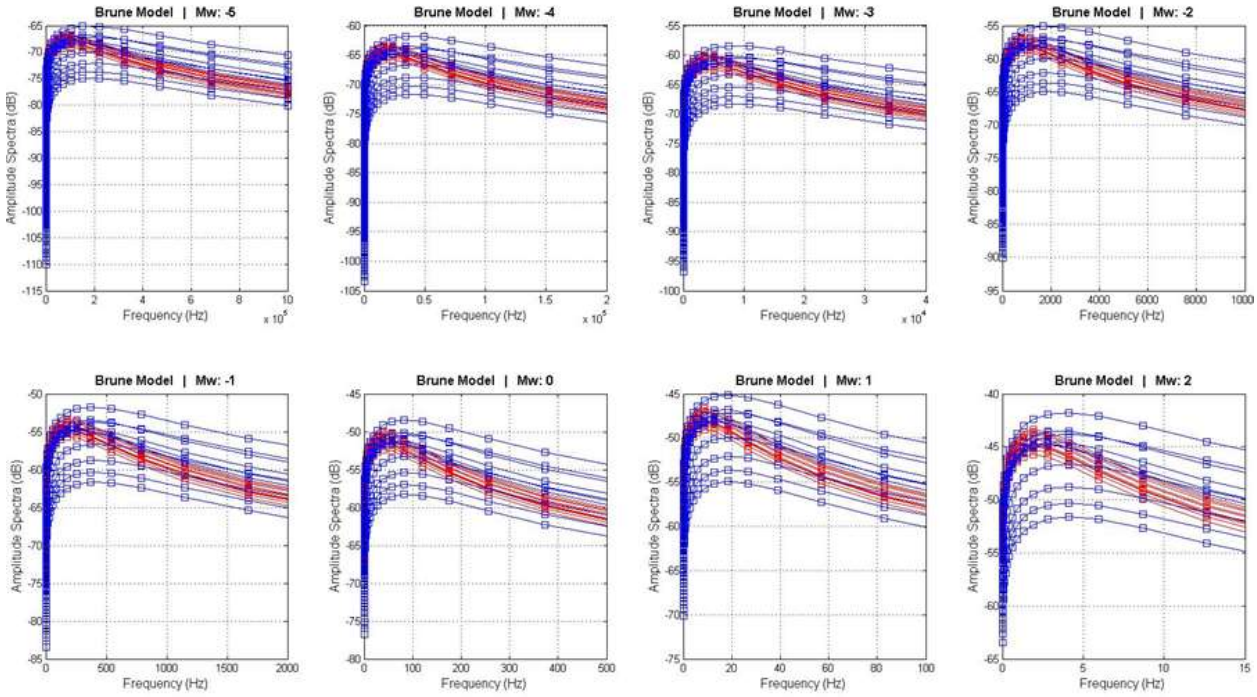

Figure 10: Amplitude spectra using Brune earthquake model.

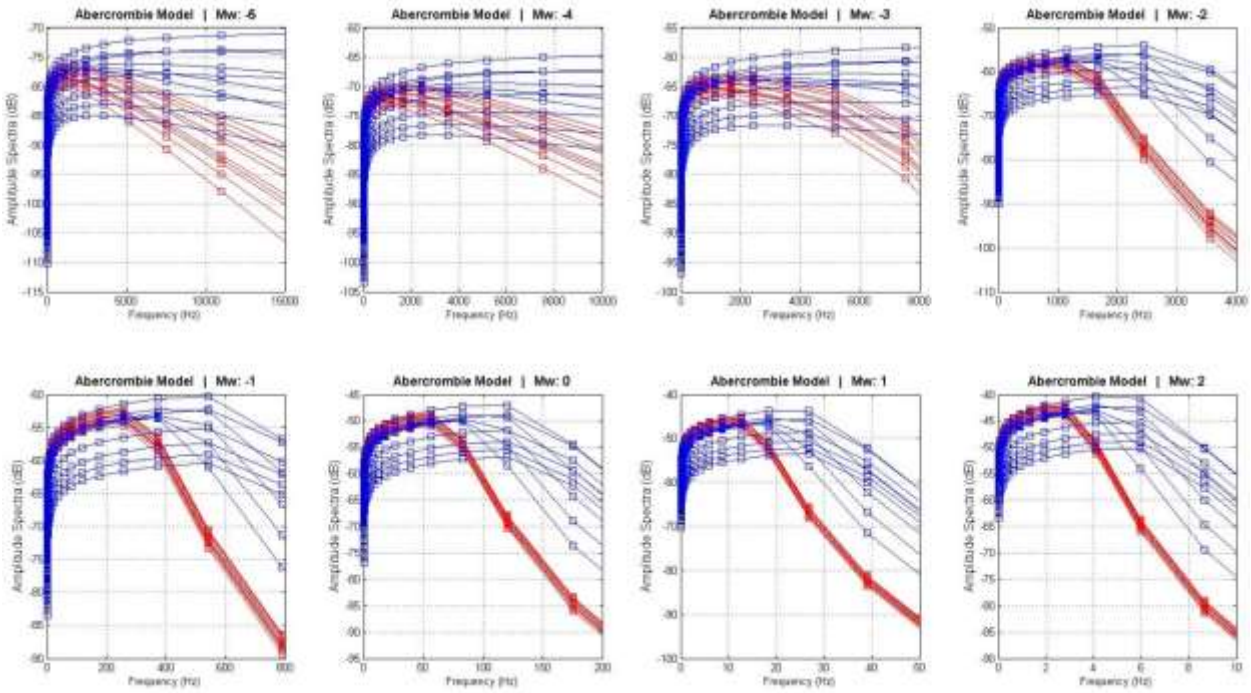

Figure 11: Amplitude spectra using Abercrombie earthquake model.

We can map the events by relative displacements for a sample source for all possible receiver locations and using a predefined threshold spectrum obtained for the geophone instruments to be used in the survey, analyze the effectiveness of each receiver in mapping a series of sources based on the expected stimulated reservoir volume during the experimental completion. Figure 12 shows the modeled displacements for a sample survey design.

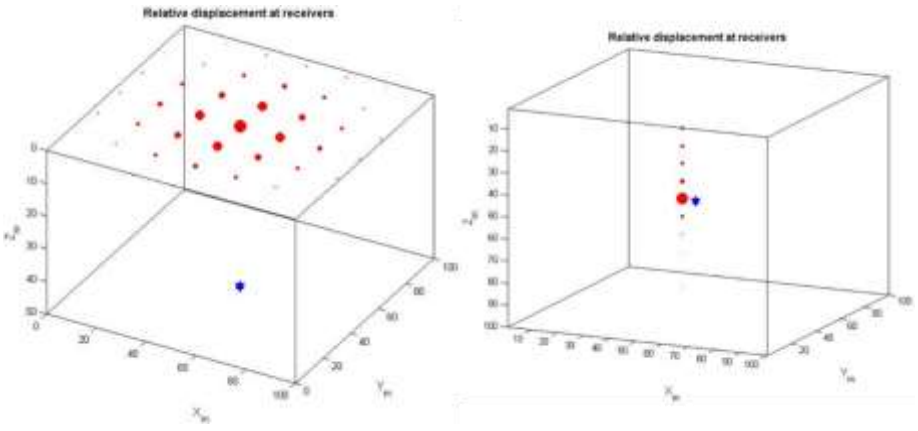

Figure 12: Modeled displacement patterns for s sample event and receiver geometry.

Survey design optimization (for imaging algorithms)

In recent years, a number of solutions are being provided for improved microseismic mapping by making use of imaging algorithms (such as scanning emission tomography(Duncan, Lakings, & Flores, 2010), reverse time migration(Wang & Cheng, 2013), etc.). The biggest upside to using these algorithms is their relative immunity towards high noise (low SNR conditions) as well as improved understanding of reservoir behavior pre-, peri- and post-injection. However, the downside to imaging algorithms is their need for proper triangulation and very high degree of redundancy (by using large number of widely distribute geophones) in order to improve results from stacking (which is critical in enhancing the underlying signal strength over noise). Most available solutions utilize large surface deployments which can lead to significant financial and legal/ regulatory issues. GTI proposes the use of a sparse deployment which will combine the traditional horizontal wellbore deployment with a few carefully located "near surface" geophones. The near surface geophones will be tightly clustered in order to remove any move-out effects and the resulting (stacked) signals will be used to improve the imaging results. A more detailed analysis of the process involved is discussed in Appendix F. Figure 13 shows a near surface deployment with 49 equally spaced sensors as well as the mapped "semblance weighted" emission observed from the corresponding synthetic gather. For these test cases, we placed the simulated "source" at the center of the defined grid space (24 × 24 × 24) within a 3D mesh (48 × 48 × 48) used for waveform modeling and emission mapping.

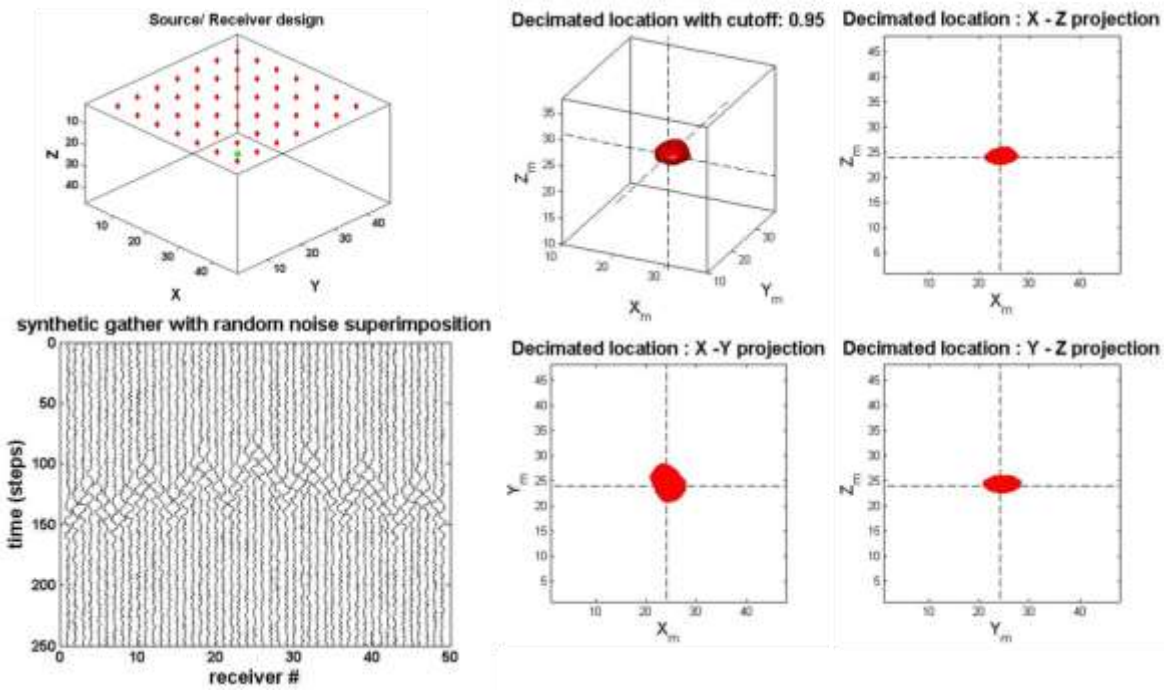

Figure 13: Emission tomography results (test case with evenly dispersed surface deployment).

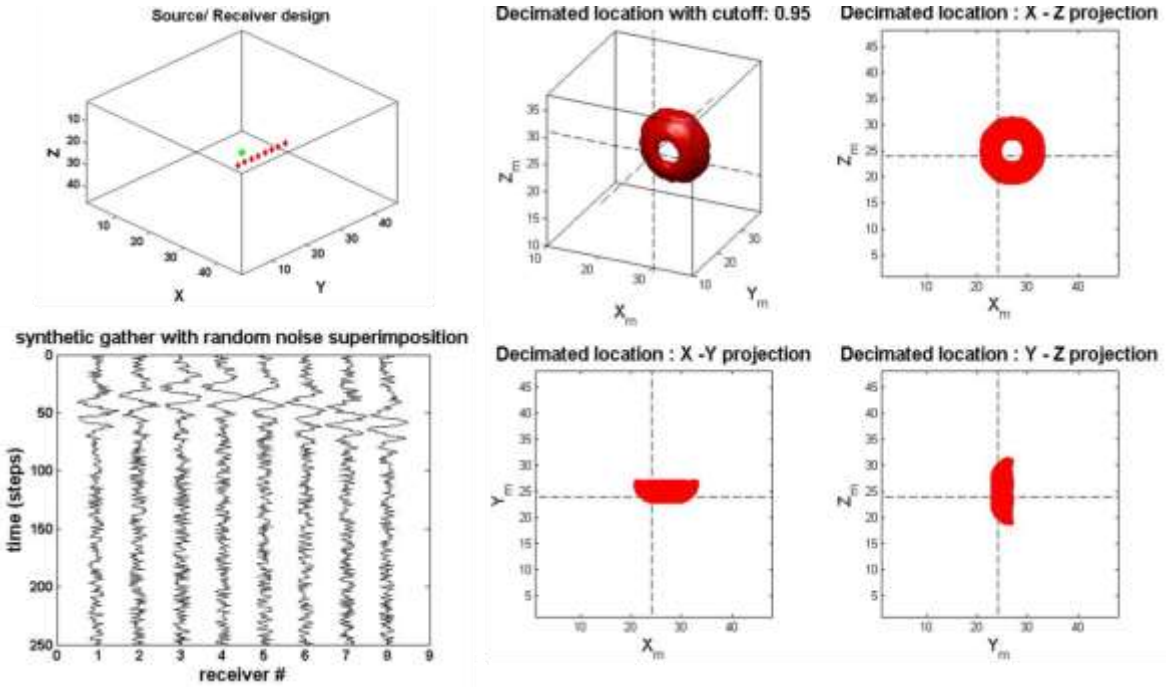

Figure 14: Emission tomography results (test case with wellbore - horizontal deployment).

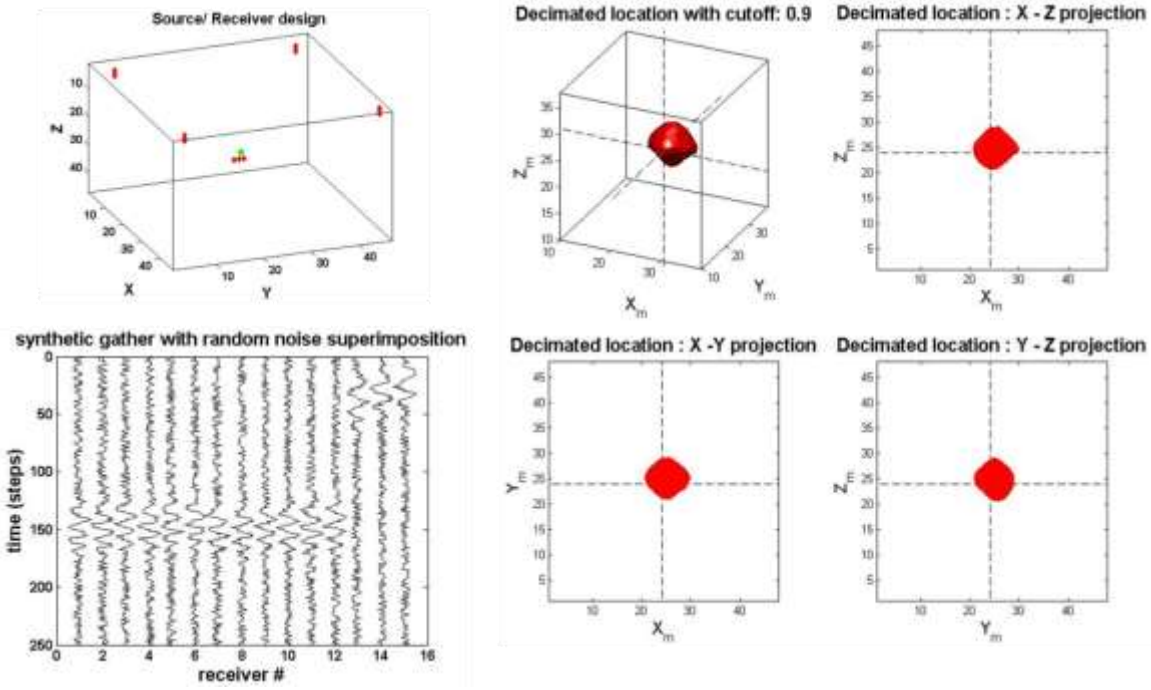

Figure 15: Emission tomography results (test case with both wellbore and sparse surface deployment).

Analyzing the decimated volume from Figure 13, we observe that the uncertainty in the vertical plane is reduced substantially (and is lower compared to uncertainty in horizontal plane). Similarly, when we look at the case with a single horizontal geophone sensor array (Figure 14) close to the perturbed (injection) zone (as is the case with the monitoring program used in phase 1 of this project), we observe the limitations posed by the Source-Receiver geometry which results in a donut shaped high energy zone around the actual (simulated) event. The results are the same with a vertical deployment (except that the axis of the donut is oriented vertically). Finally, Figure 15 shows a possible deployment with a wellbore array and a few near surface deployments. In this case, we observe improved imaging despite the non-uniqueness and inaccuracy coming in through the wellbore signals. We also observe that the vertical resolution is lower compared to test case shown in Figure 13. At the same time, the improvement in horizontal resolution while present is not substantial. This indicates that increasing the number of surface constraints beyond a certain threshold may not provide substantial improvements in the results. Next, we look into array optimization studies that were conducted to try and identify the best possible deployment scheme for future monitoring programs with imaging based processing workflows in mind. The aim is to minimize the deployment costs my placing minimum possible surface sensors by utilizing available resources (shallow water wells or existing wells) or by drilling some shallow monitoring wells and using the collected data to constrain the solutions obtained from the primary (wellbore) geophone array. A number of simulations were run to identify the best possible deployment scheme for surface sensors provided we had the subsurface array available. Figure 16 shows the optimal location for surface sensors based on the said tests.

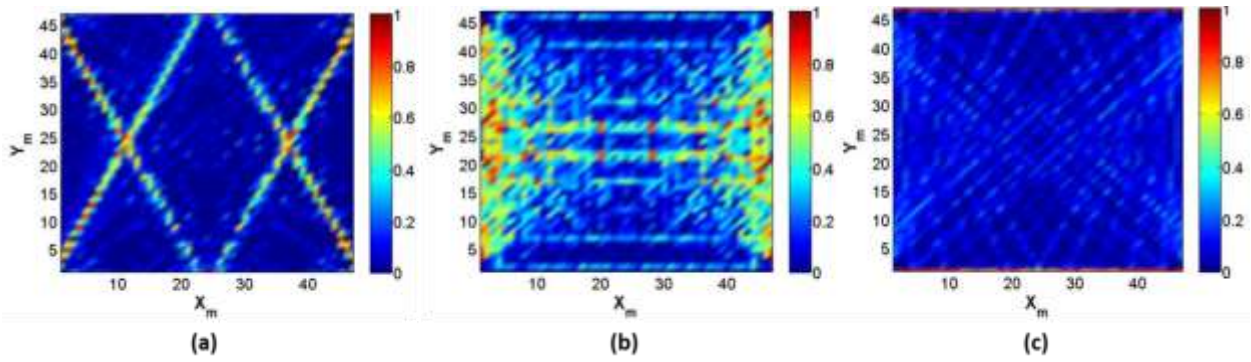

Figure 16: Optimization function maps at surface (with additional wellbore constraints through 8 sensor subsurface array) for (a) single surface constraint, (b) dual surface constraint and (c) triple surface constraint.

It should be noted that the source is located at the mid-point of the simulation grid volume (48 × 48 × 48 grid cells) with a horizontal wellbore array located at a lateral offset from the simulated source. As observed from the spatial distribution of the optimization function, for a single surface constraint, the optimum locations seem to fall along angular offsets based on the subsurface array, for two surface constraints (Figure 16b), the optimum locations seem to fall at the periphery of the test area with some higher values close to the center (hourglass map). High values tend to follow linear offsets from the selected wellbore array geometry and reduce with distance along the plane of array. With three surface constraints (Figure 16c), we observe that the optimum locations fall along the periphery of the test area indicating that the optimum results can be obtained with the sensors being placed as far away from the source as possible (however attenuation effects need to be considered to strike a balance). Table 1 gives the average errors and uncertainties obtained for the test runs and as expected, increasing surface constraints tend to improve the location estimates.

Table 1: Uncertainties and errors associated with simulation runs to identify improved array design workflow for microseismic imaging.

	Borehole + 1	Borehole + 2	Borehole + 3	Baseline
# iterations	100	10000	10000	1
# maxima within ± 500 ft.	7 (7%)	836 (8.36%)	1704 (17.04%)	1
Average volume after decimation (cutoff: 0.9)	949	716	393	166
Location error measure over all iterations (2D)	5.39	4.68	4.43	2
Avg. location error over all iterations (3D)	7.21	6.93	5.88	2

It should be noted that the baseline test run involved an equi-spaced surface array (Figure 13) for comparative analysis. We observe that the number of test deployments with relatively high accuracy increases with the additional surface constraints ({Baseline} > {Borehole + 3} > {Borehole + 2} > {Borehole + 1}). This indicates that for the best possible imaging results, the aim should be to place as many surface constraints as possible. In future projects, it will be critical to look into the error maps observed for different source locations for a simple equi-spaced surface array to determine sensor behavior as a function of source parameters. This analysis has to be done both for 2D and 3D simulation grids to understand the best possible

deployment schemes for multi-array monitoring (both limited surface as well as the wellbore arrays).

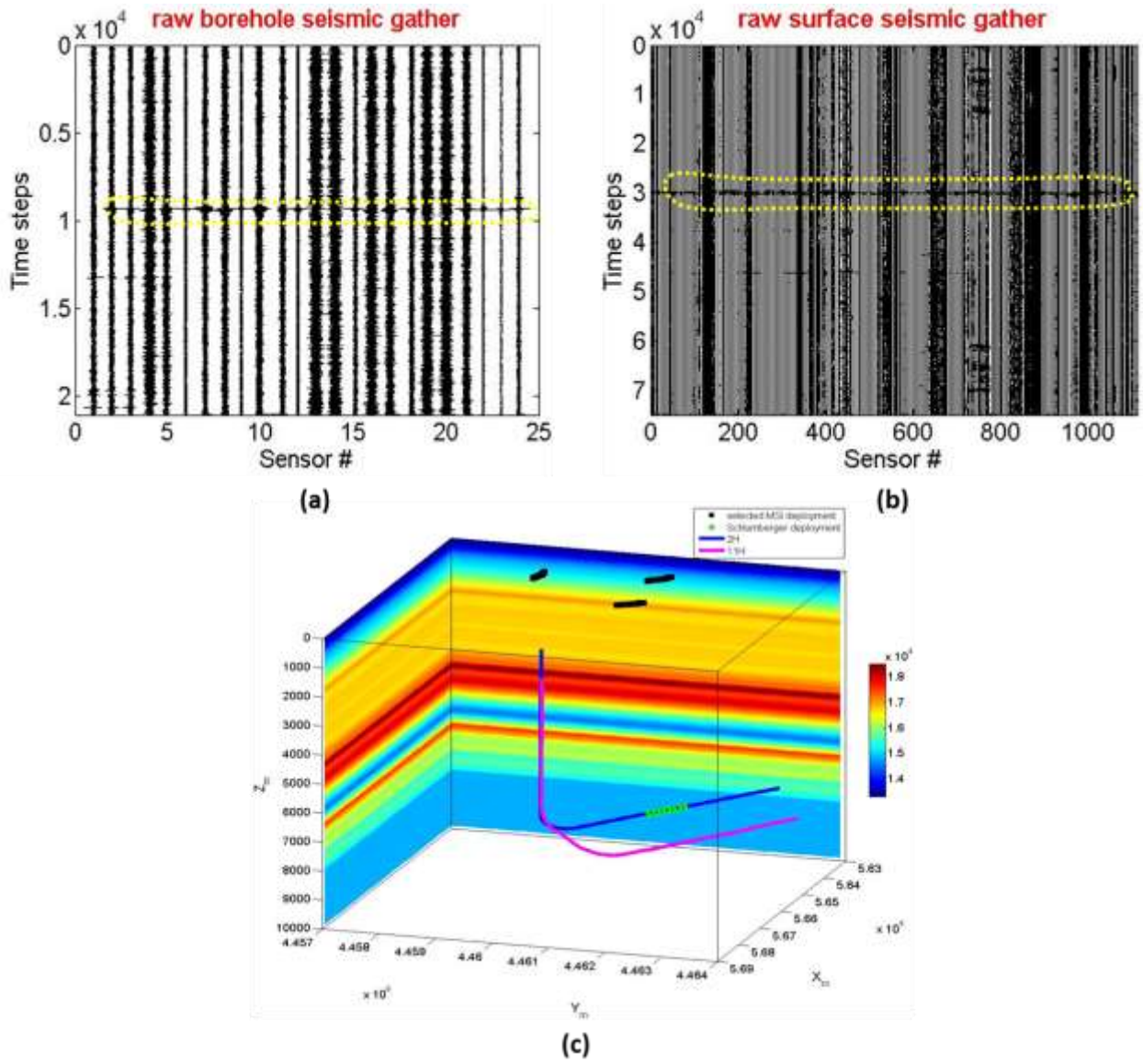

Figure 17: Identified event from (a) borehole and (b) surface data and (c) final configuration of borehole and surface sensors used for event processing. The background density map in (c) highlights the compressional velocity model used (ft/sec).

Finally, based on actual wellbore and surface data collected for an earlier RPSEA project (RPSEA 09122), tests were conducted for identified events to validate the applicability of the proposed methodology for real data. A high SNR event was first identified based on the

processed wellbore data and the corresponding continuous data from the surface measurements was extracted (based on time stamp) and analyzed to identify the same event (based on approximate S-R separation and expected move-out). The identified event is shown in Figure 17 (a, b) while Figure 17c shows the final configuration selected for processing to test applicability of imaging approach. Figure 18 shows the final results including the move-out match obtained (for both wellbore and surface data) as well as the decimated volume/ location of the identified event correlated spatially with the treatment/ observation wells.

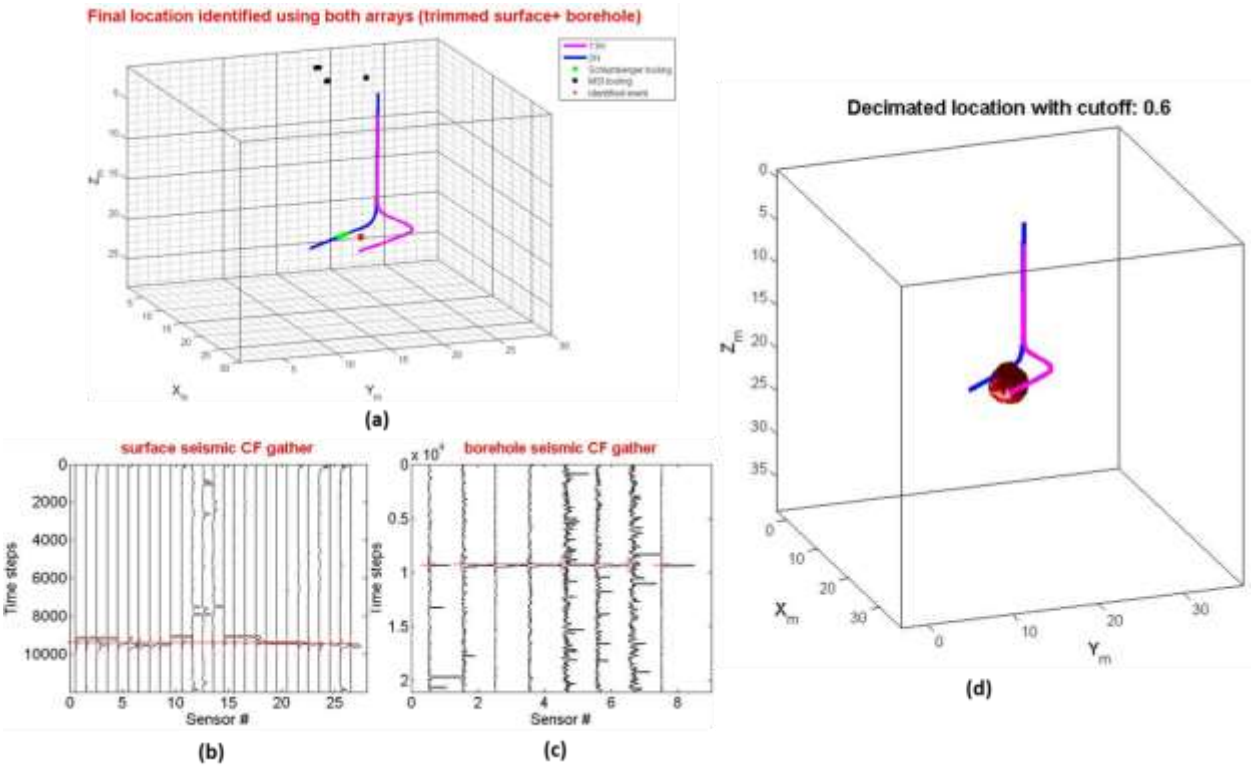

Figure 18: Subplot (a) shows the final identified event location based on "emission" maxima. Subplots (b) and (c) show the synthetic moveouts and their match with the derived characteristic functions from microseismic gathers. Subplot (d) shows the decimated volume indicating reduced event location uncertainty.

Potential Application

For future microseismic survey programs, we will initiate and conduct a robust survey design and analysis and collaborate with the relevant microseismic and other service companies as required to optimally place additional sensors as necessary to validate the methodology and refine the design workflow as required. Moreover, GA-SA ray-tracer introduced in this study

can help with survey design and also help with accurate processing of data wherever accurate synthetic arrival times are needed without having to resort to full waveform modeling.

References

[1] Abercrombie, R. E., (1995), 'Earthquake source scaling relationships from -1 to 5 M_L using seismograms recorded at 2.5-km depth', J. Geophys. Res., 100 (B12), 24015-24036.

[2] Brune, J. N., (1970), 'Tectonic stress and seismic shear waves from earthquakes', J. Geophys. Res., 75, 4997-5009.

[3] Duncan, P. M., Lakings, J. D., & Flores, R. A., (2010), *Patent No. 7,663,970 B2.* USA.

[4] Eaton, D. W., (2011), 'Solid angles and the impact of receiver-array geometry on microseismic moment-tensor inversion', Geophys. J. Int., 76.

[5] Sabatier, P. C., (1977), 'On geophysical inverse problems and constraints', Geophys. J. Int., 43.

[6] Wang, C. L., & Cheng, J. B., (2013), 'Microseismic Event Location Using Reverse-Time Focusing and Interferometric Techniques for Surface and Borehole Observations', *Chinese Journal of Geophysics,* 56(5), 584-597

Appendix J: Spreadsheet analysis of bimodal production decline curve in a hydraulically-fractured shale-gas reservoir

Status of Objectives

We implemented in an Excel spreadsheet an expanded version of a semi-analytical solution for a bimodal production decline curve for hydraulically-fractured shale-gas reservoirs. The toolbox has been implemented within Microsoft Excel platform. Curve-fitting to field data can be done by trial and error or automatically using the Solver tool within Excel, to determine flow and transport properties, fracture geometry parameters, and reservoir operating conditions. In this report, we list the underlying assumptions, we present and discuss the problem solution, we describe the use of the spreadsheet, and we examine in detail and analyze results from two example datasets that we have tested using the designed toolbox. The spreadsheet-based analysis is fast and simple yet powerful, and provides improved understanding of the hydraulic fracturing process, thus enabling future operations to be done more efficiently in addition to providing insights for more economical operation with reduced environmental impact.

Introduction

Background

Hydrocarbon production from tight reservoirs has experienced explosive growth over the last few years. Gas production from shale and tight-sand deposits has proven remarkably successful in increasing substantially both gas production and reserves estimates in the U.S. In addition to its indisputable financial benefits, the development of technology to produce fossil fuels in previously inaccessible domestic geologic systems is considered a substantial contributor to energy security.

The universal feature of all tight reservoirs is the unavoidable need for well and reservoir stimulation: the matrix permeability is extremely low (often at the nano-Darcy level) and, even with the presence of a system of natural fractures, it cannot support flow at anything approaching commercially viable rates without permeability enhancement. Such enhancement/stimulation is provided by a number of methods, all of which are designed to develop a new system of artificial fractures that increase the permeability of the system and increase the surface area (over which reservoir fluids flow from the matrix to the permeable fractures) to provide access to larger volume of the reservoir. Thus, stimulation techniques

are the only means of rendering resource-rich but unproductive natural reservoirs into commercially viable entities. Fundamentally, it is stimulation technology that made gas and oil production from shales possible and it is this same technology that has affected production increases of orders of magnitude over the last few years. Thus, production from such resources in the U.S. has exploded from zero levels at the beginning of 2000, to 6% of the gas produced in 2005 (U.S. EIA, 2007), to 23% in 2010, and is expected to reach 49% by 2035 (U.S. EIA, 2012). Additionally, the advent of effective reservoir stimulation methods have more than doubled the estimates of technically recoverable shale gas reserves in the US from 353 TCF to 827 TCF (US EIA, 2011).

Conventional stimulation techniques involve the creation of a system of individual fractures emanating from particular points along the wellbore. Although it may be possible to develop additional fractures (e.g., stress release fractures), the fracture system resulting from conventional stimulation is dominated by the "main" fractures (planar or dendritic) that occur at the locations of stimulation treatment.

Conventional stimulation techniques are usually variants of hydraulic fracturing (King, 2012), in which the near-incompressibility of liquids is exploited to deliver a shock that induces rock fracturing stemming from the target point. In this case, the artificial fracture system is induced by the injection of water or of a water-based medium into the fractures and the matrix of the geologic medium.

Hydraulic fracturing of tight shale-gas formations greatly improves production, but there is a need for greater understanding of the ensuing reservoir fluid flow and production from the complex fractured system resulting from such reservoir stimulation. The production rate in hydraulically fractured wells generally declines quickly, necessitating additional fracture stages (a re-fracturing process) or new wells both of which are expensive and carry increased environmental-impact risks. The complexity of the geologic systems resulting from the hydraulic fracturing of gas-bearing shales, coupled with the strong non-linearity of the flow of the highly compressible natural gas through the interacting fracture-matrix continua, create significant challenges in the analysis of production data because of the difficulty of extracting the necessary data describing the system properties. These are crucial for understanding the fracture characteristics (geometry, extent, aperture, orientation, etc.) and their effect on matrix-fracture mass exchanges. Such knowledge can provide a greater understanding of the flow geometry in the stimulated reservoir zone (SRZ), leading to improved estimates of expected production and a more accurate assessment of reserves and recoverable resources. Such knowledge can also offer guidance for additional/subsequent hydraulic fracturing operations, as well as important insights that have the potential to help design enhanced

fracturing processes that minimize costs, water usage, drilling footprints, and other associated environmental concerns.

Statement of the Problem, Objective and Approach

To obtain the necessary knowledge on the fracture and matrix properties, it is necessary to have the capability to conduct a rapid, near real-time model-based analysis of data collected during production from operating tight/shale gas fields. Depending on the complexity of the system under investigation, model-based analysis of oil and gas production can range from simple analytical solutions to complex numerical models. Often, the complexity of fractured media with strong non-linear flows and significant pressure and temperature gradients preclude the use of simple analytical models, leaving numerical models as the only option. Such an endeavor is time-consuming, expensive, and requires experienced modelers. It is therefore worthwhile, if the system under investigation lends itself to valid linearizations and approximations without violating basic laws of physics, to begin the analysis in a much simpler way, using an idealized representation of the real problem. The objective of this study is to develop a simple, Excel-based tool for the analysis of the complex problem of gas production from a fractured tight/shale gas reservoir that is based on a model that remains faithful to the underlying physics and can provide rapid estimates of the important parameters governing the system behavior.

That is the approach taken here. The scientifically robust model used as the basis for the Excel model is a significant modification of the bimodal production decline curve of Silin and Kneafsey (2012), hereafter referred to as mS&K. Using this expanded version of mS&K, we programmed the semi-analytical solution for production decline into an Excel spreadsheet and developed an interactive, user-friendly, Excel-based application for curve matching of well production data to the bimodal curve, by varying the aggregate (composite) variables defined in S&K. In a second step, the individual matrix and fracture properties that compose the aggregate variables can be extracted. In so doing, we can gain significant insight into the model parameters that control its behavior and production: the geometry of the hydraulically-induced fracture network, its flow and transport properties, and the optimal operational parameters.

In addition to providing the information on the induced fracture network needed to make informed choices about future operations, the curve-fitting process is valuable in several different ways. First, curve-fitting is essentially history matching, so a calibrated model can then be used to predict future production rate, including expected ultimate recovery and the useful lifetime of the stage or the well. Second, if curve-matching is not successful, that is, if no combination of aggregate parameters can provide a good match between the data and the

bimodal curve, this indicates that the real system is not behaving as predicted by the idealized mathematical model and, therefore, that the assumptions of the idealized model are not met. In that case, the use of a more complex numerical model to analyze the system is the only recourse. The semi-analytical solution is also useful as a reference for the verification/validation of numerical models. Finally, if the bulk of the production data can be fit to the bimodal curve, then data points that do not fit the curve suggest local or short-term anomalous behavior or measurement error.

This paper is organized as follows. In section 2, the idealized problem and the original semi-analytical solution of Silin and Kneafsey (2012) are introduced, along with the generalization of the expanded mS&K solution that enables a broader range of data to be analyzed. Section 3 presents the Excel spreadsheet methodology, Section 4 illustrates the curve-fitting procedure with two example problems, and Section 5 provides concluding remarks.

2. Idealized Problem and Semi-Analytical Solution

Assumptions

The Silin and Kneafsey (2012) problem (hereafter referred to as S&K) is illustrated in Figure 1, which shows several fracture stages along a horizontal well. Each fracture stage consists of a stimulated reservoir volume (SRV) of areal extent A and thickness D, consisting of a planar primary fracture perpendicular to the wellbore and a network of fractures orthogonal to the primary fracture. It is assumed that for a tight gas reservoir, production only occurs from the SRV. Additionally, it is assumed that the permeability of the primary fracture is so great that the pressure in the primary fracture is uniform and equals the pressure in the well. Hence the semi-analytical solution only models flow through the orthogonal fracture network. The solution can be applied to the SRV resulting from a single hydraulic fracture stage or to multiple SRV's resulting from identical stages that were created simultaneously, in which case A would be the sum of the areal extents of all the stages.

The fluid is assumed to be single-phase, constant-compressibility gas, which flows according to Darcy's law, and is in equilibrium with gas adsorbed on the rock (for more details, see S&K). The system is assumed to remain at constant temperature and all thermophysical properties, such as density, viscosity, and sorption coefficient, are a function of pressure only. Initially, the gas in the reservoir and the well is at a constant pressure, pR; at time zero the pressure at the well is dropped to pW, where it is held constant during the production process.

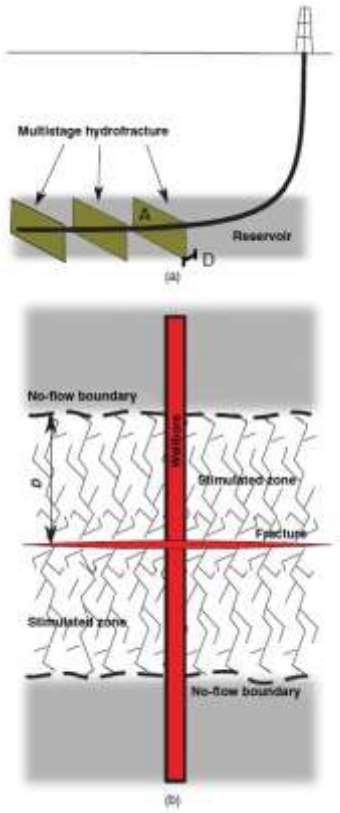

Figure 1: Schematic of the idealized problem (modified from S&K).

The S&K Bimodal Solution for Production Decline Curve

The production period is divided into two regimes: An early-time regime before the extent of the SRV is felt, where an analytical similarity solution for gas production rate can be obtained, and a late-time regime where the rate can be approximated with an exponential decline, or more accurately with a semi-analytical solution obtained by numerical integration. The key parameters controlling the solution are characteristic time t0, characteristic flow rate Q_0, and parameter u_0, which is the square of the ratio of well pressure to reservoir pressure and which determines the transition time between early-time and late-time regimes t*.

The solution for dimensionless production rate $Q_D = Q/Q_0$ as a function of dimensionless time $\tau = t/t_0$ and parameter u_0, is given by S&K Eq. (A-13) as

$$Q_D = \frac{2(1-u_0)}{\alpha\tau^{1/2}} \qquad \text{for } \tau < \frac{1}{\alpha^2} \qquad (1a)$$

$$= 2\beta(\tau)(1-u_0) \qquad \text{for } \tau > \frac{1}{\alpha^2} \qquad (1b)$$

Where $\beta(\tau)$ is the solution of the ordinary differential equation given by S&K Eq. (JA-9)

$$\frac{d\beta(\tau)}{d\tau} = -\frac{3}{2}\beta(\tau)\sqrt{u_0}\left[1 + \frac{u_0+\beta(\tau)(1-u_0)}{\sqrt{\beta(\tau)(1-u_0)u_0}}\arctan\sqrt{\frac{\beta(\tau)(1-u_0)}{u_0}}\right] , \quad (2)$$

Which can be approximated for small values of β as S&K Eq. (JA-12)

$$\beta(\tau) = \exp\left[-3\sqrt{u_0}\left(\tau - \frac{1}{\alpha^2}\right)\right]. \quad (3)$$

The parameter α is given by S&K Eq. (JA-8) as

$$\alpha = \sqrt{6\left(\sqrt{u_0} + \frac{1}{\sqrt{1-u_0}}\arcsin\sqrt{1-u_0}\right)}. \quad (4)$$

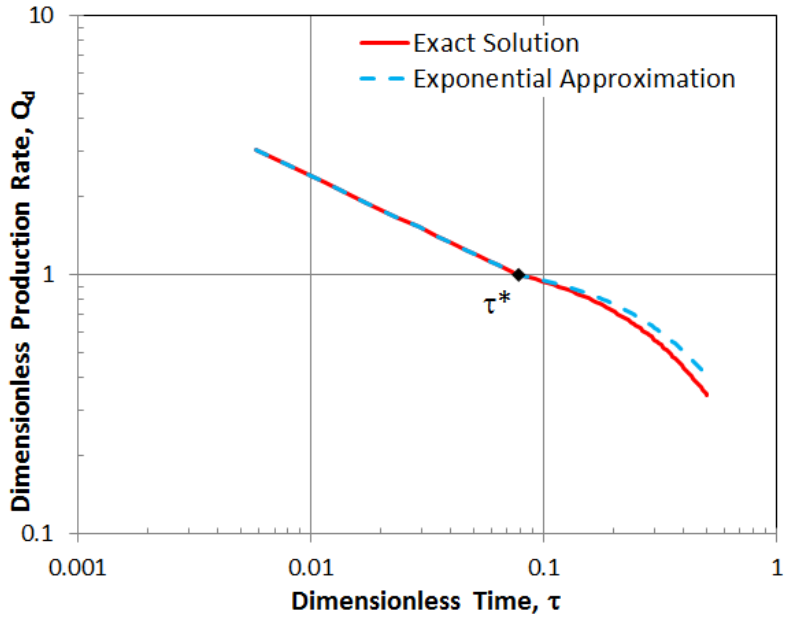

Figure 2: S&K bimodal solution; dimensionless transition time τ* is shown by the black diamond.

Figure 2 shows a log-log plot of Q_D versus τ, for $u_0 = 0.75$. Note that the early-time solution is linear with a slope of -½, as specified in Equation (1a). The late-time solution shows both the exponential approximation given by Equation (3) and the exact solution given by numerical integration of Equation (2). The dimensionless transition time τ* is given by

$$\tau^* = \frac{1}{\alpha^2} \quad (5)$$

And $\beta(\tau^*) = 1$ to assure continuity of Q_D at τ^*.

The definitions of aggregate parameters u_0, t_0, and Q_0 are given by

$$u_0 = \left(\frac{p_W}{p_R}\right)^2. \tag{6}$$

$$t_0 = \left(1 + \frac{\rho_0 \rho_k S_k c_f}{c_g \phi}\right) \frac{\mu \phi D^2}{k_D p_R} \tag{7}$$

$$Q_0 = \frac{A c_g k_D p_R^2}{\rho_0 \mu D} \tag{8}$$

See Nomenclature for a definition of all variables.

Figure 3 shows Q_D versus τ for a range of u_0 values. As u_0 gets smaller (well pressure fixed at a smaller fraction of reservoir pressure), production rate increases, as expected. The dimensionless transition time τ^* and the curvature of the late-time solution depend weakly on u_0, but the early-time slope is always -½. Figure 3 indicates that the approximate exponential solution for late-times is not a very good approximation for small values of u_0.

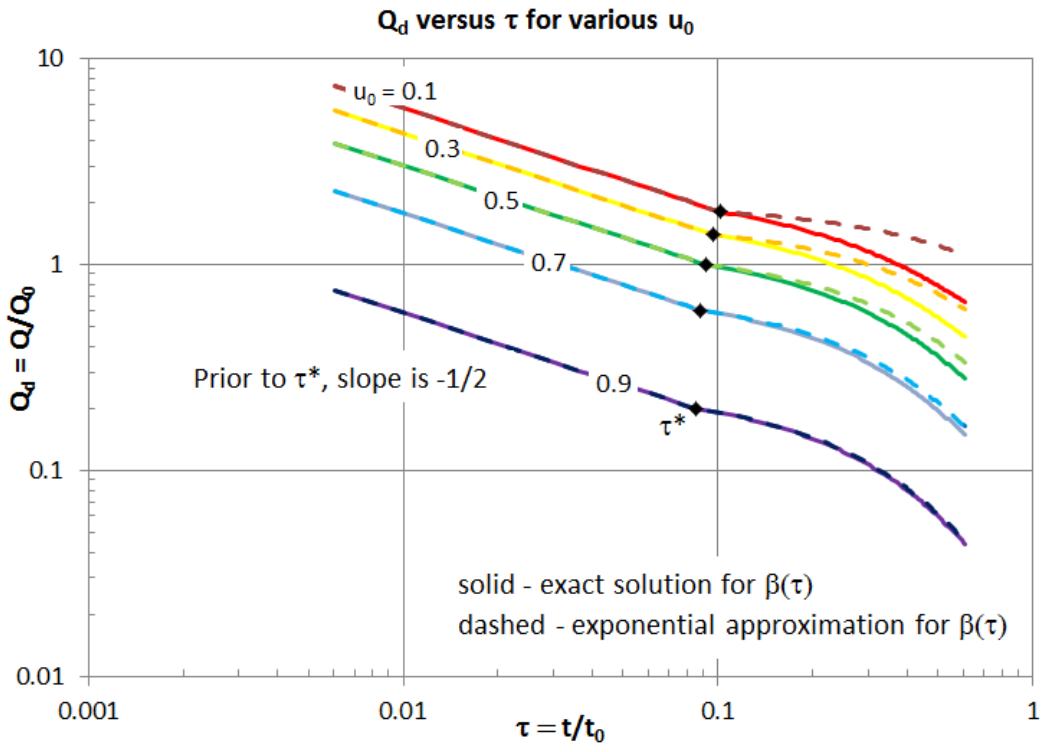

Figure 3: S&K bimodal solution for a range of values of u_0.

Some typographical errors were found in the equations in the original S&K paper; corrected versions of the equations are given in Appendix JA.

Generalization of Early-time Power-law Exponent from -½ to -n

Examining log-log plots of production decline curves from a variety of wells (personal communication, D. Silin, 2013) indicates that while most show a -½ slope at early time, some do not. Detailed numerical simulations (Olorode et al., 2012) confirm this finding, and indicate that different early-time slopes arise from non-ideal geometry of the primary fracture (i.e., fracture orientation at non-right angles with respect to the horizontal well), such that flow from the SRV to the primary fracture does not have the linear flow geometry assumed for the S&K solution. Moreover, Barker (1988) conducted well-test analyses for infinite reservoirs with flow dimension *d* ranging from 1 to 3, where *d* = 1 is linear flow to a planar sink (the geometry of the S&K problem), *d* = 2 is radial flow to a line sink, and *d* = 3 is spherical flow to a point sink. His solutions show that when pressure change is plotted as a function of time on a log-log plot, the late-time response is linear with a slope that depends on *d*. Hence it seems plausible that the slope of the bimodal production decline curve before the influence of the boundary is sensed by the system (i.e., when the SRV is infinite acting), is also controlled by *d*. For fractured rocks, the flow dimension *d* is determined by the fracture-network connectivity, so we are essentially hypothesizing (with appropriate supporting information) a relationship between early-time slope of the production decline curve and the properties of the induced fracture network.

The S&K solution produces an early-time slope of -½, but in the expanded mS&K version we generalize the solution to yield an early-time slope of -*n*, where *n* can be adjusted to fit the production decline curve. The late-time solution is unchanged from the original S&K paper. Numerical simulations described in Appendix B simulate gas production from fracture networks with different flow dimensions *d* ranging from 0.25 to 3. Figure 4 shows that for *d* = 1, the numerical solution has an early-time slope of -½ and matches the entire bimodal decline curve quite well, verifying that the numerical simulation correctly represents the original S&K problem. For other values of *d*, the numerical solutions provide a relationship between *d* and *n*, and motivate adjustments that are needed for the generalized bimodal solution: a vertical shift on the log-log plot to produce the correct production rate at some initial time t_1, and a delay in the transition time τ* when *n* < 0.5. Details are provided in Appendix JB, and the final form of the dimensionless production rate in mS&K is

$$Q_D = \frac{2(1-u_0)}{\alpha \tau^n} \qquad \text{for } \tau < \tau^* \qquad (9a)$$

$$Q_D = 2\beta(\tau)(1-u_0) \qquad \text{for } \tau > \tau^* \qquad (9b)$$

Where the dimensionless transition time τ* is given by

$$\tau^* = \frac{\tau_r^*}{\alpha^2} \tag{10}$$

Where

$$\tau_r^* = 1 \qquad \text{for } n \geq ½ \tag{11a}$$

$$\tau_r^* = 10^{0.5(d-1)} \qquad \text{for } n < ½. \tag{11b}$$

The value of β(τ*) is chosen to assure continuity of Q_D at τ*

$$\beta(\tau^*) = \frac{1}{\alpha \tau^{*n}}. \tag{12}$$

The differential equation for β (Equation 2) in the late-time solution for Q_D (Equations 9b) is unchanged, but the exponential approximation (Equation 3) is multiplied by 1/ ($\alpha\tau^{*n}$). The definitions of α, u_0, and t_0 are unchanged from Equations (4), (6), and (7), respectively, but the parameter Q_0 is modified:

$$Q_0 = \frac{Ac_g k_D p_R^2}{\rho_0 \mu D} \tau_1^{(n-0.5)} A_r, \tag{13}$$

Where $\tau_1 = t_1/t_0$ and A_r is an area-reduction factor for the primary fracture given by

$$A_r = 1 \qquad \text{for } n \geq ½ \tag{14a}$$

$$A_r = \left(\frac{r_p}{D}\right)^{(d-1)} \qquad \text{for } n < ½, \tag{14b}$$

Where r_p is the half-aperture of the primary fracture and D is the thickness of the SRV. Note that Equations (9) through (13) all simplify to the original S&K forms and $A_r = 1$, when $d = 1$ and $n = ½$.

As shown in Figure 5, Equation (9a) for early-time production rate agrees well with the numerical simulation results for all d values, but the simplistic approximation of not altering the late-time solution is only accurate for d values that are not too different from 1 (roughly $0.75 < d < 1.25$). For this range of d, the early-time slope $-n$ is related to d according to

$$n = 1 - d/2, \tag{15}$$

Making the range of applicability $0.375 < n < 0.625$. A more rigorous treatment for all n will be the subject of future studies, but the present approximation is still useful because actual production data from multiple plays and from geographically diverse locations indicate that wells in operation often show an early-time slope -n in this limited range.

The physical interpretation of d and n can be summarized as follows:

- $d = 1$, $n = ½$: (original S&K case) well-connected fracture network in SRV, uniform primary fracture

- $d < 1$, $n > ½$: (mS&K case, steeper decline) sparse or poorly-connected fracture network in SRV, uniform primary fracture
- $d > 1$, $n < ½$: (mS&K case, shallower decline) well-connected fracture network in SRV, heterogeneous primary fracture with only localized zones of high permeability

The essential difference between $n > ½$ and $n < ½$ is that for $n > ½$, there is a diverging geometry for the flow from the fracture network to the primary fracture, and for $n < ½$, there is a converging geometry. For $n = ½$, Figure 1 illustrates the linear flow geometry of the original S&K solution that separates these two domains.

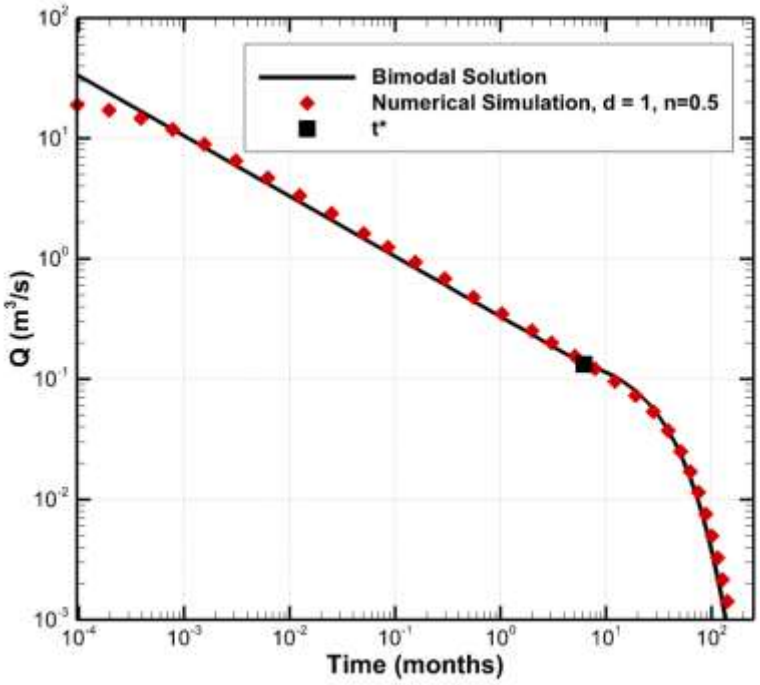

Figure 4: Comparison of original S&K bimodal decline curve (line) and a numerical simulation for flow dimension d = 1 (symbols), for which early time slope -n = -0.5.

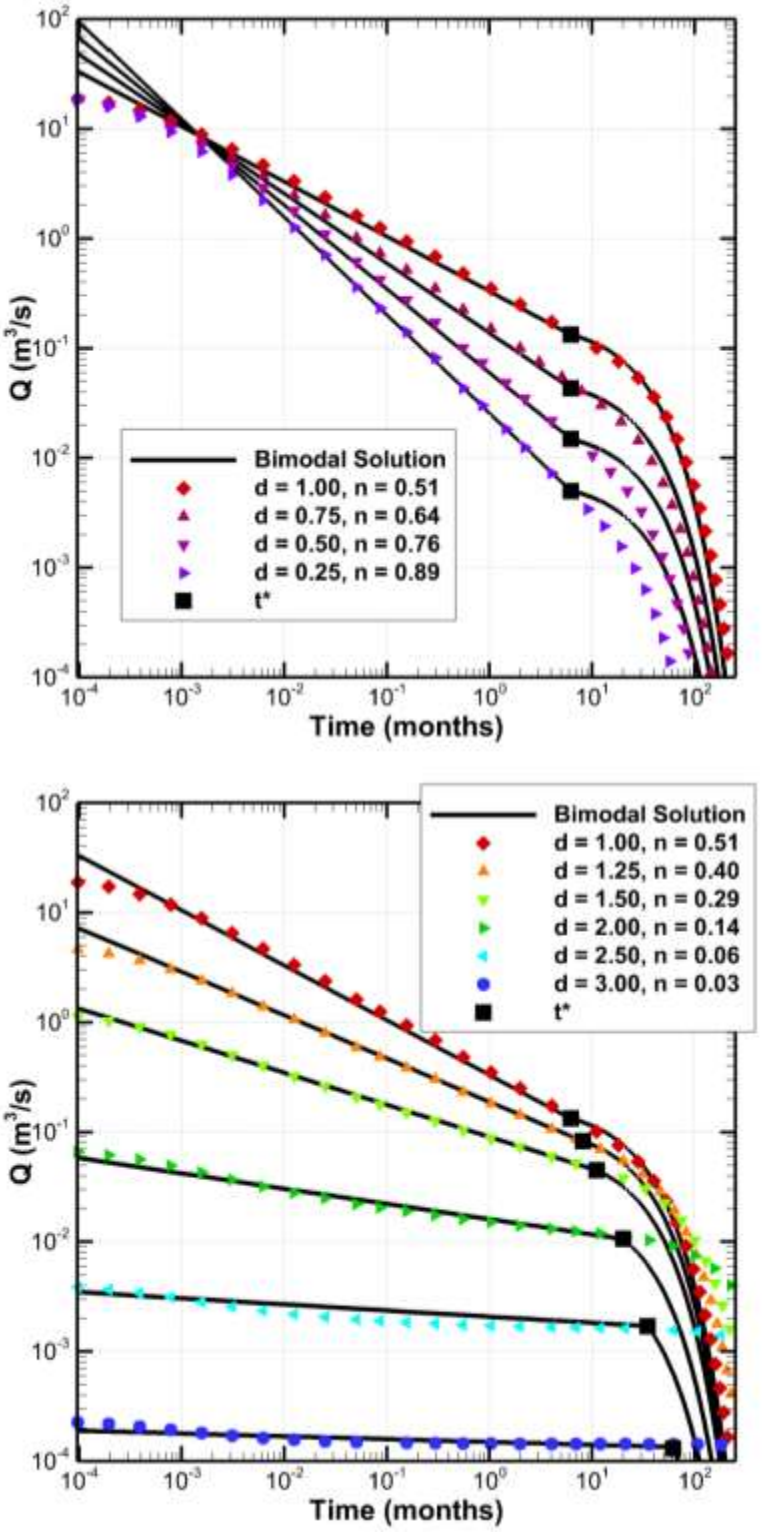

Figure 5: Comparison of solutions from the generalized bimodal mS&K decline curve (lines) and from numerical simulations for various values of flow dimension d (symbols). Top frame: n ≥ 0.5; bottom frame: n ≤ 0.5.

3. Excel Spreadsheet for Curve-Fitting

The semi-analytical mS&K solution for the production rate that is given by Equations (9) - (15) was programmed into an Excel spreadsheet. The spreadsheet was developed using Excel 2010 under Windows 7 and it has also been tested using Excel 2003 under Windows XP and Excel 2013 under Windows 8. It is recommended that users set up Excel so that variable names and formulas for cells are shown by selecting View/Show/Formula Bar. It is also advantageous to use a sufficiently large monitor so that both plots and parameters can be seen at a reasonable scale without scrolling. The primary input expected from the user is shown in red text in a cyan box, or in blue text in a pink box. The spreadsheet contains four tabs, as described below.

Basics Tab

The Basics tab includes plots of the fundamental solution for dimensionless pressure-squared u as a function of dimensionless distance (ξ) and dimensionless time (τ) taken from S&K Eqs. (JA-5) and (JA-6), and dimensionless production rate Q_D versus τ from Equations (1a) and (1b). The late-time solution uses the exponential approximation for β from Equation (3), which is not very satisfactory for small values of u_0, as shown in Figure 3. The dependences of α from Equation (4) and dimensionless transition-time $\tau^*=1/\alpha^2$ on u_0 are also shown. Q_D versus τ for various values of u_0 (Equations 1a and 1b) are shown on linear-linear, log-linear, and log-log plots. Each form of the plot highlights different features of the solution, and the user may prefer one or the other for different analyses. All these plots use $n = ½$. To examine the effect of n, the Equation (JB3) form of Q_D versus τ is shown on a log-log plot for a range of n values. As discussed in Appendix JB, in Equation (JB3) the terms $\tau_1^{(n-0.5)}$ and A_r appear explicitly in Q_D, rather than being part of the normalization Q_0, to illustrate their physical effect on production rate.

User input: For the $n = ½$ case, the user can provide as inputs various values of u_0 and observe the effect on u and Q_D. For $n \neq ½$, the user can provide input values for u_0, r_D, D, and τ_1 to observe their effect on Q_D for a range of n values.

CurveFit Tab

Overview and Data Preparation

Curve-fitting is accomplished in two steps: first the aggregate variables are determined by matching modeled production decline curves to field data. Second, the individual parameters that comprise the aggregate variables are determined. Both steps of the curve-fitting process can be executed by trial and error or automatically using the Solver tool in Excel (see Appendix JC for a general description of the Solver tool). Before attempting automated curve-fitting, it is strongly recommended to first use the trial and error approach in each step of the curve-fitting

process in order to gain experience with the sensitivity of the solution to different parameters and to determine reasonable initial guesses of unknown parameters. As in any application of an inverse method (i.e., in history-matching), it is a sound practice to repeat the fitting process using different initial guesses for the various parameters to assess the possibility of non-uniqueness of the solution.

Figure 6 and Figure 7 show screen shots of the Curve-Fit tab, with sample data taken from S&K. The tab is color coded as follows:

- *Green*: Production data, with time in column A, rate in original units in column B, and rate in SI units (m^3/s) in column C.
- *Blue*: Dimensionless production data (Q_D, τ).
- *Yellow*: Runge-Kutta numerical integration to determine $\beta(\tau)$ from the ODE for $d\beta/d\tau$, Equation (2).
- *Purple*: Modeled production rate.
- *Orange*: Model/data differences in production rate, for the Step 1 objective function. The Step 1 objective function itself is in cell X20, so it can easily be viewed on the same screen as the curves being matched and the parameter values.
- *Cyan box*: Aggregate variables (fitting parameters for Step 1 shown in red).
- *Pink box*: Individual variables: material properties, fracture geometry, reservoir conditions (fitting parameters for Step 2 shown in blue). The objective function for Step 2 is in cell X28.

User Input – Data Preparation: The user must place production data in columns A and B. If time is in months and production rate is in mcf/mo (1000 cubic feet per month at standard conditions), the data unit conversion factors in cells Z2 and Z3 should be set to 1. Otherwise, it is necessary to enter in cell Z2 the appropriate conversion factor that will result in months as the unit of time, and to enter in cell Z3 the conversion factor that will yield production rates in mcf/mo. If an objective function is being used for Step 1 (optional for trial and error curve fitting, mandatory for automatic curve fitting), then the user must verify that all the desired data entries are included in the SUM row at the bottom of the orange objective function columns. If the user's data set includes more than 140 entries, then the SUM row needs to be moved down to the row below the final data point and columns C through V need to be auto-filled to execute the necessary calculations using all the data. The plots will also need to be modified to show all the data.

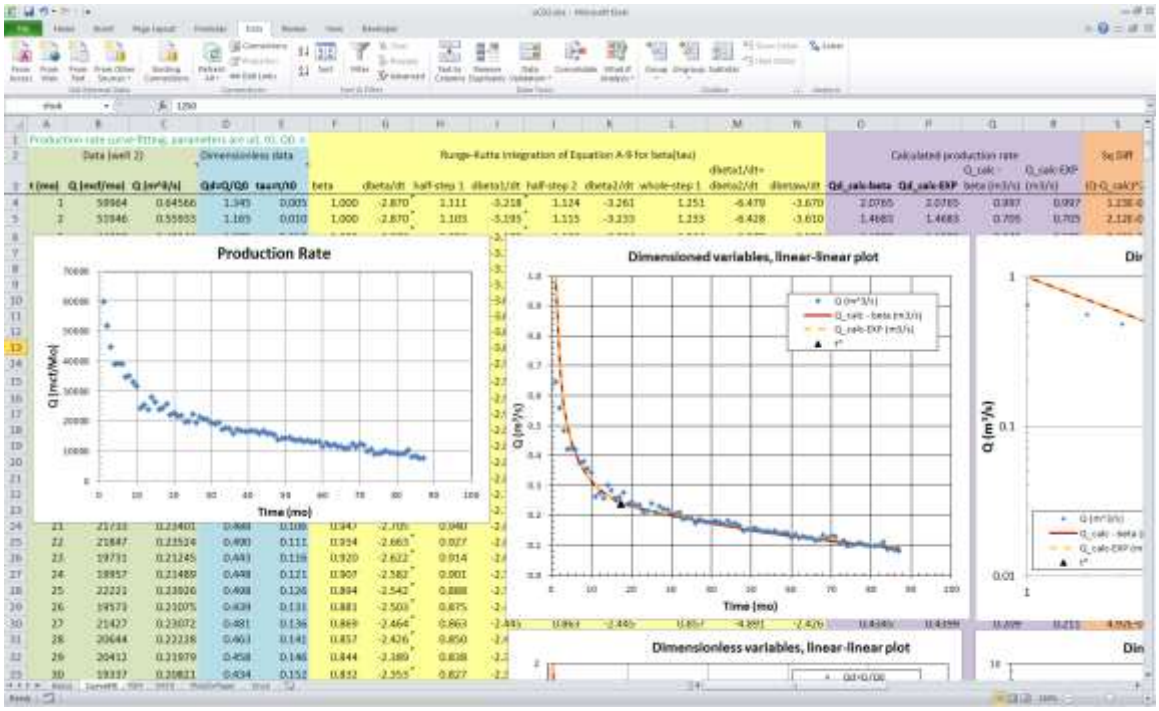

Figure 6: Screen-shots of the Excel spreadsheet tab for curve-fitting (sample 1).

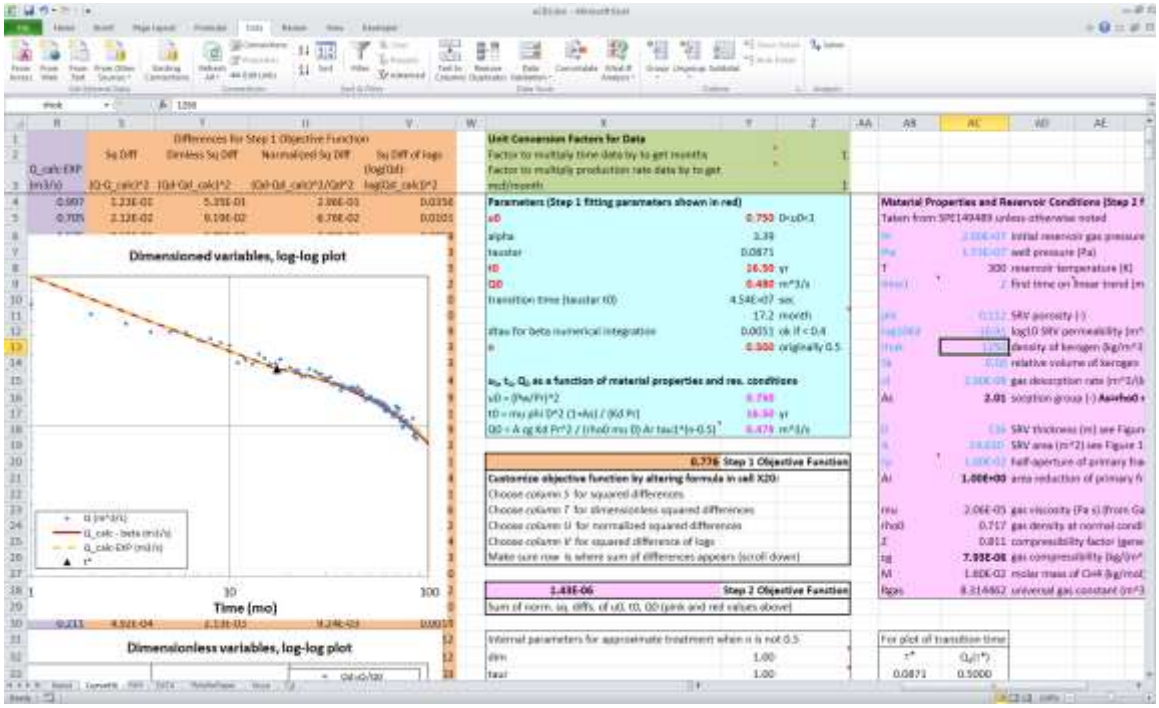

Figure 7: Screen-shots of the Excel spreadsheet tab for curve-fitting (sample 2).

Step 1 – Fitting Aggregate Variables

The aggregate variables u_0, t_0, Q_0, and n are the unknown parameters, and the objective function to be minimized is the sum of errors between the modeled production decline curve (Equation 9) and the data. The modeled curve includes the variable exponent n for the early-time solution and the exact numerically-determined value of $\beta(\tau)$ for the late-time solution (the exponential approximation is also shown for comparison, but fitting is done to the numerical solution – e.g., "Dimensioned variables – log-log plot" in Figure 7). The parameter Q_0 includes the effects for $n \neq ½$, as defined by Equation (13) (note that Equation (13) simplifies to the original definition of Q_0 given in Equation (8) when $n = ½$). The actual time data are converted into the dimensionless times $\tau = t/t_0$, and these are the times at which the model calculates Q. The production data are first converted to SI units (m^3/s), then converted to dimensionless form $Q_D = Q/Q_0$. Note that on a log-log plot, changing t_0 and Q_0 will merely shift the decline curve along the horizontal and vertical axes, respectively, whereas changing u_0 and n will change the shape of the curve, as is shown in Figure 3 and Figure 5. If the value of any parameter is considered as known, it is not varied in the curve-fitting process.

User Input - Aggregate-Parameter Fitting: u_0, t_0, Q_0, n (red entries in cyan box)

Step 2 – Fitting Individual Variables

The material properties of the SRV (flow properties ϕ, k_D; sorption properties ρ_k, S_k, c_f), fracture geometry (A, D, r_p) and reservoir conditions (p_W, p_R, t_1) that determine the aggregate variables u_0, t_0, and Q_0, through Equations (6), (7), and (13) are the unknown parameters, and the objective function to be minimized is the difference between (a) the values of u_0, t_0, and Q_0 calculated with these parameters (shown in pink in the cyan box) and (b) the values of the same variables that were determined in Step 1 (shown in red in the cyan box). As in Step 1, any properties that are considered known are not varied. When $n = 1/2$, t_1 is not used, and when $n \geq ½$, r_p is not used. For improved numerics, the log of permeability rather than permeability itself is used as an unknown parameter.

Other parameters that must be specified, but are not expected to be part of the fitting process, are the temperature T, the gas molar mass M, the gas viscosity μ, a reference gas density ρ_0, and the gas compressibility factor Z. Values of μ, ρ_0, and Z for pure gases and mixtures may be found from the GasEOS website (http://lnx.lbl.gov/gaseos/home.html). If the reservoir pressure P_R changes significantly from its initial guess during the fitting process, the thermophysical properties μ and Z should be reset because they are pressure-dependent.

User Input - Individual-Parameter Fitting: ϕ, $\log_{10}(k_D)$, ρ_k, S_k, c_f, A, D, r_p (when $n < ½$), p_W, p_R t_1 (when $n \neq ½$) (blue entries in pink box) and fixed values for T, M, μ, ρ_o, and Z.

Trial and Error Curve-Fitting

Step 1: The simplest way to use the spreadsheet is to enter the values of u_0, t_0, Q_0, and n, examine the production decline curves visually for a match between model and data, and adjust the variable values to achieve successively improved fits by trial and error. The user should examine different forms of the production decline curve (e.g., dimensioned versus dimensionless, log versus linear) to determine the most convenient form to use for a particular problem, and drag the chosen plot close to the fitting parameters, so that everything be visible on the screen at the same time. On dimensioned plots, the data remain fixed and the bimodal solution shifts as t_0 and Q_0 are varied, whereas the opposite occurs in dimensionless plots. Because n controls mainly the early-time slope, it can often be determined first and independently of the other parameters. The user may employ expert judgment in matching the production decline curve, for example by placing emphasis on getting a good match at particular times, or by ignoring spurious (in his/her judgement) data points. It can be valuable to look at the match using other forms of the production decline curve from time to time, to obtain a broader view of the goodness of the match.

Step 2: The user varies material properties, fracture geometry, and reservoir conditions by trial and error until the corresponding u_0, t_0, and Q_0 match the values returned by Step 1. In many cases, multiple sets of parameter values may give an equally good match. Therefore, it is important to make use of all the available information about the problem to constrain the ranges of the unknown parameter values. It can be useful to try a series of initial guesses for one parameter value, and examine the resulting values for the other parameters.

Automated Curve-Fitting

Automated curve-fitting requires (1) defining an appropriate objective function and (2) choosing the parameters to optimize, including possible constraints, within the Solver tool.

Step 1: The objective function (cell X20) may be the sum of squared differences (dimensioned or dimensionless), which tends to emphasize large production rates (early times), or the sum of normalized squared differences, which assigns equal weights to all data points. There is also an option to define the objective function as the sum of squared log differences; this is the most analogous to what is done when shifting curves on a log-log plot, and has proven to be especially useful for noisy data. The user chooses the form of the objective function by entering the appropriate cell name in objective function cell X20, according to the directions provided in the spreadsheet. For example, to use an objective function defined as the sum of normalized squared differences, the entry in cell X20 would be "=U141", because column U calculates normalized squared differences, and row 141 contains the sum of all the entries in column U (U141 = SUM(U4:U140)). If individual data points appear questionable, they can be omitted from the

objective function by replacing the corresponding variable value (column B) by a number less than or equal to zero. Sections of the data can be removed from consideration by altering the range in the sum used to calculate the objective function (bottom of orange columns, row labeled SUM). For example, if the first four entries of the pressure decline curve did not show a linear trend (e.g., "Dimensioned variables – log-log plot" in Figure 7), they could be eliminated from the objective function by replacing the sum in cell U141 with SUM (U8:U140).

Unknown parameters can be any or all of u_0, t_0, Q_0, and n. The initial guesses in Solver are the red entries in the cyan box, and the values returned by the Solver overwrite the guesses if the user accepts the match. The robustness of Solver increases with a decreasing number of unknown parameters. If the initial guess is bad (i.e., deviates significantly from the actual value of the parameter under consideration), the Solver can get stuck in a local minimum or run to the limit of the parameters. The problem may be significantly aggravated if there are many unknown parameters. Thus, it is recommended to conduct preliminary trial and error curve-fitting in order to get reasonable initial guesses for all parameters.

Given the bi-modal form of the production decline curve, it would seem appealing to use the transition time t^* or the dimensionless transition time τ^* directly as one of the unknown parameters instead of u_0 because, for $n = ½$, τ^* only depends on u_0, through α(see Equations (4) and (5)). We investigated this option but rejected it as impractical for two reasons. First, when the early-time slope parameter n is considered an unknown, then τ^* is a function of both n and u_0. Second, even if $n = ½$, τ^* cannot be expressed explicitly as a function of u_0 and determining u_0 for a given τ^* would require an additional iterative loop within the optimization process. However, within the Excel Solver tool, it is possible to apply constraints on parameters during the optimization, and a constraint on t^* or τ^* can be imposed, even if it is not one of the unknown parameters. Thus, if the production data show a definite signature of a transition between early-time and late-time behavior at a given time, that time can be held fixed during the optimization for parameters u_0, t_0, Q_0, and n.

Instructions for loading the Solver tool in Excel are provided in Appendix JC. The following choices for Solver options are recommended, but after some practice with Solver, the user is encouraged to try different constraints or solving methods to see if they produce improved results.

- *Set Objective* (specify cell with objective function): **X20**
- *To*: **min** or *value of* **1e-5** (something smaller than the value that the objective function is expected to reach)
- *By changing Variable Cells*: (Specify which variables to use as unknowns, can identify by cell number or variable name): any desired combination of **u0**, **t0**, **Q0**, **n**
- *Subject to the Constraints*: (suggest physically meaningful constraints)

n <= 0.62, n >= 0.38, u0 <= 0.95, u0 >= 0.05

- Check box for *Make Unconstrained Variables Non-negative*
- *Select a Solving Method*: **GRG Nonlinear**
- *Options*: suggest using defaults
- Can check box for *Use Automatic Scaling* to see if it improves search (untested)
- Can show intermediate results of search by checking box *Show Iteration Results*

Step 2: The objective function (cell X28) is simply the sum of the normalized squared differences between the red and the pink values of u_0, t_0, and Q_0 shown in the cyan box. Recall that the red spreadsheet entries are the aggregate variables returned by the Step 1 optimization and the pink spreadsheet entries are the aggregate variables calculated from the individual variables shown in the pink box. The unknown parameters can be any or all of p_R, p_W, t_1, ϕ, $\log_{10}(k_D)$, ρ_k, S_k, c_f, D, A, and r_p. The initial guesses for each parameter (the blue spreadsheet entries in the pink box) should be as physically realistic as possible. If all parameters are allowed to vary over a significant range, the solution returned by Solver is not likely to be unique. The user should experiment with different starting guesses and constraints.

Suggested Solver Options

- *Set Objective* (specify cell with objective function): **X28**
- *To*: **min** or *value of* **1e-5** (something smaller than the value that the objective function is expected to reach)
- *By changing Variable Cells*: (Specify which variables to use as unknowns, can identify by cell number or variable name): any desired combination of **Pr, Pw, time1, phi, log10Kd, rhok, Sk, cf, D, A, rp**
    - *Subject to the Constraints:* (suggest physically meaningful constraints)

      Pr >= 1.e6, Pw >= 1.e5, phi >= 0.001, phi <= 1, etc.

- Do **not** check box for *Make Unconstrained Variables Non-negative* because log10Kd is negative.
- *Select a Solving Method*: **GRG Nonlinear**
- *Options*: suggest using defaults

Direct Examination of the Effect of Individual Variables

The form of the production decline curve (Equation 9), with many parameters contained in the aggregate variables t_0 and Q_0, is convenient for curve-fitting, but does not lend itself for developing insights into the effect of individual parameters. This can be done if the user sets the red entries for u_0, t_0, and Q_0 in the cyan box to be equal to the definitions of these parameters

(the pink entries in the cyan box, which are named **u0def**, **t0def**, and **Q0def**, respectively). Then the values of the individual parameters in the pink box can be varied by hand to determine their effect on both the production decline curve and the aggregate variables.

RK4 Tab: Numerical Integration for Exact β(τ)

In Figure 3, the comparison of the approximate solution for β(τ) given by Equation (3) to the exact solution obtained by numerically integrating Equation (2) indicates that, for small values of u_0, the approximate exponential solution does not provide an accurate solution. Therefore, the numerical integration of Equation (2) is the preferred option. This is accomplished within the Curve-Fit tab of the Excel spreadsheet, which invokes a fourth-order Rung-Kutta algorithm from Numerical Recipes (Press et al., 1986). The integration step size is taken to be the time interval between observed data points, which is typically one month. For user-specified values of u_0, the RK4 tab of the spreadsheet shows the numerical integration results using two different integration step sizes to validate the correctness of using the interval between data times as the integration step size. This choice for step size has produced accurate results for all combinations of parameters tried thus far.

The exponential approximation for β(τ) is also included in this tab of the spreadsheet as an option, so the interested user can compare the approximate and the exact solutions.

User input: Values of u_0 for numerical integration tests, two trial integration step sizes.

Data Tab

Production rate data are expected to be provided at even time intervals, typically monthly. If production data from multiple wells or multiple stages within one well are available, it is convenient to store all the data in the Data tab, then cut and paste individual data sets into the appropriate location in the CurveFit tab for analysis. It can be extremely useful to plot all production decline curves on the same plot before doing a quantitative curve-fit analysis, as this allows identification of trends and qualitative comparison of features.

If any production rate data points appear questionable, they can be omitted from the matching process by replacing the data value with a number less than or equal to zero, or by leaving the cell blank, but the time corresponding to that datum should be retained. Modeled production rate is then calculated for the valid entries in the list of times. Production data can be provided in any units, but the user must supply the unit conversion factors to months (for time) and to mcf/mo (for production rates) in the CurveFit tab.

4. Example Applications of Curve-Fitting

Example Problem 1

To illustrate the method and the Excel tool, we use the production data shown in Figure 10 of S&K, kindly provided by D. Silin. The data set consists of 87 monthly measurements. When these are pasted into column B of the CurveFit tab, they occupy rows 4-90, so in the orange columns where the objective functions are calculated, the row labeled SUM (row 141) is modified to compute the sums over rows 4 through 90 (this modification is actually not necessary if the Column B entries below the final data time are blank). In the objective function cell (X20) we refer to cell U141, so the objective function will be the sum of normalized squared differences.

For Step 1, the initial values of u_0 = 0.75, n = 0.5, t_0 = 10 years, and Q_0 = 0.4 m^3/s (left over from a previous problem) produce a poor match to the data (Figure 8) and a value of 18.7 for the objective function. We assume that u_0 is known and n = 0.5 provides a reasonable estimate of the early-time slope. A few trial and error adjustments of the inputs to t_0 = 11 years, Q_0 = 0.6 m^3/s, yields a better match (Figure 9) and a value of 2.9 for the objective function. This is the starting point for the automatic curve-fit with Solver. The Solver input is shown in Figure 10. Solver returns t_0 = 16.5 years, and Q_0 = 0.48 m^3/s, and a value of 0.78 for the objective function. The curve fit, shown in Figure 11, over-estimates production corresponding to the first four time data points, but is very good for all times after 4 months.

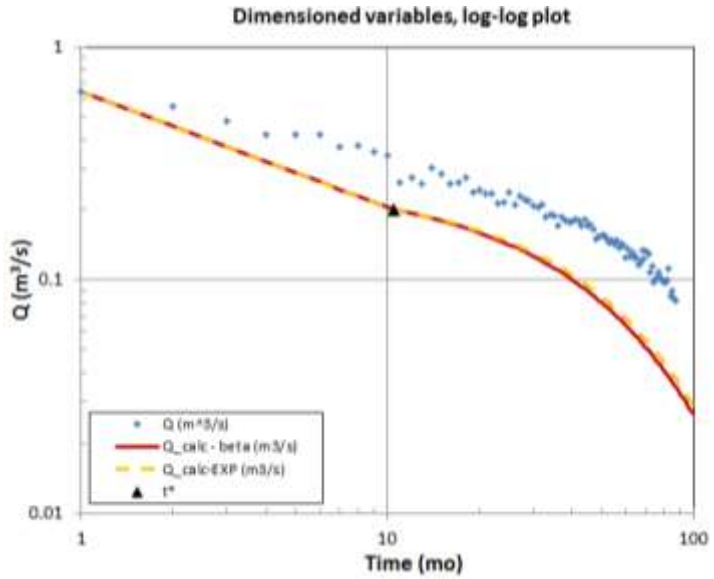

Figure 8: Production decline curves for data (symbols, taken from S&K, Figure 10) and model (lines) using poor initial guesses for parameters (taken from another problem).

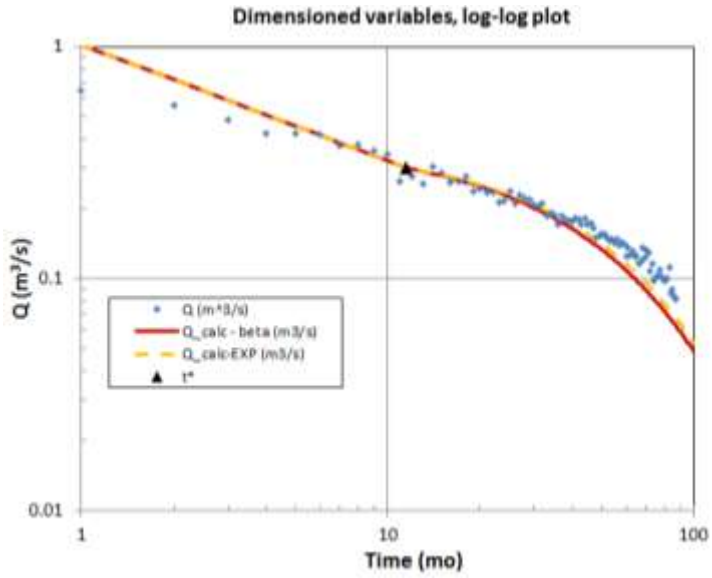

Figure 9: Step 1 curve-fit obtained by trial and error; rough match to provide better initial guesses for automatic curve-fitting using Solver.

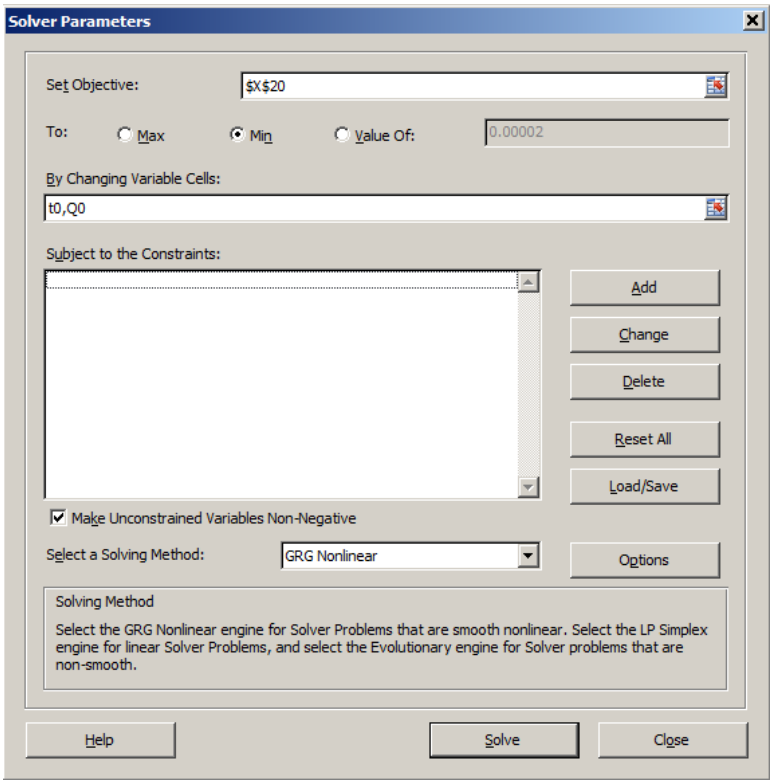

Figure 10: Step 1 input to Solver.

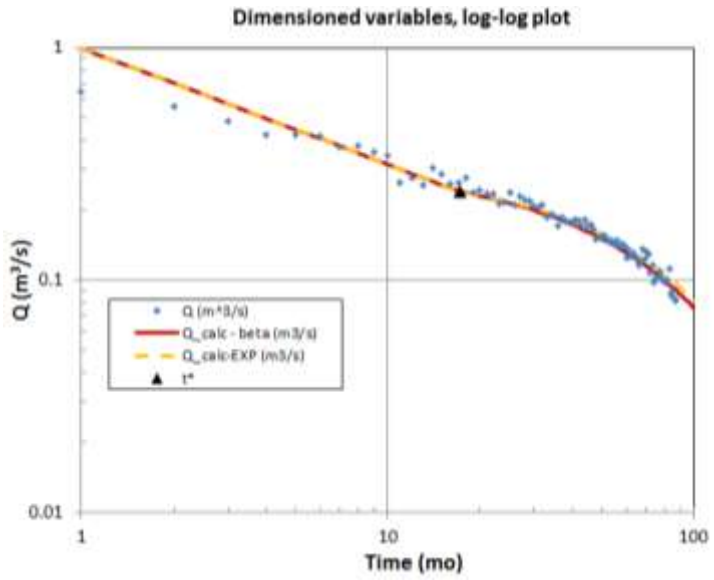

Figure 11: Step 1 curve-fit obtained by Solver when n is held fixed at ½.

Very early data are often ignored in the curve fitting analysis because they may be controlled by near-wellbore effects that are not accounted for in the idealized analytical solution. However, if the 2-to-4 month data shown in Figure 10 are considered reliable, they could be included in the fitting process by using a value of $n < ½$. Trial and error shows that $n = 0.4$ produces results that match the early time slope well for all times after 1 month. Taking $u_0 = 0.75$, $n = 0.4$, $t_0 = 16.5$, $Q_0 = 0.6$ as initial guesses, Solver returns a good fit for $t_0 = 15.7$ years, and $Q_0 = 0.66$ (Figure 12) with a value of 0.36 for the objective function.

For Step 2, we assume that the reservoir pressure p_R is known, so the well pressure p_W can be immediately determined from u_0, as $p_W = u_0^{1/2} p_R$. For $u_0 = 0.75$ and $p_R = 200$ bars, $p_W = 1.73E7$ Pa =173 bars. We focus on (a) the flow properties ϕ and k_D and (b) the fracture geometry parameters D and A, and we consider the $n = ½$ case, so t_1 and r_p are not used. The initial guesses (taken from another problem) are $\phi = 0.12$, $\log_{10} k_D = -16.90$ ($k_D = 1.26E\text{-}17$ m^2 = 0.013 mD), $D = 167$ m, and $A = 30000$ m^2. The Solver input is shown in Figure 13. The Solver matches the Step 1 values of t_0 and Q_0 closely, yielding an objective function of 4.6E-9, and returns parameter values of $\phi = 0.11$, $\log_{10} k_D = -16.98$ ($k_D = 0.01$ mD), $D = 124$ m, and $A = 26754$ m^2. These values are all physically reasonable. However, if an order of magnitude smaller porosity value (0.01) is used as an initial guess, the Solver obtains an equally good match (objective function 1.7E-6), returning $\phi = 0.01$, $\log_{10} k_D = -16.91$ ($k_D = 0.012$ mD), $D = 163$ m, and $A = 29353$ m^2. Note that these values of k_D, D, and A are not very different from the values returned for $\phi = 0.1$, implying that within this range, the solution is not very sensitive to porosity. This lack of sensitivity can be verified by examining

Equation (7) for t_0. When ϕ is small, the second term within the parenthesis is large, and the □ terms in t_0 cancel out. In contrast, if a 100 times larger or 100 times smaller value of k_D is used as an initial guess, the Solver returns solutions with similar values for all parameters, as shown in Table 1, indicating that the solution is sensitive to k_D in this range. Varying the initial guess of all parameters in this way can provide useful information on the reliability of the parameter values returned by Solver.

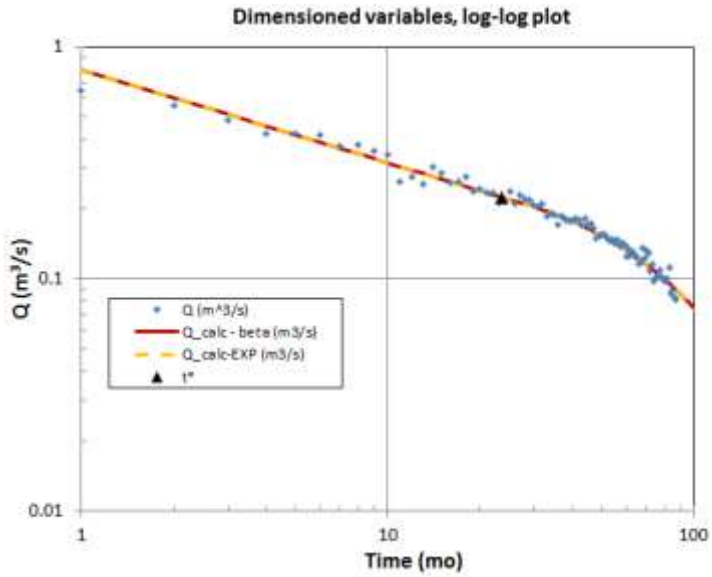

Figure 12: Step 1 curve-fit obtained by Solver when n is held fixed at 0.4.

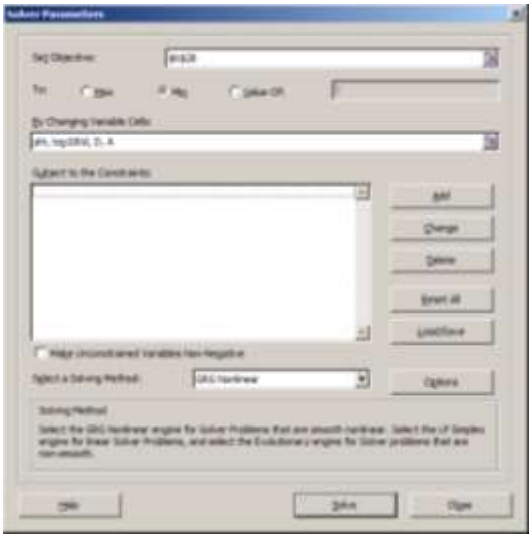

Figure 13: Step 2 input to Solver.

Table 1: Example problem 1, Step 2 results for different initial guesses of log10kD. In all cases initial guesses for other parameters are ϕ = 0.12, D = 167 m, A = 30,000 m^2.

Initial guess for $\log_{10}k_D$	Objective function	ϕ	$\log_{10}k_D$ (k_D in m^2)	D (m)	A (m^2)
-14.9	4.7E-8	0.113	-16.89	138	24140
-16.9	4.6E-9	0.113	-16.98	124	26754
-18.9	1.4e-6	0.112	-16.91	136	24610

Example Problem 2

The second example problem includes daily production data (provided by X. Xiong) for 137 days. To use these data in the CurveFit tab, we set the time data conversion factor to 0.0328 = 1/30.48 to convert days to months, and the production rate conversion factor to 30.48 to convert mcf/day to mcf/mo. As shown in Figure 14a, the production decline curve does not show the typical shape of the bimodal decline curve (Figure 2). In particular, the sharp increase in production rate at about 60 days cannot be modeled with the bimodal decline curve, which is always monotonically decreasing (Figure 2 to Figure 5). To analyze the production data, we hypothesize that, for times before the first 60 days, wellbore or other effects that are not included in the bimodal decline model control the production rate. Thus, we only consider the data after the first 60 days. Figure 14b shows that the production rate declines linearly on a log-log plot, with no evidence of a transition to an exponential decline, indicating that the outer boundary of the SRV has not been reached within 137 days. Fitting the slope of the line (by trial and error) yields a value of n = 0.285. The parameter u_0 is estimated to be 0.5 by independent means, leaving t_0 and Q_0 as the unknown parameters. Because we only have the early-time (linear) part of the bimodal solution to compare to, we cannot estimate t_0 and Q_0 independently because we can match the data equally well by a shift along the horizontal or vertical axis. To quantify the relationship between t_0 and Q_0, note that Equation (9a) for the early-time production rate Q_D can be rearranged to show that the product $Q_D\tau^n$ is a constant, and some simple algebra shows that the same relationship holds for t_0 and Q_0. Thus, if we fit the data with a particular (t_0, Q_0) pair, call it (t_{00}, Q_{00}), then for any other t_0, we have $Q_0 = Q_{00}(t_{00}/t_0)^n$. Here, we take t_{00} = 2.3 years, Q_{00} = 1.1 m^3/s, which gives a transition time t^* = 140 days, just beyond the final data time. Other possible (t_0, Q_0) pairs would produce longer transition times and smaller values of Q_0. Thus, when production data do not show a transition time, we can only obtain a lower bound for t_0 and an upper bound for Q_0.

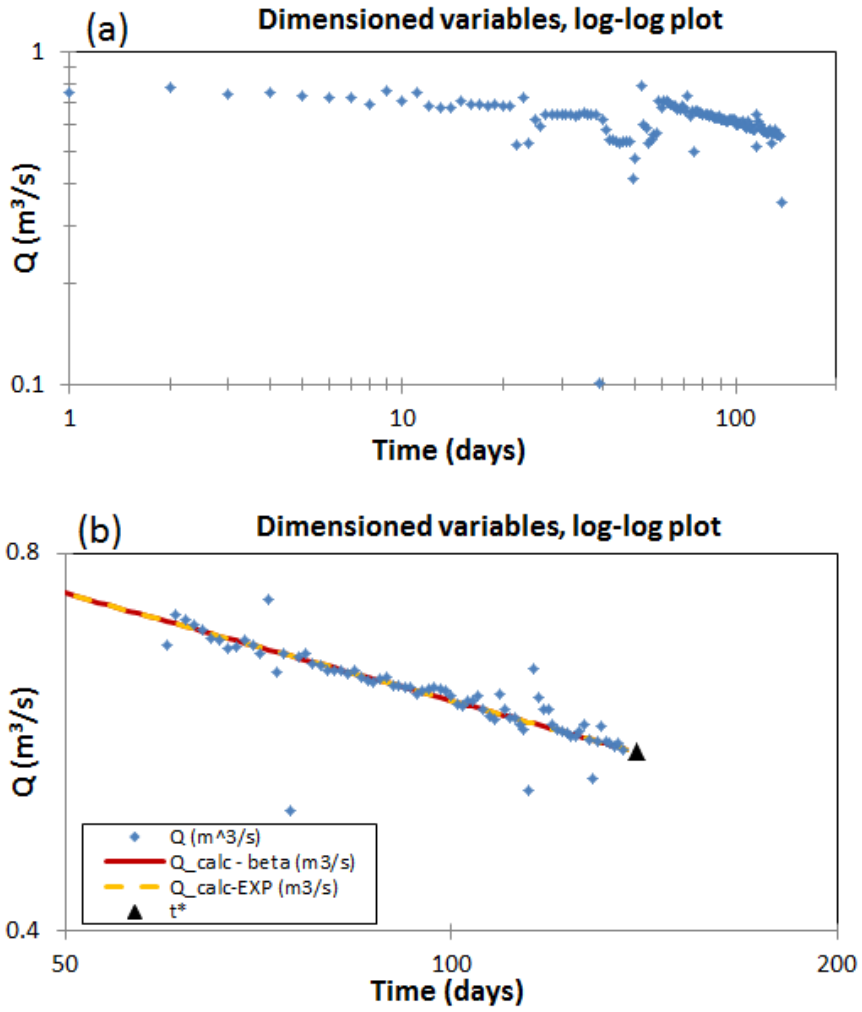

Figure 14: Example problem 2 showing (a) all data, and (b) data after 60 days with one possible fit to the linear portion of the bimodal decline curve. Other fits will follow the same line, but have a later transition time t*.

5. Conclusions

We have developed a simple, Excel-based tool for the analysis of the complex problem of gas production from a fractured tight/shale gas reservoir, based on curve-fitting production decline data to a semi-analytical solution. It is simple to use and can provide rapid estimates of the important parameters governing the system behavior, but scientifically robust as it incorporates the key features of hydraulically fractured gas reservoirs: gas is produced from a finite SRV consisting of a primary fracture and a secondary fracture network; exchange with adsorbed gas is also considered. The semi-analytical solution for production rate is bimodal, with a power-law

decline for early times (before the outer boundary of the SRV is felt) and an exponential decline at later times. We generalized the original bimodal solution of Silin and Kneafsey (2012) so that the power-law exponent is a parameter –*n*, rather than fixed at -½, to represent a broader range of fracture-network geometries and facilitate matching production decline curves that do not show a -½ slope at early times.

Curve-fitting enables an improved understanding of the hydraulic fracturing process by estimating fracture geometry properties (A, D, n, r_p), SRV flow and transport properties (k_D, ϕ, A_s), and operational parameters (p_W, p_R, t_1). This understanding provides guidance for deployment of future stages and wells, thereby improving the efficiency of the hydraulic fracturing process, making it more economical and lessening its environmental impact.

Additional benefits include the ability to predict future production decline, including the productive lifetime of the stage. Moreover, the semi-analytical solution can provide verification for complex numerical models. Finally, the present approach, although designed for shale-gas production, should be adaptable to many gas-flow problems in dual-permeability media, whether hydraulically or naturally fractured or highly heterogeneous sedimentary rock, such as geothermal energy extraction, CO_2 storage, environmental remediation, and nuclear waste isolation.

Future work will include further analysis of the relationship between the parameter n and fracture-network connectivity, and the addition of more physical processes such as retrograde condensation (which will result in two-phase flow) and compaction (which will require a coupled flow/geomechanics approach).

Acknowledgements

We thank Dmitriy Silin for providing us with the production decline data used in developing the spreadsheet application. We appreciate the scientific discussions with members of the Gas Technology Institute, particularly Xinya Xiong, Jordan Ciezobka, and Iraj Salehi. This work was performed at Lawrence Berkeley National Laboratory of the US department of Energy (DOE) under Contract No. DE-AC02-05CH11231. It was funded by the Research Partnership to Secure Energy for America (RPSEA) through the Ultra-Deepwater and Unconventional Natural Gas and Other Petroleum Resources program authorized by the US Energy Policy Act of 2005. RPSEA is a nonprofit corporation whose mission is to provide a stewardship role in ensuring the focused research, development, and deployment of safe and environmentally responsible technology that can effectively deliver hydrocarbons from domestic resources to the citizens of the US. RPSEA, operating as a consortium of premier US energy research universities, industry, and

independent research organizations, manages the program under a contract with DOE's National Energy Technology Laboratory.

Nomenclature*

A	area of SRZ (m^2) [A]
A_r	area reduction factor of primary fracture [Ar]
A_s	sorption group, $A_s = \rho_0 \rho_k S_k c_f/(c_g \phi)$ [*As*]
c_f	gas desorption rate ($kg/(m^3 Pa)$) [cf]
c_g	gas compressibility ($kg/(m^3 Pa)$), $c_g = M/(ZRT)$ [cg]
D	thickness of SRZ (m) [D]
d	flow dimension [dim]
k_D	permeability of SRZ (m^2) [log10Kd]
M	gas molar mass (kg/mol) [M]
n	absolute value of slope of early-time log Q vs log t [n]
p	pressure (Pa)
p_R	reservoir pressure (Pa) [Pr]
p_W	well pressure (Pa) [Pw]
Q	production rate (m^3/s) [Q]
Q_0	characteristic production rate (m^3/s) [Q0]
Q_D	dimensionless production rate, $Q_D = Q/Q_0$ [Qd]
R	Universal gas constant ($m^3 Pa/(K\ mol)$) [Rgas]
r	radial distance (m)
r_p	half-aperture of primary fracture (m) [rp]
S_k	relative volume of kerogen [Sk]
T	temperature (K) [T]
t	time (s)
t_0	characteristic time (s) [t0, years]
t_1	earliest time production rate falls on a linear trend (s) [time1, mo]
t^*	transition time (s) [tstar, mo]
u	dimensionless pressure squared, $u = (p/p_R)^2$
u_0	dimensionless well pressure squared, $u_0 = (p_W/p_R)^2$ [u0]
Z	gas compressibility factor [Z]
α	parameter controlling early-time solution for Q [alpha]
β	function controlling late-time solution for Q [beta]
ϕ	porosity of SRZ [phi]
μ	gas viscosity (Pa·sec) [mu]

ρ_0 gas density at standard conditions (kg/m^3) [rho0]
ρ_k density of kerogen (kg/m^3) [rhok]
τ dimensionless time, $\tau = t/t_0$ [tau]
τ_1 dimensionless t_1, $\tau_1 = t_1/t_0$ [tau1]
τ^* dimensionless transition time, $\tau^* = t^*/t_0$ [taustar]
τ_r^* transition-time delay factor [taur]
ξ dimensionless distance

*Entries in square brackets indicate the variable name used in the CurveFit tab of the spread sheet, where subscripts and Greek symbols are not used. If different units are used in the spreadsheet, they are also shown.

References

[1] Barker, J.A., A generalized radial flow model for hydraulic tests in fractured rock, Water Resources Research, 24(10), 1796-1804, 1988.

[2] Edwards, A.L. TRUMP: A computer program for transient and steady state temperature distributions in multidimensional systems, National Technical Information Service, National Bureau of Standards, Springfield, VA, 1972.

[3] King, G. E., Hydraulic Fracturing 101: What every representative, environmentalist, regulator, reporter, investor, university researcher, neighbor and engineer should know about estimating frac risk and improving frac performance in unconventional gas and oil, in SPE 152596, SPE Hydraulic Fracturing Technology Conference, pp. 1–80, Society of Petroleum Engineers, Woodlands, TX, 2012.

[4] Narasimhan, T.N. and P.A. Witherspoon. An integrated finite difference method for analyzing fluid flow in porous media, Water Resources Research, 12(1), 57 – 64, 1976.

[5] Oldenburg, C.O., G.J. Moridis, N. Spycher, and K. Pruess, EOS7C Version 1.0: TOUGH2 module for carbon dioxide or nitrogen in natural gas (methane) reservoirs, Rep. LBNL-56589, Lawrence Berkeley National Laboratory, Berkeley, CA, 2004.

[6] Olorode, O.M., C.M. Freeman, G.J. Moridis, and T.A. Blasingame, High-resolution numerical modeling of complex and irregular fracture patterns in shale gas and tight gas reservoirs, SPE 152482, presented at SPE Latin American and Caribbean Petroleum Engineering Conference, Mexico City, Mexico, 16-18, April 2012.

[7] Press, W.H., B.P. Flannery, S.A. Teukolsky, and W.T. Vetterling, Numerical Recipes: The art of scientific computing, Cambridge University Press, New York, 1986.

[8] Pruess, K., C. Oldenburg, and G. Moridis, TOUGH2 User's Guide, Version 2.0, Rep. LBNL-43134, Lawrence Berkeley National Laboratory, Berkeley, CA, 1999.

[9] Pruess, K., The TOUGH Codes—A Family of Simulation Tools for Multiphase Flow and Transport Processes in Permeable Media, Vadose Zone Journal, 3, 738-746, 2004.

[10] Silin, D. and T. Kneafsey, Shale gas: nanometer-scale observations and well modelling, SPE 149489, J. Canadian Petroleum Technology, 464-475, November 2012.

[11] U.S. Energy Information Administration (EIA), Annual Energy Outlook 2012, with projections to 2035. U.S. Department of Energy, http://www.eia.gov/forecasts/aeo/pdf/0383(2012).pdf , 2012.

[12] U.S. Energy Information Administration (EIA), Annual Energy Review 2011. U.S. Department of Energy, //http://www.eia.gov/totalenergy/data/annual/pdf/aer.pdf , 2011.

[13] U.S. Energy Information Administration (EIA), 2006 Manufacturing Energy Consumption Survey Form EIA-846. U.S. Department of Energy. http://www.eia.doe.gov/emeu/mecs/mecs2006/EIA- 846A_2006.pdf , 2007.

Appendix JA: Errata for Silin and Kneafsey (2012) SPE 149489

Equation (14) is two separate equations

$$\Psi(p) = \frac{1}{2} c_g p^2 \quad \text{and} \quad F'(p) = c_g$$

Equation (34)

$$t_s \approx \left(1 + \frac{\rho_0 \rho_k S_k c_f}{c_g \phi}\right) \frac{\mu \phi D^2}{k_D p_R} \frac{1}{\alpha^2}$$

Equation (35)

$$Q(t) = 2A \frac{c_g}{\rho_0} \sqrt{\left(\phi + \frac{\rho_0 \rho_k S_k c_f}{c_g}\right) \frac{k_D}{\mu p_R}} \frac{p_R^2 - p_W^2}{\alpha \sqrt{t}}$$

Equation (36)

$$Q(t) = 2A \frac{c_g k_D (p_R^2 - p_W^2)}{\rho_0 \mu D} exp\left[-3 \frac{p_W}{p_R} \left(\frac{1}{\phi + \frac{\rho_0 \rho_k S_k c_f}{c_g}}\right) \frac{k_D p_R}{\mu D^2} t - \frac{1}{\alpha^2}\right]$$

Equation (JA-14)

$$-\int_0^\infty \left.\frac{\partial u}{\partial \xi}\right|_{\xi=0} d\tau = \frac{2}{3} \frac{(1-u_0)^{3/2}}{[\sqrt{u_0(1-u_0)} + \arcsin\sqrt{1-u_0}]} + \frac{2}{3} \frac{(1-u_0)}{\sqrt{u_0}}$$

Appendix JB: Numerical Simulations of Gas Production Using One-column Grids with Different Flow Dimensions

A series of numerical simulations were done with the TOUGH2 code (Pruess et al., 1999; Pruess, 2004) using the equation of state module EOS7C (Oldenburg et al., 2004) to investigate gas production from a hydraulically fractured medium, for a range of flow geometries for the network of fractures making up the SRV and the primary hydraulic fracture. In general, EOS7C includes components water, brine, methane, carbon dioxide, and nitrogen, which partition among

aqueous, gaseous, and supercritical phases. Here we consider gaseous methane to be the only mobile fluid phase, with immobile water also present.

The numerical simulator TOUGH2 uses the integral-finite-difference method (Edwards, 1972; Narasimhan and Witherspoon, 1976) for spatial discretization. In this method, the volumes of grid blocks and the areas of interfaces between grid blocks are specified, without reference to a global coordinate system. This feature enables creation of one-column grids that can represent linear flow geometry (all grid blocks have equal volumes and interface areas), radial flow geometry (grid-block volume increases in proportion to r^2 while interface area increases in proportion to r), and spherical flow (volume increases in proportion to r^3 while area increases in proportion to r^2), where r is the distance from the origin of the grid to a given grid block. This concept can be generalized to non-integral flow dimensions (i.e., fractal dimensions). For a flow dimension d ($0 < d < 3$), one can create a one-column grid to represent d-dimensional flow by making grid-block volume proportional to r^d and interface area proportional to r^{d-1}.

The original case considered in S&K assumes $d = 1$, as gas flows uniformly through the SRZ toward a planar primary fracture with uniform high permeability. Gas flow perpendicular to the primary fracture has linear flow geometry, and this flow is uniform over the entire area of the fracture. However, if one considers a non-uniform primary fracture, with localized regions of high permeability, it is possible to imagine flow from the SRZ converging to these portions of the fracture, yielding $d > 1$. In the extreme case of just one point on the primary fracture providing high permeability, with spherically symmetric flow from the SRZ entering the facture at that one point, one would have $d = 3$. If quasi-linear regions of the primary fracture provided high permeability, with radial flow from the SRZ entering the fracture along those lines, then one would have $d = 2$. Different patterns of localized high permeability in the primary fracture could produce non-integral values of $d > 1$ also. On the other hand, if the primary fracture had uniform, high permeability, but flow paths through the SRZ were limited due to a sparse or poorly-connected fracture network, then $d < 1$ would also be possible.

A series of grids with d = 0.25, 0.5, 0.75, 1, 1.25, 1.5, 2, 2.5, and 3 were created to model gas production from the stimulated reservoir volume surrounding a hydraulic fracture. One end of the one-column grid ($r = 0$) is the primary fracture and the opposite end ($r = D$) is a no-flow boundary, to represent the outer limit of the SRZ, beyond which permeability is assumed to be negligible. The length of the column (D = 150 m) and the number of grid blocks (300) are the same for each grid. In keeping with the conceptual model described in the previous paragraph, for $d < 1$, the area of the primary fracture (at $r = 0$) is equal to the area of the SRV, A, and area decreases as r increases, to represent a sparse fracture network. In contrast, for $d > 1$, the area at $r = D$ is set at A, and area decreases as r decreases to represent flow converging to the heterogeneous primary fracture.

To model gas production, the first grid block, which represents the primary fracture, is held at a constant pressure p_W lower than the reservoir pressure p_R, and the gas mass flow rate into that grid block Q is converted to volumetric flow rate at standard conditions by dividing by ρ_0. The thickness of the grid block is r_p, the half-aperture of the primary fracture. For comparison to the bimodal solution, the numerically simulated value of Q must be doubled, to account for flow into both sides of the primary fracture. Porosity is 0.12 and permeability is 0.013 mD. Sorption is neglected by assuming $S_k = 0$. Initial conditions are P = 200 bar, T=28°C, a methane saturation of 0.85, and a water saturation of 0.15 with water immobile. Two cases were considered: $u_0 = (p_W/p_R)^2 = 0.766$ and $u_0 = 0.25$. While the bimodal solution assumes gas viscosity is constant, in the numerical simulations viscosity is pressure dependent, so using a large value of u_0 minimizes pressure differences, making a fairer comparison.

The symbols in Figure 5 show numerically-simulated production rate Q as a function of time on a log-log scale, for the various d values for $u_0 = 0.766$. All the curves show a linear portion that is established within an hour, and lasts until the pressure response reaches the outermost grid block of the column at $t = t^*$, after which Q declines more rapidly. For $d = 1$, the lines in Figure 5 show the original bimodal solution of S&K. The agreement between numerical and analytical solutions is good, verifying the numerical model. For $d \neq 1$, we note the following features of early-time numerically-simulated *Q(t)* that should be present in the generalized bimodal solution.

(1) As d increases, the absolute value of the slope, n, decreases. This can be achieved by replacing the power ½ in the denominator of Equation (1a) with n:

$$Q_D = \frac{2(1-u_0)}{\alpha\tau^n} \qquad \text{(JB1)}$$

Determining n as a function of d is described below.

(2) For $d < 1$, the Q values for different values of d are the same for the time at which $Q(t)$ becomes linear on a log-log plot. We denote this time t_1. The corresponding dimensionless variable is $\tau_1 = t_1/t_0$ and Equation (JB1) becomes

$$Q_D = \frac{2(1-u_0)\tau_1^{n-0.5}}{\alpha\tau^n}. \qquad \text{(JB2)}$$

We apply this correction for all d values, but note that for $d = 1$, $n = ½$, and the τ_1 dependence vanishes.

(3) For $d > 1$, $Q(t_1)$ is proportional to the area of the primary fracture. According to the algorithm used for grid generation, the ratio of the area of the primary fracture to the area of the grid block at the opposite end of the column, denoted A_r, is equal to the ratio of the corresponding distances (r_p/D) raised to the power $(d - 1)$. Equation (JB2) becomes

$$Q_D = \frac{2(1-u_0)\tau_1^{n-0.5} A_r}{\alpha \tau^n} \tag{JB3}$$

Where

$$A_r = 1 \qquad \text{for } d \le 1 \tag{JB4a}$$

$$A_r = \left(\frac{r_p}{D}\right)^{d-1} \qquad \text{for } d > 1\,. \tag{JB4b}$$

(4) For $d < 1$, transition time t^* is unchanged from the $d = 1$ case, but for $d > 1$, t^* increases with d. A plot of log(t^*) versus d for the numerical simulations is roughly linear and yields the following relationship between t^* and d:

$$\frac{t^*(d)}{t^*(d=1)} = 1 \qquad \text{for } d \le 1 \tag{JB5a}$$

$$\frac{t^*(d)}{t^*(d=1)} = 10^{0.5(d-1)} \qquad \text{for } d > 1. \tag{JB5b}$$

We denote this ratio the transition-time delay factor, τ_r^* , and using Equation (5) for τ* when d = 1, write the generalized value of dimensionless transition time τ* as

$$\tau^* = \frac{\tau_r^*}{\alpha^2}. \tag{JB6}$$

The value of β(τ*) is chosen to assure continuity of the early- and late-time solutions for Q_D at τ*:

$$\beta(\tau^*) = (a^2\tau_1)^{(n-0.5)} A_r (\tau_r^*)^{-n}. \tag{JB7}$$

The variation of β with τ, given by Equation (2), is not changed. As shown in Figure 5, this approximation is only good for values of d that are not too different from 1.

For convenience in curve fitting, so that there is only one unknown parameter that produces a vertical shift on a log-log plot, the coefficient $\tau_1^{(n-0.5)} A_r$, which appears in Equations (JB3) and (JB7), can be absorbed into Q_0, resulting in

$$Q_D = \frac{2(1-u_0)}{\alpha \tau^n} \qquad \text{for} \quad \tau < \tau^* \tag{JB8a}$$

$$Q_D = 2\beta(\tau)(1-u_0) \qquad \text{for} \quad \tau > \tau^* \tag{JB8b}$$

$$\beta(\tau^*) = \frac{1}{\alpha \tau^{*n}} \tag{JB9}$$

$$Q_0 = \frac{A c_g k_D p_R^2}{\rho_0 \mu D} \tau_1^{(n-0.5)} A_r. \tag{JB10}$$

The definitions of α, u_0, and t_0 are unchanged from Equations (4), (6), and (7), respectively.

Figure 15 shows a plot of n as a function of $d' = 3 - d$ obtained from the numerical simulations. The variable d' is used rather than d to expedite fitting a simple functional form to the n versus d values. As shown in Figure 15, a linear function for $d < 1$ and a quadratic function for $d > 1$ do a reasonable job of fitting the simulation results:

$$n = 1 - d/2 \qquad \text{for } d \le 1 \qquad \text{(JB11a)}$$

$$n = a(3-d)^2 + b(3-d) + c \qquad \text{for } d > 1 \qquad \text{(JB11b)}$$

With $a = 0.1277$, $b = -0.0142$, and $c = 0.028$. These coefficients a, b, and c are for the $u_0 = 0.766$ case, but the values for the $u_0 = 0.25$ case are quite similar. Other numerical simulations using one-column grids with different values of D and A, and different grid resolution all yielded comparable results for n and t^* as a function of d.

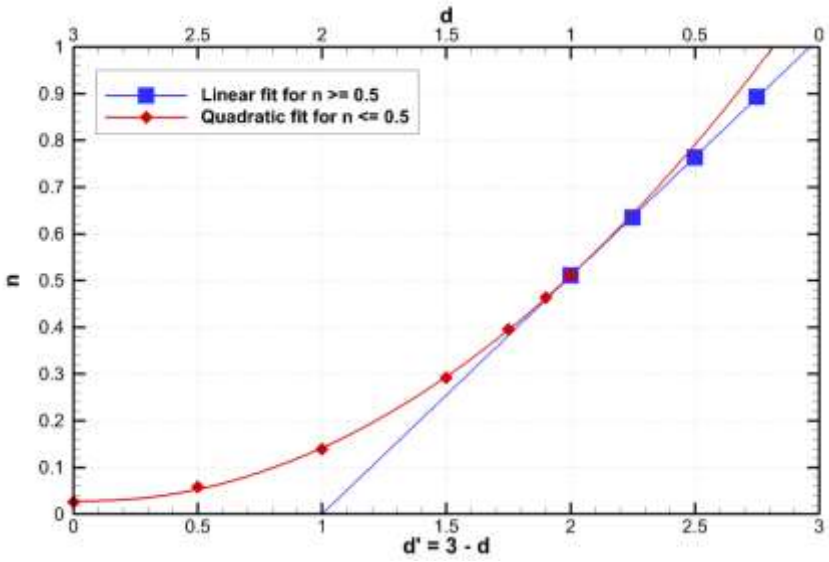

Figure 15: Absolute value of the slope of the linear portion of the production decline curve, n, as a function of flow dimension d. Symbols show numerical simulation results and the lines are a curve-fit based on linear (for n ≥ 0.5) and quadratic (for n ≤ 0.5) functions.

To determine a flow dimension d from field data, which provides n, it is necessary to invert the expression (JB11b) for n. This can be readily done using the quadratic formula, which yields closed form expressions for d as a function of n:

$$d = 2(1-n) \qquad \text{for } n \ge \tfrac{1}{2} \qquad \text{(JB12a)}$$

$$d = 3 - \left[\frac{-b+\sqrt{b^2-4a(c-n)}}{2a}\right] = 2.9 - 2.8\sqrt{n-0.028} \quad \text{for } n < \tfrac{1}{2}. \qquad \text{(JB12b)}$$

Note from Figure 15 that the linear approximation, Equation (JB12a), is reasonable for values of *n* as small as 0.4, which is the smallest value of *n* for which the approximate generalization to the bimodal solution is valid for all times. For smaller values of *n*, Equation (JB12b) should be used to infer *d*, and only the early-time portion of the decline curve, prior to τ*, should be used for curve-fitting.

In summary, if field production data show a linear trend on a log-log plot of production rate versus time, then the absolute value of the slope *n* may be used to estimate the flow dimension *d* that is characteristic of the SRZ, using Equation (JB12). The concept of a single flow dimension being representative of an entire SRZ is an extreme simplification, but one that may prove useful in predicting future production decline.

Appendix JC: Using the Solver Tool in Excel

As described in the Excel 2010 documentation, "Solver is part of a suite of commands sometimes called what-if analysis tools. With Solver, you can find an optimal (maximum or minimum) value for a formula in one cell — called the objective cell — subject to constraints, or limits, on the values of other formula cells on a worksheet. Solver works with a group of cells, called decision variables or simply variable cells that participate in computing the formulas in the objective and constraint cells. Solver adjusts the values in the decision variable cells to satisfy the limits on constraint cells and produce the result you want for the objective cell." Within the Solver, there is a choice of three algorithms to find the optimal value of the objective cell:

1. Generalized Reduced Gradient (GRG) Nonlinear: Use for problems that are smoothly nonlinear.
2. LP Simplex: Use for problems that are linear.
3. Evolutionary: Use for problems that are non-smooth.

Both optimization steps in the mS&K problem are non-linear, but the objective function varies smoothly with the unknown parameters, so the GRG method is recommended.

<u>For more information on the Solver, contact:</u>

Frontline Systems, Inc.
P.O. Box 4288
Incline Village, NV 89450-4288
(775) 831-0300
Web site: http://www.solver.com
E-mail: info@solver.com

Loading Solver into Excel 2010 and Excel 2013 (if it does not appear under the DATA header in Excel)

- File/Options/Add-Ins
- Manage Excel Add-ins - GO
- Check box for Solver Add-in, then OK.
- Solver will appear under the Analysis section of the DATA header.

Loading Solver into Excel 2003 (if it does not appear under the TOOLS menu)

- Tools/Add-Ins
- Check box for Solver Add-in, then OK.
- Solver will appear under the TOOLS menu

Appendix K: Benefit Analysis of Reservoir Engineering

Summary

In this report, we have evaluated the well performance of four wells on two well pads to compare the advanced variable rate hydraulic fracturing routine demonstrated as part of this project with conventional fracturing routine. In each pad, the experiment well is fractured using variable rate in alternating stages with a nearby offset well fractured using conventional fluid pumping scheme. The total production of four wells was looked into. The production rates were analyzed using bimodal decline scheme. Bimodal production decline analysis scheme is further illustrated in Appendix. It provides a simple indirect estimate of initial production decline rate and fracture geometry parameters. The second well pad exhibits production decline without too much operation interruptions and are therefore looked into using bimodal decline analysis carefully. The experiment well on second pad which went through more rapid fracture rate changes in alternating stages demonstrated a slower decline rate. Assuming they are draining from a uniform SRV, the experiment well developed a more effective fracture network than its offset well on the same pad. The production logs showed direct indication of 19% increased production in variable rate fracturing stages of experiment well.

Introduction

Facing the environmental and economic challenges of hydraulic fracturing in shale/tight gas reservoirs, to develop a more effective fracture design leading to increased production per unit volume of water and proppant pumped is essential. In the first experiment, we implemented a ramped pump schedule every other stage. The proppant and water volume injected during pumping is the same for all stages. Variable rate stages consistently showed more micro-seismicity than constant rate fracture stages, however no significant difference in production contribution between stages are observed. Determined that rate changes were not aggressive enough, we performed more rapid rate variations in every other stage in second experiment. Injected fluid volume and proppant mass are all same. Production logs were ran after observing decreased treating pressure after rate variations. The average gas production per stage of variable rate treated stage is higher than conventional treated stage. Four wells are still in production till now. The production data till the end of 2014 were collected and analyzed from the perspective of cumulative production, cumulative production per lateral length and per mass of proppant pumped. The dynamics of production could also be an indicator of fracture network development. The physical model of production dynamics is based on bimodal decline curve of Silin and Kneafsey (2012), with modification of variable decline rate instead of constant -0.5 decline rate. The modified bimodal decline curved was solved semi-analytically and was programmed into Excel spreadsheet. The details of application are in Appendix J [report

generated by Lawrence Berkeley National Laboratory]. The approximate estimate of fracture geometry and decline rate provided by modified bimodal analysis was utilized to analyze fracture development and flow conditions.

Benefit Analysis

The benefit analysis of advanced hydraulic fracturing consists of three parts. Two direct measurements are total production and production logs. One indirect measurement is fracture geometry and production decline rate estimate from daily production analysis.

Cumulative Production

Table 1: Production and Hydraulic Fracturing Summary for experiment and offset wells

Well	Cum Prod, Mscf	length of well, ft.	# of stages	volume of proppant, 100lbs	Mscf/ft.	Mscf/100lbs
Well #1	439025.72	5675	18	57769	77.36	7.60
Well #2	386045.45	4340	14	44804	88.95	8.62
Well #3	436989.22	4902	27	54705	89.15	7.99
Well #4	849092.86	5211	28	82457	162.94	10.30

The total production till December 1st, 2014 was summarized in Table 1. Due to a lot of inconsistencies between wells on the same pad, cumulative production of experiment wells (well #1 and well #3) didn't show advantageous production over offset wells (well #2 and well #4). Neither does cumulative production per lateral length or per mass of proppant pumped show increased production from experiment wells. Partial reason for second well pad could be explained from well trajectory map in Figure 1. One third of Well #3 lateral goes into upper layer and thus induced fractures may not be fully developed in target zone. Secondly, well #3 is located between two producing wells with well #5 in production before well #3 and well #4 on the other side, shown in Figure 2. While the adjacent wells compete for gas with well #3, the outlier well #4 has a vast of gas replenish from untapped reservoir. Therefore, cumulative production is not a good indicator to distinguish variable rate fracturing with constant rate fracturing.

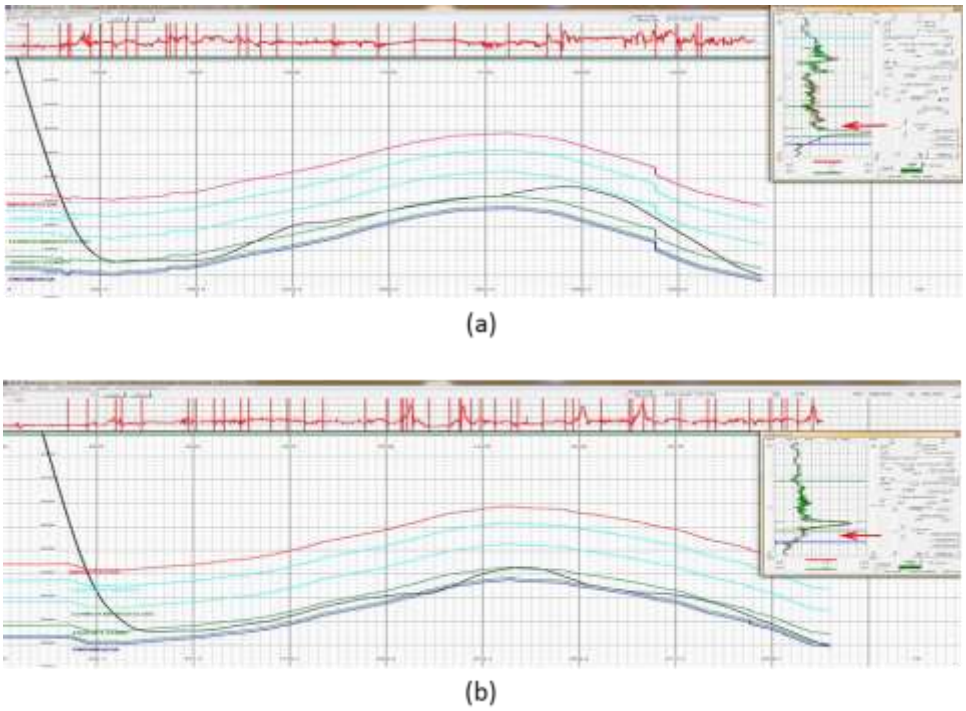

Figure 1: Well trajectory (a. well #3, b. well #4)

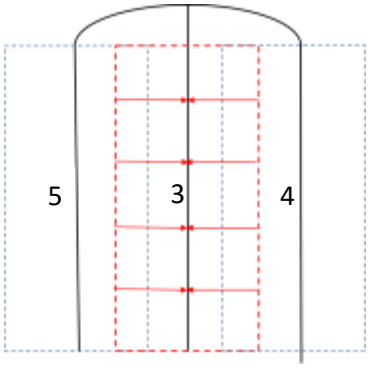

Figure 2: Well Pad

Bi-Modal Production Decline Analysis

The bimodal production decline analysis scheme is developed by Silin and Kneafsey (2012), and further modified by LBNL to include different fracture-network geometries in the early production period. The details of model setup and development of analytical solutions could be found in Appendix. Gas flow is restricted to stimulated reservoir volume (SRV) of areal extend A and thickness D. In the circumstance of multiple hydraulic fractures in a horizontal well, each fracture stage is treated identically. A could be the sum of areal extend of all stages. D could be

the distance from center of fracture to no-flow boundary or boundary between two fractures. The gas flow rate declines with a power-law relationship in the early times before the outer boundary is felt, and then declines exponentially after pressure transient reaches the no-flow boundary. The underlying assumption for all decline curves is constant flowing bottom-hole pressure.

Table 2: Input data for Bi-Modal production decline analysis

Well	#1	#2	#3	#4
FBHP, psi	1174	1160	1499	N/A
PR, psi	2545.3	2556.3	4111	4111
u_0	0.46	0.45	0.36	0.36*

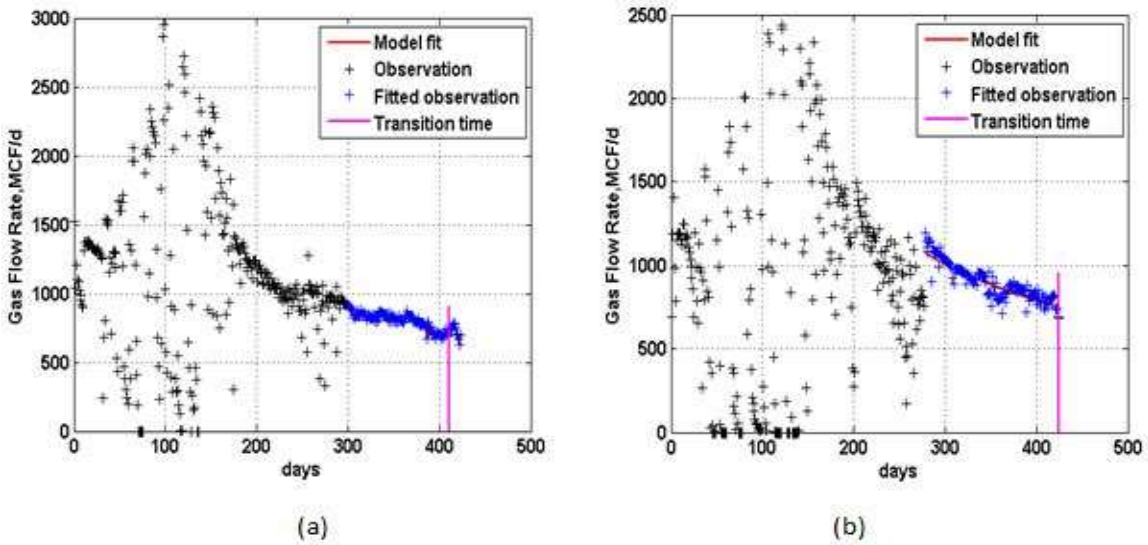

Figure 3: Observed production rates for (a) experiment well (well #1) and (b) offset well (well #2).

Assuming fours wells are producing from SRV of uniform porosity of 0.08, uniform permeability of 1 nD and shale content of 0.1. The other input parameters are listed in Table 2. Flowing bottom-hole pressures were obtained from production logs. Reservoir pressure was obtained from well tests. Term u0 is the ratio of flowing bottom-hole pressure to reservoir pressure. The four wells undergoing production decline analysis are assumed to be operated at constant bottom-hole flowing pressure. Thus input u0 is a constant, with well #4 sharing an approximately same value with well #3.

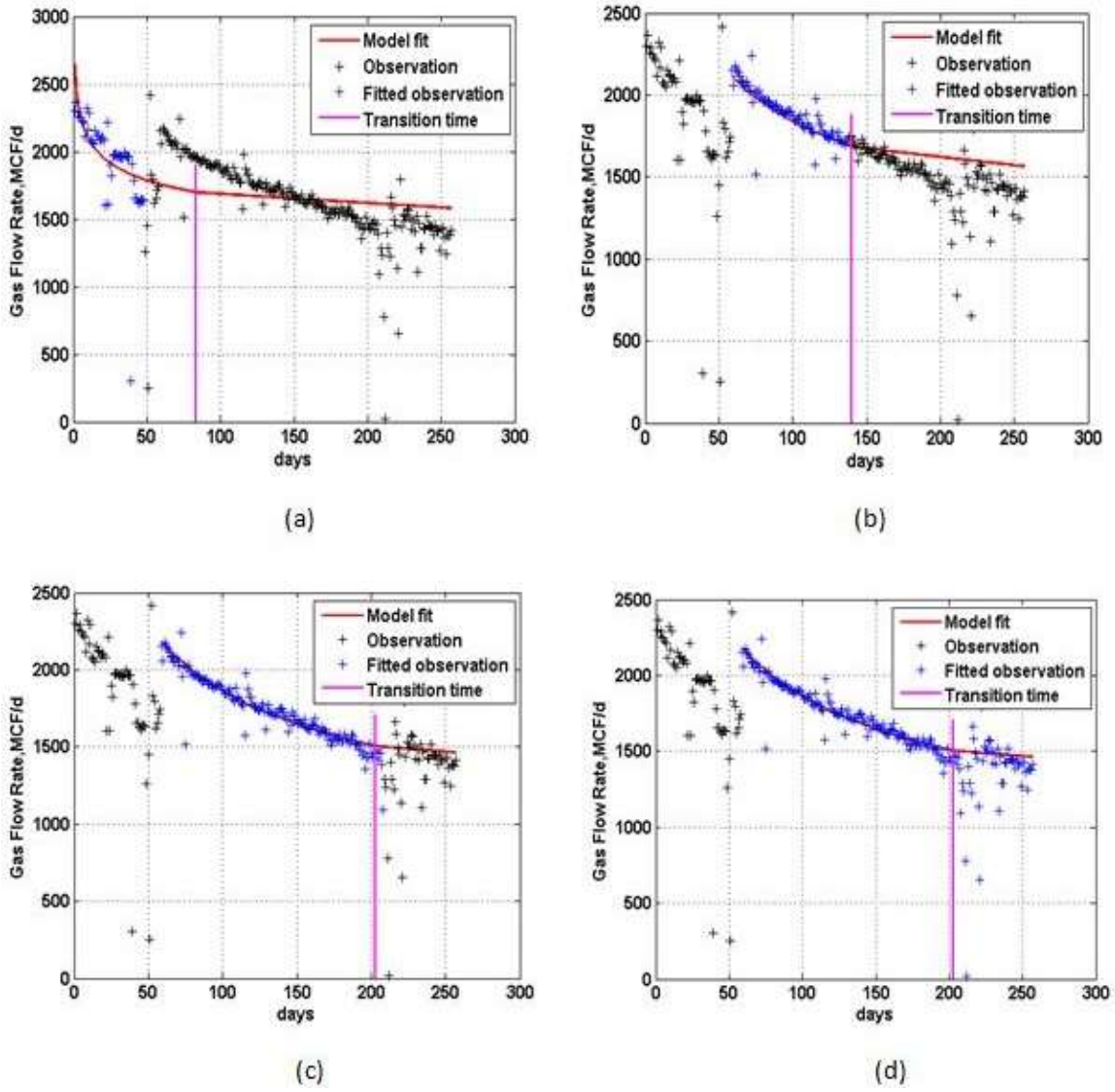

Figure 4: Production rate for well #3 [(a) 1-47 days, (b) 59-136 days, (c) 59-208 days, (d) 59-257 days]

Well #1 and well #2 are observed with abnormal well shut-ins due to salting problems in extremely low temperatures. The area of interest for production begins after around 300 days, show in Figure 3. Both of well #1 and well #2 are fitted with power-law decline, with areal extend of 200,000 ft^2 and thickness of 100 ft. The decline rate for well #1 is 0.78 and for well #2 is 0.84. Well #1 declines slower than well #2, indicating a possibly more complex fracture network. The complexity could results from more effective induced fracture propagation or existences of natural fractures.

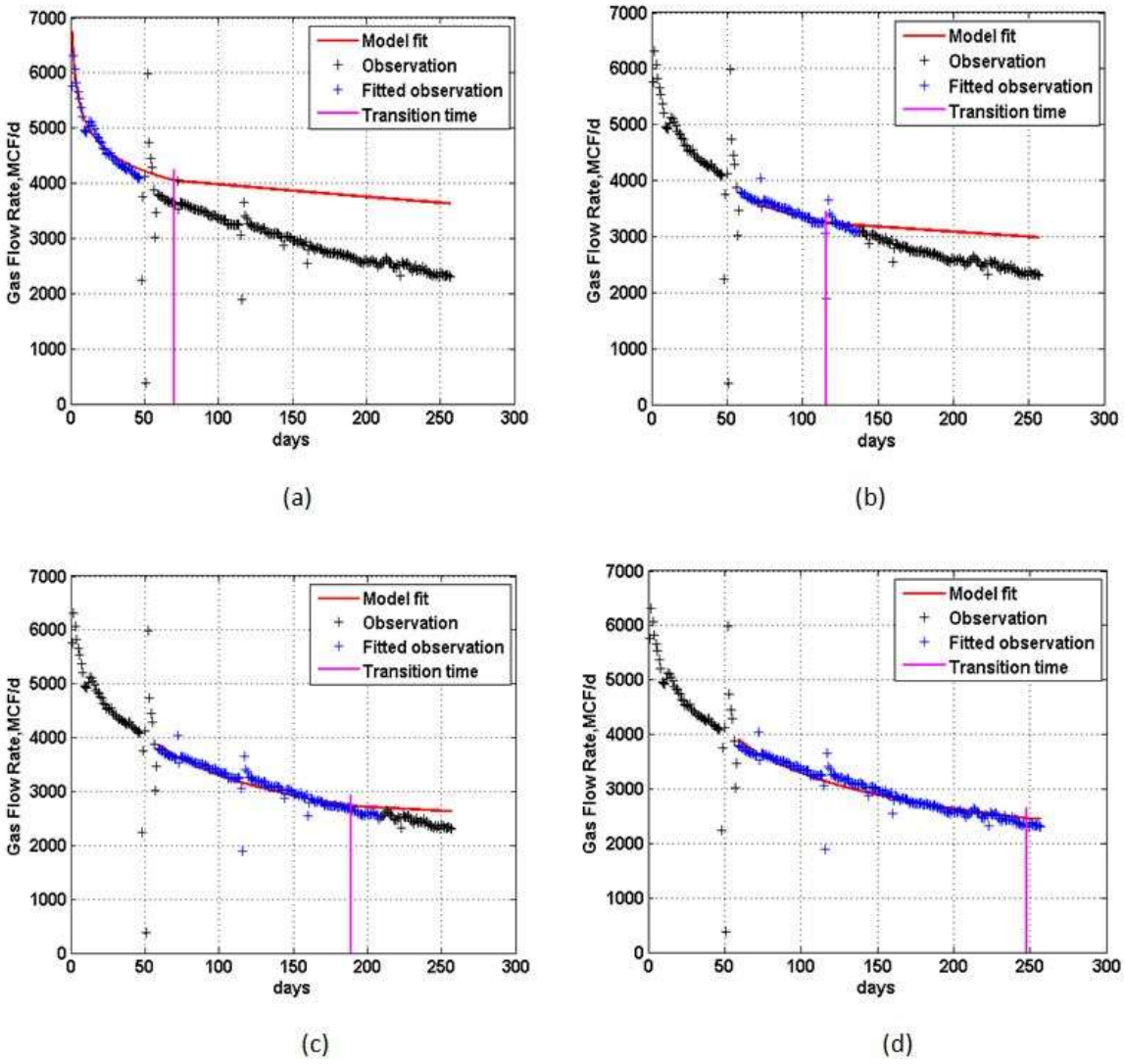

Figure 5: Production rate for well #4 [(a) 1-47 days, (b) 59-136 days, (c) 59-208 days, (d) 59-257 days]

Production curve for well #3 and well #4 are segmented into four time windows depending on data availability. In Figure 4(a) and Figure 5(a), power-law model decline fitted with initial 50 days but failed to predict future performance. That's caused by tubing installation, which changed the bottom-hole flowing pressure and well operation condition. Production data after 59 days are appropriate for bi-modal decline analysis. Comparing Figure 4(b), Figure 4(c) and Figure 4(d), transition time between power-law decline and exponential decline (represented by magenta vertical straight line) occurs around 200 days. And the corresponding areal extent A, thickness D and decline rate stabilized respectively at 400,000 ft^2, 112 ft. and 0.3.

Comparing Figure 5(b), Figure 5(c) and Figure 5(d), transition time evolved with time and stopped at around 250 days. The areal extent of well #4 is estimated to be a constant of 700,000 ft^2, while thickness is kept increasing from 108 ft. to 120 ft., as transition time evolved. The decline rate for well #4 is 0.3 in Figure 5(b) and then increased to 0.32 in Figure 5(c) and Figure 5(d). Well #4 declines at the same rate as well #3 until 208 days. The initial decline rate includes impact of many factors besides effectiveness of hydraulic fracture and reservoir heterogeneity. Given the SRV is assumed the same for both wells, well #3 declines slower than well #4 simply by change fracturing rate more rapidly in odd stages. Whether initial decline rate is directly related with fracture network effectiveness will be known with more tests.

Production logs

Production logs were ran for well #1 and well #3 after fracturing. The first experiment, implemented ramp-up pump schedule every other stage didn't show significant in production contribution between stages (Figure 6) And therefore the second experiment were fracturing using more aggressive rate variations. 14 odd stages were pumped with intended variations and 13 even stages were pumped with no intended rate variations. On average, odd stages produced 4.02% of total gas and even stages produced 3.37% of total gas. There is 19% increase in production due to rate variations (Figure 7).

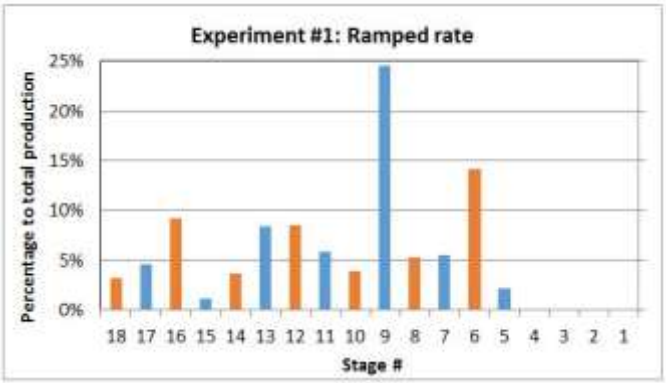

Figure 6: Production log for well #1

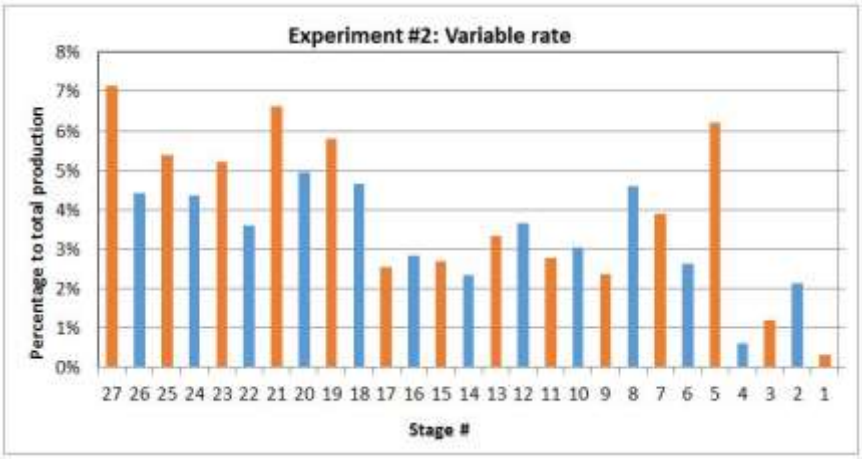

Figure 7: Production log for well #3.

Other Models

Typical production profiles from tight shale formations comprises of a few set of mechanisms, the combination of which is unique to such tight formations. These include desorption of fluids within the matrix governed by Langmuir isotherms, transport of the fluids within matrix towards the fracture face (either hydraulic or natural) governed by Darcy flow and finally, transport of free fluids within the fractures towards the wellbore. The degree of contribution to overall flow from natural fractures can vary widely from one play to another and also within plays. Some gas plays (such as Barnett) show lack of contributing natural fractures (or even absence altogether) based on field observations (over-pressured system, calcite filled fractures). However, for analytical modeling of hydraulically stimulated wells, there is broad consensus within the scientific community and the industry that the following flow regimes could be observed during the course of a well's productive lives:

- Bilinear/ Linear (flow normal to fracture face)
- Early radial/ elliptical (flow through fracture tips and fracture interference begins)
- Compound formation linear [CFL] (drainage area defined by the length of lateral and fractures)
- Pseudo-radial/ elliptical (effect of flow beyond perturbed zone starts dominating)
- Reservoir boundary dominated flow

CFL flow regime for most plays is typically observed anywhere from 6 to 12 years after a well is brought into production (Walton and McLennan, 2013).

Based on the semi-analytical solution proposed by Walton and McLennan, the early time infinite acting solution for dimensionless flow rate for shale gas is defined as:

$$q_{D0} = \frac{1}{\sqrt{\pi t_D}} \quad \rightarrow \quad Q_{D0} = 2\sqrt{\frac{t_D}{\pi}} \tag{1}$$

During this period, the cumulative production under surface conditions can be estimated as:

$$Q_S = A\frac{k_m}{Z_{ch}}\frac{T_S}{T_w}\frac{Z_s}{p_s}m_{ch}2\sqrt{\frac{t_m}{\pi}}\sqrt{t} \tag{2}$$

Cumulative production under surface conditions can be rephrased as:

$$Q_S = C_P\sqrt{t} \tag{3}$$

C_P helps characterize the early time solution in a way that can be estimated from available well production data. From equations (2) & (3), we can define C_P as follows:

$$C_P = A\frac{k_m}{Z_{ch}}\frac{T_S}{T_w}\frac{Z_s}{p_s}m_{ch}2\sqrt{\frac{t_m}{\pi}} \tag{4}$$

In the above relation for C_P, p_S gives the surface pressure, T_S is the surface temperature and T_W is the wellbore temperature. A is the productive fracture surface area, Z_{ch} is the characteristic gas compressibility factor, Z_S is the gas compressibility factor under surface conditions, m_{ch} gives the characteristic gas pseudo-pressure and t_m characterizes the pressure diffusion in matrix.

$$t_m = \frac{c\emptyset_m\mu(L/2)^2}{k_m} \tag{5}$$

L is the inter-fracture spacing, c is the gas compressibility, ϕ is the porosity, k_m is the matrix permeability and μ is the viscosity of the fluid. From equations (3) & (4), we clearly see that cumulative production varies with square root of production time (based on the above early-time solution of said semi-analytical mode) and time scale t_m defined the upper limit for applicability of this method. Since the production data from wells available from this project is not adequately long to allow robust analysis using this solution, we looked at data from a prior RPSEA program (09122; Troyer Pad) as well as data available from open source [Pennsylvania DCNR]. Figure 8 shows production vs. time while Figure 9 shows production vs. square root of time for data from Troyer Pad. We observe linear relationship as predicted by the model (early time solution) and this trend behavior carries for the entire duration that the data is available for. We note that data

from first year of production is removed due to severe impact of drawdown conditions, as well as operational and inter well interference artifacts.

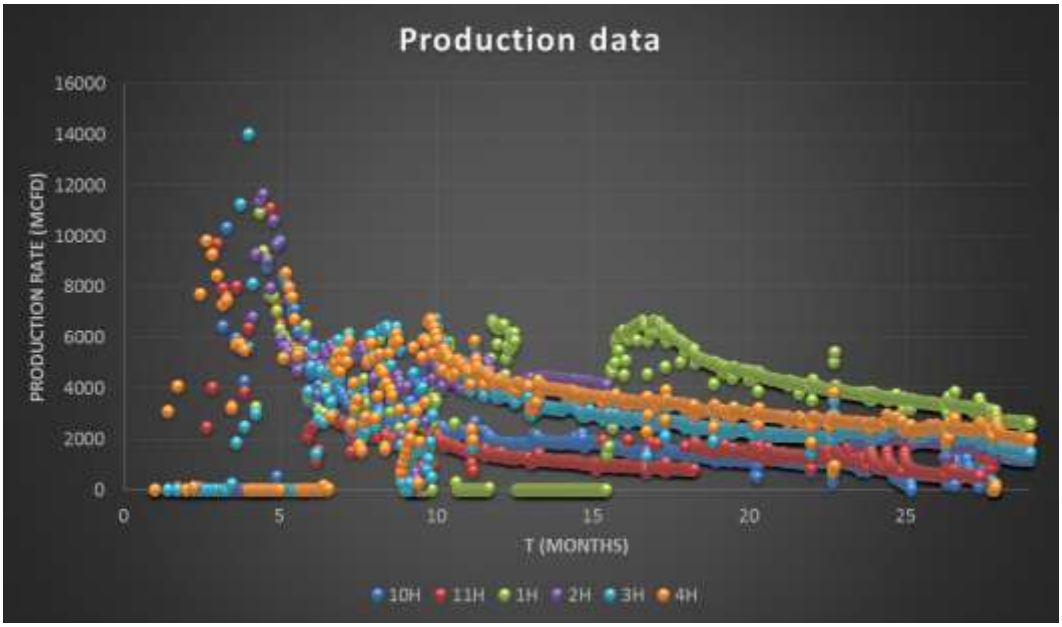

Figure 8: Production data for Troyer pad wells 1H, 2H, 3H, 4H, 10H & 11H [Refer RPSEA 09122].

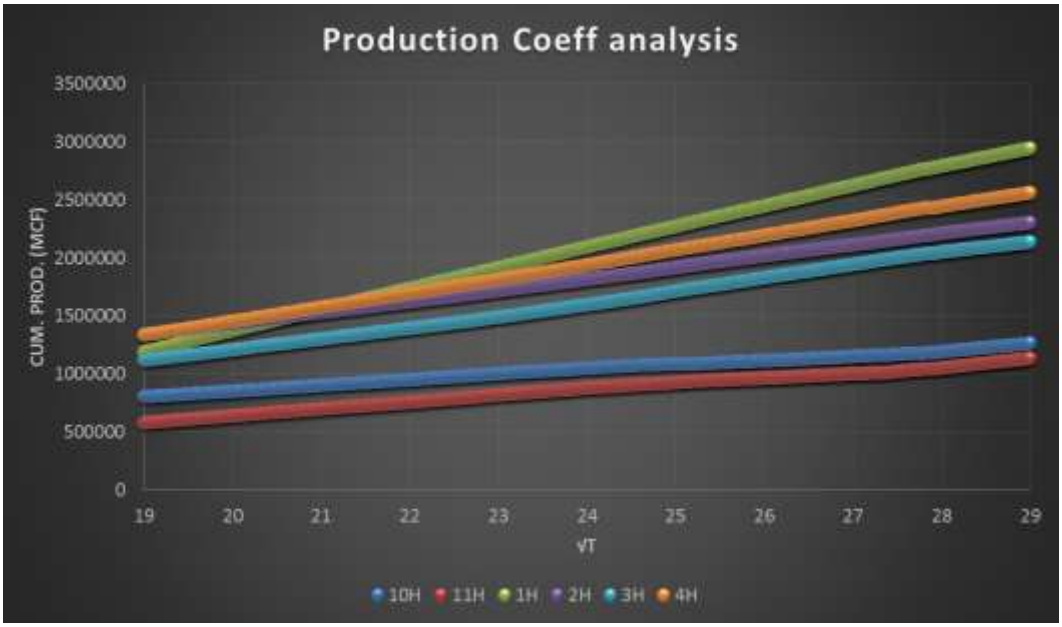

Figure 9: Production coefficient (C_P) analysis for Troyer pad wells 1H, 2H, 3H, 4H, 10H & 11H. Observe the varying slopes associated with these wells.

Figure 10 shows a composite of individual wells from Troyer pad and the C_P values based on linear best fits through regression. We observe significantly higher C_P for well 1H compared to well 10H. We note here that wells 1H and 4H are peripheral wells with significantly higher virgin reservoir contact compared to wells 10H which is the middle well of this pad.

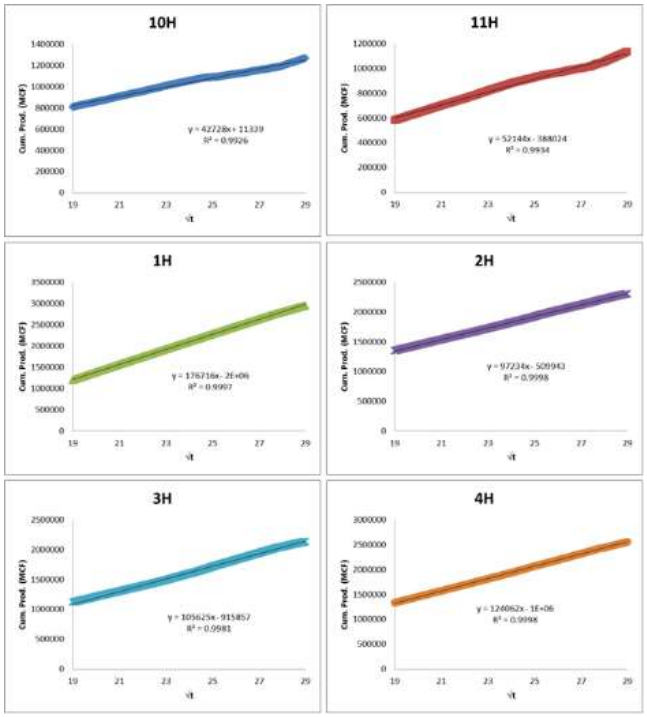

Figure 10: Production coefficient (C_P) analysis for Troyer pad wells. Wells with C_P values in decreasing order are: 1H, 4H, 3H, 2H, 11H, 10H.

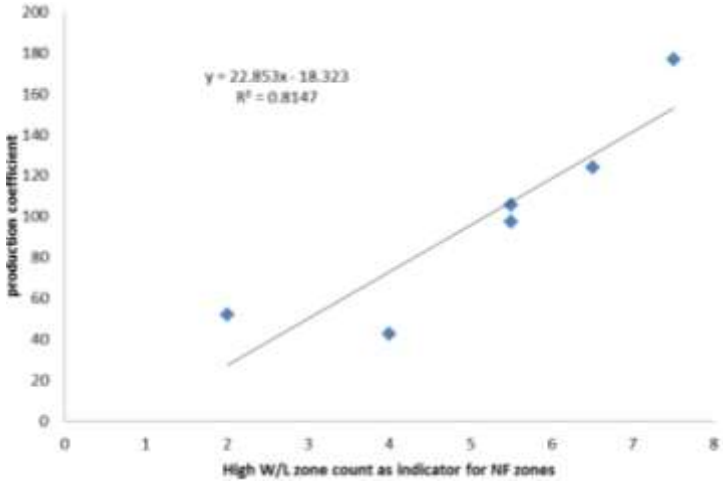

Figure 11: W/L analysis results (indocator of NF) correlated with fitted C_P values.

Despite the obvious correlation with type of stimulated reservoir the wells are in contact with based on location, we looked at how C_P values correlate with L/W (Length/ Width) ratio of microseismic event distributions available for all of these wells (Figure 11). For details regarding L/W computation and its use as an indicator of fracture complexity and natural fracture presence, please refer to the project report from prior RPSEA project as cited earlier.

Next we looked at some other wells operated by WPX energy in the Marcellus play which are in geographical proximity of the Troyer Pad. We share results from 3 separate pads in Figure 12, Figure 13 & Figure 14. We observe that for one of the pads, the significant discrepancy in observed productivity from one of the wells compared to the other two is explained by the spatial distribution of said wells. However for the other two pads, we don't see this behavior. Moreover, the range of discrepancy in C_P distribution seems to vary widely from one pad to another and these differences cannot be accounted for simply based on well location alone. In future studies, there is a scope to look at the identified C_P values as well as "A" values from bi-modal decline analysis and identify correlations between these two sets of parameters. Since both estimate early time contact area, the expectation is that we should get similar results. This will help further validate results from bi-modal decline analysis. Other independent data (such as microseismic, 3D seismic, petrophysical and image logs, etc. can potentially be used for similar analysis.

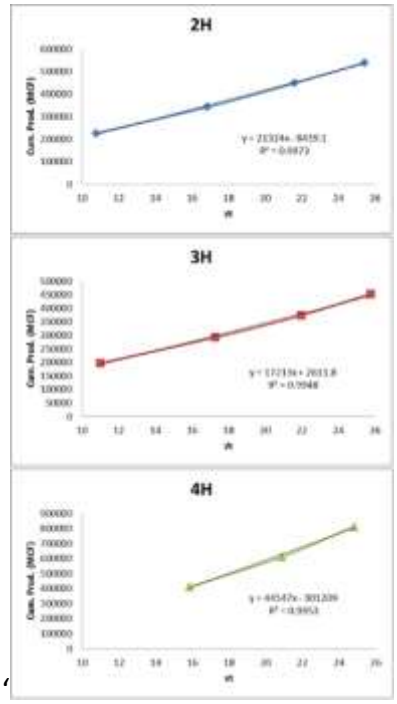

Figure 12: Analysis of wells from Panizi pad. Well 4H potentially has a lot more effective fracture surface area based on observed C_P values compared to wells 2H & 3H.

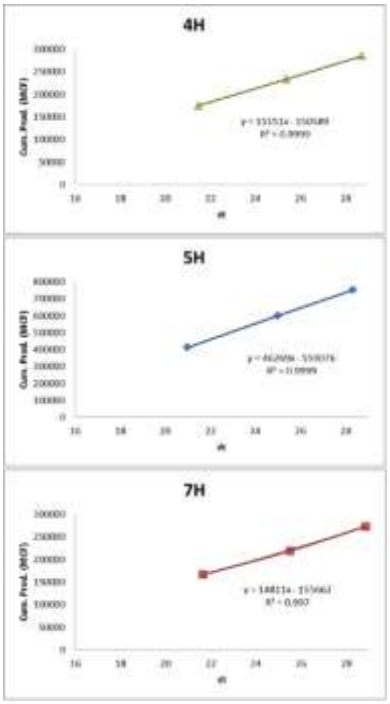

Figure 13: Analysis of wells from Eaglehouse pad. Well 5H potentially has a lot more effective fracture surface area based on observed C_P values compared to wells 4H & 7H.

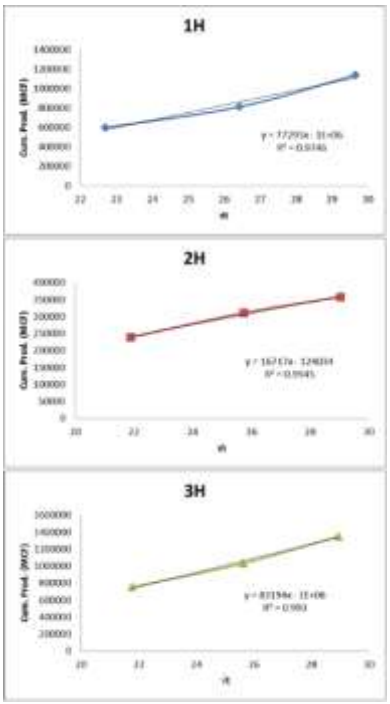

Figure 14: Analysis of wells from Slavek pad. Wells 1H & 3H potentially has a lot more effective fracture surface area based on observed C_P values compared to well 2H.

Conclusions

Cumulative production, production logs and bi-modal production decline analysis using up-to-date production data are reviewed on well basis. Cumulative production per lateral length and per mass of proppant pumped is not a good evaluation indicator for hydraulic fracture development. Bi-modal decline analysis with sufficient production data could provide information of fracture geometry parameters, prediction of production in the future and estimate of ultimate recovery once no-flow boundaries has been felt. Bi-modal decline analysis gave a slower decline rate in variable rate fracturing well. The extension to say initial decline rate is an indicator for fracture network effectiveness still needs validation on more wells. Production logs give direct measurements of gas contribution from each fracture stage. The variable rate fracturing in alternating stages exhibited 19% increase in production. Production log is so far the most straightforward and reliable method to prove that variable rate fracturing improves gas production per unit of fluid and proppant injected. Finally, other semi-analytical models can also be used to validate some of the diagnostic tools developed as part of this project for future applicability.

Reference

[1] Ian Walton, John McLennan, 2013. The Role of Natural Fractures in Shale Gas Production, In Andrew P. Bunger, John McLennan and Rob Jeffrey (Ed.). *Effective and Sustainable Hydraulic Fracturing.* ISBN: 978-953-51-1137-5.

[2] Dmitriy Silin, Timothy J. Kneafsey, 2011. Gas Shale: from nanometer-scale observations to well modeling. Canadian Unconventional Resources Conference, Calgary, Alberta, Canada, 15-17 Nov.

Appendix L: Laboratory Scale Hydraulic Fracturing Experiments

Summary

The goal of this project is to conduct **laboratory experiments** involving passive seismic monitoring in order to **understand better** the hydraulic fracturing process.

From the project we have generated the following deliverables:

- Quarterly reports to summarize the project progress, obstacles and possible alternatives.
- Experimental design of the laboratory at a national conference on hydraulic fracturing.
- Experimental descriptions and interpretations of single-component seismic data sets derived under non-dimensional experimental conditions.
- An appropriate number of multi-component sensor clusters will provide the necessary data to generate tables of event location during the course of the experiments.
- Results of the influence of a simulated fault will on interpreted seismic mechanisms (Mode-I versus mixed-Mode)
- An analysis and discussion of the scalability of these results to field conditions and comparison to previous laboratory experiments will be published.
- An educational deliverable will be the training of student workers in this field,

Detailed as follows:

1. Quarterly reports to summarize the project progress, obstacles and possible alternatives

Quarterly updates were provided to Jordan Ciezobka along with annual reports from 2013 and 2014. Refer file: "Reports_portfolio.pdf".

2 (A) Experimental design of the laboratory at a national conference on hydraulic fracturing.

Digital Seismic Hardware

We installed a microseismic acquisition computer for the laboratory, under a RedHat Enterprise Linux OS 6.6 (Figure 1). Benchmark tests show that reading and writing speeds range from 780-980 MB/s. The maximum expected data acquisition rate during experiments is ~ 480 MB/s. Acquisition rates are estimated

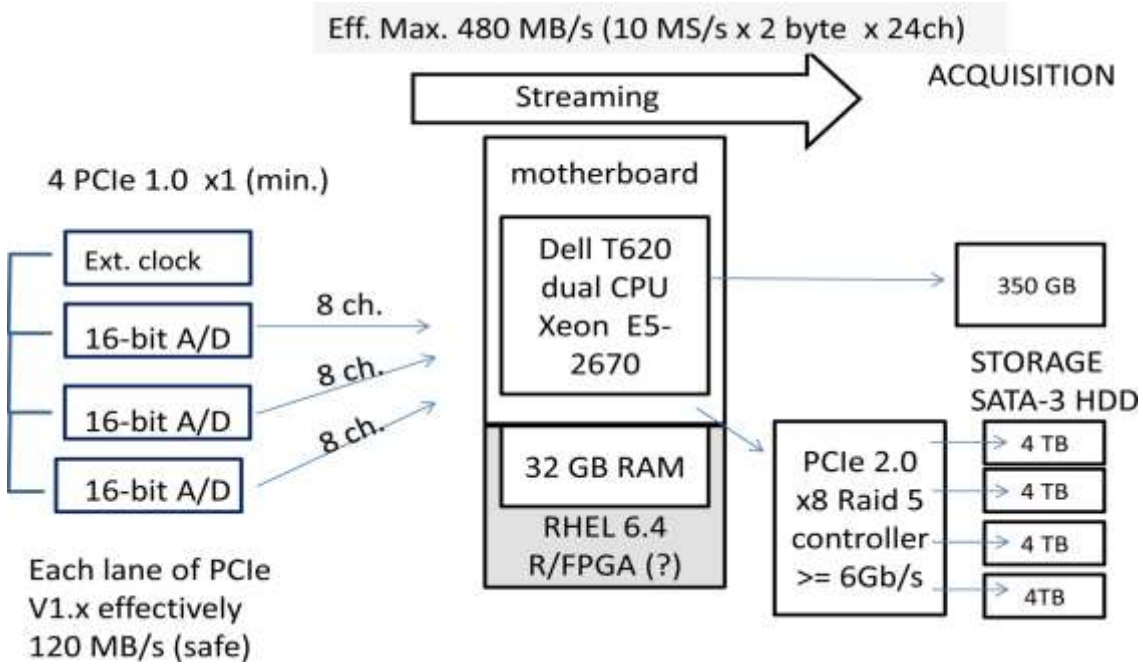

Figure 1. Schematic outline of technical requirements for fast microseismic laboratory acquisition system are met by an off-the-shelf Dell T620 server. Fast acquisition speeds are achieved through PCIe-bus technology.

based on 24 sensors each collecting data at a rate of 10 MS/s and 16-bits of resolution. Benchmark tests for our 350 GB solid-state-drive show reading and writing speeds in the range of 780-980 MB/s. Even with an expected maximum delay of 25%, caused by software and hardware overhead, our system is capable of handling the expected data flow rates. We expect that direct writing to RAID during some experiments could be used if the sample rates were reduced significantly.

We surveyed all available fast analog-digital acquisition (AD) and timing cards. Based on necessary acquisition speeds and resolution, we selected a USA manufacturer (Innovative Integration Inc.) to provide three 8-channel AD cards (X3-2M) plus associated installation software and hardware. Cards are

synchronized to each other via an external clock and trigger card (X3-timing XMC module). Free vendor libraries control driver and hardware. Binary files are saved in a proprietary but well-described format.

A PCIe-XMCe adapter that accompanies each AD card provides access to one "lane" of the fast onboard PCIe bus. According to the manufacturer a maximum, effective, reliable, transfer rate of ~160 MB/s per card can be achieved when using a maximum of 8 channels on each card. Each card allows up to 12 incoming channels.

For the objective of our proposal we used the standard capabilities of 8 channels per card at the maximum data transfer rate. However, in future, the current hardware, could be scaled to collect on 12 channels per card (a maximum of 36 channels). Future development would require software to employ the onboard FPGA (field-programmable gate array) which is programmable via MATLAB modules. MATLAB is a

Figure 2: Opened acquisition computer reveals one AD card (acquisition card and bus adapter) in bottom-right corner. Three slots (light blue, right-hand side) remain for three additional AD cards.

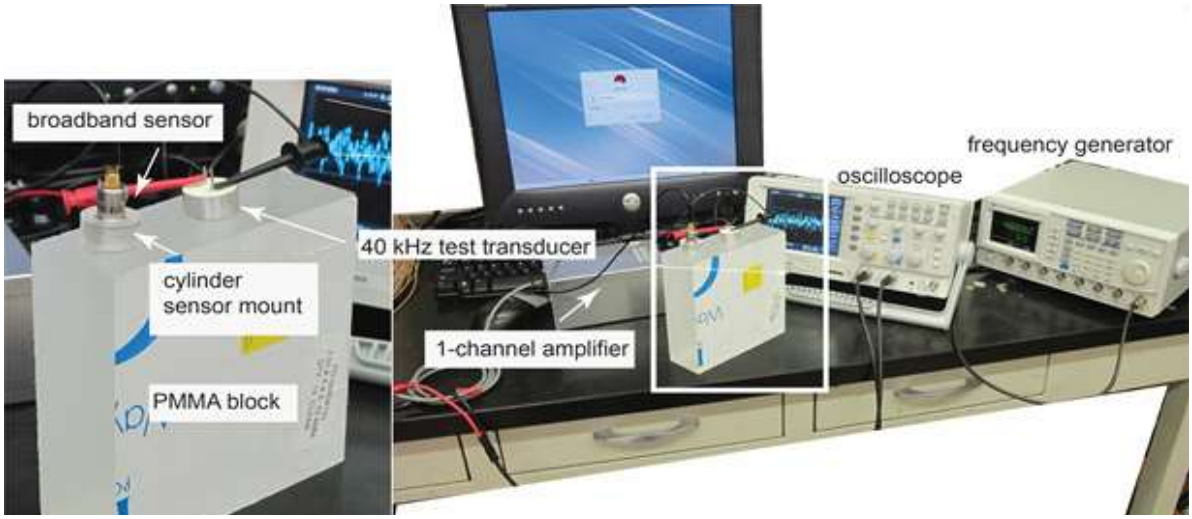

block of transparent Poly (methyl methacrylate) PMMA (5 cm x15 x 15 cm) serves as an initial test body on which to mount sensors. The blocks that were hydraulically fractured also included larger samples; 10-15 cm in length and width. For the setup above, a weak 40 kHz sinusoidal signal is detected by the sensor, then pre-amplified 10-fold and displayed on the oscilloscope. High-frequency instrument noise was also detected and identified for later removal.

common commercial software language useful for vectorized calculations. By selectively culling unwanted noise, real-time processing of the data stream via the FPGA can incorporate up to 12 channels of data (4 additional channels) into the written data stream.

Seismic Acquisition Seismic Timing Cards

Trigger and clock synchronization is achieved through a specialized card (card X3-timing XMC module) that ensures that the start of recording and all the signals themselves are simultaneously. We highlight that in contrast to some commercial, ultrasonic non-destructive testing units we use analog-to-digital acquisition

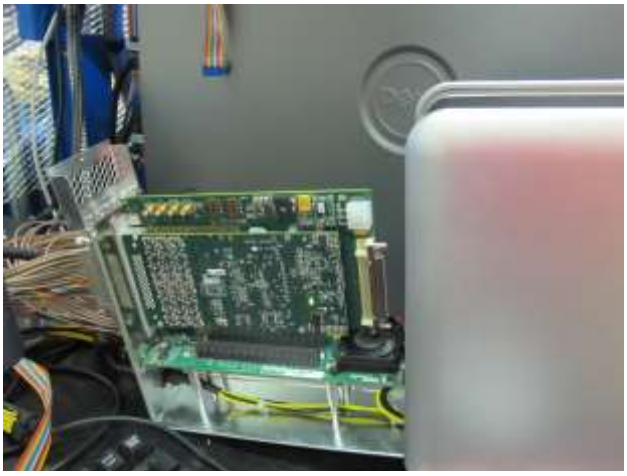

Figure 4. Third and final acquisition card is mounted on an external PCIe expansion bus and brings the acquisition capacity to 24 channels, for use in 8x 3-component stations.

cards that do not have to provide power directly to sensors. Our pre-amplifier serves that purpose and leaves us with a more modular system that provides flexibility to update AD cards in future independently of the pre-amplifier.

Pre-amplifier (prior to digital capture) for 24-channels of Microseismic Data

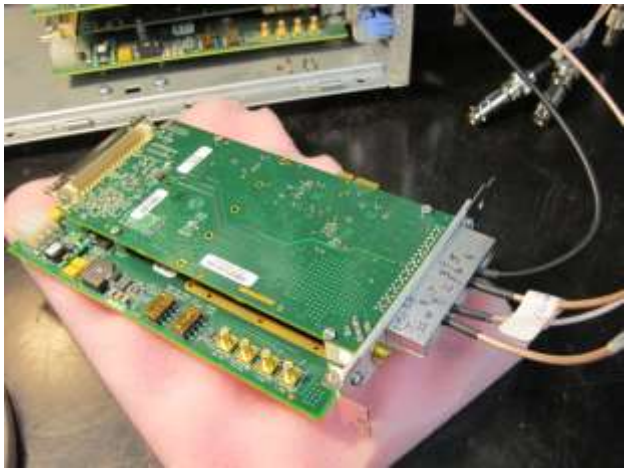

Figure 5. Timing card via external connector (cables) relays trigger pulses and through a reference clock synchronizes acquisition sampling.

We modified the original task in the proposal so that instead of multiplexing incoming data streams, we simultaneously sample of all data arriving from 24 channels (non-multiplexing). That is, we have a dedicated data channel for each of the 24 sensors. As a result we also found it cheaper and more flexible to proceed with the design and construction of our own pre-amplifier. An early, single-channel prototype pre-amplifier was used in an early trial and was presented at a group meeting in Palo Alto, November 2013.

Our pre-amplifier serves two purposes: (1) to condition signal coming from the sensors and transmitted on the AD cards and (2) to provide power to the seismic sensors.

The final working version of the pre-amplifier design (Figure 6) has four optional gains: x4, x20, x60, x100

Figure 6. 12-channel differential amplifier connected to one single-component sensor mount with sensor. Our final working pre-amplifier consists of two such units which provide power to the sensors, condition the signal with a differential amplifier before transmission to AD cards.

(prototype had only unity gain) while maintaining a broad sensitivity of 2 kHz – 2 MHz range of frequencies. Both input and output connectors are of BNC type, for convenience and lower noise (prototype unit one had only wire connectors). We use differential signal output pairs to reduce transmission noise.

A tool to synchronize among three different data-acquisition systems (Q4, 2014)

During the more advanced and final two experiments we collected not only microseismic data with the above acquisition hardware but we also recorded pressure data and made video recordings of the developing fractures within the samples. In order synchronize all three data types during experiments (Figure 41) we built a simple, inexpensive timing electronic circuit. Recorded images, pressure data and micro-seismic data are recorded on three separate acquisition systems. Because we required a timing signal to synchronize seismic events to pressure and camera data for cross-analysis, we built our own electronic tool for this purpose.

In order to better compare events in time between the camera images and the other two acquisition systems (seismic and well-head pressure, and pump pressure) we flash a red LED within the camera frame of view. Synchronously a square wave pattern is induced into the signal voltages of the other two recording systems.

The timing electronics circuit uses an oscillating square wave at a frequency of 20 kHz. A single-frequency square wave (3-V offset, and 5 Vpp amplitude) establishes the following timing signals among the different acquisition systems:

1. Switches on a red LED for the video camera.

2. Capacitively couples a timing signal (voltage) into the pump-pressure data stream.

3. Inductively couples a timing signal (voltage) into the well-pressure and microseismic data stream.

During the post-processing stage timing marks in each of the data sets can be correlated. A written log of the approximate times (within a few seconds of accuracy) is also made to facilitate later correlation.

Sensors and Sensor Mounts

After a review among all the available commercial microseismic sensors, we selected a high-quality test contact sensor. We settled on using a Glaser-NIST sensor (Figures 7, 8) because it provides the most constant frequency response over the range of signal frequency we expect to collect (< 0.1 MHz- ~ 2 MHz).

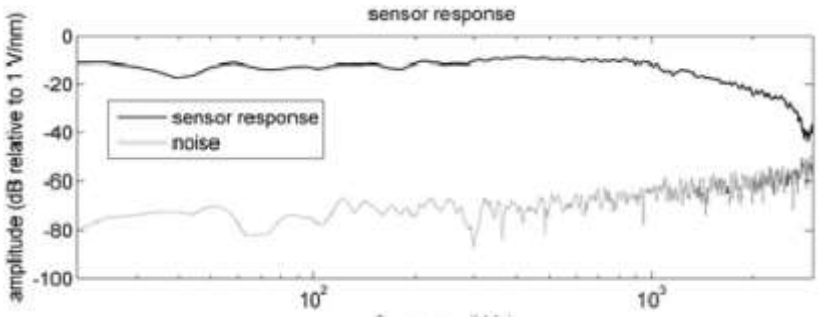

Figure 7 The NIST-Glaser sensor provides a broad consistent response to very high frequency signals as expected in future experiments

We employed a maximum number of 24 Glaser-NIST broadband (100 kHz-1MHz) point-contact, high-frequency sensors (KRN Services).

Because sensors need to be couple mechanically to the poly (methyl methacrylate) or PMMA test blocks, we designed, built and tested two types of sensor mounts. A single-component mount (Figures 3, 6) allows 24 individual single-component sensors the sensors to be distributed at 24 locations whereas a 3-component "Galperin" mount (Figure 8) is used when 3-component motion is required at a station location. PMMA is a transparent thermoplastic, with elastic properties suitable for scaling expected results up to field conditions. No commercially available equivalent sensor supports exist. We note that coupling between the sensor and the PMMA test sample is improved by using a sensor support of the same acoustic impedance and so we use the same material for the sensor mounts as for the tested blocks. PMMA has a suitable Young's modulus that permits up-scaling of our experimental results to field conditions. Use of PMMA is also advantageous because it has been well-characterized material by the biomedical industry.

During this project we gradually increased the number of sensors as the system was built and tested. In earlier experiments we collected data across first 1, then 6, and then 12 channels in groups of 3-component data (N-S, E-W, and vertical). During Q3, 2014, we added the final and third acquisition card which increased the acquisition capabilities to 8 x 3-component sensors (also N-S, E-W, and vertical)

A 3-component sensor mount in a Galperin configuration (Figure 8) three identical, single-component geophones are mounted at an angle of 35.3° to the horizontal (or 54.7° to the vertical) and at 120° relative to each other. Ralston and Steeples, (2002) show that the transformation from a Galperin co-ordinate system to an XYZ (or, equivalently NEZ) system is equivalent to the following general 3D rotation transformation matrix:

$$\begin{pmatrix} X \\ Y \\ Z \end{pmatrix} = \begin{pmatrix} 0 & cos\alpha cos\beta & -cos\alpha cos\beta \\ cos\alpha & -cos\alpha sin\beta & -cos\alpha sin\beta \\ sin\alpha & sin\alpha & sin\alpha \end{pmatrix} \begin{pmatrix} u \\ v \\ w \end{pmatrix}$$

We built two differently sized Galperin-type sensor mounts and selected a second prototype version of the Galperin 3-axis sensor. The second prototype sensor support uses slightly larger (1 1/4" diameter) optically transparent cylindrical rods of PMMA. A larger diameter-material permits more space for two more threads of the seismic sensor and therefore firmer coupling. We recommend using approximately 6-inch-ounces of torque (0.04 N.m) to seat the sensors in this preferred 3-component sensor mount.

We tested different arrangements for mechanically coupling the mount to the underlying PMMA block (Figure 3) as well as coupling the between the sensor to the mount. As a standard signal we used a 40 kHz

Figure 8 Galperin-type mounts allow 3-component data at 8 stations in addition to single-component readings at 24 stations around sample.

transducer, normally used for acoustic distance-ranging in air.

The best mechanical coupling between the sensor mount and PMMA substrate block is achieved by first fine sanding of all contact surfaces followed by solvent bonding such as acetone or "Superglue". Whereas acetone may improve coupling as well as remove microscopic surface relief created by the machining process (Ogilvie et al., 2010), we prefer "Superglue" because it is less toxic and readily available. Mounts that are bonded to the sample with "Superglue" can be easily pried off their base, sanded and reused in other experiments without any noticeable reduction in sensor coupling.

Water and grease can also be used coupling agents which provide a weak bond between the mount and the PMMA but we found that best increase in signal strength occurred when light pressure was applied between the pieces even under dry conditions.

We also tested using two circular depressions acted as receiving sites for the sensor mounts, each with a different fitting tolerance: 0.001", 0.01" in the second. These would serve to reduce amplitude of the surface waves but are more complicated to machine than direct bonding.

Direct insertion of the sensor into the large PMMA test block was considered but deemed as too complicated because the acoustic contrast between the walls of the sensor and the PMMA could produce unnecessary reflections in the data. Future work would be needed to evaluate completely the usefulness of direct insertion. While conducting pulse signal tests with breaking pencil leads (ASTM standard) we were not able to detect significant contributions to noise in the data caused by internal resonance

Uni-axial (first stage) and Bi-axial Hydraulic Press

Figure 9 Student worker completes assembly of first 50-ton (maximum force) uni-axial press

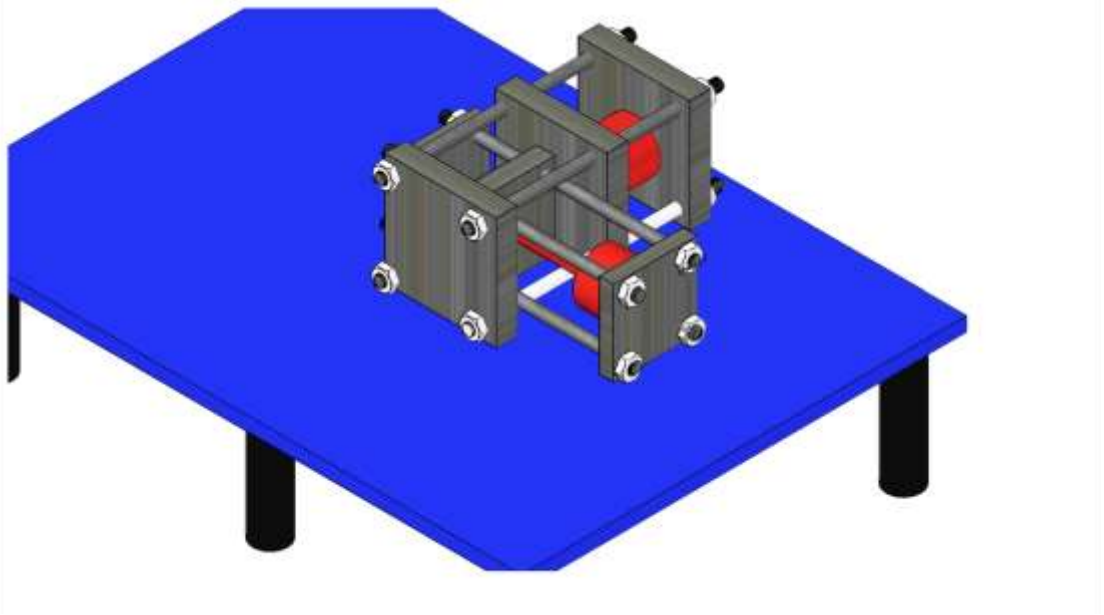

Figure 10 The biaxial press generates a stable nominal pressure of 500 psi – 1000 psi along two horizontal axes; provided by two 50-ton ram and cylinders (red). Six anti-vibration posts (black cylinder) help reduce low-frequency background noise.

In parallel with the development of the seismic acquisition system, we completed construction and installation of the hydraulic press is stages. First, we build and tested a uni-axial hydraulic press prototype (Figure 9) and finally we completed a bi-axial hydraulic press (Figure 10). In order to approach homogeneous stress field conditions, as close as possible, we take care to use steel of high flexure strength so that the arch height during bending is minimum and that the platen remains as flat as possible against the sample so as to prevent unwanted deviations complications in the stress field. In the uniaxial press we use three platens (16" x 16" x 3") made from AS-4140 chromium-molybdenum alloy steel, heat treated and

quenched to achieve a tensile strength of 100,000 psi. The three platens are connected with high-strength steel shafts (1 -1/2“diameter).

We completed construction and installation of the orthogonal-biaxial press by adding another set of smaller platens (12” x 12” x 2”) platens and a second ram and cylinder. When needed we also place appropriately-sized PMMA loading blocks between the platens the experimental block. The bi-axial press uses two 50-ton (force) ram and cylinders at right angles to each other. In both the 'N-S' and 'E-W' direction the presses have the capacity to impose a directed pressure of 1000 psi (considering safety factor of 2). The cylinders can achieve a safe, working stress of 500 – 1000 psi over sustained work periods over several days. Manual pumps were chosen so as to minimize experimental noise. Many geomechanical laboratories employ electrically powered hydraulic presses but we excluded these types because of their more elevated cost and the additional noise they could potentially contribute to the experiment.

Through testing we found that both sample PMMA blocks and any additional loading blocks placed between the experimental block and the steel platens had to be milled to an adequate tolerance. In sample #5 (from April’s 2014 report) although both horizontal presses were active at the same time we did not achieve a horizontal crack as expected and a near-vertical crack was generated. We attributed the cause to poor mechanical coupling between the sample and the platens or loading blocks because their faces did not touch evenly throughout. As a result, from May 2014 onward, we had both loading and sample blocks milled so that each opposed set of faces were parallel to each other with a tolerance of .005” and this issue was not observed again.

Safety Cage around Biaxial Press

In order to protect the user from possible release of high-pressure water or PMMA fragments we isolated the computer and controller-pump by construction a wooden cage around the instrumentation.

Normally the pump controller is operated at low flow rates (< 40 microliters/minute) so that the quick pressure drop which occurs when the crack reaches the surface of the acrylic block quickly (< ~5 s) lowers the pressure to safe levels (50 psi).

Figure 11. Safety Cage around Biaxial press. Three large (16” x 16” x 3”) steel platens are oriented in a ‘N-S’ direction while three smaller (12” x 12” x 2”) steel platens are oriented at right angles (‘E-W’ direction). Each cylinder is capable of exerting 50 tons of force on to a 4”-diameter ram. Blue wall of Plexiglas and mesh protect user and equipment for hydraulic line failures. A Perspex and laminated plywood cage around the sample catches sugary fluid in a plastic pan, protects the adjoining electronic equipment from spillage.

Despite potentially dangerous conditions under high fluid pressures, Perspex panels successfully protect the viewer and camera from possible flying plastic fragments and water. In order to prevent possible breaking hydraulic hoses from and damaging equipment we separate the high-pressure press from the work area, with mesh and Plexiglas. As an added precaution, and because of the thickness of the steel platens we expect that any Plexiglas shards possibly ejected during an experiment would not endanger laboratory workers**.**

Workbench, Baseplates, and Vibration-isolation Supports

Although our seismic signals are expected in the ultrasound range during fracturing experiments we can reduce the background level of intrinsic environmental noise (building, air-conditioning, pumping) in the 10-50 Hz range through the use of a passive (low maintenance) pneumatic vibration-isolation supports

Figure 12. (Left) Workbench with square (12" x 12") leg plates is centered, with use of a crane, over six vibration-isolation supports (Jie Shen, graduate students helps with the crane). (Above, right) Cylindrical vibration-isolation support is ~ 23 inches (600 mm) high. (Thor Labs – Model PTH 602)

under the work table (Figure 12).

High-pressure syringe pump

Figure 11 Syringe pump and controller injects water into sealed sample well. Teledyne ISCO 100 DM syringe pump and controller capable of pulseless pressures at 10 - 10,000 psi and ultra-low flow rates of 0.00001 – 30 ml/m

The loads should not exceed 3000 lb. as we employ a factor of safety ~>2. Platens from the two presses, rams, cylinders and pumps weigh ~ 1500 lb. Six heavy-duty passive vibration-isolation supports and raise the work surface to a comfortable working height of 39 ". A hydraulic rolling crane positions the platens

whose combined weight will be ~1100 pounds. The work tables attach rigidly to 12" x 12" x ½" steel plates. These plates are required in order to distribute weight evenly to each vibration-isolation support. The work tables (each 36"x48") are also rated to support a combined weight of 6,000 lb.

Poly (methyl methacrylate) (PMMA) Sample Preparation Procedures

Machining well features into acrylic blocks (PMMA) during Q1 of 2014

We also experimented with different types of pre-cracks. Pre-cracks are equivalent to field perforations. In order to allow the cracks to develop at relatively low fluid pressures, we pre-weaken the walls of the well by engraving narrow pre-crack indentations. Otherwise, tensile strength can range from 7,000-11,000 psi (McMaster-Carr, 2014, Daikon Industries, 2014; www.mcmaster-carr.com).

In the case of cases when we used the uniaxial press, "pre-cracks" or indentations were made with their

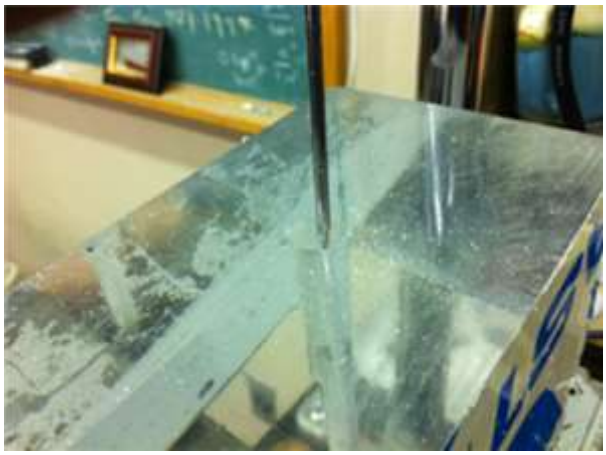

Figure 12. Underside of acrylic block shows ~ 0.5" diameter access hole that we used initially to facilitate engraving. In this case we access the well from below. An engraving tool is about to enter the bore to inscribe an initial cut in the walls of the well. Additional tests show that suitable, pre-crack indentations are best achieved from the top of the acrylic block, through a single borehole of smaller diameter (11/32").

major axis along the length of the model borehole (Figure 12) —their dimensions were approximately ~ 1 mm wide and ~8-15 mm high (along borehole) and 2-3 mm deep (radial direction). Two indentations were located on symmetrically opposite faces of the well at similar depths from the top of the acrylic block face. These pre-cracks permitted vertical fracture wings to develop. In order to create vertical pre-cracks along the length of the well wall we used an engraving tool s to create an initial groove to guide additional engraving. For this purpose we used a 4.5"-long, 1/8"-diameter profiler a 15^{o}-sloping triangular tip 0.005" across. The sloping head suitably engages the walls at middle depths in the borehole. In a second stage we complete the indentation by hand-inscribing a deeper rut with a narrow, 3-tooth-tipped saw (< 1/8" diameter) that has a beveled and sharpened tip.

For experiments conducted using the biaxial press, pre-cracks were horizontally cut around the wall of the model well (Figure 14). The model well is also vertical, approximately 11/32"in diameter and approximately 3" deep in the PMMA blocks that that are 2" thick x 6" x 6" and approximately 2" in the blocks that are 4"x 6" x 6" thick.

By June, 2014 we achieved the simplest, drilling procedure. The narrow borehole for (Figure 13) feeding the fracking fluid was removed. We now recommend supplying the fracking fluid from a single large-diameter borehole that spans down to half each sample height (Figures 14, 15)

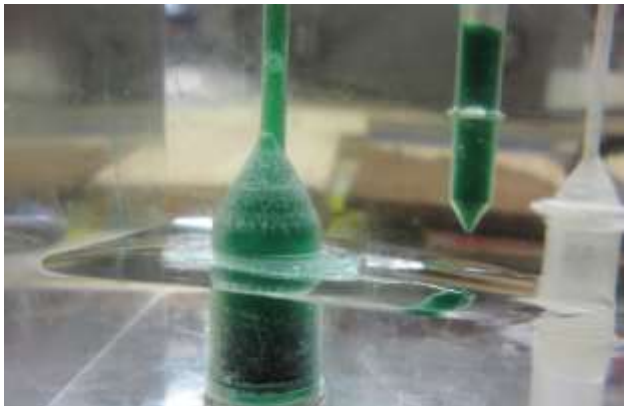

Figure 13. (LEFT) PMMA sample block shows one strategy for generating horizontal pre-cracks around the periphery of the model well wall. Fracking fluid is colored green (1 cps). On the lower side of the block, a large-diameter borehole (~3/4") permits is used to lower the tool that notches out the pre-crack. From the upper side of the block we see a narrower borehole which matches 1/8" NPT valve fitting from the high-pressure low-flow displacement pump. The transition between the two boreholes occurs across the funnel-shaped region.

In the background of this sample we also see a single narrower borehole which is an example of a narrow well with a pre-crack notched at middle depth.

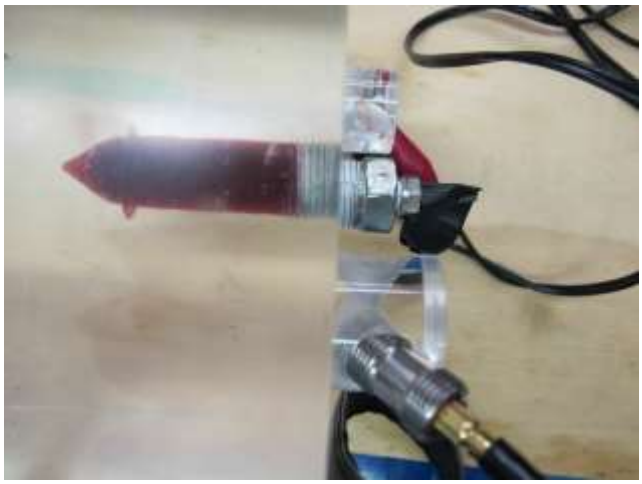

Figure 14. (LEFT) Side view of PMMA sample block shows the recommended and preferred (June, 2014) well geometry devised. On the top side of the block (right side) a large-diameter borehole (~3/4") permits access to the tool that notches out the pre-crack. Fracking fluid is fed through the 1/8" NPT valve fitting from the high-pressure low-flow displacement pump.

A widening of the borehole (filled with colored fracking sugar solution, ~ 1000 cps) occurs toward the middle of the PMMA block, about 2" from the top. This red ring, is the pre-crack, notched mechanically and etched with acetone for a minute.

PMMA Annealing procedure

Pre-existing stress concentrations in the PMMA create the chance of interfering with the crack propagation during the experiments. In order to remove thermal stresses generated in our PMMA blocks either during casting, extrusion, or during milling in our lab, we thermally annealed our PMMA blocks for ~33-36 hours at 75-80 °C, followed by cooling over 24 hours (process was developed in Q1, 2014). Blocks were cooled to room temperature at a rate no faster than 15°C/hour.

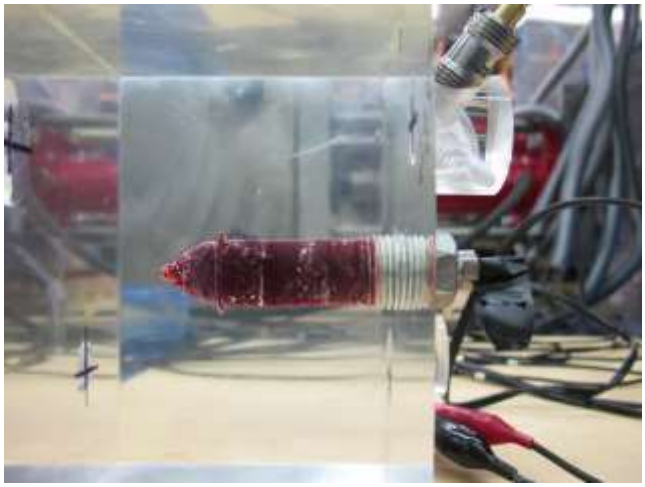

Figure 15. A single, ¾"-diameter borehole provides access to the pre-crack zone (image of sample #8)

Cross-polarizing film chamber--Interference Figures to Verify Annealing Effectiveness (Q3, 2014)

Both the effects of thermal annealing can be examined qualitatively by examining the sample blocks between cross-polarizing film before and after the treatment. In this manner we confirmed that a ~ 1mm translucent zone (caused by drilling) around the periphery of the model wells was removed (Figure 16). However, we continue to verify that after thorough thermal annealing, the residual interference figures that appear under cross-polarized light indicated a residual anisotropy that may be considered during data interpretation.

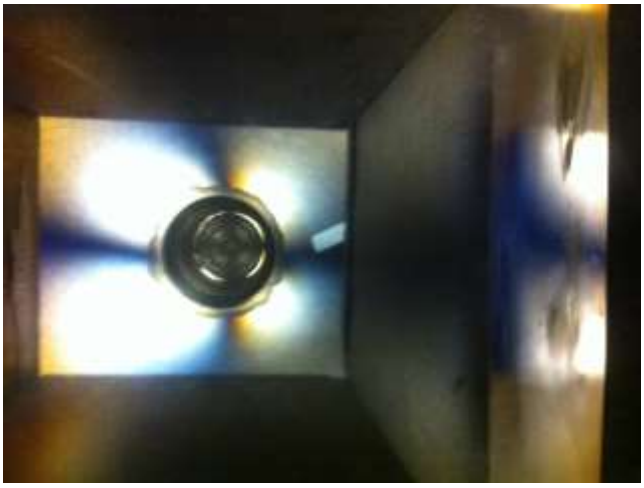

Figure 16. (LEFT) PMMA sample block viewed from top face between two sheets of cross-polarizing plastic film. Alternating lighter and darker bands around the central borehole indicate residual anisotropy. Reflections from the walls of the light box create are visible on the right the edges of the image. Prior to installation of a valve and pipe fittings and after thermal annealing, each sample block continues to displays this biaxial interference cross.

Cross-polarizing-film chamber for Viewing Crack Growth

Crack growth during experiment changes the stress field in the PMMA sample that is readily visible as a color change within a cross-polarizing film chamber. For this reason, the biaxial press cavity which confines the sample during hydraulic fracturing was also fitted with two sheets of polarizing plastic film: one beneath the sample and one above. The sample was illuminated from below by a diffuse fluorescent light source.

Within the cross-polarizing film chamber, light crosses the sample after passing through an initial polarizing plastic film. Light leaves the sample, passing through a second sheet of polarizing film oriented at right angles to the first. The entire sample is blocked from external light sources with black fabric except for a small circular aperture above the sample for photography and visual inspection (Figure 17)

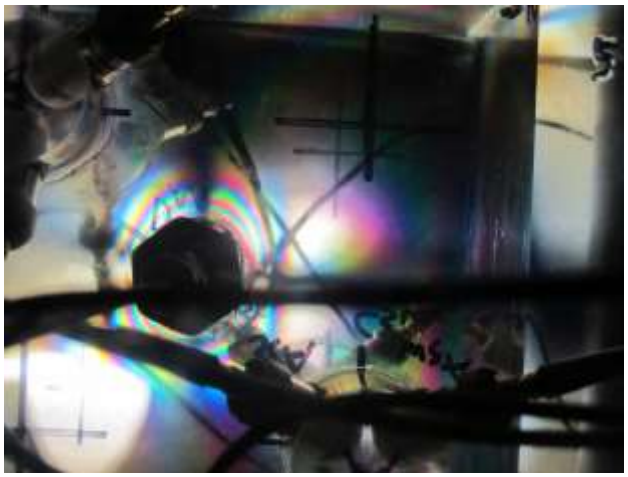

Figure 17. (LEFT) PMMA sample block viewed from top face between cross polarizing films during running of an experiment Alternating colored bands around the central borehole indicate stress created while inserting and tightening the NPT-standard fluid valve. Dark lines consist of a high-pressure fluid line and cables to the3-compnent sensor mounts (top left and bottom right of image).

As an example of additional stresses induced during sample preparation, insertion of the screwed-high-pressure pipe fitting (NPT) into the PMMA block creates a ringed pattern of colors around the shallow portion of the borehole (Figure 18). Despite these residual stresses crack growth maintains a planar and circular geometry centered around the model well.

Fracking Fluid Preparation Procedures

We first developed sugar-water-based solutions of up to ~1,000 centipoise viscosity to act as fracturing fluids. The first two hydraulic fracturing experiments conducted used tap water (~1 cps). PMMA block samples #5 (April Report) and #6 (May Report) used a simple colored water solution at 1 cps. In sample # 7 (May report) we used a ~ 1000 cps solution, 78 % by weight of sucrose dissolved in water (Figure 21). Initial dissolution of sugar requires vigorous agitation and repeated heating in a microwave oven.

In the first year, we tested (unsuccessfully) development of a dextrose (glucose) solution at 15,000 cps. A

Figure 18. (LEFT) PMMA sample block (#12-110514) viewed from side face between two sheets of cross-polarizing plastic film. Residual stresses after thermal annealing show as colored bands.

glucose solution was prepared using 453.6 grams of glucose and 45.2 ml of water. This solution had a calculated viscosity of 15.6 Pa-s, or 15,600 cps. This solution was dyed using Kool-Aid. Kool-Aid contains citric acid, salt, calcium phosphate, colors and flavors, and vitamin C. However we could not keep the glucose solution from crystallizing within a few hours.

During June, 2014 we finalized our preferred procedure for creating the most viscous sugar-water solutions.

Figure 19. Warming sugar solution at 78 % concentration by weight provides a 1000 cps fracking fluid. Addition of colorant (brand name strawberry Kool-Aid) permits better visualization of cracks. Colorant may affect viscosity although to a degree our results have not yet noticed.

We make sure to prefill the model well with the same fracking fluid and remove any residual pockets of air.

By adding glucose to a sucrose solution we were able to extend viscosity to that of thick taffy without initiating crystallization. We now recommend a sucrose-to -glucose weight ratio of 80.95:19.05. That is, 425 g sucrose, 100 g glucose, 100 ml water. Without the glucose we could not keep sucrose alone in solution for more than a few minutes. Sugar at about 78% by weight is calculated to produce 1000 cps. We estimate the current solution has a viscosity ~100,000 cps. During Q3, 2014, and thanks to a new Brookfield Digital Viscometer (1% accuracy and 2 % repeatability), we confirmed an estimated viscosity of 96,000 cps for this solution. This solution was dyed using Kool-Aid. Kool-Aid contains citric acid, salt, calcium phosphate, colors and flavors, and vitamin C.

Highly viscous solutions have to be prepared for low-P suction into the pump chamber. We first need to reduce the viscosity of these solutions by heating (Note, that the fracturing experiments are conducted after the fluids in the chamber equilibrate to room temperature). However, during the initial warming process excessive evaporation at the surface of the fracture fluid (Figure 19) can also lead to dextrose exsolving and crystallizing. In order to reduce evaporation, we also experimented with heating the dextrose under low pressure vessel (1st Quarterly Report, 2014, final figure).

Figure 20. A heated pressure vessel at 60 psi will assist loading of high-pressure fluids. The stainless steel tubing has an inner diameter of 0.69" and an outer diameter of .125"

Post-Acquisition software R-based software for Managing and Analyzing Microseismic Data

In order to develop the seismic catalog we created an R-based software package to RHFM (R-based Hydraulic Fracture Mapping Tools) Version 1.1 is able to demultiplex binary data streams from either one, two or three acquisition cards (up to 24 possible acquisition channels). Data can be then cross-correlated for timing re-alignments, length-trimming and finally rotated into a common N-S, E-W and vertical (UP down) right-handed coordinate system. Through RHFM package we currently are able to perform principal component analysis, so as to back-project micro-event source directions.

A tarred RHFM package is included with this final report. R Documentation and full program examples are embedded in the help files in R-markup style language as well as in a pdf-formatted file: "RHFM(software)_portfolio.pdf".

2 (B) Experimental design of the laboratory at a national conference on hydraulic fracturing.

National Presentations of Experimental Design in 2013

On December, 10, 2013 we co-convened and chaired special session at the San Francisco American Geophysical Union fall meeting, on hydraulic fracturing that brought presenters from both industry and academia to exchange technological advancements and geomechanical modeling approaches in a session (NS23C) entitled "Advances in Near Surface Fracture Studies".

Conference oral presentations in 2014

-Major effort and time was spent in preparing data and results for presentation of key results at Annual Meeting of the American Geophysical Union, entitled:

"Effects of fracturing fluid viscosity on Wave Emissions during Hydraulic fracturing: An Experimental Study", NG33B- Tuesday, December 16, 201408:45 AM - 09:00 AM Marriott Marquis Salon 8

- PowerPoint presentation is made available: "Lorenzo_NG33B-3831_AGUFM2014.pdf"

Papers published in 2014

Taleghani, A.D., Gonzalez, M., Puyang, P., **Lorenzo**, J.M., (2014) Post-treatment assessment of induced fracture network Hydraulic Fracturing Journal. V1/3, 24-33

3 Experimental descriptions and interpretations of single-component seismic data sets derived under non-dimensional experimental conditions.

Non-dimensional analysis Detournay (2004) predicts that low flow rates (microliters per minute)., when coupled with viscous fluids in the lab are analogous to field conditions. High viscosity fluids allows to experiment under conditions closer to those found in many field cases-- in the viscous-dominated regime. In order to evaluate the feasibility of our experimental setups, in a first stage (Q1, 2014) we conducted 2 hydraulic fracture experiments under a fluid rate of 40-100 μl/minute and 1 centipoise viscosity. Samples failed when internal pump pressures reach ~ 2000 psi (Figures 21, 22, 23).

Fracture experiments under uniaxial confining stress (Q1, 2014)

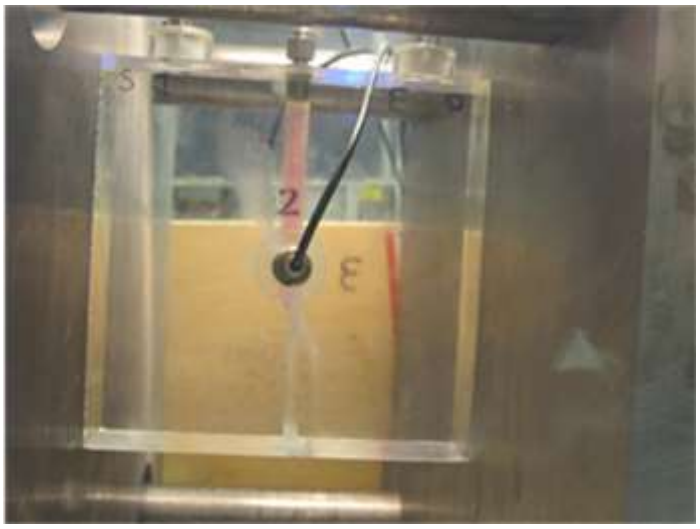

Figure 22. In this side view, a sample (6"x6") lies confined between two steel platens (16 "x16") at ~ 100 psi. Horizontally directed pressure is only directed with the left-to-right orientation. Four sensors are used to test microseismic event acquisition. Water (pink) completely fills well. A single-wing crack developed in the plane of the observation. A detail of the crack is seen in Figure 23.

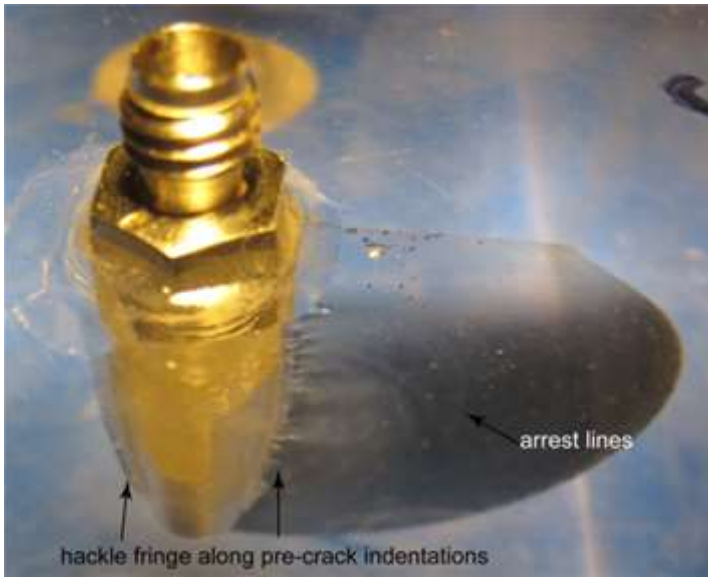

Figure 23 Crack propagation in the adjacent sample initiated at middle depths in the well and moved outwardly in the direction of the maximum horizontal stress direction. We interpret that a narrow fringe of hackles is created parallel to a curvilinear indentation that was engraved vertically along the walls of the well before the hydraulic fracturing treatment began. A penny-shaped crack that intersects the surface to the right of the high-pressure fitting at the well appears as a grey ellipse. Probably the drop of fluid pressure when the crack intersected the top surface was responsible for halting crack propagation from the opposite side of the well.

Video record of fracture experiments (Q1, 2014)

Over the course of the project we concluded that we were able to record crack propagation adequately while using a 30 frame-per-second video camera. For the uni-axial experiments conducted with low-viscosity fracturing fluid (Figures 21, 22, 23) we estimated from examination of the oscilloscope waveforms that crack propagation speeds were of the order of 102m/s. At this speeds a 60,000 fps camera (rental) would be needed. Later, as we developed biaxial experiments and increased the viscosity of the fracturing fluid to ~100,000cps, crack propagation speeds were at least 3 orders of magnitude slower, and the required camera shot at only 30 fps (Figure 24 A & B).

Early in the work, we located a Cordin 550 high speed imaging system (up to 1.5 million frames per second) at Southern University of Baton Rouge in the Mechanical Engineering Department. This camera is limited to 24 frames.

Video recording of crack propagation at 30 frames per second (Q4, 2014)

At a rate of 30 frames per second, at a resolution of 640x480 pixels, a 4 GB file takes in approximately 50 minutes of the experiment. File sizes are limited to the size of the onboard Smart Card (~ 4 GB). Video from our experiments have been made available with quarterly reports. Because of their large size, we do not include those files with this report. Additional copies of these videos can also be made available as required.

Figure 24 A and B show one images before (A-left) and after (B-right) the clear appearance of fracture propagation. These two images (640x480 pixels) are taken from recorded videos using a Canon G10. Top edge of images is oriented E-W. The top of the image points toward N. The dashed line shows approximate location of half of the presumed cracking front. The circular boundary between the fracture-fluid filled crack and the surrounding PMMA is more obvious and left uninterpreted.

4. An appropriate number of multi-component sensor clusters will provide the necessary data to generate tables of event location during the course of the experiments.

Seismic catalogs for the principal experiments (folders: "SeismicCatalog_100114", "SeismicCatalog_110514", "SeismicCatalog_120914") are available per requirement.

Seismic Catalogs (Q 3-4, 2014)

We initiated our seismic catalog of experiments (hyperlinked scans of representative microseismic events) for the most meaningful experiments. The purpose of the catalogs is to classify potential events for future analyses. Each catalog is presented in an Excel spreadsheet which also includes hyperlinks to some images showing plots of the seismic traces. Original binary data is of the order of ~ 10 TB and can be requested with reference to the catalogs included.

Events are classified into short-lived ("spike") lasting a few milliseconds, and longer arrivals that last as long as 200 ms. Of interest too, are any large-amplitude events whose digital counts exceed a threshold value of 90-100. Absolute values of 32,768 have indicated saturation the recording differential amplifier with extremely high-amplitude events. A noise level of -60dB below this maximum is characteristic for all experimental data. "Card" columns (in Excel spreadsheet headings) note which digital cards held these events and the start and end times columns indicate approximately where the event appears in the digital file.

Experiment Descriptions under Bi-axial Stress Conditions

Experiment (Sample #5):

Hydraulic joint was generated in sample (#5- 050814), at 3260 psi, at a flow rate of 40 μl/min. This block had dimensions of 4" x 6" x 6". Bidirectional horizontal stresses were between 200-280 psi on four of the six faces. The fracturing solution had a viscosity of 1 cps at RTP, and was stained with a green food colorant. On the free faces (unconfined) two sensors were symmetrically installed to the top and bottom of the sample, half way along each of the diagonals on the top and bottom surfaces. The well was pre-etched with a 3 mm-deep skirt, cut around the whole well at one depth.

Based on the complete duration of all the seismic signals, and if we assume they span the start of cracking at the well and end of cracking after the fluid pressure drops when the crack intersects the sample wall, then the rate of crack propagation was ~ 380 m/s. Material property sheets show that compressional wave velocities in generic PMMA are an order of magnitude larger (2750 m/s).

Unexpectedly, the resultant crack propagated in a nearly 'N-S' direction along a near-vertical path, inclined ~ 60 degrees to the horizontal). The N-S direction was along the major axis of one of the presses. Because the horizontal stresses were equal in the 'N-S' and 'E-W' directions and the vertical faces were free of stress, we expected the crack to propagate in a near-horizontal plane, equally in all directions until intersecting the edges of the block. However, the orientation of the crack indicates that the major compressional direction was oriented in a more northerly direction and that the minimum principal stress direction was inclined to the horizontal striking in an easterly direction.

Experiments (Q2, 2014)

Hydraulic joint were generated in two samples (#6- 052314; Figure 25; #7-060514; Figure 26) using two different fluid viscosities and flow rates. Both sample blocks had similar dimensions of 4" x 6" x 6". We applied bidirectional horizontal stresses of ~830 psi on four of the six faces in both a N-S and E-W direction. The other two vertical faces (top and bottom) were open to room conditions.

For sample #6, the fracturing fluid solution had a viscosity of 1 cps at RTP, and was stained with a green food colorant. On the free faces (unconfined) two sensors were symmetrically installed to the top and bottom of the sample, half way along each of the diagonals on the top and bottom surfaces. The well was pre-etched with a 6-8 mm-deep skirt, cut around the whole well at one depth. In order to facilitate the initiation of cracking we introduced acetone into the pre-crack for 1 minute

Figure 25. (LEFT) Close-up of sample #6 (052314) A large elliptical crack extends to the edges of the block.

For the case of sample #6, we did not collect seismic data. Based on the behavior of sample #5 which was

Figure 26. Sample #7 Horizontal crack viewed obliquely from the lower face of the PMMA block. Two sensors were placed symmetrically about the seal on the underneath face of the PMMA block. Note the curved crack as a result of the fracture bowing toward the free surface.

Figure 27. Sample #7 Horizontal crack viewed obliquely from above. The crack surface bows downward. Three seismic sensors on the upper free surface (not seen here). Note up to three arrest lines surrounding and parallel to the original notched pre-crack (darker red). Secondary linear radial cracks are prevalent but most apparent on the rightmost corner.

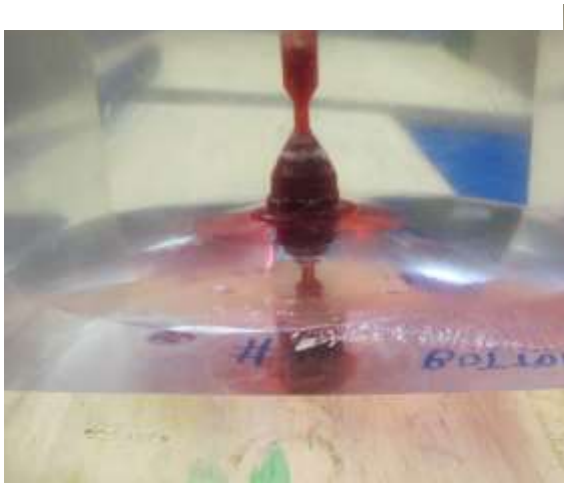

similarly notched we expected fluid pressure to initiate at up to 3260 psi. Actual fluid pressure at crack initiation was improved—lower, at 2400 psi.

For the case of sample #7, we collected seismic data for approximately two minutes at a sample rate of 4MS/s on 5 seismic channels. A sixth channel was left to acquire pressure signals from the pump, synchronized to the seismic acquisition. In contrast to last month's tests the cracks developed in the horizontal plane as expected. Proper milling of PMMA blocks, thermal annealing and chemical etching to weaken the pre-crack may have been important contributing factors.

Noticeably, sample #7 (May, 2014), displayed up to 10 large seismic events which spanned at least 30 seconds and the crack propagation rate decreased markedly with respect to April's experiment (#5). The large microseismic events saturate the digitizer, at the lowest gain. Given the dimensions of the block, and assuming a radially symmetric propagation distance of 3 inches, the average speed of the propagation is estimated to be ~0.154 m /s. By comparison to April's estimated propagation speeds (~380 m/s) we appear to have a reduction by four orders of magnitude. We think that the reduced speed is the result of the increase by 3 orders of magnitude in viscosity for the fracking fluid, over April's experiment.

Multiple internal reflecting events were not a major concern in the examined microseismic data. We detected only ~29 visible events during over a 50 second period. The slower crack propagation speed allowed easier identification of events.

During June (2014), we ran an experiment of sample #8 (Figure 29) with a red, sucrose solution (est. ~1000 cps). Data were collected for the first time in 3 D component seismic stations with 3 accelerometer-sensors arranged in a Galperin formation—that as if along the tilted edges of a cube corner. We used four stations, two on the top surface and one on the bottom surface for a total of 12 channels (Figure 29). Until now we

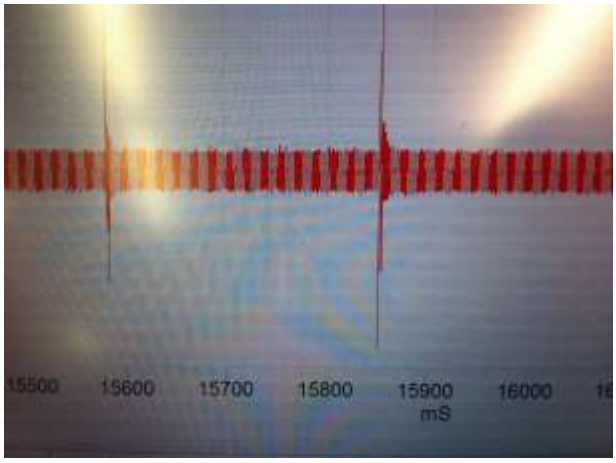

Figure 28. For sample #7 two distinct microseismic events on channel 0 (out of 5 channels). Their separation in time is approximately, 0.25 s

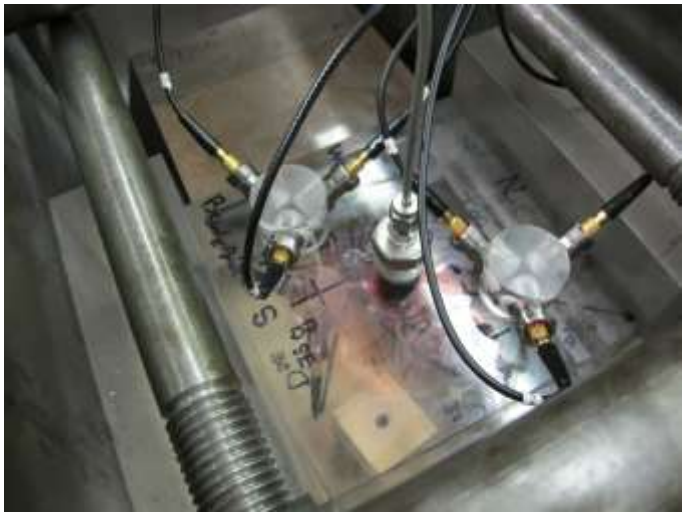

Figure 29 In the latest sensor layout we use groups of 3-component accelerometers—two stations on the top surface and two stations on the bottom of the PMMA block.

had only used 4 and 6 sensors. As for sample #7 (May, 2014) we raised the biaxial pressure to ~ 700 psi along both horizontal directions (N-S & E-W). Data acquisition rates were 120 MB/s continuously for at least 5 minutes.

For sample #8, (Figures 29, 30) and at a flow rate of .01 ml/min breakdown pressure occurred when the fracking fluid reached 1860 psi. At that point, a well-defined circular crack front grew out from the pre-crack area. Flow rates were raised to 1 ml/min in order to continue crack propagation which we observed

Figure 30 In addition to the pre-crack notch that rings the model well, four crack arrest fronts (indicated with short shite lines) are visible. In the front plane, a line of red droplets mark where the horizontal crack intersects a vertical edge of the PMMA block. The concentric crack fronts, bow slightly toward the edges.

to take place during three additional phases of crack growth, until the crack breached one edge of the block. For each phase of crack growth we are able to identify only a few microseismic events.

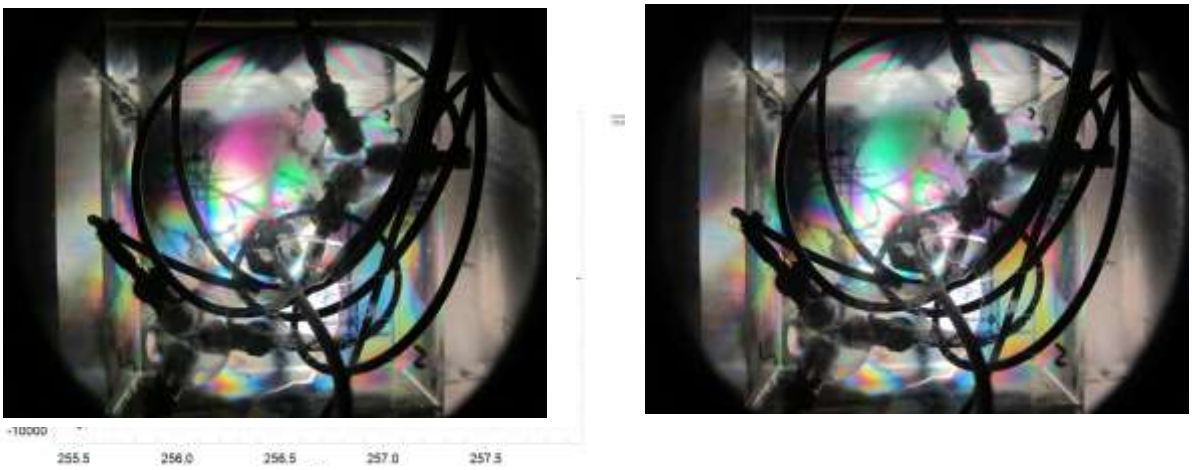

Figure 31. Changes are noticeable in the interference colors of the stress field before (LEFT) and after the first large pressure drop

Experiment (Sample #9- 080114) (Q3, 2014)

We generated a hydraulic joint, using water at a 4 microliter/min flow rate. Non-dimensional analysis showed that the sample broke in the toughness-dominated regime. The flow rate was the lowest in all

samples containing water (low viscosity) as the fluid. As expected, the lower flow rate reduced the

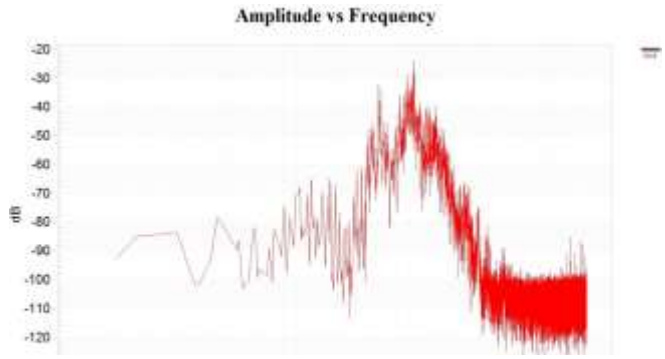

Figure 32 For low-viscosity fracking fluid, dominant frequency content of microseismic events (Sample #9) lies between 10^3 and 10^4 Hz.

amplitude of the resultant microseismic events and distributed them over a longer period of time.

In sample #9, fluid pressure at crack initiation was higher than expected (2700 psi). For comparison, the previous test (Sample #8) we initiated the crack propagation at ~1834 psi.

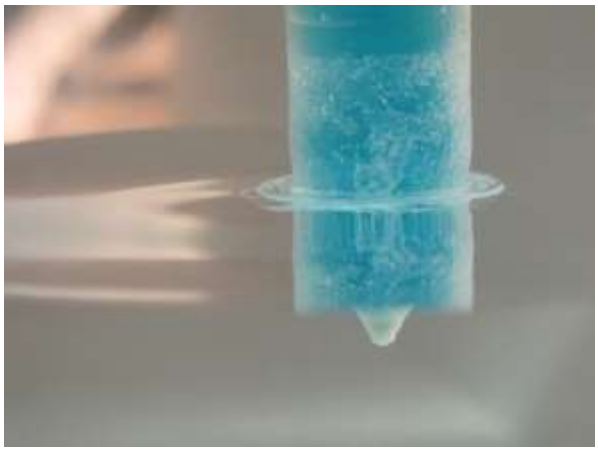

Figure 33. Sample #9 Horizontal crack viewed obliquely from above the PMMA block. The blue-green region to the right marks the vertical model borehole (3/4" diameter). Although the crack surface is relatively smooth, and the pre-crack area stands out adjadent to the borehole, concentric some irregularities exist over parts of the horizontal crack.

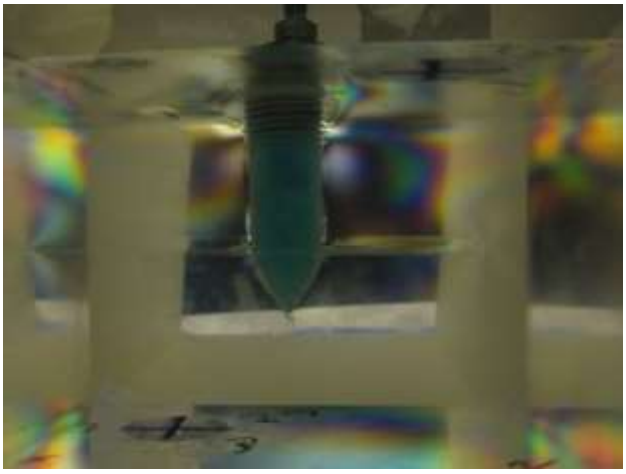

Figure 34. Sample #9 Horizontal crack viewed obliquely from below the PMMA block through cross-polarization filters. Crack is located where the borehole changes from cylindrical to conical shape. Color bands indicate that residual stress above the borehole possibly from the tightly screwed valve. No color bands are visible below the crack. White horizontal and vertical bands are reflections from the walls of the white viewing chamber.

Experiment (Sample #10- 081914) (Q3, 2014)

We generated a hydraulic joint (Sample #10- 081914), using highly-viscous fluid (92,280 cps+/-1%). at 1 microliter/min flow rate (Figure 32) under 1000 psi of confining horizontal pressure. Non-dimensional analysis shows that the sample broke in the viscous-dominated regime. The sample broke unexpectedly at 800 psi fluid pressure across a hairline crack that developed during fast uni-directional clamping in the biaxial press. Similar surface features are visible as in case of 1000 cps (sample #8, second Quarterly report, 2014). We are currently repeating this experiment taking care to raise the confining pressure from both horizontal directions simultaneously. If sample #8 results are a guide, we expect that the frequency content should range in 10^3-10^4 Hz.

Figure 35. Birefringence bands after the horizontal crack propagation are dominated by the orange color of the fracture fluid located just below the central pipe fitting.

Loading of the pump with high-viscous fluid at low negative pressures (no less than –14 psi) requires careful treatment. First, we use 1/8" tubing of the widest internal diameter. The tubing is no more than 4" in length and must remain heated above 150 degrees Fahrenheit externally during the transfer of fluid into the pump chamber. Second, the fluid must be at around 210 degrees Fahrenheit at room temperature and pressure.

Experiment (Sample #11- 100114) (Q3, 2014)

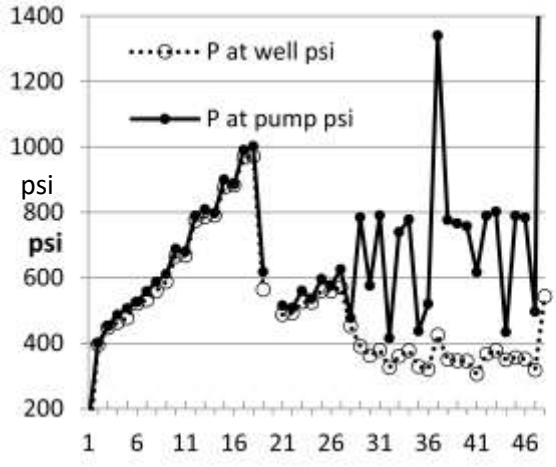

Figure 36. Pressure variations at the pump and well head, (~6 feet separation) both increase until the first interpreted fracture occurs (mark 16 along horizontal axis).

Flow rates are held steady at 4 microliters/min. except near well "mark" 36 and "mark" 48 -- at 400 and 100 microliters/min. respectively.

Well pressure measurements were taken manually every ~ 6 minutes manually. By Q4, 2014 we had automated digital recording of well pressure.

Approximately 280 GB of microseismic data were collected for this experiment. Near-well pressure values were recorded with the seismic data on a spare data channel.

Fluid pressure at the pump was recorded manually approximately every 6 minutes and once the fracturing commenced well-pressure values were recorded at the same rates as the seismic data, 1 MS/s. The sample breakdown pressure was ~ 1000 psi. (Figures 36, 37) As expected, comparison between pressure values at the well and at the pump shows consistently greater pump pressures than at the model well, more so when pressure rates drop after the interpreted start of hydraulic fracturing. Fracturing fluid viscosity was high (~96,000 cps) and flow rates were held relatively constant at a nominal flow rate of 4 microliters per minute, although on two occasions after the start of fracturing, these rates were increased to values of 400 and 100 microliters per minute for a few minutes at a time. For our PMMA sample, our non-dimensional toughness was ~1.3 and in the viscous-dominated regime.

Experiment Data Processing (Sample #11- 100114)

Selected waveform data was rotated from a Galperin orientation into geographic coordinates (RHFM software) One example (Figure 38) shows an interpreted microseismic event generating dominantly

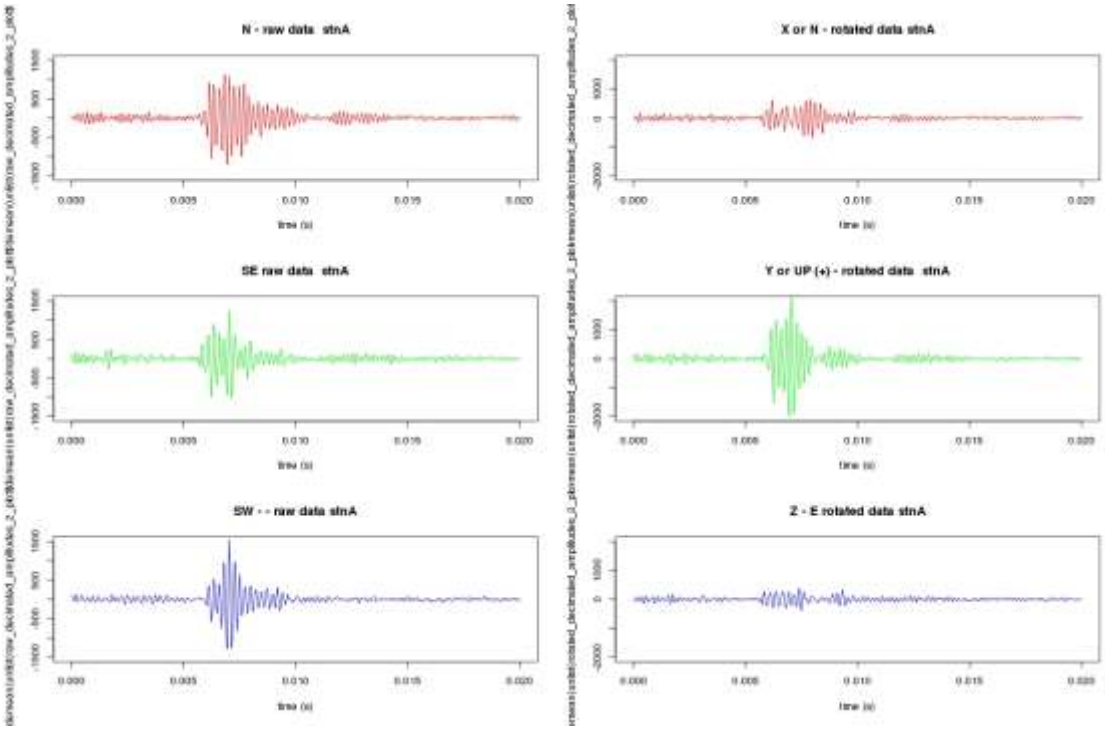

Figure 38 Selected waveform data from the NE corner of the sample block on the top face, before and after (right-hand side) rotation into the N-Z-E right-handed coordinate system.

vertical particle motion, (probably compressional body wave) followed immediately by two dampened oscillations.

Experiment # 12 (Q4 2014) 110514

Pressure Recordings (Q2, 2014)

The first of two dedicated data channels to record pressure during the experiments was incorporated into

Figure 39 Pressure sensor lies within 8 inches of model well and provides a current output source between 4 and 20 mA that is proportional to inline pressures of 0 –6000 psi. Sensor values are digitized at and synchronized to the same rate as the seismic sensors; i.e., sample rates can vary between 1 – 10 MS/s

the digital seismic system. The first data channel records the pressure sensed at the pump controller which, produces an output analog voltage of about 0.1V / 69 bars. Pressure measurements at the exit to the pump are recorded at a lower rate of 100 S/s, after a running average is performed on every 10 adjacent samples (Figure 36). We note that substantial changes in the interference colors during the experimental cracking of sample #11 (100114; Figure 36) implied that continuous video recordings in later experiments would be useful.

Two Sets of Digital, Pressure Recordings (Q4, 2014)

We later installed a second data channel to record inline pressure sensor to incorporate into our experiments to record pressure changes nearest the model borehole, just outside the sample.

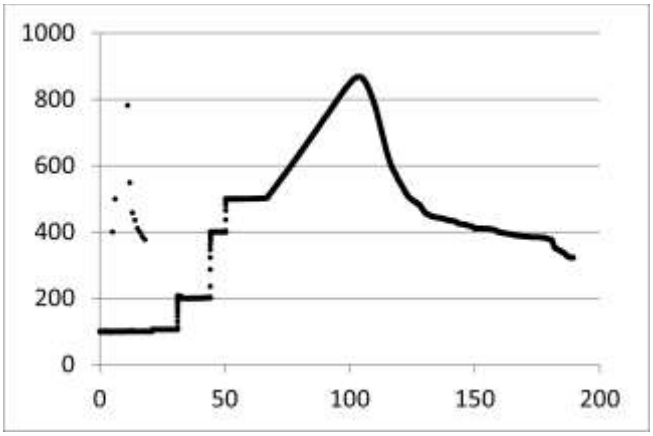

Figure 40 Digitally recoded pressure values at the syringe pump, over a > 3 hour period (~200 minutes). Sampl is first pressurized at constant pressure changes until ~ 500 psi. Thereafter flow rates are held constant at 4 microliters/minute. Pressure leading to principal initiation of crack propagation is linear while decrease in pressure measured at the pump head decays rapidly afterward.

This inline pressure sensor adjacent to the experimental sample (see 3rd Quarterly report, 2014) generates calibrated currents which are recorded in parallel to the seismic measurements at the same rate (e.g., 1 MS/s).

Experimental Repeatability (Q4, 2014)

We verified that the sample-preparation protocol and running conditions produced overall repeatable results. We ran sample (# 12), with a high viscosity fluid (~92,000 cps), at a slow flow rate of 4 microliters/minute. Horizontal pressures from a N-S and E-W direction were again 1000 psi applied to four

vertical sides of a 4" x 6" x 6" cast PMMA block. The conditions and material are scalable to viscous-dominated regime found in many field cases. Break-down pressure of the pre-cracked sample is consistently below 1000 psi. (Sample #11, 100114 1002 psi, Sample #12, 110514, 868 psi).

We note again that three-component sensor stations in a Galperin-geometry arrangement were distributed at the top and bottom of each sample maximize the angular coverage around micro-seismic events. Four stations were located on the top and another four on the base of the block.

Recordings with 8x3-component sensor stations and 2 Pressure sensors (Q 4, 2014)

A full-acquisition run with high-viscosity fluids approximately 80 minutes generates data that comprise:

- 18 x 20 GB seismic binary data files, at sustained rates of 60 MB/sec. Recording noise absolute amplitudes are usually are < 1/300 of the maximum amplitude that can be recorded accurately.
- 4 GB of color video images recorded at 30 frames per second.
- Pressure-pump readings are collected 100 S/sec while near-well-pressure readings are streamed with the seismic data at nominal rates of 1 MS/sec and 2 bytes per sample.

Figure 40. Two views of PMMA sample, prepared with 8x3 component stations above and below the model well (red, filled with high-viscosity fracture fluid).

Comparison of previous results

sample #	dates	fluid type	dynamic viscosity cps	non-dimensional toughness	viscosity error	dynamic viscosity MPa s	flow rate ul/min
5	50814	water	1	13	0.1	0.001	40
7	60514	sucrose	1000	0.80867	0.2	1	3000
8	71514	sucrose	1000	1	0.2	1	1000
11	100114	sucrose + glucose	92280	1.36	0.1	92.28	4
12	110514	sucrose + glucose	92280	1.36	0.1	92.28	4
13	120914	sucrose + glucose	92280	1.36	0.1	92.28	4

	H1 H2 psi	H1-H2 (MPa)	press H1 H2 ton force	Breaking Pressure psi	Breaking Pressure MPa	MS/s	# channels
5	500	0.34474	6	3260	22.477	1	4-Z
7	833.333	0.574567	10	730	5.0332	4	4-Z
8	833.333	0.574567	10	1830	12.6175	5	4-3C
11	1000	0.68948	12	1002	6.90859	1	4-3C
12	1000	0.68948	12	810	5.58479	1	8-3C
13	400	0.275792	5-6	1700	11.7212	1	8-3C

Table shows main characteristics of past key experiments (date and sample #) including fracking fluid flow rates, fluid composition and viscosities, as well as horizontal confining pressures (H1,H2) seismic sample rates (MS/s), seismic stations numbers and whether the seismic data were single vertical component (Z) or multi-component (3C)

5. Results of the influence of a simulated fault will on interpreted seismic mechanisms (Mode-I versus mixed-Mode) [Also see section 6]

Through multiple experiments we have developed a protocol for sample preparation and standard acquisition tools. We now collect:

- Seismic binary data files at 8 stations, each with 3-component sensor at 1 MB/s and 16-bit resolution
- Color video images recorded at 30 frames per second, with a resolution of 320 x 240 pixels
- Pressure-pump readings are collected 1000 S/s and 16-bit resolution.
- Well-pressure readings at 1 MS/s and 16-bit resolution.

Fault-block and Fracking Experiment that includes a pre-existing fracture (model fault); (# sample 13; 120914)

We prepared a sample containing a synthetic model faults glued. We will test the effect of this pre-existing crack in the otherwise homogeneous PMMA block. The high-strength epoxy cement (3960 psi trensile strength) will control whether a hydraulic fracture is able to propagate across the artificial fault. we may see an increase in the number of double-couple seismic micro-events relative to the previous cases (Table 1). At present, we cannot make a better prediction of the results because the toughness of the epoxy cement and its shear strength is not publicly available.

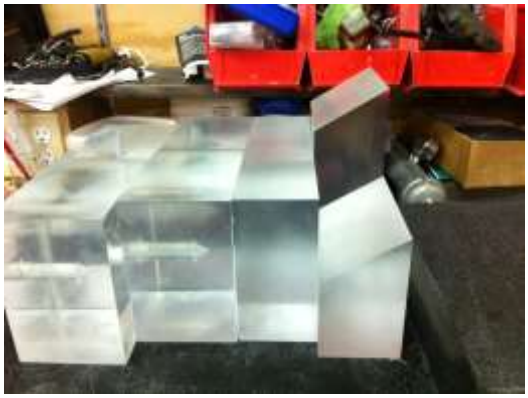

Figure 41 PMMA blocks during preparation for testing. The blocks on the far right (inclined tops) will server to emulate the effects of a hydraulic fracture interacting with a pre-existing model fault.

(* See Table 1., Dec. 2014 report for more complete characteristics of past key experiments --date and sample #, including fracking fluid flow rates, fluid composition and viscosities, as well as horizontal confining pressures (H1,H2) seismic sample rates (MS/s), seismic stations numbers and whether the seismic data were single vertical component (Z) or multi-component (3C))

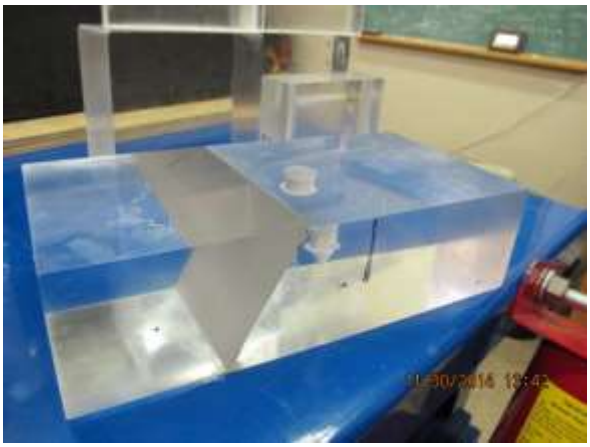

Figure 42. Left image above shows a 45-degree dipping pre-cut plane, now glued with a commonly-available high-strength epoxy cement (right-hand image)

Sample # 13 -Experiment 120914

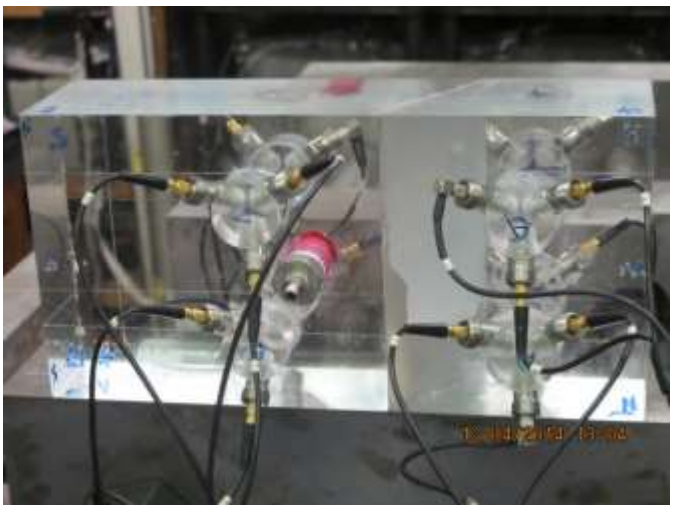

Figure 43 Sample shows four 3-C sensor mounts on the top surface of two glued PMMA blocks; one on either side of the model fault. Two other 3-C mounts exist on the bottom surface; also placed on either side of the model fault.

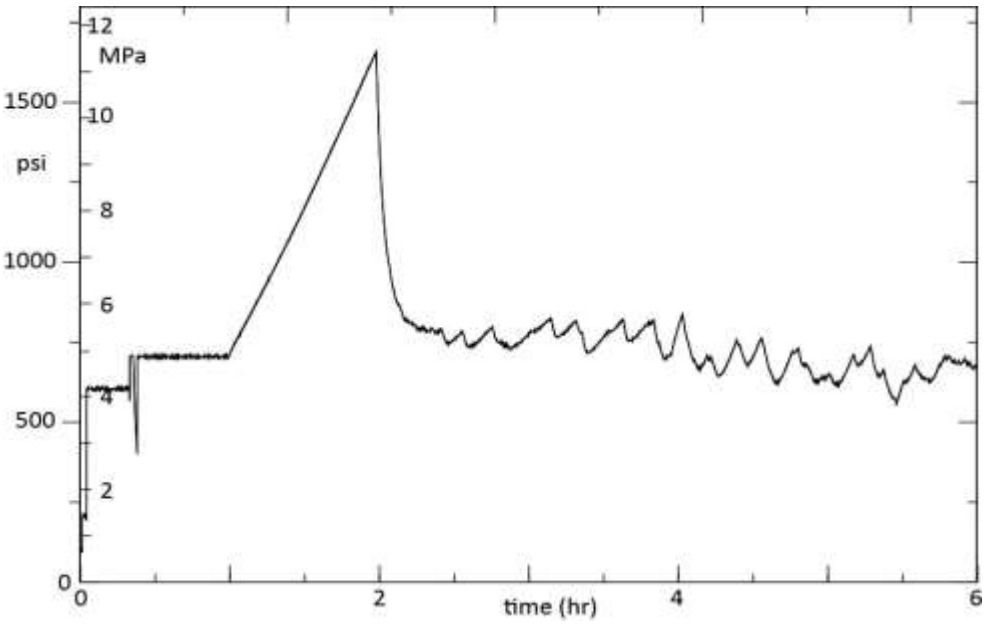

Figure 44. Fracking Experiment that includes a pre-existing model fault. Pressure-versus-time plot from constant-flow (4 microliters/min.), high-pressure-pump sensor. Pressure response at the well is expected to be lower and time-delayed, and will be extracted for comparison and analysis during January 2015. In comparison to prior experiments, a pre-existing model fault creates sharp oscillatory pressure variations.

Although not foreseen in the original proposal, we now collect pressure data because they are deemed necessary for relating engineering and seismic process models in later analyses. For example, by visual inspection, we determined that initiation of these oscillatory pressure variations at the pump sensor, occurred before the hydraulically induced fracture physically contacts the pre-existing model fault.

Sample# 12 110514

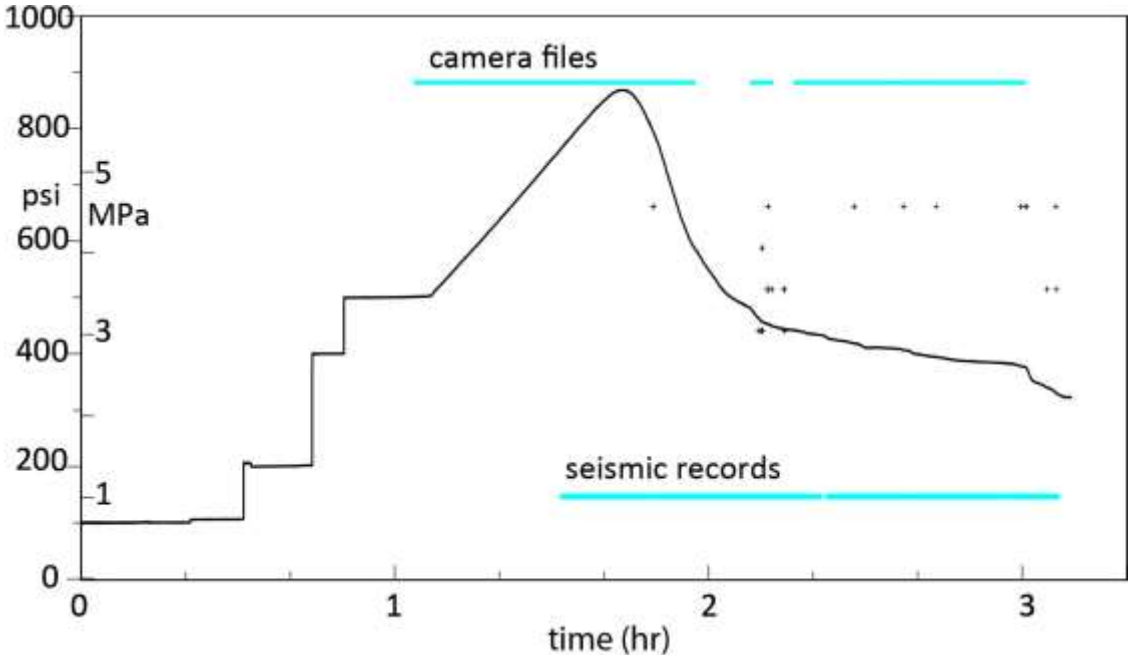

Figure 45. Three different types of data (video camera (see Oct. 2014 report files), microseismic, and pump pressure) are linked in time using new, in-house, simple, inexpensive timing circuitry. Digitally recorded pressure values at the syringe pump, cover a > 3 hour period (~200 minutes). Fluid pressure within sample (#12) is raised in steps until ~ 500 psi. Thereafter, flow rates are held constant at 4 microliters/minute for the duration of the whole experiment. Pressure leading to principal initiation of crack propagation is linear while decrease in pressure measured at the pump head decays rapidly afterward. Sample #12 –Experiment 110514

For this high-viscosity experiment*, a relatively small number (17) of low-amplitude (low-energy release) microseismic events are currently detectable. Fracking experiment without pre-existing fractures. Pressure-versus-time plot from constant-flow (4 microliters/min.), high-pressure pump sensor. Non-dimensional toughness = 1.4 High-viscosity (92,280 cp, 92 Pa.s). 17 events Seismic events (small crosses) are noticeable after the peak (breakdown) pressure is reached toward the end of hour 1. Microseismic events are divided into four groups based on their duration: highest row indicates the longest duration. Events are classified as lasting spike-like, ~ 0, 1 s, ~0, 5 s, and longer than 0.5 s duration. Three different types of data (video camera (see Oct. 2014 report files), microseismic, and pump pressure) attempt to record the fracturing processes.

6. An analysis and discussion of the scalability of these results to field conditions and comparison to previous laboratory experiments will be published.

Detection of differences in microseismic event strength based on detected amplitudes under various viscosity conditions indicate that (1) there is no noticeable change in the number of events, (2) magnitude of the events decreases and (3) crack propagation speeds diminish. The first result is most applicable to scaled viscous- dominated field regimes.

Theory suggests that observed field frequencies of microseismic events should be lower than those observed in the field (Taleghani and Lorenzo, 2011). Also whereas field data often displays many double-couple events we expect that pure extensionally produced fractures (tension fractures, Mode I) should be more numerous. One possible reason for the abundance of double-couple events is because of the interaction of

new fractures with pre-existing natural fractures; this interaction is poorly understood and is one of the aspects this research has looked into.

Experiment 050814

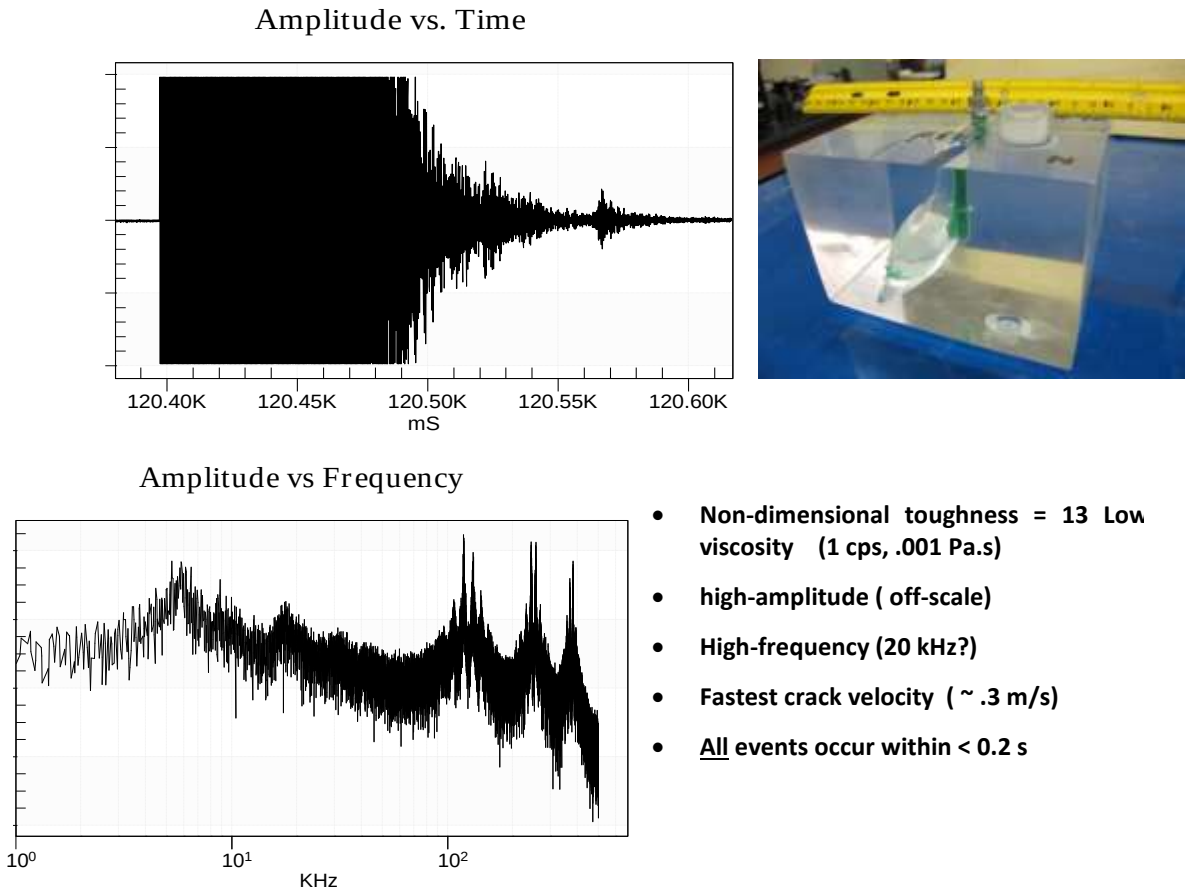

Figure 45. Low-viscosity fracking fluid accompanies the fastest average crack propagation rate (0.3 m/s) and highest magnitude events. (LEFT) Spectral maxima span 5-15 kHz. (Higher frequency peaks derive from electronic noise)

We aim to quickly diagnose new tensile fractures versus reactivation of pre-existing fractures by a combination of amplitude, frequency content of seismic events in combination with pressure history.

Working Hypothesis:

Under extensional conditions, lower energy events are expected because samples are weaker than under shear-fracture conditions. One implication at present of this result is that in the field, lower-energy events would indicate more tensile-dominated fractures, and that higher-energy events would indicate events related to more shearing mechanisms.

Comparison of experiments 050814 (Figure 45) and 060514 (Figure 46) indicated that higher-viscosity fluids accompany lower-amplitude events. For experiment 060514 (Figure 50), S-wave events are not apparent, and indicate possibly that only a P-wave extension-related oscillatory signal is produced during tensile fracture opening, as can be expected.

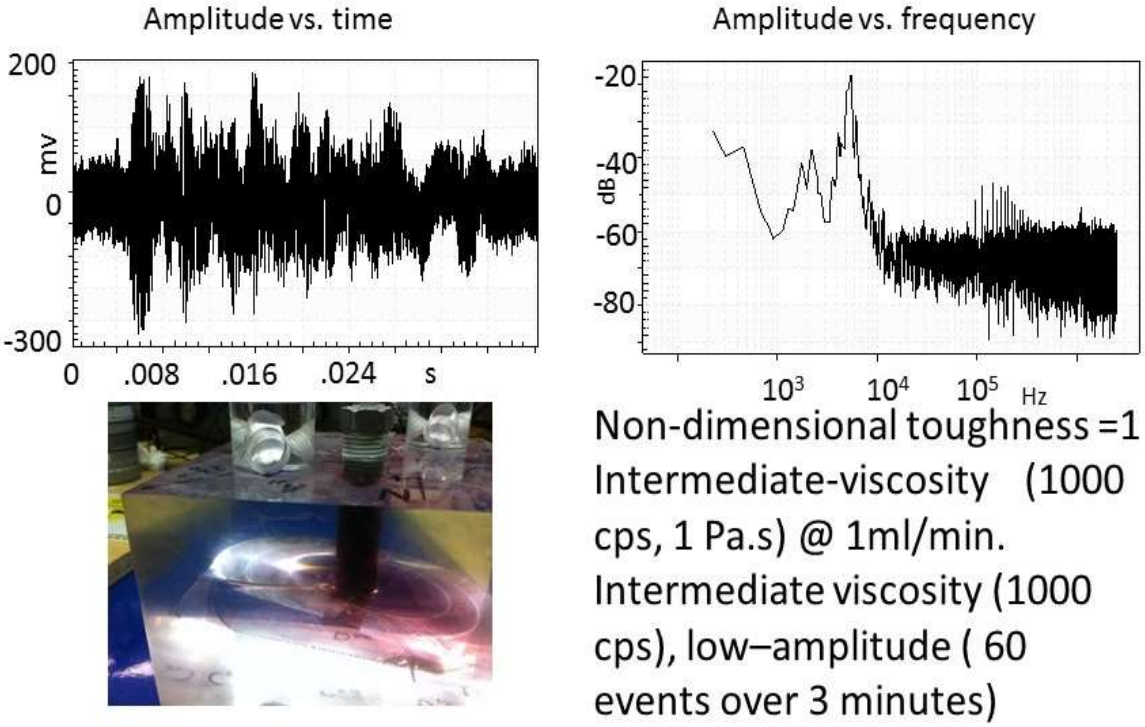

Figure 46 Experiment 060514 shows relatively low-energy few events (TOP LEFT) at lower viscosity than experiment 050814; dominant frequencies (TOP RIGHT) are lower. Of note are the lack of clear S-wave arrivals and the tremor-like nature of the seismograms (top LEFT) created during fracture growth in sample (BOTTOM LEFT)

Outcomes

The experiments in this project use homogeneous, relatively impermeable, transparent materials (PMMA) to evaluate fracture behavior in the lab. In the field, materials are far more heterogeneous and conditions more complex. Nevertheless our observations suggest interesting implications which are not in disagreement with other theoretical and empirical approaches to micro-seismic monitoring.

A workflow to build a hydraulic fracturing lab for collect seismic and flow data

We have created a unique, step-by-step guide for other researchers to build a cost-effective, hydraulic fracturing microseismic laboratory. In addition, we supply an open-source set of software tools (in R--open-source) to read vendor formatted digital data and conduct preliminary seismic analyses (pp. 6-20).

Distinguishable differences observed between seismic events collected in toughness dominated regime and viscous dominated regime.

Throughout our work we have taken great care to scale our geomechanical conditions to either a toughness or viscous-dominated regime (See p. 34 for comparisons among different experiments and original proposal for details). In general there is an unexpected similarity in the frequency content of

microseismic events produced in both regimes (kHz). However, the toughness dominated events display a slightly higher frequency (20 kHz versus 5 kHz; Figures 45, 46).

Field conditions are usually conducted in the viscous-dominated regime. For these cases, our dominant frequencies we observed are 1-2 orders of magnitude different from the field. Our sample size (10 - 15 cm) scale to 10's meters in the field.

7. Pressure Analysis of Fracturing

Although we did not originally propose to collect pressure data while conducting experiments, we did instrument our experiments to measure in-situ as well as pump-versus time variations. Laboratory results show a good similarity with expected relationships often used to analyze formation stimulation during symmetric fracture propagation. The analysis of these pressure curves suggests that our experimental behavior bears similarity to field cases.

Experiments

In this section, we try to study pressure response during hydraulic fracturing experiments in the lab with a closer look. Due to uniaxial loading condition and geometry of initial crack in the sample, the induced fracture in the PMMA block has a radial geometry (Figure 47). In other words, the induced fracture is neither PKN nor KGD but Penny-shaped crack. This fracture geometry is occurring in the field at the beginning of pumping stage in horizontal wells before fracture reaches upper and lower barriers like bedding planes. The radial model is also applicable in homogeneous reservoir condition where the injection zone can be practically assumed to be point source. We conduct pressure analysis to scrutiny fracture propagation regime in terms of hydraulics. Later, these analyses can be used to investigate possible correlations between bottom hole pressure fluctuations and recorded microseismic events in the geophones. For instance via a rough investigation in Figure 48, it can be seen that some large magnitude events are occurring simultaneous with pressure fluctuations during fracture propagation. It is notable that pressure measurement always involves some sorts of fluctuations, however the frequency of these fluctuation are different from pressure fluctuations generated during fracture propagation and will be removed by movable averaging.

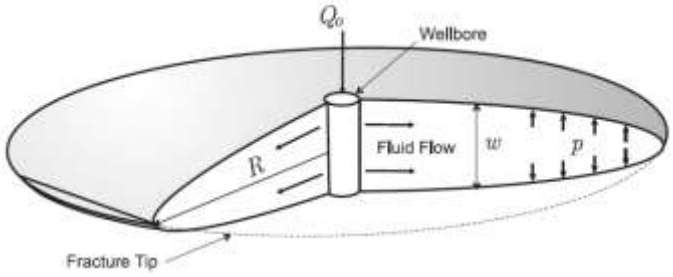

Figure 47. Schematic of a radial or Penny-shaped hydraulic fracture.

Considering the fact that the core of most of the commercial hydraulic fracturing software like Stimplan and FracPro are written with Boundary Element Methods, they are only suitable for fracturing problems in

infinite medium not for a finite size sample considered in this experiment. In an effort to match pressure obtained through experiment, we used StimPlan software to reproduce experiment results, however, results show big differences between test and simulation results (See Figure 49). To match the injection pressure, the mechanical properties of the PMMA and injection rate are used as input. The simulation uses Pseudo-3D model for fluid flow and fracture propagation. To address difficulties associated with pressure matching, we resort to analytical asymptotic solutions for radial fractures.

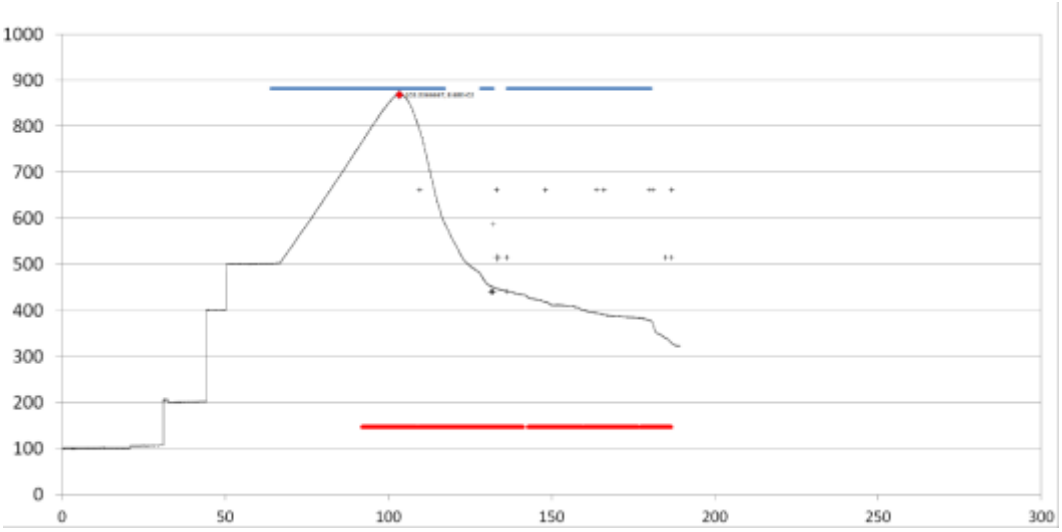

Figure 48. Treatment pressure and major microseismic events during an experiment (Experiment 110514, sample#12) conducted in this project.

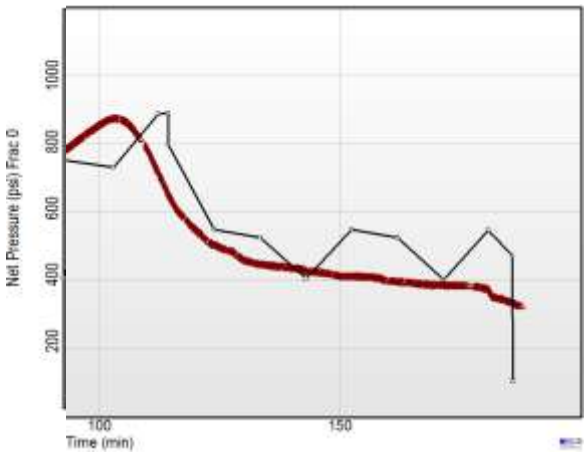

Figure 49. Pressure match using StimPlan.

A typical net pressure during a microfrac or DFIT test is shown in Figure 50. In the experiments conducted in this project, minimum principal stress was zero, therefore recorded pressure is net pressure (Figure 48). The experimental results obtained in our project follow the same pattern in large extent, however, our experimental data does not include Shut-in and closure time periods. The major pressure drop at the end of pumping time in Figure 48 is related to the situation that fracture reaches sample boundaries. In

general, toughness or tip effects become important for cases where fracture height is unconfined (e.g. radial or circular fractures) or for very soft rocks. For treatments using low viscosity fluid or pumping at very low rates, the viscous term of the net pressure equation becomes small, and fracture toughness becomes a dominant parameter. Although many cases fall into one of these extremes, neither effect should be overlooked for the prudent application of fracturing. To address this issue, fracturing fluid with very different viscosities have been used in this project.

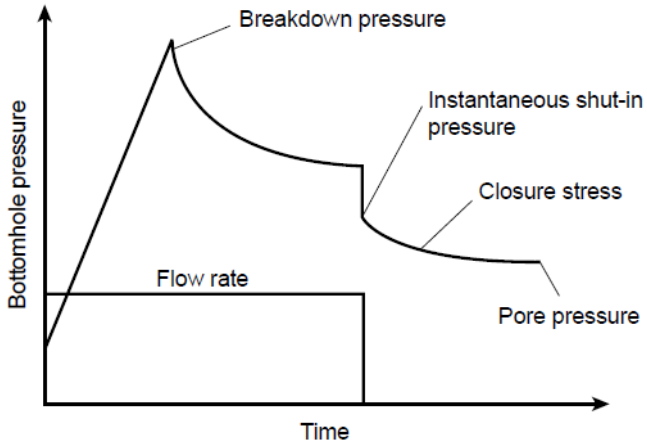

Figure 50. A typical net pressure response during a micro-frac test.

Pressure during pumping

Equations for interpreting pressure during fracturing are developed by combining the basic equations of material balance, fluid flow and rock deformation (elastic and or plastic). The relation between the fracture geometry and pressure during pumping was initially presented by Nolte and Smith (1981), with specific application to the PKN type fracture geometry. This analysis was subsequently generalized for application to each of the basic fracture geometry models (Nolte, 1986). Extensions were also proposed by Nolte (1991) to consider deviations in the fracture geometry from the idealized 2D fracture geometry conditions.

The pressure slope in the log-log plot versus pumping time can provided some information about the fracture propagation mode. As mentioned earlier in previous reports, fracturing experiments were done in PMMA samples to not only satisfying scaling issue but also due to impermeable nature of PMMA, fluid leak off is removed from analyses.

The fundamental relationship between pressure and time can be derive from principle equations. By combination lubrication equation and fracture compliance, we can find that

$$\frac{dp}{dx} \propto \frac{K}{\left(c_f p_{net}\right)^{1+2n}} \left(\frac{q_i}{h_f}\right)^n .$$

Integration over the length with the assumption that p_c is a constant and that p_{net} is negligible at the fracture tip gives

$$p_{net} \propto \left[\frac{K}{c_f^{1+2n}} \left(\frac{q_i}{h_f} \right)^n L \right]^{1/(2n+2)}$$

By combining the above relationship with the mass balance developed for radial fracture, we will have

$$p_{net} \propto \left(E'^{2n+1} K q_i^n \right)^e \left[\frac{1}{R^{3n}} \right]^e$$

where e= 1/(2n+2) and n is the power-law index. With further analysis and assuming constant injection rate, we can show that

$$p_{net} \propto \left(K E'^{n+1} \right)^{1/(n+2)} (t^*)^{-n/(n+2)}$$

Where n is equal to 1 for Newtonian fluids. By ignoring leak-off, we can have

$$p_{net} \propto t^{-n/(n+2)}$$

Questions surround laboratory physical analogs regarding the scalability of both geomechanical and seismic results obtained from these experiments. In part, we rely on the use of non-dimensional idealizations of the physical processes taking place during the fracture process. We note that it is common practice to use non-dimensional numbers in interpreting pressure conditions during hydraulic fracturing, for example, when considering the effect of turbulence in pumping fluids to explain pressure losses due to friction in pipes through the Reynolds number (Stokes, 1851). Laminar instead of turbulent flow is expected for lower dimensionless Reynolds numbers. Of course local complexity, e.g., surface roughness is not considered in the idealized version of this non-dimensional number and should be used as a guide in field cases.

In our experiments we also assume ideal conditions in order to simplify and up-scale our observations and interpretations to field-scale conditions via the use of non-dimensional toughness. For example, for our two cases above we calculate a dimensional toughness ~ 1.4 (See previous conference presentation from December activities, slide# 9). Non-dimensional toughness is calculated function of viscosity, pump rate, layer thickness, rock toughness (Detournay, 2004) presentation and assumes simple linear fracture theory conditions. A non-dimensional toughness value close to 1 approximates field conditions of hydraulic fracturing activities, so that although our flow rates appear to be low (4 microliters per minute) by field standards (measured in bpm) and viscosity high (92,280 cp, 92 Pa.s cf. ~ 1cp in field cases) the non-dimensional number indicates that the fracturing process still occurs under a viscous-dominated regime.

It is true that analytical solutions in fracture models are limited to very simple planar geometries embedded in an infinite-size homogeneous isotropic medium, but these solutions provide important insights into the asymptotic behavior of the pressure distribution near the fracture tips. Analytical solutions have revealed the controlling role of two dissipative processes: fracturing of rock (toughness) and dissipation in the fracturing fluid (viscosity). Depending on the competition between these two mechanisms, the singularities at the fracture tip will vary with stress, deformation, and height growth. Small-scale fracturing with real rocks will be dominated primarily by the toughness mechanism regime. In contrast, field-size fracturing treatments are usually under the influence of the viscosity dissipation mechanism.

Cepstrum analysis to assure that observed seismic events are not influenced by the reflection from sample sides.

From a cepstrum analysis of the data we consider that the sample and hydraulic press are not generating resonant frequencies. Cepstrum analysis is a commonly used spectrum analysis technique used in voice recognition studies to determine characteristic human pitch. The observed 5 kHz pitch matches the frequencies observed in the seismic events and not before the start of the fracking (Figure 51)

In order to confirm that the low frequency events were not the result of the new experimental setup we

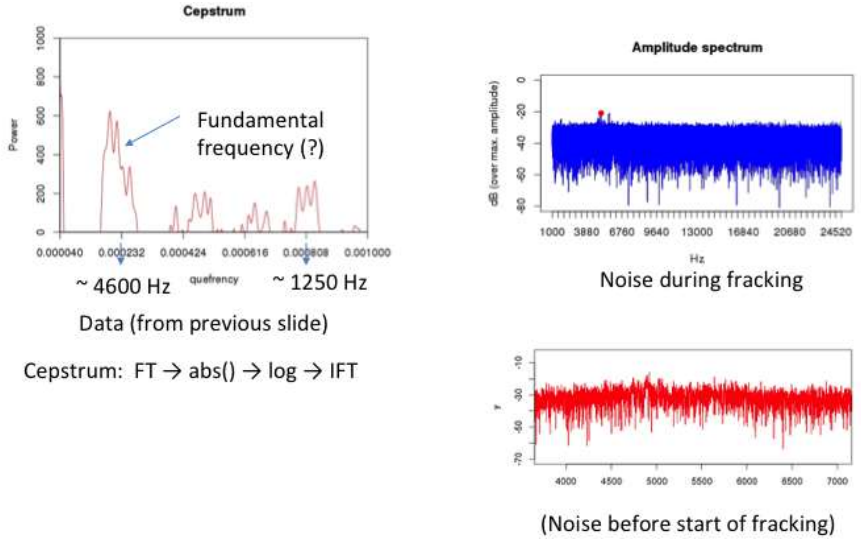

Figure 51 A fundamental frequency of 5 kHz is observed during fracking in the laboratory, but not before treatment while the acquisition system is running and broad-band sources of noise exist to excite resonance.

conducted a pencil test. Breaking of a 0.5 mm pencil lead is a common method for generating high frequencies, (US National Institute of Standards and Technology). We conclude, for now, that the lower frequency observed in the microseismic events is indicative of the mechanical process and not equipment effects

Analysis of all the available data indicate the background frequencies within the noise level show similar frequency distributions to that in microseismic events. If so, there is potential to study microseismic activity by examining the background noise level. This observation also suggests that energy dissipation

may be more continuous than previously in freed by only microseismic activities. An advantage of our laboratory setting is that the noise level is lower than in field conditions and so allows us to observe microseismic activity at low energy levels.

Most of the events acquired in the lab are tensile (CLVD) events (Mode I). No Double-couple was found in the lab data

To date we have not been able to detect shear wave data. Hodogram analysis indicates signals are primarily compressional waves (Figures 52, 53, 54). Therefore traditional earthquake locational algorithms will not work well with these data. For now, the absence of Mode II or mixed mode may be surprising, especially for the case of the model fault (Experiment #13, 120914). However, because of the homogeneous nature of the PMMA (thermally annealed, and machined to high tolerances), Mode I is the observed form of fracture development and is well supported by the clear circular growth geometry. It is to be expected that in the field, where conditions are much more heterogeneous (than usually considered), Mixed Mode, Mode-II and double-couple microseismic events should be the norm rather than the exception. So, for the reasons we repeatedly do not observe S waves in our data we should expect that Mode-I events should also be relatively rare in the field.

Back-projection of Seismic Events

We are now able to locate the azimuth and dip of the source event location at each sensor via polarization analysis, or principal component analysis. In a least-square sense, we find the best-fitting ellipsoid to a particle-displacement trajectory map (hodogram – Figure 53) of the microseismic event. We assume that our experimental material (PMMA) is relatively homogeneous, so that from the resultant eigenvalues and eigenvectors of the hodograms we can obtain several important attributes. Of interest to locating the microseismic event is the principal direction of oscillation of the first-arriving P wave. We incorporate the supolar module of opensource seismic processing system SeismicUnix into our R-Hydraulic Fracture

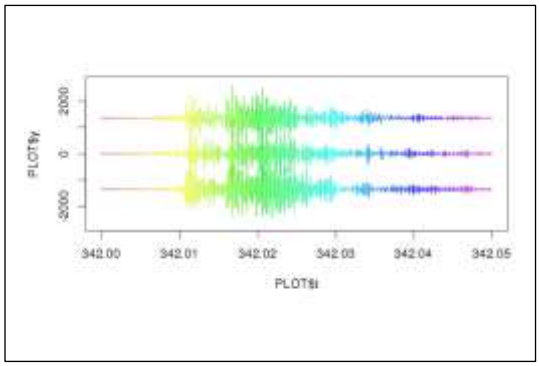

Figure 52 Data from experiment 110514-station C between times 342 and 342.05 s. Data are rotated into an N-Z (+ve up)-E coordinate system (from top to bottom) orthogonal RHS. Colors of the seismograms allow comparison with plots in figures 12 and 15.

Module package (RHFM manuals and code have been made available).

As an example of the backprojection analysis we show a microseismic event from experiment 110514 (e.g., Figure 52). From the data, events can be most easily interpreted as purely P-wave arrivals (Figure 52). In summary, P-wave arrivals are expected to dominate for the case of our Mode-I tension crack. Our sensors are located on the upper and lower surfaces of a rectangular block and for a penny-shaped crack

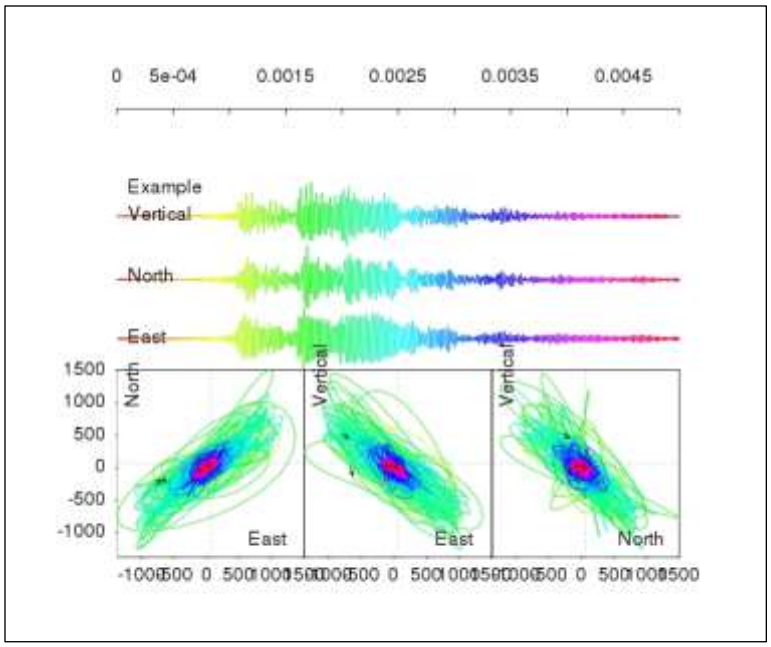

Figure 53. Hodogram representation of particle motion for data (Figure 52) of a microseismic event for experiment 110514.

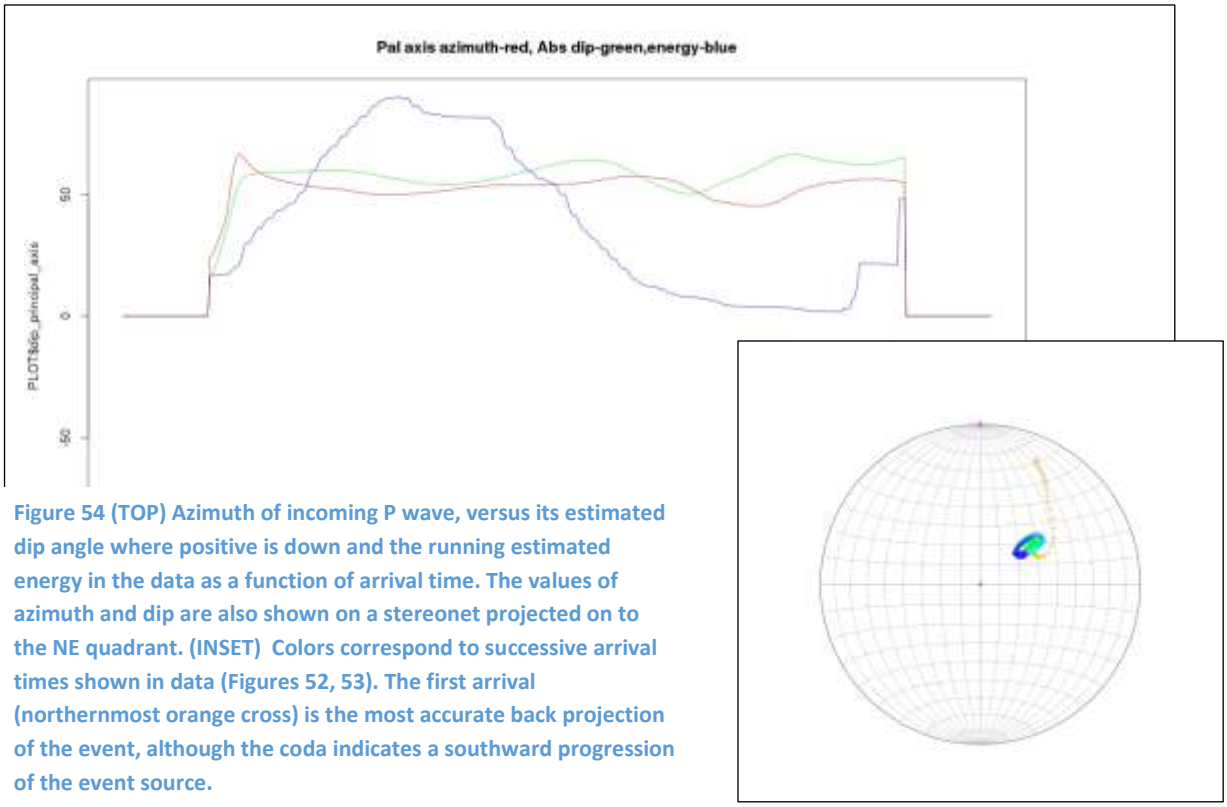

Figure 54 (TOP) Azimuth of incoming P wave, versus its estimated dip angle where positive is down and the running estimated energy in the data as a function of arrival time. The values of azimuth and dip are also shown on a stereonet projected on to the NE quadrant. (INSET) Colors correspond to successive arrival times shown in data (Figures 52, 53). The first arrival (northernmost orange cross) is the most accurate back projection of the event, although the coda indicates a southward progression of the event source.

propagating in the horizontal plane directivity of P-waves is also supposed to be greatest at the top and lower faces.

During back-projection analysis we can obtain attributes such as the average energy of the event, the azimuth of the first, incoming P-wave and its dip with respect to the horizontal (positive angle downward (Figures 53, 54). A stereographical map can locate the location of the event and to the degree the location of the event migrates we can infer a migration in the backprojected path (Figure 54-inset).

Pressure fluctuations observed in the sample with a pre-existing crack (model fault)

Thanks to the recorded treatment pressures and the recorded video camera images of the propagating crack across a model pre-existing fault in the PMMA block, we observed that pressure in the model well (Figures 44, 55) started to vary notably occurring before the propagating crack intersected the pre-existing crack model fault. (Figures 56, 57) That is, the presence of the fault changes the pressure in the borehole. The pressure continues to oscillate even after intersection with natural fracture. Nevertheless only Mode I events have been observed so far. For comparison, no such pressure fluctuations were observed in a previous almost identical experiment (Figure 48) , which did not contain a model fault in the PMMA.

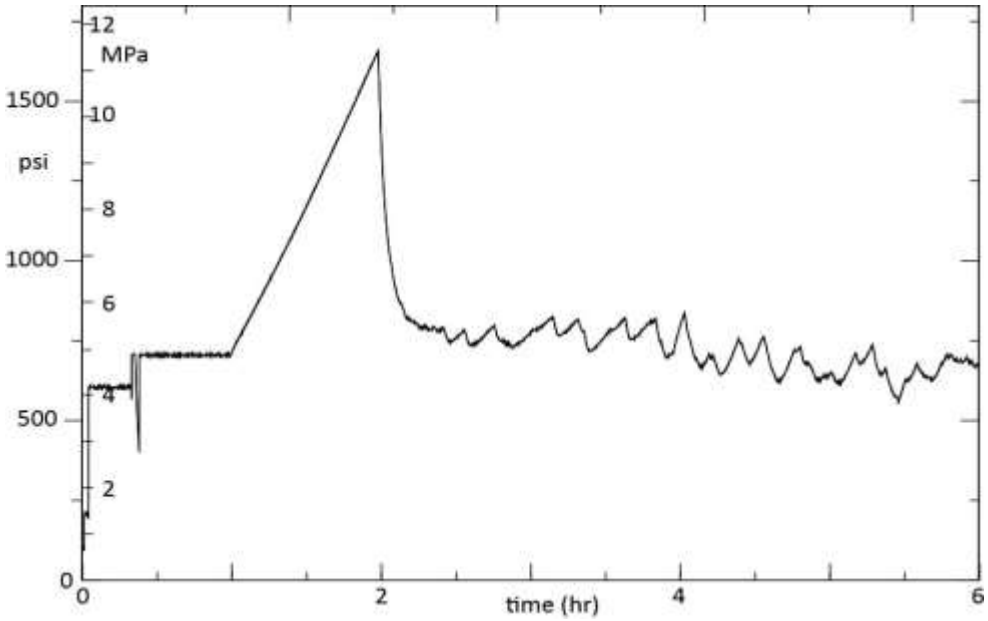

Figure 55 Fracking Experiment that includes a pre-existing model fault. Pressure-versus-time plot from constant-flow (4 microliters/min.), high-pressure-pump sensor. In comparison to prior experiments, a pre-existing model fault is responsible to generating sharp oscillatory pressure variations.

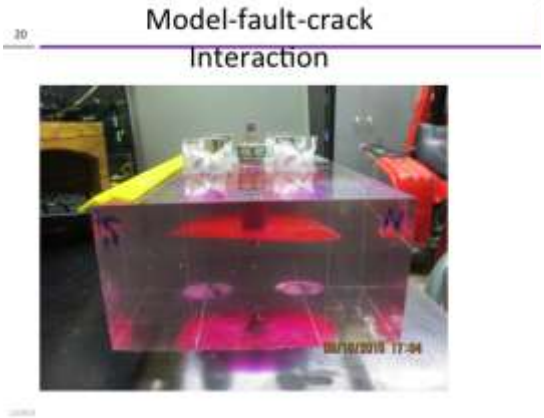

Figure 56. Side view of PMMA block (120914; sample #13) after fracture (red fracking fluid) has propagated across model fault (into page)

8 An

educational deliverable will be the training of student workers in this field

Figure 57 Top view (PMMA block (120914; sample #13) after fracture (red fracking fluid) has propagated across model fault and down the fault interface. The sloping interface is the model fault sandwiched between two PMMA blocks. The PMMA block to the right of the fault is transparent but continuous with the top surface of the block

We obtained additional funding from our university with which we took on two new graduate students (Trudy Watkins and Abigail Maxwell) to complete an MS program by fall 2016 on the subject of Advanced Hydraulic Fracturing in the RPSEA-funded laboratory. We recall that one MS student who worked on developing inversion code for this project already graduated in 2014 (Chennu Fan). One undergraduate work-study student, Jack Cadigan (Dept. Petroleum Engineering) and Daniel Carter (Chancellor's Aid Scholar – Dept. Geology and Geophysics) both assist with sample preparation and experiments.

Appendix M: A re-look at contractor supplied geophysical data

Summary and Accomplishments

GTI took a second look at the raw and cataloged microseismic dataset from Wootton Pad test well. The raw data was processed using in-house processing capabilities at GTI. Various techniques were used in an attempt to derive maximum value from the data and aid in our interpretation and analysis, particularly to validate variable rate fracturing scheme that was a key task undertaken as part of this project. Finally, this study provided an opportunity to take a second look at the microseismic data supplied by the relevant service companies tasked with collecting and processing the data. The major accomplishments from this task have been:

- Successfully conducted independent data quality analysis including identification of acquisition and processing artifacts.
- We successfully validated the primary inversion product from the vendor (microseismic event hypocentral locations) for a subset of the data acquired for this project.
- In depth spatio-temporal b-value analysis to better understand the nature of observed seismicity.
- We were able to identify long period long duration events (LPLD) highlighting their presence in the Marcellus shale play.
- Correlated completion data with b-value analysis to identify fracture indicators observed during hydraulic fracturing.
- Correlated fractures, mud log gas shows, production logs and observed inter-well interference as diagnostic tools validating observations.

Introduction

We undertook a detailed analysis of the microseismic data made available from service provider (Halliburton). The aim was to better understand the seismicity behavior by doing a seismicity distribution study (b-value analysis). We also utilized a novel event detection routine to apply an imaging algorithm and compared our results with those cataloged using a traditional inversion based workflow from the service provider. In the course of this study, we have quickly realized the major limitations posed by the data quality itself as well as the challenge of imaging the subsurface using a single horizontal array of geophones. These challenges and issues will be shared in this report. We also looked into additional data/ properties that were collected as part of this project. These include mud log information (gas shows), image log data, interference data (between Wootton pad wells 10H &12H) and other seismic derived attributes (such as b-value and length/width ratios of the observed seismicity spreads) to better understand the stimulated zone behavior within the reservoir setting. These results have also been discussed in in this report.

Geophysical data for Wootton Pad well 10H

Frac treatment for well Wootton 10H was monitored using a downhole sliding geophone array for the 18 stages completed as part of this treatment. Initial observations indicate good containment with fractures reaching the top of Hamilton. Downward growth was limited and we did not observe significant seismicity below the Onondaga limestone. Figure 1 highlights the seismicity observed over the treatment and its containment based on inversion results (side view). Figure 2 shows a similar distribution of events (top view) for reference.

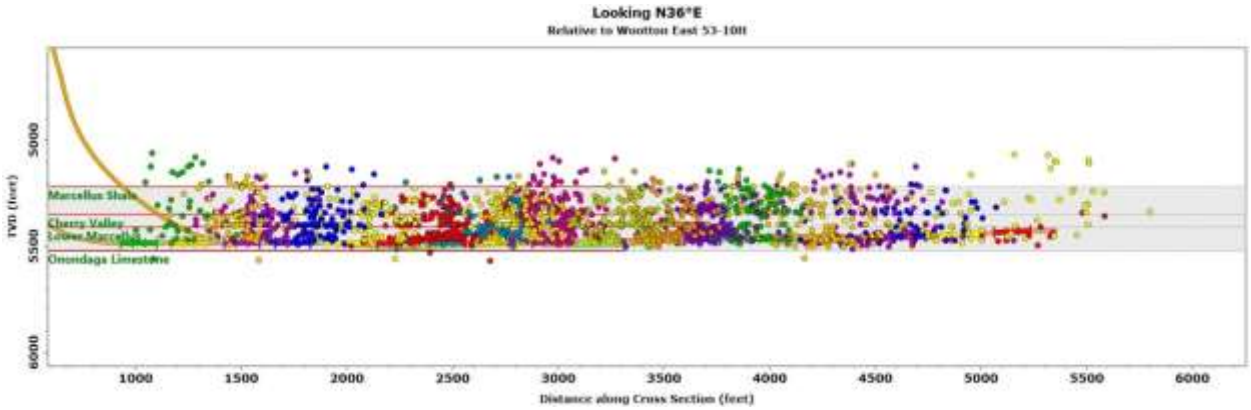

Figure 1: Side projection of microseismicity observed during treatment of well 10H.

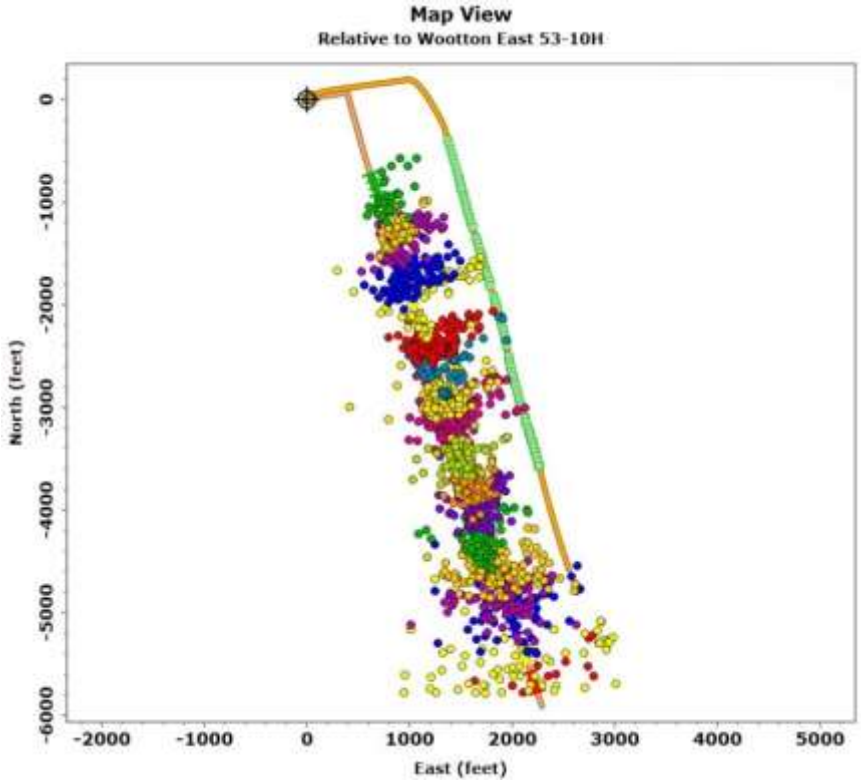

Figure 2: Top projection of microseismicity observed during treatment of well 10H.

The primary fracture azimuths from seismicity distribution for most stages suggests a N67°E orientation which correlated well with known SH_{max} estimates. Typical fracture network length (X_f) is estimated at ~620 ft., width at ~420 ft. and height at ~400 ft. Complexity seems low to moderate and spatially confined (such as stages 9 & 10). The seismicity distribution from figure 2 indicates issues of directional and separation bias in terms of events successfully located as well as identified locations and errors associated with inversion. This can be seen in the relatively large event spreads in X-Y for early stages compared to later stages. However, the distributions as observed indicate good fracture containment in the vertical plane with adequate confidence. This can be further observed from the height growth data as obtained from the inversion results. Figure 3 shows the height growth during treatment.

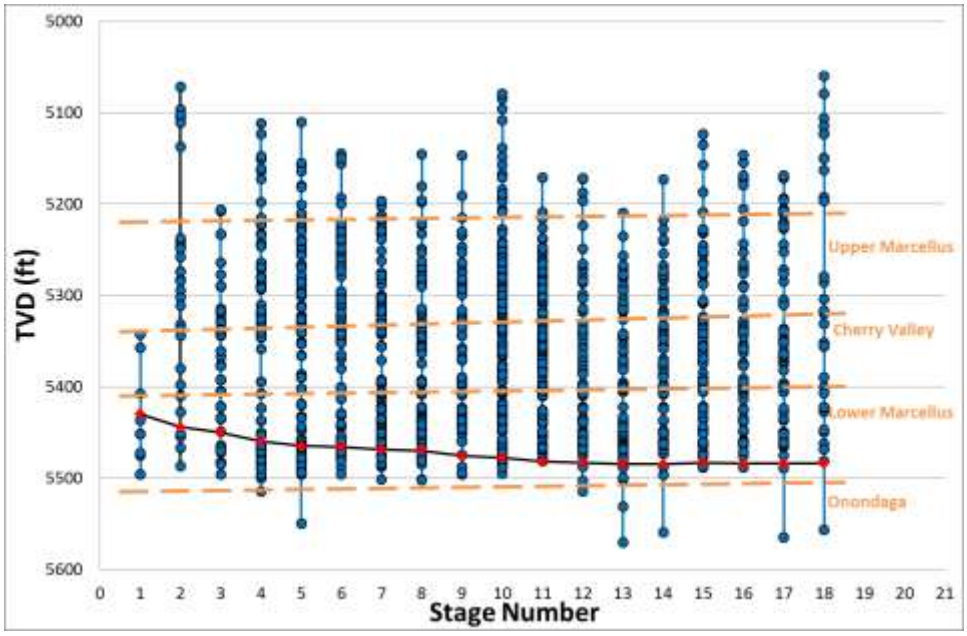

Figure 3: Fracture height growth as per microseismic data spread.

Seismicity spread both in vertical and horizontal plane can allow for an improved understanding of fracturing behavior. The 10th and 90th quantile cutoffs for spatial spreads are shows in figure 4 and table 1. This further validates reasonably good containment within the Marcellus layer. Moreover, overall magnitude distribution across stages suggests very small events with the maximum observed magnitude at ~ -1.2 on Richter scale. Based on event distribution patterns, we believe that the relatively high X, Y and Z directional spreads in event distribution associated with the first few stages is due to distance bias which leads to lower event count and increased event location uncertainty. Moreover, as we move from the toe towards heal of the well, the event clouds gradually shift closer towards the observation well which follows slightly enhanced intra-well offsets. This could be again indicative of separation and coverage biases. We also note that due to said biases, the uncertainties associated with events in X-Y plane are quite significant. However, the uncertainty in the Z direction is relatively modest and we have reasonably high confidence in the containment of seismicity within the desired formation.

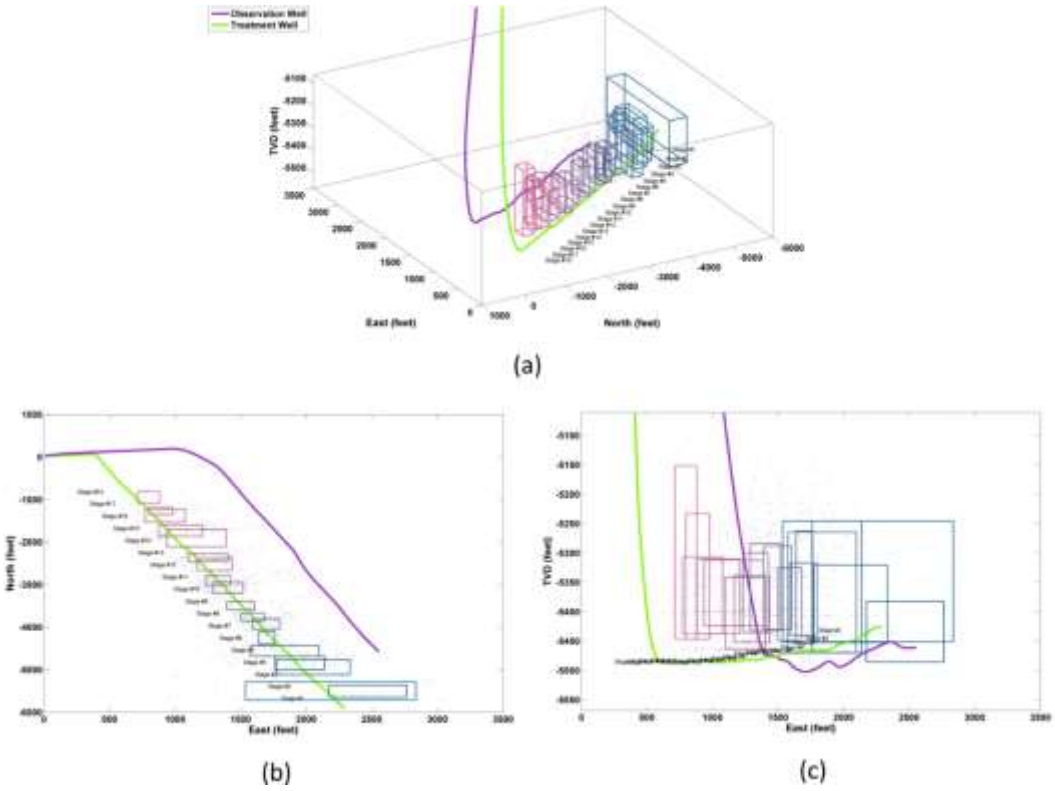

Figure 4: Event distribution based on upper 90th and lower 10th quantile cutoffs in X, Y and Z directions for all completed stages in treatment well. Subplots (b) and (c) show the top and side view respectively.

Table 1: Event spreads along X, Y and Z direction based on 10th and 90th quantile cutoffs.

Stage #	X - min	X - max	Y - min	Y - max	Z - min	Z - max	Magnitude - min	Magnitude - max
1	2175.095	2764.595	-5642.685	-5361.24	-5382.725	-5485.68	-2.58	-2.13
2	1536.21	2835.645	-5708.725	-5288.62	-5245.58	-5451.21	-2.47	-1.28
3	1772.778	2333.536	-5115.969	-4767.048	-5320.44	-5452.548	-2.63	-1.38
4	1760.187	2139.154	-4999.744	-4685.925	-5245.691	-5469.537	-2.8	-1.64
5	1575.62	2097.988	-4686.397	-4434.233	-5264.397	-5470.096	-2.92	-1.65
6	1637.06	1763.835	-4399.435	-4106.37	-5262.485	-5451.465	-2.85	-1.14
7	1594.145	1798.215	-4051.245	-3800.745	-5317.005	-5440.705	-3.07	-1.31
8	1499.514	1679.95	-3855.723	-3669.869	-5325.066	-5449.427	-2.91	-1.49
9	1390.965	1604.598	-3600.802	-3400.326	-5288.279	-5430.587	-2.79	-1.46
10	1289.013	1518.816	-3200.212	-2947.951	-5283.997	-5432.237	-3.36	-1.21
11	1231.321	1425.484	-3014.356	-2785.178	-5300.039	-5435.703	-3.34	-1.51
12	1166.517	1435.288	-2666.051	-2385.355	-5338.507	-5452.019	-3.06	-1.47
13	1098.925	1404.605	-2455.615	-2278.815	-5341.745	-5463.915	-3.03	-1.51
14	936.86	1390.31	-2112.505	-1704.255	-5312.06	-5424.055	-3.33	-1.83
15	878.073	1208.583	-1862.734	-1599.494	-5310.395	-5437.494	-2.96	-1.27
16	772.263	1077.873	-1533.619	-1228.725	-5306.62	-5438.06	-3.25	-1.49
17	795.499	978.58	-1353.479	-1181.087	-5233.397	-5446.675	-2.91	-1.65
18	714.48	881.922	-1095.061	-812.84	-5152.214	-5446.393	-3.01	-1.58

Based on the information obtained from the seismicity distribution, conservative estimates of perturbed zone length, width and height as well as potential overlap with prior stages is highlighted in table 2.

Table 2: Perturbed zone length, width, height and observed overlap of seismicity with previously completed stages.

stage #	Length	Width	Height	Overlap
1	589.5	281.445	102.955	-
2	1299.435	420.105	205.63	yes
3	560.758	348.921	132.108	no
4	378.967	313.819	223.846	yes
5	522.368	252.164	205.699	no
6	126.775	293.065	188.98	no
7	204.07	250.5	123.7	no
8	180.436	185.854	124.361	yes
9	213.633	200.476	142.308	no
10	229.803	252.261	148.24	no
11	194.163	229.178	135.664	yes
12	268.771	280.696	113.512	no
13	305.68	176.8	122.17	yes
14	453.45	408.25	111.995	no
15	330.51	263.24	127.099	yes
16	305.61	304.894	131.44	no
17	183.081	172.392	213.278	yes
18	167.442	282.221	294.179	no

Leakoff into previously completed stages (potentially caused by pre-seating activities) was observed. For some stages (e.g. stage #2 and stage #4), there seems to be limited forward growth of fractures along the lateral with most growth occurring towards or within previously completed stage (in this particular case, it could be separation bias and associated processing artifact). These have been correlated with other properties (SWE) in Appendix F. One of the reasons for looking into alternative processing approach as described in said appendix section was to tide over the issue of small magnitude “non-locatable” events. Figure 5 shows two examples highlighting an easy to locate event and another which was not inverted (stage 16).

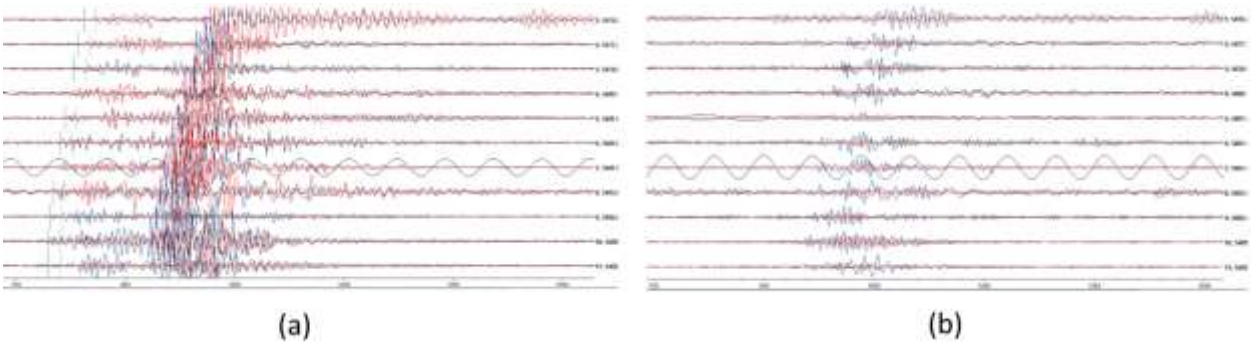

Figure 5: Data quality parameters such as event magnitude, attenuation impact (S-R separation), signal SNR, etc. can all influence the final "event" quality and thereby determine whether it can be located using traditional inversion algorithms or not. We can observe the distinguishable phases from (a) “locatable” event as compared to (b) “non-locatable” event.

Revalidation of inversion based hypocentral locations using emission based mapping

Re-validation of microseismic data processing using in-house GTI workflow was carried out for relatively large magnitude events to increase credibility of the processed catalog. Figure 6, 7 & 8 show

examples of a subset of reprocessed events with both the original event location as provided by Pinnacle and the event location obtained as a result of re-analysis at GTI.

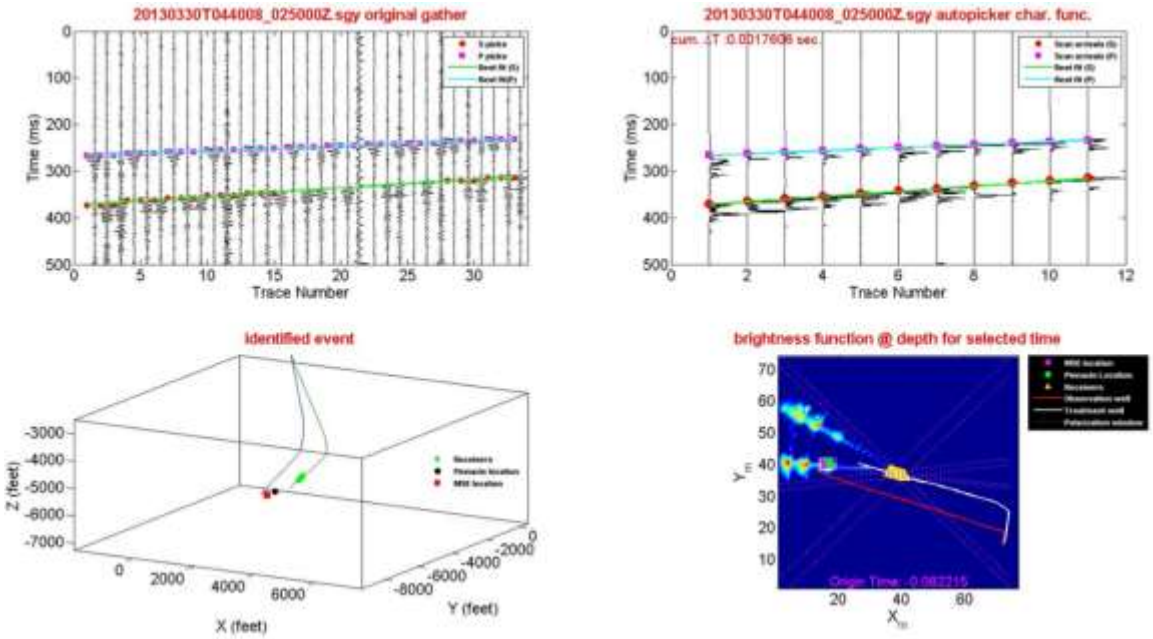

Figure 6: Comparison of event location solutions from contractor (Pinnacle) and the same event processed internally by GTI with results falling within a few search grids indicating reasonably strong match.

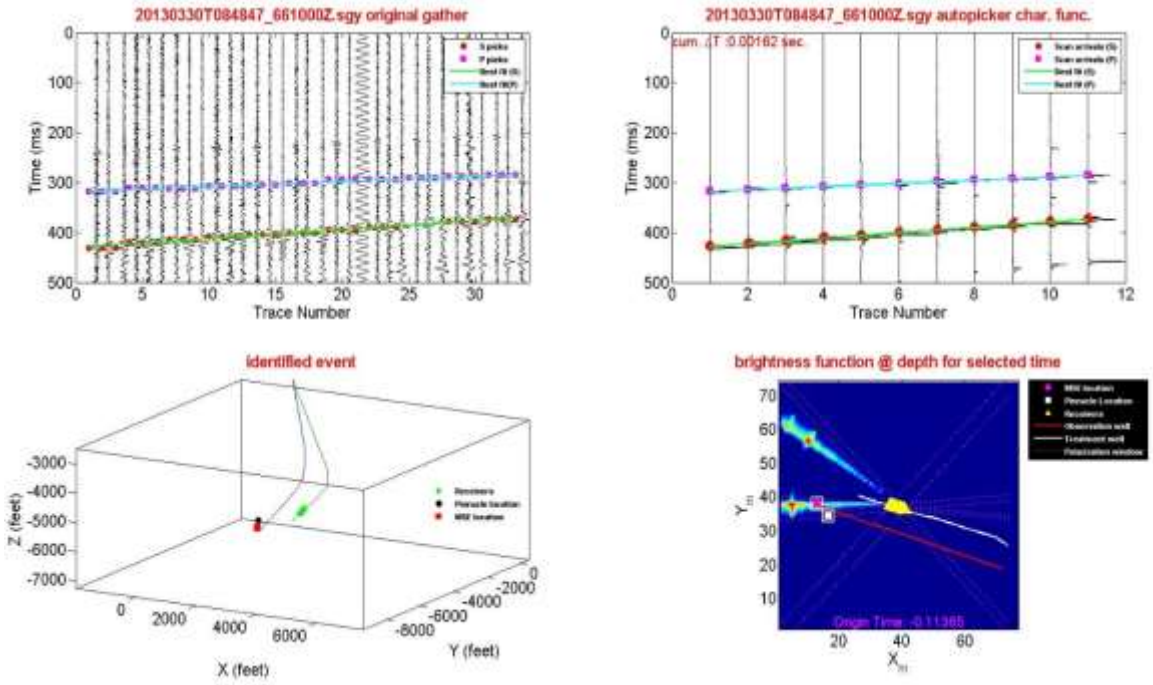

Figure 6: Comparison of event location solutions from contractor (Pinnacle) and the same event processed internally by GTI with results falling within a few search grids indicating good match.

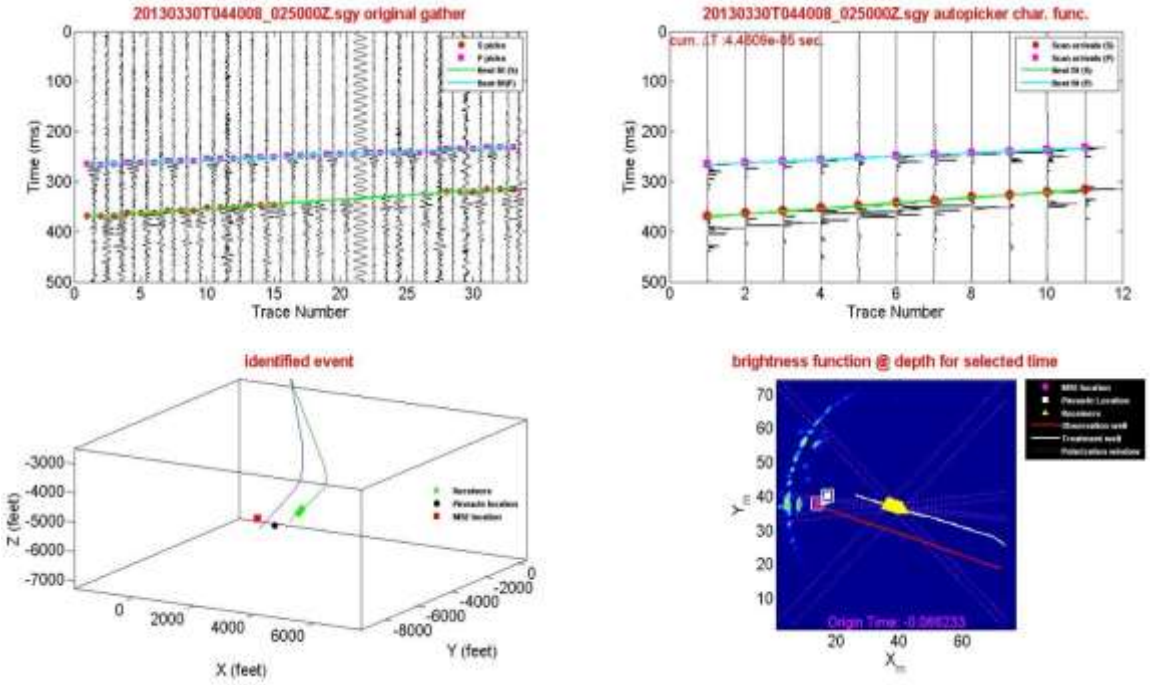

Figure 6: Comparison of event location solutions from contractor (Pinnacle) and the same event processed internally by GTI with results falling within a few search grids indicating good match.

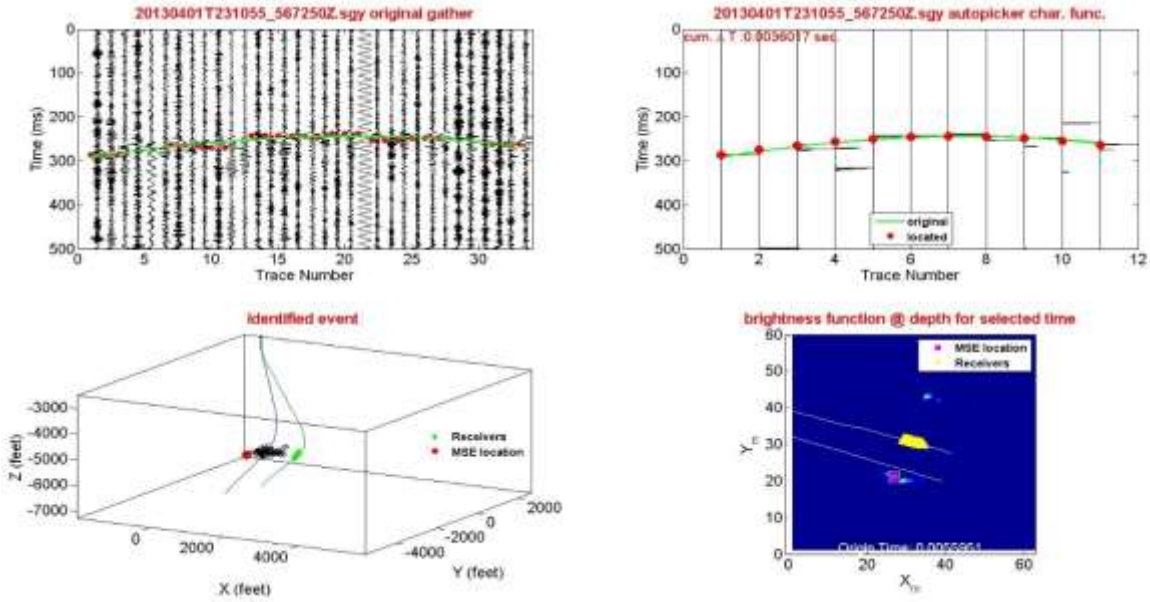

Figure 7: Wootton 10H stage # 16 sample event identified using GTI workflow.

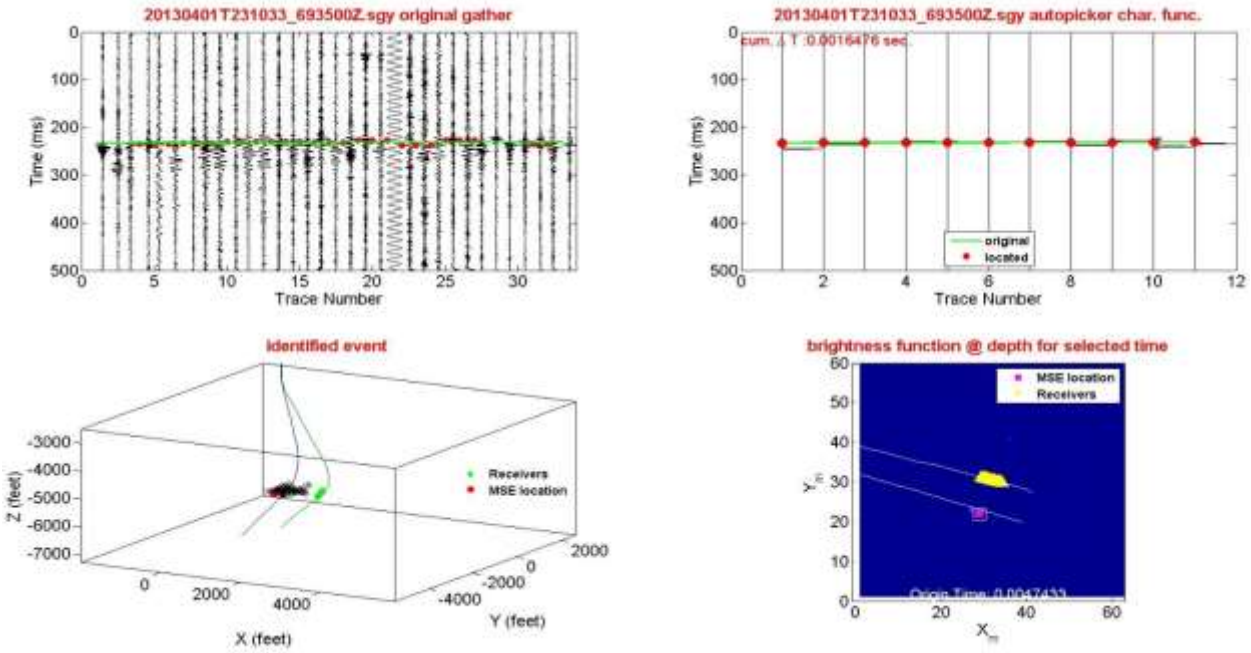

Figure 8: Wootton 10H stage # 16 sample event identified using GTI workflow.

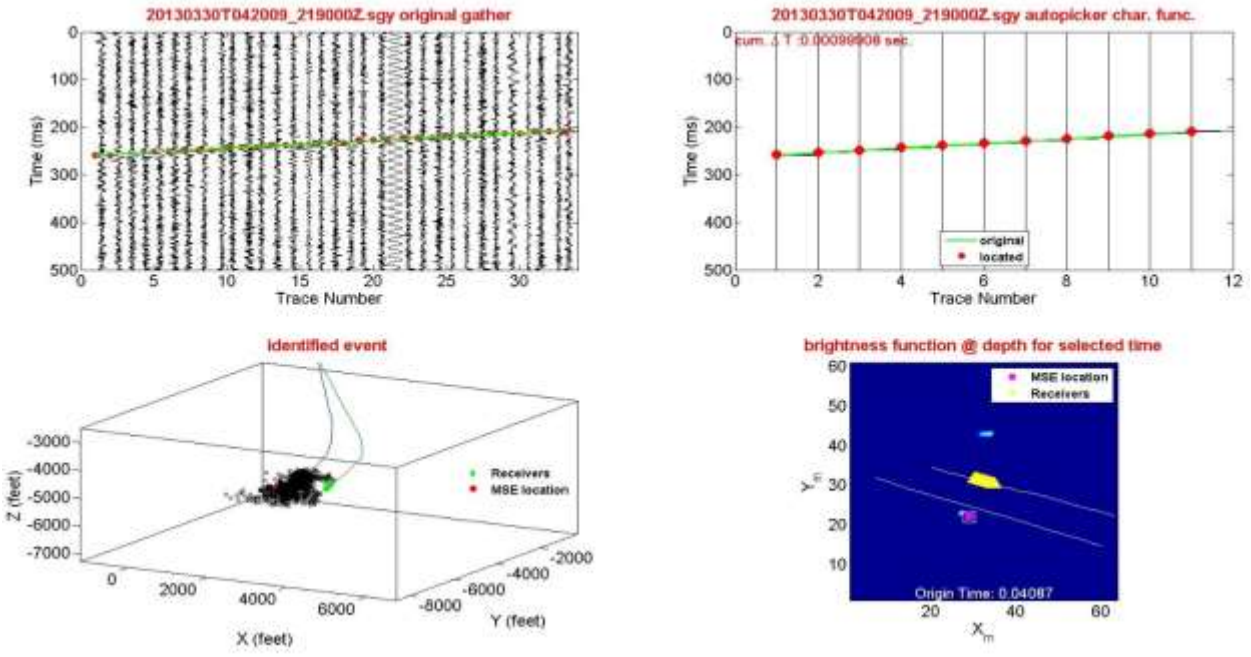

Figure 9: Wootton 10H stage # 8 sample event identified using GTI workflow.

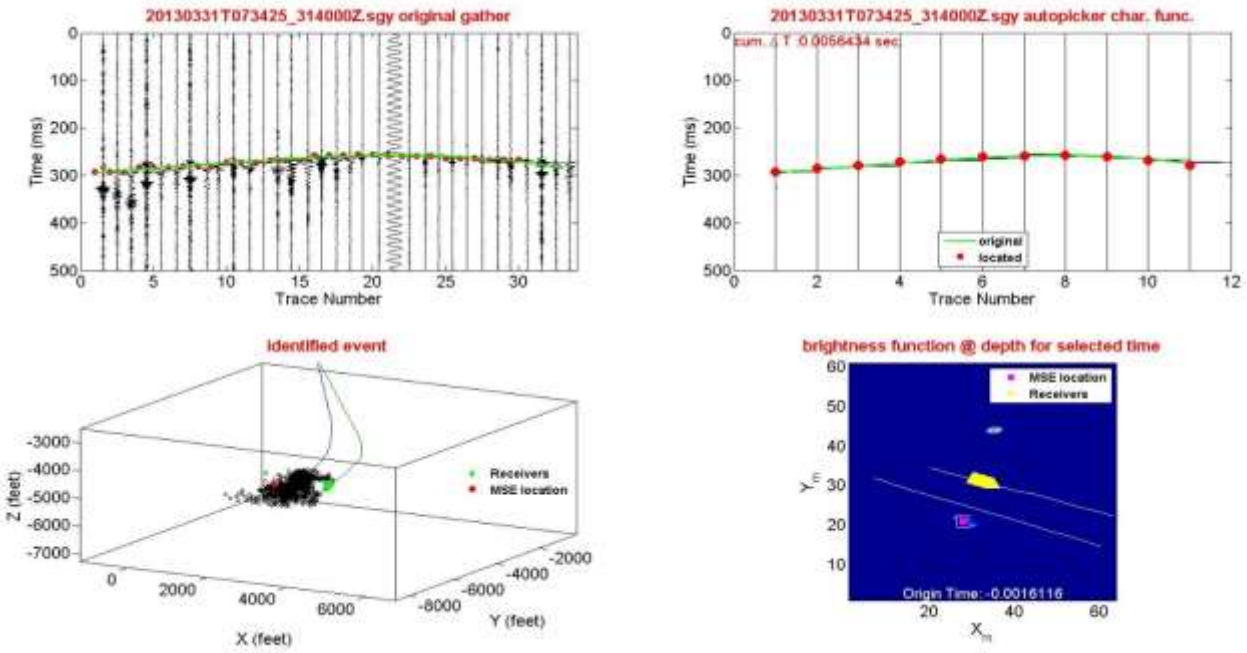

Figure 10: Wootton 10H stage # 8 sample event identified using GTI workflow.

A source-scanning algorithm and p wave polarization information is used to calculate the event location. For the tested events (a total of 10 large magnitude events with high signal-to-noise were tested), we found reasonably good match between the two sets of locations for the same events. The range of mismatch between the hypocentral locations in terms of separation was from 26 ft. to 213 ft. We deemed these events to be close enough so as to validate the results available from Pinnacle. Using GTI workflow, we were able to identify many events which were absent from the catalog due to poor waveform characterization and missing phase arrivals. Figure 7, Figure 8, Figure 9 and Figure 10 highlight examples from 2 stages where such events were successfully characterized.

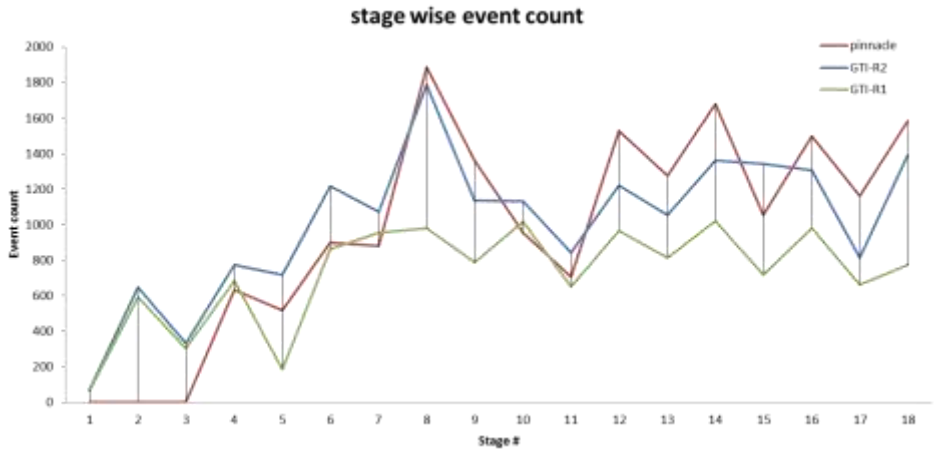

Figure 11: Good match between total events detected by Pinnacle and those by GTI.

The mismatch we observed was probably a result of velocity model accuracy as the GTI workflow superimposed a single model used in the original inversion by Pinnacle on a discretized grid (100 ft. cell size) for imaging workflow. The source scanning algorithm used by GTI searches within all available grid points for the best possible Δt (travel time difference b/w P & S wave) match and at the same time, it tries to maximize the "brightness function" which is a measure of energy associated with each identified event. Both these parameters are closely related to the actual picks and their accuracy. Discrepancies here can easily lead to errors. Figure 11 shows the comparison of stage wise events as detected by Pinnacle and from GTI workflow.

"b-value" analysis

While b-value [1] analysis is typically associated with earthquake seismology, in recent years, some research groups have tried to identify the potential use of b-value as a tool to better understand the seismicity and isolate outliers (such as possible fault activations) or stress regime changes both spatially and temporally (such as work on seismicity correlated with brittleness [2] and relation between tress regimes and b-values [3]). The attribute "b-value" is based on the original Gutenberg-Richter relationship which proposes a semi-logarithmic relationship between the number of events (N) belonging to a particular magnitude scale or higher (M). This relationship is as follows:

$$log_{10}N = a - bM$$

Figure 12 shows the overall analyses when we take into consideration all the identified events for each stage for Wootton pad well 10H which was monitored as part of our project. We can clearly observe the impact sensor positioning has on the total event count (as detected) as well as their impact on the magnitude of completeness (M_C) at which the relationship starts to develop. Here, stage 6 at lateral offset from recording geophone array leading to lower event count. This is demonstrated through comparisons with similar distribution for stage 9 events which did not have any such offset.

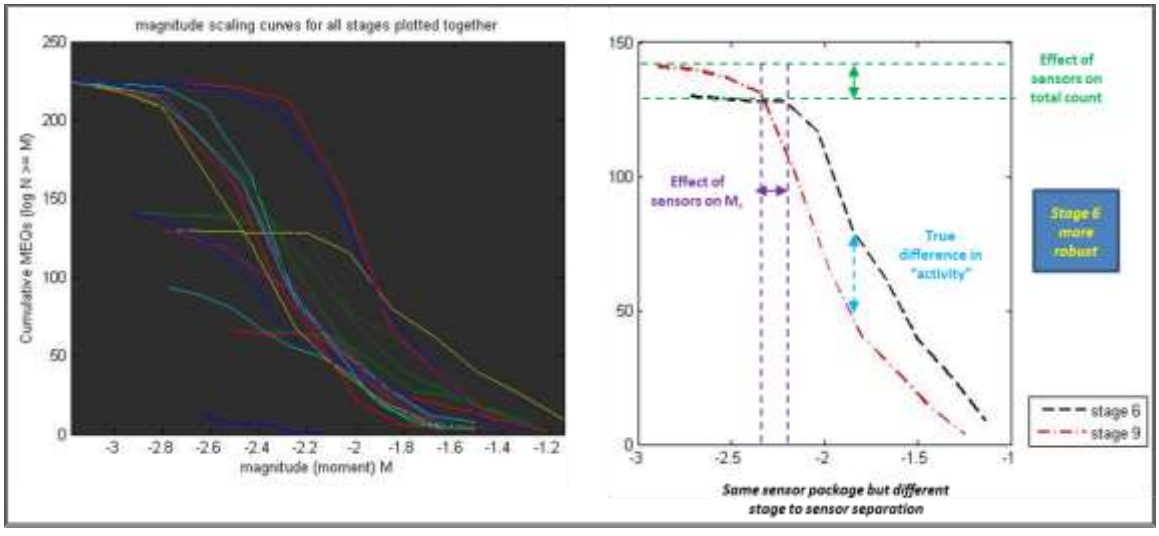

Figure 12: Stage wise b-value mapping showing that event count itself may not be adequate to judge a stage.

We carried out b-value analysis in both space as well as time to understand the behavior of the microseismicity across stages. We carried out this analysis using the catalog provided to us by Pinnacle and made some possible interpretations with respect to possible failure modes as well. Figure 13, Figure 14 and Figure 15 show examples of the said interpretation based on the temporal microseismicity distribution for two of the stimulated stages.

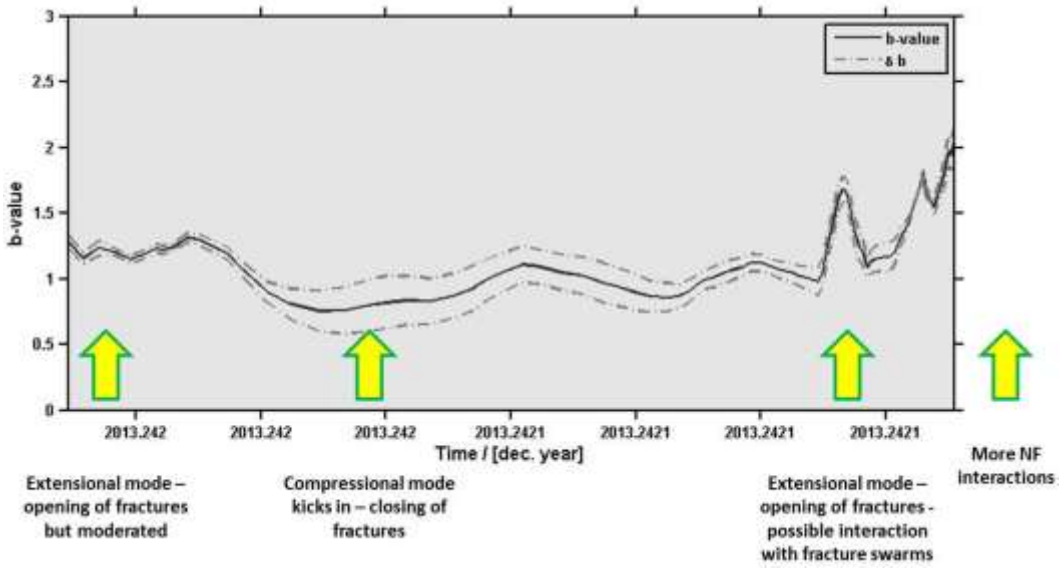

Figure 13: Temporal b-value analysis of events observed during stage 6 stimulation. Based on the behavior of the attribute at different periods during the stage, we can hypothesize the possible mechanisms.

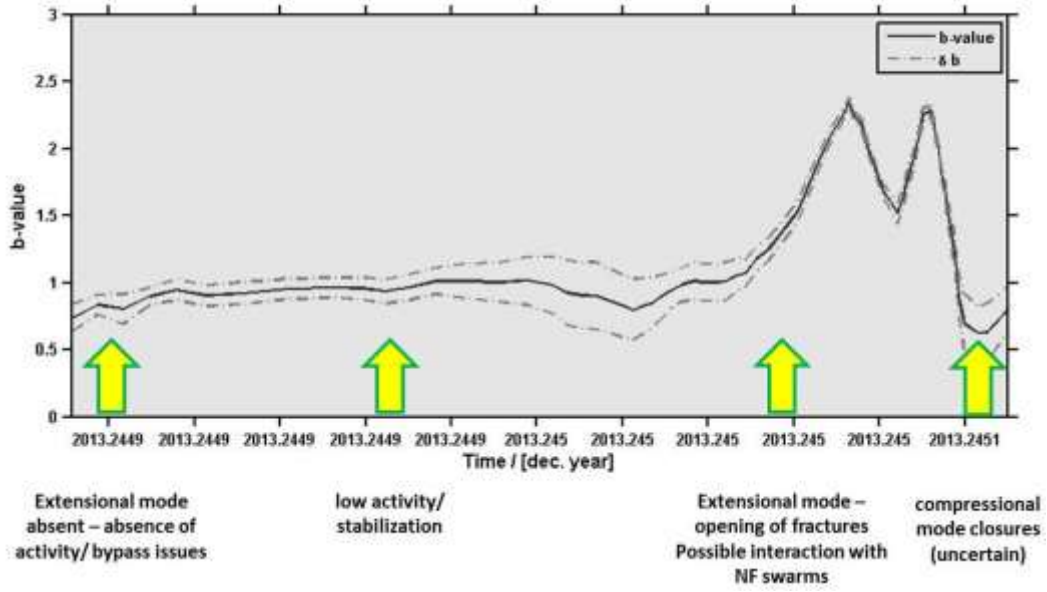

Figure 14: Temporal b-value analysis of events observed during stage 12 stimulation. Based on the behavior of the attribute at different periods during the stage, we can hypothesize the possible mechanisms.

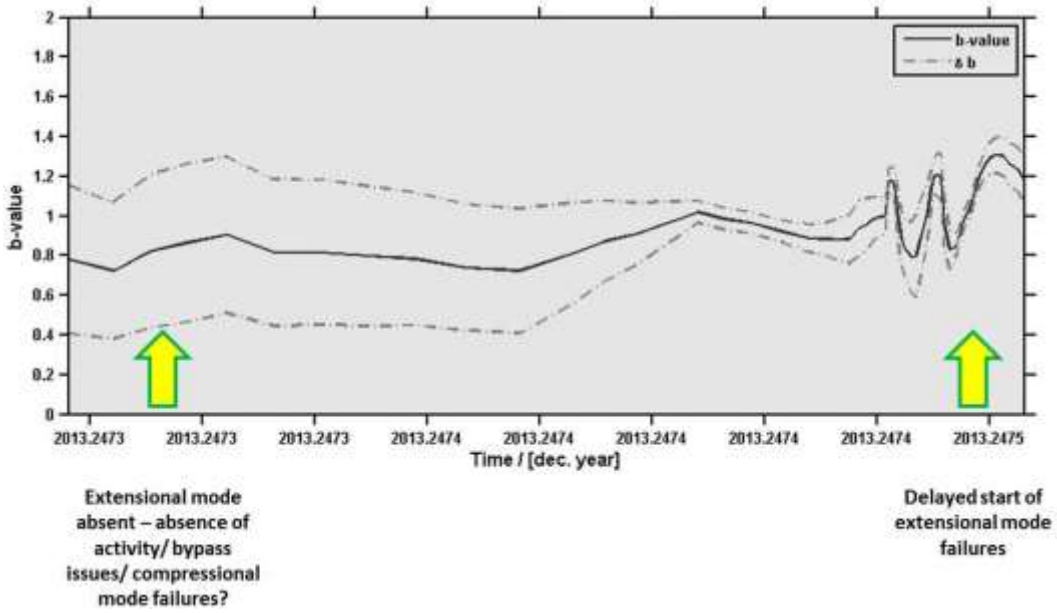

Figure 15: Temporal b-value analysis of events observed during stage 16 stimulation. Based on the behavior of the attribute at different periods during the stage, we can hypothesize the possible mechanisms.

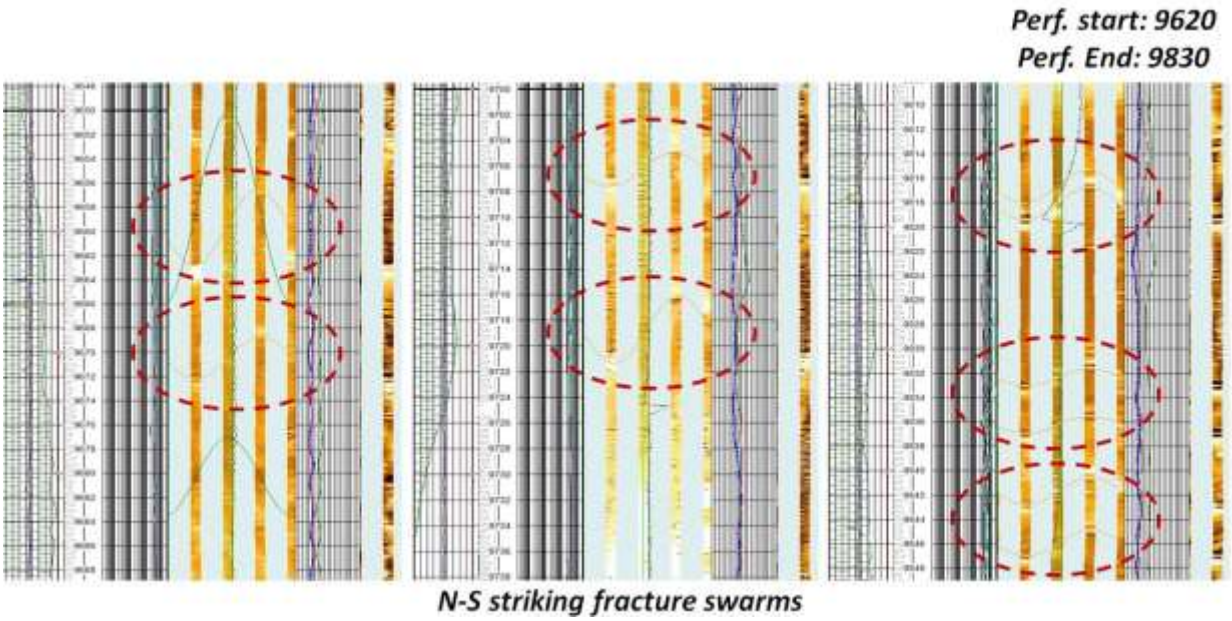

Figure 16: Sample of identified fractures for stage 6 from image logs (10H)

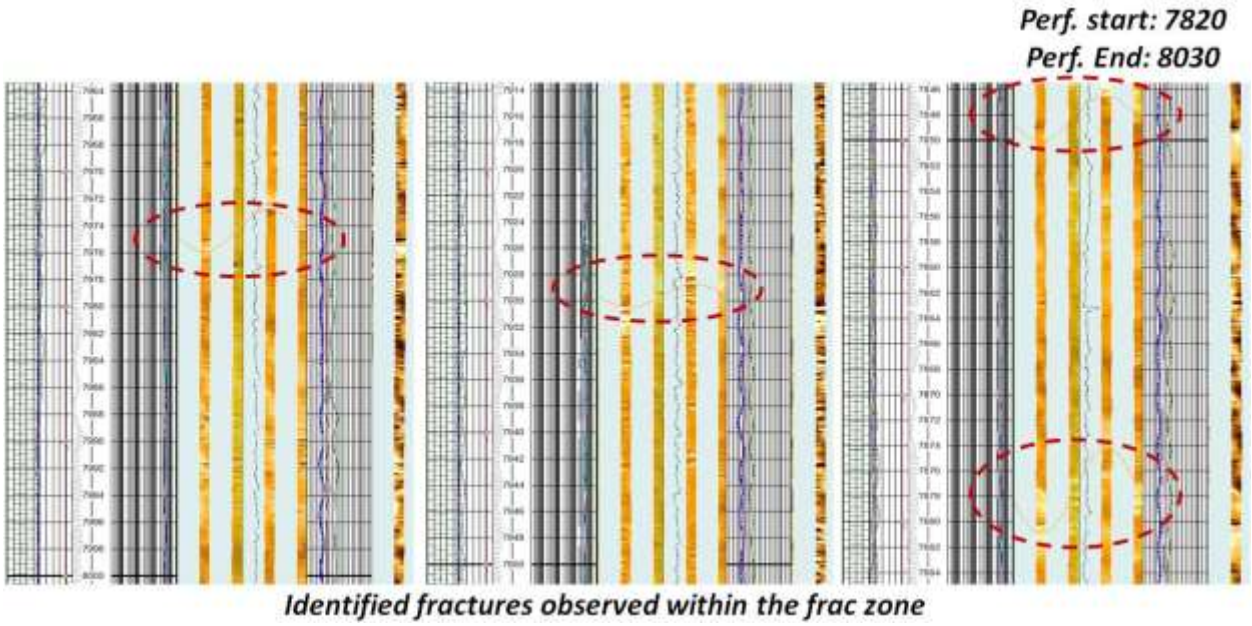

Figure 17: Sample of identified fractures for stage 12 from image logs (10H)

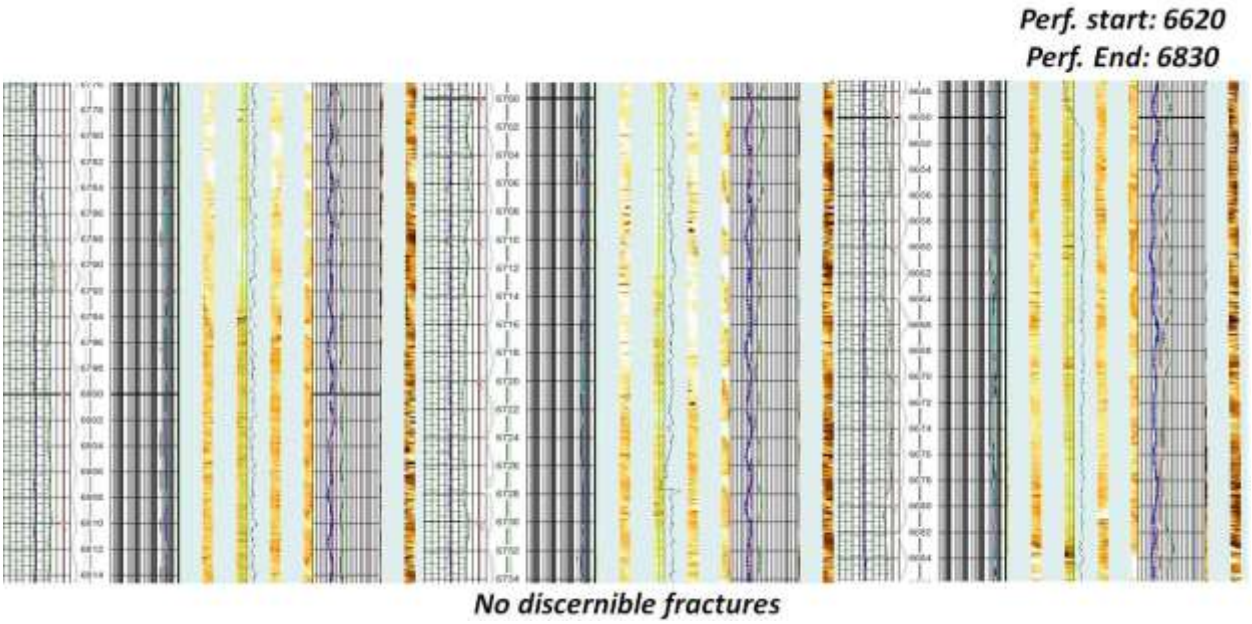

Figure 18: Sample of identified fractures for stage 16 from image logs (10H)

Based on independent data available to us in the form of image logs, we try to correlate the observations from seismicity with the image log analysis as a means to validate the hypothesized failure mechanisms with observed fractures/ swarms near wellbore. While this is fraught with uncertainty due to lack of information away from the wellbore and other aspects associated with the physics of interaction of injected fluids/ hydraulic fracture with natural fractures, we still observe reasonable correlation between b-value and interpreted fractures for many of the treatment stages. Figure 16, Figure 17 & Figure

18 show the interpreted fractured intervals from the image log for well 10H for stages referenced earlier. We note that for most other depth (MD) intervals, the fracture count is significantly lower and the observed temporal b-value maps show different trends. Figure 15 and Figure 18 show the temporal b-value distribution and image log extracts for stage 16 as an example of such behavior. Later discussions (Figure 27) will show a reasonably strong correlation between the cumulative b-value for events mapped for each stage and the interpreted fracture density.

With good quality seismic catalogs, there exists a possibility to identify spatial fracturing behavior during stimulation and use this information to interpret the prevalent stress regime during said treatment. Borrowing from earthquake seismology, b-values tending towards 2 may suggest fracture growth through 3D network of fractures influenced by presence of fluids. Values tending towards 1.5 are characteristic of failures associated with 3D distribution of network of fractures. Finally, values closer to 1 is associated with slippage along single plane of weakness along a predominant orientation [4]. Accurate moment tensor inversion solutions are needed to understand features and failure mechanisms associated with hydraulic fracturing. However, due to uncertainties associated with data quality and processing as well as acquisition geometry issues, the results can be inconclusive. Frequency-magnitude distributions [1] and spatial distributions [5] have theorized and demonstrated the power law behaviors which have been validated for thousands of datasets since then.

The b-value parameter is believed to be an indicator of the stress regime as the latter tends to influence the size of the rupture and as such, the magnitude of the event. D-values (fractal dimension) are a quantification of the shape of the event clusters thereby emphasizing rock weaknesses. Schorlemmer [6] showed that the value of b varies according to the tectonic stress regime. They found a b-value above 1 for normal (extensional) type of faulting (stress regime where the vertical stress is dominant), b around 1 for the strike-slip regime (with an intermediate vertical stress), and b below 1 for reverse (compressive) type of stress regime (the vertical stress is minimum). The statistical quantification of the spatial distribution of events is done by plotting the number of pairs of events separated by a distance smaller than a given distance in a log-log space. In our study we used an independent box counting technique. The D-value varies according to the clustering of the events. If D equals 0, all events occur at the same place (a point); if it's close to 1, events are aligned; if its value is around 2, events are distributed over a plane; and if it equals 3, then events are spatially uniformly distributed. Given the rock deformation happening in extensional and compressive stress regimes, a D-value around 3 is usually observed whereas D is found to be equal or less than 2 for strike-slip regimes. According to the significance of b and D values, these statistical coefficients can be used to infer the local stress regimes at the time when the corresponding MEQ's are occurring [3]. Indeed a b value over 1 coupled with a D value above 2 can reveal an extensional stress regime. If $b \approx 1$ and $D < 2$, the local stress regime is likely strike-slip. And $b < 1$ and $D > 2$ can indicate a compressive regime.

We use data from a prior RPSEA project [09122] due to a more complete catalog and more monitored wells for that project for our analysis. Figure 19 shows the evaluated b-value distribution for well D from the Troyer Pad experiment.

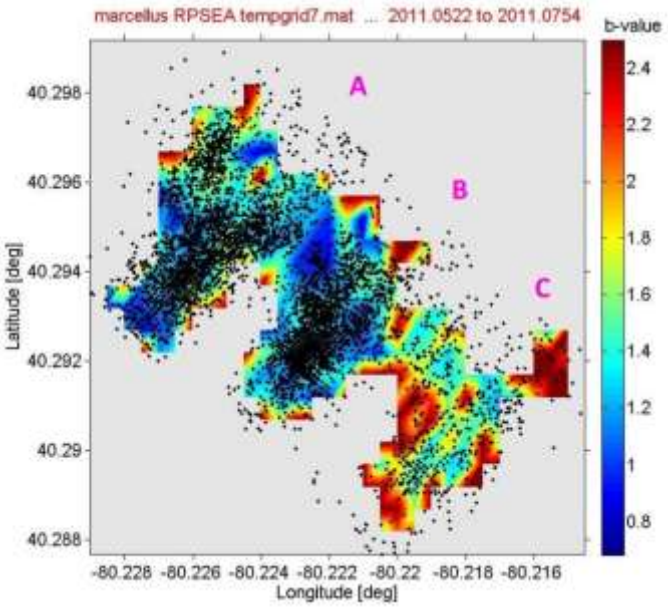

Figure 19: b-value map with actual event distribution.

When we compare the distribution for individual stages (Figure 20), we can observe a good correlation with results from post completion production logging data. Stage A shows higher values compared to stage B indicating more complex 3D fracture network associated with stage A and thereby, higher expected productivity.

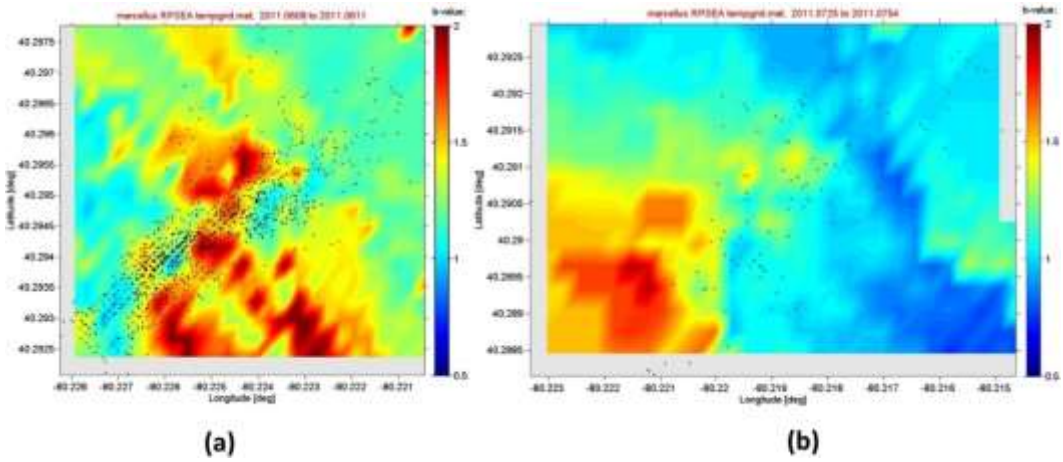

Figure 20: b-value map for (a) stage A and (b) stage B. We also see much higher event count for stage A compared to stage B.

Based on the b value and D value distribution, stress regime maps can be generated which are indicative of either normal faulting regime, compressive faulting regime or strike slip regime. We can generate 3D stress regime distributions (Figure 21) in this manner. Based on earlier discussion, the identification framework is as follows:

- Compressive:- $b < 0.9$ & $D > 2$

- Strike-Slip:- 0.9 < b < 1.05 & D < 2
- Extensional:- b > 1.05 & D > 2

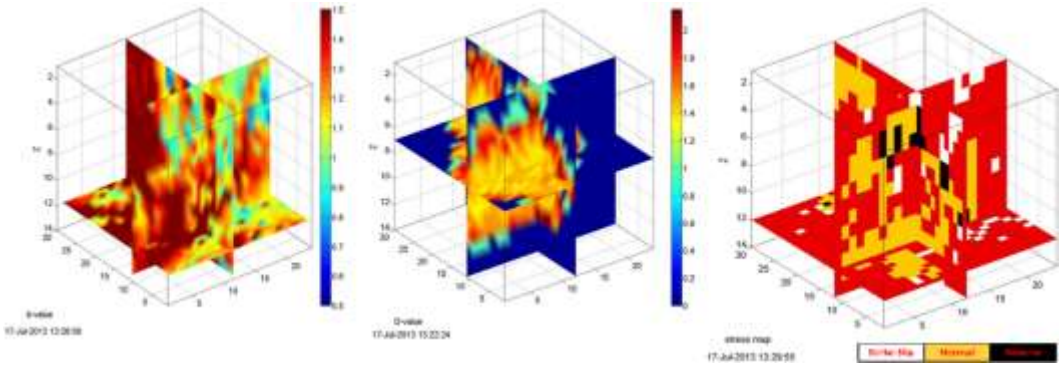

Figure 21: b-value, D-value and stress regime maps for a small 3D space along fracture stage.

The stress maps can be used to interpret fracturing process in terms of fracture growth and interaction with the reservoir. Figure 22 shows example of stress mapped for one of the stages and a particular depth range. For most stages, we predominantly see extensional failure along most of the stimulated zone. We do see some strike slip and compressional failures but they seem to congregate far field. This makes sense since far field stress perturbations can cause strike-slip failure along pre-existing natural fractures. The distribution also helps understand where we probably have more natural fractures and associated reactivations as well as potentially abnormally stressed zones within the reservoir. From Figure 22, we see highly stressed reservoir and associated strike slip and compressional failures on one flank of the well compared to the other. This could be due to one flank having already fractured stages nearby from the neighboring well of the Troyer pad compared to the other flank where we did not have any fracturing in the neighbor yet.

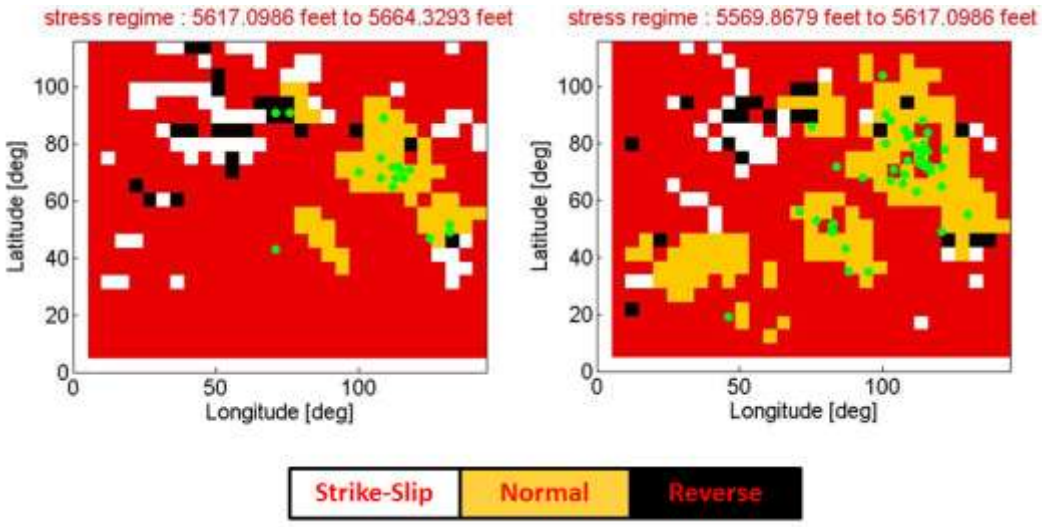

Figure 22: Stress regime mapped at two depth intervals for one of the stages from well D. Note highly stressed zone showing strike slip and compressive failures towards one flank of the well.

Correlating "b-value" with modified "Nolte-Smith" approach

Analyzing pressure data as a means to understand treatment behavior has been a part and parcel of the oil and gas industry for many decades now. Pressure data can help identify fracturing behavior, proppant transport issues, screen out situations, limited entry calculations, etc. to name just a few of its uses. However, with the increasing use of multi-stage hydraulic fracturing treatments, many of these traditional techniques no longer hold validity and newer techniques are considered desirable for improved treatment diagnostics. In this paper we consider a recently proposed diagnostic technique which builds upon a very popular real-time fracturing analysis technique and demonstrate the utility as well as pitfalls associated with using such techniques.

Pressure Data Analysis

Simple fracture models were proposed by Perkins and Kern [7] who suggested that the fracturing pressure at the wellbore should be a power function of treatment time (Eq. 1) with a large value of exponent indicating better fluid containment within developing fracture.

$$p(t) \propto t^{e} \tag{1}$$

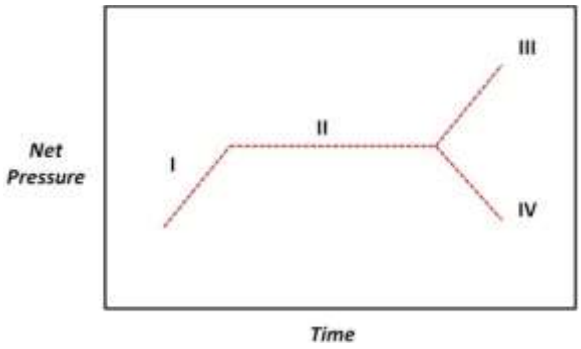

Figure 23: Nolte-Smith Interpretation Guide (log P_{net} vs. log T). Mode I indicates constrained height with unrestricted extensional growth; Mode II indicates Stable growth; Mode III indicates restricted extension or screenout conditions; Mode IV indicates unstable fracture height growth.

This and other work by Nordgren [8] formed the basis for real time completion analysis technique as proposed by Nolte and Smith [9]. They concluded that fracture propagation may follow one of four predefined modes based on the slope of net pressure plotted against time as shown in Figure 23. The basic power law equation guiding the propagation of hydraulic fractures is given as follows:

$$\log(p - p_{closure}) \propto e \times log(t) \tag{2}$$

Recent proposals include modifications to the original Nolte-Smith approach to take into account intermittent nature of fracture propagation and the well-known phenomenon of natural and hydraulic fracture interaction during treatment in shale plays [10][11]. Developing upon the power function defined by Eq. 1, and considering the reference time (t_i) for fracture growth initiation, we have:

$$p - p_i = C(t - t_i) \tag{3}$$

$$(t - t_i)\frac{\delta p}{\delta t} = eC(t - t_i)^e \tag{4}$$

$$(t - t_i)\frac{\delta p}{\delta t} = e(p - p_i) \tag{5}$$

Based on Nolte's generalization [12] for the bounds applicable on Eq. 1 for non-Newtonian fluids, we expect the exponent to range close to 0.25. If the fracture is dilating, the exponent will have a value close to 1. If the growing hydraulically created fracture interacts with natural fracture swarms, we expect rapid loss of fracturing fluid into the natural fracture system with the pressure behavior to be similar to fast leak off scenario (Figure 23, Mode IV) provided the pressure is stable or increasing. At the same time we understand that as soon as pressure drops due to such fluid loss, the fissures tend to close as it drops below the stress holding them open. However upon closure, the pressure starts to rise again and there is a corresponding opening of closed fissures. This opening-closing cycle should produce rapid fluctuations in the exponent as an indicator of natural fracture interaction during treatment as will be shown later.

This modified Nolte-Smith approach with varying reference time has been detailed by Pirayesh and others [10]. We use the same approach to estimate time variant exponent 'e' during treatment and use the results in our analysis. The calculations involve evaluating the exponent and constant at each point of time (during treatment) and then integrating the results from the reference to the current time.

$$e_t = \frac{dp/dt}{(p_n - p_i)/(t_n - t_i)} \tag{6}$$

$$c_t = \frac{p_n - p_i}{(t_n - t_i)^{e_t}} \tag{7}$$

$$E = \frac{1}{(t_n - t_i)} \int_{t_i}^{t_n} e_t dt \tag{8}$$

$$C = \frac{1}{(t_n - t_i)} \int_{t_i}^{t_n} c_t dt \tag{9}$$

Next we can estimate BHP by using the E & C values and identify the error from the actual BHP value available either through downhole pressure instrumentation or surface pressure data corrected for downhole conditions.

$$BHP_{est} = p_n + C(t_n - t_i)^E \tag{10}$$

$$\varepsilon = |BHP_{est} - BHP_{calc.}| \tag{11}$$

If the calculated error mismatch, ε, is higher than a predefined threshold, the initial reference point (t_i) is shifted to the current evaluation time. This provides us with a varying value for exponent e for the entire treatment and this can then be used for our diagnostic interpretations. As an example, Figure 24 shows pressure match obtained for a reference stage and the error in evaluation. We note that for this analysis, we used a threshold limit of 5 psi in order to obtain a close match between the estimated BHP and the calculated BHP. We note that it is preferable that we use downhole pressure data instead of calculating BHP from surface measurements. The potential pitfalls of using BHP calculated from surface data compared to downhole measurements will be looked into later on.

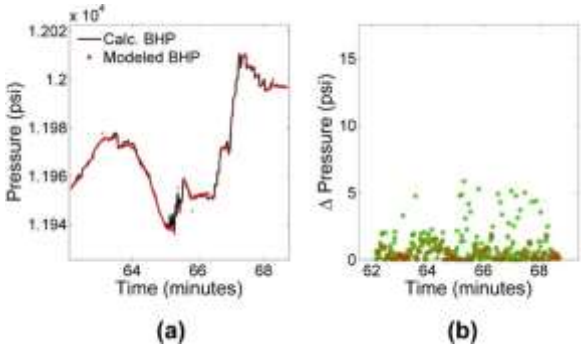

Figure 24: (a) Comparison of calculated BHP and estimated BHP (Eq. 10) and (b) observed ΔP mismatch for a short window extracted from completion data for a sample hydraulic fracturing stage.

After validation of adequate accuracy in the net pressure prediction, the exponent variability with completion time can be interpreted as required. Figure 25 shows the variability of exponent 'e' for the same treatment data subset shown earlier and we can clearly identify those sections of the treatment where we either had Mode I, Mode III or Mode IV fracturing based on the distribution of the exponent values. We observe that there is significant interaction with natural fractures and we also observe that towards the end of the period in question, extensional growth of the fracture network occurs with fluid injection. The exact range used for the zones indicating the three modes are: -1.00 to -0.10 for mode IV; 0.10 to 0.30 for Mode I and 0.75 to 1.00 for Mode III.

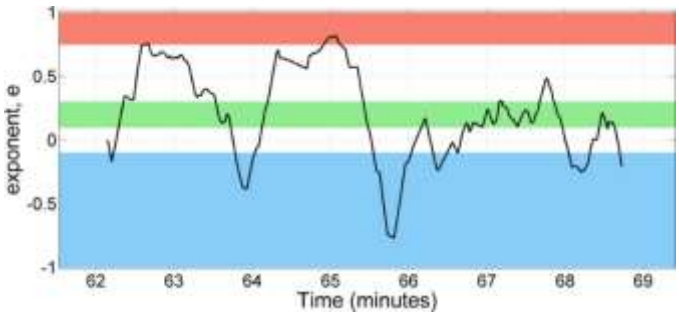

Figure 25: Modeled modified Nolte-Smith exponent 'e'. The red region indicates restricted flow and fracture dilation, green indicates unrestricted fracture extension and blue indicates natural fracture interactions or rapid height growth.

While real time diagnostic application has already been studied for multi stage shale gas completions by Soliman [11], we want to look at the predicted fracturing behavior and identify possible ways to characterize the completion effectiveness using the modeled parameters. This is achieved by defining certain diagnostic parameters computed for each stage. For the three modes (I, III and IV) identified, we calculate two separate diagnostic parameters as defined below:

$$DP_{1-S} = \sum_{t=1}^{t_{end}} \delta_{tt_S} |e| \, \Delta t \tag{12}$$

$$DP_{2-S} = \sum_{t=1}^{t_{end}} \delta_{tt_S} \, \Delta t \tag{13}$$

Here δ represents the Kronecker delta, tend represents the end of evaluation period and t_S is the set with the time stamps that correspond with the value of exponent 'e' falling within the three modes in question. Finally, Δt is the time step in seconds. The reason for using the above definitions for the diagnostic parameters $DP_{1\text{-}S}$ & $DP_{2\text{-}S}$ was that the extent that the exponent 'e' stays within each modal region should provide an indication of how much extensional growth, dilatational growth as well as interaction with natural fractures occurs during completion.

Microseismic Data Analysis

We use b-value distributions as highlighted earlier for our analysis. While evaluating b-value, care should be taken to fit the data using maximum likelihood method [13]. Datasets with very few earthquakes should not be considered for analysis. Also, error in magnitude can cause significant uncertainty in the slope estimation as well as identifying the M_C (Magnitude of completeness). In our analysis, we assume that the errors in magnitude within our catalogs are negligible.

For local seismicity scenarios, variations in b-value can be attributed to reservoir heterogeneity, thermal gradients across the perturbed zone, applied stress through injection as well as other factors [14]. For induced fracturing, this relationship was originally observed by Scholz [15] and has been further validated in recent years [16] [17]. Finally, recent studies have also indicated some correlation between

observed b-value distribution and the local stress regime guiding rock failure [18] [19]. In general, when it comes to local or microseismicity, b values less than 1 are rare and represent compressive failure modes; b values close to one indicate strike-slip regime similar to observations during failure of faults (from earthquake seismology) and b values higher than 1 are indicative of extensional failure modes.

Data

We apply this technique on two separate wells from the Appalachian Basin (Marcellus shale gas play). Both the wells were completed as essentially dry gas wells with reasonable water cuts. The choice was based on the fact that both these wells involved microseismic monitoring during completion which was a necessary element of our analysis. Well # 1 located in northern Pennsylvania involved pumping of ~ 300,000 lbs. of proppant for each stage with a total of 18 stages. Well # 2 located in western Pennsylvania again involved pumping of ~ 300,000 lbs. of proppant for each individual stage with a total of 13 stages. Both completions were monitored by downhole sliding microseismic monitoring arrays placed in nearby horizontal observation wells. For b-value analysis, we used microseismic event catalogs generated by using standard P (compressional) & S (shear) wave travel time inversion approach. Production logs were run post treatment for both the wells and these are also used in our study. For Well # 1, we also have data from OBMI log and we also use the interpreted stage-wise fracture density from this log for our analysis.

Results

As stated earlier, we apply both these techniques; namely modified Nolte-Smith approach to fracture diagnostics as well as stage wise b-value mapping on the data from the two wells under study. For both wells, we generate the diagnostic parameters ($DP_{1\text{-}S}$ and $DP_{2\text{-}S}$) for each of the fracturing mode under study defined by subscript S (Mode I, III and IV). Based on the identified parameter values, we cross-correlate the same with available production log data (fractional gas flow) from post completion production logging runs. Figure 26 shows how the modeled diagnostic parameter results for Well # 1 correlate with observed stage wise productivity from production logs. We notice weak positive correlation for both mode I and mode IV results but no correlation with mode III results.

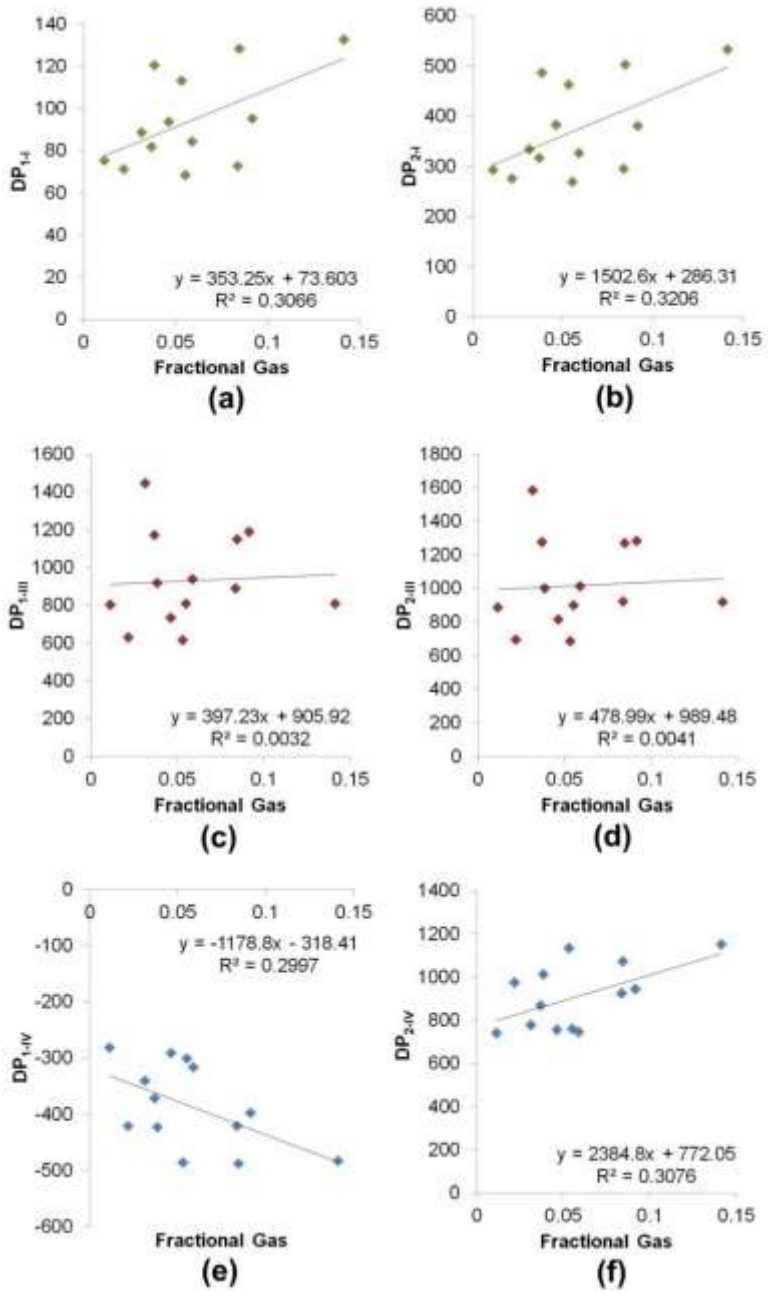

Figure 26: Production data (fractional gas flow) compared with extensional diagnostic parameters (a) ($DP_{1\text{-}I}$), (b) $DP_{2\text{-}I}$, dilatational diagnostic parameters (c) $DP_{1\text{-}III}$, (d) $DP_{2\text{-}III}$, natural fracture interaction diagnostic parameters (e) $DP_{1\text{-}IV}$ and (f) $DP_{2\text{-}IV}$ for Well # 1.

Figure 27 shows the same parameters evaluated for Well # 2 under study and their correlation with stage wise productivity. Once again, we observe weak positive correlation for both the mode I and mode IV parameters and no correlation whatsoever with mode III results.

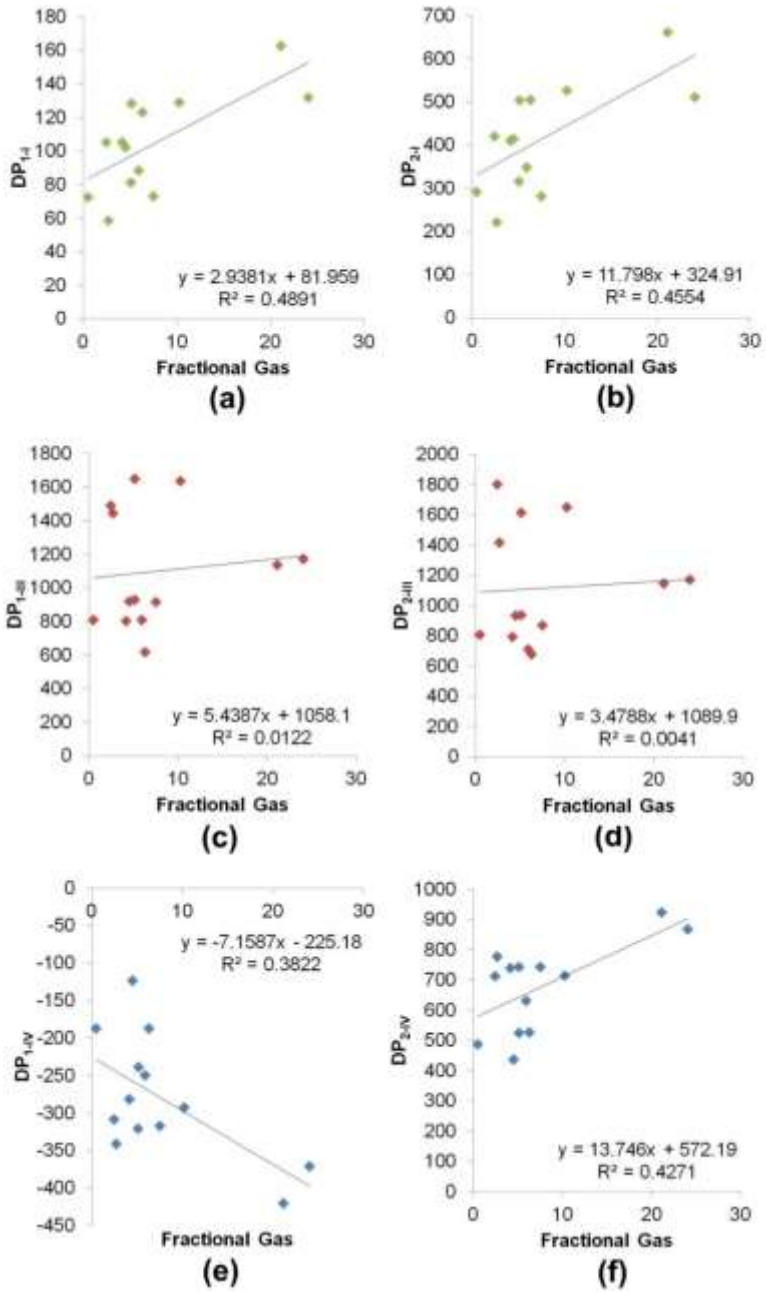

Figure 27: Production data (fractional gas flow) compared with extensional diagnostic parameters (a) ($DP_{1\text{-}I}$), (b) $DP_{2\text{-}I}$, dilatational diagnostic parameters (c) $DP_{1\text{-}III}$, (d) $DP_{2\text{-}III}$, natural fracture interaction diagnostic parameters (e) $DP_{1\text{-}IV}$ and (f) $DP_{2\text{-}IV}$ for Well # 2.

Since observations from both sets of analysis seem to validate each other, we can argue that this observation is non-unique and should hold for more completions. We do note that the correlations are weakly positive and may not signify much. However, in essence, these observations indicate that the productivity from any hydraulically fractured stage shows slight correlation with the extent of extensional fracture growth taking place during the treatment as well as any interaction with natural fractures observed during treatment. Moreover, we can clearly state that the degree of dilatational fracture growth

has no impact on the productivity of the completed zone. These observations are also intuitive as we would not expect fractures ballooning due to fluid fill-up to have any impact on productivity as any far field fracturing due to stress perturbation may not be contributing due to them being spatially isolated. Extensional growth and growth into natural fractures on the other hand should lead to more productivity due to higher fractured area through the connected hydraulically created as well as natural fractures.

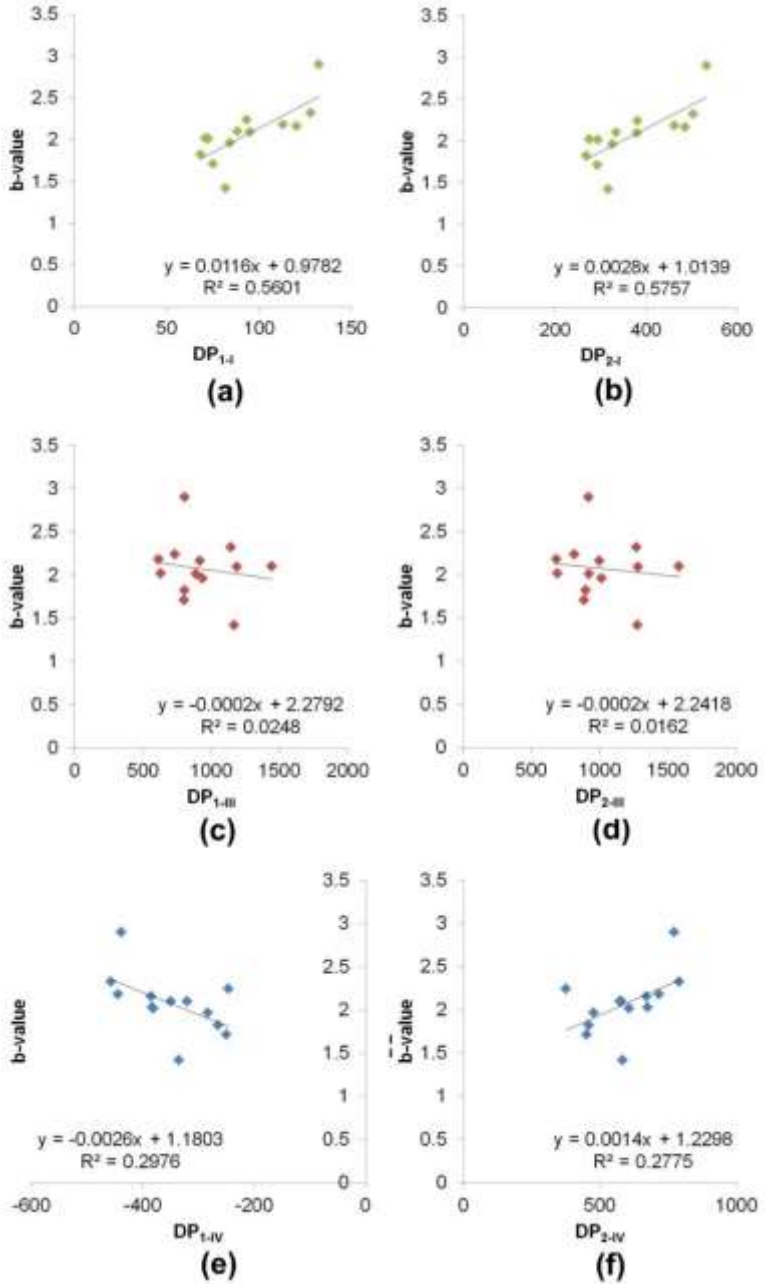

Figure 28: Microseismic derived b-value compared with extensional diagnostic parameters (a) ($DP_{1\text{-}I}$), (b) $DP_{2\text{-}I}$, dilatational diagnostic parameters (c) $DP_{1\text{-}III}$, (d) $DP_{2\text{-}III}$, natural fracture interaction diagnostic parameters (e) $DP_{1\text{-}IV}$ and (f) $DP_{2\text{-}IV}$ for Well # 1.

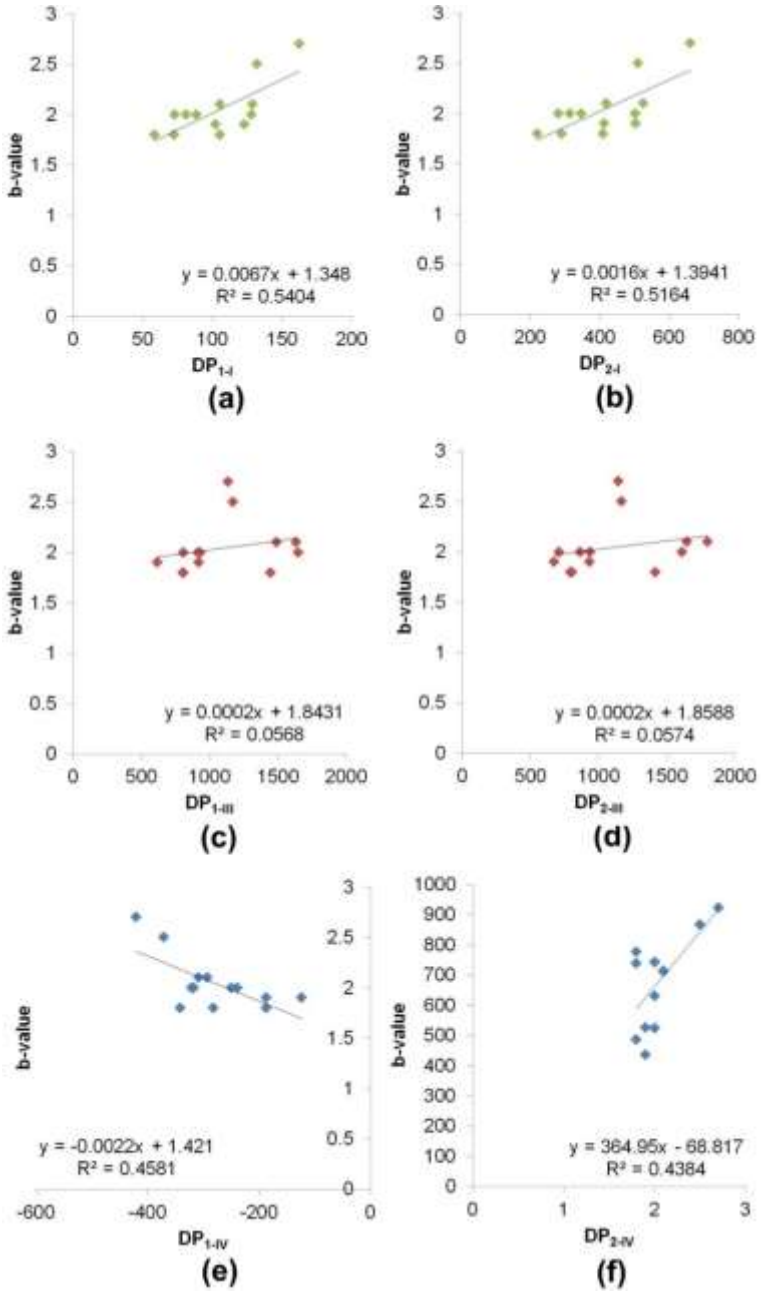

Figure 29: Microseismic derived b-value compared with extensional diagnostic parameters (a) ($DP_{1\text{-}I}$), (b) $DP_{2\text{-}I}$, dilatational diagnostic parameters (c) $DP_{1\text{-}III}$, (d) $DP_{2\text{-}III}$, natural fracture interaction diagnostic parameters (e) $DP_{1\text{-}IV}$ and (f) $DP_{2\text{-}IV}$ for Well # 2.

Next we look at the b-value analysis results and how they correlate with the modeled parameters shared above. Careful selection was made from the microseismic event catalogs to make sure that the analysis was valid including removing outliers. Those stages with very low event count were not considered in this analysis (stages 1 through 5 for well # 1). Finally fitting to identify slope was done using maximum likelihood technique as mentioned earlier. We understand that higher b values (and consequently higher fractal dimensions) are indicative of more complex fractured network or values

higher than 1 indicating extensional fracture growth [20]. In our analysis, for all stages studied, we found b-values close to or higher than 1. Any b-value close to or higher than 2 could be a result of microseismic data quality or could indicate fluid rich completions. Also, as observed from Figures 28 & Figure 29, b-value shows a much stronger correlation with extensional growth parameters compared to natural fracture interaction related parameters. Finally, b-value shows no correlation with dilatational fracture swelling related parameters.

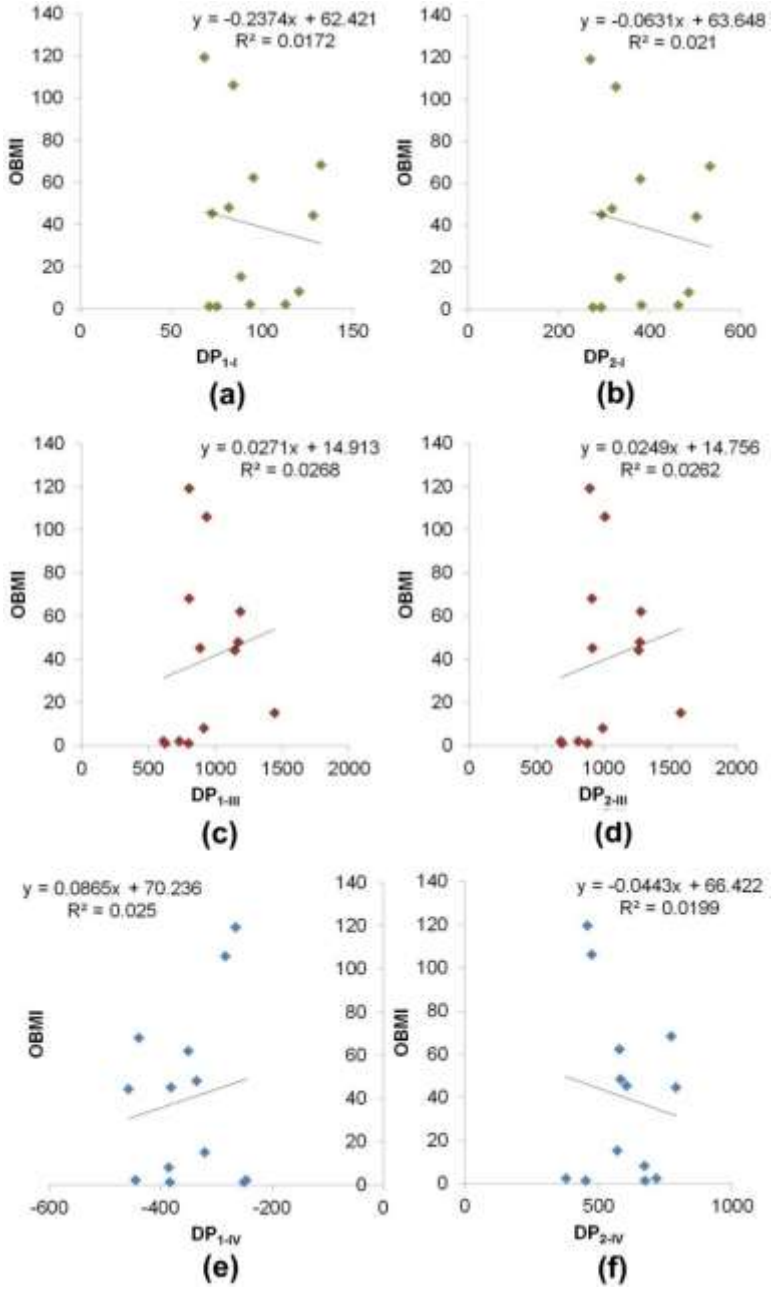

Figure 30: OBMI log derived fracture density compared with extensional diagnostic parameters (a) ($DP_{1\text{-}I}$), (b) $DP_{2\text{-}I}$, dilatational diagnostic parameters (c) $DP_{1\text{-}III}$, (d) $DP_{2\text{-}III}$, natural fracture interaction diagnostic parameters (e) $DP_{1\text{-}IV}$ and (f) $DP_{2\text{-}IV}$ for Well # 1.

This is again expected as extensional growth through fracture propagation should create extensive three dimensional microseismicity and so should interaction with natural fractures. However, we note that with fluid filling up dilating fractures, seismicity will be limited in size (small shear tip or far field failures). Next, we look at correlation with OBMI log in Figure 30. We can clearly see no apparent correlation between the derived fracture density from OBMI logs and the modeled diagnostic parameters. This is expected since the OBMI logs provide a snapshot of wellbore or near wellbore fracturing and cannot estimate the presence or absence of actual fractures in the formation. Eyeballing the modeling results using the pressure data can provide indicators to make judgement calls by identifying stages with significant interactions with natural fractures during treatment. Figure 31 shows sample stages from Well # 1 showing the modeled exponent. We validate the observations by comparing the corresponding b-values as shown in Figure 32.

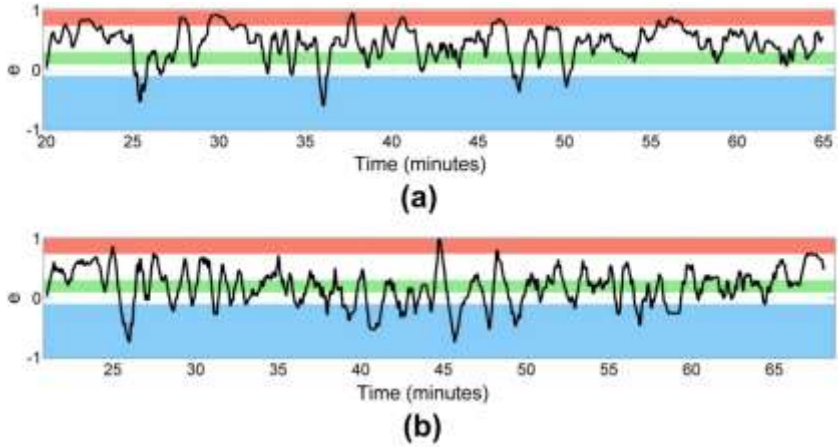

Figure 31: Modeled exponent 'e' for two stage treatments during proppant injection phase. Subplot (a) shows lower productivity for stage 'A' compared to subplot (b) showing productivity for stage 'B' from production log data.

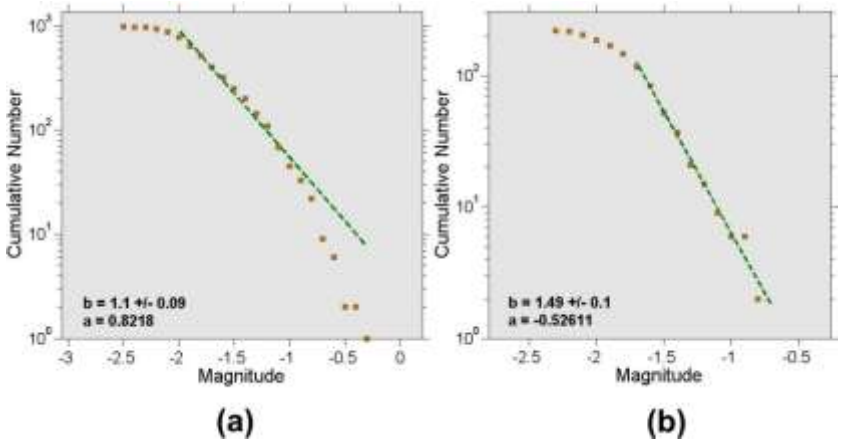

Figure 32: Results from b-value analysis for (a) stage 'A' and (b) stage 'B' using Maximum Likelihood approach.

As observed from results for the two stages shared in Figure 31, stage corresponding to Figure 31a (stage 'A') shows relatively lower degree of interactions with natural fractures. Moreover significant sections of the treatment show dilatational behavior compared to stage corresponding to Figure 31b (stage 'B'). These observations are validated by actual observations from production log data with stage 'A' showing 1.135% gas flow contribution compared to 14.139% for stage 'B' from post completion production log. Furthermore, the corresponding b-value evaluation shows significant differences with stage 'B' showing a higher value (1.5) indicating higher fracture complexity compared to stage 'A' (1.0).

Treatment artifacts such as screenout can also be evaluated on the basis of "e" behavior and correlated with geophysical data. Figure 33 shows a composite with one of the stages completed for Well # 1. We can clearly observe dilatational characteristics close to the transition from mesh # 100 proppant pad. The fluid is not able to go through extending fractures of natural fractures easily and no new fractures are being formed. The same is validated by the distribution of "e" for that duration. Correlation with seismicity (temporal event distribution) shows a lack of seismicity during this period as well. This is expected as any seismicity associated with extensional failure will be relatively smaller in magnitude compared to shear or strike slip failure.

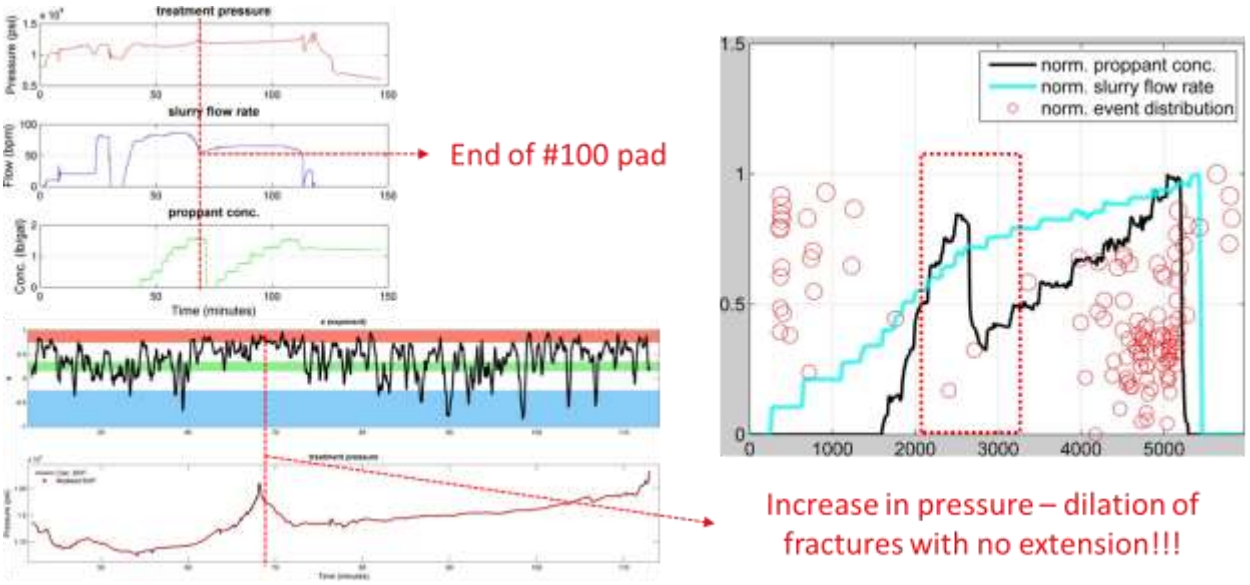

Figure 33: Diagnostic using modified Nolte-Smith and observed seismicity during completion of a representative stage from Well #1.

Pitfalls in Analysis

We need to carefully consider the limitations and assumptions made in our analysis and highlight adequate caution required when conducting similar analysis. Before looking into the models themselves, the most important constraint with any diagnostic methodology is the actual data quality collected from the field and used in analysis. With pressure data, downhole pressure measurement is extremely rare in long multi-stage horizontal hydraulic fracturing programs due to cost issues. Downhole data is necessary as assumption of net pressure being equal to the calculated BHP can be highly flawed due to uncertainties

in models used for these calculations including corrections for air entrainment, frictional losses and impact of proppant loads. With microseismic data, errors in inversion, limitations of array design, deployment issues, etc. can significantly alter the overall quality of the microseismic catalogs and thereby undermine any interpretations. When it comes to the actual physical fracture model used, we need to highlight that it is by very nature highly simplistic. Moreover, the variability in exponent, though very useful, can be interpreted in multiple ways. As an example, negative exponent values could mean natural fractures as suggested in this work. But at the same time, they could also mean uncontrolled rapid height growth into lower closure stress zones (particularly with decreasing pressure) or interaction with local faults. Similarly, with b-value analysis, sometimes the data artifacts require manual mapping of the slopes resulting in significant non-uniqueness in the selected values. Therefore we believe that for proper utilization of this technique, more robust analysis of data as well as analysis of other information in addition to those shared in this work may be necessary. All of these considerations will influence our future work with new wells.

Conclusions

Novel completion diagnostic techniques such as those applied in this study provide valuable tools which can be very useful in helping understand the behavior of long lateral multi-stage hydraulically fractured wells. Judicious selection of data, analysis methodology and a careful consideration of potential pitfalls is also necessary in order to add value to any such diagnostic workflow. In this study, we have demonstrated two ways of identifying potential fracture growth mechanisms available today and have tried to correlate the two to highlight a reasonable match between the results as per our observations. However, more careful analysis of methods as well as better models are deemed necessary before any such technique can find widespread use within the fracking industry. This is because of a high degree of uncertainty and non-uniqueness possible in the interpretations. The issue of frictional pressure heads and non-availability of downhole monitoring data is the primary constraint towards successful validation and application of this technique.

Observed interference and other properties:

Based on the interpreted and mapped properties discussed in the previous sections, we also identified if we could observe any pressure interference during completion of well 12H using a pressure transducer fitted on well 10H. Figure 34 shows a 3D distribution of many of these interpreted properties across wells 10H and 12H. We observe two perforated zones having “positive” interference on well 12H and the nearby zones along well 10H show high fracture density as interpreted from image logs providing an understanding of the underlying flow behavior as well as observed production. As per above observation, we expect a strong communication close to this zone due to higher fracture density leading to potential communication pathway between the two wells. With an inter-well separation of around 1000 ft., it is plausible that some of the hydraulic fracture pathways do communicate between the two wells. We also observe high production along two of these zones (one within well 10H and the other in 12H) indicating preferential flow behavior despite hydraulic connectivity which could be due to drawdown conditions in place. Certain sections of the reservoir may have higher natural fracture presence compared to others (natural fracture swarms) and these may have had an impact on observations.

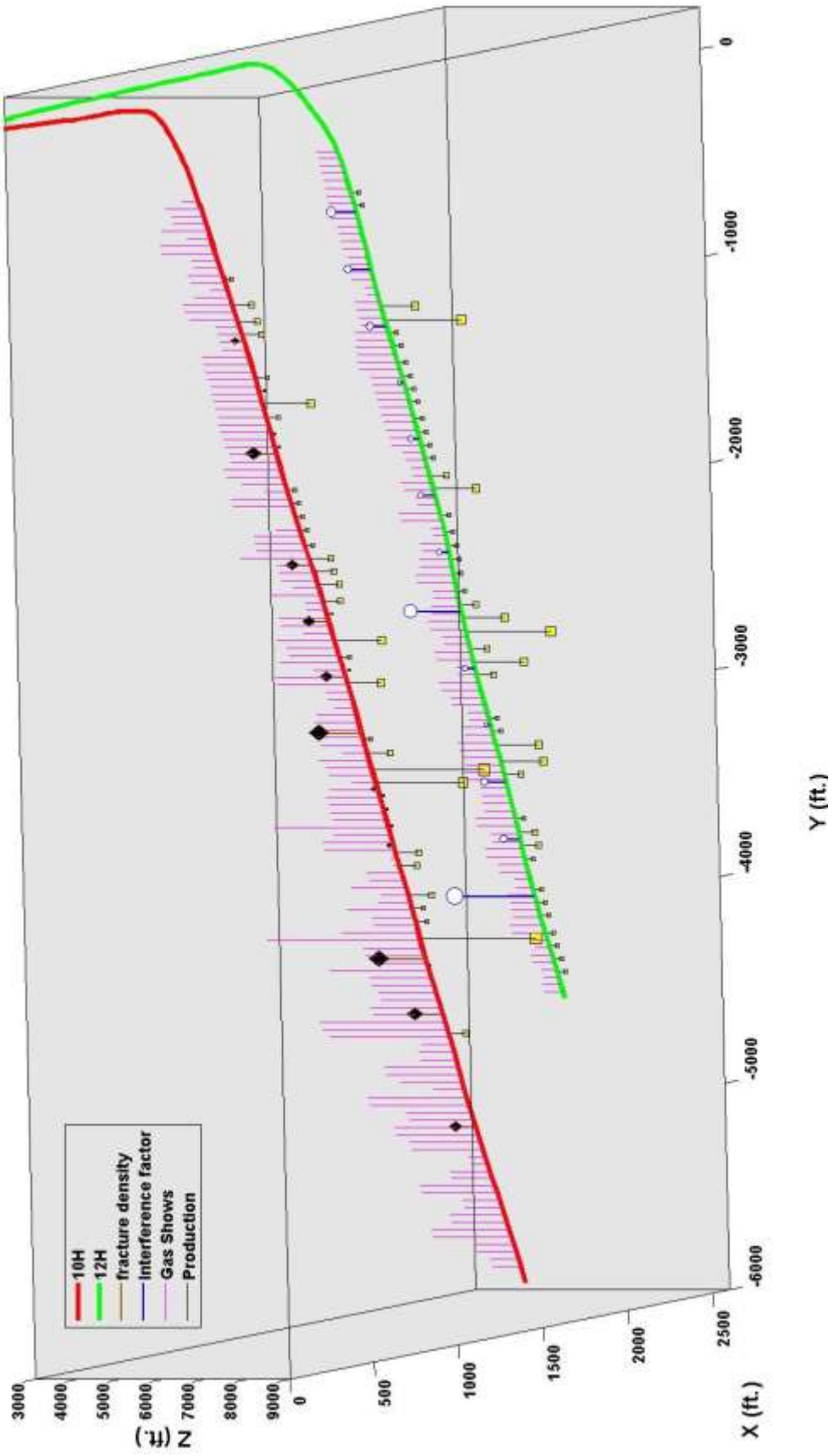

Figure 34: Observed fracture density (OBMI log), interference factor, mud log gas shows and production log data (early period) to detect potential correlations.

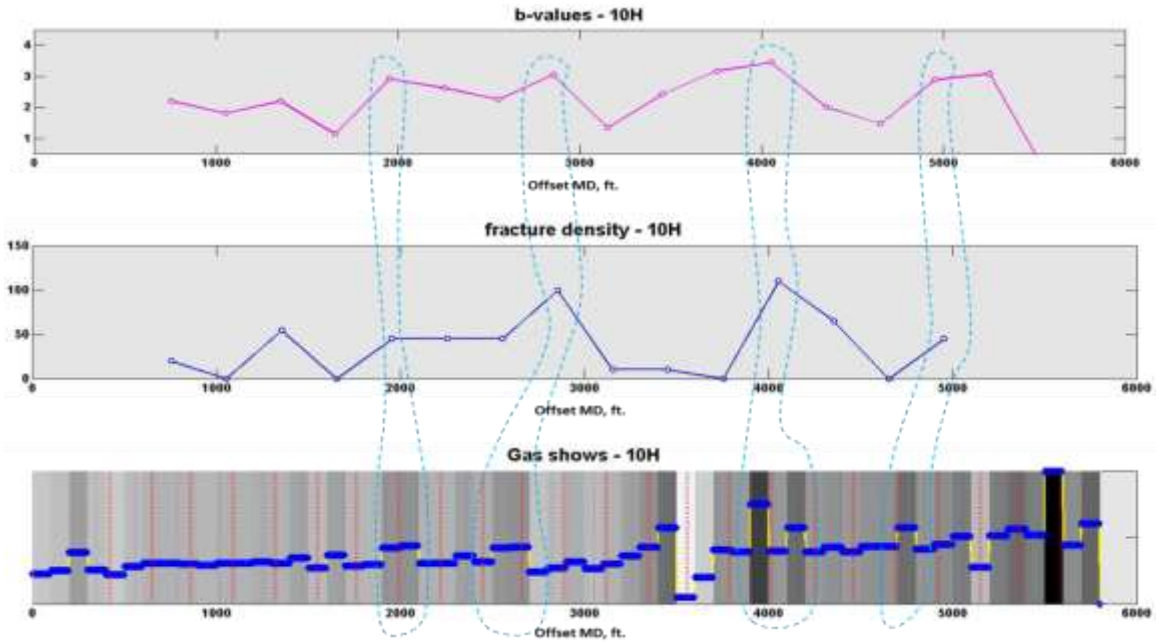

Figure 35: b-value (from seismicity), fracture density (from OBMI) and mud log gas shows correlated for well 10H.

Finally, we looked into the mud log gas shows and tried to identify if they showed any correlation with other properties as measured along the wells (including OBMI logs). Mud log gas shows can show erratic behavior and do not always show strong correlation with other attributes due primarily to scale/ resolution issues as well as accuracy concerns. The gas shows were up-scaled so as to take some of these uncertainties into account. Figure 35 shows well 10H correlated with two separate attributes for a comparative analysis (fracture density from OBMI as well as b-value mapped for every stage). We observe reasonably strong correlation between the mapped properties within ±100 feet of each perforation cluster center (considering typical depth errors from mud logs) and the observed correlation suggests that mud log gas shows can be a valuable indicator of natural fractures. Moreover, strong correlation between measured b-values (and D-values not shared in this report) with fracture density observed from image logs provides a strong basis for the possible use of b-value maps as indicators of natural fracture presence. Correlations with early period production logs also show a reasonably strong correlation between observed gas cuts from production logs and observed properties along stage/ perforation clusters.

Long Period Long Duration (LPLD) events

Evidence of Long Period Long Duration events has been observed in the downhole microseismic data acquired for this project. We identified these events based on duration and waveform characteristics from raw datasets. We compared their waveform characteristics with standard microseismic arrivals as well as noise artifacts. Figure 36 shows examples of typical microseismic and tube wave arrivals for one of the stages from the Wootton Pad. We can clearly see that microseismic signals show body wave characteristics with distinct arrivals with high P-wave energy while tube waves show absence of propagation characteristics of traditional body waves. We also observe microseismic events to have a smaller period (~0.01 seconds) compared to tube waves (~0.02 seconds).

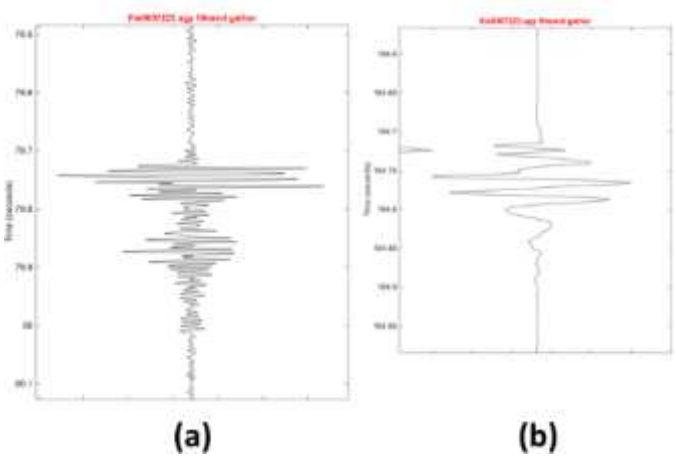

Figure 36: Typical (a) microseismic and (b) tube wave signals. Notice significant difference in waveform characteristics.

Figure 37 shows three examples of detected LPLD events with event duration varying anywhere from ~10 seconds to ~40 seconds.

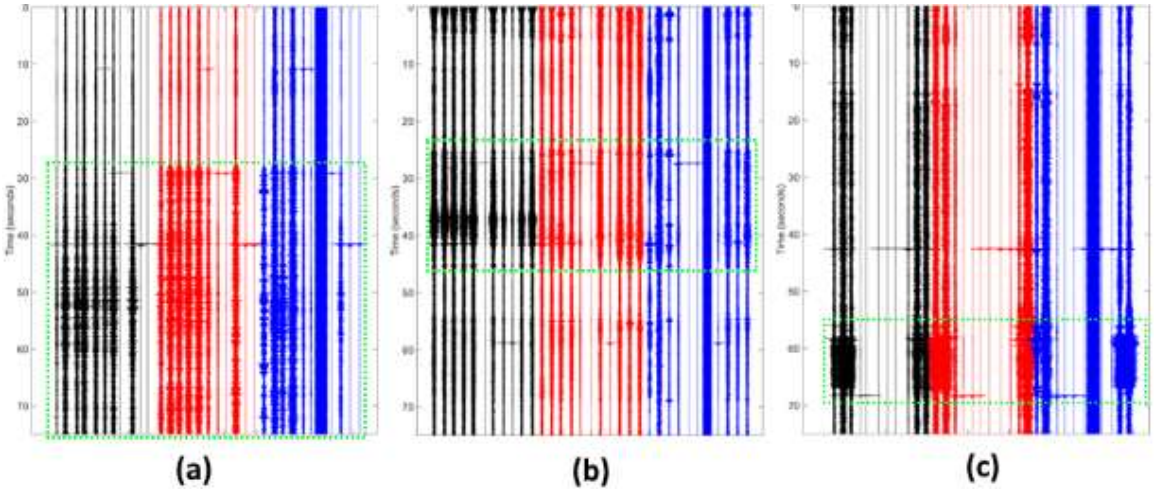

Figure 37: Typical examples of LPLD events observed from Wootton well 10H microseismic data.

The observed period of these LPLD events from Marcellus play was found to be in the range of 0.04 to 0.05 seconds. The period observed is quadruple that of typical microseismic events associated with this treatment. Within each LPLD wavetrain, we observe interpreted arrivals which though broadly similar, show subtle differences. This ties with observations made by Das & Zoback [21]. Moreover, the observed period matches well with other reported values from Pembina Cardium formation (Central Alberta) as reported by St. Onge [22] as well as for Marcellus shale (0.03 to 0.06 seconds) reported by Das & Zoback [21]. A comparison between the frequency spectrum for a typical LPLD event and a microseismic event (Figure 38) shows that typical microseisms show lower amplitude levels compared to LPLD events and they release higher energy as well (by factor of 10). Note that in Figure 38, we have only analyzed 1 second of data for the LPLD event and so the cumulative moment will be much higher for this event. We also note that with most LPLD events, we have observed many interbedded and straddling microseismic

events. A rigorous analysis is required to know if these originate from a location close to where the LPLD events originate.

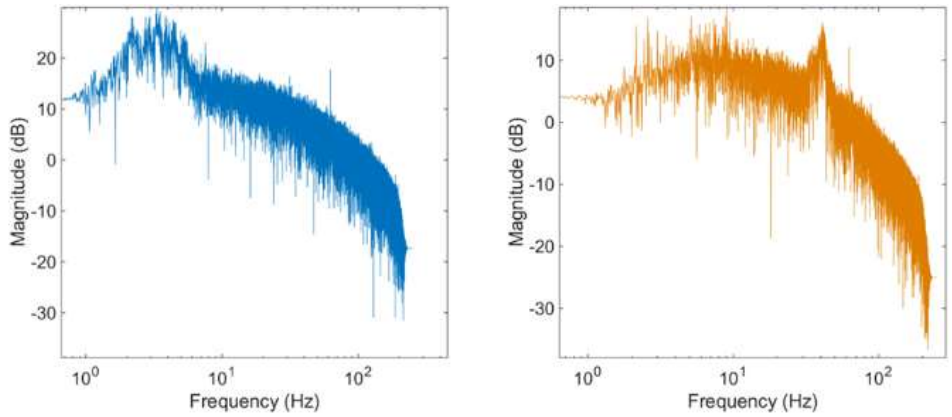

Figure 38: Comparing power spectrums of typical microseismic and LPLD events.

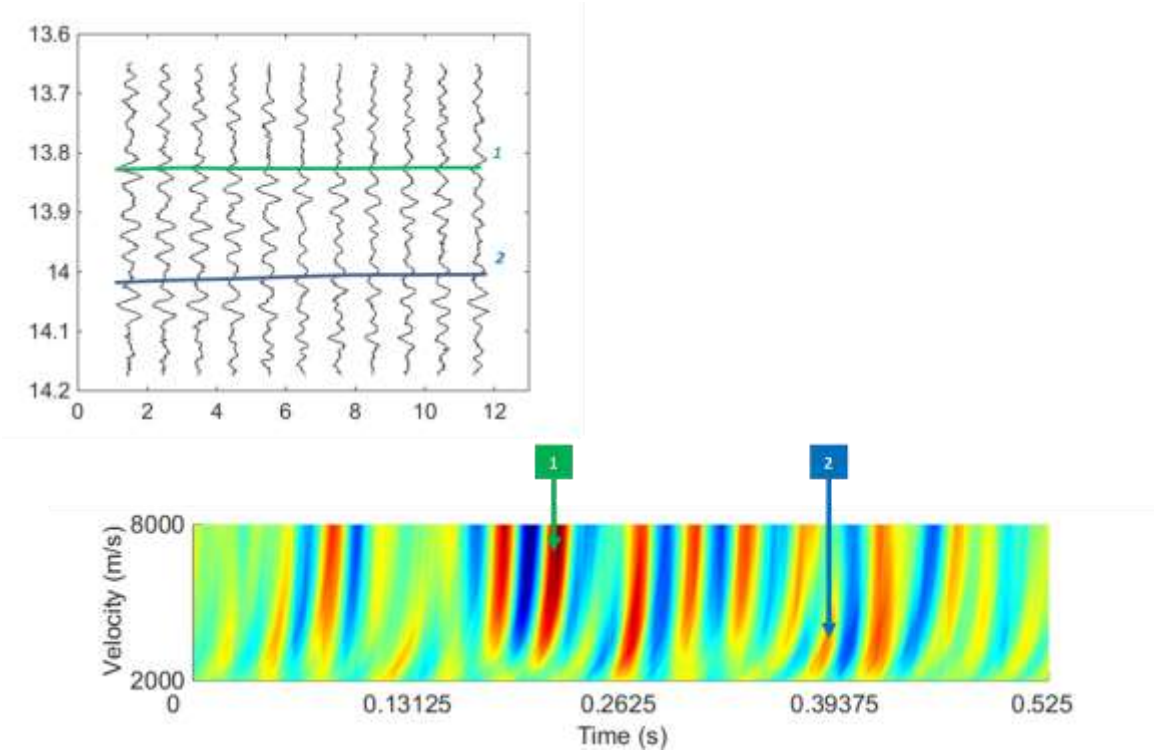

Figure 39: Gather (Z component) along with computed vespagram highlighting variation in velocities of individual arrivals.

We observed highest coherency across the vertical components (rotated for orientation) compared to the two transverse components for the LPLD events. We computed the velocity spectrum by stacking the amplitudes based on the expected arrivals along the geophone array for varying velocity values after setting the arrivals for deep offset traces as t_0. Figure 39 shows a 1.5 second section vespagram along one of the identified LPLD events. We can clearly observe significant changes in apparent velocities for the two arrivals that we identified. Thus the observed energy release during an LPLD event

could potentially be from a slowly shearing slippage along existing natural or hydraulic fractures due to fluid injection during fracturing. Moreover, the interbedded microseismic emissions could be associated with triggered events along associated fractures along the main shear plane or change in the shear plane through dislocated/ connected fracture systems.

Through visual inspection, we were able to isolate possible LPLD events by first locating potential long period energy bursts and then examining the dominant period from the filtered data around identified events. Table 1 highlights the number of identified events for various stages from Wootton Pad well 10H dataset.

Table 1: Stage wise LPLD event count

Stage No.	# LPLD	Stage No.	# LPLD	Stage No.	# LPLD
1	0	*7*	1	*13*	2
2	0	*8*	0	*14*	3
3	1	*9*	0	*15*	6
4	0	*10*	1	*16*	9
5	0	*11*	1	*17*	3
6	0	*12*	2	*18*	5

We do not observe significant LPLD events for the first 9 stages despite rigorous examination of the data gathers. This could be due to higher source-receiver separations leading to lower signal strength and higher noise. Moreover, for stages 10 through 13, we do not observe any LPLD events post injection. This could be a result of low energy release associated with slow shear failures hypothesized for LPLD events. Modeling of such failures could provide better understanding of the observations we make.

References

[1] B. Gutenberg and C. F. Richter, *Seismicity of the Earth and Associated Phenomena*, pp. 16-25, Princeton University Press, Princeton, New Jersey, (1949).

[2] D. Amitrano, Brittle-ductile transition and associated seismicity: experimental and numerical studies and relaitonship with the b-value. *J. Geophys. Res.,* **108(B1)**, 2044, (2003).

[3] M. Grob, & M. van der Baan, Statistical Analysis of Microseismic Event Locations and Magnitudes and their Geomechanical Implications. Calgary: CSEG, (2011).

[4] T. Urbancic, A Baig and S. Bowman, Utilizing b-values and Fractal Dimention for Characterizing Hydraulic Fracture Complexity. Calgary: CSPG/ CSEG/ CWLS GeoConvention, (2010).

[5] P. Grassberger and I. Procaccia, *Phys. Rev. Lett.*, **50**, 346, (1983).

[6] D. Schorlemmer, S. Weimer, and M. Wyss, Variations in earthquake-size distribution across different stress regimes, *Nature*, **437**, 539 – 542, (2005).

[7] T. K. Perkins and L. R. Kern, Widths of Hydraulic Fractures. *J. Petr. Tech*. **13**. 937-949, (1961).

[8] R. P. Nordgren, Propagation of a Vertical Hydraulic Fracture. *Soc. Petrol. Eng. J.* **253**. 306-314, (1972).

[9] K. G. Nolte and M. Smith, Interpretation of Fracturing Pressures. *J. Petr. Tech*. **33**. 1767-1775, (1981).

[10] E. Pirayesh, M. Y. Soliman and M. Rafiee, Make Decision on the Fly: A New Method to Interpret Pressure-Time Data during Fracturing – Application to FracPack, *SPE Annual Technical Conference and Exhibition.* (2013).

[11] M. Y. Soliman, M. Wigwe, A. Alzahabi and E. Pirayesh, Analysis of fracturing Pressure Data in Heterogeneous Shale Formations. *Hydraulic Fracturing Journal.* **1(2)**. 8-13, (2014).

[12] K. G. Nolte, Determination of Fracture Parameters from Fracturing Pressure Decline, *SPE Annual Technical Conference and Exhibition*. (1979).

[13] K. Aki, Maximum likelihood estimate of b in the formula log (N) = a − bM and its confidence limits, *Bull. Earthq. Res. Inst. Tokyo Univ*. **43**. 237-239, (1965).

[14] J. Farrell, S. Husen, and R. B. Smith, Earthquake swarm and b-value characterization of the Yellowstone volcano tectonic system. *J. Volcanol. Geoth. Res*. **188.** 260-276, (2009).

[15] C. H. Scholz, The frequency-magnitude relation of microfracturing in rock and its relation to earthquakes. *Bull. Seismol. Soc. Am.* **58**. 399-415, (1968).

[16] S. Wessels, M. Kratz and A. De La Pena, Identifying fault identification during hydraulic simulation in the Barnett shale: Source mechanism, b values, and energy release analyses of microseismicity, *81st SEG annual meeting expanded abstracts*, Volume **30**, pp. 1463-1467 (2011).

[17] S. Sil, B. Bankhead, C. Zhou and A. Sena, Analysis of B value from Barnett Shale Microseismic Data, *74th EAGE Conference & Exhibition.* (2012).

[18] M. Grob and M. van der Baan, Inferring in situ stress changes by statistical analysis of microseismic event characteristics. *The Leading Edge*. **30(11)**. 1296-1302, (2011).

[19] M. Grob and M. Van der Baan, Statistical analysis of microseismic event characteristics helps monitor in-situ stress changes, *21st Canadian Rock Mechanics Symposium*. (2012).

[20] T. Urbancic, A. Baig and S. Bowman, Utilizing b-values and Fractal Dimensions for Characterizing Fracture Complexity, *CSPG/ CSEG/ CWLS GeoConvention.* (2010).

[21] I. Das and M. D. Zoback, Long-period Long-duration seismic events during hydraulic stimulation of shale and tight-gas reservoirs – Part 1: Waveform Characteristics. *Geophysics*. **78(6)**. KS106 – KS118. (2013).

[22] A. St-Onge and D. W. Eaton, A long-period long-duration microseismic event: evidence of Cardium formation induced microseismicity? *GeoConvention*. (2014).

Appendix MA: Temporal b-value maps for all Wootton 10H stages

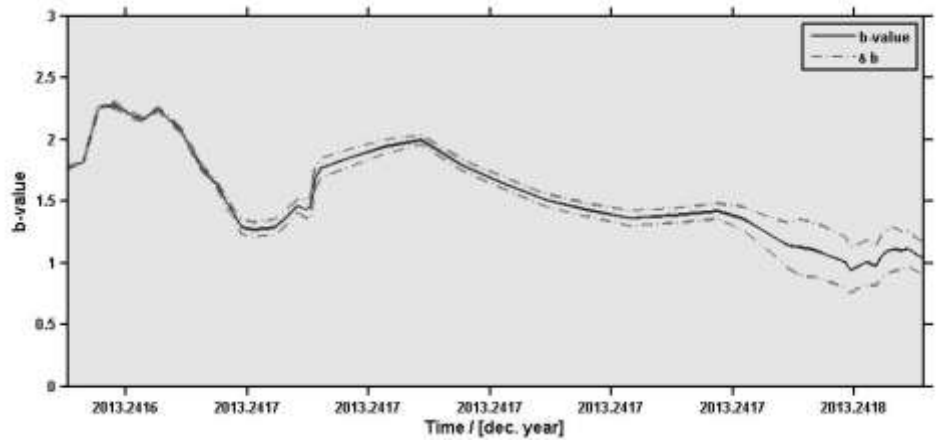

Figure 1: Stage 2 temporal b-value map

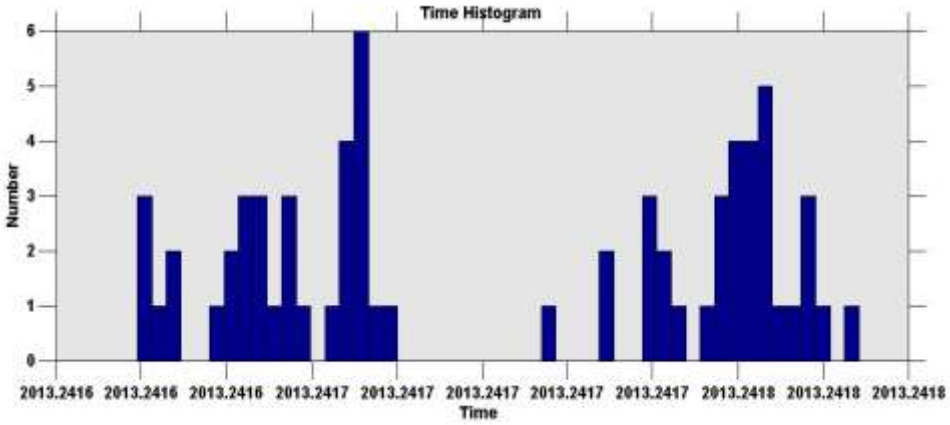

Figure 2: Stage 2 temporal event distribution map

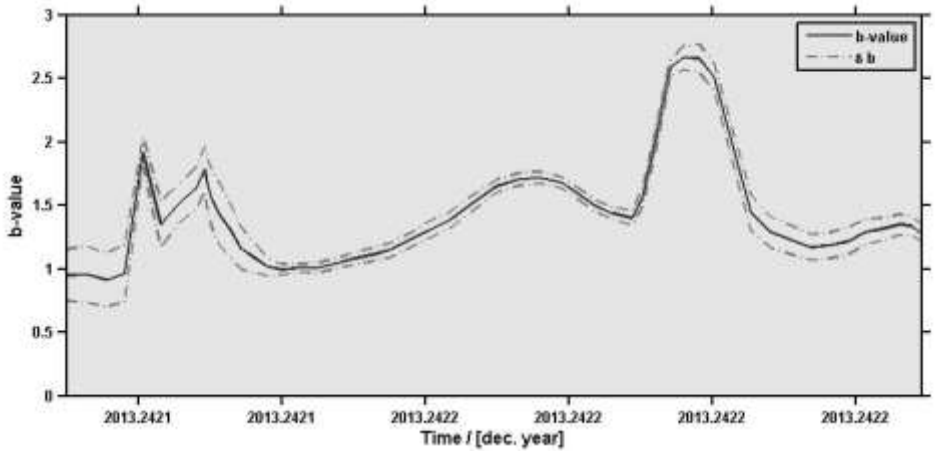

Figure 3: Stage 3 temporal b-value map

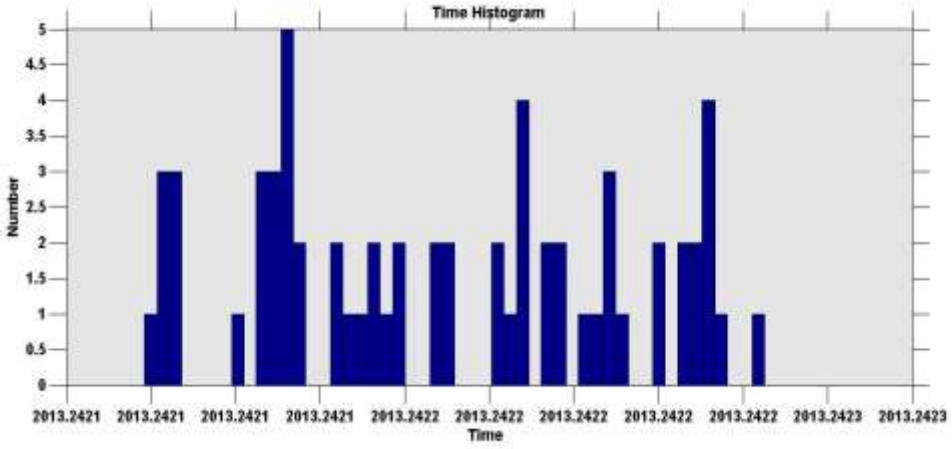

Figure 4: Stage 3 temporal event distribution map

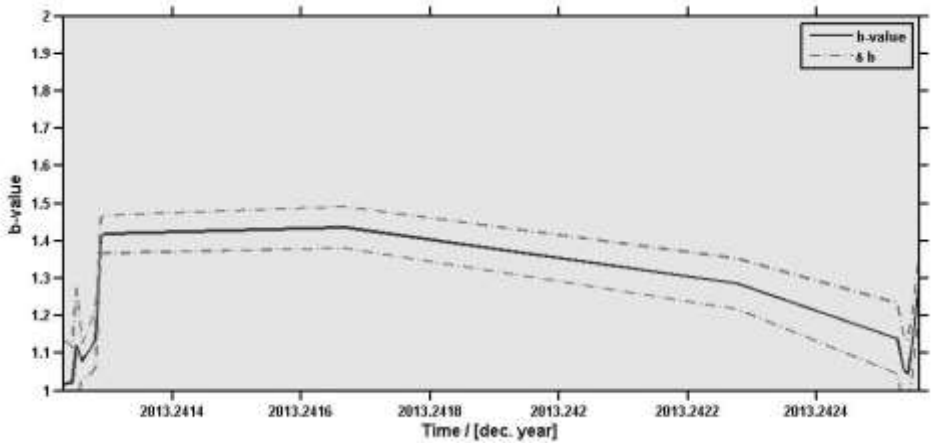

Figure 5: Stage 4 temporal b-value map

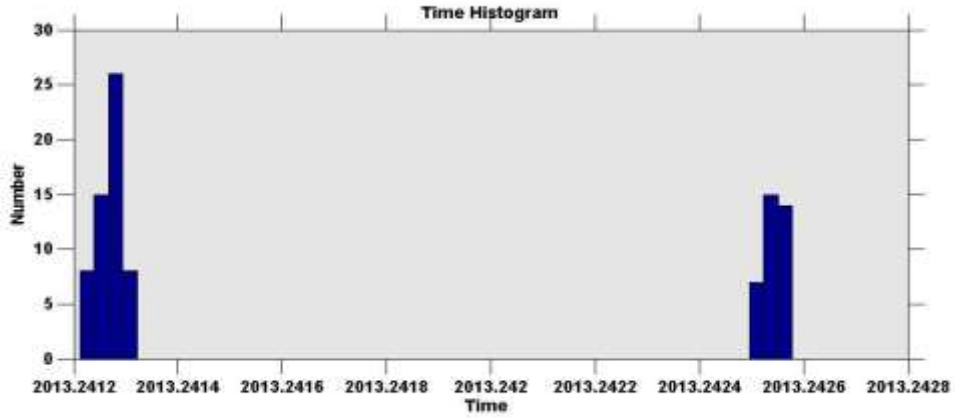

Figure 6: Stage 4 temporal event distribution map. Due to irregular distribution, b-value analysis has to be limited to certain time windows which correspond with relatively high event distribution.

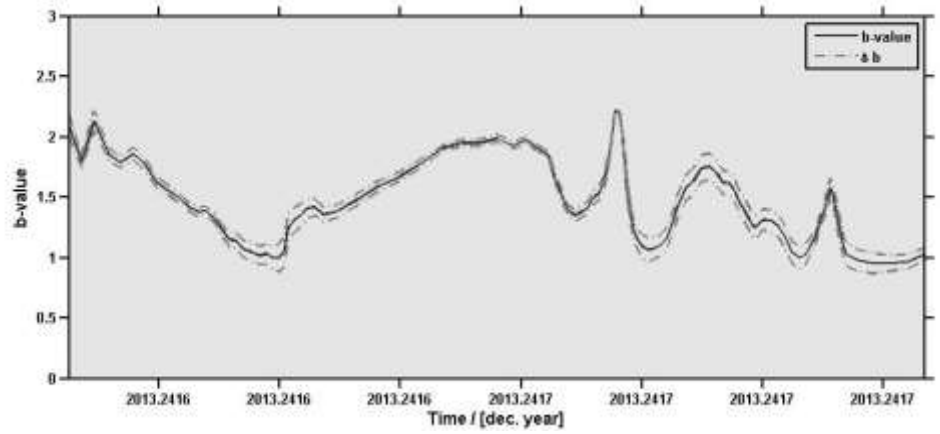

Figure 7: Stage 5 temporal b-value map

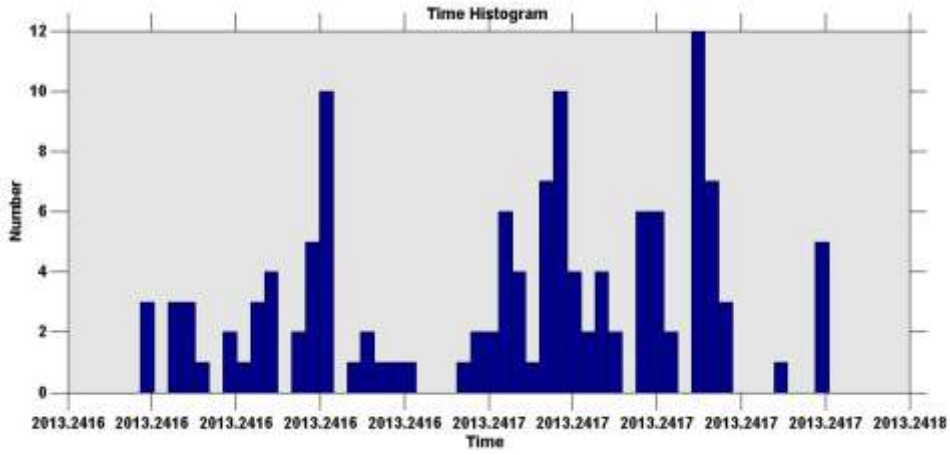

Figure 8: Stage 5 temporal event distribution map

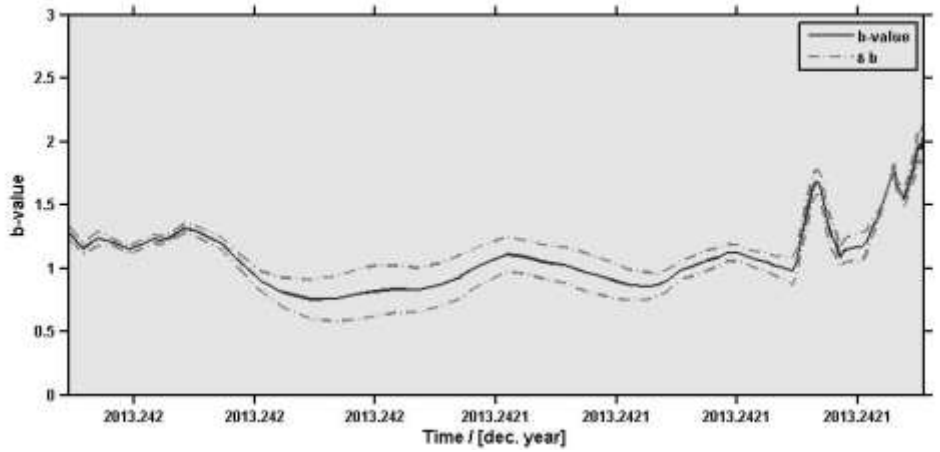

Figure 9: Stage 6 temporal b-value map

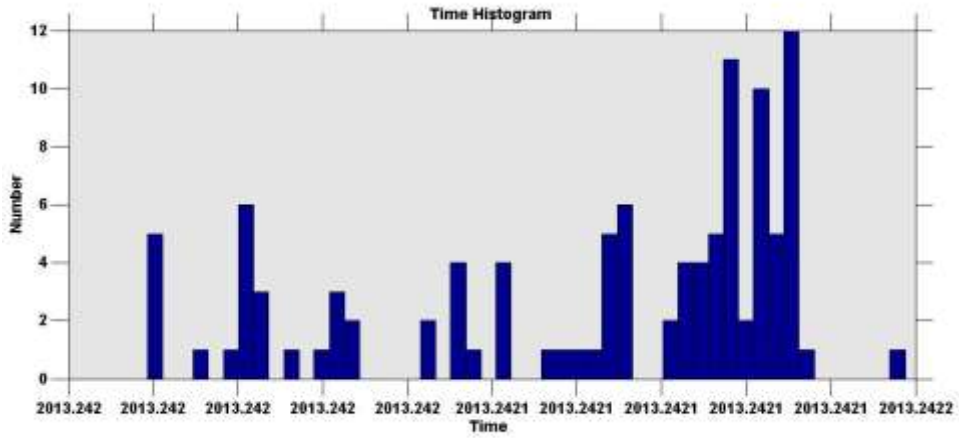

Figure 10: Stage 6 temporal event distribution map

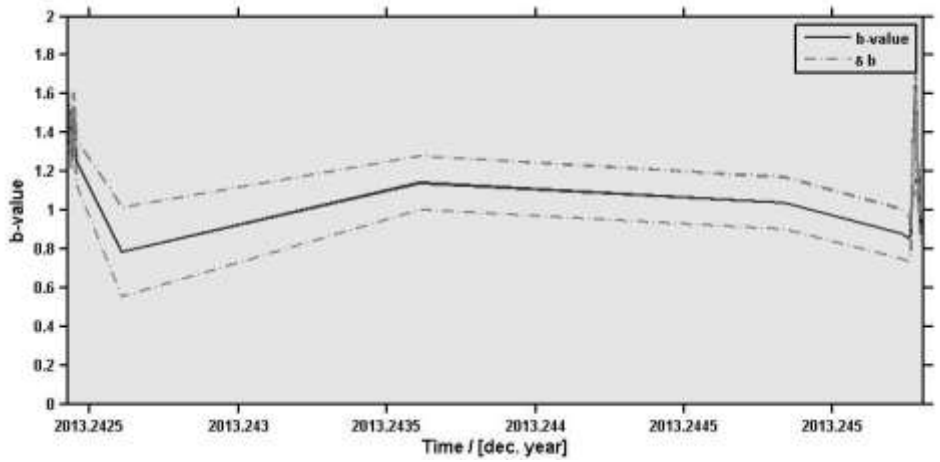

Figure 11: Stage 7 temporal b-value map

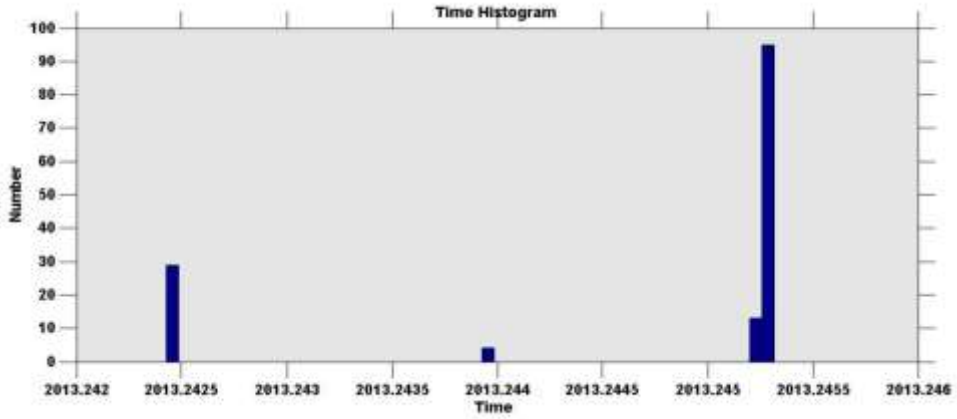

Figure 12: Stage 7 temporal event distribution map. Due to irregular distribution, b-value analysis has to be limited to certain time windows which correspond with relatively high event distribution.

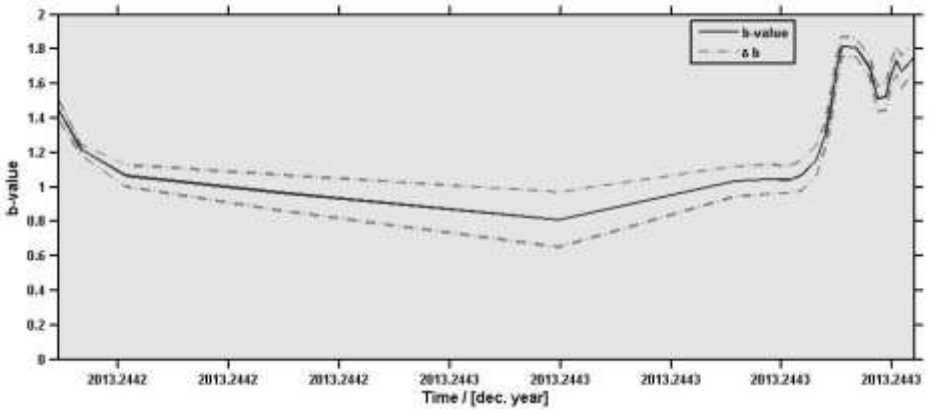

Figure 13: Stage 8 temporal b-value map

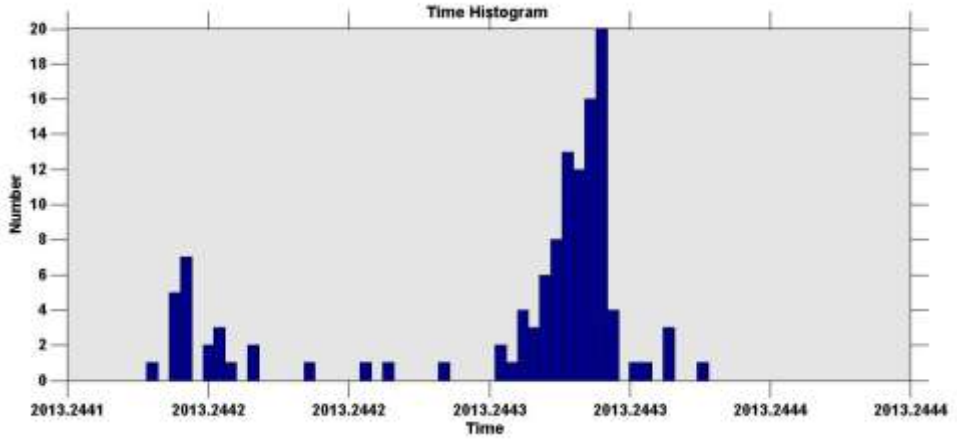

Figure 14: Stage 8 temporal event distribution map

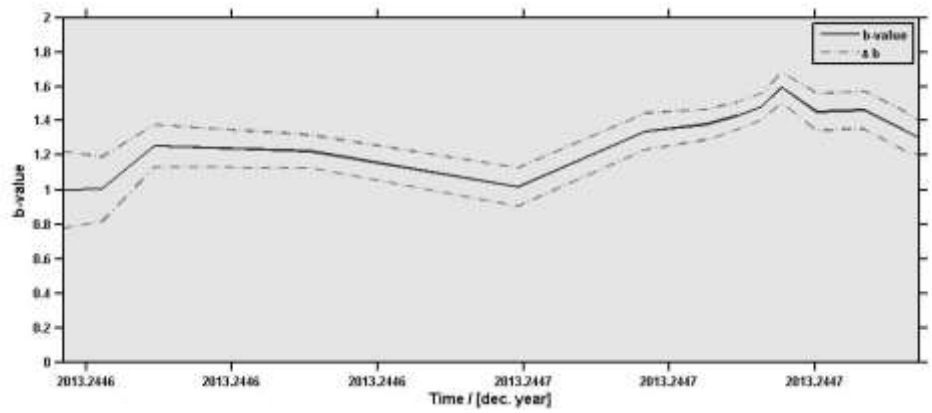

Figure 15: Stage 9 temporal b-value map

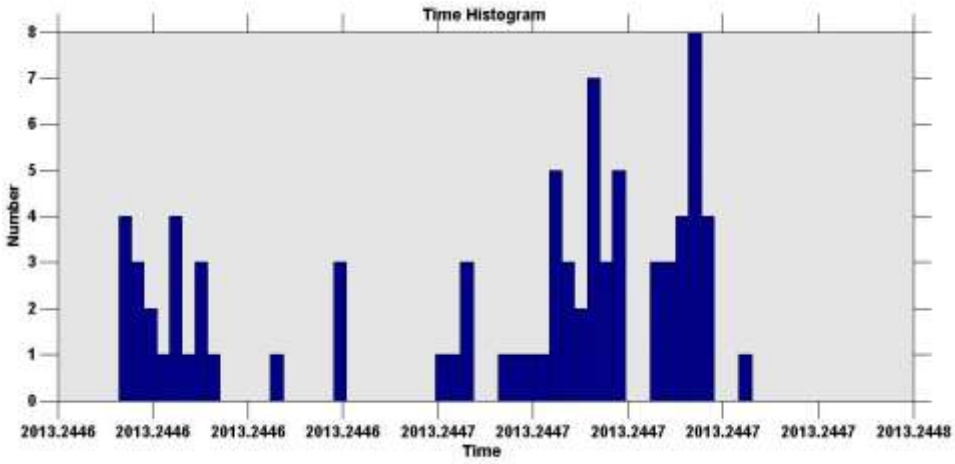

Figure 16: Stage 9 temporal event distribution map

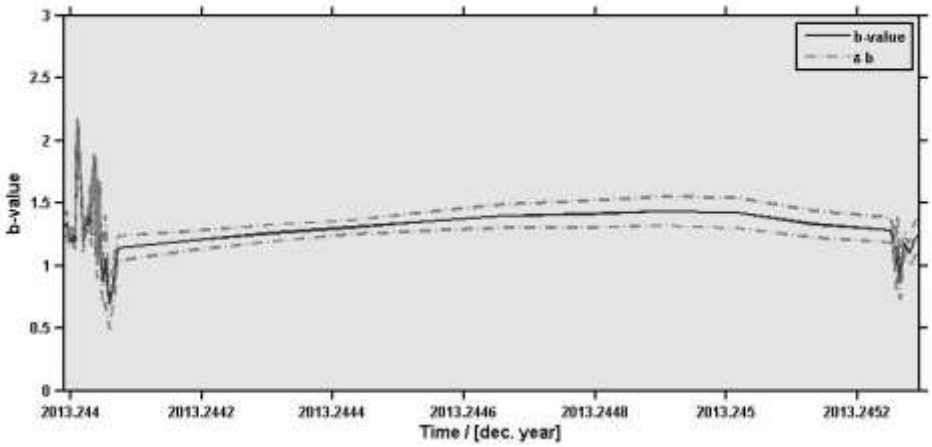

Figure 17: Stage 10 temporal b-value map

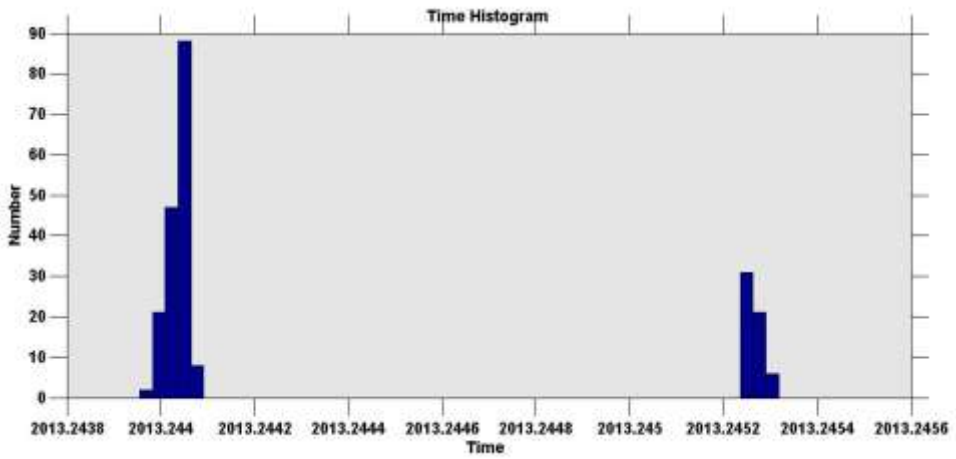

Figure 18: Stage 10 temporal event distribution map. Due to irregular distribution, b-value analysis has to be limited to certain time windows which correspond with relatively high event distribution.

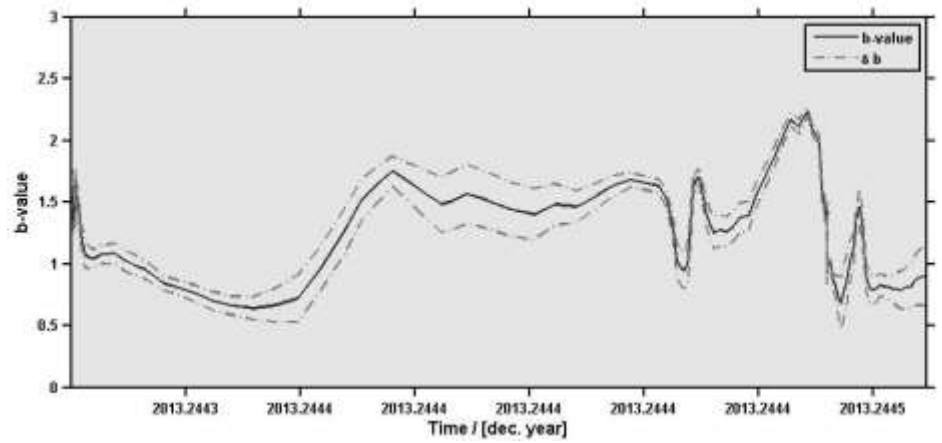

Figure 19: Stage 11 temporal b-value map

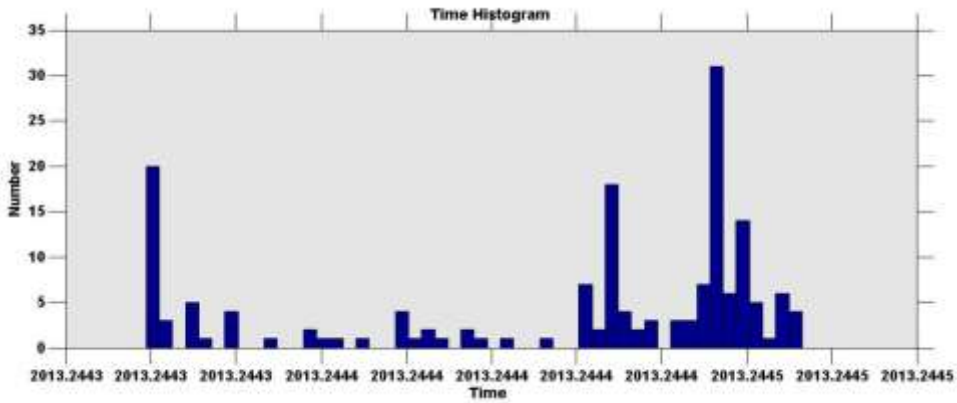

Figure 20: Stage 11 temporal event distribution map

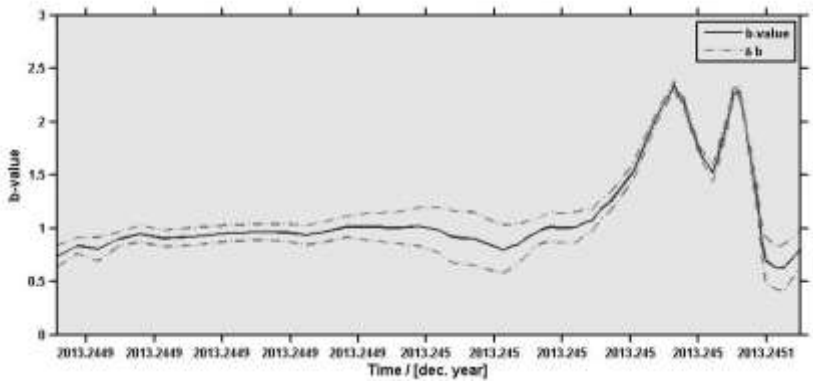

Figure 21: Stage 12 temporal b-value map

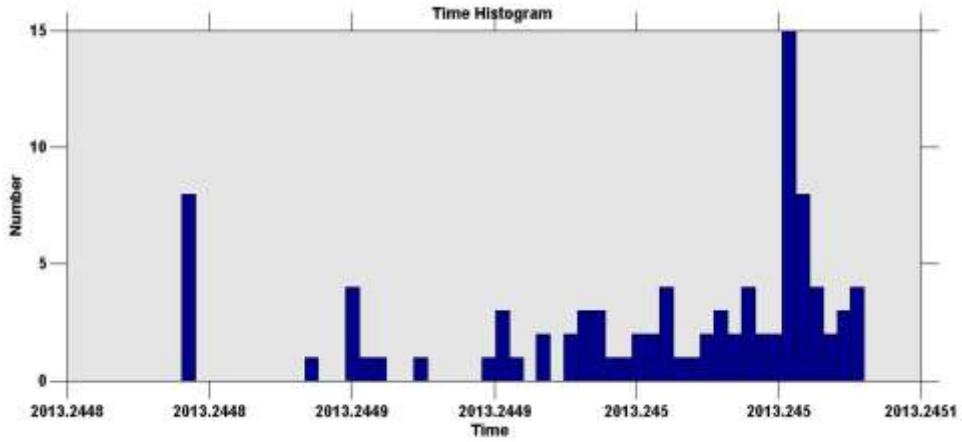

Figure 22: Stage 12 temporal event distribution map

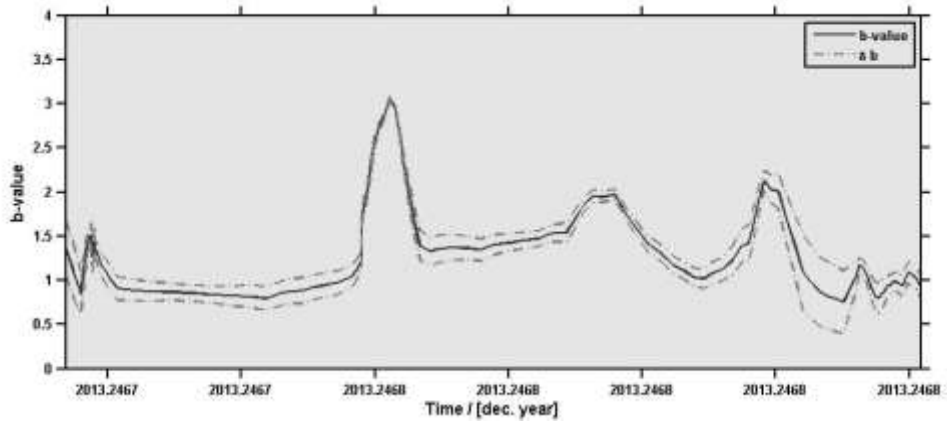

Figure 23: Stage 13 temporal b-value map

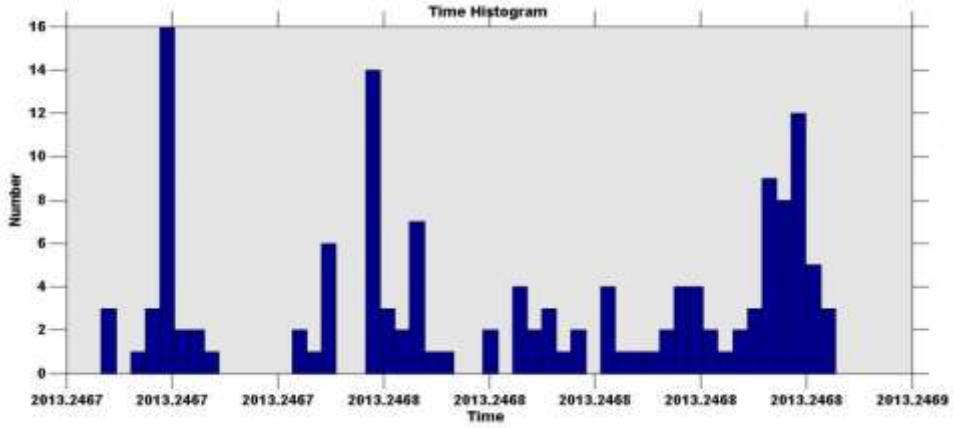

Figure 24: Stage 13 temporal event distribution map

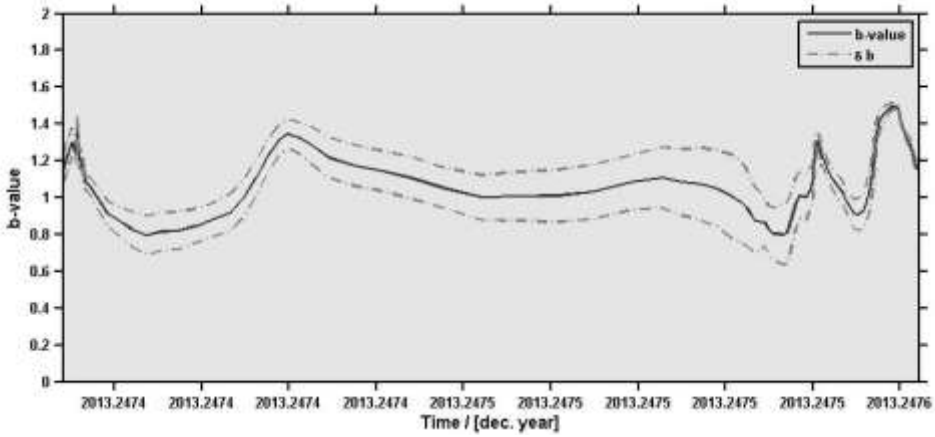

Figure 25: Stage 14 temporal b-value map

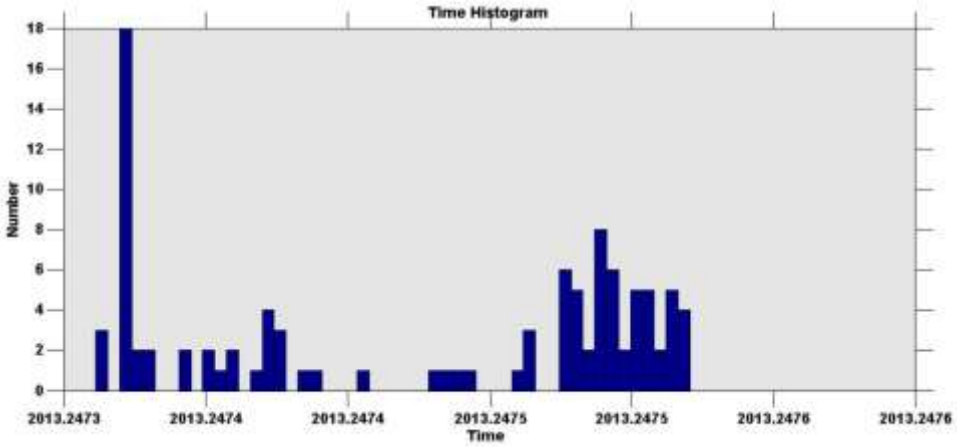

Figure 26: Stage 14 temporal event distribution map

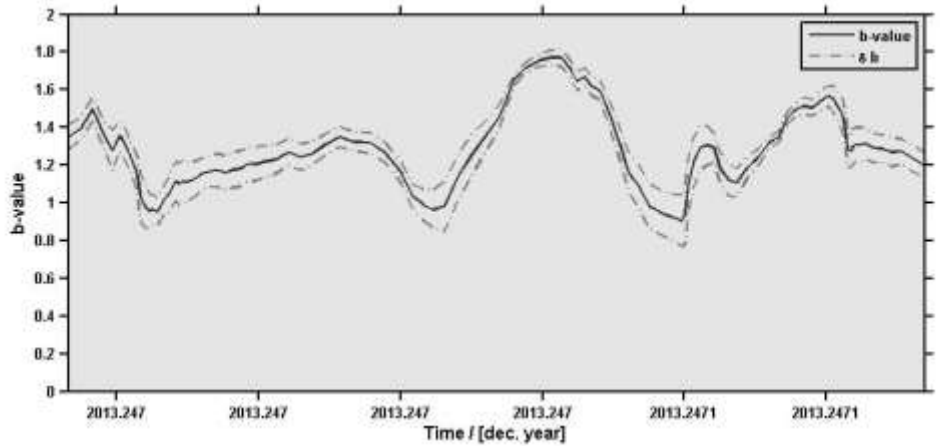

Figure 27: Stage 15 temporal b-value map

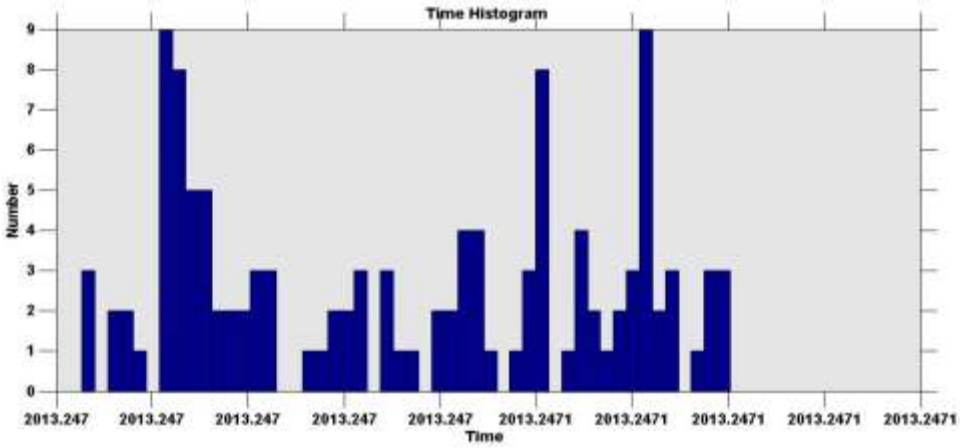

Figure 28: Stage 15 temporal event distribution map

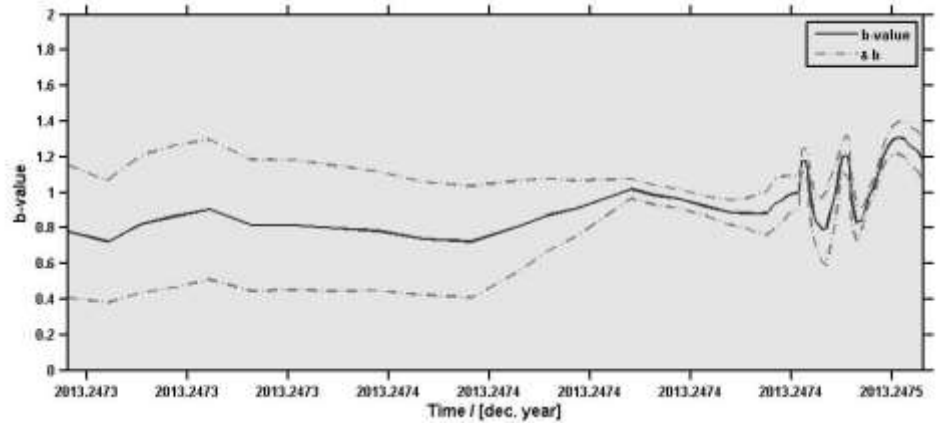

Figure 29: Stage 16 temporal b-value map

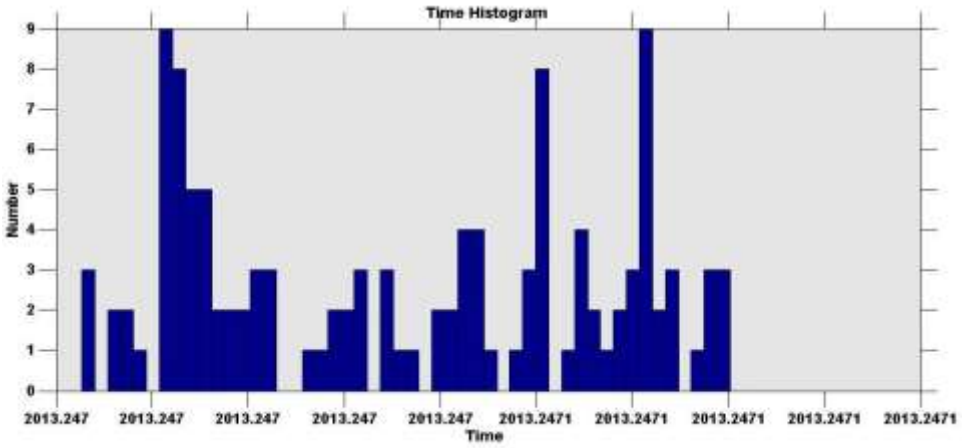

Figure 30: Stage 16 temporal event distribution map

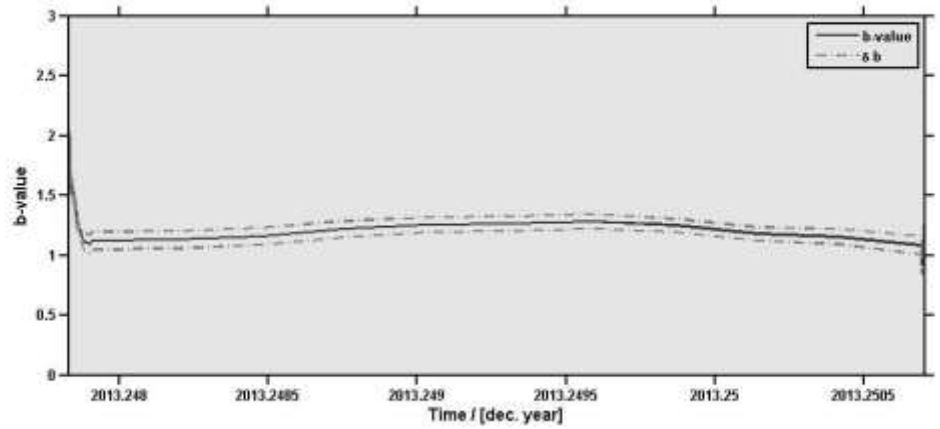

Figure 31: Stage 17 temporal b-value map

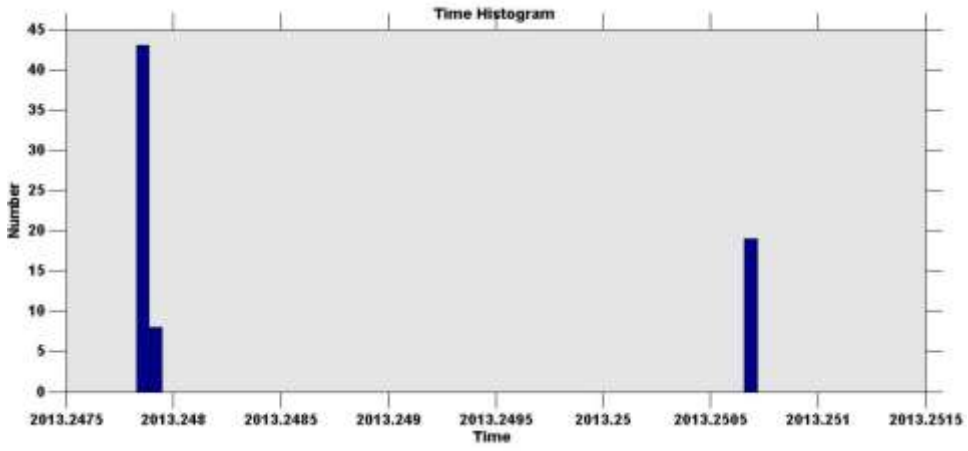

Figure 32: Stage 17 temporal event distribution map. Due to irregular distribution, b-value analysis has to be limited to certain time windows which correspond with relatively high event distribution.